Quaternary geometry, kinematics and paleoearthquake history at the intersection of the strike-slip North Island Fault System and Taupo Rift, New Zealand

Vasiliki Mouslopoulou

A thesis
Submitted to the Victoria University of Wellington
in fulfillment of the requirements for the degree of
Doctor of Philosophy
in Geology

Victoria University of Wellington
2006

Foreword

the red of the sunset at Ohope

the smile of the locals at Waimana

the ancient whisper of the creek at Wharepora

the mercurial silhouette of the peka-peka at Tawhiwhi

the tip of the flame dancing under the raindrops at Mangatoatoa

the quicksilver of the moonlight caressing the waves and your eyes at

O t a r a w a i r e r e

the call of the morepork hollowing through the silent night at Whirinaki

the steaming horse galloping on the overgrown track at Ruatahuna

the teardrop of the fern a misty morning at Takaroa

the upstream flight of the Whio at Waikare

the dance with the Whakatane River

the echo of our dreams

…is the ultimate pay back of this land for missing the eyes of my Parents

and the Blue of the Aegean Θάλασσα all these years.

This thesis is dedicated to Andy Nicol,

Who taught me that

The wider our view of the World is

The deeper the insight into our self grows …

ABSTRACT

The North Island of New Zealand sits astride the Hikurangi margin along which the oceanic Pacific Plate is being obliquely subducted beneath the continental Australian Plate. The North Island Fault System[1] (NIFS), in the North Island of New Zealand, is the principal active strike-slip fault system in the overriding Australian Plate accommodating up to 30% of the margin parallel plate motion. This study focuses on the northern termination of the NIFS, near its intersection with the active Taupo Rift, and comprises three complementary components of research: 1) the investigation of the late Quaternary (c. 30 kyr) geometries and kinematics of the northern NIFS as derived from displaced geomorphic landforms and outcrop geology, 2) examination of the spatial and temporal distribution of paleoearthquakes in the NIFS over the last 18 kyr, as derived by fault-trenching and displaced landforms, and consideration of how these distributions may have produced the documented late Quaternary (c. 30 kyr) kinematics of the northern NIFS, and 3) Investigation of the temporal stability of the late Quaternary (c. 30 kyr) geometries and kinematics throughout the Quaternary (1-2 Ma), derived from gravity, seismic-reflection, drillhole, topographic and outcrop data.

The late Quaternary (c. 30 kyr) kinematics of the northern NIFS transition northward along strike, from strike-slip to oblique-normal faulting, adjacent to the rift. With increasing proximity to the Taupo Rift the slip vector pitch on each of the faults in the NIFS steepens gradually by up to 60°, while the mean fault-dip decreases from 90° to 60°W. Adjustments in the kinematics of the NIFS reflect the gradual accommodation of the NW-SE extension that is distributed outside the main physiographic boundary of the Taupo Rift. Sub-parallelism of slip vectors in the NIFS with the line of intersection between the two synchronous fault systems reduces potential space problems and facilitates the development of a kinematically coherent fault intersection, which allows the strike-slip component of slip to be transferred into the rift.

[1] The NIFS is equivalent to the North Island Shear Belt (NISB) or North Island Dextral Fault Belt (NIDFB) (Beanland, 1995) and here we focus specifically on the western strand which includes the Wellington-Mohaka-Ruahine-Waiohau-Whakatane-Waimana-Waiotahi and Waioeka faults.

Transfer of displacement from the NIFS into the rift accounts for a significant amount of the northeastward increase of extension along the rift. Steepening of the pitch of slip vectors towards the northern termination of the NIFS allows the kinematics and geometry of faulting to change efficiently, from strike-slip to normal faulting, providing an alternative mechanism to vertical axis rotations for terminating large strike-slip faults. Analyses of kinematic constraints from worldwide examples of synchronous strike-slip and normal faults that intersect to form two or three plate configurations, within either oceanic or continental crust, suggest that displacement is often transferred between the two fault systems in a similar manner to that documented at the NIFS - Taupo Rift fault intersection.

The late Quaternary (c. 30 kyr) change in the kinematics of the NIFS along strike, from dominantly strike-slip to oblique-normal faulting, arises due to a combination of rupture arrest during individual earthquakes and variations in the orientation of the coseismic slip vectors. At least 80 % of all surface rupturing earthquakes appear to have terminated within the kinematic transition zone from strike-slip to oblique-normal slip. Fault segmentation reduces the magnitudes of large surface rupturing earthquakes in the northern NIFS from 7.4-7.6 to c. 7.0.

Interdependence of throw rates between the NIFS and Taupo Rift suggests that the intersection of the two fault systems has functioned coherently for much of the last 0.6-1.5 Myr. Oblique-normal slip faults in the NIFS and the Edgecumbe Fault in the rift accommodated higher throw rates since 300 kyr than during the last 0.6-1.5 Myr. Acceleration of these throw rates may have occurred in response to eastward migration of rifting, increasing both the rates of faulting and the pitch of slip vectors. The late Quaternary (e.g. 30 kyr) kinematics, and perhaps also the stability, of the intersection zone has been geologically short lived and applied for the last c. 300 kyr.

Acknowledgements

The years of my PhD will never finish.

For each of you, the ***People*** I have encountered on this land, and the ***Land*** itself, have spilled few eternal drops of ***Beauty*** and ***Pain*** in the *Thalassa* of my essence. And when Beauty (she) encounters Pain (him), the wrestle is so ardent, that what is merely left is Poetry. And is the Poetry that invited corals and anemones to grow on my seafloor. That created currents to whirl within my body and even, an island to emerge through my waves. How I hope that one day my *Poseidon* will come and settle on this island!

I am able to write these words today, not because anyone ever invited me here but simply because I always knew that the unexplored life is not worth living. For when you do explore *her*, almost certainly, *she* is going to reward you with:

K n o w l e d g e

Andy (Nicol) and ***Tim*** (Little), in your faces collectively, I have found the **best** guidance. For your individual characteristics perfectly complemented each other's virtues, leaving me with a complete spectrum of colours on my rainbow. For you stood by my side and believed in me during the very first days of uncertainty. For you inspired me to such an extent that the beauty of *tectonic faults* captured my heart. For you offered me the best of yourselves throughout, transforming me into a scientist who can now understand better, think deeper, assess critically, write effectively and persist through hardship. Andy, your name is equivalent to endless inspiration and balance for me. The challenge now is to continue without you. Tim, I already feel the *Pain* turning into *Skill*. Thank you for trusting me your 'poetic' face as well.

Friendship

John *(Begg)*, deep into Te Urewera forest, where everything is filtered by Beauty, I found a life's *Taonga* that was made of water, fire and rock. It was your elemental *Wairua*. Ever since, your unconditional devotion has stamped both my thesis and my *Psyche*. To all those moments of *Wonder* that we shared and which now have turn into lyrics; to all those river crossings that you led me holding firmly my hand; and to the one that was left uncrossed. Where does Music go after it has existed? Where does the Light of Te Whetu go after dawn has come?

Biljana & Zoran *(Lukovic)*, inside your hearts you are carrying all the pride, culture, warmth and knowledge of an historic country that does not exist anymore, *Yugoslavia*. Your little '*Balkan*' corner here is like the fire on the snow. Like the homeland within an, often, incomprehensible culture. Biljana, in your beautiful face I have found a trusted friend; a model of a dedicated mother, loving wife and a gifted woman who knows how to walk in this life. And dance!

Dave *(Heron)* you were, perhaps, the most *stable* presence throughout this journey. Your friendship was a garden with lots of beautiful native trees, fresh water creeks and an unlocked hut that I could shelter anytime. That is why all these years with you were full of *moments*, not just minutes… To the moments yet to come, to the dances yet to be danced…

Dick *(Beetham)*, you gave me your hand in times of uncertainty. You trusted and supported me by all means, as a friend, 'father' and scientist. You were the first to introduce me to Te Urewera! You became my link to Ohope, Betty & Douglas, and EBoP. Wish one day I can give you back some of what you've offered me.

Betty & Douglas *(Beetham)*, you are my 'New Zealand grandparents'. Ohope now, thanks to you, has turn into a symbol in my mind. The love & the sea I found by your side gave me strength during fieldwork and helped me complete this thesis. May the gentle ocean breeze keep you healthy and content for the years to come.

Sameer (*Vayalam*), you were always there each time I needed a break. Thank you.

Djees *(Markovic*), my friend the Wind…

Rafael (Benites), walking and discussing, discussing and walking; about everything; without being constrained by anything. Uniquely.

Shona (de Sain), ***Tim & KC*** (Little), thank you for your support and friendship.

Wisdom

Tuhoe *(tangata whenua)*, your support was "*Me uru kahikatea*- like a grove of kahikatea".

(Kahikatea, is the tallest growing of the NZ native trees and its preferred growing habitat is swampy ground that is very unstable. This, and the height that it grows, made it especially vulnerable to the natural elements such as stormy winds. So to counter that, kahikatea grew in groves whereby the roots of all the trees intertwined and in so doing, gave each individual tree strong additional support, but underground and therefore not seen by the above ground observers. Hence, the support given was strong but discreetly unobtrusive. Tuhoe teach us to provide strong support to each other but without making it so obvious).

'Kei toku whatumanawa koutou katoae tau ana. No reira, Ngai ***Tuhoe****, tena koutou, tena koutou, tena koutou katoa.'*
'You have landed in my emotional heart -whatumanawa- and there you will always stay. To all Tuhoe people, greetings, greetings, greetings to you all.'

Waaka *(Vercoe),* you introduced me to the poetic world of Maori. You showed me how similar geographically distant cultures can be. Your Matangi Mariri (gentle breeze) is always going to stay with me, reminding me of your beautiful mind.

Noti *(Teepa) and* ***Te Kiatou Sonny*** *(Biddle),* your knowledge of the trees, the birds, the land and the people is the foundation that each of us should have and on which, the rest of our life should be based.

Sokratis (Tolias) you encouraged me to fly from Greece to New Zealand with my own wings. You were certain of the result. Wish you were here today to see it. But instead, you went yourself to explore the *Skies*. Before time….

Eirini **&** ***Nikos*** *Mouslopoulos* (Mama & Mpampas), this journey wouldn't have started, let alone been completed, if you hadn't turn the pain that my absence caused into *love* and *spirit*, that quietly supported and protected me every single day. My gratitude is due to my extended family as well.

G e n e r o s i t y

Land access permission: Tuawhenua Trust Board, Western Executive Tuhoe Trust Board, Sonny & Amelia Biddle, Noti Teepa, Richard Temara, Aubrey Temara, Timoti Purewa, Frank Vercoe, Don & Paul Atkinson, Puna Melbourne, Rongokarae Marae in Ruatoki North, Liz & Richard (and kids) Apanui, Rahiri Marae in Waimana, Bob Weil and Uwhiarae Marae in Ruatahuna. Troy Apatu from Ruatoria is thanked for his big heart.

Field assistance: Hannu Seebeck, Dick Beetham and John Begg are sincerely thanked for they repeatedly dedicated resources and time to facilitate my fieldwork throughout this study. The field assistance of Peho Tamiana, Rob Langridge, Kelvin Berryman, Glenn Hughes, Suz Toulmin, Graham Duncan, Pilar Villamor, Kate Wilson, Noti Teepa, Biljana Lukovic and Dave Heron is deeply appreciated.

Technical assistance: Ian Nairn (tephra identification – thank you for your numerous visits in my trenches), John Patterson (glass chemistry analyses – thank you for your friendship as well), Vaughan Stagpoole and Derek Woodward (process of the gravity data), Stewart Bush (production of glass-slides).

Scientific discussions: John Begg, John Walsh, Kelvin Berryman, Rafael Benites, Paul Froggatt, Nicola Litchfield, Rob Langridge, Russell Robinson, Phil Shane. Julie Rowland, John Townend and Lisa McNeill are thanked for their thorough reviews that improved this thesis.

Financial support: This study wouldn't have been completed within this timeline without the support of the: *Earthquake Commission of New Zealand*, *Foundation of Research Science and Technology* and *GNS Science (2-year Bright Future – Enterprise Scholarship)*, *Victoria University of Wellington (PhD completion Scholarship). Environment Bay of Plenty (EBoP)* generously supported most of my fault-trench excavations. Special thanks to Russ Martin (EBoP). My gratitude is also due to Mark Rattenbury for offering me the Q-map award and Steve Everitt for supporting my FRST Enterprise Scholarship application.

CONTENTS

CHAPTER FIVE: PALEOEARTHQUAKE SURFACE RUPTURE IN A TRANSITION ZONE FROM STRIKE-SLIP TO OBLIQUE-NORMAL SLIP, NORTH ISLAND FAULT SYSTEM, NEW ZEALAND

CHAPTER SIX: QUATERNARY TEMPORAL STABILITY OF A STRIKE-SLIP AND NORMAL FAULT INTERSECTION, NORTH ISLAND, NEW ZEALAND

LIST OF FIGURES

LIST OF TABLES

CHAPTER ONE

INTRODUCTION

1.1 The Fabric

The interaction of *two* synchronously active auras within me, led ultimately to the creation of this thesis (the *fabric*). The *scientific inspiration* (the *warp*) derived from a strike-slip and normal fault intersection in North Aegean, Greece, while my *ethereal Muse* (the *weft*) appeared in Bay of Plenty, Aotearoa[1], where an analogous fault intersection occurs (Fig. 1.1). This Ph.D. thesis aims to explore the interaction between synchronously active strike-slip and normal faults in the upper crust, during earthquake and geological timescales. It also aims to better understand the natural World *(the people and the land)* within which this work was carried out, and, of which, we are all children. The *fabric*, the journey, is one. It is only the colour of the thread that changes, in this coherently interwoven cloth…

The name of *Bay of Plenty* is indicative of its character. Long ago, *plenty* of trees resided on this land to turn the stony hills into a green grove populated by native birds. Through time, *plenty* of earthquakes shook this forested land to incise long deep valleys. *Plenty* of rain filled these valleys with waters to create powerful rivers. *Plenty* of spirits inhabited these rivers, calling the Tuhoe into Te Urewera country. The mystical beauty of this ***plenty*** invited the author's heart to explore this small piece of land on our World….

[1] New Zealand.

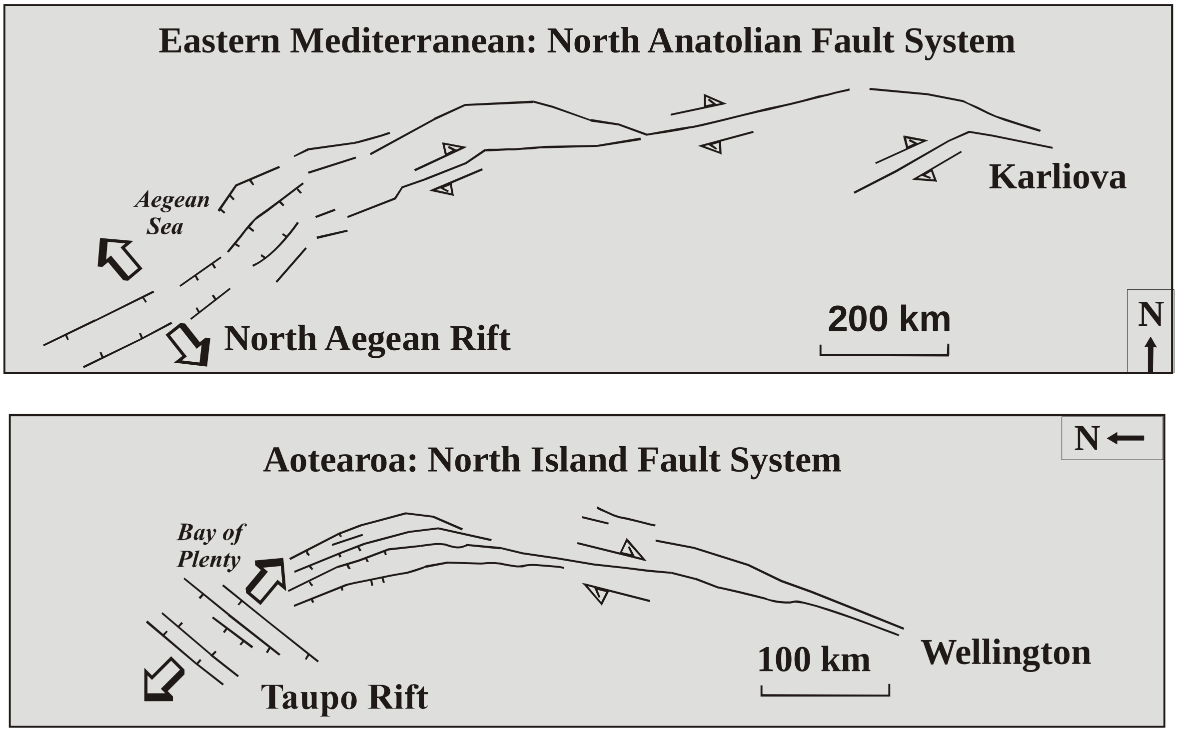

Fig. 1.1 The *warp* (upper) and the *weft* (lower) of the fabric.

1.2 Scientific aim and objectives of this study

Fault interactions are an essential feature of all fault systems and are generally accommodated either by hard-linkage, in which faults physically link, or by soft-linkage, in which displacement is transferred by distributed (i.e. ductile) deformation of the rock volume between faults. Fault interaction is associated with the transfer of slip between structures and in some cases can continue for prolonged periods to produce kinematic coherence within a fault system (Dahlstrom, 1969; Walsh and Watterson, 1991)[2].

Fault interaction and displacement transfer must also occur where different types of synchronous fault systems intersect. Such intersections display a wide variety of fault geometries and kinematics. The angle of intersection between the strike of the component fault systems may, for example, vary between 0-90° and, as a consequence, the intersecting faults can define either a two- or three-‘plate’ kinematic system (McKenzie & Morgan, 1969). Although intersecting active strike-

[2] See individual chapters for citation of references.

slip and extensional fault systems are found globally, on both oceanic and continental crust, the kinematics by which they interact is often poorly understood. The principal purpose of this thesis is to shed light on the deformational processes that can accommodate fault-slip across the intersection between two mutually active strike-slip and normal fault systems. I principally study an active fault intersection in New Zealand where the strike-slip North Island Fault System (NIFS)[3] intersects and terminates against the Taupo Rift[4] (Fig. 1.2). Insights into the geometry and kinematics of the intersection zone are afforded by new data from a previously poorly known part of the NIFS and by compilation of existing information from the adjacent Taupo Rift.

In order to achieve the primary aims of this thesis, I address the following six research objectives:

1) examine the along strike variations in the late Quaternary (c. <30 kyr) geometry and kinematics (e.g., slip vectors and displacement rates) of the NIFS with increasing proximity to its termination against the active Taupo Rift;

2) explore how the intersection between the NIFS and Taupo Rift operates kinematically;

3) provide insight into the larger question of how other strike-slip and normal fault intersections globally, with different kinematic relationships, intersection geometries and/or type of crust (i.e. oceanic or continental) operate;

4) chart the rupture lengths, magnitudes and recurrence intervals of paleoearthquakes within the northern NIFS;

5) address how the late-Quaternary change in the kinematics of the northern NIFS is achieved by the accumulation of incremental slip during individual earthquakes or earthquake cycles;

6) explore the longevity of the geometry and kinematics of the intersection zone between the NIFS and the Taupo Rift during the Quaternary.

[3] In the past this fault system has been referred to as the *North Island Dextral Fault Belt (NIDFB)* (Beanland, 1995). Here, *'belt'* has been replaced by *'system'* to more accurately reflect the presence of an array of subparallel faults and *'dextral'* is omitted due to the significant amount of normal or reverse slip along some sections of the fault.

[4] The term *'Taupo Rift'* was first introduced by Villamor & Berryman (2006) and is equivalent to the *'Ruaumoko Rift'* (Rowland & Sibson, 2001).

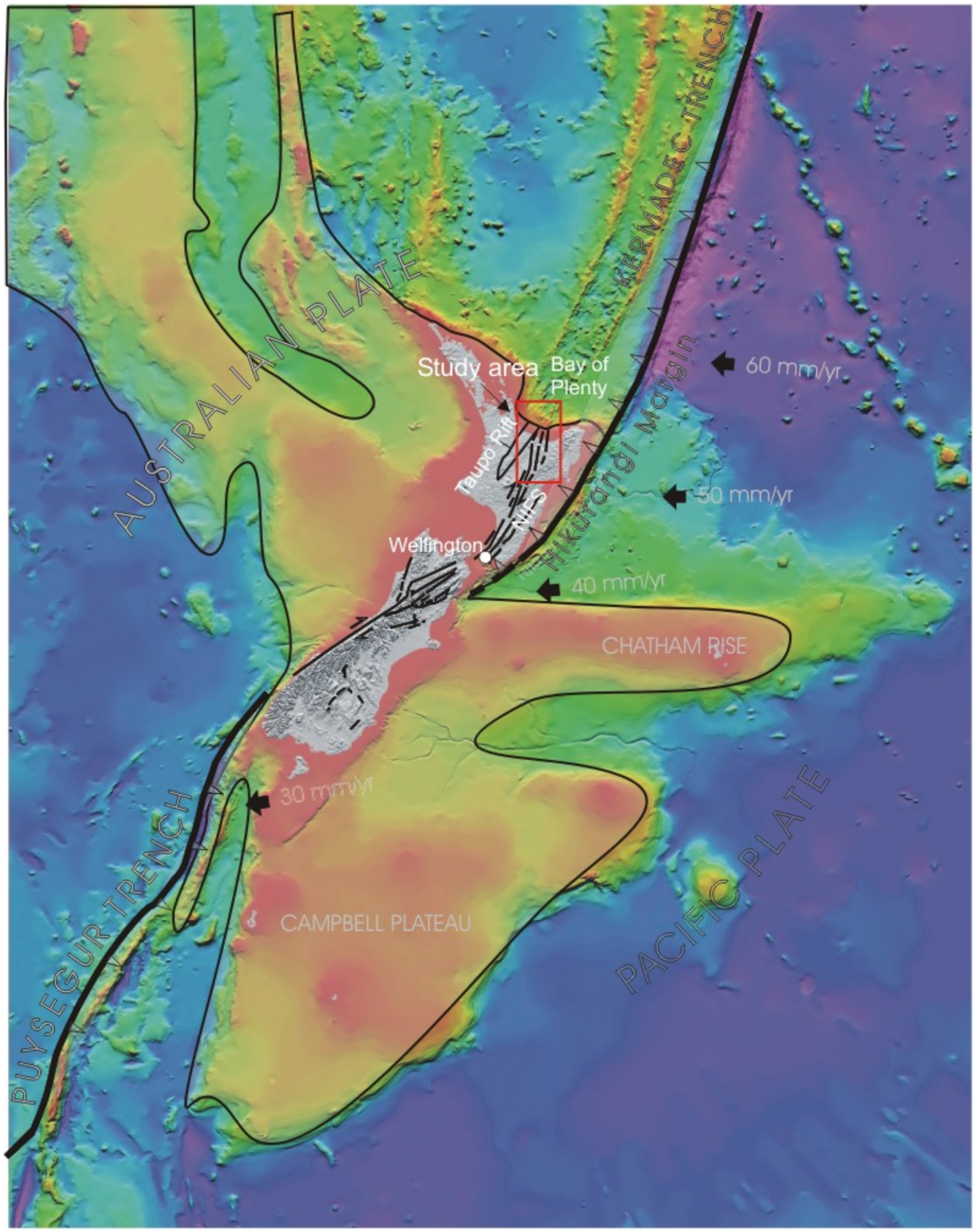

Fig. 1.2 Major structural elements of the present day Australian – Pacific plate boundary in New Zealand. The study area is indicated. Black outline represents the margin of the continental crust. Map after NIWA.

1.3 Geological background

The North Island in New Zealand straddles the active boundary along which the oceanic Pacific Plate is being obliquely subducted beneath the continental Australian Plate (Fig. 1.2). The active strike-slip NIFS and the extensional Taupo Rift are the longest and highest slip rate active fault systems in the upper plate of the Hikurangi margin. The NIFS comprises two main strands, the eastern and the western strand (Beanland, 1995) (Fig. 1.2). This thesis focuses on the northern termination of the western strand and hereafter refers to this strand as the NIFS. The NIFS is at least 500 km long and extends from Wellington to the Bay of Plenty. In the southern North Island the NIFS accommodates c. 10 mm/yr strike-slip and accounts for up to 30% of the margin-parallel relative plate motion (Beanland, 1995). In the Bay of Plenty, at the northern end of the NIFS, the late Quaternary rate of strike-slip is only about 4 mm/yr (this study). This is significantly less than the c. 10-15 mm/yr rate of NW-SE horizontal extension across the nearby northern Taupo Rift (Wallace et al., 2004). At its northern termination the NIFS intersects the Taupo Rift obliquely (c. 45°) to define a type of triple junction. As the NIFS branches into 5 splays (Waiohau, Whakatane, Waimana, Waiotahi and Waioeka faults) within 100 km of the Bay of Plenty coastline, the intersection is not defined by a point but rather by a zone which is distributed c. 40 km along and up to 50 km across (i.e. perpendicular) the southeast margin of the Taupo Rift.

The NIFS is defined by active traces that are discontinuous in map-view. The fault offsets dateable landforms which enabled Beanland (1995) to compile late Quaternary slip rates and slip vectors along its entire length. Beanland's work dramatically improved our understanding of the NIFS and, in doing so, highlighted the need for further work. In the northern NIFS Beanland (1995) recognised the northward along-strike change from strike-slip to oblique normal-slip, using mainly unpublished New Zealand Geological Survey client reports (i.e., Beanland 1989b). These observations provided a catalyst for my study, and an inspiration, and also supplied a valuable template of kinematic data to the south of the intersection of the NIFS with the Taupo Rift. Beanland's work provided a stable substratum on which this work was built.

Unlike the intersection between the strike-slip North Anatolian Fault and the North Aegean Rift in Greece which is covered by the Aegean Sea (Fig. 1.1), much of the intersection of the NIFS and the Taupo Rift can be seen onshore. The active fault trace displaces landforms, including abandoned streams, river terrace margins and ridges. The landscape in the Bay of Plenty has been blanketed by tephras from the Taupo and Okataina volcanic centres, which provide important time lines for constraining the timing of deformation. These late Quaternary tephras are primarily <30 kyr in age and are underlain by volcanic deposits and marine strata which are estimated to be 1.5 Ma in age and younger (Nairn & Beanland, 1989; Bailey & Carr, 1994). These pre 30 kyr Quaternary deposits, which include the 280 kyr old Matahina ignimbrite, rest on Torlesse greywacke basement (Mortimer, 1994) and thicken northwards along the NIFS and towards the Taupo Rift. Displacements of Quaternary stratigraphy constrain faulting rates over earthquake (tens to hundreds years) and geological (thousands to million years) timescales.

1.4 Methods

To address the main aims of this thesis a combination of existing and new information has been used. The principal methods employed to collect, analyse and, in some cases, re-interpret data are discussed in detail in the main body of the text or in an appendix. These methods are briefly listed below:

- Detailed mapping of active fault traces in the northern NIFS at sixty eight new sites. There, fault measurements were made to constrain the late Quaternary displacements, displacement rates, slip-vector orientations (pitch, azimuth, slickenlines), strike and dips on faults in the NIFS. Most measurements (n=54) are from offset geomorphic features such as, ridge crests, stream channels, river terrace margins. Displacements range from 3 to 90 m while the sense of slip varies from predominantly strike-slip (h:v=10) to predominantly normal dip-slip (h:v=0.4). Thirty microtopographic contour maps were constructed by Global Position System Real Time Kinematics surveys to constrain displacement measurements. The remainder of the offsets (n=24) were measured directly using a tape measure.
- Examination of twenty trenches located within the northern NIFS and the Taupo Rift. Ten of these fault-trenches (each c. 15 m long, 3 m wide and 3-6 m deep) were

excavated along the northern NIFS (Whakatane and Waimana faults) as part of this thesis. These new trenches crossed faults in the kinematic transition zone and constrain the spatial and temporal distribution of earthquakes across this transition zone. Published trench data incorporated in this thesis are from Hull (1983), Ota et al., (1988), Beanland (1989b), Beanland (1995), Woodward-Clyde (1998), Hanson (1998) and Berryman et al. (1998). Trench logs from Hanson (1998) and Woodward-Clyde (1998) have been re-interpreted in this study.

- Augering of ten offset landforms was undertaken in order to constrain the stratigraphy, age and the slip rate for the offset feature.
- Dating of landforms was achieved mainly from tephrochronology. Dateable volcanic tephra layers, sourced from two major volcanic centers located adjacent to the NIFS (Nairn & Beanland, 1989), produced up to thirteen late Quaternary (i.e., 0-30 kyr BP) tephras. Seventy four individual tephra layers of known ages have been identified by comparing their distinctive glass chemistry, as measured by electron micro-probe equipment at Victoria University of Wellington, to a New Zealand database of results (Froggatt & Solloway, 1986; Lowe & Hogg, 1986; Lowe, 1988; Eden et al., 1993; Manning (and references therein), 1995; Newnham et al., 1995; Lowe et al., 1999; Wilmhurst et al., 1999; Shane & Hoverd, 2002; Pillans & Wright, 1992; Nairn et al., 2004). Further constraints on the age of landforms is provided by nineteen radiocarbon dates.
- Gravity survey was pursued across four active faults in the northern NIFS and the Edgecumbe Fault in the Taupo Rift. Two E-W oriented profiles were collected to model the depth of top-basement surface and to estimate its vertical displacement across the intersection zone between NIFS and Taupo Rift. During this survey 186 new gravity stations were established.
- Compilation of a worldwide database of published information on the geometries and kinematics of intersecting regional scale strike-slip and normal fault systems. In addition to the NIFS-Taupo rift intersection, data have been compiled and analysed from four intersections in continental crust, and nine mid-ocean ridge-transform fault intersections.
- Seismic-reflection profiles from Woodward (1988), O'connor (1988) and Davey et al. (1995) have been reinterpreted using current outcrop, gravity and drillhole data. Reinterpreted seismic reflection data have been combined with interpretations

of additional seismic reflection lines, and with gravity, to constrain vertical displacements on horizons ranging in age from 280-1500 kyr (Rogan, 1982; Woodward, 1989; Nairn & Beanland, 1989; Beanland et al., 1989; Woodward-Clyde, 1998; Stagpoole & Bibby, 1999; Nairn, 2002; Taylor et al., 2004; Lamarche et al., 2006; Nicol et al., Unpubl. data).

1.5 Structure of the thesis

The seven chapters in this thesis first establish the late Quaternary geometry and kinematics of the NIFS-Taupo Rift intersection zone and relate this to other global examples (chapters 2 and 3), then document how the intersection zone functions on the time-scale of individual earthquakes (chapters 4 and 5), and finally look back in time to evaluate the geological longevity of the New Zealand case study (Chapter 6). To aid the publication of results, chapters are written and formatted as manuscripts for journal submission. Chapters 2 and 3 are currently in press (Special Publication of Geological Society of London and Journal of Structural Geology, respectively). In recognition of the guidance and support of A. Nicol, T. Little, J. Begg and J. Walsh they appear as co-authors in all/some of the papers. Their role in this work, however, was strictly supervisorial in nature; that is, limited to the provision of advice, discussion, commentary, criticism, and editing of the written work. The field observations, scientific analyses, tables, maps, graphs, illustrations and written text in this thesis are all entirely my own work.

Because the thesis was produced as a series of manuscripts, each chapter includes its own abstract, introduction, conclusions and references. The majority of chapters are self-contained and can be read independent of one another. To produce stand-alone chapters some degree of repetition and overlap was necessary, especially in the description of the general kinematic characteristics of the NIFS.

Chapter 2 tracks the late Quaternary (≤ 30 kyr) pattern of fault kinematics on each fault in the northern NIFS (Waiohau-Ruahine, Mohaka-Whakatane, Waimana and Waiotahi faults) and documents how these vary northward, along strike, and towards their termination against the Taupo Rift. The mechanism through which the strike-slip NIFS terminates, is compared to rotations about vertical axis.

Chapter 3 examines the interaction and displacement transfer between active intersecting strike-slip (or transform) and extensional fault systems and the factors that might control it. The data from the NIFS-Taupo Rift fault intersection in New Zealand (Chapter 2) are compared to a global dataset of 13 strike-slip and normal fault intersections that form either two or three plate configurations in continental or oceanic crust.

Chapter 4 documents the temporal and spatial distribution of large earthquakes that have ruptured the ground surface in the northern NIFS during the last c. 18 kyr. The seismic hazard (earthquake recurrence and earthquake magnitudes) in the Bay of Plenty region is also discussed.

Chapter 5 investigates the process by which the accumulation of individual earthquake ruptures might produce the long-term (< 30 kyr), along-strike, kinematic change that characterise the northern NIFS. The spatial relationship between the location of the kinematic transition zone and fault segmentation is discussed. Simple kinematic modelling is undertaken in order to explore whether fault segmentation alone can account for the long-term kinematic transition.

Chapter 6 examines the intermediate- and longer-term (i.e. 280-1500 kyr) temporal stability of the kinematics in the intersection zone between the NIFS and the Taupo Rift. Regional changes in fault kinematics are discussed.

Chapter 7 summarises the main conclusions of this study.

The thesis contains a series of appendices. The locations, site descriptions and maps for sites of detailed fault studies are presented in **Appendix I**. The units encountered in the fault-trenches are documented in **Appendix II**. The electron microscope analyses of glass geochemistry of late-Quaternary tephras are presented in **Appendix III**. The raw gravity data, the method used for gravity data reduction and modeling are presented in **Appendix IV**. The radiocarbon and calibrated ages obtained for this project are presented in **Appendix V**.

CHAPTER TWO

TERMINATIONS OF LARGE STRIKE-SLIP FAULTS: AN ALTERNATIVE MODEL FROM NEW ZEALAND

Abstract

The 500 km long strike-slip North Island Fault System (NIFS) intersects and terminates against the Taupo Rift. Both fault systems are active with strike-slip displacement transferred into the rift without displacing normal faults along the rift margin. Data from displaced landforms, fault-trenching, gravity and seismic-reflection profiles, and aerial photograph analysis suggest that within 150 km of the northern termination of the NIFS, the main faults in the strike-slip fault system bend through 25°, splay into five principal strands and decrease their mean dip. These changes in fault geometry are accompanied by a gradual steepening of the pitch of the slip vectors and by an anticlockwise swing (up to 50°) in the azimuth of slip on the faults in the NIFS. As a consequence of the bending of the strike-slip faults and the changes in their slip vectors, near their intersection, the slip vectors on the two component fault systems become sub-parallel to each other and to their mutual line of intersection. This sub-parallelism facilitates the transfer of displacement from one fault system to the other, accounting for a significant amount of the northeastward increase of extension along the rift, whilst maintaining the overall coherence of the strike-slip termination. Changes in the slip vectors of the strike-slip faults arise from the superimposition of rift-orthogonal differential extension outside the rift margin resulting in differential motion of the footwall and hangingwall blocks of each fault in the NIFS. The combination of rift-orthogonal heterogeneous extension (dip-slip) and strike-slip, results in a steepening of the pitch of the slip vectors on the terminating fault system. Slip vectors on each splay close to their terminations are, therefore, the sum of strike-slip and dip-slip components with the total angle through which the pitch of the slip vectors steepens being dependent on the relative values of both these two component vectors. In circumstances where interaction of the velocity fields for the intersecting fault systems cannot transition to a slip vector that is boundary coherent, either rotation about vertical axes of the terminating fault relative to the through-going fault system may take place to accommodate the termination of the strike-slip fault system, or the rift may be offset by the strike-slip fault system rather than terminating into it. At the termination of the NIFS an earlier phase of such rotations may have produced the 25° anticlockwise bend in fault strike and contributed up to about one third of the anticlockwise deflection in slip azimuth. On the terminating strike-slip NIFS, therefore, rotational and non-rotational termination mechanisms have both played a role but at different times in its evolution, as the thermal structure, the rheology and the thickness of the crust in the rift intersection region have changed.

2.1 Introduction

Continental strike-slip faults commonly traverse the Earth's upper crust for tens to hundreds of kilometers. They often operate as transform faults, linking and transferring displacement between other plate boundary segments (Joffe & Garfunkel, 1987; Freymueller et al., 1999; Norris & Cooper, 2000), as large strike-slip faults within continental plate boundary zones (Davis & Burchfiel, 1973; Bellier & Sébrier, 1995; Quebral et al., 1996; Tsutsumi & Okada, 1996; Chapter 3, this study) or as isolated structures within otherwise rigid plates (Molnar & Lyon-Caen, 1989; Taymaz et al., 1991; Jackson et al., 1995; Bayasgalan et al., 1999). Each of these different forms of strike-slip faults must terminate, yet the mechanisms by which they terminate are often poorly resolved by the available data.

Terminations of strike-slip faults are of three basic types (Fig. 2.1). A) A free tip termination in which the strike-slip fault dies out within a rock volume that appears unfaulted at a regional scale of observation (Fig. 2.1a). The E-W striking left-lateral faults of the Gobi-Altay fault system in western Mongolia are an example of this type of termination (Baljinnyan et al., 1993). B) A termination produced by normal or reverse faults that intersect the tip of the strike-slip fault (i.e. horsetail splay). Slip azimuths on the normal or reverse faults ideally will be parallel, and of equal magnitude, to those of the strike-slip fault (Fig. 2.1b). This type of termination is a two-plate geometry in classical plate tectonic terminology (Le Pichon & Francheteau, 1976) and can be observed where the eastern tip of the strike-slip Artz Bogd Fault in Mongolia ends on a reverse fault (Bayasgalan et al., 1999), where the Sumatra Fault in Indonesia terminates in the Sunda Strait Rift (Lelgemann et al., 2000), where the Median Tectonic Line in Japan ends in the Yatsushiro Graben (Kamata & Kodama, 1994) and at the northeastern tip of the Hope Fault in New Zealand (Van Dissen & Yeats, 1991). C) A termination produced where strike-slip fault intersects and terminates against (often in an abutting relation) another through-going reverse, normal or strike-slip fault system (Fig. 2.1c). This 3-plate setting can be observed where the Dead Sea Transform intersects the Red Sea Rift (Joffe & Garfunkel, 1987), at the western end of the Garlock Fault where it intersects the San Andreas Fault (Davis & Burchfiel, 1973) and at the southwestern tip of the Hope Fault where it intersects the Alpine Fault of New Zealand (Freund, 1974).

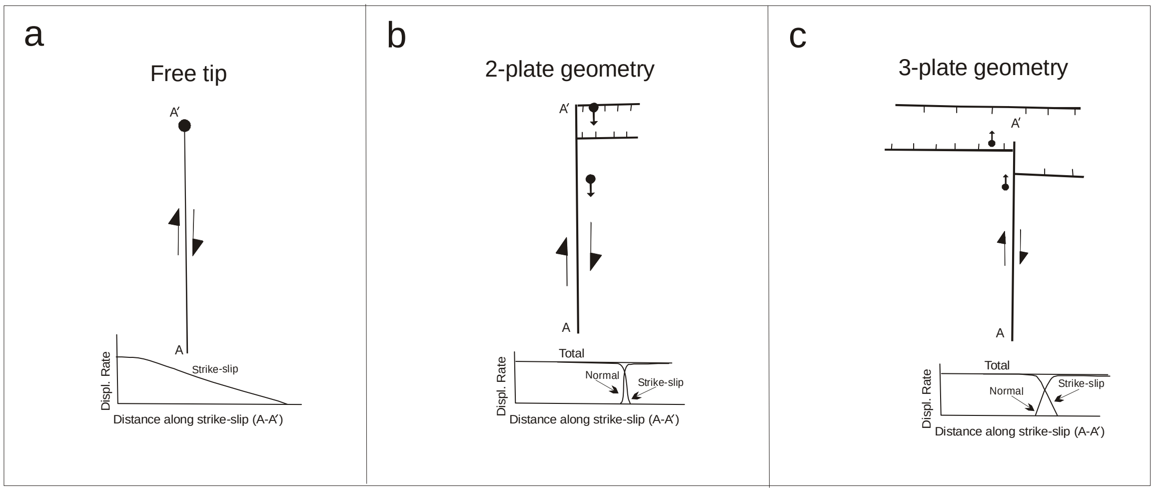

Fig. 2.1 Schematic diagram illustrating the three basic types of strike-slip fault termination: (**a**) Strike-slip fault terminates within undeformed rock (free tip), (**b**) Strike-slip terminations produced by normal or reverse faults formed at their tips (2-plate geometry) and, (**c**) Strike-slip fault terminates against another through-going fault or fault system (3-plate geometry). Arrows attached to filled circles represent slip vector azimuths. Schematic displacement profiles along each strike-slip fault system are indicated.

Each of the three types of strike-slip fault terminations may be associated with vertical-axis rotations of the rock close to the tip, as has been suggested by Bayasgalan et al., (1999) and Kim et al., (2000) for the tips of the Artz Bogd Fault in Mongolia (e.g., Fig. 2.2a) and the small scale strike-slip faults at Crackington Haven in southwest England (e.g., Fig 2.2b), respectively, and/or with branching of the principal slip surface into multiple splays, as occurs at both tips of the Doruneh Fault in Iran (Freund, 1974) (e.g., Fig. 2.2c). These processes decrease the displacement on the principal fault surface by redistributing the slip into the rock volume around the fault.

Both vertical-axis rotations and fault bifurcation appear to contribute to the northern termination of the strike-slip North Island Fault System (NIFS), New Zealand, against the Taupo Rift. In this New Zealand example, however, neither vertical-axis rotations nor fault bifurcation by itself either decreases strike-slip to zero at the rift margin or permits transfer of strike-slip into the rift without displacing the rift margin. In this chapter it is shown that, in addition to an earlier phase of vertical-axis rotations and fault bifurcation, termination of the NIFS and transfer of strike-slip into the Taupo Rift is achieved today because rift-related heterogeneous extension is distributed into the fault blocks outside the rift and is differentially accommodated in footwall and hangingwall blocks of each of the main faults in the NIFS. As a result of this heterogeneous extension, slip vectors on the northern end of the strike-slip faults become gradually sub-parallel to slip vectors in the rift and to the line of intersection between the two fault systems. This sub-parallelism of fault slip vectors reduces potential space problems at the intersection of the two fault systems, allowing the kinematics and geometry of faulting to change efficiently while accommodating the overall deformation imposed by the regional kinematics and without the requirement of vertical-axis rotations.

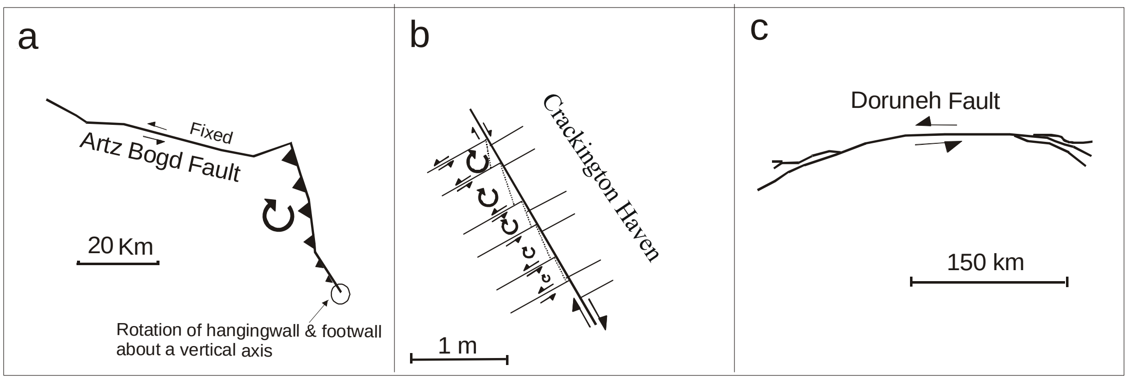

Fig. 2.2 (**a**) The eastern termination of the Artz Bogd Fault in Mongolia is achieved through the development of a rotating thrust at its tip. The displacement on the thrust decreases with distance from the strike-slip fault as a result of the relative rotation of the footwall and hangingwall blocks of the thrust about a vertical axis (map modified after Bayasgalan et al. (1999)). (**b**) The termination of the small-scale strike-slip fault at Crackington Haven, southwest England. Strike-slip displacement gradually decreases towards the tip of the fault in association with rotational deformation of small blocks in the wall rock that are bounded by bedding discontinuities. Dotted lines indicate extensional cracks formed by rotation (map modified after Kim et al. (2000)). (**c**) The Doruneh Fault, Iran, terminates at both tips through bifurcation of the principal slip surface (map modified after Freund (1974)).

2.2 Tectonic setting and fault data

The North Island Fault System (NIFS) is the principal strike-slip fault system in the upper Australian Plate of the Hikurangi margin, which is forming in response to oblique (c. 40-70°) subduction of the Pacific Plate (De Mets et al., 1994) (Fig. 2.3, inset). Oblique relative plate motion produces a margin-parallel component of motion of 26-33 mm/yr which is mainly accommodated by regional vertical-axis rotations of the deforming Hikurangi margin with respect to relatively stable Australian Plate and by strike-slip faulting in the upper plate, with little or no strike-slip on the subduction thrust (Wallace et al., 2004). The NIFS accommodates between 20 and 70% of the margin-parallel relative plate motion at the northern and southern ends of the fault system, respectively (Beanland, 1995; Wallace et al., 2004).

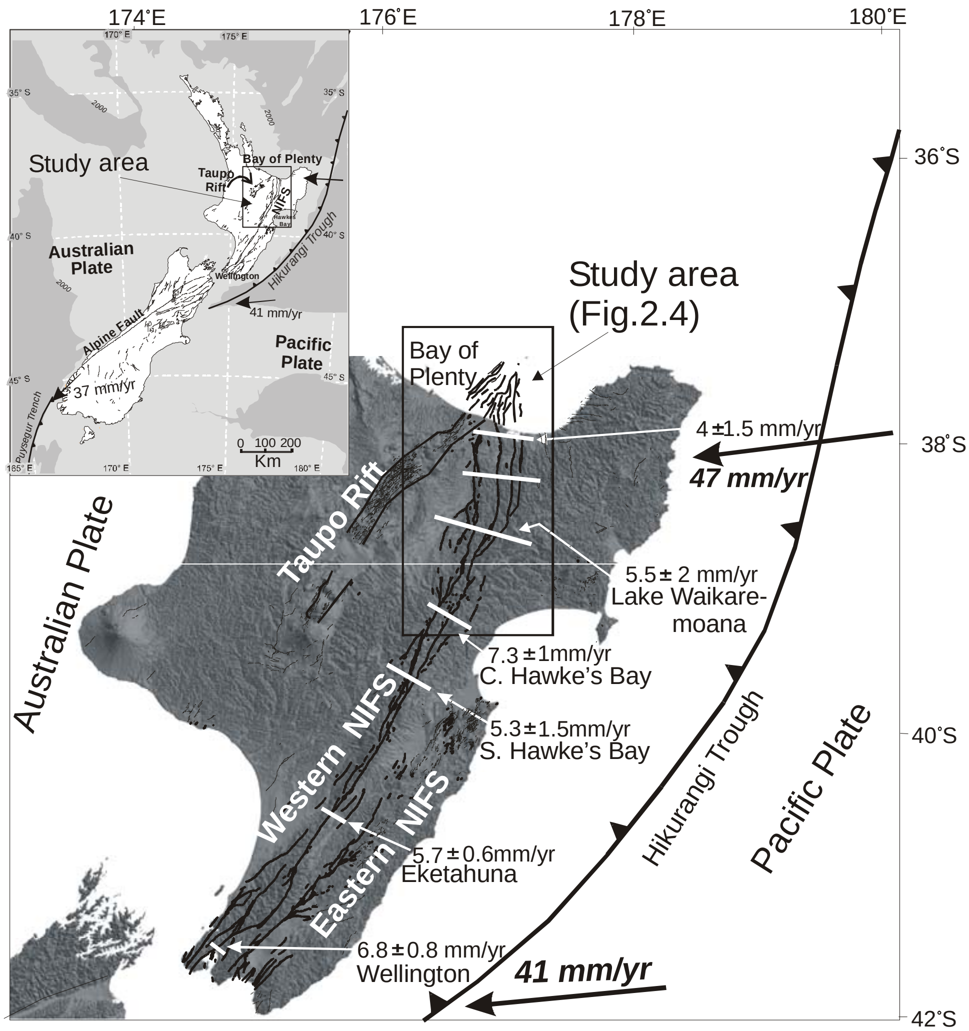

Fig. 2.3 Digital Elevation Model illustrating the large strike-slip North Island Fault System (NIFS) traversing the North Island of New Zealand and terminating against the Taupo Rift. The eastern strand of the NIFS extends from Wellington to Hawke's Bay, whilst the western strand traverses the North Island from Wellington to the Bay of Plenty. The Taupo Rift is also indicated. The black lines that bound the rift indicate its geographic extend. The along strike variation of the strike-slip rate for the western strand of the NIFS are shown for six transects. Slip rate data from: Beanland & Berryman (1987); Cutten et al. (1988); Kelsey et al. (1998); Beanland (1995); Van Dissen & Berryman (1996); Schermer et al. (2004); Langridge et al. (2005); this study. Arrows with associated velocities indicate relative plate motion between the Pacific and Australian plates (De Mets et al., 1994). Inset: New Zealand plate boundary setting; the study area is located on the upper plate of the Hikurangi subduction margin.

The NIFS comprises two main strands, here referred to as the eastern and the western strand (Beanland, 1995) (Fig. 2.3). Each strand traverses rugged terrain of Mesozoic greywacke basement along much of their length, both exploiting pre-existing terrane boundaries and mélange zones and cutting across these structures to define their own path (Mortimer, 1994; Begg Pers. comm., 2006). The eastern strand extends for approximately 250 km, from the Wellington region in the south to southern Hawke's Bay in the north, where it is mainly a reverse-dextral fault (Beanland, 1995) (Fig. 2.3). The western strand is approximately 500 km long and traverses the North Island from Wellington to the Bay of Plenty coastline (Fig. 2.3). This chapter focuses on the northern termination of the western strand and hereafter refers to this strand as the NIFS.

The NIFS ends where it intersects at a c. 45° strike angle the active Taupo Rift, a 200 km long and up to 40 km wide extensional basin associated with intense volcanic activity (Fig. 2.3) (Wilson et al., 1995; Rowland & Sibson, 2001). At its northern termination the NIFS comprises five main splays, spaced at a distance of 5-10 km, that distribute the displacement of the fault system across a zone that is 40-50 km wide. The intersection of the two fault systems is in part exposed onshore providing an excellent opportunity to examine the geometry and kinematics of the termination of the strike-slip faulting.

The active NIFS has accommodated up to 5-8 km of strike-slip during the last 1-2 Ma (Beanland, 1995; Kelsey et al., 1995). Aggregated late Quaternary dextral strike-slip rates, across the two main strands of the NIFS (i.e. eastern and western) range from c. 18 mm/yr in the south (Beanland, 1995; Van Dissen & Berryman, 1996; Langridge et al., 2005), near Wellington, to c. 4 mm/yr in the north (this study), near the Bay of Plenty (see Fig. 2.3 for further details). During the late Quaternary, the southernmost c. 400 km of the NIFS has chiefly carried dextral strike-slip and only minor reverse or normal-slip (typical horizontal:vertical slip ratios are 10:1) (Beanland, 1995). Along the northern c. 100 km of the fault system, however, strike-slip and normal dip-slip decrease and increase northwards respectively, resulting in a change of the horizontal to vertical slip ratio (H:V) from 10:1 to <1:1 (Beanland, 1995; this study).

In this chapter displaced landforms ≤ 50 kyr in age, fault-trench data, gravity profiles and seismic-reflection lines are used to track changes in the kinematics and geometries of the NIFS approaching its intersection with the Taupo Rift. Eighty-eight sites were studied along the northernmost 250 km of the four main strands in the NIFS (Waiohau-Ruahine, Whakatane-Mohaka, Waimana and Waiotahi faults) (Fig. 2.4, Table 2.1 & Appendix I). Fault geometries were determined from outcrop exposures, trenching, air-photo interpretation, gravity modelling and seismic-reflection profiles. Slip-directions

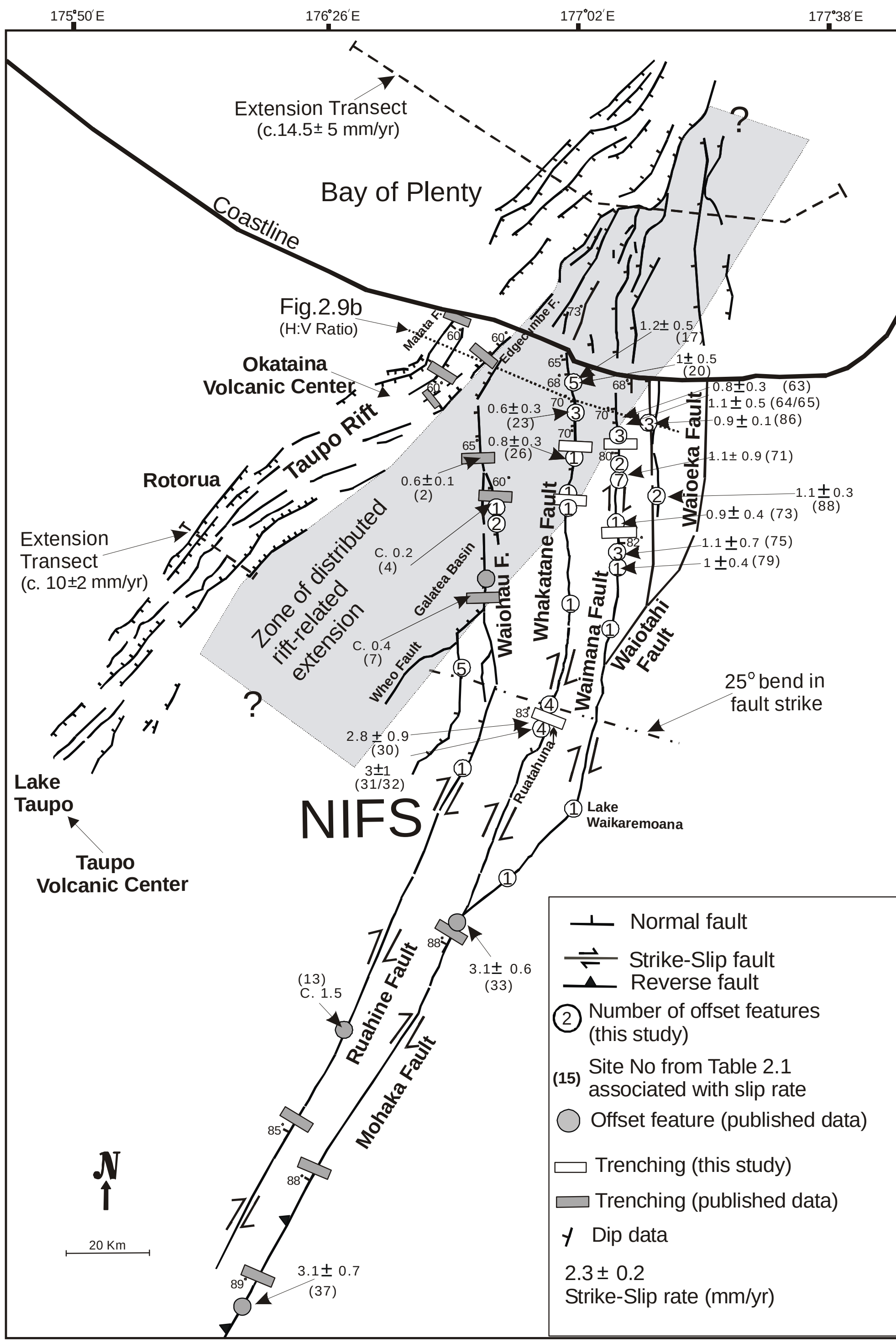

Fig. 2.4 Map shows the strike-slip North Island Fault System (NIFS) terminating against the Taupo Rift in the Bay of Plenty, North Island, New Zealand. The sites studied and the associated strike-slip rates (where available) are indicated (see also Table 2.1). Dashed transects indicate locations of extension profiles, one across the onshore and one across the offshore Taupo Rift. The approximate location of the H:V slip ratio transect across the intersection of the two fault systems in Fig. 2.9b, is indicated by the dotted line. Regional distributed extension outside the rift indicated by grey shading. Published data are from: Hull (1983); Raub (1985); Hanson (1998); Ota et al. (1988); Beanland et al. (1989); Beanland (1989b); Berryman et al. (1998); Woodward-Clyde (1998); Taylor et al. (2004). Offshore data from Davey et al. (1995), Lamarche et al. (2000) & Taylor et al. (2004).

were derived from the analysis of offset geomorphic linear markers (e.g. spurs, abandoned stream axes, river margins) and slickenside striations, and slip-rates were estimated from offset landforms, 3D-trenching (i.e. perpendicular and parallel to the fault) and dating of key geomorphic stratigraphic markers by tephrochronology (Table 2.2) and ^{14}C dating (Fig. 2.4, Table 2.1).

Most of the slip-rate estimates derive from fault traces that traverse and displace young geomorphic surfaces (≤ 50 kyr) which are often mantled by alternating layers of loess, paleosols and volcanic tephra. Dateable volcanic tephra layers were sourced from two major volcanic centers located adjacent to the NIFS (Taupo and Okataina volcanic centers) and have erupted repeatedly throughout the late Quaternary (Fig. 2.4, Table 2.2) (Nairn & Beanland, 1989). Individual tephra layers of known ages have been identified by comparing their distinctive glass chemistry to a New Zealand database of results (see caption of Table 2.2 for references). Wherever possible these ages were confirmed by radiocarbon dating of associated sediments (Table 2.1). Most of the displaced landforms (i.e. abandoned stream channels, river terrace risers and ridges) occur in proximity to fluvial aggradational terrace surfaces that are today elevated above modern river beds. In the study area, these river terraces have typical ages of c. 5 kyr, 13.8 kyr, 17.6 kyr, 30 kyr and 50 kyr (Table 2.2 & references therein).

Fault displacements and slip vectors have been measured using topographic surveys (GPS - Real Time Kinematic) of linear landforms that are offset by the fault to produce piercing points (e.g. Fig. 2.5, Appendix I) (Table 2.1). These piercing points were identified and correlated across faults by constructing detailed topographic maps, from which profiles were made parallel (and adjacent) to the fault in both footwall and hangingwall (e.g. Fig. 2.5). Where the displaced lineaments have been eroded or modified by deformation close to the fault, they have been projected as an inclined lineation to intersect the fault surface from both sides of the fault. Errors in slip estimates are chiefly derived from projection uncertainties rather than measurement precision (i.e. Fig. 2.5a). Kinematic attributes such as fault strike, dip, displacement components and late Quaternary slip-rates at ninety-seven localities in the northern NIFS (N=88) and Taupo Rift (N=9) are summarized (with estimated errors) in Table 2.1.

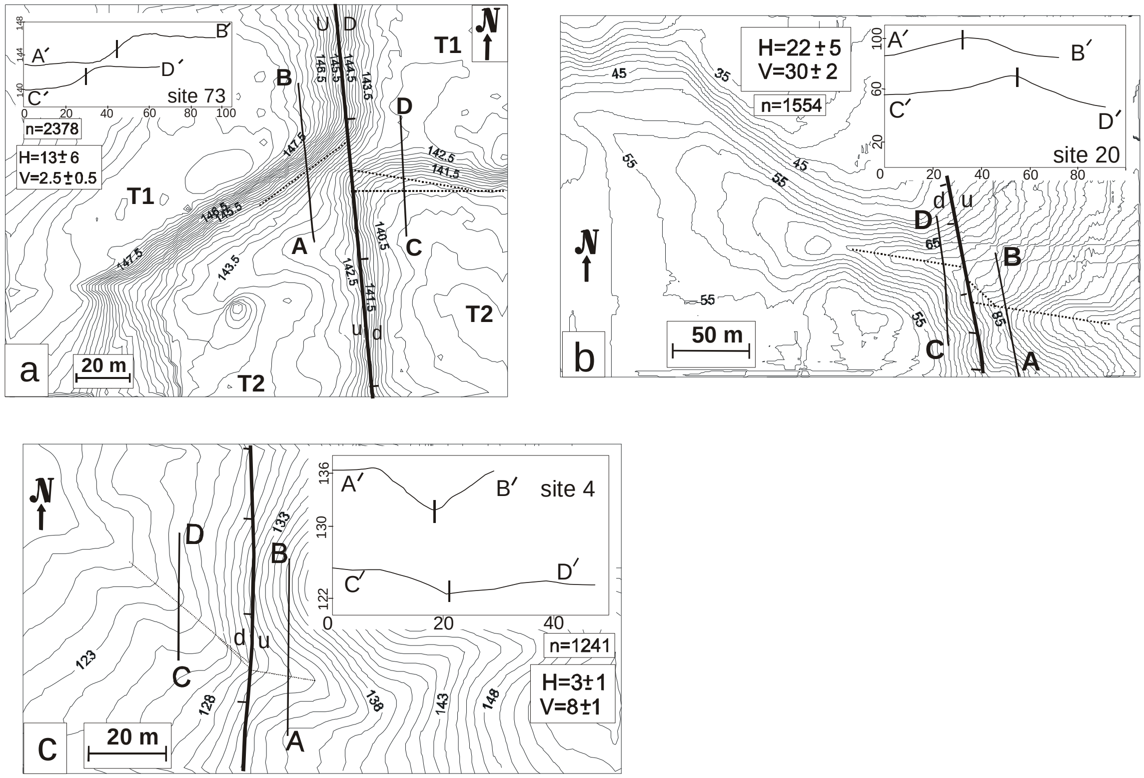

Fig. 2.5 Detailed contour maps of three representative offset features from faults within the northern NIFS constructed by GPS-Real Time Kinematics. The topographic data were gridded, contoured and "sliced" in order to estimate slip-vectors. Offset profiles (e.g. A-B line) were derived by sampling a data-line approximately perpendicular to the offset marker and parallel to the fault plane. These profiles were projected onto the fault plane on each side of the fault (e.g. A′-B′) and matched with one-another to produce a series of piercing points (the actual piercing point utilized are indicated by the thick vertical lines on each profile). Dashed lines represent offset piercing points while their divergence represents error in the projection. (**a**) Displaced river margin on the Waimana Fault (T1= higher river terrace, T2= younger river terrace), (**b**) Displaced ridge spur in northern Whakatane Fault, (**c**) Displaced stream channel on the Waiohau Fault (see Table 2.1 for more details on each of these sites). Downthrown side is indicated. n = number of topographic data points/site. The associated displaced profiles are indicated as: A-B profile parallel to the fault plane. A′-B′ projection of A-B on the fault plane.

2.3 Northern termination of the NIFS

2.3.1 Fault geometries

Strike-slip faults in the NIFS strike NNE-SSW along the southernmost 350 km of their length (Fig. 2.3). To the north of Lake Waikaremoana, however, this consistent northeast strike swings c. 25° anticlockwise to a N-S direction (Figs 2.3 & 2.4). This change in strike, the possible origin of which is discussed in the 'fault termination' section, is accompanied by some bifurcation of the main faults. Immediately south of the bend the NIFS consists of two main faults, the Mohaka and the Ruahine faults while north of the bend, the Mohaka Fault splays into the Whakatane, Waimana, Waiotahi and Waioeka faults and the Ruahine Fault becomes the Waiohau Fault which is associated with other secondary splays (e.g. Wheo Fault) (Fig. 2.4). These five main splays extend northwards for a distance of ~100 km on land and up to 50 km offshore and form a 40-50 km wide zone at their northernmost onshore extent. Still farther north, however, the N-S striking faults deflect clockwise in strike by c. 20-35° to NE within c. 10-15 km of the rift's southeast margin (Fig. 2.4). For the Waiohau Fault, this change of strike close to the intersection takes place onshore whereas for the Whakatane, Waimana and Waiotahi faults it occurs offshore (Fig. 2.4) (Lamarche et al., 2000; Taylor et al., 2004; Chapter 3, this study). Similarly, the faults of the Taupo Rift, south of their intersection with the NIFS, strike ENE while northwards, as the intersection is approached, they swing anticlockwise by c. 20° to a NE strike (Fig. 2.4).

Along the southern 350 km of the NIFS, the faults often dip steeply at the surface, c. 80-90°, either to the east or west (Beanland, 1995). Close to the northern termination of the NIFS, however, the dips of the faults gradually become shallower, at 60-70°, and are consistently west-dipping and downthrown to the west (Fig. 2.4) (e.g., sites 1, 15, 16, 57, 58, 83 in Table 2.1). The lower dips at the northern end of the NIFS are comparable to those measured on normal faults in the Taupo Rift itself from Beanland et al. (1989), Lamarche et al. (2000) and Taylor et al. (2004) (for details see Fig. 3.4 from Chapter 3).

2.3.2 Late Quaternary displacement rates and slip vectors

The relatively uniform late Quaternary strike-slip rate recorded along the southernmost c. 350 km of the Wellington-Mohaka Fault (c. 6.8 mm/yr in Wellington region, c. 5.7 mm/yr in Eketahuna, c. 5.3 mm/yr in south Hawke's Bay, c. 7.3 in central Hawkes Bay) begins to decrease northwards within c. 100 km of its intersection with the Taupo Rift (Figs 2.3, 2.4 & 2.8). In order to assess how the termination of the northern NIFS is accomplished, I examine changes in the late Quaternary rates of strike-slip, dip-slip, and net-slip on four of the main strands of the fault system towards its northern tip. These changes are reflected in corresponding changes of the slip vectors along each of the strands of the NIFS as they approach the Taupo Rift. In this section, the northward decrease in the H:V slip ratio from 10 to 1 is documented, signifying a steepening of the pitch of the slip vectors.

➢ Waiohau-Ruahine Fault

The Waiohau Fault, which is the westernmost strand of the NIFS, has been the least active fault within the NIFS during the last c. 17 kyr (Fig. 2.6). In the south, where this strand is referred to as the Ruahine Fault, it is predominantly strike-slip (H:V=5.5, site 14 in Table 2.1), has a late Quaternary dextral slip-rate of c. 1.5 mm/yr (site 13 in Table 2.1 and Fig. 2.4) and slip vectors plunging c. 10° N on a steeply dipping (i.e. 85°) fault (Hanson, 1998). The geomorphic signature of the Waiohau Fault along its northernmost 60-70 km, however, differs significantly from that of the Ruahine Fault. Steep scarps > 100 m high and triangular facets occur along the eastern margin of the Galatea Basin, where they record a significant component of normal displacement on this section of the fault. Estimates of late Quaternary slip-rates, on the northern Waiohau Fault (Beanland, 1989b; Woodward-Clyde, 1998; this study) (sites 2-5 & 7 in Table 2.1, Fig. 2.5c) indicate a strike-slip rate of < 0.5 mm/yr, significantly less than the slip-rate of 1.5 mm/yr documented on the Ruahine Fault in the south. This northward decrease in the strike-slip rate is associated with a steepening in the pitch of the slip vectors by up to 60° (i.e. from 10° to 69° W) and a 20° shallowing in the mean dip of the fault (i.e. from 80-90° to 60° W). These changes in slip vector pitch are associated with a c. 50° clockwise rotation of the slip azimuth and also a 50% decrease in the net-slip rate from 1.5±0.5 mm/yr in the south, to 0.7±0.2 mm/yr in the north (site 4 in Table 2.1).

➢ Whakatane-Mohaka Fault

The Whakatane Fault is presently the fastest moving of the splays in the northern NIFS and, like the Waiohau Fault, experiences a change in its kinematics towards its northern end (Figs 2.4 & 2.6). In the south, at Ruatahuna (see Fig. 2.4 for location), the Whakatane Fault strikes 020°, has a relatively straight trace and is a strike-slip dominated fault with an average H:V ratio of c. 6.5. Dextral offsets of c. 4.5 to 90 m were observed with respect to eight channels, five spurs and one river terrace (sites 30-48 in Table 2.1). At site 32, for example, 3D-trenching across an abandoned channel incised into mainly pre-Holocene deposits (Fig. 2.7), indicates a dextral offset of 22±2 m. Based on trenching of the channel it is suggested that the youngest deposits that pre-date incision of the channel are about 10 kyr old (Rotoma tephra, cal. 9.5 kyr BP, Table 2.2), while a radiocarbon date of 5728-5586 calibrated yrs BP from a peat layer close to the base of channel infill deposits indicates that the channel was abandoned about 6 kyr ago (Fig. 2.7). From these values, the age of the offset channel is estimated to be 8±2 kyr which, in combination with strike-slip of 22±2 m, indicates a dextral slip-rate of c. 3±1 mm/yr.

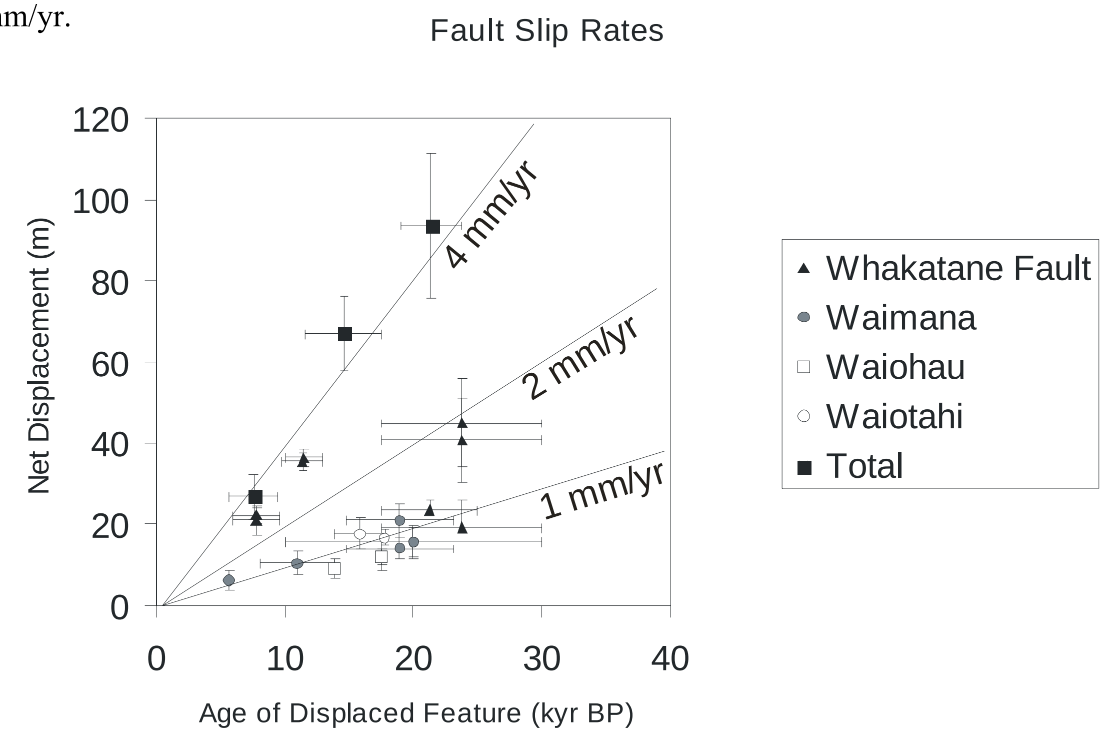

Fig. 2.6 Displacement rates for the faults within the northern NIFS. Data suggest that the Whakatane Fault is presently the most active fault within the northern NIFS. The total displacement rate is c. 4 mm/yr and has remained approximately uniform for the last c. 30 kyr.

At the northern end of the fault, within 10 km of the coastline, the fault consistently dips to the west and has a significant component of normal dip-slip. Normal displacements are indicated by numerous prominent scarps that are down to the west (e.g. Fig. 2.5b), a normal slip recorded in a fault trench (site 25 in Table 2.1) and by a westward throw of at least 660 m on the top of the basement inferred from modelling of a gravity survey (site 16 in Table 2.1) (this study). Accordingly, the average dip-slip rate on this part of the fault is 1.5±0.5 mm/yr (sites 17-21 in Table 2.1). Dip-slip rates at these localities are greater than associated strike-slip rates of c. 1.1±0.5 mm/yr during the last c. 30 kyr. In summary, the strike-slip rate along the Whakatane Fault decreases from c. 3±1 mm/yr in the south, to c. 1 mm/yr some 65 km to the north. This decrease in strike-slip rate is accompanied by an increasing component of dip-slip rate from c. 0.2 in the south to c. 1.5 mm/yr near the coast. Despite this change in the individual components of slip, the magnitude of the net-slip rate remains approximately constant along the northernmost 100 km of the Whakatane Fault (Table 2.1).

As expected, the changing kinematics along the Whakatane Fault is expressed by a northward steepening in the pitch of measured slip vectors (Table 2.1). In the south these are sub-horizontal (i.e. 0-10°) (sites 50 & 53 in Table 2.1) whereas further north, close to the coast, they steepen to a c. 55° northwest pitch (sites 17 & 20 in Table 2.1). This northward transition occurs gradationally over a strike distance of c. 60 km (see also Fig. 3.6a from Chapter 3) in conjunction with a northward shallowing in the dip of the faults (from 80-90° to c. 60°down to the west) and is reflected as a 50° anticlockwise deflection in the slip azimuth.

- **Waimana Fault**

The Waimana Fault, which splays eastwards from the Whakatane Fault, is the second most active fault within the northern NIFS (Figs 2.4 & 2.6). Within the onshore study region, the Waimana Fault is predominantly strike-slip. Near the coastline and offshore, however, it appears to become increasingly dip-slip (Davey et al., 1995; this study).

Along the northernmost 35 km of its onshore trace, the Waimana Fault strikes approximately N-S and has fault scarps that face either to the east or west (Fig. 2.4). The fault traverses a diachronous landscape with displaced surface features spanning from <5.6 to 23 kyr age (Table 2.1). I observed dextral displacements of five channels, three spurs and three river terraces by offsets of 5.5 - 24 m (Figs 2.4 & 2.5a, sites 62-79 in Table 2.1). The average H:V ratio along this section of the fault is c. 6.5 with slip vectors plunging at c. 10° N on a fault that dips > 80° (e.g. sites 64, 68, 76 in Table 2.1). The fault has a uniform late Quaternary strike-slip rate of c. 1 mm/yr over an onshore strike-distance of c. 35 km. Dip-slip rates are typically only c. 0.1 - 0.2 mm/yr (Table 2.1).

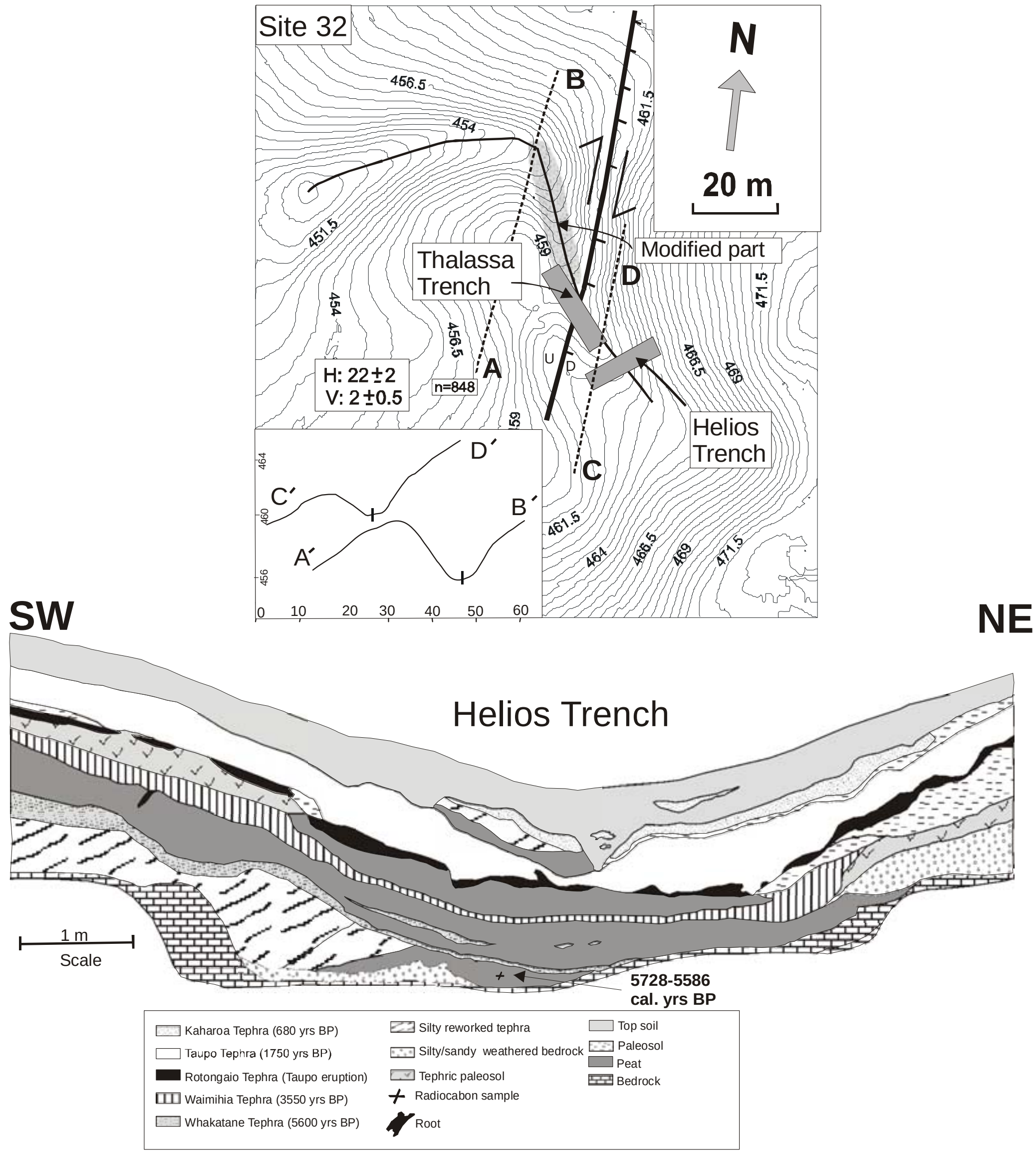

Fig. 2.7 Detailed contour map of site 32, Ruatahuna, where the Whakatane Fault displaces dextrally an abandoned stream channel by 22±2 m. Tephra stratigraphy revealed by trenching across and parallel to the fault helped to determine a slip rate of 3±1 mm/yr for this section of the fault (see text for further discussion). The log of the northwest wall of the stream crossing trench 'Helios', excavated normal to the stream channel (see site map for location), shows the record of volcanic and sedimentary layers deposited in the abandoned channel.

Along its northernmost 50 km, the Waimana Fault accumulates increasing normal displacement as its dip decreases (sites 57, 58 in Table 2.1). Gravity and seismic-reflection profiles acquired at the coast (site 58 in Table 2.1) and some 40 km offshore (site 57 in Table 2.1) respectively, suggest that the kinematics and geometries of the fault in the north, near the rift, differ from those observed along its onshore trace further south (Davey et al., 1995; this study). For example, the c. 500 m cumulative throw on the top of the greywacke basement during the past c. 600 kyr (sites 57, 58 in Table 2.1), suggests an increase in the dip-slip rate of the Waimana Fault from 0.1 - 0.2 mm/yr onshore to c. 0.8 mm/yr offshore. This increase in the normal displacement occurs in conjunction with a decrease of the fault-dip from > 80° in the south to c. 60° W offshore (Table 2.1).

The changing kinematics, from onshore to offshore along the Waimana Fault, is manifest as a northward steepening in the pitch of its late Quaternary slip vectors (Table 2.1). The pitch of the slip vectors onshore, in the south, is sub-horizontal (i.e. 10° N) (sites 65, 72, and 73 in Table 2.1) and based on the documented increase of the normal dip-slip rate, it is inferred that the pitch of the slip vectors increases significantly into the offshore region in conjunction with an anticlockwise deflection in the azimuth of this vectors.

- **Waiotahi Fault**

The Waiotahi Fault splays eastwards from the Waimana Fault and, similar to the Waimana Fault, does not change kinematics in the onshore study area although it does appear to become more dip-slip in the offshore region proximal to its northern termination. Onshore and some 10-20 km south of the coastline, the Waiotahi Fault strikes N-S and is chiefly a strike-slip fault with a H:V slip ratio of c. 8 and dextral offsets of up to 17 m. These offsets are associated with horizontal and vertical slip-rates of c. 1 mm/yr and < 0.2 mm/yr, respectively (sites 86 & 88 in Table 2.1 and Figs 2.4 & 2.6).

In the north, however, gravity modelling and seismic surveys suggest a gradual increase in the normal (down to the west) displacement on a relatively shallow (i.e. 60°) fault plane near the coast and offshore (Davey et al., 1995; this study). As expected, these changes are reflected in the gradual northward increase of the dip-slip rate on the Waiotahi Fault from < 0.2 mm/yr some 20 km south of the coastline, to c. 0.5 mm/yr at the coast and up to 0.7 mm/yr some 40 km north of the coastline and close to its northern end (sites 83-85 in Table 2.1) (Davey et al., 1995; this study).

In a similar manner to the Waimana Fault, the northward change in kinematics on the Waiotahi Fault is associated with corresponding deflections in the pitch of the late Quaternary slip vectors. The pitch of the slip vectors in the south is sub-horizontal (i.e. 7° N) (sites 86 & 88 in Table 2.1), and it is inferred that the increase of the normal dip-slip rate offshore to the north is accompanied by a steepening in the pitch of the slip vectors on the Waiotahi Fault together with an anticlockwise deflection of its slip azimuth.

2.3.3 Extension Rates

Strike-slip rates aggregated across all splays of the NIFS decrease from c. 5.5 mm/yr in the south, near Lake Waikaremoana, to c. 4 mm/yr close to Bay of Plenty coastline (Figs 2.8 & 2.3). This decrease in the horizontal slip-rate is accompanied by an increase in the aggregated dip-slip rate across all strands of the NIFS from ≤ 0.5 mm/yr in the south to c. 2.5 mm/yr at the coast (Table 2.1). These changes in cumulative strike-slip and dip-slip rates produce a net-slip rate aggregated across all fault strands which, within the uncertainties, is approximately constant for the northern 150 km of the NIFS. For example, the 5.5±1.8 mm/yr of aggregated net-slip rate across the coastal section is comparable to the 6±2 and 7.3±1 mm/yr estimated for the Waikaremoana and central Hawke's Bay slip-rate transects, respectively (Table 2.1 & Fig. 2.8).

Figure 2.9 illustrates how the H:V slip ratio and the component of rift-orthogonal NW-SE extension decreases and increases, respectively, along and across the NIFS towards the Taupo Rift. Figure 2.9a indicates a progressive kinematic transition on the Whakatane-Mohaka Fault (black triangles) from minor transpression (strike-slip with minor reverse component) in the south, to minor transtension (strike-slip with minor normal component) and to oblique-normal slip in the north, over a strike distance of c. 150 km.

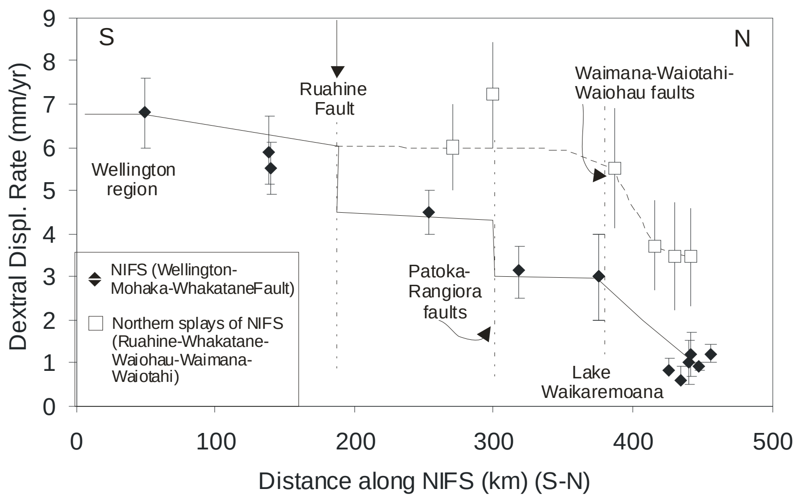

Fig. 2.8 Displacement profile along the Wellington-Mohaka-Whakatane Fault (filled rhombs) and its splays to the north (open squares). Each of the steps on the profile coincide with a branch point and the transfer of some displacement onto additional fault splays. Note that the total strike-slip across the NIFS decreases northwards. Fault-slip rate data from: Hull (1983); Raub (1985); Beanland & Berryman (1987); Cutten et al. (1988); Ota et al. (1988); Beanland et al. (1989); Beanland (1989b); Beanland (1995); Van Dissen & Berryman (1996); Berryman et al. (1998); Hanson (1998); Kelsey et al. (1998); Villamor & Berryman (2001); Schermer et al. (2004); Langridge et al. (2005).

Similarly, Figure 2.9b suggests that oblique-normal slip is accommodated on the Waiohau and Whakatane faults outside the rift, while the onshore Waimana and Waiotahi faults are principally strike-slip. These relationships indicate that the component of dip-slip within the NIFS increases northwestwards towards the Taupo Rift. The southeastward transition from oblique-normal slip to strike-slip across the NIFS and the corresponding increase in H:V slip ratio (Fig. 2.9b) has led us to map a kinematic boundary which trends sub-parallel to the margin of the rift and at c. 45° to the NIFS and separates a region of oblique extension to the NW from one dominantly strike-slip to the SE (shaded zone in Fig. 2.4).

The presence of normal oblique-slip in the northern NIFS indicates that some rift-orthogonal extension is distributed outside the main rift. This extension, which here is inferred to have formed in association with NW-SE rifting across the crust of the Taupo Rift, increases towards the rift (Figs 2.9a & b) and covers an area that is at least 150 km long (i.e. parallel to the rift) and up to 50 km wide (i.e. perpendicular to the southeast margin of the rift) (Fig. 2.4). Rift-parallel normal faulting in the region to the southeast of the topographically defined rift margin is supported by offshore seismic-reflection data acquired across the Taupo Rift (Davey et al., 1995; Lamarche et al., 2006) (see northern extension transect in Fig. 2.4), which show that zones of minor normal faults occur beyond the main rift. The rate of NW-SE extension to the southeast of the main rift margin is c. 1 mm/yr (Davey et al., 1995; this study) and appears to be comparable to rates of extension to the northwest of the main rift (Davey et al., 1995), accounting for between c. 6 and 15% of the estimated total 7-15 mm/yr extension across the greater Taupo Rift (Davey et al., 1995; Darby et al., 2000; Villamor & Berryman, 2001; Wallace et al., 2004) (see extension transects in Fig. 2.4).

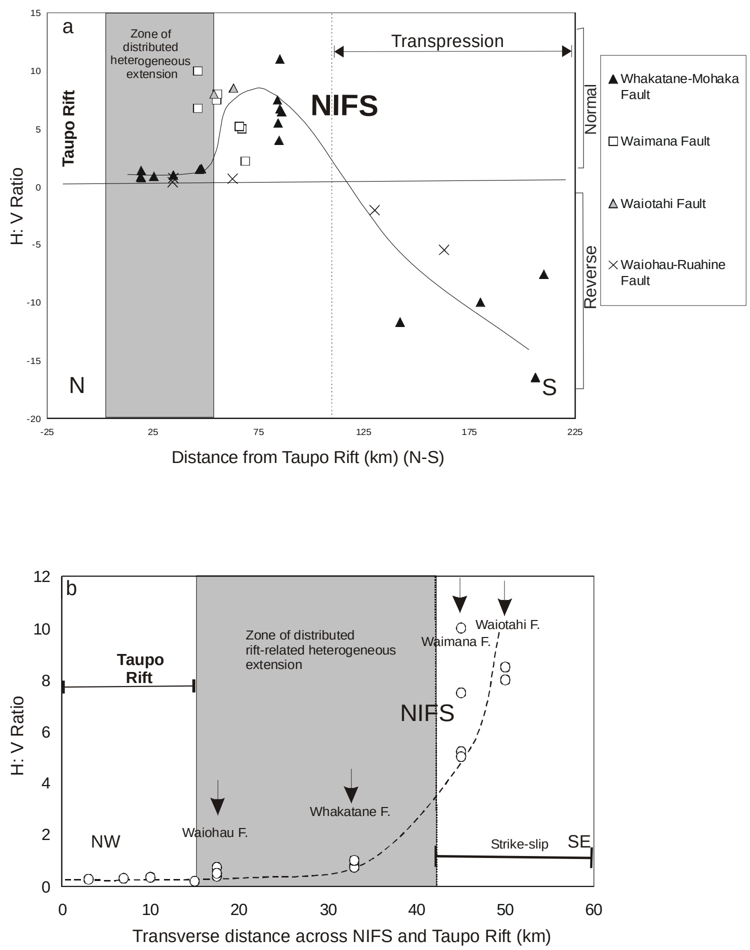

Fig. 2.9 Horizontal to vertical (H:V) slip ratios for each of the faults of the NIFS determined using displaced landforms. The data suggest that the ratio of strike-slip to dip-slip decreases both, along (**a**) and across (**b**) the NIFS towards its intersection with the Taupo Rift. Regional distributed extension outside the rift indicated by grey shading. See Figure 2.4 for the location of the H:V transect across the two fault systems. Lines among data-points indicate average values.

2.4 Fault Termination

At the termination of the NIFS, these strike-slip faults are not orthogonal to the Taupo Rift and therefore the far-field slip azimuths on the component faults are non-parallel. As the margins of the rift do not appear to have been displaced by the strike-slip faults, the termination of these faults can not be attained by rigid block translations. Instead, at their northern termination, the faults in the NIFS undergo a change in their slip vectors such that these become parallel to the (steeply plunging) line of their intersection with the Taupo Rift. This parallelism allows the intersecting fault systems to be kinematically coherent and the displacement to be transferred into the rift without any offset of the margin of the rift. The present quasi-stability on this triple junction may have been aided by an earlier phase of anticlockwise vertical-axis rotations of the northern tip of the faults in the NIFS relative to the southern part of the fault system and the Taupo Rift (e.g. Fig. 2.10a), and currently it is conditioned by an additional swing in the slip vectors along each fault that takes place in proximity to the rift margin (Fig. 2.10c). The inferred vertical-axis fault rotations (25° change in fault strike near Lake Waikaremoana) and changes of the slip vectors due to heterogeneous distributed extension may account for about one third and two thirds of the total 75° required swing in slip azimuths, respectively. In the following sections it is documented how the termination of the northern NIFS has included aspects of fault bending and bifurcation as well as the currently operating swing in their slip vectors that is permitted by distributed and heterogeneous off-fault extension orthogonal to the rift.

2.4.1 Vertical-axis fault-block rotations

Vertical-axis rotations of rocks proximal to the tips of large strike-slip faults have been widely discussed as a mechanism for their termination (Jackson & McKenzie, 1984; McKenzie & Jackson, 1986; Taymaz et al., 1991; Little & Roberts, 1997). Figures 2.10a & b illustrate termination of a strike-slip fault by vertical-axis rotations of the truncated fault system relative to the through-going one. A fault termination mechanism similar to the end-member illustrated in Figure 2.10a is documented on the northeast tip of the strike-slip Clarence Fault in New Zealand (Little & Roberts, 1997) whereas, a mechanism similar to the one illustrated in Figure 2.10b is proposed for central Greece, where clockwise rotations of the northwest trending normal faults accommodate the oblique right-lateral motion documented on the northeast trending faults of the North Anatolian Fault and allow abrupt changes in the type of faulting (Taymaz et al., 1991).

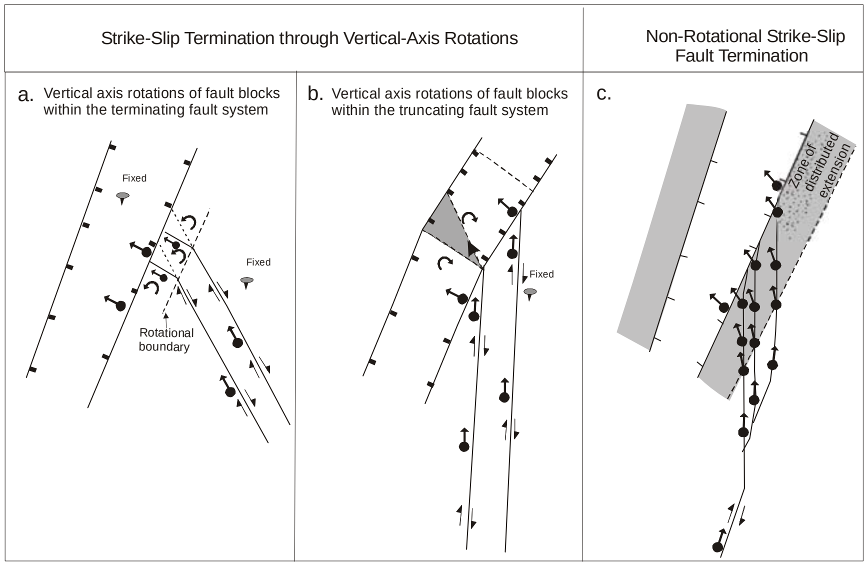

Fig. 2.10 Schematic end-member termination models for regional strike-slip faults that terminate against another fault or fault system. Termination can be achieved either through: (**a**) rotations about vertical axis of the crust enclosed between the tip of the fault and the truncating fault or fault system (i.e. Little & Roberts, 1997), (**b**) rotations about vertical-axis of the crust enclosed within the truncating fault or fault system (i.e. Taymaz et al., 1991) and/or (**c**) superimposition of heterogeneous extension onto strike-slip resulting in changes in the slip vectors of the strike-slip fault (this study). Dotted pattern indicates higher strain rates. Regional distributed extension outside the rift indicated by grey shading. Arrows attached to filled circles represent slip vector azimuths.

Anticlockwise vertical-axis rotations of the northern NIFS fault blocks relative to the southern part of the fault system and the Taupo Rift may have produced the abrupt 25° anticlockwise bend (i.e. from NNE-SSW to N-S) in the strike of the NIFS c. 150 km south of the Taupo Rift (Figs 2.3 & 2.4). Paleomagnetic data from sites to the east of the bend in the NIFS suggest that the change in fault strike may have resulted from differential vertical-axis rotation of the faults on either side of the bend (Walcott, 1989; Thornley, 1996). Such a change in strike of the faults might produce a comparable deviation in the strike-slip azimuths without any change in the pitch of those vectors. This appears to be the case in the NIFS. In addition, fault rotation is facilitated by the bifurcation of the strike-slip fault. Bifurcation reduces displacement gradients on individual faults and transfers displacements from faults into the adjacent blocks which subsequently are not rigid. A consequence of such a vertical-axis rotation, therefore, would have been to decrease the divergence in the slip azimuths between the two intersecting fault systems from c. 75° to c. 50° and therefore to increase the compatibility of fault motions between the rift and the NIFS by bringing the strike of the northern end of the NIFS more parallel with its line of intersection with the rift. Global Positioning System (GPS) data provide no evidence that the differential rotation required to produce the observed 25° anticlockwise bend in the NIFS is still operating today (Wallace et al., 2004). As this relict anticlockwise bend of fault strike occurred in the opposite sense of the one expected for a dextral strike-slip fault that terminates through “horsetail type” splaying, here it is argued that this rotation about vertical axis took place during an initial stage of the development of the NIFS–Taupo Rift intersection, when the crust was thicker and colder, in order to increase the compatibility between the fault motions. As the rift evolved, the crust in proximity to the Taupo Rift-NIFS junction becomes thinner through stretching and associated normal faulting and the termination of the strike-slip fault occurs in conjunction with heterogeneous extension distributed outside the main margin of the Taupo Rift.

2.4.2 Slip vector changes due to distributed heterogeneous extension

Data from the NIFS (Table 2.1) suggest that the azimuth and pitch of slip vectors on each of the main faults in this system change by up to 60° from south to north, approaching the fault system termination (i.e. Fig. 2.10c). Here it is suggested that these adjustments in slip vectors on the NIFS are produced by heterogeneous NW-SE directed extension distributed across the off-fault regions to the southeast of the rift margin. How these changes in extension produce the observed changes in fault slip vectors can be visualized with the aid of Figure 2.11 in which the termination of the NIFS and the velocities of the three blocks (AUST, RAUK and AXIR) adjacent to the fault system tip are shown. The boundaries between these three blocks are the NIFS (between RAUK & AXIR blocks) and Taupo Rift (between AUST & RAUK and AUST & AXIR blocks). The Australian

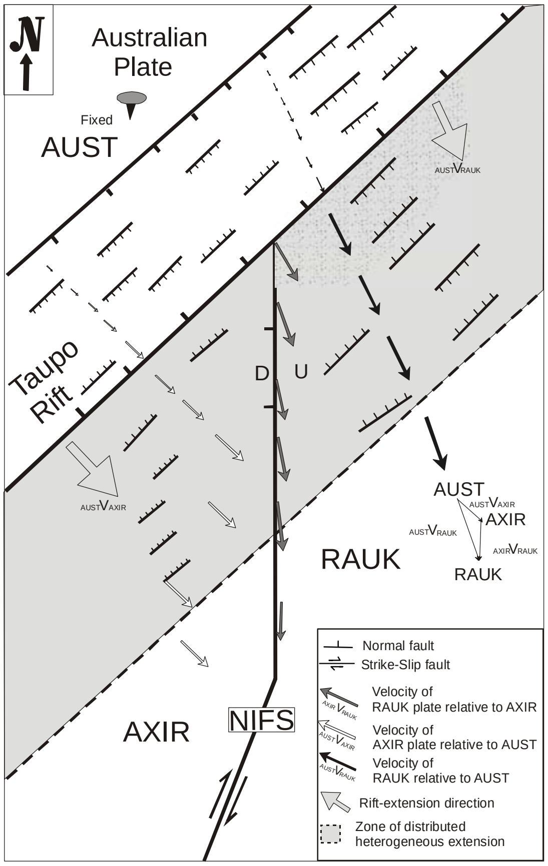

Fig. 2.11 Schematic cartoon illustrating deformation and velocity vectors for the three blocks (i.e. Australian (AUST), Raukumara (RAUK) and Axial Ranges (AXIR)) enclosing the NIFS termination. Regional distributed differential extension outside the rift indicated by grey shading. The velocity field of each block relative to the fixed Australian Plate is indicated. Note that the rates of extension are different, and unevenly distributed, in the footwall and hangingwall blocks (RAUK and AXIR) of the NIFS (dotted pattern indicates higher strain rates). Also note that all faults of NIFS are collapsed onto a single slip surface. The far field velocity circuit is indicated. The differential extension between the RAUK and AXIR blocks reflects the oblique-slip documented in northern NIFS.

block is assumed to be fixed. Within the rift, extension increases to the northeast with increases in the rift extension primarily taking place across the main faults of the NIFS (Wallace et al., 2004; Chapter 3, this study). Within RAUK block the highest rates of extension outside the rift occur close to the main rift-bounding fault (black arrows within stippled region in Fig. 2.11), whereas rates of extension to the southeast of the Taupo Rift are distributed more evenly across the AXIR block (white arrows in Fig. 2.11). The velocity vectors (with respect to a fixed Australian block) across the rift and within the RAUK & AXIR blocks are shown schematically in Figure 2.11. In proximity to the southeastern margin of the Taupo Rift, in the area of localized high strain-rate on RAUK block, the differential extension between RAUK & AXIR blocks requires a local component of extension on the transcurrent fault separating these blocks. This extension introduces a net oblique slip on the faults of the NIFS (Fig. 2.12). Indeed, when each of the faults of the NIFS enters this zone of distributed differential extension, a component of normal dip-slip is added onto its strike-slip (Fig. 2.12). At each location along the NIFS and within this zone of distributed off-fault deformation, therefore, slip vectors are the sum of strike-slip and dip-slip with the total angle through which the pitch of these vectors deflect being dependent on the relative displacements of the interacting fault systems outside the rift and close to the termination of the strike-slip fault system (Fig. 2.12). Because the strike-slip on these faults decreases to the north and the normal dip-slip increases in this direction, the pitch of slip on the fault surfaces steepens towards the NIFS termination. The angular change in the pitch of slip vectors of the terminating fault system will depend on a number of factors, including the difference in strike of the two intersecting fault systems, and the relative values of strike-slip and extension accommodated by the terminating fault. If, for example, no differential extension were accommodated across the northern NIFS outside the rift, then the slip vectors on the strike-slip faults would not change in magnitude or orientation. In such cases the strike-slip fault would simply offset the margin of the rift. Therefore, a key element of the proposed model is that significant NW-SE extension is distributed in a heterogeneous way outside the rift. This heterogeneous extension, which is associated with the formation of the weak Taupo Rift, therefore captures the pre-existing strike-slip faults of the NIFS.

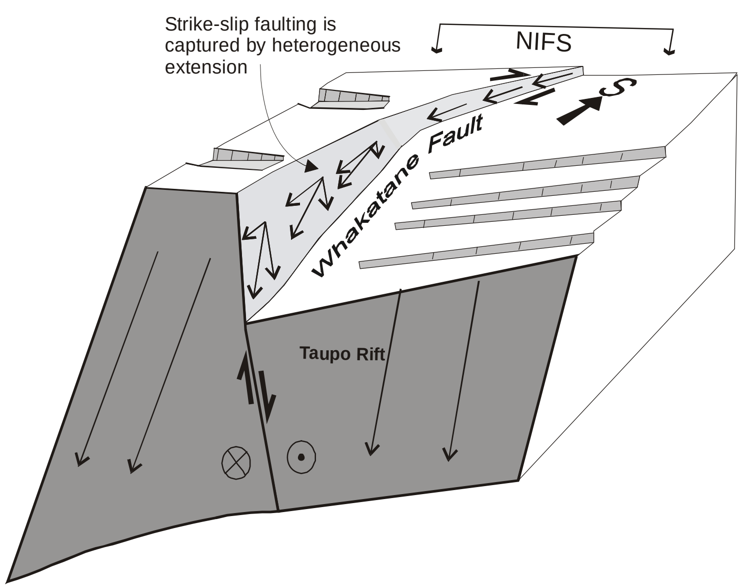

Fig. 2.12 Block diagram illustrating the gradual superimposition of rift-related dip-slip onto strike-slip as the NIFS termination is approached. Given that extension and strike-slip rates increase and decrease towards the Taupo Rift respectively, the pitch of the slip vectors steepens as the northern end of the fault is approached. The sub-parallel slip at the junction of the two fault systems results in the kinematic coherence of the termination.

For the NIFS each of the splays accommodates 1-2 mm/yr of normal dip-slip rate and c. 1 mm/yr of strike-slip rate close to their northern tips (Table 2.1, Fig. 2.4). About 50 km south of the termination of the NIFS the rate of normal dip-slip is approximately zero while the strike-slip rate is 1- 3 mm/yr (Table 2.1, Fig. 2.4). The change in the rates of strike-slip and dip-slip along the main faults of the NIFS, results in significant northward steepening (by up to c. 60°) of the pitch of the slip vectors on the fault plane and in a northward 50° anticlockwise swing in the slip azimuth (Fig. 2.13). These changes of the slip vectors take place onshore for the Waiohau and Whakatane faults and offshore for the Waimana and Waiotahi faults. The change in slip vector orientations in the NIFS results in the sub-parallelism of the slip azimuths on the intersecting fault systems (Fig. 2.13). Slip vectors are also oriented sub-parallel to the line of intersection of the planes of the two fault systems, permitting strike-slip transfer into the rift without lateral offset of the rift margin faults.

Termination of the NIFS may be assisted by fault bifurcation. Within 150 km of their northern end the faults in the NIFS bifurcate, distributing fault slip across a wider area and reducing the strike-slip on individual faults within the system. The Mohaka and Ruahine faults splay northwards into five sub-parallel slip surfaces (Fig. 2.4), resulting in the redistribution of the total c. 7 mm/yr of strike-slip rate onto multiple slip surfaces each accommodating 1-1.5 mm/yr strike-slip. Decreases in strike-slip along the faults of the NIFS arising from fault bifurcation may influence the degree to which the slip vector orientations and magnitudes change approaching the rift, by reducing the required intra-fault block strain rates. The potential influence of fault bifurcation can be rationalized if it is considered that for each fault within the NIFS the rates of normal dip-slip close to the rift is approximately the same (c. 1-2 mm/yr) and (within the uncertainties) appear not to vary with changes in the rates of strike-slip. Therefore, northward steepening in slip vector pitch is dependent on a reduction in strike-slip rate. Where the strike-slip rate is higher than the dip-slip the change in the pitch of the slip vector will be less and additional off-fault strain will be required. If, for example, the northern tip of the NIFS had not bifurcated and all 7 mm/yr strike-slip was carried on a single displacement surface into the rift, the H:V ratio would have remained high (e.g. 3.5-7), and the pitch of the slip vectors on the fault would not have steepened into sub-parallelism with the

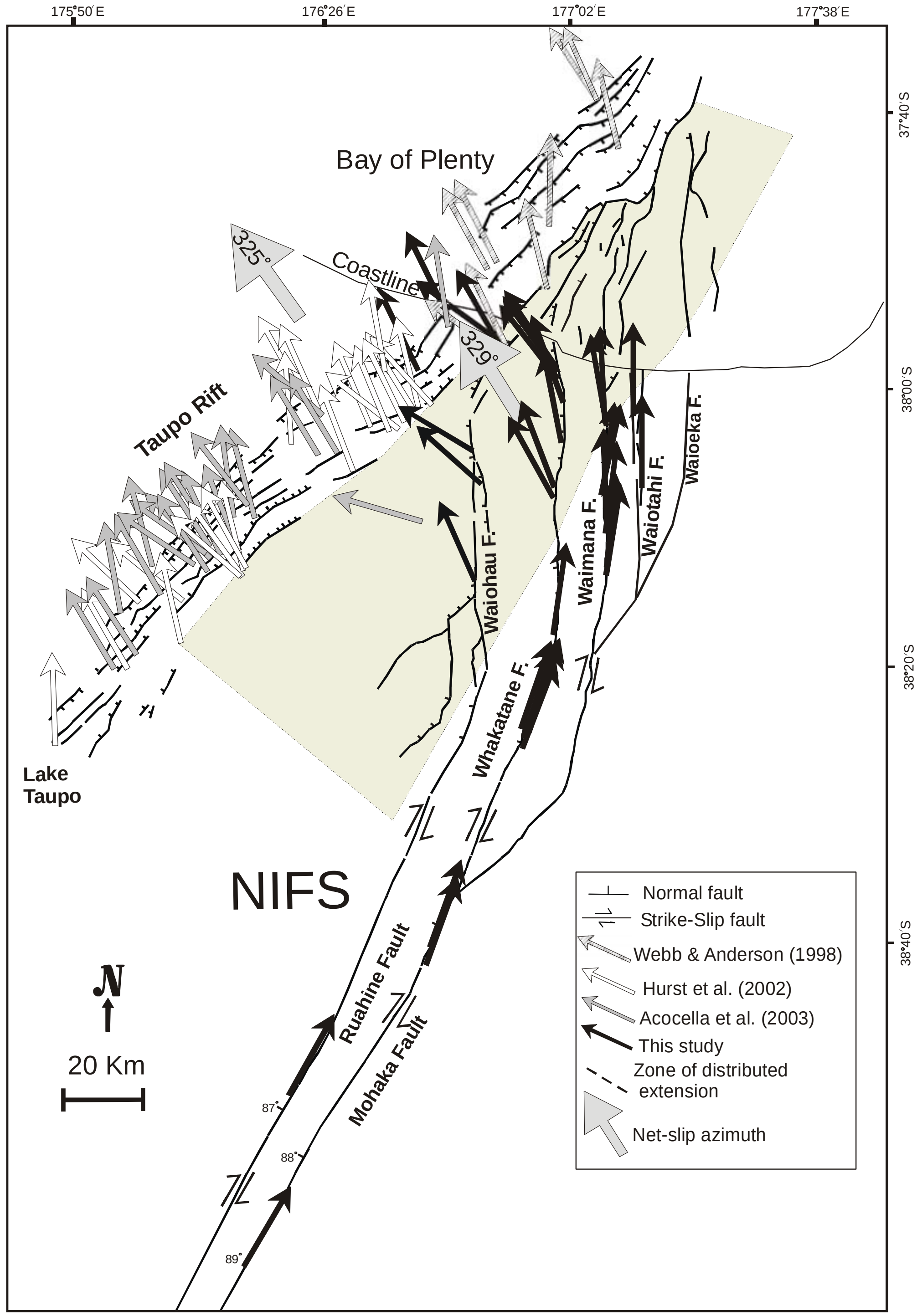

Fig. 2.13 Map showing the azimuths of the net-slip vectors for the NIFS (Hull, 1983; Raub, 1985; Hanson, 1998; this study) and the Taupo Rift (Webb & Anderson, 1998; Hurst et al., 2002; Acocella et al., 2003) which have been derived from a combination of outcrop geology and focal mechanism solutions. Note the anticlockwise deflection in the azimuth of net-slip on the faults in the northern NIFS, such that these become sub-parallel to the slip azimuth documented on the faults within the rift. Regional distributed differential extension outside the rift indicated by grey shading. Large grey arrows represent average values of net-slip azimuths for the onshore Taupo Rift and northern NIFS. Note that the two arrows are approximately parallel.

line of fault intersection, and perhaps the strike-slip fault would have displaced the margin of the rift. Moreover, the bifurcation of the fault results in the distribution of the strike-slip related deformation over larger rock volume and reduces the requirements for strain accommodation on each of the displacement surfaces while the total displacement budget across the fault system is preserved. Lower displacement and displacement gradients on each splay would, therefore, decrease volumetric problems that may arise at the intersection of two fault systems with non-parallel slip vectors.

2.5 Discussion

One question associated with the evolution of the NIFS is why it terminates to the north. To answer this question, the regional kinematics of the North Island and their impact on the kinematics of the NIFS is considered. Along the Hikurangi margin the margin-parallel motion of the oblique subduction of the oceanic Pacific Plate beneath the continental Australian Plate is principally accommodated by clockwise vertical-axis rotations (of the northeast North Island relative to stable Australian Plate) and strike-slip faulting in the overriding Australian Plate (Fig. 2.3) (Walcott, 1989; Wallace et al., 2004). Figure 2.14 illustrates this interrelation between faulting and rotations, as derived by geological and GPS data respectively, by comparing the margin-parallel rate of the relative motion between Australia and Pacific plates with the strike-slip rate on eastern and western strands of the NIFS, the rate of the extension in the rift which is parallel to the margin and the rotational velocity of the northeast North Island relative to stable Australia at six margin-normal transects located at different latitudes (see Figs. 2.3 & 2.4 for location of the transects). Collectively these data suggest that there is a gradual northward increase of the clockwise rotational velocity of the northeast North Island relative to stable Australian Plate from c. 20 to c. 26 mm/yr (Fig. 2.14). At the latitude of the NIFS termination, vertical-axis rotation of the northeast North Island relative to stable Australian Plate accounts for more than 80% of the total Pacific-Australian margin-parallel velocity accommodated across the entire actively deforming plate boundary zone. These high rotational velocities documented in the northeastern North Island (Wallace et al., 2004), significantly decrease the requirement for strike-slip faulting in the upper plate. The northward increase in clockwise vertical-axis rotations of the northeast North Island is accompanied by a decrease in strike-slip on the NIFS in the same direction from c. 7 mm/yr to c. 4 mm/yr (Fig. 2.8). Despite the northward changes on the fault-slip rates and rotational velocities, the summation of those two components (rotational velocity and fault slip rates) on each of the transects, compares favourably to the total margin parallel motion between the Australia-Pacific plates. The slightly higher values of the summed slip and rotational velocities (as compared to the total margin-parallel relative plate motion) may be due to uncertainties in fault-slip and vertical-axis rotational velocities (Fig. 2.14).

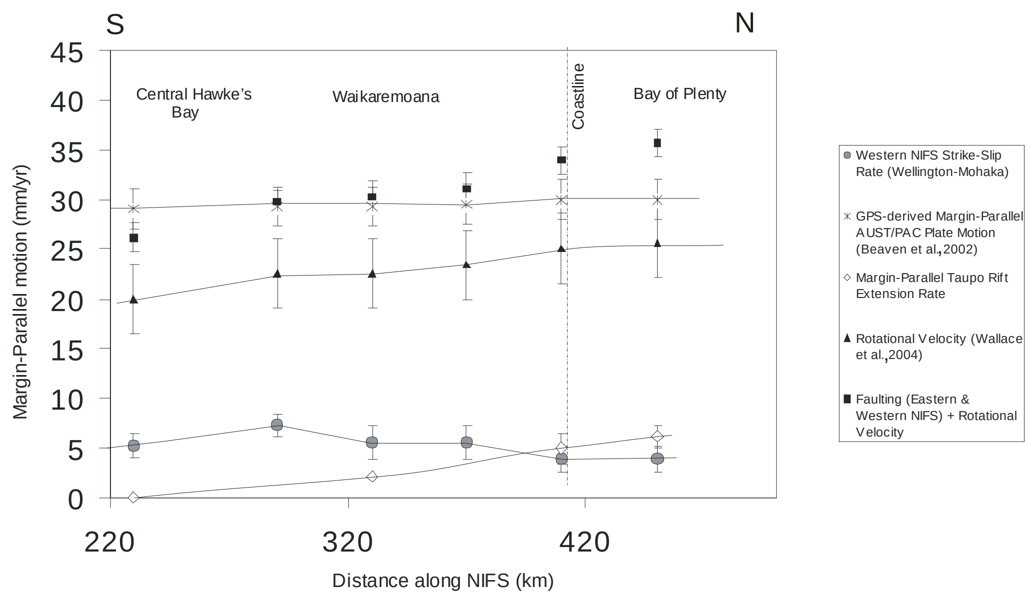

Fig. 2.14 Plot summarizing the horizontal kinematics of the northern North Island in New Zealand. Strike-slip rates for the NIFS are summed for Wellington-Mohaka Fault and its northern splays (Ruahine, Waiohau, Whakatane, Waimana, Waiotahi). The calculated extension rate within the Taupo Rift is estimated for a margin-parallel direction. Rotational velocities show the margin-parallel component of relative plate motion accommodated by clockwise vertical-axis rotations (Wallace et al., 2004). Refer to Wallace et al. (2004) for further discussion of conversion of vertical-axis rotation to margin-parallel motion in mm/yr. Margin-parallel component of the relative Australian/Pacific plate motion from Beavan et al. (2002). Onshore transects are shown in Fig. 2.3 while offshore in Fig. 2.4. Fault slip rate data from: Hull (1983); Raub (1985); Beanland & Berryman (1987); Cutten et al. (1988); Ota et al. (1988); Beanland et al. (1989); Beanland (1989b); Beanland (1995); Van Dissen & Berryman (1996); Berryman et al. (1998); Hanson (1998); Kelsey et al. (1998); Villamor & Berryman (2001); Schermer et al. (2004); Langridge et al. (2005). Distance reference in x-axis is Wellington city.

Although the strike-slip fault system terminates at the edge of the rift, the c. 4 mm/yr strike-slip does not and is transferred into the rift. Because the strike-slip faults in the NIFS strike at 45° to the rift, the slip transferred from the NIFS is expected to produce about 3 mm/yr strike-slip and extension within the rift. The additional extension contributed by the NIFS into the Taupo Rift, therefore, accounts for a significant component of the observed northeastwards increase in extension rates within the rift and is illustrated in Figure 2.15 by the difference between the AUST/AXIR and AUST/RAUK relative plate motion (rates estimated for Euler poles published in Wallace et al., 2004). An additional effect of the increase of the extension along the rift and across its junction with the strike-slip, is the transition from sub aerial to submarine rifting across the intersection zone in Bay of Plenty.

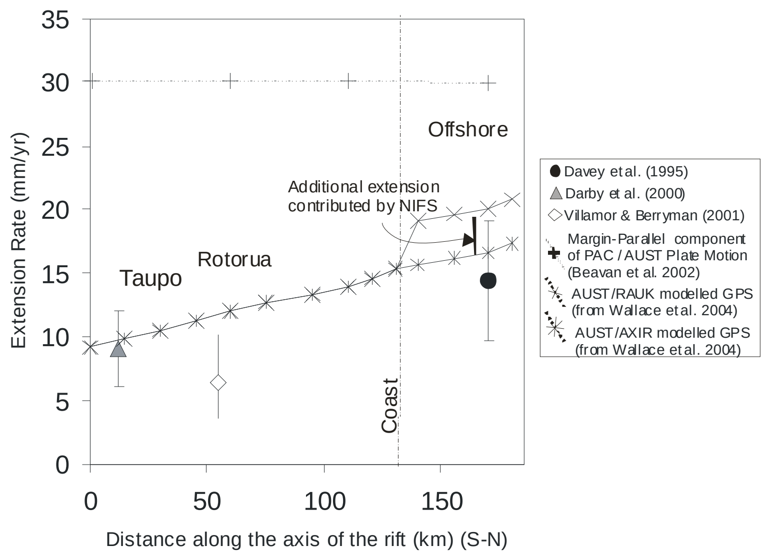

Fig. 2.15 Plot illustrates extension rates within the Taupo Rift plotted against distance along the axis of the rift. Extension transects across the Taupo Rift and the NIFS are indicated in Fig. 2.4. Both GPS and geological data indicate a northward increase of the extension rate (see text for further discussion). The margin-parallel vector of the relative Pacific-Australia plate motion is plotted. Note that the extension rate associated with the NIFS accounts for a significant amount of the difference between the AUST/AXIR and AUST/RAUK relative plate motion (rates estimated from poles published in Wallace et al., 2004). The AUST/AXIR extension rates are calculated c. 30 km to the north of the northern end of AUST/AXIR block boundary in Wallace et al. (2004). Distance reference in x-axis is Lake Taupo.

The strike-slip fault termination accommodated by rift-orthogonal heterogeneous extension may be a generally applicable mechanism for strike-slip terminations globally. For this reason it is worthwhile considering under what circumstances this non-rotational termination mechanism that involves slip vector changes may take place instead of fault-block rotations about vertical axis. The New Zealand example shows that the presence of some distributed heterogeneous off-fault deformation associated with the truncating fault (i.e. the rift) and the relativity in the rates of the two interacting velocity fields (i.e. rates of the truncating fault vs. rates of the terminating strike-slip fault) may play important roles in the functionality of the proposed model. If, for example, all deformation on the truncating fault was confined to a single slip surface, then the displacement fields of the intersecting faults would not overlap and the slip vector on the terminating fault would be constant up to the intersection. Therefore the superimposition of the velocity fields helps produce sub-parallel slip vectors at the fault intersection.

For superimposition of the velocity fields to significantly impact on the slip vector, however, the displacement rate of the strike-slip fault should not significantly exceed the rate associated with the distributed deformation on the truncating fault. The ratio between strike-slip and dip-slip rates controls the total angle through which the pitch of the slip vectors on the strike-slip faults deflects from the horizontal. In circumstances where the strike-slip rates are far larger than the rates of the truncating fault system, slip vector changes will be small and may not bring slip on the terminating fault into sub-parallelism with the line of fault intersection. In circumstances where slip vectors do not swing into sub-parallelism with the line of intersection, vertical-axis rotations of the terminating strike-slip fault relative to the truncating one may become important. The western termination of the strike-slip North Anatolian Fault against rotating blocks that are bounded by normal faults in central Greece (Taymaz et al., 1991) (Fig. 2.10b) is such an example.

Moreover, the rheology of the crust may control whether fault rotations about vertical-axis would be the dominant termination mechanism as compared to non-rotational. Relative vertical-axis rotations between rigid fault blocks and abutting strike-slip fault systems are most likely to occur where the former consists of a cold and thick continental crust (McKenzie & Jackson, 1986; Little & Roberts, 1997) (Fig 2.10a & b). On the contrary, a strike-slip fault system transected by a rift that has hotter and thinner continental crust could terminate by distributed extension outside the rift, allowing the rift to “capture” the strike-slip fault system by means of its differential extension. It is anticipated that the potential for temporal transition from continental to oceanic crust during rifting, will produce localization of the rift-related deformation and therefore, narrower transition zones from strike-slip to dip-slip faulting (Chapter 3, this study). The NIFS in New Zealand, however, has employed both mechanisms, at different times of its evolution, to meet the requirements for sub-parallel slip at the intersection of the two fault systems.

2.6 Conclusions

The strike-slip North Island Fault System in New Zealand intersects the Taupo Rift at 45° and terminates without displacing the margin of the rift. Examination of the northern end of the strike-slip fault system suggests that its termination is accomplished by bending and splaying of the main faults into numerous strands, and by changes in the trend and pitch of the slip vectors by up to 50°. Slip vectors progressively change on faults within the NIFS as they approach the rift. These changes arise because rift-orthogonal extension distributed outside the margins of the rift is accommodated differentially in the footwall and hangingwall blocks of each fault in the NIFS. The combination of rift-related differential extension (dip-slip) and strike-slip results in a steepening of the pitch in the slip vectors on the terminating fault system. Interaction of the velocity fields of the two intersecting fault systems produces a northward gradual sub-parallelism of the slip vectors on the terminating fault system with the line of fault intersection. This sub-parallelism facilitates the transfer of strike-slip displacement into the rift while maintaining the overall coherence of the strike-slip termination. In cases where the superimposition of the two velocity fields does not provide sub-parallelism of the slip vectors of the two intersecting fault systems, fault rotations about vertical axes may take place. In the proposed model such rotations, that have taken place in the past, account for up to one third of the termination mechanism while today rift-orthogonal extension, distributed into the fault blocks outside the rift and differentially accommodated across the northern NIFS, accounts for the primary termination mechanism. Although the NIFS terminates, its displacement is transferred into the Taupo Rift, resulting in a northeastward increase in rift-related extension.

Acknowledgements: A. Nicol, T. Little, J. Walsh and J. Begg provided constructive reviews of this chapter. I am grateful to Fred Davey for providing me with raw seismic-reflection data. Special thanks go to the QMAP team of GNS Science and Hannu Seebeck for assisting in the fieldwork, and to the Maori tribe of Tuhoe for welcoming us into their home: Te Urewera forest.

References

Acocella, V., Spinks, K., Cole, J. and Nicol, A., 2003. Oblique back-arc rifting of Taupo Volcanic Zone, New Zealand. Tectonics, 22, 4, 1045, doi:10.1029/2002TC001447.

Baljinnyan, I. et al., 1993. Ruptures of major earthquakes and active deformation in Mongolia and its surroundings. Memoirs of Geological Society of America, 181, 62pp.

Bayasgalan, A., Jackson, J., Ritz, J. F. and Carretier, S. 1999. Field examples of strike-slip fault terminations in Mongolia and their tectonic significance. Tectonics, 18, 394–411.

Beanland, S. & Berryman, K.R., 1987. Ruahine Fault reconnaissance. New Zealand Geological Survey Report, EDS 109.

Beanland, S., Berryman, K.R. and Blick, G.H., 1989. Geological investigations of the 1987 Edgecumbe earthquake. New Zealand Journal of Geology and Geophysics, 32, 73-91.

Beanland, S., 1989b. Detailed mapping in the Matahina Dam region, New Zealand. New Zealand Geological Survey Client Report, 89/8, 45pp.

Beanland, S., 1995. The North Island Dextral Fault Belt, Hikurangi Subduction margin, New Zealand. PhD Thesis, Victoria University of Wellington, New Zealand.

Beavan, J., Tregoning, P., Bevis, M., Kato, T. and Meertens, C., 2002. Motion and rigidity of the Pacific Plate and implications for plate boundary deformation. Journal of Geophysical Research, 107, B10, 2261, doi:10.1029/2001JB000282.

Bellier, O. & Sébrier, M., 1995. Is the slip rate variation on the Great Sumatran Fault accommodated by fore-arc stretching? Geophysical Research Letters, 22, 15, 1969-1972.

Berryman, K.R., Beanland, S., Cutten, H.N.C., Darby, D.J., Hancox, G.T., Hull, A.G. and Read, S.A.L., 1988. Seismotectonic hazard evaluation for the Mohaka River Power Development. New Zealand Geological Survey Contract Report.

Berryman, K.R., Beanland, S. and Wesnousky, S., 1998. Paleoseismicity of the Rotoitipakau Fault Zone, a complex normal fault in the Taupo Volcanic Zone, New Zealand. New Zealand Journal of Geology and Geophysics, 41, 449-465.

Beu, A.G., 2004. Marine mollusca of oxygen isotope stages of the last 2 million years in New Zealand. Part 1: Revised generic positions and recognition of warm-water and cool-water migrants. Journal of the Royal Society of New Zealand, 32, 2, 111-265.

Cutten, H.N.C., Beanland, S. and Berryman, K., 1988. The Rangiora Fault, an active structure in Hawkes Bay. New Zealand Geological Survey Record, 35, 65-72.

Darby, D.J., Hodgkinson, K.M. and Blick, G.H., 2000. Geodetic measurement of deformation in the Taupo Volcanic Zone, New Zealand: the north Taupo network revisited. New Zealand Journal of Geology and Geophysics, 43, 157-170.

Davey, F.J., Henrys, S. and Lodolo, E., 1995. Asymmetric rifting in a continental back-arc environment, North Island, New Zealand. Journal of Volcanology and Geothermal Research, 68, 209-238.

Davis, G.A. & Burchfiel, C.B., 1973. Garlock fault: an intracontinental transform structure, southern California. Geological Society of America Bulletin, 84, 1407-1422.

De Mets, C.R., Gordon, R.G., Argus, D. and Stein, S., 1994. Effect of recent revisions to the geomagnetic reversal time scale on estimates of current plate motions. Geophysical Research Letters, 21, 2191-2194.

Eden, N.D., Palmer, A.S., Froggatt, P.C., Trustrum, N.A. and Page, M.J., 1993. A multiple-source Holocene tephra sequence from Lake Tutira, Hawke's Bay, New Zealand. New Zealand Journal of Geology and Geophysics, 36, 233-242.

Fleming, C.A., 1955. Castlecliffian fossils from Ohope Beach, Whakatane (N69). New Zealand Journal of Science and Technology Section, B36, 511-522.

Freund, R., 1974. Kinematics of transform and transcurrent faults. Tectonophysics, 21, 93-134.

Freymueller, J. T., Murray, M. H., Segall, P. and Castillo, D., 1999. Kinematics of the Pacific-North America plate boundary zone, Northern California. Journal of Geophysical Research, B, Solid Earth and Planets, 104, 4, 7419-7441.

Froggatt, P.C. & Solloway, G.J., 1986. Correlation of Papanetu Tephra to Karapiti Tephra, central North Island, New Zealand. New Zealand Journal of Geology and Geophysics, 29, 303-314.

Hanson, J.A., 1998. The neotectonics of the Wellington and Ruahine faults between the Manawatu Gorge and Puketitiri, North Island, New Zealand. PhD Thesis, Massey University, New Zealand.

Hayward, B., Cochran, U., Southall, K., Wiggins, E., Grenfell, H., Sabaa, A., Shane, P. and Gehrels, R., 2003. Micropaleontological evidence for the Holocene earthquake history of the eastern Bay of Plenty, New Zealand. Quaternary Science Reviews, 23, 1651-1667.

Hull, A.G., 1983. Trenching of the Mohaka Fault near Hautapu River, Hawkes Bay. New Zealand Geological Survey report, file 831/26.

Hurst, W.A., Bibby, H.M. and Robinson, R.R., 2002. Earthquake focal mechanism in the Central Volcanic Zone and their relation to faulting and deformation. New Zealand Journal of Geology and Geophysics, 45, 527-536.

Jackson, J.A. & Mckenzie, D.P., 1984. Active tectonics of the Alpine-Himalaya Belt between western Turkey and Pakistan. Geophysical Journal of Royal Astronomical Society, 77, 185-264.

Jackson, J., Haines, J. and Holt, W., 1995. The accommodation of Arabia-Eurasia plate convergence in Iran. Journal of Geophysical Research, 100, 15,205-15,219.

Joffe, S. & Garfunkel, Z., 1987. Plate kinematics of the circum Red Sea - a re evaluation. Tectonophysics, 141, 5-22.

Kamata, H. & Kodama, K., 1994. Tectonics of an arc-arc junction: an example from Kyushu Island at the junction of the Southwest Japan Arc and the Ryuku Arc. Tectonophysics, 233, 69-81.

Kelsey, H.M., Cashman, S.M., Beanland, S. and Berryman, K.R., 1995. Structural evolution along the inner forearc of the obliquely convergent Hikurangi margin, New Zealand. Tectonics, 14, 1, 1-18.

Kelsey, H.M., Hull, A.G., Cashman, S.M., Berryman, K.R., Cashman, P.H., Trexler, J.H. and Begg, J.G., 1998. Paleoseismology of an active reverse fault in a forearc setting: the Poukawa fault zone, Hikurangi forearc, New Zealand. Geological Society of America Bulletin, 110, 9, 1123-1148.

Kim, Y.S., Andrews, J.R. and Sanderson, D.J., 2000. Damage zones around strike-slip fault systems and strike-slip fault evolution, Crackington Haven, southwest England. Geosciences Journal, 4, 2, 53-72.

Lamarche, G., Bull, J.M., Barnes, P.M., Taylor, S.K. and Horgan, H., 2000. Constraining fault growth rates and fault evolution in New Zealand. EOS, Transactions, American Geophysical Union, 81 (42), 481, 485, 486.

Lamarche, G., Barnes, P.M. and Bull, J.M., (in press). Faulting and extension rate over the last 20,000 years in the offshore Whakatane Graben, New Zealand continental shelf, Tectonics.

Langridge, R.M, Berryman, K.R. and Van Dissen, R.J., 2005. Defining the geometric segmentation and Holocene slip rate of the Wellington Fault, New Zealand: the Pahiatua section. New Zealand Journal of Geology and Geophysics, 48, 591-607.

Lelgemann, H., Gutscher, M-A., Bialas, J., Flueh, E., Weinrebe, W. and Reichert, C., 2000. Transtentional basins in the western Sunda Strait, Geophysical Research Letters, 27, 21, 3545-3548.

Le Pichon, X. & Francheteau, J., 1976. Plate Tectonics. New York: Elsevier.

Little, T.A. & Roberts, A.P., 1997. Distribution and magnitude of Neogene to present-day vertical-axis rotations, Pacific-Australia plate boundary zone, South Island, New Zealand. Journal of Geophysical Research, 102, B9, 20,447-20,468.

Lowe, J.D. & Hogg, A.G., 1986. Tephrostratigraphy and chronology of the Kaipo Lagoon, an 11,500 year-old montane peat bog in Urewera National Park, New Zealand. Journal of the Royal Society of New Zealand, 16, 1, 25-41.

Lowe, J.D., 1988. Stratigraphy, age, composition, and correlation of late Quaternary tephras interbedded with organic sediments in Waikato Lakes, North Island, New Zealand. New Zealand Journal of Geology and Geophysics, 31,125-165.

Lowe, J.D., Newnham, M.R. and Ward, M.C., 1999. Stratigraphy and chronology of a 15 Ka sequence of multi-sourced silicic tephras in a montane peat bog, eastern North Island, New Zealand. New Zealand Journal of Geology and Geophysics, 42, 566-579.

Manning, D.A., 1995. Late Pleistocene tephrostratigraphy of the eastern Bay of Plenty, North Island, New Zealand. PhD Thesis, Victoria University of Wellington, New Zealand.

Mckenzie, D. & Jackson, J.A., 1986. A block model of distributed deformation by faulting. Journal of Geological Society of London, 143, 349-353.

Molnar, P. & Lyon-Caen, H., 1989. Fault plane solutions of earthquakes and active tectonics of the Tibetan plateau and its margins. Geophysical Research International, 99, 123-153.

Mortimer, N. 1994. Origin of the Torlesse Terrane and coeval rocks, North Island, New Zealand. International Geology Review, 36, 891-910.

Nairn, I.A. & Beanland, S., 1989. Geological setting of the 1987 Edgecumbe earthquake, New Zealand. New Zealand Journal of Geology and Geophysics, 32, 1-13.

Nairn, I.A., Shane, P.R., Cole, J.W., Leonard, G.J., Self, S. and Pearson, N., 2004. Rhyolite magma process of the AD 1315 Kaharoa eruption episode, Tarawera volcano, New Zealand. Journal of Volcanology and Geothermal Research, 131, 265-294.

Newnham, R.M., Lowe, D.J. and Wigley, G.N.A., 1995. Late Holocene palynology and paleovegetation of tephra-bearing mires at Papamoa and Waihi Beach, western Bay of Plenty, North Island, New Zealand. Journal of the Royal Society of New Zealand, 25, 2, 283-300.

Norris, R.J. & Cooper, A.F., 2000. Late Quaternary slip rates and their significance for slip partitioning on the Alpine Fault, New Zealand. Journal of Structural Geology, 23, 2/3, 507-520.

Ota, Y., Beanland, S., Berryman, K.R. and Nairn, I.A., 1988. The Matata Fault: active faulting at the north-western margin of the Whakatane graben, eastern Bay of Plenty. New Zealand Geological Survey record, 35, 6-13.

Pillans, B. & Wright, I., 1992. Late Quaternary tephrostratigraphy from the southern Havre Trough-Bay of Plenty, northeast New Zealand. New Zealand Journal of Geology and Geophysics, 35, 129-143.

Quebral, R.D., Pubellier, M. & Rangin C., 1996. The onset of movement on the Philippine Fault in eastern Mindano: a transition from a collision to a strike-slip environment. Tectonics, 15, 4, 713-726.

Raub, M.L., 1985. The neotectonic evolution of the Wakarara area, Hawke's Bay. MSc thesis, University of Auckland, New Zealand.

Rowland, J.V. & Sibson, R.H., 2001. Extensional fault kinematics within the Taupo Volcanic Zone, New Zealand: soft-linked segmentation of a continental rift system. New Zealand Journal of Geology and Geophysics, 44, 271-283.

Schermer, E.R., Van Dissen, R.J., Berryman, K.R., Kelsey, H.M. and Cashman, S.M., 2004. Active faults, paleoseismology, and historical fault rupture in northern Wairarapa, North Island, New Zealand. New Zealand Journal of Geology and Geophysics, 47, 1, 101-122.

Shane, P. & Hoverd, J., 2002. Distal record of multi-sourced tephra in Onepoto basin, Auckland, New Zealand: implications for volcanic chronology, frequency and hazards. Bulletin of Volcanology, 64, 441-454.

Taylor, S.K., Bull, J.M., Lamarche, G. and Barnes, P.M., 2004. Normal fault growth and linkage in the Whakatane Graben, New Zealand, during the last 1.3 Myr. Journal of Geophysical Research, 109, B2, B02408.

Taymaz, T., Jackson, J. and Mckenzie, D., 1991. Active tectonics of the north and central Aegean Sea. Geophysical Journal International, 106, 433-490.

Thornley, R.S.W., 1996. Tectonics of the Raukumara Peninsula, New Zealand. PhD thesis, Victoria University of Wellington, New Zealand.

Tsutsumi, H. & Okada, A., 1996. Segmentation and Holocene surface rupture faulting on the Median Tectonic Line, southwest Japan. Journal of Geophysical Research, 101, B3, 5855-5871.

Van Dissen, R. & Yeats, R.S., 1991. Hope Fault, Jordan Thrust, and uplift of the seaward Kaikoura Range, New Zealand. Geology, 19, 393-396.

Van Dissen, R.J. & Berryman, K.R., 1996. Surface rupture earthquakes over the last ~1000 years in the Wellington region, New Zealand, and implications for ground shaking hazard. Journal of Geophysical Research, 101, B3, 5999-6019.

Villamor, P. & Berryman, K., 2001. A late Quaternary extension rate in the Taupo Volcanic Zone, New Zealand, derived from fault slip data. New Zealand Journal of Geology and Geophysics, 44, 243-269.

Walcott, R.I., 1989. Paleomagnetically observed rotations along the Hikurangi margin of New Zealand. In Kissel, C. and Laj, C. (eds). "Paleomagnetic rotations and continental deformation" Kluwer Academic Publishers, Dordrecht, p. 459-471.

Wallace, L.M., Beaven, J., McCaffrey, R. and Darby, D., 2004. Subduction zone coupling and tectonic block rotations in the North Island, New Zealand. Journal of Geophysical Research, 109, B12, 2406, doi:10.1029/2004JB003241.

Webb, T. & Anderson, H., 1998. Focal mechanisms of large earthquakes in the North Island of New Zealand: slip partitioning at an oblique active margin. Geophysical Journal International, 134, 40-86.

Wilmhurst, J.M., Eden, D.N. and Froggatt, P.C., 1999. Late Holocene forest disturbance in Gisborne, New Zealand: a comparison of terrestrial and marine pollen records. New Zealand Journal of Botany, 37, 523-540.

Wilson, C.J.N., Houghton, B.F., Mcwilliams, M.O., Lamphere, M.A., Weaver, S.D. and Briggs, R.M., 1995. Volcanic and structural evolution of Taupo Volcanic Zone, New Zealand: a review. Journal of Volcanology and Geothermal Research, 68, 1-28.

Woodward-Clyde, 1998. Matahina Dam strengthening project. Geological completion report to Electricity Corporation of New Zealand.

Zachariasen, J. & Van Dissen, R., 2001. Paleoseismicity of the northern Horohoro Fault, Taupo Volcanic Zone, New Zealand. New Zealand Journal of Geology and Geophysics, 44, 391-401.

Table 2.1: Summary of the geometric and kinematic attributes of the faults at the sites studied. *Distance from Bay of Plenty coast; [†]Re-interpreted data; [‡]Fleming (1955) and Beu (2004); # Calibrated ages from Zachariasen & Van Dissen (2001); [∂]Real Time Kinematics; [a]Tephrochronology; [b] 14 C dating.

Site No	Site Name	Grid Ref (NZMS 260)	Strike (°)	Dip (°)	Distance along Fault (km)*	Dextral separation (m)	Vertical separation (m)	H:V ratio	Down Side	Offset feature	Data source	Age # (max-min) (kyr)	Net Slip Rate (mm/yr)	Pitch (°)	Reference
WAIOHAU-RUAHINE															
1	Matahina gr	V16/453360	360	65±5	23	-	700±100	-	W	Basement	Gravity profile	1000± 200[‡]	0.7±0.2 (throw rate)	-	This study
2	Tasman 1	V16/453298	350	65±5	29	-	c. 7 (min)	0.4	E & W	Scarp	Trench	17.8 [a,b]	0.7±0.2	70	Woodward-Clyde 1998†
3	Cornes tr	V16/472252	360	65±10	34	-	c. 7	-	W	Scarp	Trench	25 [a,b]	-	-	Woodward-Clyde 1998†
4	Cornes	V16/472251	360	65±10	34.2	3±1	8±1	0.4	W	Stream	RTK[∂]	13.8 [a]	0.7±0.2	69	This study
5	Waiohau1	V16/471246	008	-	34.7	3±2	4±2	0.75	W	Stream	Tape measure	-	-	-	This study
6	Waiohau2	V16/475213	040	-	38.2	-	5±3	-	W	Scarp	Tape measure	-	-	-	This study
7	Troutebeck	V17/446057	010	c. 70	55	-	c. 9	0.5	W	Scarp	Trench	17.6 [a]	0.7±0.2	63	Beanland 1989b
8	Whirinaki	V17/401916	340	-	79.1	c. 24	-	-	W	Stream	Air photo	-	-	-	This study
9	Whirinaki1	V17/401913	340	-	79.4	38	-	-	W	Spur	Air photo	-	-	-	This study
10	Whirinaki2	V17/402914	340	-	79.3	c. 24	-	-	W	Spur	Air photo	-	-	-	This study
11	Whirinaki3	V17/397928	340	-	78	c. 24	-	-	W	Spur	Air photo	-	-	-	This study
12	Skips Hut	V18/404692	-	-	92.8	-	-	-	W	Basement	Mapping	-	-	-	This study
13	Gorge Stream	U20/083061	020	-	130	c.10	c.5	2	W	River margin	Tape measure	c. 3.5 [a]	1.5±0.5	-	Beanland & Berryman 1987
14	Davis	U20/092077	015	85	163	55	10	5.5	W	Scarp	Trench	c. 13.8[a]	-	10	Hanson 1998
WHAKATANE-MOHAKA															
15	F1	W14/787761	360	60±10	c. - 40	-	c. 610	-	W	Basement	Seismic reflection profiles	600± 30[‡]	c. 1.2 (dip-slip)	-	Davey et al. 1995†
16	Poroporo	W15/599532	-	65±5	6	-	660±100	-	W	Basement	Gravity profile	600± 30[‡]	1.1±0.2 (throw rate)	-	This study
17	Pukehoko	W15/614459	345	-	9	26±5	32±2	0.81	W	Spur	Tape measure	17.6-30[a]	2.2±1	51	This study
18	Anemos	W15/614455	345	-	9.2	23±5	-	-	W	Spur	Tape measure	17.6-30[a]	-		This study
19	Galini	W15/615452	345	-	9.4	5±4	5±1	1	W	Spur	RTK	-	-	45	This study

Site No	Site Name	Grid Ref (NZMS 260)	Strike (°)	Dip (°)	Distance along Fault (km)*	Dextral separation (m)	Vertical separation (m)	H:V ratio	Down Side	Offset feature	Data source	Age # (min-max) (kyr)	Net Slip Rate (±mm/yr)	Pitch (°)	Reference
20	Tophouse	W15/617450	345	68±10	9.5	22±5	30±2	0.73	W	Spur	RTK	17.6-30[a]	2.2±0.9	54	This study
21	Karenza	W15/618444	345	-	9.8	25±5	-	-	W	Spur	Tape measure	17.6-30[a]	-	-	This study
22	Awahou1	W16/622389	360	-	15.3	5±3	-	-	W	Stream	RTK	17.6-30[a]	-	-	This study
23	Awahou2	W16/621388	355	70±10	15.4	14±6	13±2	1.07	W	Spur	RTK	17.6-30[a]	1±0.5 (min)	43	This study
24	Awahou grav	W16/622346	-	70±5	18	-	500±100	-	W	Basement	Gravity profile	600±30[‡]	0.8±0.4 (throw rate)	-	This study
25	Te Whetu	W16/619327	010	68±2	19	-	10±1	-	W	Scarp	Trench	c.30[a,b]	0.4 (min)	-	This study
26	Noti	W16/615298	010	-	24.5	15±7	15.5 (min)	0.97	W	Spur	RTK	25-17.6[a]	1.5 (min)	46	This study
27	Te Marama	W16/603193	350	55±5	37	-	1.7±0.3	-	W	Terrace margin	Trench	Post c. 0.8[b]	-	-	This study
28	Matangi Mariri	W16/603177	342	-	38	4±0.5	2.7±0.5	1.5	W	Stream on river terrace	Tape measure	< 3.5[a]	-	34	This study
29	Waikare	W17/608984	009	65±2	57	-	-	-	W	Basement	Striations	-	-	70 & 50 NW	This study
30	Ru-1/ Armyra	W17/556802	018	81±5	75.1	20±2	3±1	6.67	E	River margin	RTK/ Trench	c. 6-9.5[a,b]	3±1.1	9	This study
31	Ru-2	W17/555802	020	-	75.3	22±2	2±0.5	11	E	Stream	RTK	c. 6-9.5[a,b]	3.1±1	5	This study
32	Thalassa / Helios	W17/555800	020	85±5	75.3	22±2	2±0.5	11	E	Stream	Trench	c. 6-9.5[a,b]	3.1±1	-	This study
33	Ru-3	W17/555800	020	-	75.6	8.5±6	-	-	-	Stream	RTK	-	-	-	This study
34	Ru-4	W17/555799	017	-	75.9	9.5±5	-	-	-	Stream	RTK	-	-	-	This study
35	Ru-5	W17/555799	020	-	76	17±7	2±0.5	14	E	Spur	RTK	-	-	7	This study
36	Ru-7	W17/559811	020	-	74	15±2	2±0.5	7.5	W	Spur	Tape measure	-	-	8	This study
37	Ru-8	W17/559810	020	-	74.3	12±5	-	-	-	Stream	RTK	-	-	-	This study
38	Ru-9	W17/558809	020	-	74.4	15±5	-	-	E	Spur	RTK	-	-	-	This study

Site No	Site Name	Grid Ref (NZMS 260)	Strike (°)	Dip (°)	Distance along Fault (km)*	Dextral separation (m)	Vertical separation (m)	H:V ratio	Down Side	Offset feature	Data source	Age # (min-max) (kyr)	Net Slip Rate (±mm/y)	Pitch (°)	Reference
39	Ru-10	W17/558808	020	-	74.6	5.5±1.5	1.2±0.3	4.5	W	Spur	RTK	-	-	14	This study
40	Ru-11	W17/557805	022	-	74.9	14±1	-	-	-	Stream	Tape measure		-	-	This study
41	Ru-13	W17/561817	020	-	73.6	11±5	-	-	-	Stream	RTK	-	-	-	This study
42	Ru-15	W17/565828	028	-	73	15±8	2±1	7.5	E	Spur	RTK	-	-	10	This study
43	Ru-16	W17/566829	028	-	72.8	-	2±0.5	-	E	Scarp	RTK	-	-	-	This study
44	Ru-17	W17/566829	028	-	72.75	4.5±2.5	-	-	W	Stream	RTK	-	-	-	This study
45	Ru-18	W17/567832	022	-	72.5	15±5	3±1	5	E	Spur	RTK	-	-	11	This study
46	Opuhou	W17/562821	020	-	73.3	-	0.5±0.2	-	W	Scarp	Tape M.	-	-	-	This study
47	Opuhou1	W17/562821	020	-	73.2	90±10	-	-	-	Stream	Tape measure	-	-	-	This study
48	Kakanui	W17/551795	048	-	76.5	-	2±1	-	SE	Scarp	Tape measure	-	-	-	This study
49	Te Hoe	V19/379395	020	87	132	-	2.9	-	-	Scarp	Trench	9.5[a]	3.5±0.8	-	Hull 1983
50	N. Te Hoe	V19/373400	020	88	131.7	c. 40	3±1	11.70	W	Stream	Tape measure	9-13[a,b]	3.7±0.3	5	Berryman et al. 1988
51	Syme	V20/137986	030	85	170	60	6	10	E	Scarp	Trench	10.1[a,b]	-	-	Hanson 1998
52	McCool 1	U21/010746	020	89	196	66	4	16.5	W	Stream	Trench	16.8± 0.5[a,b]	c. 4.2	-	Hanson 1998
53	C. Mohaka	U22/876485	024	90	225	c. 33	4.5	7.5	W	River margin /Scarp	Tape measure	10-13[a]	3.2±0.6	8	Raub 1985
54	Hughes 1	T24/377761	030	87	314	60±5	1.5±1	40	SE	Stream	Tape measure	c.10.8[b]	4.9-6.2(max) (dextral)	-	Langridge et al. 2005
55	Bennet	T24/372753	037	86	315	50±6	-	-	NW	Stream	RTK	c. 8.5[b]	5.1-6.7 (min) (dextral)	-	Langridge et al. 2005
56	Emerald Hill	R27/873102	062	-	c. 400	104-940	10-90	c. 10	SE	River margins	Tape measure	14 - 140[a]	6-7.6 (dextral)	-	Van Dissen & Berryman 1996
WAIMANA															
57	F2	W14/817760	360	60±5	c. - 40	-	390±100	-	W	Basement	Seismic reflection profiles	600± 30[‡]	c. 0.8 (dip-slip)	-	Davey et al. 1995†
58	Ohope	W15/769485	-	68±3	0.1	-	500±100	-	W	Basement	Gravity profile	600± 30[‡]	0.8±0.4 (throw rate)	-	This study

Site No	Site Name	Grid Ref (NZMS 260)	Strike (°)	Dip (°)	Distance along Fault (km)*	Dextral separation (m)	Vertical separation (m)	H:V ratio	Down Side	Offset feature	Data source	Age # (min-max) (kyr)	Net Slip Rate (mm/yr)	Pitch (°)	Reference
59	Ohiwa1	W15/748458	-	-	3.1	-	2	-	-	Holocene sediments	Drill hole	2.7-8 [a]	-	-	Hayward et al. 2003
60	Ohiwa2	W15/743438	-	-	5.2	-	2	-	-	Holocene sediments	Drill hole	2.7-8 [a]	-	-	Hayward et al. 2003
61	Ohiwa3	W15/737426	-	-	6.5	-	2	-	-	Holocene sediments	Drill hole	2.7-8 [a]	-	-	Hayward et al. 2003
62	Don1	W16/725377	350	-	11.3	24±15	-	-	-	Stream	RTK	-	-	-	This study
63	Don2	W16/725379	350	-	11.2	13.5±2	2±0.5	6.75	W	River margin	RTK	15-23 [a,b]	0.8±0.4	-	This study
64	Moana-Iti	W16/725379	360	88±2	11.2	20±3	2±1	10	W	Scarp	Trench-RTK	15-23 [a,b]	1.2±0.5 (max)	-	This study
65	Moana	W16/725379	357	47±2	11.25	20±3	2±1	10	W	Stream	Trench-RTK	15-23 [a,b]	1.2±0.5 (max)	0 & 20	This study
66	Don3	W16/727371	345	-	11.6	19±2	-	-	-	Stream	Tape measure	-	-	-	This study
67	Stevens2	W16/728342	350	-	15	20±2.5	-	-	W	Stream	Tape measure	-	-	-	This study
68	Nukuhou-gr	W16/724328	-	>80	15.3	-	< 50 m	-	W	Basement	Gravity profile	600± 30	-	-	This study
69	SH2	W16/716329	010	-	15.5	-	4±1	-	W	Scarp	Tape measure	-	-	-	This study
70	Tom1	W16/707293	018	-	18.8	20±5	-	-	W	Spur	Tape M.	-	-	-	This study
71	Timoti 2	W16/703278	014	-	20.3	13±7	2±1	6.5	E	Spur	RTK	9.5-30 [a]	1.2±0.9	9	This study
72	Timoti 1	W16/702276	010	-	20.4	12±6	2±1	6	E	Spur	RTK	9.5-30 [a]	1.1±0.9	9	This study
73	Sonny Riser	W16/704170	360	-	31	13±6	2.5±0.5	5.2	E	River terrace riser	RTK	13.8 [a] (max)	1±0.5 (min)	11	This study
74	Sonny scarp	W16/704180	360	-	30.5	-	5±1	-	E	Scarp	RTK				This study
75	Ahirau 4	W16/705158	007	-	32.3	10±5	2±1	5	W	Stream	RTK	8-13.8 [a]	1.2±0.8	11	This study
76	Ahirau1	W16/705161	008	82	31.6	-	2±1	-	E	Scarp	Trench	9,5 [a,b]	-	-	This study
77	Ahirau2	W16/705161	352	70	31.7	-	2±1	-	E	Scarp	Trench	9,5 [a]	-	-	This study
78	Tuhora 2	W16/705160	352	-	32.1	18±2	-	-	E	Spur	Tape M.	-	-	-	This study

Site No	Site Name	Grid Ref (NZMS 260)	Strike (°)	Dip (°)	Distance along Fault (km)*	Dextral separation (m)	Vertical separation (m)	H:V ratio	Down Side	Offset feature	Data source	Age # (min-max) (kyr)	Net Slip Rate (mm/yr)	Pitch (°)	Reference
79	Waiiti	W16/704145	010	-	33.8	5.5±2	2.5±0.5	2.2	W	River margin	Tape measure	5.6 (max) [a]	1. 2±0.5 (min)	24	This study
80	Panoanoa	W18/672902	020	-	60	330±50	-	-	-	Stream	Air-photo	-	-	-	This study
81	Hopuruahine	W18/632701	020	-	80.5	-	-	-	-	Basement	Fault gouge	-	-	-	This study
82	Mangatoatoa	W18/515537	020	-	100	-	5±2	-	W	Scarp	Mapping	-	-	-	This study
WAIOTAHI															
83	F3	W14/898756	360	60 ±10	c. - 40	-	300±70	-	W	Basement	Seismic reflection profiles	600± 30‡	0.6±0.2 (dip-slip)	-	Davey et al. 1995†
84	F4	W14/912755	360	60 ±10	c. - 40	-	330±70	-	W	Basement	Seismic reflection profiles	600± 30‡	0.7±0.2 (dip-slip)	-	Davey et al. 1995†
85	Waiotahi Beach	W15/775485	-	68±3	0.1	-	300±50	-	W	Basement	Gravity profile	600± 30‡	0.5±0.1 (throw rate)	-	This study
86	Waiotahi N	W16/766397	350	-	9	16±1	2±0.5	8	W	Stream	Tape measure	17.6 [a]	1±0.1	7	This study
87	Waiotahi n	W16/767396	340	-	9.1	-	5±1	-	W	Scarp	Tape measure	-	-	-	This study
88	Waiotahi S	W16/761308	340	-	18	17±3	2±0.5	8.5	W	Stream	Tape measure	13.8-17.6 [a]	1. 2±0.4	7	This study
WHAKATANE GRABEN															
89	Edgecumbe1	V15/477502	055	55±5	9.2	-	4.7±0.8 (dip slip)	-	W	Scarp	Trench	Today-1.8 [a,b]	2.6±1.4	-	Beanland et al. 1989
90	Edgecumbe 2	V15/477502(?)	055	55±5	6-12	-	2.5±0.2	-	W	Cultural features	Topo-graphic survey	March 1987	-	55 (plunge)	Beanland et al. 1989
91	Rotoitipakau	V15/345436	055	60	20.5	-	11.5±0.7 (dip slip)	-	W	Scarp	Trench	5.6 [a,b]	2.2±0.25	-	Berryman et al. 1998
92	Braemar	V15/358480	045	60	16	-	5.5±2.2 (dip slip)	-	E	Scarp	Trench	8.7 [a,b]	0.7±0.3	-	Beanland 1989b
93	Matata	V15/414602	045	60	1.5	-	9.2	-	E	Scarp	Trench	5.6[a,b]	1.8±0.2	-	Ota et al. 1988

Site No	Site Name	Grid Ref (NZMS 260)	Strike (°)	Dip (°)	Distance along Fault (km)*	Dextral separation (m)	Vertical separation (m)	H:V ratio	Down Side	Offset feature	Data source	Age # (min-max) (kyr)	Net Slip Rate (mm/yr)	Pitch (°)	Reference
94	White Island Fault	c. W15/670676	c. 040	67±2	c. -20	-	-	-	W	Scarp	Seismic reflection profiles	-	-	-	Taylor et al. 2004
95	R1	c. W15/650708	c. 057	61±2	c. -20	-	830±130 (max)	-	W	Scarp	Seismic reflection profiles	1340± 510	1.4±0.3	-	Taylor et al. 2004
96	R2	c. W15/648719	c. 057	61±2	c. -20	-	830±130 (max)	-	W	Scarp	Seismic reflection profiles	1340± 510	1.4±0.3	-	Taylor et al. 2004
97	R3	c. W15/642727	c. 057	61±5	c. -20	-	830±130 (max)	-	W	Scarp	Seismic reflection profiles	1340± 510	1.4±0.3	-	Taylor et al. 2004

Grid Ref (NZMS 260)	site(s)	SiO2	TiO2	Al2O3	FeO	MnO	MgO	CaO	Na2O	K2O	Cl	TOTAL	n	Tephra ID	Cal. Age (kyr)	Sample code	Reference
W15/617450	17-21	78.0244	0.15031	12.4825	0.91618	0.09809	0.1472	0.82431	3.84558	3.29132	0.21708	100	10	Rotoehu	c. 50	Q3	5,10
W15/614455	17-21	78.2043	0.12524	12.3396	0.89701	0.09401	0.1281	0.78996	3.85677	3.40353	0.1644	100	10	Rotoehu	c. 50	An	5,10
W16/615298	26	76.4835	0.16363	13.1423	1.1511	0.13221	0.2395	1.08962	4.52813	2.88348	0.18804	100	10	Mangaone	c.30	NF	5
W16/621388	23	77.249	0.16396	13.103	1.06603	0.08211	0.189	1.01461	4.04158	2.91515	0.17345	100	10	Mangaone	c.30	Awa Manga	5
W16/703278	71 & 72	77.2377	0.17561	13.047	1.20911	0.06691	0.17219	1.03117	4.00386	2.87956	0.18268	100	10	Mangaone	c.30	TimotiD	5
W17/555800	30-32	78.2898	0.13843	12.2588	1.17833	0.08503	0.1196	1.09413	3.57948	3.07656	0.17625	100	10	Kawakawa	26	T(0)	1,10
W16/615298	26	78.045	0.14204	12.509	1.02861	0.05229	0.14274	0.88094	3.60364	3.41326	0.17835	100	10	Te Rere	25	Noti B	1,9
W16/615298	26	77.3678	0.13499	12.5283	0.8623	0.08383	0.18264	0.83069	3.96904	3.88264	0.15776	100	10	Rerewhakaaitu	17,6	Ng	2,3,4,7,9
W15/617450	17-21	78.1355	0.13941	12.3442	1.0234	0.03204	0.15078	0.9065	3.60833	3.51732	0.14559	100	10	Rerewhakaaitu	17,6	TH/c	2,3,4,7,9
W15/617450	17-21	78.2619	0.13246	12.4529	1.07122	0.05692	0.12495	0.97149	3.47012	3.27404	0.1799	100	10	Rerewhakaaitu	17,6	GB	2,3,4,7,9
W16/705158	75	78.0802	0.12937	12.6656	0.81349	0.09411	0.119	0.81546	3.78036	3.34705	0.15674	100	10	Waiohau	13,8	Ah4-C	2,4,7,9
W16/704170	73 & 74	78.3415	0.12545	12.5896	0.85871	0.07752	0.1116	0.80137	3.69121	3.2543	0.1359	100	10	Waiohau	13,8	Auger4	2,4,7,9
W16/725379	63-65	78.1579	0.13303	12.7822	0.93085	0.06105	0.14001	0.84139	3.61339	3.17302	0.16719	100	10	Waiohau	13,8	T1-Moana	2,4,7,9
W17/555800	30-32	77.9107	0.14586	12.3728	0.95374	0.08546	0.12688	0.87341	3.97888	3.37208	0.18149	100	10	Rotoma	9,5	T1	2,3,7,9
W16/705161	76 & 77	78.5925	0.13731	12.5177	0.93153	0.0497	0.12037	0.81598	3.31757	3.36959	0.14433	100	10	Rotoma	9,5	TuhD	2,3,7,9
W16/725379	63-65	77.7384	0.1214	12.9795	0.9096	0.09503	0.12707	0.77064	3.66643	3.43703	0.15371	100	10	Rotoma	9,5	M29	2,3,7,9
W16/704145	79	77.8385	0.12046	12.3925	0.78971	0.0855	0.10924	0.7204	3.95576	3.82794	0.15746	100	10	Whakatane	5,6	Sonny1	2,7

Table 2.2 Representative electron microscope analyses of late Quaternary tephras. For details of each site refer to Table 2.1. Glass chemistry determined using Electron microprobe (10 μm beam diameter). Analyses recalculated to 100% (volatile-free). Tephra correlations from 1 = Froggatt & Solloway (1986); 2 = Lowe & Hogg (1986); 3 = Lowe (1988); 4 = Eden et al. (1993); 5 = Manning (and references therein) (1995); 6 = Newnham et al. (1995); 7 = Lowe et al. (1999); 8 = Wilmhurst et al. (1999); 9 = Shane & Hoverd (2002); 10 = Pillans & Wright (1992); 11 = Nairn et al. (2004); n= Number of analyses per sample.

CHAPTER THREE

DISPLACEMENT TRANSFER BETWEEN INTERSECTING STRIKE-SLIP AND EXTENSIONAL FAULT SYSTEMS

Abstract

Interaction and displacement transfer between active intersecting strike-slip (or transform) and extensional fault systems are examined. Outcrop data from a well preserved strike-slip fault and rift intersection in New Zealand are compared to a global dataset of 13 such intersections in both continental and oceanic crust. Displacement transfer between strike-slip and normal faults is typically accomplished by gradual changes of fault orientations and slip vectors close to the intersection zone. For two and three plate configurations these changes result in sub-parallelism of the slip vectors of the component faults with their line of intersection. The dimensions of the area over which fault-strike and slip vectors change is principally controlled by the extent to which displacements on the dominant of the two intersecting fault systems are confined to a single slip surface or distributed across a zone. Where slip is spatially distributed, the region in which the two displacement fields are superimposed produces transtension and associated oblique slip. This distributed off-fault deformation facilitates the development of a quasi-stable configuration of the fault intersection region, maintaining both the regional geometry and kinematics of the intersection zone which, in many cases, would not be possible for rigid-block translations. The dimensions of the transition zone are larger for continental crust than for oceanic crust because oceanic crust is thinner, fault geometries in oceanic crust are simpler two-plate configurations and the slip vectors of the component intersecting fault systems are sub-parallel.

3.1 Introduction

Fault interactions are an essential feature of all fault systems and are generally accommodated either by hard-linkage, in which faults physically link, or by soft-linkage, in which displacement is transferred by distributed (i.e. ductile) deformation of the rock volume between faults. In circumstances where faults are active synchronously, interaction promotes displacement transfer and kinematic coherence within a fault system (Dahlstrom, 1969; Walsh & Watterson, 1991). Kinematic coherence (i.e. interdependence of displacement rates of all faults of the interacting fault systems) would be expected where different types of faults co-exist in close proximity and collectively accommodate regional strains imposed, for example, by plate motions. Despite its likely importance, kinematic coherence may be difficult to document using outcrop datasets which are rarely complete. This chapter explores how kinematic coherence and associated displacement transfer are achieved between intersecting strike-slip (or transform) and extensional fault systems in the upper crust.

Figure 3.1 illustrates two fundamental plate geometries for intersecting strike-slip and normal fault systems: 1) Geometries in which both normal and strike-slip faults terminate in the intersection zone, equivalent to a two-plate configuration (Fig. 3.1a). These two-plate geometries may occur at the tips of large strike-slip or transform faults, where strike-slip displacements are transferred into a rift, such as occurs between the termination of the Sumatra Fault and the Sunda Strait Rift (Fig. 3.1b). 2) Geometries in which one of the fault systems terminates against the other are analogous to triple junctions where the faults define three plates with summed slip azimuths across the intersection equal to zero (Fig. 3.1c). The Sinai triple junction in the Arabian Peninsula represents such a case (Fig. 3.1d).

Three-plate configurations appear to be stable in two-dimensions (i.e. map-view) when the two arms of the strike-slip (or transform) fault are in alignment (T-T-R triple junction) (McKenzie & Morgan, 1969) or when the two arms of the rift intersect at 90° to each other (R-R-T triple junction) (York, 1973). Under any other configuration, such a triple junction is considered to be unstable and requires temporal adjustments in the angle of fault intersection (e.g., by vertical-axis rotations) and/or changes in the velocity slip azimuths between each rigid block. For two-plate geometries, however, changes from normal to strike-slip faulting can be achieved by rigid block translations independent of the fault intersection angle and do not necessarily require changes of slip azimuth across the intersection zone (Fig. 3.1a).

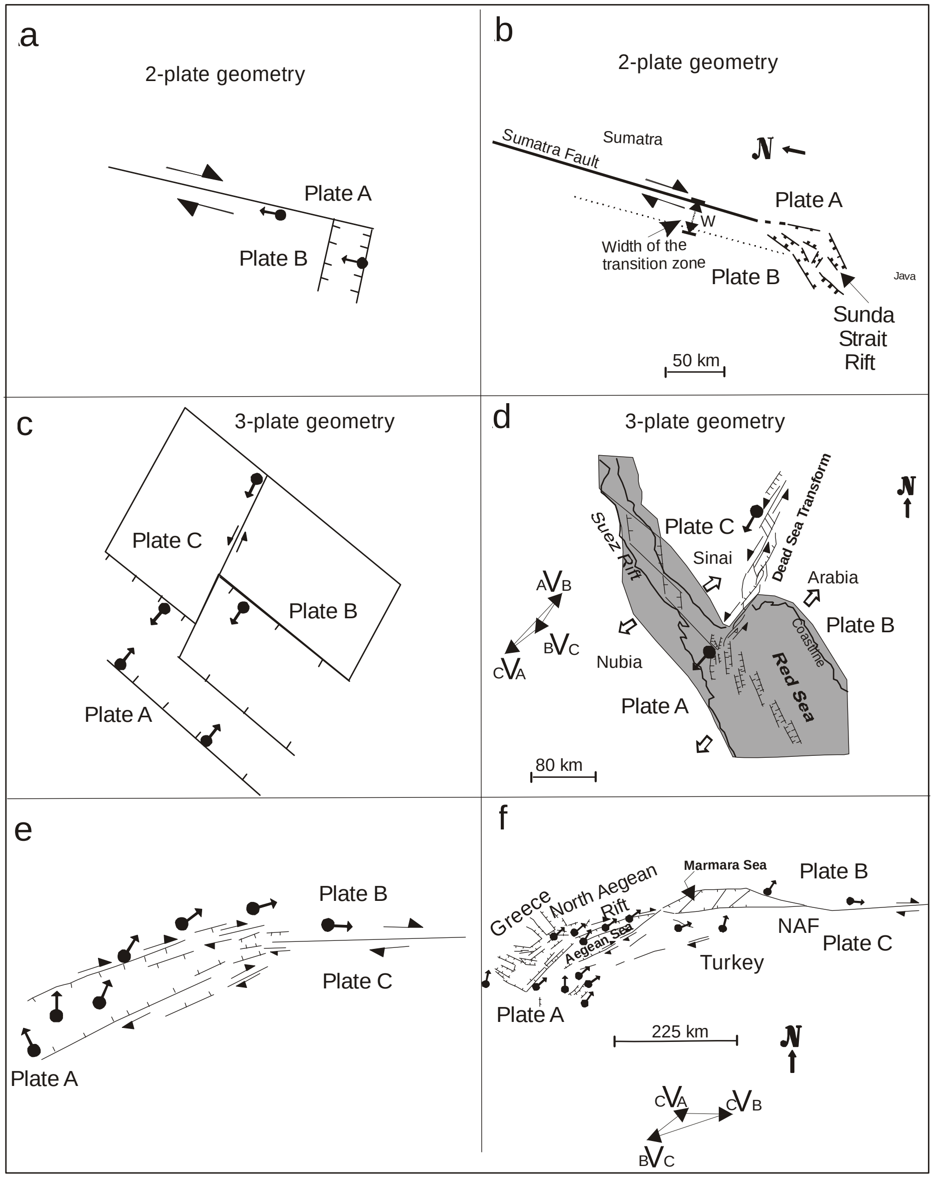

Fig. 3.1 a) Displacement transfer model for a 2-plate intersection assuming rigid block translations. **b)** Schematic fault map illustrating the southern termination of the Sumatra Fault against the Sunda Strait Rift. The change of strike of the normal faults at the tip of the strike-slip fault occurs within a transition zone, the width of which is shown (modified after Lelgemann et al. (2000)). **c)** Displacement transfer model for a three-plate configuration assuming rigid block translations. **d)** Schematic fault map of the Red Sea Rift – Dead Sea Transform – Suez Rift triple junction (modified after Courtillot et al. (1987)). Large unfilled arrows show the extension direction of rifting while the grey shaded area outlines the extent of the rift. **e)** Schematic diagram illustrating displacement transfer through gradual rotation of slip vector azimuths towards parallelism across the intersection zone of the fault systems. **f)** Schematic fault map of the intersection of the North Anatolian Fault (NAF) and the North Aegean Rift, Eastern Mediterranean. Slip vectors, derived from focal mechanisms across the intersection of the two fault systems (Taymaz et al., 1991), indicate the direction of motion of the north side of the faults relative to the south. Note the gradual westward rotation of the slip vector azimuths towards the intersection (faults within the western Aegean domain from Papanikolaou et al., 2002). Horizontal projections of slip vectors are indicated by the filled circles and attached arrows for all figures.

For three-plate geometries, the acute angle between the strikes of the intersecting fault systems can vary from 0-90º. For sub-perpendicular fault intersection angles, such as the intersection of the Red Sea Rift and the Dead Sea Transform on the Arabian Peninsula (Fig. 3.1d), the relative slip azimuths on the intersecting strike-slip and normal faults are approximately parallel to one another and the change in fault kinematics could be achieved by rigid-block translations with displacements confined mainly to the principal fault surfaces (Fig. 3.1b). For non-orthogonal intersections in which the slip vectors on the intersecting faults are not parallel, as is the case at the intersection between the North Anatolian Fault and the North Aegean Rift (Fig. 3.1f), displacement transfer requires rotation of the slip azimuth in the region where the faults intersect. In the upper portion of continental crust these readjustments of slip vectors in the intersection zone must be accompanied by distributed off-fault deformation on small-scale faults (King, 1983) (Fig. 3.1e). Whether displacement transfer between intersecting strike-slip and normal faults (i.e. three plate geometries) is more often accommodated by rigid-block translation or by distributed deformation in the intersection zone remains unresolved.

This chapter investigates how displacement is transferred between synchronous intersecting regional strike-slip and normal fault systems with two or three plate configurations. In particular, the chapter examines how displacement is transferred between dip-slip and strike-slip faults, to what extent displacement transfer is achieved by different patterns of off-fault deformation and how the style of displacement transfer impacts on the life expectancy, and therefore stability, of the intersection zone. To answer these questions I draw on detailed data from the intersection of the strike-slip North Island Fault System (NIFS) and the Taupo Rift in onshore New Zealand and four more such intersecting strike-slip and normal fault systems in continental crust, and from nine mid-ocean ridge-transform fault intersections. The majority of these intersecting fault systems, including the New Zealand example, occur in active plate boundary zones and carry slip rates of at least 5 mm/yr. Collectively these case studies indicate the occurrence of displacement transfer between different types of faults, the propensity for slip vectors to change plunge and azimuth across the intersection zone of a two and three-plate configuration respectively, and the requirement for significant distributed deformation within the main fault blocks of these intersecting systems (on the scale of regional fault maps).

3.2 Intersecting Fault Systems

Intersecting regional strike-slip and normal faults that are presently active and moving synchronously are found globally (i.e. Joffe & Garfunkel, 1987; Taymaz et al., 1991; Chapter 2, this study). To gain a better understanding of how these intersections form and evolve, three strands of data are utilized: 1) geometric and kinematic data from the intersection of the strike-slip North Island Fault System (NIFS) and the Taupo Rift in the North Island of New Zealand (which is analogous to a triple junction), 2) published data for four examples of active intersecting strike-slip and normal faults in continental crust with two or three-plate geometries and, 3) published data for nine mid-ocean ridge-transform fault intersections.

The Taupo Rift and the NIFS in the North Island of New Zealand**,** combine to provide an excellent example of active intersecting regional strike-slip and normal fault systems which strike at c. 45º to each other (Fig. 3.2). The onshore parts of these two fault systems extend along their strikes for approximately 200 km (rift) and 450 km (NIFS). Close to their intersection, the Taupo Rift and the NIFS accommodate about 10-15 and c. 4 mm/yr of extension and right lateral strike-slip, respectively (Wallace et al., 2004; Chapter 2, this study). These fault systems are key elements of the Hikurangi margin, along which the Pacific Plate is being obliquely subducted westward beneath the Australian Plate (Fig. 3.2-inset). The NIFS is the principal zone of strike-slip faulting in the overriding Australian Plate. It breaks up into five main splays (i.e. Waiohau, Whakatane, Waimana, Waiotahi and Waioeka faults) approaching the northern termination where it intersects with the Taupo Rift. Within the intersection zone the strike-slip faults of the NIFS accommodate an increasing component of normal dip-slip in a northward direction in proximity to the Taupo Rift (Beanland, 1995; Chapter 2, this study), suggesting that the boundary between the two intersecting fault systems is gradational.

The transition between the rift and the strike-slip NIFS straddles the coastline, and provides one of the few active examples worldwide where elements of both intersecting fault systems are well exposed onshore (Fig. 3.2). In the plate tectonics nomenclature the kinematics of this intersection is comparable to that of a ridge-ridge-transform triple junction. Figure 3.2 illustrates the three plates A, B, C comprising this configuration and presents the relative velocity circuit for these three blocks (i.e. ${}_{B}V_{C,}$ ${}_{C}V_{A}$ and ${}_{A}V_{B}$) based on fault slip data (Webb & Anderson, 1998; Hurst et al., 2002 Acocella et al., 2003; Chapter 2, this study). Within the uncertainties in the data, the far-field fault slip azimuths form a closed triangle, but their corresponding boundary velocities (i.e. ab, bc, and ca) do not meet at a point suggesting that this configuration is not stable in 2D. The kinematics of this intersection would be stable if the two rift systems intersected at right angles (York, 1973) and/or their plate velocities were parallel to one another. These requirements would be achieved if the strike of the strike-slip fault rotated to become normal to the rift or if slip azimuths of each fault system swing in trend to become parallel to one another.

Data from Chapter 2 are utilised to document how changes in fault orientations and late Quaternary slip-vectors might be producing a quasi-stable three-plate configuration today. In detail, changes in fault attitudes, displacement vectors and displacement rates are documented on both fault systems in proximity to the intersection zone during the last 500 kyr. Ninety-seven sites were studied along the main faults in the northernmost 250 km of the NIFS and the northern 50 km of the Taupo Rift and across its intersection with the NIFS (Fig. 3.2). Fault attitudes (i.e. strike and dip) for both fault systems were estimated from a combination of outcrop geology, air-photo interpretation, trenching, seismic-reflection lines and gravity profiles, while slip directions are calculated from the 3D offset of various geomorphic markers (e.g. ridges, abandoned stream channels and terrace margins) and slickenside striations. Slip rates on the faults were calculated using radiocarbon dating and identification of key dated volcanic tephras on displaced landforms. Uncertainties on fault orientations and displacement rates are indicated on Figs 3.2, 3.4 & 3.6b. Details of these data are included in Chapter 2 and Appendix I.

In addition to the New Zealand example, four regions of continental crust in which strike-slip and normal fault systems intersect are examined. Three of the continental examples (i.e. the Red Sea and Dead Sea in Arabian Peninsula, the Median Tectonic Line and the Hohi Volcanic Zone in Japan and the North Anatolian Fault and the North Aegean Rift in eastern Mediterranean), provide some analogies to triple junctions, while the Sumatra case more closely resembles a simple two-plate intersection. To complement these data I also draw on a large volume of literature on the development of ridge-transform intersections in oceanic crust (Lachenbruch & Thompson, 1972; Crane, 1976; Fujita & Sleep, 1978; Choukroune et al., 1978; Fox & Gallo, 1984; Gallo et al., 1984; Goud & Karson, 1985; MacDonald et al., 1986; Gallo et al., 1986; Pockalny et al., 1988; Taylor et al., 1994). Although oceanic crust at mid-ocean ridges is hotter, thinner and stronger than most continental crust (Kohlstedt et al., 1995), the structural evolution of ridge-transform intersections appears to be comparable to those in continental crust. Thus, while upper crustal deformation mechanisms in the intersection zones of these faults can differ between oceanic and continental crust, the kinematic requirements for displacement transfer may not. The details of each example in this worldwide database, which includes the examples presented in Fig. 3.1, are summarized in Table 3.1. These examples share many features in common with the New Zealand case but also highlight differences in the way in which upper crustal fault mosaics accommodate two and three plate fault junctions (e.g., Figs 3.1 & 3.2).

In the following sections it is considered in some detail how various geometrical attributes (such as fault strike, slip azimuth and fault displacement) of intersecting fault systems adjust as the zone of intersection is approached. These changes provide important constraints on how the fault systems interact and on the deformation required to achieve displacement transfer.

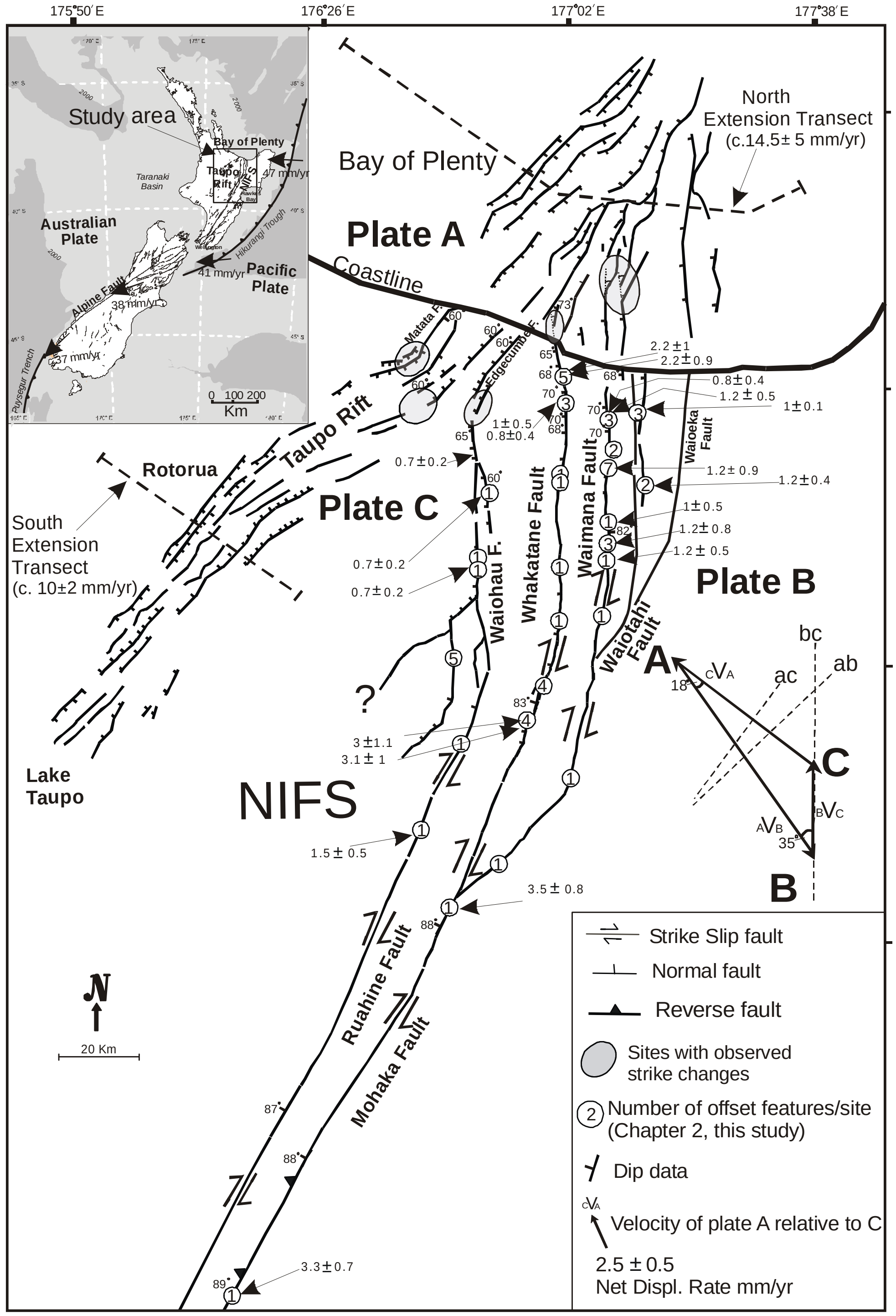

Fig. 3.2 Map of the intersection of the strike-slip North Island Fault System (NIFS) and the Taupo Rift in the North Island of New Zealand. Dashed transects indicate locations of extension profiles across the Taupo Rift (south) and at the northern end of the intersection zone of the two fault systems (north) (see text for discussion). The three plates (A, B, C), their relative velocities (${}_{B}V_{C}$, ${}_{C}V_{A}$, ${}_{A}V_{B}$) and the loci of reference frame velocities (ab, bc, ac) are indicated. The displacement rate data are from Chapter 2 in this study and the references therein. Offshore faults from Davey et al., (1995), Lamarche et al., (2000) and Taylor et al., (2004). Inset: New Zealand plate boundary setting; arrows indicate relative plate motion. The study area is located on the upper plate of the Hikurangi subduction margin.

Name	Location	Dominant fault system	Angle between fault strikes (°)†	Angle between far field velocity vectors(°)*	Horizontal Cumulative Slip Rates (mm/yr)		Width of Transition Zone (km)	Length of Transition (km)	References
					Dominant	Secondary			
Taupo Rift-NIFS	New Zealand	Rift	c. 45	c. 45	10-15	4-6	45-55	60-90	1,2,3,4
NAF-Aegean Rift	Eastern Mediterranean	Strike-Slip	0-20	90-70	17-23	25-35	50-70	100-200	5,6
Red Sea Rift-Dead Sea	Arabian Peninsula	Rift	65-75	20-10	7.5	6	80-120	100-140	7,8,9
Sumatra-Sunda Rift	Sumatra	Strike-Slip	40-50	50-40	6±4	<<10	c.20	40-60	10,11
MTL/Hohi VZ	Japan	Strike-Slip	35-45	55-45	<<4-9	>>1	15-25	70-80	12,13
Vema FZ / MAR	Mid-Atlantic Ridge	Oceanic Transform	88-90	2-0	24	24	9-12	9-12	14,15
Clipperton FZ / EPR	East Pacific Rise	Oceanic Transform	88-90	2-0	110	110	4-10	4-10	16
Willaumez FZ / Manus ridge	Manus Basin	Oceanic Transform	c. 70	c.20	c. 103	c. 103	5-11	10-15	17
Kane FZ / MAR	Mid-Atlantic Ridge	Oceanic Transform	84-88	6-4	30	28	5-14	5-14	18
Oceanographer FZ/ MAR	Mid-Atlantic Ridge	Oceanic Transform	83-87	7-3	60	60	10-14	10-14	19
Tamayo FZ / EPR	East Pacific Rise	Oceanic Transform	88-90	2-0	60	60	4-6	4-6	20
TF-A / MAR	Mid-Atlantic Ridge	Oceanic Transform	75-80	10	c. 20	c. 20	2-4	2-4	21,22
TF-B / MAR	Mid-Atlantic Ridge	Oceanic Transform	88-90	2-0	c. 20	c. 20	6-8	6-8	21
Siqueiros FZ / EPR	East Pacific Rise	Oceanic Transform	88-90	2-0	60	60-69	5-15	5-15	23

Table 3.1 Worldwide database presents the details of the 14 examples utilized in this study. 1=Beanland, 1995, 2=Villamor & Berryman, 2001, 3=Wallace et al., 2004, 4= Chapter 2, this study, 5=Taymaz et al., 1991, 6=Papanikolaou et al., 2002, 7=Joffe & Garfunkel, 1987, 8=Picard, 1987, 9= Moustafa, 1997, 10=Bellier & Sébrier, 1995, 11=Lelgemann et al., 2000, 12=Kamata & Kodama, 1994, 13=Tsutsumi & Okada 1996, 14=Macdonald et al., 1986, 15=Van Andel et al., 1971, 16=Gallo et al., 1986, 17=Taylor et al., 1994, 18=Pockalny et al., 1988, 19=Otter, 1984, 20=Gallo et al., 1984, 21=Goud & Karson, 1985, 22=Choukroune et al., 1978, 23= Crane, 1976. MAR=Middle Atlantic Ridge, EPR=East Pacific Rise, NIFS= North Island Fault System, NAF=North Anatolian Fault, MTL=Median Tectonic Line, †Acute

3.3 Fault intersection geometries

Intersections between strike-slip and normal fault systems in continental crust are characterised by significant variability in their geometries (Fig. 3.3). The strikes of the two intersecting fault systems may range from being sub-parallel to sub-perpendicular, the dominant fault system (i.e. the system not terminated at the intersection or the longer of the two fault systems) may be strike-slip or normal while the number of faults in each system may also change (two vs. three plate geometry). Figure 3.3 excludes the situation in which neither fault system terminates at the intersection; that is, where the fault systems are entirely mutually cross-cutting, because review of the literature suggests that this four-plate geometry is rare in nature.

The New Zealand example of intersecting faults has a three-plate configuration in which rifting truncates strike-slip faulting and the component fault systems strike at about 45° to each other outside the intersection zone (Fig. 3.2). The strike and dip of faults in the NIFS change northwards towards its intersection with the rift. The average strike of the NIFS throughout the North Island is NNE-SSW, with the northernmost c. 100 km of the faults striking N-S (Fig. 3.2). This N-S strike changes abruptly again within 5-15 km of the intersection between strike-slip faults and the main rift-bounding fault, with each of the main strike-slip faults swinging clockwise in strike by up to 20-35° (Fig. 3.2). This abrupt change in strike may result from the "capture" of the strike-slip fault system by the NE-SW striking normal faults (outside the main rift-bounding fault) as has been observed in brittle-ductile analogue modeling (Basile & Brun, 1999). Similarly, the NE to ENE striking normal faults of the Taupo Rift swing anticlockwise in strike by up to c.20° to a more NNE strike, as they approach the intersection with the strike-slip faults of the NIFS (Fig. 3.2). The net effect of these changes in the strike of the two fault systems in proximity to their mutual intersection is a reduction of the divergence of strike between the two systems from 35-45º to <10º.

These changes in fault strike occur in conjunction with a change in the dip of faults in the NIFS. To the south, some 120 km from the rift, the strike-slip faults at the ground surface dip steeply at 80-90° either to the east or west. These dips gradually decrease northwards towards the rift until they reach values of c. 60-70° to the west within 10-20 km of the rift (Fig. 3.4). The lower dips at the northern end of the NIFS are comparable with those measured on normal faults in the upper crust and at the ground surface in the rift by seismic-reflection profiles and fault trenching (Chapter 2, this study and references therein) (Figs 3.2 & 3.4). The observed changes of fault strikes and dips suggest a tendency for both fault systems to become sub-parallel in the proximity of their intersection. This trend is mirrored by the strike-slip fault system acquiring an increasing dip-slip component northwards towards the rift intersection (see next section for further discussion).

The changes in the geometries of intersecting faults in the New Zealand example are similar to changes in intersecting strike-slip and normal fault systems elsewhere in the world. For example, at the three-plate junction of the extensional Hohi Volcanic Zone (HVZ) and the strike-slip Median Tectonic Line (MTL), the strike of the secondary fault system (in this case the rift) swings by up to 20-35° within c.70 km of the intersection zone to become sub-parallel to the strike-slip fault system (Fig. 3.5a). The MTL also swings in strike (c.20°) across the intersection zone towards sub-parallelism with the faults of the rift (Fig. 3.5a). The change in the strike of normal faults in the HVZ within the intersection zone is consistent with a component of off-fault distributed dextral strike-slip forming up to 20 km NW of the MTL. Similarly, at the intersection of the strike-slip North Anatolian Fault and the North Aegean Rift (Fig. 3.1f), both the strike-slip fault and the rift axis change in orientation by about 20º as they approach the zone of fault system intersection (Taymaz et al., 1991; Papanikolaou et al., 2002).

In continental crust where both normal and strike-slip faults terminate at the intersection (i.e. two-plate configurations) similar strike transitions between the two fault systems have also been documented in a number of locations and settings. The southern tip of the strike-slip Sumatra Fault, for example, appears to terminate in the Sunda Strait Rift. Distal to the intersection zone the strikes of the two fault systems differ by 40-50° (Fig. 3.1b) (Lelgemann et al., 2000). High resolution bathymetry data across the intersection zone reveal a swing in the strike of the rift-bounding normal faults at c. 50 km from the southern tip of the Sumatra Fault. This change in fault strike, results in sub-parallelism in the attitudes of the faults within the rift and the Sumatra Fault near the intersection zone (Lelgemann et al., 2000).

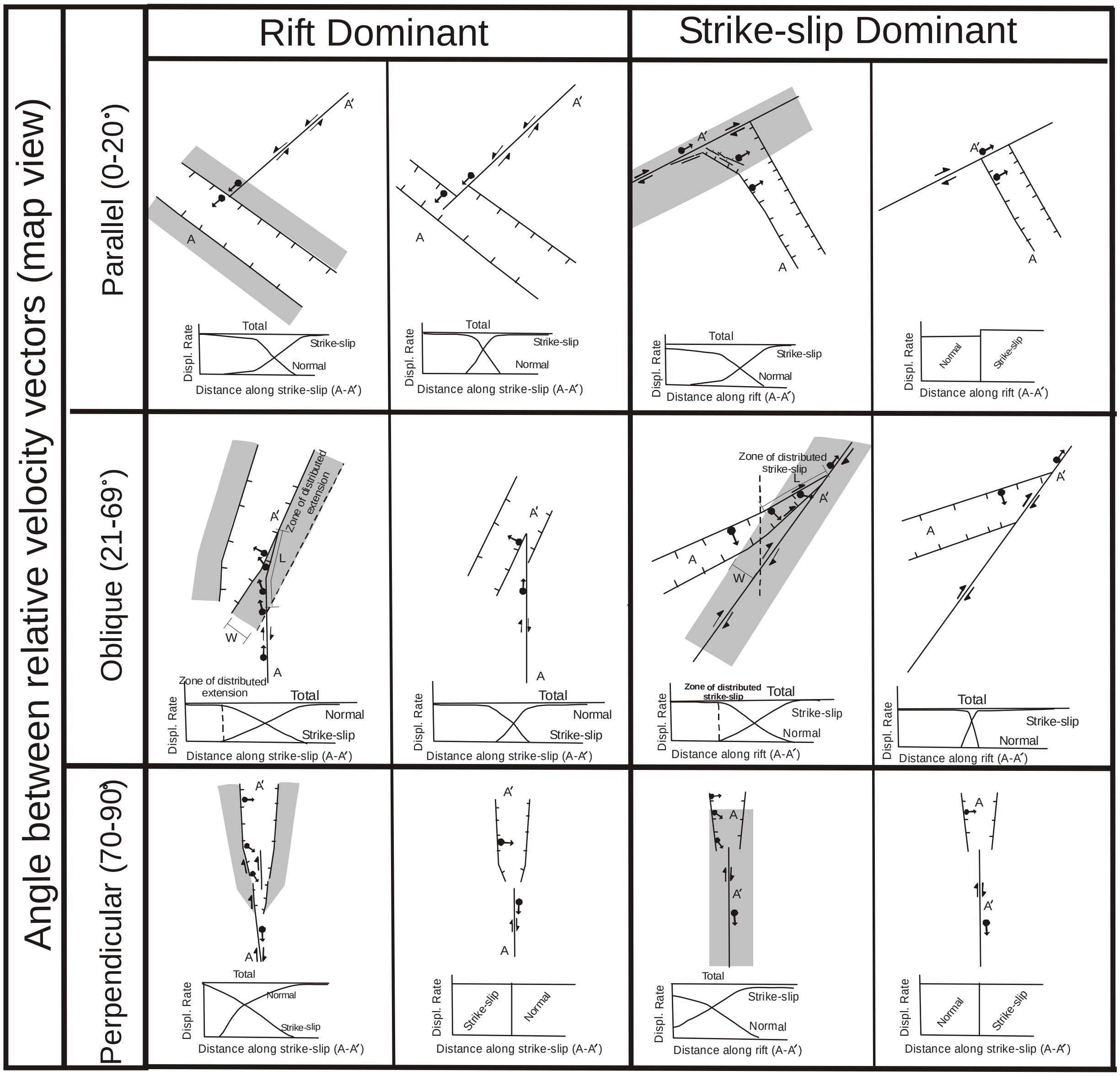

Fig. 3.3 Schematic diagram illustrating end-member geometries and slip vector azimuths for intersecting strike-slip and normal fault systems. In cases of 3-plate geometries, the dominant fault system is the system not terminated at the intersection (i.e. through-going), whilst for the 2-plate configuration it is the longer of the two fault systems. Schematic displacement profiles along the secondary fault system are indicated and permit comparison of the gradients between different intersecting geometries. Total displacement rate is uniform and conserved in its entirety across the intersection. The gradient is assumed to be equal and opposite on the component faults (these conditions may not always be met in Nature). Regions of distributed off-fault deformation are shaded grey. Horizontal projections of slip vectors are indicated by the filled circles and attached arrows.

The changes in the geometries of the intersecting fault systems described above are all for intersection angles of ≤ 50°. In cases where the component fault systems are pure strike-slip and dip-slip and strike perpendicular to each other, either under a three or two-plate configuration, their slip azimuths will be in near alignment. Because of this sub-parallelism strike-slip and normal faults intersecting at 90° can slip simultaneously without requiring significant changes in fault strike to effect the required displacement transfer. This argument is consistent with the apparent lack of change in strike of the Dead Sea Transform as it approaches the Red Sea Rift (e.g. Figs 3.1c, 3.1d & 3.3) but appears to be inconsistent with many Ridge-Transform systems in oceanic crust. In these systems, which most often strike perpendicular to each other, normal faults bounding the walls of the rift (ridge) typically swing in strike by 30-90° towards the strike of the transform fault (MacDonald et al., 1986 and references therein) (Fig. 3.5b) resulting in sub-parallelism of the component fault systems where they intersect. Changes in strike of normal faults approaching a transform have been documented in both slow and fast spreading centers (MacDonald et al., 1986; Gallo et al., 1986; Taylor et al., 1994) and appear to be independent of displacement rates. The swing in fault strikes has been inferred to result from local re-orientation of the stress trajectories through the transmission of transform-related distributed shear into the spreading center domain (Fox & Gallo, 1984; Morgan & Parmentier, 1984; Basile & Brun, 1999). The amount of curvature of each fault is thought to depend on the ratio of the rift normal to transform shear stress exerted on the rock volume that encloses the fault (Morgan & Parmentier, 1984).

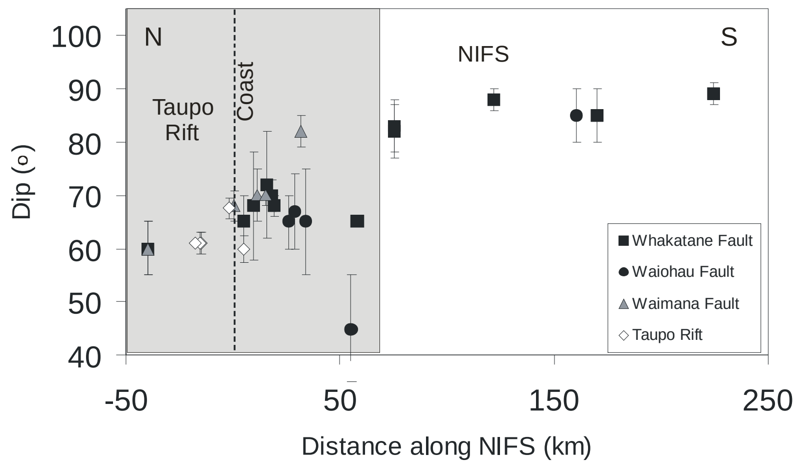

Fig. 3.4 Plot of measured dips for the main faults of the NIFS (Waiohau, Whakatane, Waimana) and for the main offshore faults of the Taupo Rift versus along-strike distance measured relative to the coastline. Dip data derived from trenches, seismic-reflection and gravity profiles and outcrop geology (see Table 2.1 from Chapter 2 (this study) and the references therein). Symbols differentiate dips for each fault. Strike distance over which changes in dip of the faults are documented is shaded grey.

3.4 Slip Vectors

A requirement of synchronous slip on intersecting strike-slip and normal faults is that the orientations of two or more of the principal incremental strain axes must flip by 90° across the intersection zone. Where strike-slip and dip-slip faults form a three-plate configuration and do not intersect at an angle of 90º, the azimuth of their slip vectors must be non-parallel. For these geometries to remain stable, changes in the orientations of the principal strain axes in the intersection zone must be accompanied by a change in the fault-slip vectors, which in turn requires non-rigid block (i.e. internal) deformation. In a two-plate setting, however, where the slip azimuths of each fault system are already parallel, the motions can take place through rigid block translations across the region of fault intersection without any change in slip vector azimuth. Two and three plate intersections share the requirement that the slip vector must change from chiefly horizontal to chiefly dip-slip across the zone of fault intersection. For these reasons, only the change in the plunge of slip vectors can be compared between two and three plate geometries.

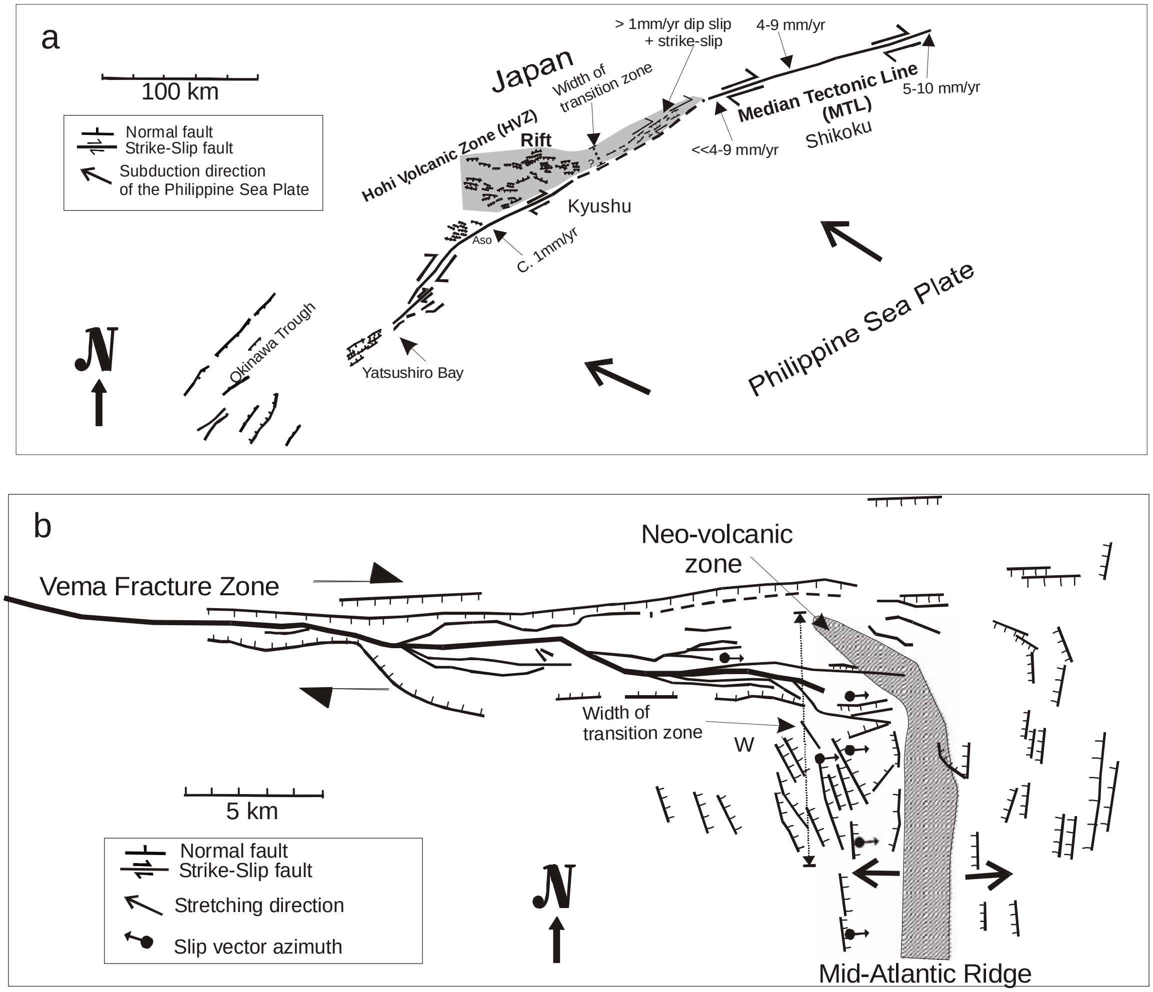

Fig. 3.5 a) Intersecting strike-slip (Median Tectonic Line) and normal faults (Hohi Volcanic Zone) on Kyushu and Shikoku islands, southwest Japan (modified after Kamata & Kodama (1994)). A swing in strike of the normal and strike-slip faults across the intersection zone occurs over a c. 75 km long transition zone (dotted line), which is defined as the distance along the strike of the secondary fault over which the normal faults rotate their slip vector azimuths. Black arrows represent the subduction direction of the Philippine Sea Plate. **b)** The eastern intersection of the Vema Fracture Zone with the Mid-Atlantic Ridge (modified after Macdonald et al. (1986)). The swing in strike of the axial normal faults, approximately 10 km from the intersection (dotted line), indicates the width (=length) of the transition zone and the associated rotation of their slip vector azimuths. Note that the swing in the strike of the neovolcanic zone occurs much closer to the intersection than the distance over which normal faults change in strike.

Figure 3.3 schematically illustrates a range of possible patterns of slip-vector azimuths for a number of different three and two plate fault geometries. Slip vectors on the intersecting fault systems and outside the intersection zone may be oriented parallel

(0-20º), oblique (21-69º) or perpendicular (70-90º) to one another, with displacements being accommodated on the principal slip surfaces and/or within the rock volume surrounding these fault surfaces (indicated by the grey shaded zones). As a consequence of this distributed deformation, a combination of strike-slip and normal dip-slip would be expected in the intersection zone where slip may be oblique.

In the New Zealand example, slip vectors show a gradual change in both their trend and plunge along the faults in the NIFS northwards proximal to the rift (e.g. Fig. 3.6a and Fig. 3.7). These changes accompany changes in the strike and dip of faults. On the Whakatane Fault, which is presently the fastest moving fault in the NIFS (Chapter 2, this study), slip vectors are approximately horizontal in the south (>50 km from the coast) but become progressively more dip-slip (with a pitch of ca. 55° to the northwest) close to the Bay of Plenty coastline and up to 30 km south of the main rift-bounding fault (shaded area in Fig. 3.6a). This gradational steepening in slip-vector pitch takes place over a strike distance of approximately 60 km and is associated with a c. 50° anticlockwise (westward) deflection in the azimuth of the slip vectors on the Whakatane Fault, a transition that could be predicted from the velocity triangle plotted in Figure 3.7; that is, the CB motion is converted to a BA motion across the intersection. About 100 km to the south of Bay of Plenty coastline, there is a 25° anticlockwise change in strike of the NIFS, from NE-SW to N-S. It is interesting to note that an effect of this change is to increase the strike angle between the two fault systems, from c. 50° to c. 70°, and also to reduce the required change in slip azimuth across the intersection from c. 75° to c. 50°, correspondingly.

I also plot on Figure 3.6a the plunge of the slip vector (derived by outcrop geology) of the Mw 6.6 1987 Edgecumbe earthquake (dashed line), which occurred on the Edgecumbe Fault, the large normal fault which bounds the eastern margin of the Taupo Rift (Beanland et al., 1989). The plunge of this earthquake slip vector is approximately parallel (i.e. within 10º) to the average plunge of the slip vectors on the northern Whakatane Fault and to the general plunge of the fault intersection (solid line intersecting the x-axis at -25 km). This sub-parallelism permits displacements to be transferred from the principal strands of the 'strike-slip' fault system to the normal faults which bound the eastern margin of the rift. The sub-parallelism of the slip vectors at the intersection of the two fault systems is consistent with the apparent absence of strike-slip offset of the southeastern margin of the rift.

The northward changes in the relative proportions of strike-slip and dip-slip along the Whakatane Fault (Fig. 3.6b) are accompanied by a decrease in the net-slip rate. This decrease arises in large part due to c. 50% of its displacement being transferred onto the three other, more eastern strands of the NIFS (Fig. 3.2). If we take this displacement transfer into account the net displacement rate across the NIFS may only decrease slightly from about 7.3 mm/yr at the southern part of the fault system (Beanland, 1995) to about 5.5 mm/yr at the coastline (Chapter 2, this study). The steepening of the slip vectors on the fault planes away from the horizontal is therefore associated with no more than a 25% loss of net slip on the principal faults in the NIFS. This loss may in part be achieved by a corresponding increase in slip on small-scale faults between the main strands of the NIFS.

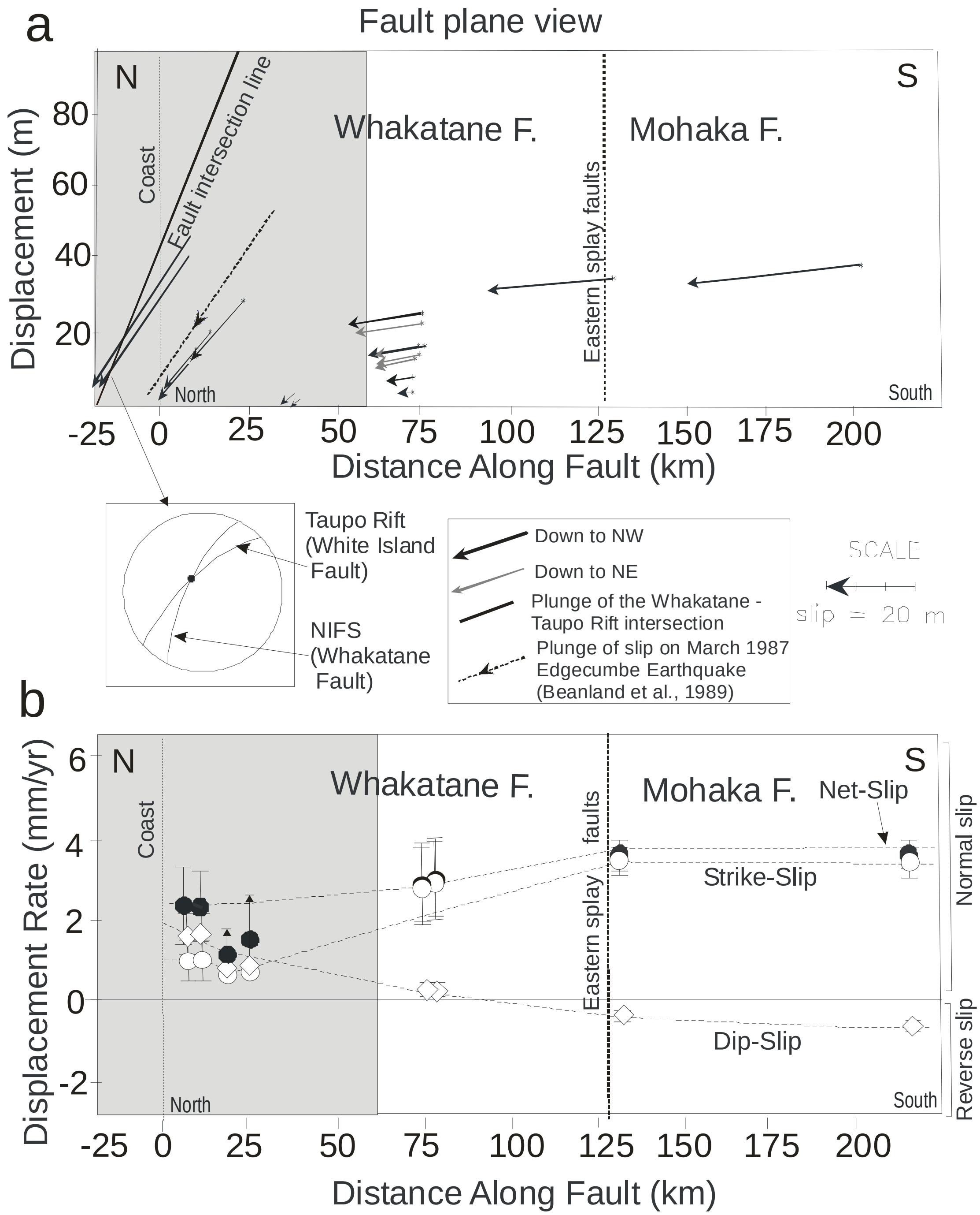

Fig. 3.6 a) Fault plane view illustrating the pitch of the slip vectors along the Whakatane-Mohaka Fault. Length of arrows is proportional to the magnitude of the slip. Black arrows represent slip down to the NW whereas grey arrows represent slip down to the NE. The plunge of the slip vector of the M 6.6 1987 Edgecumbe Fault (Beanland et al., 1989) earthquake is indicated (dashed line) as is the plunge of the line of intersection (thick black line) between the Edgecumbe Fault and the Whakatane Fault. **b)** The three components of slip (i.e. dip-slip, strike-slip and net-slip) of the Whakatane-Mohaka Fault are plotted against distance along the strike of the fault. Data are consistent with a kinematic transition from strike-slip to dip-slip northwards as the Whakatane Fault approaches the Taupo Rift. Transition of strike-slip (minor transtension) to oblique-slip northwards occurs progressively over a distance of approx. 60 km. Strike distances over which changes in the kinematics of the faults are documented are shaded grey.

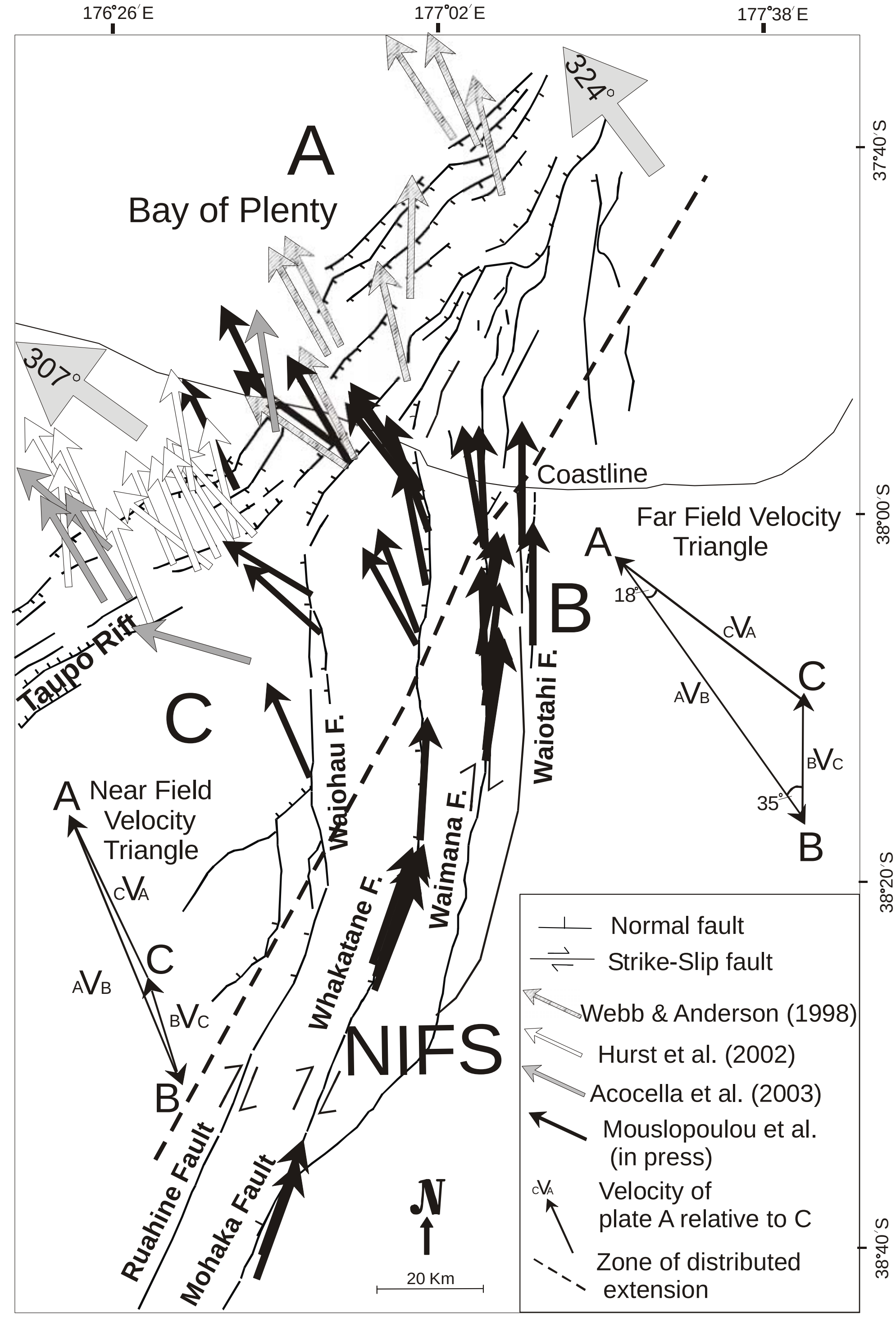

Fig. 3.7 Map of slip azimuths derived from outcrop geology and earthquake focal mechanisms plotted along the strike of the two fault systems and across their intersection zone. Large shaded arrows represent the average extension direction along the rift, southwest and northeast of its intersection with the NIFS, and confirm the c. 18° predicted (using far field velocity vectors) clockwise rotation of the extension direction across the intersection. Stereographic procedure used to evaluate the extension directions are from Marret & Allmendinger (1990). Note the anticlockwise rotation of the slip azimuths along the NIFS. The far-field and near-field velocity triangles are indicated.

The aggregation of strike-slip in the NIFS ($_{B}V_{C}$ vector) and extension in the southwestern part of the rift ($_{C}V_{A}$ vector) would be expected to result in a progressive clockwise (northeastward) swing in the extension direction in the rift from SW to NE across the intersection zone (Fig. 3.7). The direction of fault slip in the rift from outcrop geology (Acocella et al., 2003) and focal mechanisms (Webb & Anderson, 1998; Hurst et al., 2002) are broadly consistent and compatible with a northeastward increase in the obliquity (i.e. normal plus dextral) of fault slip in the rift. A running average of the slip azimuth for groups of five measurements suggests a c. 20º clockwise change in slip azimuth (i.e. 325º to 345º trend). This change is accompanied by a 20º anticlockwise swing in the strike of normal faults of the rift from south to north. These changes in fault kinematics in the rift combine to produce a clockwise 17º northeastward change in the trend of the extension direction (i.e. 307 to 324º trend) across its intersection with the NIFS. Given the uncertainties on fault-slip direction (in some cases up to ±10º) the observed changes in extension direction are consistent with the 18º predicted by summing the far field velocity vector from the strike-slip system ($_{B}V_{C}$) with that of the rift SW of the intersection ($_{C}V_{A}$) (Fig. 3.7). The magnitude of the observed and predicted change in extension direction northwards along the rift (and across the intersection zone with the NIFS) is comparable to the 21º (i.e. 312 to 330º trend) predicted from modelling of GPS data (Wallace et al., 2004). The c. 5-6º discrepancy in the trends of the modelled GPS and observed extension directions may be due to uncertainties in fault-slip directions, produced by the incompleteness of both the GPS and geological datasets. Furthermore, the observed (20º) northward clockwise swing in the trend of the extension direction along the rift and across its intersection with the NIFS, produces a west to east reduction in the total along-strike anticlockwise rotation of slip azimuths on faults of the NIFS (Fig. 3.7).

The observed changes in slip vectors across the intersection zone of the NIFS and the Taupo Rift are similar to those seen elsewhere for oblique strike-slip-rift triple junctions from the global data set. Across the intersection of the North Anatolian Fault and Aegean Rift, for example, earthquake focal mechanisms (Taymaz et al., 1991) indicate a progressive rotation of the slip vector azimuth over a strike distance of 100-200 km from strike-slip in the North Anatolian Fault to mainly normal dip-slip in the

Aegean Rift (Fig. 3.1e). Similarly, at the intersection of the strike-slip Median Tectonic Line and the Hohi Volcanic Zone in Japan, seismic-reflection profiles from the Sea of Iyo suggest the presence of both strike-slip and dip-slip faults in the rift proximal to the Median Tectonic Line (Fig. 3.5a) (Tsutsumi & Okada, 1996; Kamata & Kodama, 1994). The combination of strike-slip and dip-slip in the intersection zone produces bulk transtension with summed slip vectors across the zone, intermediate in trend and in plunge between the slip vectors in the rift and on the Median Tectonic Line. Thus, the required relative velocity changes between the several mutually intersecting blocks are expressed by changes in slip-vector azimuths across transition zones of finite width.

The intersection of the Red Sea Rift and the Dead Sea Transform (Fig. 3.1d), is an example of a triple junction within continental crust in which the transition from strike-slip to dip-slip is achieved without apparent rotations of the slip azimuths across the intersection zone. In this special case, the slip azimuths on the intersecting strike-slip and normal faults are approximately parallel and the change in fault kinematics could be achieved by rigid-block translations with displacements confined mainly to the principal fault surfaces (Fig. 3.1c). The transition from strike-slip to extension takes place mostly within the rift (i.e. in the offshore Red Sea) and up to c. 20 km onshore and parallel to the main rift-bounding faults (Moustafa, 1997; McClay & Khalil, 1998), and as a consequence the transform fault displaces the northeast margin of the rift (Fig. 3.1d).

Mid-ocean ridges, where strike-slip and dip-slip faults are orthogonal and slip azimuths parallel, have two-plate geometries. The geometry and kinematics of ridge-transform intersections together with finite element models of these systems indicate that the angle between the minimum horizontal compressive stress direction (σ_3) and the strike of the transform fault increases approaching the intersection (Morgan & Parmentier, 1984). Local rotation of the minimum horizontal compressive stress direction induces re-orientation of the principal strain axes and of the faults. In cases where the slip azimuths are constant across the intersection zone the re-orientation of fault strikes results in oblique slip and associated transtension in the transition zone between the two fault systems. Such oblique slip has been inferred close to the intersection of the Siqueiros transform and the East Pacific Rise (Crane, 1976), in the 10-15 km wide intersection zone of the Manus ridge and Willaumez Transform Fault in

Manus Basin (Taylor et al., 1994), and adjacent to the intersection of the Fracture Zone B and the Mid-Atlantic Ridge (Goud & Karson, 1985).

Figure 3.8 schematically illustrates a transition from normal to strike-slip faulting achieved through changes of the strikes and obliquity of slip on normal faults proximal to the intersection of a ridge-transform. Oblique extension results where the two displacement fields (strike-slip and normal) are superimposed on one another. The region in which strike-slip rates dominate over normal rates is restricted to a zone immediately adjacent to the transform fault. With increasing distance from the transform, decreasing strike-slip is associated with a complementary increase in dip-slip, i.e. net slip is fixed (see displacement profiles in Fig. 3.8). The horizontal incremental strain ellipses for each stage of the transition illustrate changes in the orientations of the principal horizontal extension axes across the intersection zone. The transition from strike-slip to normal faulting is expected to be achieved in a similar way for two-plate junctions in continental rocks (e.g. Sumatra Fault and Sunda Strait Rift).

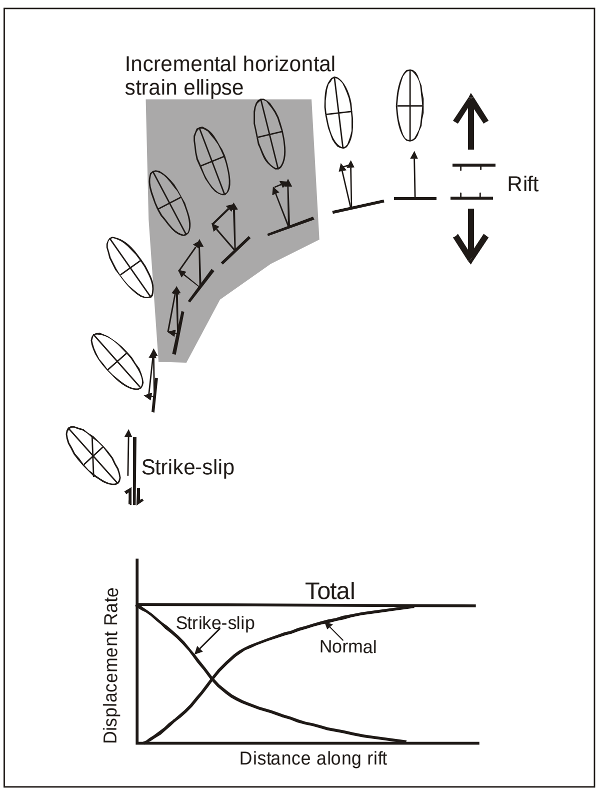

Fig. 3.8 Schematic diagram illustrating how the displacement transfer between orthogonal extensional and strike-slip fault systems may be achieved by rotating only the fault orientation and the individual components of slip but keeping the net-slip vector azimuth fixed. Incremental horizontal strain ellipses for each location illustrate changes in the orientations of the principal horizontal shortening and extension axes across the intersection zone. Schematic displacement profile along the rift is indicated.

3.5 Testing and understanding displacement transfer

Displacement transfer between intersecting strike-slip and normal faults would be expected where these faults are active synchronously and is a requirement for kinematically coherent fault systems. Displacement transfer and kinematic coherence can be tested where displacement rates for the component faults can be measured immediately outside the intersection zone. At the intersection of the Red Sea Rift and the Dead Sea Transform, for example, the 6 mm/yr displacement rate of the transform is equal to the decrease in extension in the rift across the intersection, from the Red Sea northwards to Gulf of Suez (i.e., 7.5 – 1.5 mm/yr) (Joffe & Garfunkel, 1987). In the schematic displacement rate profiles of Figure 3.3 total displacement rates are uniform and conserved in their entirety across the intersections. Displacement transfer observed for the Red Sea Rift-Dead Sea Transform junction and inferred in Figure 3.3 has not been widely documented. In this study, however, the kinematic coherence of the NIFS-Taupo Rift intersection is documented and it is anticipated that future work will help to constrain better the existing model where displacement is transferred by non-rigid block deformation.

Displacement transfer between the NIFS and the Taupo Rift can be demonstrated with reference to the northward change in extension rates and extension directions across the rift. Extension rates across the rift to the southwest of its intersection with the NIFS are c. 10±2 mm/yr in a direction approximately perpendicular to the faults (Darby et al., 2000; Villamor & Berryman, 2001; Wallace et al., 2004). North of the fault intersection rift-related extension trends at c. 20° clockwise of the rift perpendicular direction, with rates of c.15 mm/yr (Davey et al., 1995; Wallace et al., 2004). The c. 5 mm/yr increase in extension rates and 20° clockwise change in the slip azimuth across the intersection of the two fault systems, compares favourably with the c. 4 mm/yr strike-slip cumulative displacement rates at the northern end of the NIFS (Chapter 2, this study) and with the predicted 18° clockwise rotation of the fault slip azimuths within the rift and across the intersection (Fig. 3.7). The similarity of these rates together with the change in the slip azimuth along the rift and across the intersection zone, are consistent with the view that displacement is being transferred from the NIFS into the rift.

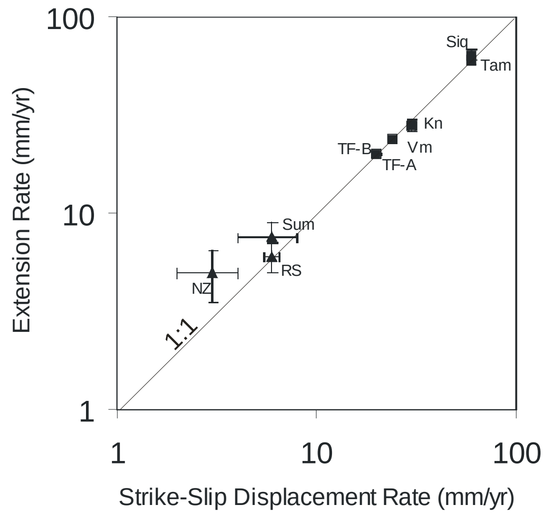

Fig. 3.9 Log-log plot of strike-slip and extension rates on the component fault systems of 9 of the examples utilized in this study (Table 3.1). In cases where both faults terminate at the intersection their strike-slip and extension are compared, while in cases where only one of the faults terminates, the strike-slip or extension of the terminating fault is compared with the difference in strike slip or extension across the intersection for the non-terminating fault. Line of equal extension and strike-slip rates is indicated. Errors at a 2σ level for the New Zealand example. The error bars for the rest of the examples derive from literature. For ridge-transform intersections errors are ≤ 0.2 mm/yr (i.e. smaller than the size of the symbols). NZ=New Zealand, RS=Red Sea, Sum=Sumatra, TF-A=Transform Fault A, TF-B=Transform Fault B, Vm=Vema, Kn=Kane, Siq=Siqueiros, Tam=Tamayo.

To test the global applicability of displacement transfer between intersecting strike-slip and dip-slip faults the strike-slip and extension rates on the component fault systems is compared (Fig. 3.9). For two-plate geometries where both faults terminate at the intersection, strike-slip and extension are compared as close as possible to the intersection zone, whilst in cases where only one of the faults terminates (three-plate configuration), the strike-slip or extension rates of the terminating fault are compared with the difference in strike-slip or extension across the intersection for the through-going fault. The data typically straddle the line along which strike-slip and extension are equal, supporting the suggestion that efficient displacement transfer between kinematically different fault systems is a widely occurring phenomenon. The data also suggest that the transfer of displacement between the two intersecting fault systems is principally accomplished by slip on the main mapped faults, with a relatively small component (e.g. < 25%) of off-fault deformation which would be sub-resolution and could result in a rate deficit. In cases where displacement rates on the intersecting fault systems are not comparable, internal faulting within the main fault blocks (i.e. sub-parallel to the main fault strands) may constitute a significant fraction of the overall slip budget. In addition, a change in relative plate motions across the intersection and/or an inability to measure rates precisely at the margins of the intersection zone may also account for differences in the rate values across the intersection zone. In the 3-plate case of the NIFS-Taupo Rift, for example, rifting is not only accommodating the horizontal translation of the NIFS but also reflects the extension induced by the southwestward oblique subduction of the Pacific Plate beneath the Australian Plate along the Hikurangi margin (Wallace et al., 2004). Therefore, the rates of extension are higher than would be expected if rifting were driven solely by displacement transfer from the strike-slip NIFS.

Determining how displacement is transferred from one fault system to another is important. Given that the transfer of displacement between two intersecting fault systems in a three plate configuration is a three dimensional process, we need to go beyond the 2D concept of plate tectonic stability and consider the likelihood of deforming rather than rigid plates and we also need to define the requirements for stable faulting in 3D. In 3D stable faulting across a fault junction is achieved when the trend and the plunge of the slip vector on each of the component faults is parallel with the intersection line of the two fault systems. Note that, these requirements for 3D stability, at least in theory, are not met by orthogonal R-T-T or T-R-R triple junctions which are stable in 2D, as the c. 65° divergence in the plunge of their slip vectors at their intersection results in a kinematically unstable system.

The schematic block diagram in Figure 3.10 shows the manner in which the triple junction examined in New Zealand attains a quasi-stable configuration in 3D. In the block diagram, the faults of the Taupo Rift are represented by one main marginal fault that bounds the eastern margin of the rift and accommodates most of the slip within it. The northern tips of the Waiohau, Whakatane and Waimana faults accommodate oblique extension, with the component of dip-slip gradually increasing from south to north and east to west towards the rift (Chapter 2, this study). Where the faults of the NIFS intersect the rift, their slip vectors are approximately parallel to the line of fault intersection. Therefore the transfer of displacement between the fault systems principally takes place along their lines of intersection which, due to their sub-parallelism with the slip vectors, remain stable. As more faults of the NIFS intersect the rift the component of strike-slip and extension increases northwards along the rift.

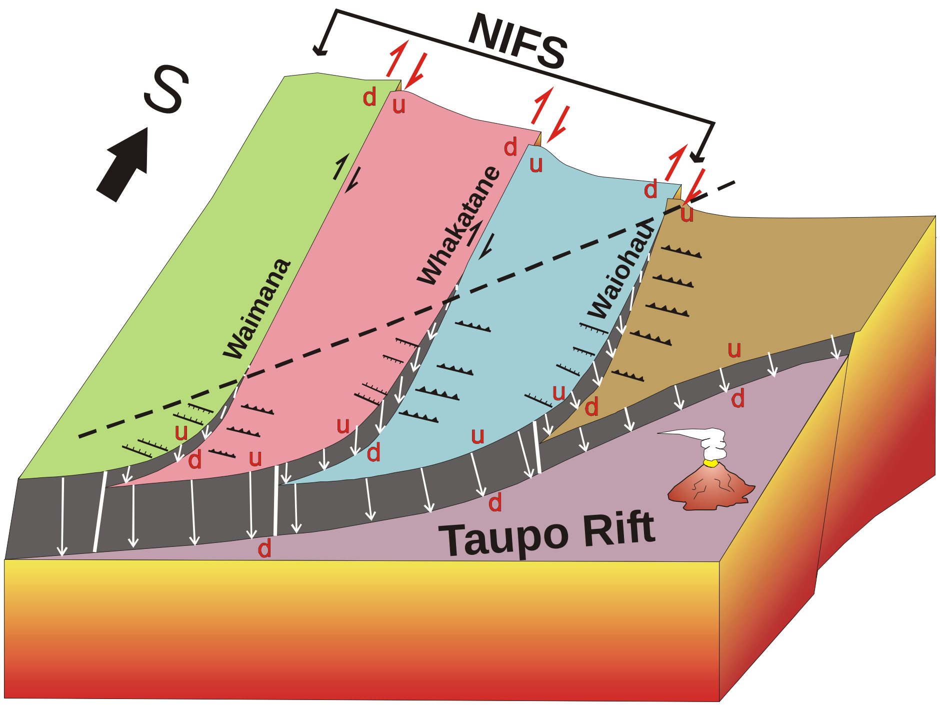

Fig. 3.10 Schematic block diagram showing the displacement transfer (from the strike-slip system to the normal) for the NIFS-Taupo Rift intersection, New Zealand. The block diagram summarizes the geometries and kinematics of the NIFS which shows a progressive northward change of strike, dip and slip vector orientations along the strike of the faults. The transfer of displacement from the NIFS to the Taupo Rift is partially facilitated by the gradual steepening of the NIFS slip vectors towards sub-parallelism with fault-slip vectors in the rift. At the intersection of the two fault systems, slip vectors in the NIFS are sub-parallel to the lines of fault intersections and to the slip vectors in the rift. Minor reverse and normal faulting in the hangingwall and footwall of the NIFS respectively, associated with a component of off-fault deformation that may arise due to displacement gradients on the strike-slip faults of the NIFS and on normal faults in the rift (see text for discussion). The zone enclosed between the black dashed line and each fault intersection accommodates rift-related distributed deformation.

Changes in the slip vectors along the NIFS require internal deformation in the fault blocks in between the main faults. In the hangingwalls of the faults in the NIFS (i.e. west of faults), strike-slip decreases northwards producing a net shortening in the horizontal plane which is indicated schematically in Figure 3.10 by small-scale reverse faulting at high angles to the main faults. However, as this northward decrease in strike-slip is also associated with an increase in dip-slip, shortening in the horizontal plane is accompanied by extension approximately parallel to fault dip. In the footwalls of faults in the NIFS the deformation is inverted with extension parallel to strike in the horizontal plane indicated schematically in the block diagram by small-scale normal faults formed at high angles to the main faults. This extension is accompanied by shortening approximately parallel to the fault dip. The magnitude of strains in fault footwalls and hanging walls cannot be determined precisely as few data are available to constrain their absolute motion during fault displacement. However, as these changes occur within an area of distributed rift-orthogonal NW-SE extension, it is more likely for normal faults to be formed at high angles to the main strike-slip faults and sub-parallel to the rift (Fig. 3.10). Further detailed mapping of the deforming zone between the main strands of the NIFS in combination with acquisition of earthquake focal mechanisms may help constrain better the pattern of off-fault deformation that can accommodate the observed displacement gradient on the main faults.

The model of displacement transfer in the New Zealand example (Fig. 3.10) is consistent with available data from other three-plate fault intersections including those of the Median Tectonic Line and Hohi Volcanic Zone, and the North Anatolian Fault and Aegean Rift. In the case of two-plate configurations, such as the junction of Sumatra Fault and Sunda Strait Rift and the ridge-transform intersections, similar changes in the plunge of the slip vectors across the transition zone can be expected.

3.6 Discussion

Important questions remain as to what controls the dimensions of the transition zone from strike-slip to normal faulting. The data indicate that changes of fault geometries and orientations of slip vectors on intersecting faults towards parallelism within the intersection zone occur regardless of whether the intersection consists of three (New Zealand) or two plates (ridge-transform examples), whether the rift (New Zealand) or the strike-slip fault (Japan and Sumatra examples) dominates or whether displacement rates are intermediate (c. 5-10 mm/yr) or high (c. 100 mm/yr). A common feature, however, of most intersecting strike-slip and normal fault systems that demonstrate kinematic and geometric changes proximal to the intersection zone, is the presence of distributed deformation on the dominant fault system. The dimensions of the area over which fault geometries and slip-vectors on the secondary fault change, is mainly controlled by the extent to which displacement on the dominant fault system is confined to a single slip surface or distributed across a zone. Where slip on the dominant fault system is spatially distributed, the region in which the two displacement fields are superimposed will produce oblique slip and transtension (Fig. 3.8). The wider the zone of spatially distributed deformation associated with the dominant fault (i.e. W in Fig. 3.11), the longer the transition zone from one type of faulting to another (i.e. L in Fig. 3.11).

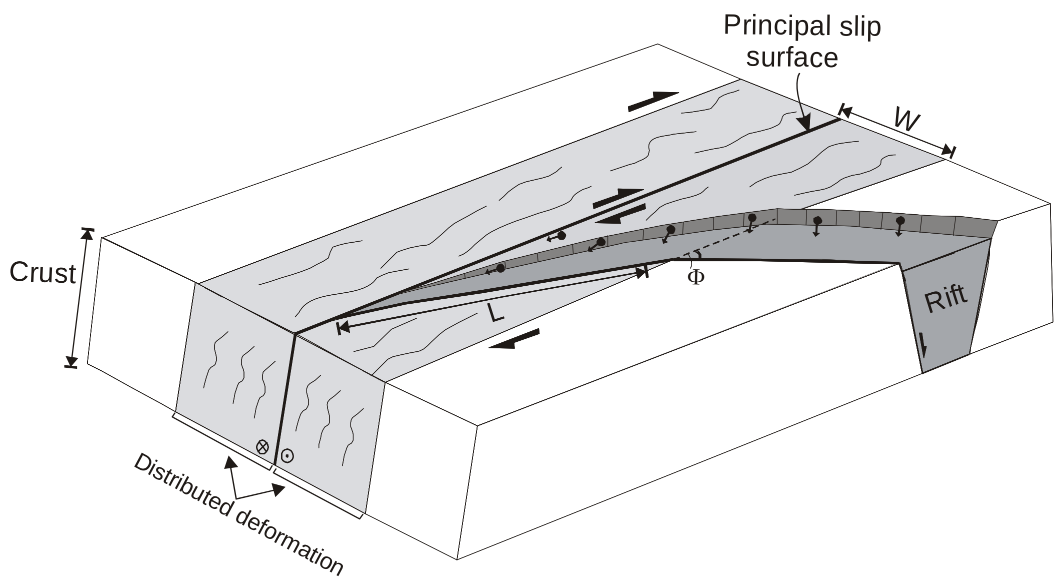

Fig. 3.11 Schematic block diagram illustrating the way fault geometries and kinematics of the rift change as the zone of intersection with the strike-slip fault system is approached. The smaller the angle of intersection (Φ) between the two component faults, the greater the angle through which the slip vectors of the secondary fault must change their pitch. The greater strains required for this change, however, are distributed over a longer distance (L). W = width of transition zone, L = length of transition, Φ = angle of intersection between the component systems.

For the purposes of describing the dimensions of the transition zone from strike-slip to dip-slip, the width and the length of the transition zone is measured. The width (W) of the transition zone is the distance, measured normal to the dominant fault and from the tip of the secondary fault, over which the deformation associated with the dominant fault is distributed. Length (L) of the transition is the distance on the secondary fault along which changes in its geometry and/or kinematics are recorded (Figs 3.3 and 3.11). Figure 3.12a and 3.12b suggest that the width (W) of the transition zone from strike-slip to dip-slip faulting and the length over which these changes are observed (L), are different for oceanic and continental examples and therefore may be influenced by crustal rheology. Deformation in oceanic crust at fault intersections more closely resembles a rigid block process with narrower zones of deformation associated with the dominant fault (Fig. 3.12). This may occur because oceanic crust is thin and strong compared to continental crust (Kohlstedt et al., 1995), resulting in a relatively confined deformation zone (Dauteuil et al., 2002) and therefore rapid spatial transitions from strike-slip to dip-slip. In addition to crustal rheology, the length (L) over which the kinematics and the geometries change may relate to the angle through which the trend of the velocity vectors must rotate, with longer distances where the angles between velocity vectors are greater (Figs 3.11 and 3.12c).[1] This relationship can be rationalized if it is considered that the greater the angle between the slip-vectors of the two component systems the higher the total deformation required in the rock volume enclosing the faults. Greater displacement gradients across the intersection zone could be achieved without increasing strain magnitudes, by increasing the distance and volume over which the deformation is distributed (Fig. 3.11). Continental transition zones are larger than the equivalent oceanic zones due to greater thickness of the continental crust and greater complexity associated mainly with three-plate configurations which are often accompanied by large ranges between the slip vectors of the component intersecting fault systems (Figs 3.12a & b).

Intriguingly, the distances over which the change in slip vector and fault strike occurs cannot be convincingly related to the displacement rates of the component faults (Figs 3.12a & b). The lack of displacement rate dependency on the dimensions of the transition zone can only be quantitatively demonstrated for examples which are in all other respects similar (i.e. crustal rheology, angle between slip vectors azimuths); such constraints on the examples discussed here do not exist.

[1] The orientations of the velocity vectors outside the intersection zone are assumed to coincide with the orientation of the slip vectors on the principal fault surfaces of each fault system.

This study has implications for the stability of strike-slip and normal fault intersections. The stability of such intersections is time and scale-dependent phenomenon. When one of the intersecting fault systems terminates, the fault configuration can be approximated to a triple junction with the dominant fault defining two arms of the junction. In 2D plate tectonic terms, triple junctions are assumed to

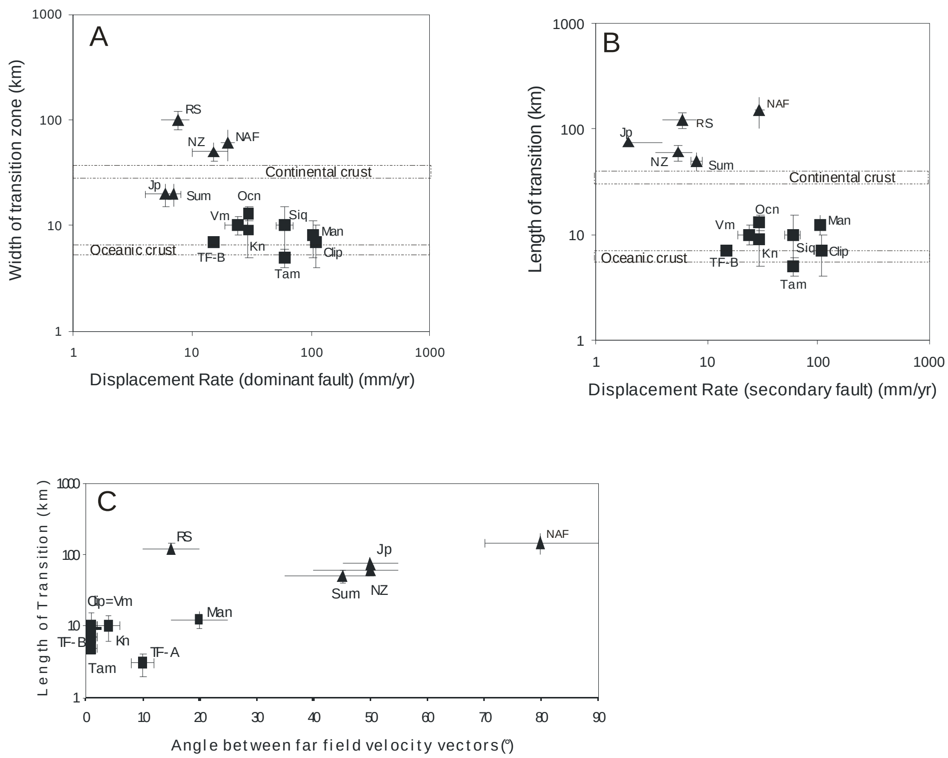

Fig. 3.12 (a) Log-log plot of displacement rates (on dominant faults) against the width of the transition zone for both oceanic (squares) and continental (triangles) strike-slip and normal fault intersections. **(b)** Log-log plot of displacement rates (on secondary faults) against the length of the transition zone for both oceanic (squares) and continental (triangles) strike-slip and normal fault intersections. **(c)** Semi-logarithmic plot showing a positive relationship between the length of the transition zone and the angle through which the trend of the velocity vectors rotate. Note that velocity vectors outside the intersection zone coincide with net-slip vector orientation on the principal fault surfaces on each fault system. NZ=New Zealand, RS=Red Sea, Sum=Sumatra, NAF=North Anatolian Fault, Jp=Japan, Man=Manus, Clip=Clipperton, Ocn=Oceanographer, TF-A=Transform Fault A, TF-B=Transform Fault B, Vm=Vema, Kn=Kane, Siq=Siqueiros, Tam=Tamayo.

develop in conjunction with rigid-blocks translations (McKenzie & Morgan, 1969; King, 1983; Patriat & Courtillot, 1984; Cronin, 1992) and considered to be stable if the geometry of the plates (McKenzie & Morgan, 1969) and the relative orientations of the plate boundaries (Cronin, 1992) remain constant over a finite time interval. This study indicates, however, that rigid blocks are rarely maintained near the intersection of strike-slip and normal faults and points to a propensity for distributed deformation. The progressive changes of fault orientations and/or slip vectors and the associated distributed deformation appear to increase the stability and geological longevity of the intersection at regional scales. This point is illustrated by the NIFS and Taupo Rift intersection, which is geometrically and kinematically comparable to a Ridge-Ridge-Transform triple junction. In formal plate tectonic terms this type of triple junction is considered unstable (rigid blocks) (York, 1973). The intersection of the NIFS and Taupo Rift may, however, have been stable at a regional scale since 300 kyr, when throw rates on the principal faults in the NIFS and the rift increased by a factor of three (this study, Chapter 6). The present fault geometries show no outward signs that strike-slip faults are displacing the rift or that the present kinematics of the active faults differ from those recorded in the last 300 kyr.

3.7 Conclusions

Transfer of displacement between active strike-slip and normal faults is typically facilitated by gradual changes of fault strikes, dips and slip vectors towards, and across, the intersection.

Three-plate intersections that strike at low to moderate angles to each other (up to c. 60°) experience rotation of their slip azimuths and fault attitudes towards parallelism approaching the intersection. Two or three plate junctions that are orthogonal to each other, and therefore have parallel slip azimuths, appear to be characterized by gradual rotation of the plunge of slip vectors and fault attitudes on the secondary fault proximal to the intersection.

The changes on fault attitudes and slip vectors are accompanied by displacement gradients on the component faults and therefore, by distributed deformation and strain in the rock volume enclosing one or both faults over fault strike distances of up to 200 km. The distance over which these changes on the secondary (i.e. terminating) fault system are observed is defined by the width of the dominant-fault related deformation and by the angle between the far field velocity vectors of the component fault systems across the intersection. The wider the dominant-fault related distributed deformation, the larger the area of transtensional oblique-slip arising on the secondary fault system from the superimposition of the two displacement fields (i.e. dip-slip on strike-slip). Overall, the dimensions of the transition zone are larger for continental crust than for oceanic crust as the latter is thinner and comprises inherently simpler two-plate configurations which are mainly associated with narrower ranges of slip vectors between the component intersecting fault systems.

Progressive changes in the plunge and azimuth in slip vectors in the proximity to fault intersections lead to a mutual parallelism of these slip vectors to the line of intersection between the two fault systems, this is the 3D requirement for slip stability, and minimizes the deformational work required for mutual slip on the two intersecting fault systems which would, otherwise, require high strains in the volume enclosing this line. Sub-parallelism of slip vectors at the fault intersection in combination with off-fault deformation increases the stability of strike-slip and normal fault intersections.

Acknowledgments: I am grateful to A. Nicol, T. Little, J. Walsh and J. Begg for beneficial discussions and reviews of this chapter. Also thanks are due to J. Begg for assistance with the Figure 3.10.

References

Acocella, V., Spinks, K., Cole, J. and Nicol, A., 2003. Oblique back arc rifting of Taupo Volcanic Zone, New Zealand. Tectonics, 22, 4, 1045, doi:10.1029/2002TC001447.

Basile, C. & Brun, J.P., 1999. Transtensional faulting patterns ranging from pull-apart to transform continental margins: an experimental investigation. Journal of Structural Geology, 21, 23-37.

Beanland, S., Berryman, K.R. and Blick, G.H., 1989. Geological investigations of the 1987 Edgecumbe earthquake. New Zealand Journal of Geology and Geophysics, 32, 73-91.

Beanland, S., 1995. The North Island Dextral Fault Belt, Hikurangi Subduction margin, New Zealand. PhD Thesis, Victoria University of Wellington, New Zealand.

Bellier, O. & Sébrier, M., 1995. Is the slip rate variation on the Great Sumatran Fault accommodated by fore-arc stretching? Geophysical Research Letters, 22, 15, 1969-1972.

Choukroune, P., Francheteau, J. and Le Pichon, X., 1978. In situ structural observations along Transform Fault A in the FAMOUS area, Mid-Atlantic Ridge. Geological Society of America Bulletin, 89, 1013-1029.

Courtillot, V., Armijo, R. and Tapponnier, P., 1987. The Sinai triple junction revisited. Tectonophysics, 141, 181-190.

Crane, K., 1976. The intersection of the Siqueiros transform fault and the East Pacific Rise. Marine Geology, 21, 25-46.

Cronin, V.S., 1992. Types of kinematic stability of triple junctions. Tectonophysics, 207, 287-301.

Darby, D.J., Hodgkinson, K. M. and Blick, G.H., 2000. Geodetic measurement of deformation in the Taupo Volcanic Zone, New Zealand: the north Taupo network revisited. New Zealand Journal of Geology and Geophysics, 43, 157-170.

Dahlstrom, C.D.A., 1969. Balanced cross sections. Canadian Journal of Earth Sciences, 6, 743-757.

Dauteuil, O., Bourgeois, O. and Mauduit, T., 2002. Lithosphere strength controls oceanic transform zone structure; insights from analogue models. Geophysical Journal International, 150, 3, 706-714.

Davey, F.J., Henrys, S. and Lodolo, E., 1995. Asymmetric rifting in a continental back-arc environment, North Island, New Zealand. Journal of Volcanology and Geothermal Research 68, 209-238.

Fox, P.J. & Gallo, D.G., 1984. A tectonic model for ridge-transform-ridge plate boundaries: implications for the structure of oceanic lithosphere. Tectonophysics, 104, 205-242.

Fujita, K. & Sleep, N., 1978. Membrane stresses near mid-ocean ridge-transform intersections. Tectonophysics, 50, 207-221.

Gallo, D.G., Kidd, W.S.F., Fox, P.J., Karson, J.A., Macdonald, K., Crane, K., Choukroune, P., Seguret, M., Moody, R. and Kastens, K., 1984. Tectonics at the intersection of the East Pacific Rise with Tamayo Transform Fault. Marine Geophysical Researches, 6, 159-185.

Gallo, D.G., Fox, P.J. and Macdonald, K.C., 1986. A sea beam investigation of the Clipperton Fracture Fault: the morphotectonic expression of a fast slipping transform boundary. Journal of Geophysical Research, 91, B3, 3455-3467.

Goud, M.R. & Karson, J.A., 1985. Tectonics of the short-offset, slow-slipping transform zones in the FAMOUS area, Mid-Atlantic Ridge. Marine Geophysical Researches, 7, 489-514.

Joffe, S. & Garfunkel, Z., 1987. Plate kinematics of the circum Red Sea - a re-evaluation. Tectonophysics, 141, 5-22.

Hurst, W.A., Bibby, H.M. and Robinson, R.R., 2002. Earthquake focal mechanism in the Central Volcanic Zone and their relation to faulting and deformation. New Zealand Journal of Geology and Geophysics, 45, 527-536.

Kamata, H. & Kodama, K., 1994. Tectonics of an arc-arc junction: an example from Kyushu Island at the junction of the Southwest Japan Arc and the Ryuku Arc. Tectonophysics, 233, 69-81.

Kelsey, H.M., Cashman, S.M., Beanland, S. and Berryman, K.R., 1995. Structural evolution along the inner forearc of the obliquely convergent Hikurangi margin, New Zealand. Tectonics 14, 1, 1-18.

King, G., 1983. The accommodation of large strains in the upper lithosphere of the Earth and other solids by self-similar fault systems: the geometrical origin of b-value. Pure and Applied Geophysics, 121, 761-815.

Kohlstedt, D.L., Evans, B. and Mackwell, S.J., 1995. Strength of the lithosphere: constraints imposed by laboratory experiments. Journal of Geophysical Research, 100, B9, 17,587-17,602.

Lachenbruch, A.H. & Thompson, G.A., 1972. Oceanic ridges and transform faults: their intersection angles and resistance to plate motion. Earth and Planetary Science Letters, 15, 116-122.

Lamarche, G., Bull, J.M., Barnes, P.M., Taylor, S.K. and Horgan, H., 2000. Constraining fault growth rates and fault evolution in New Zealand. EOS, Transactions, American Geophysical Union, 81 (42), 481, 485, 486.

Lelgemann, H., Gutscher, M-A., Bialas, J., Flueh, E., Weinrebe, W. and Reichert, C., 2000. Transtentional basins in the western Sunda Strait. Geophysical Research Letters, 27, 21, 3545-3548.

MacDonald, C.K., Castillo, D.A., Miller, S.P., Fox, P.J., Kastens, K.A. and Bonnati, E., 1986. Deep-tow studies of the Vema Fracture Zone. 1. Tectonics of a major slow slipping transform fault and its intersection with the Mid-Atlantic Ridge. Journal of Geophysical Research, 91, B3, 3334-3354.

Marret, R. & Allmendinger, R.W., 1990. Kinematic analysis of fault-slip data. Journal of Structural Geology, 12, 973-986.

McClay, K. & Khalil, S., 1998. Extensional hard linkages, eastern Gulf of Suez, Egypt. Geology 26, 6, 563-566.

McKenzie, D.P. & Morgan, W.J., 1969. Evolution of triple junctions. Nature 224, 5215, 125-133.

Moustafa, A.D., 1997. Controls on the development and evolution of transfer zones: the influence of basement structure and sedimentary thickness in the Suez Rift and Red Sea. Journal of Structural Geology, 19, 6, 755-768.

Morgan J.S. & Parmentier, E.M., 1984. Lithospheric stress near a ridge-transform intersection. Geophysical Research Letters, 11, 2, 113-116.

OTTER (Oceanographer Tectonic Research Team), 1984. The geology of the Oceanographer Transform: the ridge-transform intersection. Marine Geophysical Researches, 6, 109-141.

Papanikolaou, D., Alexandri, M., Nomikou, P. and Ballas, D., 2002. Morphotectonic structure of the western part of the North Aegean basin based on swath bathymetry. Marine Geology, 190, 465-492.

Patriat, P. & Courtillot, V., 1984. On the stability of triple junctions and its relationship to its episodicity in spreading. Tectonics, 3, 317-332.

Picard, L., 1987. The Elat (Aqaba)-Dead Sea-Jordan subgraben system. Tectonophysics, 141, 23-32.

Pockalny, R.A., Detrick, R.S. and Fox, J., 1988. Morphology and tectonics of the Kane Transform from sea beam bathymetry data. Journal of Geophysical Research, 93, B4, 3179-3193.

Taylor, S.K., Bull, J.M., Lamarche, G. and Barnes, P.M., 2004. Normal fault growth and linkage in the Whakatane Graben, New Zealand, during the last 1.3 Myr. Journal of Geophysical Research, 109, B2, B02408.

Taylor, B., Crook, K. and Sinton, J., 1994. Extensional transform zones and oblique spreading centers. Journal of Geophysical Research, 99, B10, 19,707-19,718.
Taymaz, T., Jackson, J. and McKenzie, D., 1991. Active tectonics of the north and central Aegean Sea. Geophysical Journal International, 106, 433-490.

Tsutsumi, H. & Okada, A., 1996. Segmentation and Holocene surface rupture faulting on the Median Tectonic Line, southwest Japan. Journal of Geophysical Research, 101, B3, 5855-5871.

Van Andel, T.H., Von Herzen, R.P. and Phillips, J.D., 1971. The Vema Fracture Zone and the tectonics of transverse shear zones in oceanic crustal plates. Marine Geophysical Research, 1, 261-283.

Villamor, P. & Berryman, K., 2001. A late Quaternary extension rate in the Taupo Volcanic Zone, New Zealand, derived from fault slip data. New Zealand Journal of Geology and Geophysics, 44, 243-269.

Wallace, L.M., Beaven, J., McCaffrey, R. and Darby, D., 2004. Subduction zone coupling and tectonic block rotations in the North Island, New Zealand. Journal of Geophysical Research, 109, B12, B12406.

Walsh J.J. & Watterson, J., 1991. Geometric and kinematic coherence and scale effects in normal fault systems. From Roberts, A.M., Yielding, G. and Freeman, B. (eds), 1991. The geometry of normal faults. Geological Society of London, Special Publication No 56, 193-203.

Webb, T. & Anderson, H., 1998. Focal mechanisms of large earthquakes in the North Island of New Zealand: slip partitioning at an oblique active margin. Geophysical Journal International, 134, 40-86.

Wilson, C.J.N., Houghton, B.F., McWilliams, M.O., Lamphere, M.A., Weaver, S.D. and Briggs, R.M., 1995. Volcanic and structural evolution of Taupo Volcanic Zone, New Zealand: a review. Journal of Volcanology and Geothermal Research, 68, 1-28.

York, D., 1973. Evolution of triple junctions. Nature, 244, 341-342.

CHAPTER FOUR

PALEOEARTHQUAKE HISTORY OF THE NORTHERN NORTH ISLAND FAULT SYSTEM

4.1 Introduction

Active faults generate earthquakes. The principal objective of this chapter is to chart the temporal and spatial distribution of large earthquakes that have ruptured the ground surface in the northern North Island Fault System (NIFS) during the last c. 18 kyr. By constraining the timing and location of large earthquakes along the northern NIFS we gain insight into how and why the changes in the fault kinematics, from chiefly strike-slip in the south to mainly oblique-normal slip in the north (Chapter 2), are achieved during individual earthquakes or earthquake cycles.

To address these questions, ten fault-trenches were excavated at various localities along two of the principal faults of the NIFS (Whakatane and Waimana faults) (Fig. 4.0). Fault trenching is a technique that may provide direct evidence on the timing of large past earthquakes and the magnitude of the coseismic displacement on the fault. The location of a trench on a fault is principally purpose-dependent. Knowing that the faults in the NIFS change their kinematics across a c. 60-70 km wide zone (Chapter 2), most of the fault-trenches were excavated across this kinematic transition zone, at localities chosen to maximize the information with respect to 1) the paleoearthquake history on each fault (such as the timing of past earthquakes, recurrence interval and earthquake magnitude) and, 2) the kinematics on each fault (such as fault-dip, slip direction from potential slickenside striations, slip-rates and fault zone geometry).

Five trenches were excavated on the Whakatane Fault at three different localities (Ruatahuna, Wharepora and Ruatoki North), and five trenches were excavated on the Waimana Fault at two different localities (Te Ahirau and Nukuhou North) (Fig. 4.0). Trenches oriented perpendicular to strike-slip faults typically optimize information regarding the width of the strike-slip zone and the timing of past earthquakes on it.

Trenches oriented parallel to strike-slip faults may provide data on the age of piercing points offset across the fault and therefore help constrain slip-rates on faults.

The analysis of individual prehistoric earthquakes improves our understanding of some of the North Island's most seismically active faults and contributes directly to seismic hazard evaluation in the Bay of Plenty region, a seismically active and geologically poorly understood part of New Zealand. By trenching the same fault at different localities, information may be obtained about surface-rupture length, an attribute that scales with the size of paleoearthquake magnitude. The latter contributes directly to seismic hazard models, to the impact assessment of earthquakes for local authorities and engineering vulnerability, social understanding of earthquake hazards, and general public knowledge of the physical environment. Overall, this chapter characterises the timing of paleoearthquakes and discusses earthquake hazards (recurrence interval and magnitude of paleoearthquakes) whereas the next chapter (Chapter 5) discusses how these earthquakes may produce the observed late Quaternary changes in fault kinematics along the northern NIFS.

4.2 Organization and Analysis of trench data

In this chapter, the location, timing and size of the paleoearthquakes that ruptured the ground surface in the northern NIFS over the last c. 18 kyr are characterised. Evidence for paleoearthquakes in the northern NIFS is discussed from south to north along each fault (Waiohau-Ruahine, Whakatane-Mohaka and Waimana faults). Three types of trench data have been used: 1) new fault-trench information collected as part of this PhD study (which are discussed in detail); 2) trench-data and interpretations from previous studies (Hull, 1983; Beanland, 1989b; Beanland, 1995; Woodward-Clyde, 1998; Hanson, 1998) that are summarised briefly here; and, 3) trench-data from previous work (Hanson, 1998; Woodward-Clyde, 1998) that have been re-interpreted here. These sources of data are integrated in order to evaluate the temporal and spatial distribution of paleoearthquakes within the northern NIFS (see Chapter 5 for further discussion).

At each trench site I present a brief description of the geomorphology of the site and the trench itself, the stratigraphy encountered, the geometry of the fault within the trench and the earthquake events recorded in the trenches. Slip-rates obtained from 3D trenching are presented where appropriate.

Once the description of all the sites along each fault is completed, a general discussion follows that involves the comparison of the earthquake histories between trench sites for each fault (i.e. the temporal and spatial distribution of paleoearthquakes). A mean recurrence interval and earthquake magnitude is inferred for each fault at the end of this chapter, in the Seismic Hazard section (section 4.6).

The numbering of the paleoearthquakes recorded on each trench wall is from the youngest (e.g. 1st) to the oldest (e.g. 4th). The chief dating tool involved the identification of 74 individual tephra layers and the correlation of these to well-dated tephras in the Taupo Rift. Tephra identifications were obtained by comparing their distinctive glass chemistry to a New Zealand database of results, the details of which are available in Appendix III. In addition to the tephra samples, 19 organic stratigraphic horizons were radiocarbon dated in order to provide additional constraints on the timing of past earthquakes. Details on the radiocarbon dating are provided in Appendix V. All ^{14}C ages are presented in calibrated radiocarbon years BP. The calibrated ages of the reference tephra layers are those of Zachariasen & Van Dissen (2001). For detailed description of the units encountered within the trenches see Appendix II. A summary of all trenches used in this study (such as source of data, grid reference, timing of the most recent event, etc.) is presented in Table 5.1 of Chapter 5.

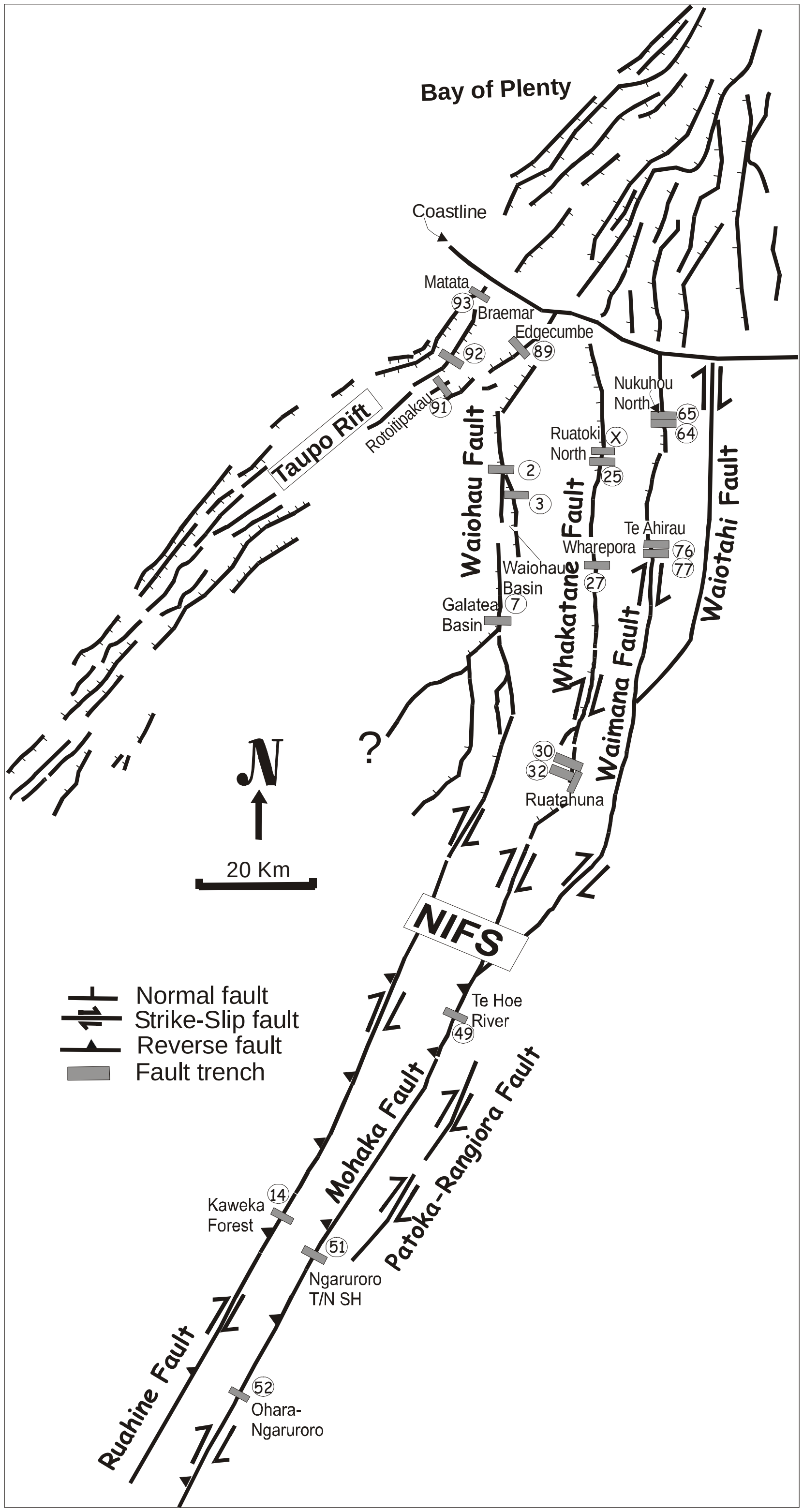

Fig. 4.0 Fault map showing the location of the 20 fault trenches across the northern NIFS (n=16) and Taupo Rift (n=4) which are discussed in Chapter 4. The details of each trench are summarized in Table 5.1 (Chapter 5).

4.1 WAIOHAU-RUAHINE FAULT

4.3.1 Kaweka Forest - Napier/Taupo Highway:

All information discussed at this site is from Hanson (1998).

4.3.1.1 Site and trench descriptions

The Ruahine Fault between the Kaweka Forest and Napier/Taupo State Highway traverses rugged terrain underlain by Mesozoic greywacke which is heavily vegetated. In places, the fault forms the boundary between the Torlesse Mesozoic greywacke, to the west, and Tertiary siltstone, to the east. It strikes NE-SW (i.e. 020-030°), dips steeply (i.e. >80°) and is a strike-slip fault. Where the fault traverses farm land, right-lateral displacement of abandoned streams, spurs and terrace risers across active traces is commonly visible.

Two trenches were excavated across the Ruahine Fault on Davis' farm (U20/092077), at the end of Whittle Road and on either side of Baldy quarry near Kaweka Forest (site 14 in Fig. 4.0). The quarry exposes basement greywacke with vertical bedding. Davis 1 Trench is located 100 m north of the quarry and it is excavated perpendicular to the fault, through a swamp where the drainage has been ponded. Davis 2 is located 500 m south of Baldy quarry and excavated across the fault scarp and through basement greywacke.

4.3.1.2 Stratigraphy and age control

Davis 1 Trench is excavated across a part of the Ruahine Fault that separates Tertiary siltstone (east) and the Mesozoic greywacke (west) (Fig. 4.1a). The middle section of the trench comprises interbedded peat, silt and volcanic tephra layers. The base of this sequence is radiocarbon dated at 8511±132 cal. kyr BP (NZ 8233). The Waimihia (3.5 kyr BP) and Taupo (1.8 kyr BP) tephras are present higher up within the bedded sequence (Fig. 4.1a).

Davis 2 Trench is excavated across weathered greywacke (Fig. 4.1b). All deposits within the trench consist of either weathered greywacke, greywacke-derived colluvium or volcanic horizons derived from the Taupo and Okataina volcanic centers. The oldest of the datable infill deposits is the Waiohau Tephra (13.8 kyr BP). Additional tephras encountered within the trench include those of Mangamate (c. 10 kyr BP), Waimihia (3.5 kyr BP) and Taupo (1.8 kyr BP). No organic material or peat deposits are present within the infill deposits, precluding radiocarbon dating.

4.3.1.3 Fault Geometries

The fault in the trenches strikes c. 015° and has a steep dip of c. 85° down to the west. In Davis 1, the fault consists of one principal, near vertical, slip surface that splays upwards into two strands which are 1-1.5 m apart. The westernmost strand is also near vertical whereas the easternmost strand dips c. 70° to the west and bifurcates upwards. In contrast, the fault in Davis 2 is vertical and comprises a single fault surface.

4.3.1.4 Timing of paleoearthquakes on Ruahine Fault between Kaweka Forest and Napier/Taupo Highway

The following is a re-interpretation of the paleoseismic history of large surface rupturing earthquakes based on the trench logs of both Davis 1 and 2 trenches of Hanson (1998).

- 1st event (most recent): Slip during this event displaces the Taupo Tephra (1.8 kyr BP) and occurred within the last 1.8 kyr. This post-Taupo Tephra event is equivalent to events 5, 6, 7 and 8 in Hanson’s (1998) interpretation.
- 2nd event: This earthquake displaces and folds the Waimihia Tephra (3.5 kyr BP) (Fig. 4.1a), a deformation that predates the deposition of Taupo Tephra (1.8 kyr BP). This event is equivalent to the 4th event in Hanson’s (1998) interpretation.
- 3rd event: Slip during this earthquake has an apparent vertical displacement (c. 17 cm) of the top of a gravel unit on the western strand of the North wall in Davis 1 (Fig. 4.1a). Dating of a peat and wood layer that is displaced by the fault and rests on top of the gravel unit but below Waimihia Tephra (3.5 kyr BP), indicates a maximum age of this event of 4055±15 yrs BP (NZ 8232). The unfaulted

Waimihia Tephra (3.5 kyr BP) suggests a minimum age of this event of 3.5 kyr BP. This event is equivalent to the 3rd event in Hanson's (1998) interpretation.

- 4th event: This event forms the colluvial wedge that rests within the peat layer at the base of the Davis 1 Tench and adjacent to the silt block (Fig. 4.1a). The formation of this wedge predates 4055±15 yrs BP. The dating of the peaty material that sits below the silt block and adjacent to the main fault, and predates block movement, indicates that faulting is post 6738±204 yrs BP (NZ 8231). There are no data for the time interval between the deposition of Mangamate Tephra (c. 10 kyr BP) and prior 6738±204 yrs BP (see Fig.4.1b, North wall in Davis 2) and therefore there may be event(s) missing.
- 5th earthquake event: Forms the colluvial wedge that rests between Waiohau (below) and Mangamate (above) tephras. Therefore, this is a post Waiohau (13.8 kyr BP) – pre Mangamate (c. 10 kyr BP) earthquake event (Fig. 4.1b). This event is equivalent to the 2nd event in Hanson's (1998) interpretation.
- 6th earthquake event (oldest): Colluvium thickening towards fault suggests fault-related depression present pre-Waiohau Tephra (13.8 kyr BP) which in turn suggests pre-Waiohau event of uncertain age (Fig. 4.1b). This event is equivalent to the 1st event in Hanson's (1998) interpretation.

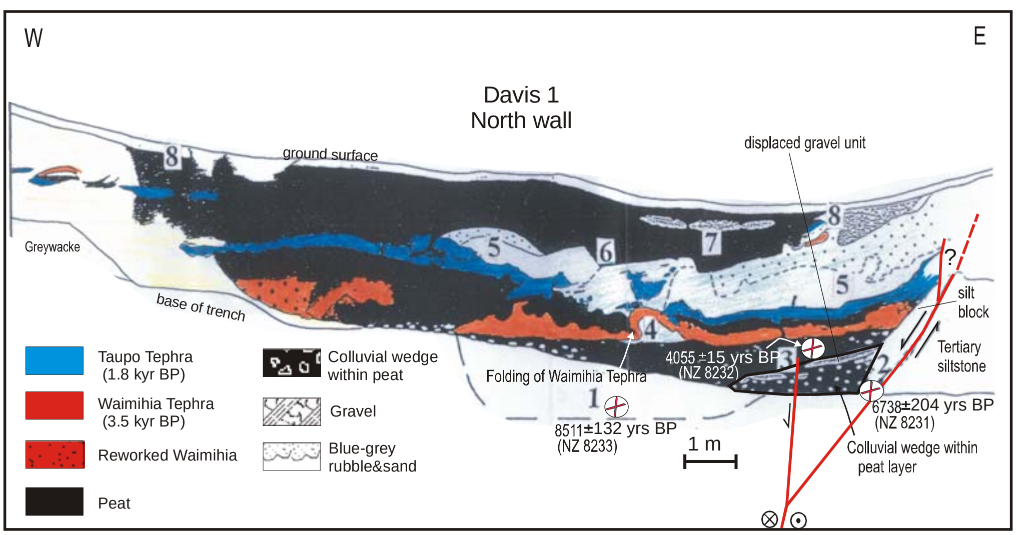

Fig. 4.1a The north wall of Davis 1 Trench from Hanson (1998). The numbers in the log represent earthquake events as interpreted by Hanson and are numbered in the reverse sense to that indicated in the text (see section 4.2).

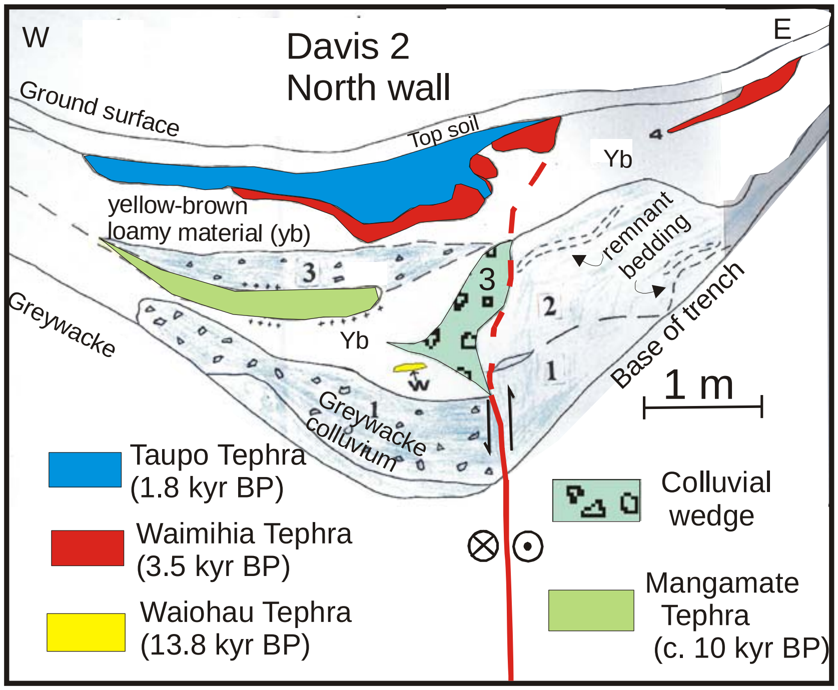

Fig. 4.1b The north wall of Davis 2 Trench from Hanson (1998). The numbers in the log represent earthquake events as interpreted by Hanson and are numbered in the reverse sense to that indicated in the text (see section 4.2).

4.3.2 Galatea Basin

All information discussed at this site is from Beanland (1989b).

4.3.2.1 Site and trench descriptions

The Waiohau Fault bounds the eastern margin of the Galatea Basin. It consists of three geometric segments which, from south to north, strike ENE-WSW (050-060°), NE-SW (c. 040°) and N-S (c. 350-010°), respectively (Map C in Appendix I). The middle segment is inferred to have the largest vertical component of displacement, because the mountain range-front is the highest (>900m) at this location, with triangular facets characteristic of normal fault displacements (Fig. 1 in Appendix I). The average dip of the Waiohau Fault in Galatea Basin is 60-70° W (S. Toulmin, Pers. comm., 2006), with displacement consistently down to the west.

The Troutebeck Trench (V17/446057) is located at the southern end of the N-S striking northernmost fault segment (site 7 in Fig. 4.0 & Map C in Appendix I). The trench was excavated across the fault trace, near a terrace riser that is covered by a younger fan. A stream subsequently cut into the fan and formed a floodplain up to 100 m wide, which remains active and is < 3m below the fan surface. To the north of the site, the fault scarp is at the base of the range-front. South of the stream the fault scarp height increases from 3 to 10 m as the displaced fan deposits (of the younger fan) thin on the downthrown side of the fault. A second trench across the active floodplain showed no evidence of faulting in the alluvium post Kaharoa Tephra (i.e. c. 0.8 kyr ago). A third trench was excavated c. 4 km to the north of Troutebeck Trench (V17/447093) (site 7a in Map C, Appendix I) into fan alluvium overlain by Taupo (c. 1.8 kyr BP) and Kaharoa (0.8 kyr BP) tephras. This trench showed the fan to be unfaulted. For further details on the geomorphology and trench site location see Beanland (1989b, 1995).

4.3.2.2 Stratigraphy / Age control

The timing of the earthquake events recorded in the Troutebeck Trench, and which are discussed in the next section, is constrained by tephra stratigraphy. The volcanic layers in the Troutebeck trench that sit stratigraphically above the basal gravels of the oldest fan include (from the bottom to the top) Te Rere (25 kyr BP), Okareka (21 kyr BP), Rerewhakaaitu (17.6 kyr BP), Waiohau (13.8 kyr BP), Rotoma (9.5 kyr BP) and Whakatane (5.6 kyr BP) tephras. Initial deposition of the oldest fan therefore predates c. 25 kyr BP. The total vertical offset on this fan is c. 9 m. The active floodplain (on which the second trench was excavated) contains Kaharoa Tephra (c. 0.8 kyr BP) near its base indicating that it mainly formed in the past 800 years.

4.3.2.3 Fault Geometries

The average strike of the fault in the trench is 010° and it dips c. 45° to the west. This very shallow dip probably does not represent the average dip of the fault in Galatea Basin which instead is thought to be about 60-70° (S. Toulmin, Pers. comm., 2006). The faulting within the trench is distributed over 3-4 m on two main slip surfaces. For further details on the geometry of the fault in the trench see Beanland (1989b).

4.3.2.4 Timing of paleoearthquakes on Waiohau Fault in Galatea Basin

Troutbeck Trench:

- 1st (most recent) & possibly 2nd events: Lack of displacement of the Taupo (1.8 kyr BP) and Kaharoa (0.8 kyr BP) tephras in the trench c. 4 km north of Troutebeck (see section 4.3.2.1) indicate the most recent rupture pre-dates Taupo (1.8 kyr BP). Offset of Waiohau (13.8 kyr BP) and Rotoma (9.5 kyr BP) tephras in the Troutebeck Trench, by the same amount, indicate at least one surface-rupturing event subsequently. That is, the most recent event is constrained between 9.5 and 1.8 kyr BP.
- No rupture of the fault is indicated between c. 13.8 and 9.5 kyr BP (as the displacement on the Waiohau and Rotoma tephras is the same).
- 3rd event (oldest): On a fault strand different to that which ruptured during the youngest (and possibly second youngest) earthquake, the Rerewhakaaitu Tephra (17.6 kyr BP) is displaced while the Waiohau Tephra (13.8 kyr BP) appears to lie unfaulted on top of the Rerewhakaaitu Tephra. This event therefore postdates the deposition of Rerewhakaaitu Tephra (17.6 kyr BP) and predates the deposition of the Waiohau Tephra (13.8 kyr BP).

4.3.3 Waiohau Basin

All information discussed at this site is from Woodward-Clyde (1998).

4.3.3.1 Site and trench descriptions

The Waiohau Fault at the Waiohau Basin partitions its slip into two strands, the eastern and the western. Both strands of the fault strike c. N-S (Map D in Appendix I). The eastern strand has a westwardly concave shape bounding the eastern margin of the basin and appears to be chiefly a normal fault dipping to the west at c. 65°. The western strand bounds the western margin of the Waiohau Basin and appears to be the northward extension of the northernmost segment in the Galatea Basin (Maps A, C & D in Appendix I). The western strand carries oblique-slip (strike-slip and normal dip-slip) displacement and is near vertical (> 80°), dipping either to the east or west. These two strands, which are less than 3 km apart, are assumed to link at depth and their paleoearthquakes are therefore discussed jointly.

Two trenches have been excavated across the Waiohau Fault in the Waiohau Basin. The Cornes Trench was excavated across a scarp at the northern end of the eastern strand of the Waiohau Fault (site 3 in Fig. 4.0 & Map D in Appendix I), about 300 m east of Galatea Road, 300 m south of Kaiwhakinokino Stream, and 30 m east of an electricity pylon (V16/472251). The Tasman 1 Trench was excavated across a scarp on the western strand of the Waiohau Fault (site 2 in Fig. 4.0 & Map D in Appendix I), c. 0.9 km north of bridge over Rangitaiki River on Galatea Road and c. 6 km south of the Matahina Dam in Tasman forestry area (V16/453298). The Tasman 1 is located on a prominent north-south oriented fault strand which extends through the Matahina reservoir.

4.3.3.2 Stratigraphy / Age control

The Cornes Trench was excavated into a fan surface. The basal fan gravels are overlain by Te Rere Tephra (25 kyr BP) and therefore they have been inferred to be at least 25 kyr BP in age. Prominent tephra units above Te Rere in the Cornes Trench include Okareka (21 kyr BP), Rerewhakaaitu (17.6 kyr BP), Waiohau (13.8 kyr BP), Rotoma (9.5 kyr BP), Mamaku (c. 8 kyr BP), Taupo (1.8 kyr BP) and Kaharoa (0.8 kyr BP).

The Tasman 1 Trench was excavated within Matahina ignimbrite (c. 280 kyr BP) overlain by c. 5 m of late Quaternary tephras and paleosols. The Tasman 1 Trench remains open today and four reference tephra layers were sampled for this study to identify their origin and age. New micro probe analysis suggests identifications for two of the tephra layers that differ from the assignments proposed by Woodward-Clyde (1998). In detail, the Woodward-Clyde ‘Waiohau Tephra’ (13.8 kyr BP) is here instead interpreted as Rerewhakaaitu Tephra (17.6 kyr BP), while their ‘Rotoma Tephra’ (9.5 kyr BP) has been reinterpreted as Waiohau Tephra (13.8 kyr BP) (for details on the probe analyses, see Tables 1-4 in Appendix III). Eruptives of Mamaku (c. 8 kyr BP), Whakatane (5.6 kyr BP), Taupo (1.8 kyr BP) and Kaharoa (0.8 kyr BP) were also recognised in the Tasman 1 Trench. In the discussion that follows, the timing of paleoearthquakes relative to the stratigraphy in Tasman 1 has been adapted from

Woodward-Clyde (1998), while the absolute timing of events has been adjusted in accordance with the new tephra identifications.

4.3.3.3 Fault Geometries and site description

The fault in Cornes Trench strikes 360° and dips 65±10° to the west. Faulting is distributed over a 4-5 m wide zone. Most of the slip surfaces dip to the west; however, there are also few antithetic splays. The geometry of faulting within the trench typifies that of normal faults as most of the units can be traced and correlated across the slip surfaces.

The fault geometry in Tasman 1 Trench is complex with at least three sets of faults exposed. One set is steep (near vertical) with an approximately north trend (330-030°), another has a shallow dip (25-40° W) also with an approximately north strike (320-005°) and a third set of near vertical faults strikes 060-070°. The shallow dipping set of faults has a 'normal' sense of motion and runs through a rotated block. Woodward-Clyde (1998) assumed that the slip on the latter 'normal' strands predates the block rotation and therefore the shallow dip is an apparent feature. Data derive from a gravity survey located 6 km to the north of the trench site (Chapter 6 & Appendix IV), suggest an average dip for the Waiohau Fault in the upper 1-2 km of crust of 65±5° W. For further details on the geometry of the fault in the trench see Woodward-Clyde (1998).

4.3.3.4 Timing of paleoearthquakes on Waiohau Fault in Waiohau Basin

Eastern strand (Cornes 1 Trench)

- Mamaku (c. 8 kyr BP) and younger tephras are unfaulted and therefore no earthquake has occurred on this strand during the last 8 kyr.
- 1st earthquake event (most recent): Rotoma Tephra (c. 9.5 kyr BP) is displaced by c. 2.5 m whereas Mamaku Tephra (c. 8 kyr BP) is not faulted. This earthquake ruptured the fault between 9.5 and 8 kyr BP.
- 2nd & possibly 3rd earthquake events (oldest): Two colluvial (scarp-derived) wedges formed in the time interval between the deposition of the Waiohau (13.8 kyr BP) and Rotoma (9.5 kyr BP) tephras and may represent two earthquakes

events on this strand of the Waiohau Fault. Each event is associated with 2 to 2.5 m of dip-slip separation. However, one event of >2.5 m cannot be ruled out.

- No earthquake event occurred on this strand between 25 and13.8 kyr BP.

<u>Western strand (Tasman 1 Trench)</u>

The absolute timing of the paleoearthquakes has been re-interpreted following the new tephra identifications (see section 4.3.3.2)

- Taupo Tephra (1.8 kyr BP) is not faulted and therefore the last event is constrained as older than c. 1.8 kyr BP.
- 1st (most recent) & 2nd earthquake events: Two major surface-rupturing events post-date deposition of the Whakatane Tephra (5.6 kyr BP) and pre-date deposition of the Taupo Tephra (1.8 kyr BP). A block that contains Whakatane Tephra (5.6 kyr BP) is displaced (and tilted) by 4.5-5 m and subsequently faulted (on a different strand) by a later event. The minimum age for the last event is estimated by McMorran & Berryman (2001) to be c. 3690 kyr BP.
- 3rd earthquake event: There is some evidence for displacement of the Waiohau Tephra (13.8 kyr BP) on north-striking faults near the western end of the south wall. This event, which postdates the deposition of the Waiohau Tephra (13.8 kyr BP), predates the deposition of the Whakatane Tephra (5.6 kyr BP).
- 4th earthquake event (oldest): Rerewhakaaitu Tephra (17.6 kyr BP) is displaced by a fault strand (c. 2 m of dip-slip separation) but Waiohau Tephra (13.8 kyr BP) is unfaulted. The oldest event recorded in this trench occurred between 17.6 and 13.8 kyr BP.

4.3.4 Timing of paleoearthquakes on the Waiohau-Ruahine Fault

Figure 4.2 summarises the temporal and spatial distributions of the late Quaternary earthquakes on the northernmost 150 km of the Waiohau-Ruahine Fault. The trench data indicate that the southern c. 90 km of the fault has ruptured more recently and more frequently than the northern c. 60 km. For example the southern section of the Waiohau-

Ruahine Fault, from Kaweka Forest to south of Galatea Basin (where the fault is known as the "Ruahine Fault") has ruptured at least once in the last 1.8 kyr while the section of the fault that extends through the Galatea and Waiohau basins appears not to have ruptured in the last at least 1.8 kyr. At least three of the earthquakes that ruptured the Kaweka section of the fault did not rupture the Galatea Basin site. In addition, at least three (more than half of the total earthquakes occurred over the last c. 18 kyr) events appear to terminate between the Troutebeck and Tasman 1/Cornes trench sites (a distance of 25 km). The non-uniform spatial distribution of paleoearthquakes along the Waiohau-Ruahine Fault appears to indicate the presence of two potential areas of rupture arrest: the southernmost between Kaweka Forest and Galatea Basin and the northernmost between Galatea and Waiohau basins. The details of the potential earthquake segments are discussed in Chapter 5.

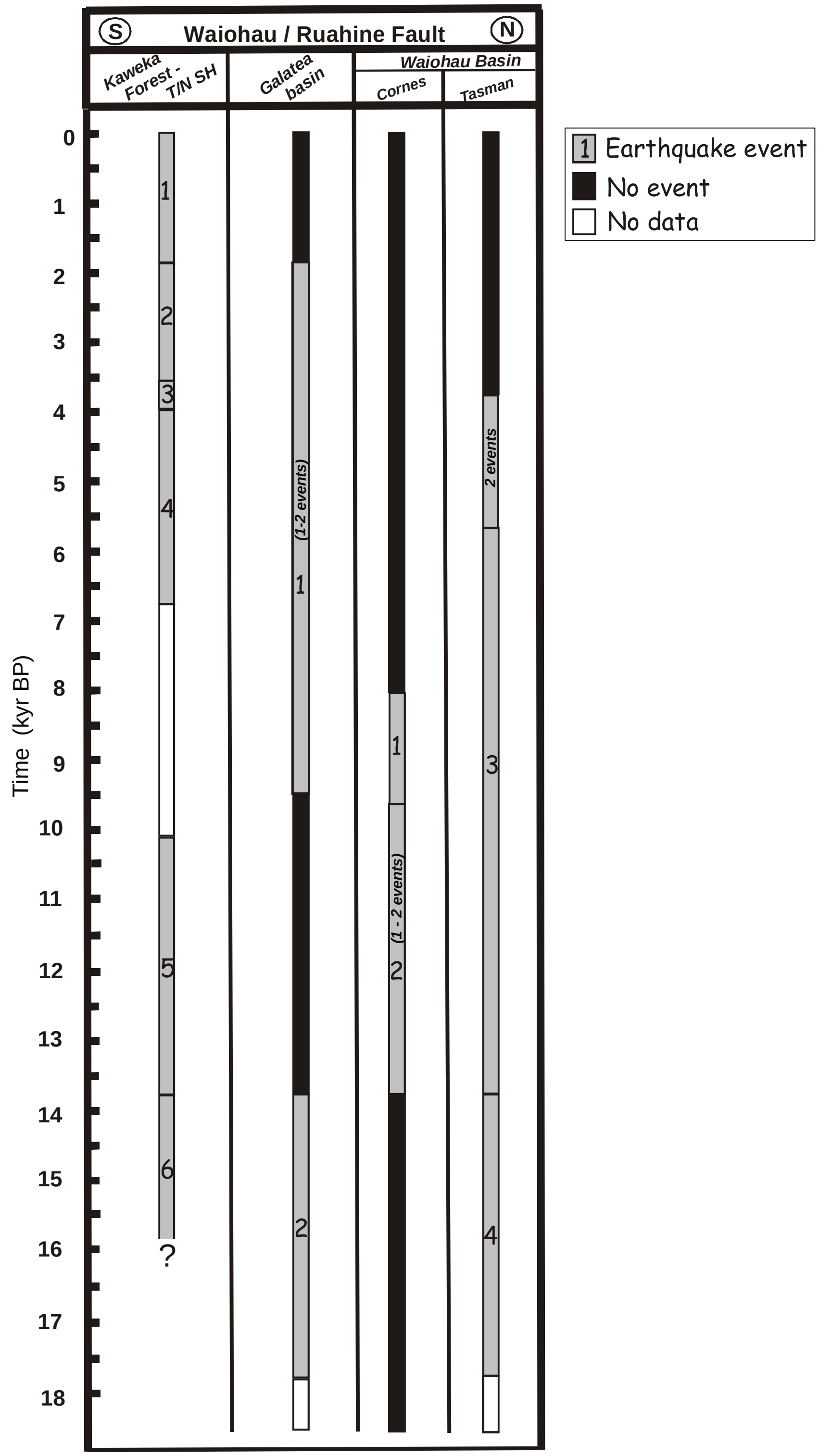

Fig. 4.2 Summary of the late Quaternary paleoearthquake history on the northernmost 150 km of the Waiohau-Ruahine Fault. Consecutive numbering of events within the grey polygons is shown. Black lines that bound the grey polygons represent minimum and maximum age for each event, respectively. T/N SH indicates Taupo/Napier State Highway.

4.2 WHAKATANE – MOHAKA FAULT

4.4.1 Ohara Depression – Ngaruroro River

All information discussed at this site is from Hanson (1998).

4.4.1.1 Site and trench descriptions

The Mohaka Fault between Ohara depression and Ngaruroro River strikes NE-SW (e.g. c. 040°) and has a near vertical dip (Fig. 2.4 in Chapter 2). The fault itself is the boundary between the Mesozoic greywacke basement, which is upthrown to the west, and Tertiary sediments, which are downthrown to the east. In this locality, the strike-slip late Quaternary trace of the fault is clear and continuous, traversing and displacing numerous spurs and streams.

One trench (McCool 1) was excavated across the fault on McCool farm at the end of Nelson Road (U21/010746) (site 52 in Fig. 4.0). At this site the fault scarp impedes a stream which is ponded on the downthrown side of the fault. Both, the north and south walls of the trench were logged and are presented in Figs 4.3a & b.

4.4.1.2 Stratigraphy and Age control

The trench is excavated on an aggradational terrace. Based on dating of carbonaceous silt resting immediately on the aggradation gravels (16810±575 / NZ 8287), the terrace is inferred to have formed at c.17 kyr ago. On the downthown (ponded) side of the fault, a 5 m thick sequence of gravels, peat and volcanic ash layers overlies the basal gravels and carbonaceous silt. The Waimihia (3.5 kyr BP) and Taupo (1.8 kyr BP) tephras are present towards the top of the sequence. Six peat samples were dated and returned ages ranging between 16810±575 (NZ 8287) and 614±20 (NZ 8291) (Figs. 4.3a & b).

4.4.1.3 Fault Geometries

The average strike of the fault in McCool 1 is 020° while its dip is near vertical (c. > 85°). The fault comprises a c. 1.5 m wide zone with two principal slip surfaces which splay upwards in secondary strands. Some of the units (e.g. carbonaceous silt) within the fault zone appear to be strongly deformed (e.g. tilted vertically) whereas other faulted units (e.g. cobbly gravel) dip only gently. The presence of off-fault deformation is indicated by the drag of Waimihia Tephra and silt layer into the fault zone (Fig. 4.3b). The easternmost strand on the south wall of McCool 1 appears to reach the base of modern soil (Fig. 4.3b).

4.4.1.4 Timing of paleoearthquakes on Mohaka Fault between Ohara Depression and Ngaruroro River

McCool 1 Trench

The following is a re-interpretation of Hanson's (1998) work.

- 1st event (most recent): At least one earthquake displaces the Taupo Tephra (1.8 kyr BP) and possibly also the peaty layer, dated at 614±20 yrs BP (NZ 8291), that rests on Taupo Tephra (sample F in Fig. 4.3a). Therefore, the most recent event postdates 1.8 kyr and possibly c. 600 yrs BP. This event is equivalent to the 5th & 6th events in Hanson's (1998) interpretation.
- 2nd event: Waimihia Tephra (3.5 kyr BP) is displaced and/or dragged downwards into the fault zone (Figs. 4.3a & b). Deformation of Waimihia Tephra is greater than that of the Taupo (Fig. 4.3b), from which it is inferred that the penultimate event occurred between the deposition of these tephras (i.e. between 1.8 and 3.5 kyr BP). This event is equivalent to the 4th event in Hanson's (1998) interpretation.
- 3rd and 4th events: Carbonaceous silt and aggradation gravels have been incorporated into the fault zone. On the north wall of McCool 1 (Fig. 4.3a) a 1-1.5 m wide block of vertically dipping carbonaceous silt is overlain by sub-horizontal cobbly gravel and peat. Deformation of the silt therefore predates deposition of the cobbly gravel and post dates deposition of the silt. The vertical bedding, the significant thickening of the carbonaceous silt in the fault zone and the mixing of aggradation gravels and silt suggest multiple fault rupture events.

As the silt is significantly more deformed than the Waimihia Tephra it is inferred that two or more events predate deposition of the cobbly gravel. The youngest of these events may have occurred at about the time of deposition of the cobbly gravel (which locally overlies the carbonaceous silt across an angular unconformity). Radiocarbon dates from immediately above and below the cobbly gravel are 5919±257 (NZ 8288) and 4728±145 (NZ 8289) yr BP, respectively (samples B and C in Fig. 4.3b). Therefore the 3rd event at this site may date from 6 kyr ago. The maximum age of the fourth event derives from the age of the silty unit which overlies the offset basal gravels and which is 16810±575 yrs BP (NZ 8287) (sample A in Fig. 4.3b). These events are equivalent to the 3rd, 2nd & 1st events in Hanson's (1998) interpretation.

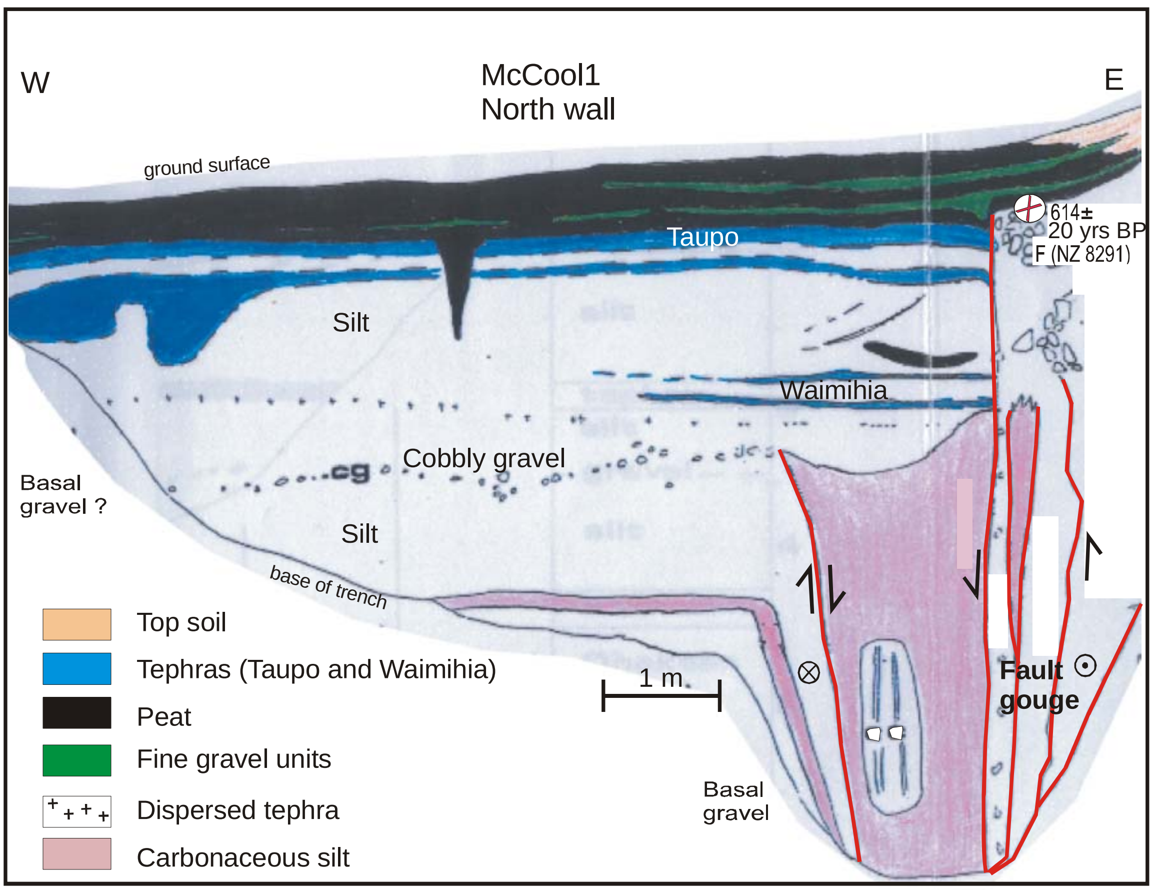

Fig. 4.3a The north wall of McCool 1 Trench from Hanson (1998).

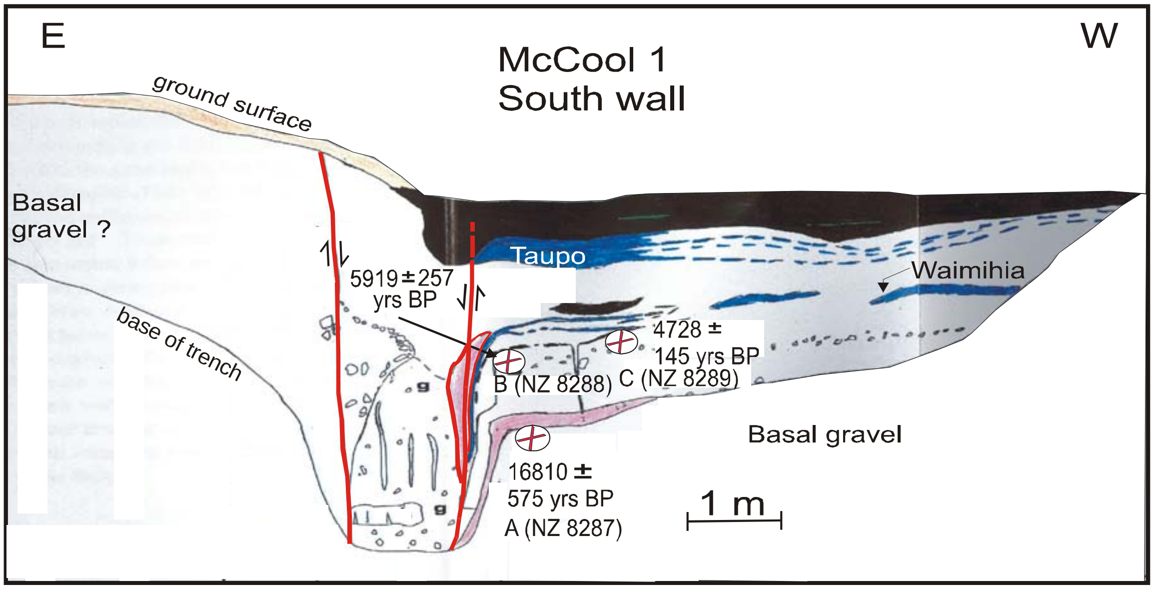

Fig. 4.3b The south wall of McCool 1 Trench from Hanson (1998).

4.4.2 Ngaruroro River – Napier/Taupo Highway

All information discussed at this site is from Hanson (1998).

4.4.2.1 Site and trench descriptions

The Mohaka Fault between the Ngaruroro River and the Napier/Taupo State Highway is a principally strike-slip fault that strikes c. 030-040° NE and its dip is near vertical. It forms scarps that face either to the east or west and often displaces right-laterally numerous streams and spurs formed on surfaces of Ohakean age (30-15 kyr BP).

The Syme Trench is located at the end of Hawkstone Road (V20/137986) (site 51 in Fig. 4.0). At this location an upstream-facing fault scarp, downthrown to the west, blocks a stream channel. The trench is excavated through the upper end of the blocked drainage, across the fault scarp into Te Weka limestone on the upthrown wall.

4.4.2.2 Stratigraphy and Age control

The west (downthrown) side of the scarp is filled in by c. 5 m thick ponded sediments and volcanics. The identification of the Karapiti Tephra (10.1 kyr BP) at the base of the infill deposits, suggests that the drainage was blocked c. 10 kyr ago. Mangamate (10 kyr BP), Waimihia (3.5 kyr BP) and Taupo (1.8 kyr BP) tephras are also present within the trench.

4.4.2.3 Fault Geometries

The average strike of the fault in Syme Trench is 030° and its dip is steep (c. 85° E). The fault zone is c. 4 m wide and comprises two steep principal slip surfaces that extend upwards to near the base of the top soil. The slip-surfaces juxtapose non-matching stratigraphic horizons indicating strike-slip. Fissures within the fault zone are filled with gravel and rubble. For further details on the geometry of the fault in the trench see Hanson (1998).

4.4.2.4 Timing of paleoearthquakes on Mohaka Fault between Ngaruroro River and Napier/Taupo Highway

<u>Syme Trench</u>

- 1st event (most recent): Taupo Tephra (1.8 kyr BP) is truncated by the fault. Therefore, at least one earthquake event post dates the deposition of the Taupo Tephra (1.8 kyr BP).
- 2nd event: This earthquake post dates the deposition of Mangamate Tephra (c. 10 kyr BP) and pre-dates formation of a colluvial wedge dated at 9831±346 (NZA 4557) kyr BP.
- 3rd event (oldest): The identification of the Karapiti Tephra (10.1 kyr BP) at the base of the infill deposits and of the trench, suggests a minimum age for the initiation of the ponding of the drainage and subsequently a minimum age for this third earthquake event. Therefore, at least one earthquake event predates 10.1 kyr BP.

4.4.3 Te Hoe River

All information discussed at this site is from Hull (1983).

4.4.3.1 Site and trench descriptions

The Mohaka Fault at Te Hoe River strikes c. NNE-SSW (e.g. 020°) and is chiefly a strike-slip fault (H:V slip ratio is >10) with a steep dip (e.g. > 85°) either down to the east or west. In proximity to Te Hoe River, the fault forms the boundary between the Mesozoic Urewera greywacke, to the west, and the Neogene sediments, to the east, and shows clear evidence of late Quaternary activity. Several streams appear to be right-laterally displaced up to 100 m. A trench was excavated across the Mohaka Fault, c. 700 m south of its intersection with the Te Hoe River, and where it forms a prominent west dipping scarp (V19/379395) (site 49 in Fig. 4.0).

.

4.4.3.2 Stratigraphy and Age control

The stratigraphic sequence recorded within the trench is entirely Holocene in age as Rotoma Tephra (9.5 kyr BP) rests directly on underlying colluvium. Additional prominent tephras encountered within the trench are Waimihia (3.5 kyr BP), Taupo (1.8 kyr BP) and Kaharoa (0.8 kyr BP). Further south, where two channels have been offset by 35 and 40 m, respectively, Opope Tephra (c. 10 kyr BP) rests directly on colluvium, without a paleosol, suggesting a Holocene age for the displaced features.

4.4.3.3 Fault Geometries

The average strike of the fault within Te Hoe Trench is 020° while its dip is near vertical. The fault in the trench is confined within a narrow zone (< 50 cm) which comprises one main steep slip surface. The uppermost units are dragged into the fault zone and can be correlated across the fault whereas near the base of the trench, the fault juxtaposes different stratigraphic units.

4.4.3.3 Timing of paleoearthquakes on Mohaka Fault at Te Hoe River

<u>Te Hoe Trench</u>

- 1st (most recent) & 2nd events: Taupo Tephra (1.8 kyr BP) is offset vertically by 1m while Kaharoa Tephra (0.8 kyr BP) is offset by 0.5 m. This suggests two events, the first post 1.8 kyr BP and the second post 0.8 kyr BP (A. Hull, Pers. comm., 2005).
- 3rd event: This earthquake postdates deposition of Waimihia Tephra (3.5 kyr BP) and predates that of Taupo Tephra (1.8 kyr BP).
- 4th, 5th & 6th events: Given that the average vertical displacement for events 1, 2 and 3 is c. 0.45 m and that the total throw on Rotoma Tephra (c. 9.5 kyr BP) is 2.9 m, 3 earthquakes could have occurred between the deposition of Rotoma (9.5 kyr BP) and Waimihia (3.5 kyr BP) tephras.

4.4.4 Ruatahuna Valley

4.4.4.1 Site and trench descriptions

Approximately 10 km to the north of the Te Hoe River trench site, the Mohaka Fault splays northwards into the Whakatane and the Waimana faults (Fig. 2.4 in Chapter 2). On the west, the Whakatane Fault extends for c. 75 km northwards, from the branch point to the Bay of Plenty coast (and offshore). On the east, the Waimana Fault further bifurcates northwards into the Waiotahi and Waioeka faults (Fig. 2.4 in Chapter 2). Trenches discussed in this section cross the Whakatane Fault in Ruatahuna Valley. The Whakatane Fault, bounds the southern and eastern side of the valley where it strikes at c. 040-050° and 010-020°, respectively (Fig. 4.4 and Map E in Appendix I). The fault-dip is near vertical (e.g. >80°) and is dominated by strike-slip.

Three trenches were excavated across and parallel to the Whakatane Fault (3D trenching). The trench sites were located c. 1.5 km north of the State Highway 38 and c. 500 m to the east of Mataatua Road (W17/555800) (Fig. 4.4 and sites 30 & 31 in Map E,

Appendix I). The two trenches were excavated where the Whakatane Fault displaces an abandoned stream channel dextrally by 22±2 m (Figs. 4.5a & b). The channel has been offset during repeated fault ruptures. A trench along the channel axis and across the fault scarp, "Thalassa*", was excavated to provide information on the paleoearthquake history of the fault. A second trench, "Helios*", was opened on the SE block of the fault and perpendicular to the stream axis, specifically to constrain both the age of the stream channel and the slip rate on the Whakatane Fault (Fig. 8 in Appendix I).

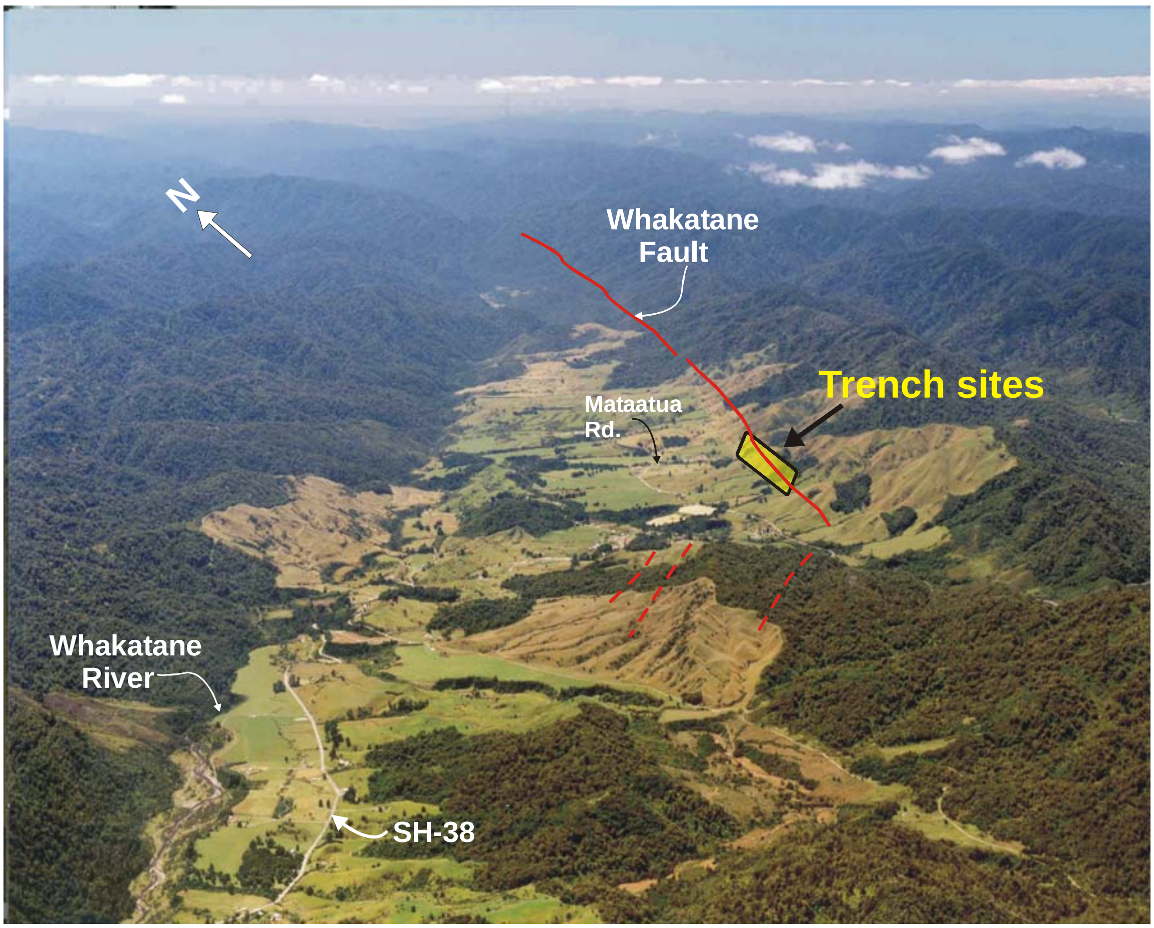

Fig. 4.4 The Whakatane Fault at Ruatahuna Valley. The location of the trench sites is indicated by the yellow polygon. The view is towards the northeast from above Mimiha Stream, with State Highway 38 in the left foreground (photograph by Lloyd Homer).

* "Thalassa" means 'Sea' and "Helios" means 'Sun' in Greek.

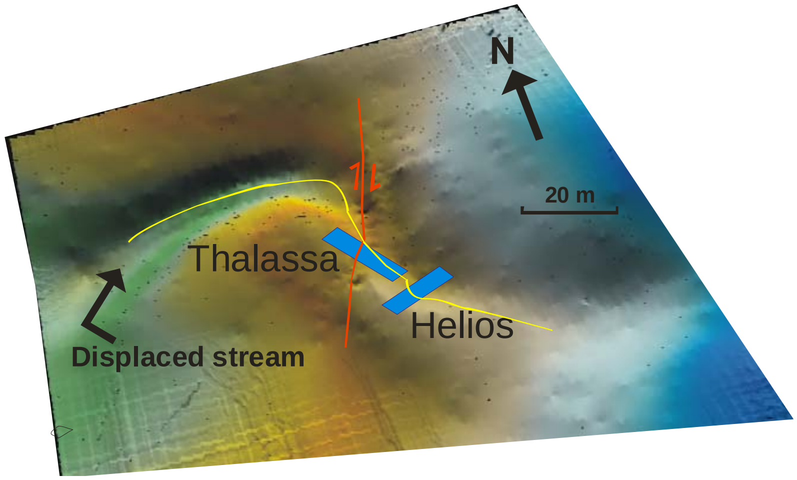

Fig. 4.5a Digital Elevation Model showing the locations of the two trenches excavated in Ruatahuna, one across the Whakatane Fault (Thalassa) and the other across the displaced channel (Helios).

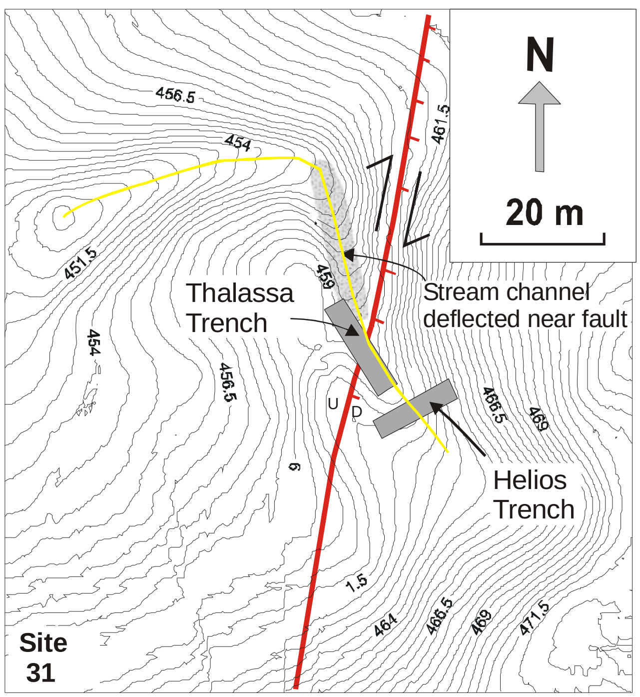

Fig. 4.5b Detailed contoured map created by GPS-RTK illustrating the geometry of the fault (red line) and the channel (axis of the channel is shown as thin yellow line). The locations of the trenches are also indicated by the grey polygons.

A third trench, "Armyra*", was excavated at site 30 (Fig. 11 in Appendix I) c. 100 m to the north (W17/556802) of the displaced channel at site 31. At this location, the drainage is blocked by an uphill-facing fault scarp (down to the east) and a small swamp has formed (Fig. 4.6). The trench was excavated across the fault and the margin of the swamp. Due to the high groundwater level, only part of the north wall was logged (Fig.

* "Armyra" means 'saltiness' in Greek.

4.11). The uppermost c. 0.5 m of the logged wall was modified by a 4WD farm track constructed prior to trenching.

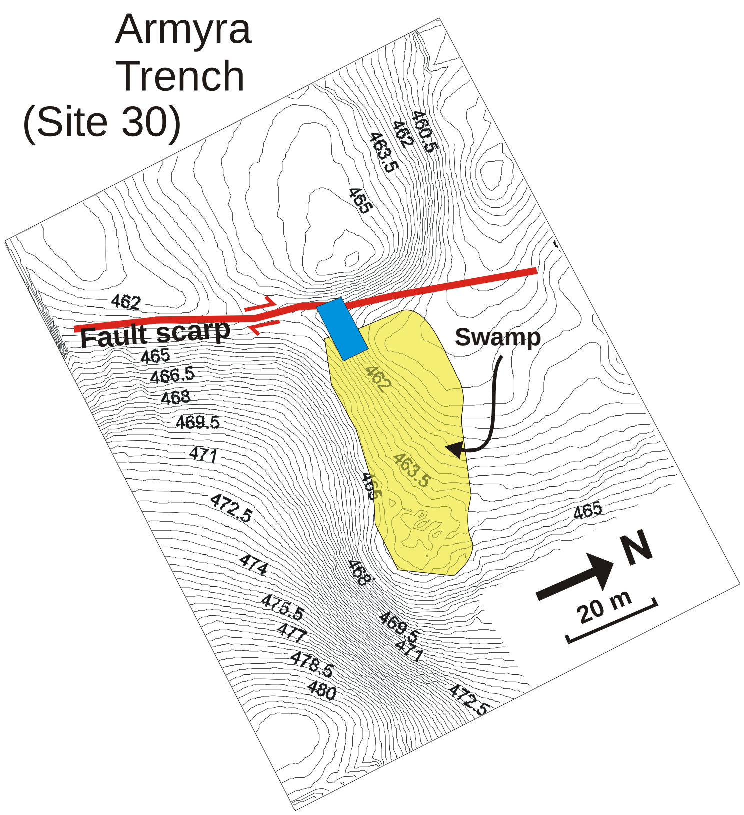

Fig. 4.6 Digital Elevation Model constructed by GPS-RTK surveying showing the Armyra trench site.

4.4.4.2 Stratigraphy and Age control

In Ruatahuna Valley, the N-S striking Whakatane Fault is the boundary between Mesozoic greywacke basement in the east, and Miocene mudstone in the west (Fig. 5 in Appendix I). Bedrock is mantled by Quaternary cover beds that range up to 50 kyr in age and which are incised by numerous stream channels (Francis et al., 1988).

These cover beds were variably deposited pre-, syn- or post- incision of the channel at site 31 (Fig. 4.7). The older, pre-incision deposits (c. 50-26 kyr), consist mainly of loess and tephric layers derived from the Okataina and Taupo volcanic centers which are located < 100 km northwest and southwest of the trench site, respectively (Fig. 2.4 in Chapter 2). Tephras interbedded within these pre-incision deposits include the Rotoehu

(50 kyr BP), which is deposited directly on Tertiary rocks within the trench (see auger-hole in Fig. 4.9), Mangaone Subgroup (c. 30 kyr BP) and Kawakawa (27 kyr BP) (Table 13, 15, 16 in Appendix III) (Figs. 4.7, 4.9, 4.10). These older tephras are unconformably overlain by a Holocene sequence of loess, tephra, peat and pebble gravel beds (Figs 4.7 & 4.8). The oldest datable layer of this younger group of sediments is the Rotoma Tephra (9.5 kyr BP) (Tables 9, 17 & 19 in Appendix III). Additional prominent tephras recorded within this Holocene sequence include Mamaku (c. 8 kyr BP), Whakatane (5.6 kyr BP), Waimihia (3.5 kyr BP), Taupo (1.8 kyr BP) and Kaharoa (0.8 kyr BP) (Tables 7, 8, 10, 11, 12, 14 & 18 in Appendix III) (Figs 4.7 - 4.11). The age of Holocene stratigraphy is further constrained by four radiocarbon dates from peats exposed in the trench walls (Table 4.1) (Figs 4.8 & 4.9).

The channel incision is interpreted to have commenced at about the start of the Holocene (Rotoma Tephra: Tables 9, 17 & 19 in Appendix III, Fig. 4.7). Furthermore, a radiocarbon date of 5728-5586 calibrated kyr BP from a peat layer close to the base of the channel infill deposits indicates that the channel was abandoned (cessation of its erosional phase) about 6 kyr ago (Fig. 4.8, Table 4.1). From these values the age of the offset channel is estimated to be 8±2 kyr, allowing a dextral slip rate of 3±1 mm/yr to be calculated from the cumulative displacement of 22±2 m. This slip rate is consistent with measured single event dextral displacement of c. 5.5±1.5 m from an offset spur c. 500 m north of the trenches (site 39 in Table 2.1 of Chapter 2) and the four earthquakes recorded within the last 9.5 kyr at this site (i.e. 4 events of 5.5 m displacement would produce 22 m of total slip in 9.5 kyr).

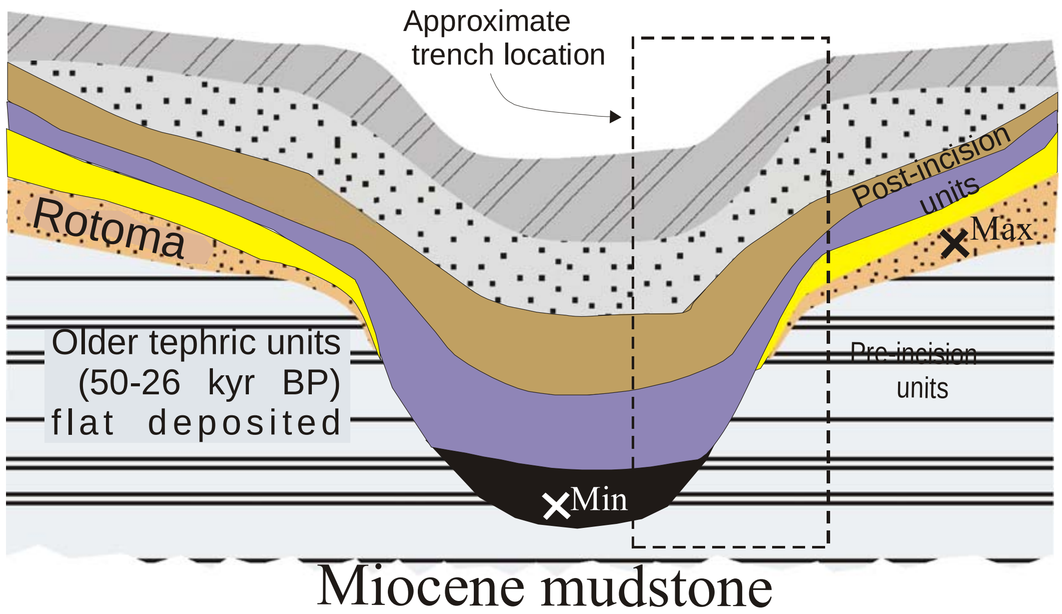

Fig. 4.7 Simplified sketch illustrating the relationships between the Tertiary basement, the older flat lying volcanics, the younger infill and mantling deposits and the channel at site 31. The oldest of the infill channel deposits approximates the time of channel abandonment (minimum age) while the youngest of the pre-incision deposits approximates the start of channel incision (maximum age).

Sample Number (*AMS date)	Method used to claim sample	Sample Description	Grid Reference	Radiocarbon Age			Data on
				Conventional age yrs B.P.	Calibrated age yrs B.P.	Calendar years (calibrated)	
NZA 19822 * (Thalassa)	Trenching	Peat/plant material	W17/ 802555	920 ± 40 BP	930 - 736 BP	1020 AD - 1214 AD	last event
Wk 14588 (Helios)	Trenching	Peat	W17/802555	4908 ± 45 BP	5728-5586 BP	3779 BC - 3637 BC	SR Max (min age)
Wk 14589 (Thalassa)	Trenching	Peat	W17/802555	2628 ± 41 BP	2783-2722 BP	834 BC - 773 BC	Event 2 (max age)
Wk 14590 (Thalassa)	Trenching	Peat	W17/802555	2031 ± 40 BP	2111-1886 BP	162 BC - 64 AD	Event 2 (min age)

Table 4.1 Summary of radiocarbon samples and dates collected from Thalassa and Helios trenches.

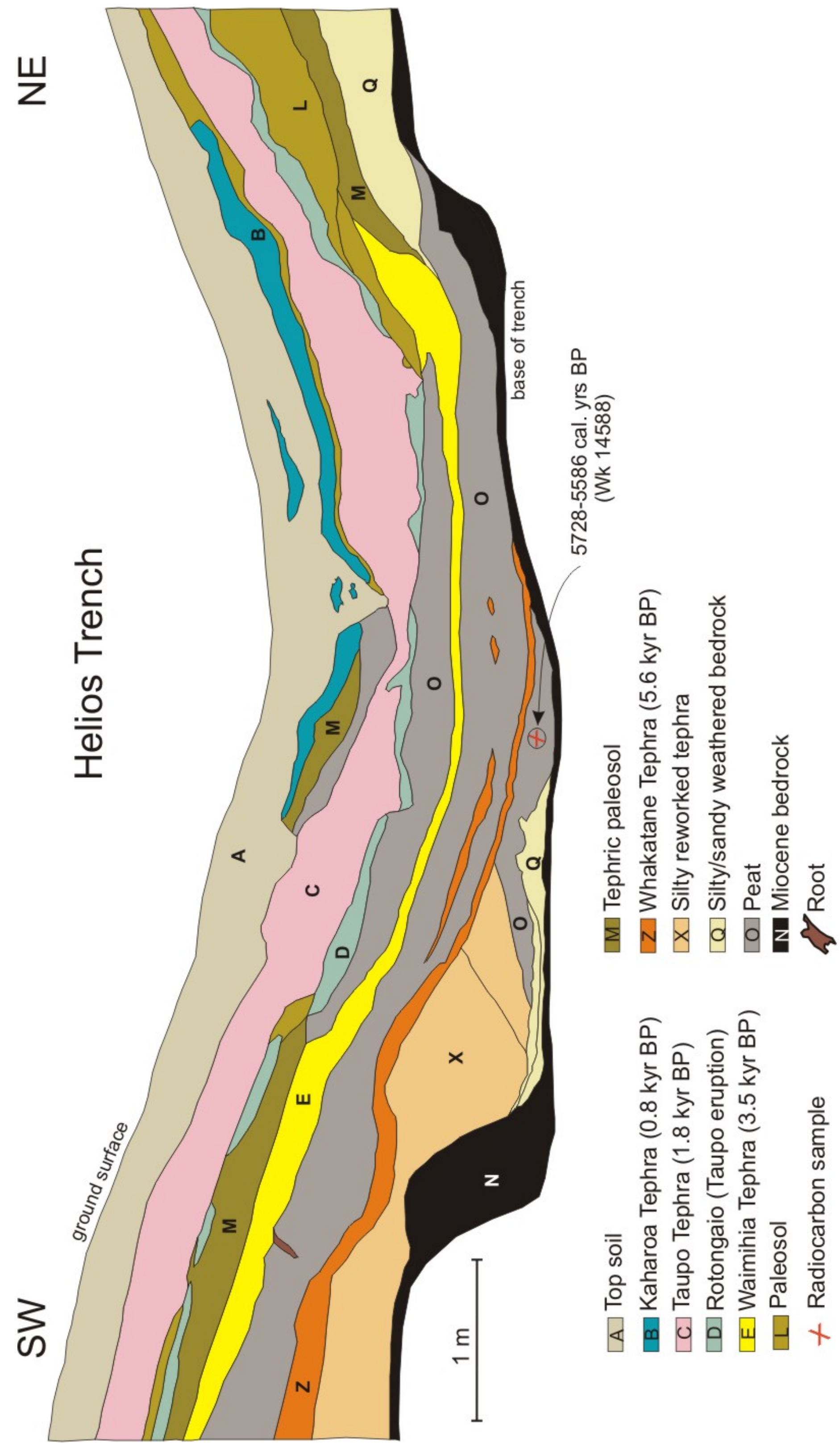

Fig. 4.8 Northwest wall of Helios Trench. Trench normal to the stream axis excavated to help constrain the slip rate on the Whakatane Fault at Ruatahuna.

4.4.4.3 Fault Geometries

The Whakatane Fault on the northeast wall of Thalassa (Fig. 4.9) strikes 020° and its dip is near vertical (87° E). The fault zone is confined to a single principal displacement surface which juxtaposes different stratigraphic units (slip surface 2 in Fig. 4.9). The fault zone at the bottom of the northeast wall is only 10 cm wide whereas upwards splays into four secondary strands and it becomes wider (i.e. 50 cm). Approximately 1.2 m to the northwest of the main fault zone, there is an isolated steep fault-strand (slip surface 6 in Fig. 4.9) that probably joins at depth with the principal fault (Fig. 4.9). There is no apparent off-fault deformation in this wall.

The fault on the southwest wall of Thalassa (Fig. 4.10) strikes 020° and dips 82° to the east. The fault here comprises a single slip surface with only minor upward bifurcation on two small slip surfaces (Fig. 4.10). However, most units proximal to the fault appear to be deformed and dragged upwards towards the fault indicating some off fault deformation.

The Whakatane Fault on the north wall of Armyra Trench (Fig. 4.11) strikes 018° and dips 81° to the east. As in the south wall of Thalassa, the fault geometry is simple, comprising a single steep slip surface, < 5 cm wide, which remains confined along its entire exposure in the trench.

4.4.4.4 Timing of paleoearthquakes on Whakatane Fault at Ruatahuna

Thalassa / Northeast Wall (Fig. 4.9):

- 1^{st} event (most recent): Slip during this event on strand 2 offsets the Taupo (1.8 kyr) and Rotongaio (earlier phase of Taupo eruption) tephras but does not displace the paleosol (unit M) that lies above them. The top of Taupo has an apparent downthrown to the east of 25±5 cm, whereas the base of the unit steps down to the east by 50±5 cm. The difference between the two measures may indicate that a small (25 cm) fault scarp existed prior to the Taupo eruption and/or that the fault had accommodated strike-slip and/or that simply part of the top of Taupo Tephra has been eroded off the upthrown side of the scarp (note thickness of Taupo on each side of the scarp). Kaharoa Tephra (c. 0.8 kyr) appears to be unfaulted. Additional age control for this event is provided by a calibrated radiocarbon age of 833±97 yrs BP dating the unfaulted paleosol between those two tephras. Therefore, the most recent event has occurred between 1800 and 833 yrs BP.

- 2nd event: Slip during this event (slip surface 2) displaces (down to the east) Waimihia Tephra (3.5 kyr BP) by at least 60 cm and forms the colluvial wedge (unit G) east of the slip surface 2. By dating the peat layers (unit O), above and below this wedge the timing of this earthquake is constrained between 2000±110 and 2752±30 yrs BP.
- 3rd event: The Mamaku Tephra (c. 8 kyr BP) on the western side of the main fault zone is abruptly truncated by fault strand 5. This rupture appears to have propagated either slightly or not at all through the paleosol (unit Q1) between the Mamaku (c. 8 kyr BP) and the reworked Whakatane tephras (5.6 kyr BP) and thus, it possibly occurred soon after deposition of the Mamaku Tephra (c. 8 kyr).
- 4th event (oldest): Secondary strand (slip surface 6 in Fig. 4.9), to the northwest of the main fault zone, has an apparent vertical displacement of Rotoma Tephra (9.5 kyr BP) by c. 20 cm, downthrown to the west, and does not appear to propagate into the overlying tephric silty clay (unit P) or to displace the overlying Mamaku Tephra (c. 8 kyr BP). Thus, the rupture post-dates 9.5 kyr BP (perhaps not by much), and predates c. 8 kyr BP.

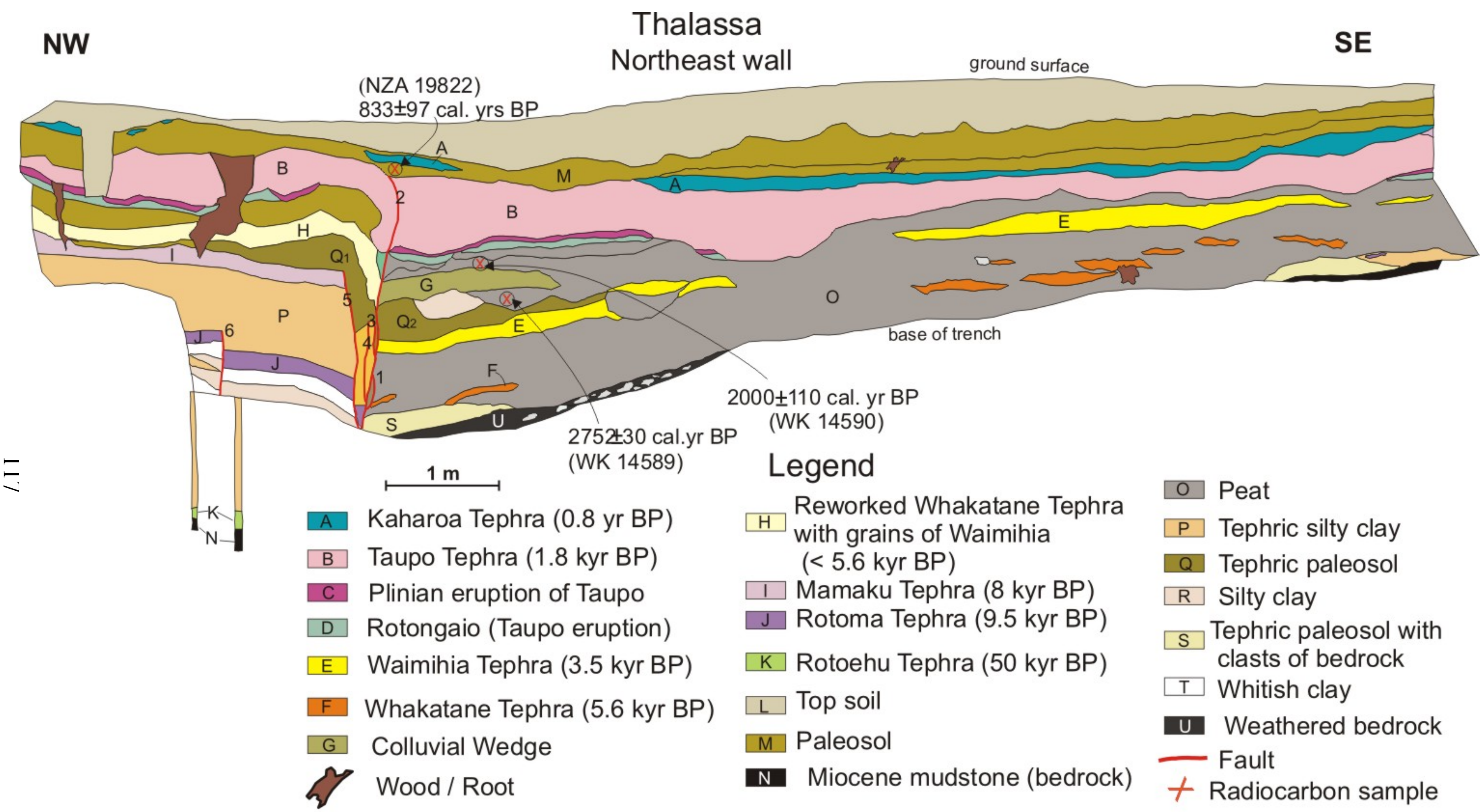

Fig. 4.9 The north wall of Thalassa Trench reveals the most complete earthquake history on the Whakatane-Mohaka Fault in Ruatahuna: 4 earthquakes during the last c. 9.5 kyr. Slip surfaces are numbered (e.g.1-6).

Thalassa / Southwest Wall (Fig. 4.10):

- 1st event: Slip during this event displaces the Taupo (1.8 kyr) and Rotongaio (earlier phase of Taupo eruption) tephras but does not displace the modern soil. The top of Taupo Tephra has an apparent downthrown to the west by 25±5 cm whereas the bottom by 50±5 cm (see argument from 1st event of north wall regarding the differences in the throw on top/base of Taupo Tephra).
- 2nd event: The volcanic horizon of Waimihia Tephra (3.5 kyr BP), southeast of the principal fault surface, is dragged upwards and unconformably overlain by the Taupo Tephra (and its eruptives). Waimihia Tephra (3.5 kyr BP) is disrupted (and deformed) to a greater extent than Taupo Tephra (1.8 kyr BP) and therefore an earthquake event probably occurred between these horizons (i.e. 3.5 and 1.8 kyr BP). This post 3.5 kyr BP earthquake is likely to be equivalent to the penultimate event recorded on the north wall which occurred between 2000±110 and 2752±30 yrs BP.
- 3rd event (oldest): Mamaku Tephra (c. 8 kyr BP) is displaced in an apparent reverse sense by the fault. The Mamaku Tephra (c. 8 kyr BP) is overlain by a colluvial wedge (unit X) which underlies, and is truncated by, the Whakatane Tephra (5.6 kyr BP). This earthquake is probably equivalent with the 3rd event recorded on the north wall of Thalassa and which is inferred to have occurred at c. 8 kyr BP.

The different sense of apparent vertical displacement recorded on some of the units on the south wall (e.g. Taupo downthrown to the west, Rotoma downthrown to the east) results from the combined effect of strike-slip motion on the fault and the steepness of the topography. In detail, the south wall is located on the southern “shoulder” of the displaced stream and very close to a steep gradient associated with the topography of the hill (Figs. 4.5b & 4.7). Therefore, the vertical displacements recorded on the south wall of Thalassa (at least on the older units) are apparent only.

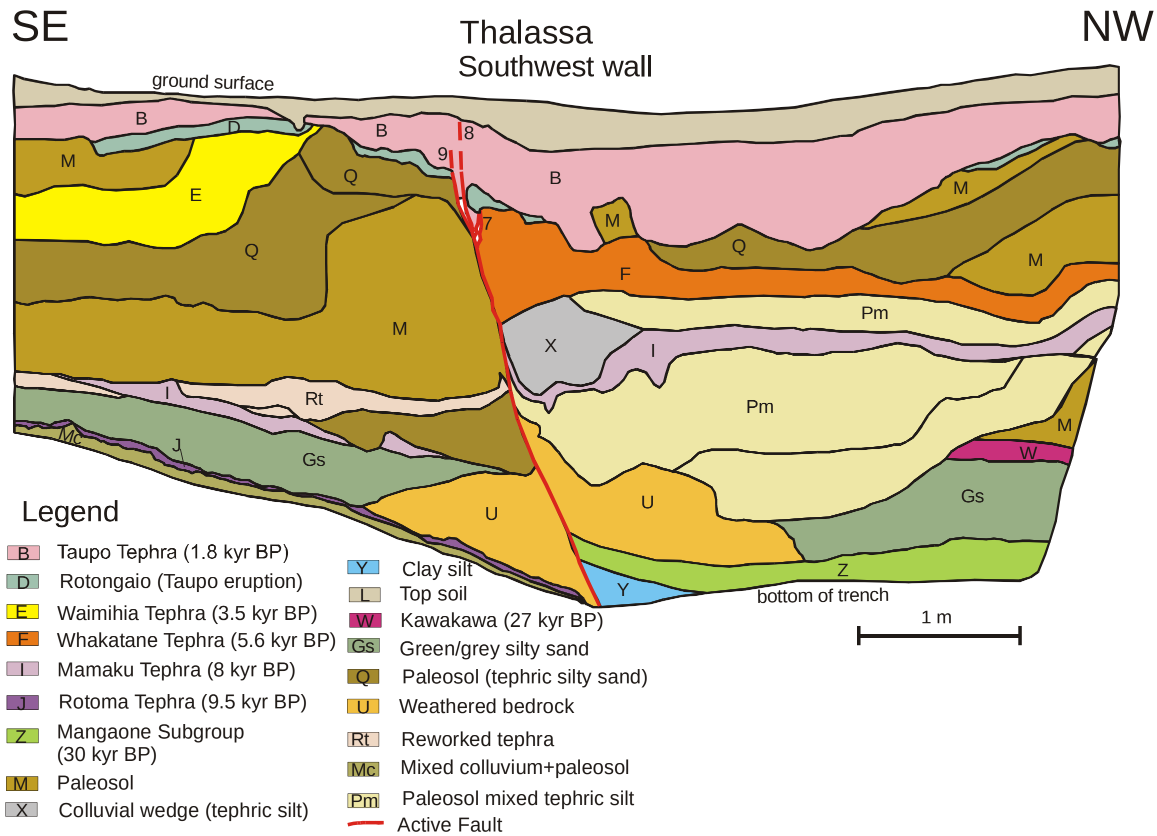

Fig. 4.10 Southwest wall of Thalassa Trench across the Whakatane Fault in Ruatahuna Basin. Slip surfaces are numbered (e.g.7-9).

Armyra Trench / North Wall (Fig. 4.11):

- 1st event (most recent): Displaces the Taupo Tephra (1.8 kyr BP) but does not appear to offset either the overlying paleosol, or the extrapolated base of the Kaharoa Tephra (0.8 kyr BP). The top and the base of Taupo are downthrown to the east by an apparent throw of c. 10-20 cm.
- 2nd event: Waimihia Tephra (3.5 kyr BP) has an apparent vertical displacement (down to the east) which is larger than that on the Taupo suggesting a possible additional earthquake event between the deposition of those two volcanic layers. The scarp formed by this event resulted in a wedge of material (units D, I, K, O) on the downthrown side of the fault between the Taupo and Waimihia tephras. These units (particularly the inter-fingering of units D and I) are inferred to have been derived from degradation of the scarp during this earthquake. This

earthquake may be equivalent to the second event recorded on the north wall of Thalassa (c. 2 – 2.7 kyr BP). Bedrock (Miocene mudstone) is found below Waimihia Tephra east and west of the fault and, therefore, in this trench there is no record of older pre-Waimihia Tephra (3.5 kyr BP) earthquakes.

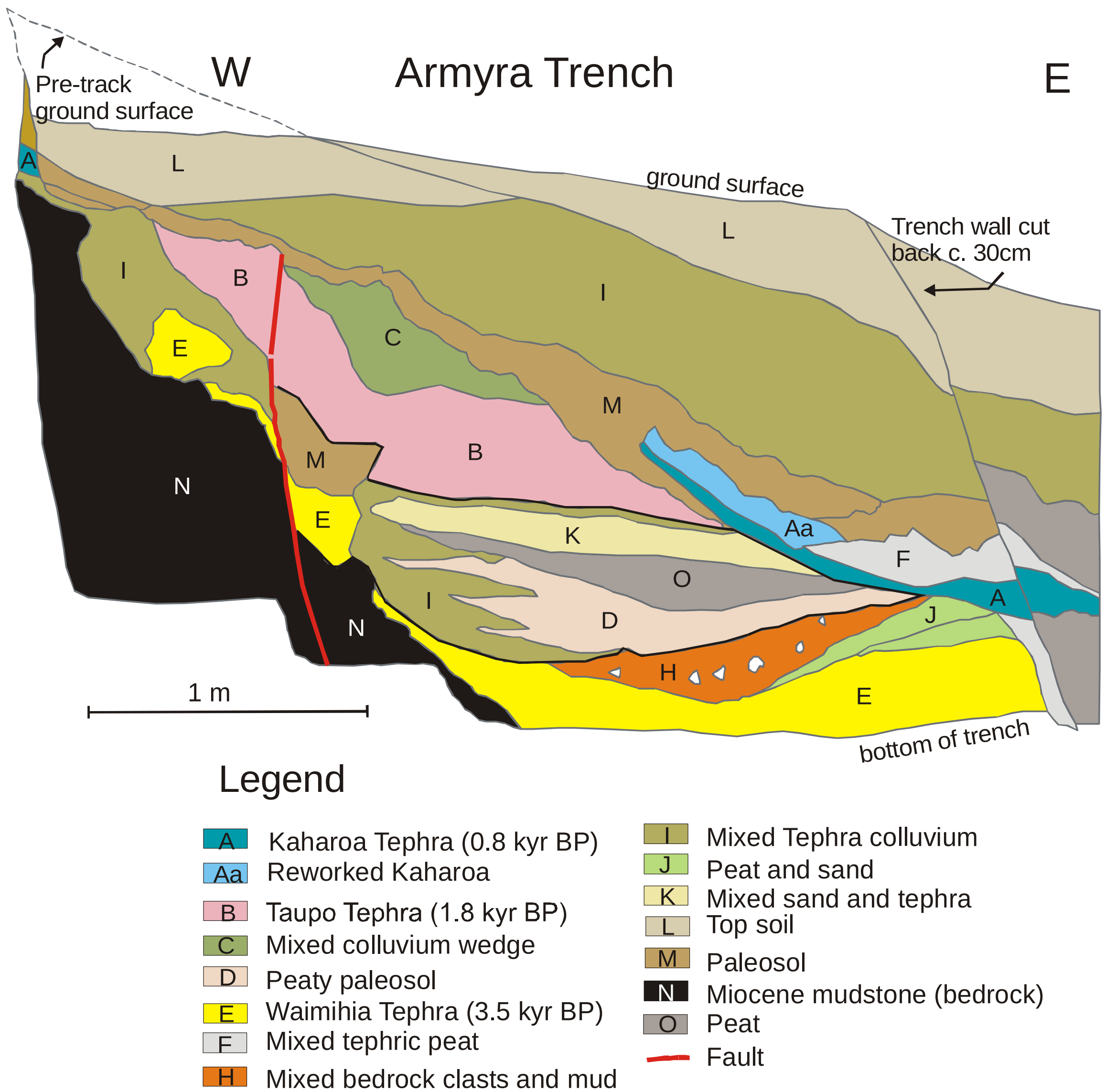

Fig. 4.11 North wall of Armyra Trench. This trench was excavated across the Whakatane Fault in Ruatahuna Basin.

<u>Summary of paleoearthquakes on the Whakatane Fault at Ruatahuna:</u>

- 1st event (most recent): This event occurred between 1800 and 833±97 cal. yrs BP (constrained on all trenched walls).
- 2nd event: This event occurred between 2000±110 and 2752±30 cal. yrs BP (constrained on all trenched walls).
- 3rd event: This event occurred c. 8000 cal. yrs BP (both walls of Thalassa).
- 4th event (oldest): This event occurred between 9500 and 8000 cal yrs BP (north wall of Thalassa).

4.4.5 Wharepora

The name of this trench is "Te Marama" (=the moon)

This trench was excavated when January's full moon was larger than all of our hopes to find the fault within Te Urewera Forest. Standing amidst the dwarfed trees, however, we felt that in this trip we were not alone...

Indeed, the good spirits of Wharepora came into sight, through contorted trunks and hanging wraithlike lichens silhouetted by the mist, to guide us to the right place... They allowed us to reveal the most recent of Ruamoko's trembles on the Whakatane Fault... For a purpose: to know that few hundred years ago, when this land was shaken by this earthquake, all the goblins that were inhabiting this forest, turned into Spirits... The Spirits that today live beneath the foundations of Wharepora...*

4.4.5.1 Site and trench descriptions

The Whakatane Fault at this location, some 40 km south of the Bay of Plenty coast, runs parallel to the Whakatane River on a c. N-S strike through the heavily vegetated Te Urewera Forest (Fig. 4.12 and Map F in Appendix I). At this site, the river valley is narrow (200-300 m wide) with the mean elevation of the Mesozoic greywacke ranges to the west of the fault being 100-200 m lower than that to the east. This difference suggests a long-term (i.e. 0-600 kyr) down to the west component of motion on the Whakatane Fault. Indeed, from this location northwards, the different elevation of the hangingwall and footwall on the Whakatane Fault increases gradually, whereas to the south the footwall and hangingwall lie at similar elevations suggesting little throw on the fault (see also Fig. 6.10 in Chapter 6).

Overall, along this section of the fault, there is little evidence of late Quaternary faulting preserved in the landscape. This is because the fault runs either within, or near

* Ruamoko is the God of Earthquakes for Maori people

to, the active river floodplain, or on heavily vegetated Mesozoic greywacke that contains no sedimentary cover. At a few locations, however, the fault traverses abandoned degradational river terraces that are preserved above the modern river bed of the Whakatane River (Fig. 29 in Appendix I). This is the case at Wharepora. The fault trace at the location of the excavation is continuous for over 1000 m (Fig. 4.12). Along most of this distance it forms a west-facing scarp of c. 1.7 m height (Fig. 28 in Appendix I). In places where the fault runs through alluvial fans, the scarp height decreases as it is buried beneath younger fan deposits. Te Marama Trench was located at a site that is distal from such fans, where the height of the scarp was c. 1.7 m (site 27 in Appendix I) (W16/603193). The trench was excavated manually and therefore is only 2.5 m long and up to 2.3 m deep (Fig. 4.14a & b).

Fig. 4.12 The Whakatane Fault within Te Urewera Forest. Te Marama Trench site is indicated by the yellow polygon.

4.4.5.2 Stratigraphy and Age control

No airfall tephra was identified within Te Marama Trench. The thickness of the sediments deposited above the basal river gravels slightly exceeds 1 m. The sedimentary cover consists mainly of buried soil horizons, reworked tephric sands and sandy silts. The absence of Taupo Tephra (1.8 kyr BP) from this terrace and a calibrated radiocarbon age (794±126 / Wk 18346) of charcoal from c. 80 cm below the ground surface (Fig. 4.14a), brackets the age of alluvial abandonment of this terrace to have been between c. 1800-794 cal. yrs BP.

Airfall Taupo Tephra (1.8 kyr BP) was found in an auger-hole (W16/603180) at a depth of 50-70 cm below the surface on the next older (higher) river terrace, c. 1 km south of site 27, on the eastern bank of the Whakatane River (Fig. 4.13) (site 28a, Fig. 26 in Appendix I). No other airfall tephra is recorded in the auger-hole. In the absence of the primary airfall Waimihia Tephra (3.5 kyr BP), the first tephra below Taupo that might be expected in this area, it is inferred that the age of abandonment of this terrace is younger than 3.5 kyr BP. This terrace is also traversed and displaced by the Whakatane Fault. Here, the Whakatane Fault splays locally into two strands forming two closely spaced west-facing scarps (Fig. 27 in Appendix I).

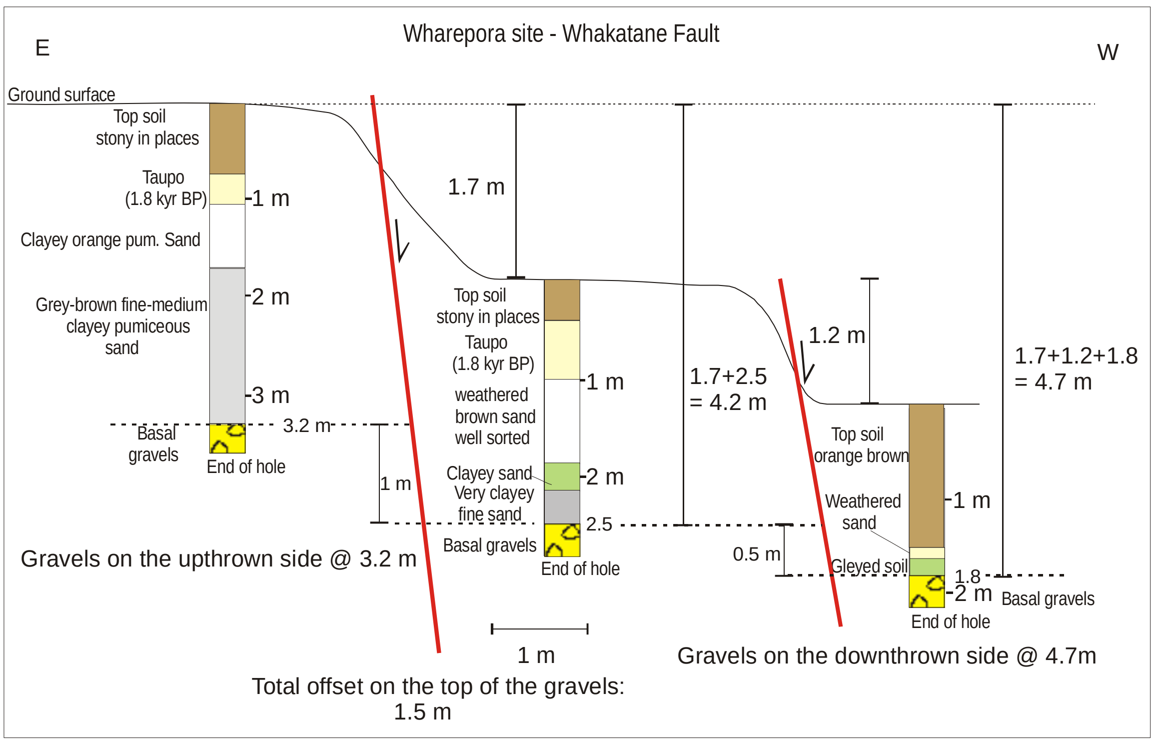

Fig. 4.13 Auger holes on displaced terrace surfaces across the Whakatane Fault at site 28a, here represented by two strands < 5 m apart. Based on the presence of Taupo and the absence of any other airfall tephra, the age of this terrace is inferred to post date the 3.5 kyr Waimihia Tephra.

Augering revealed that the cumulative throw (across the two fault strands) accrued on the top of the basal gravel is c. 1.5 m. The total height across the two west-facing fault scarps at this site, however, is c. 4.7 m. This height difference between the offset on the river gravel and the total height across the two scarps is thought to result from post-faulting erosion of the terrace by the near-by Whakatane River. This suggestion is supported by the fact that the coverbeds on the lowest (western) and middle remnant of the surface (assuming the gravel represents the same surface) are different, and have possibly been truncated by alluvial erosion. The thickness of the coverbeds on the gravel, changes markedly from the lowest surface to the middle surface (a change of 0.7 m), and from the middle surface to the top surface (also 0.7 m). So, the change of thickness of the coverbeds can only be explained by sediment retention and/or sediment erosion. The difference in stratigraphy between the lower and middle surfaces might support erosion on both the middle and lower surfaces. If we assume that the coverbeds in each auger hole can be divided into three units: A = topsoil, B = tephra, and C = gleyed soils, the approximate thickness of each of the unit on each-auger hole is:

	eastern auger hole	central auger hole	western auger hole
Unit A	0.6 m	0.4 m	1.4 m
Unit B	1.0 m	1.5 m	0.2 m
Unit C	1.8 m	0.6 m	0.3 m

1. Little variation in thickness of Unit A (topsoil) between eastern and middle auger holes, but much thicker in western auger hole (i.e., not much erosion, but thickening in the auger closest to the river).
2. Unit B (tephra) thickens from eastern to middle auger (perhaps wash from the fault scarp), then very much thinner in the auger hole closest to the river (river erosion).
3. Unit C (gleyed soils) much thicker in the eastern auger hole than in middle hole (perhaps erosion of older soil layers in the middle auger hole), then thinner again closest to the river.

Summing up this information, the offset on the gravel is about 1.5 m, but the cumulative erosion of the middle and western terraces has increased the scarp height by 3.2 m. This probable erosion almost certainly varies along strike, and may also account for the difference in scarp height between the site 27 (where Te Marama Trench was excavated), and the measured c. 4.7 m scarp height at site 28a (where the auger hole is located). Further investigation (e.g. trenching) along this section of the fault is necessary to test the suggestion that the fault scarp height was increased by river erosion.

4.4.5.3 Fault Geometries

The fault within Te Marama Trench strikes 350° and dips 55° W. This measured dip is unexpectedly low, and may be a superficial feature of the fault, as the average dip of the Whakatane Fault in the region is thought to be steeper (70-80°) (see Chapter 2). The fault at the bottom of the trench appears to be confined on a single surface. It splays upwards into three secondary steeply dipping strands. Pebbles and gravels appear to be dragged along the fault plane with their long axes oriented parallel to the slip surface.

4.4.5.3 Timing of paleoearthquakes on Whakatane Fault at Wharepora

Te Marama Trench (Figs 4.14a & b):

- 1st earthquake (most recent): There is one earthquake event recorded in both walls of Te Marama Trench (Figs. 4.14a & b). This earthquake has an apparent vertical displacement of the unit Lgss by c. 50 cm in a down to the west sense. On the west side of the fault this layer (Lgss) has been dragged and re-deposited as a wedge-shaped unit. Radiocarbon dating of charcoal derived from within the Lgss unit (south wall) constrains the timing of this event as post 794±126 yrs BP. The top of the gravel on the south wall is dragged down to the west by at least c. 1.7 m.
- 1 km south of Te Marama Trench, the Whakatane Fault splays into two strands that traverse the c. 3.5 kyr old river terrace (see section 4.4.5.2), forming two closely spaced west-facing scarps (site 28a in Map F and Fig. 27, Appendix I). Augering revealed that the cumulative throw (across the two strands) accrued on the top of the basal gravel is c. 1.5 m (Fig. 4.13, see also discussion in section 4.4.5.2). This throw is comparable to that recorded in Te Marama Trench (1.7 m) and is inferred to result from the post 794±126 yrs BP earthquake. From this, it is suggested that the Whakatane Fault at this locality has ruptured only once during the last c. 3.5 kyr.

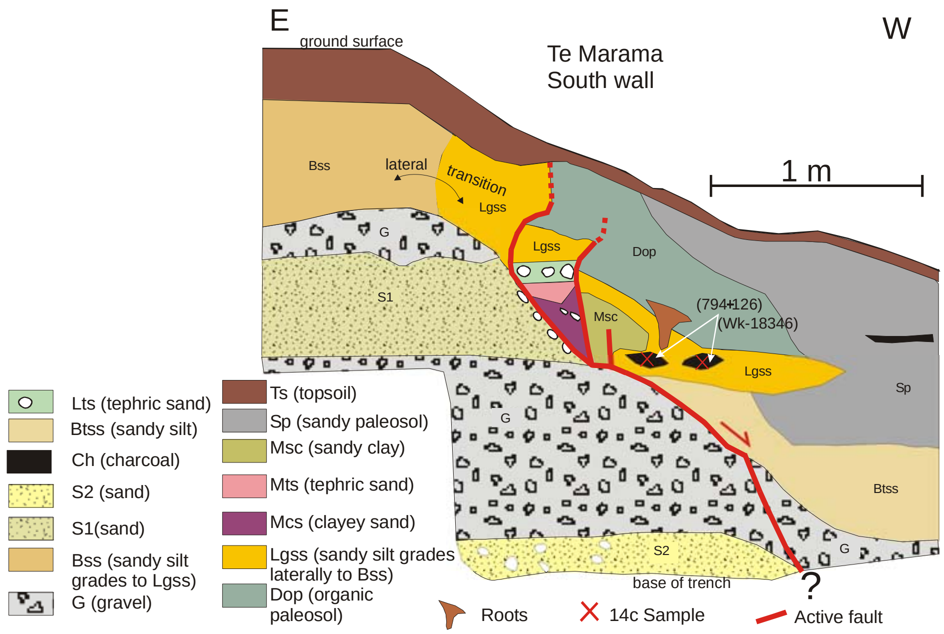

Fig. 4.14a The south wall of Te Marama Trench on the Whakatane Fault at Wharepora. For detailed description of the units see Appendix II.

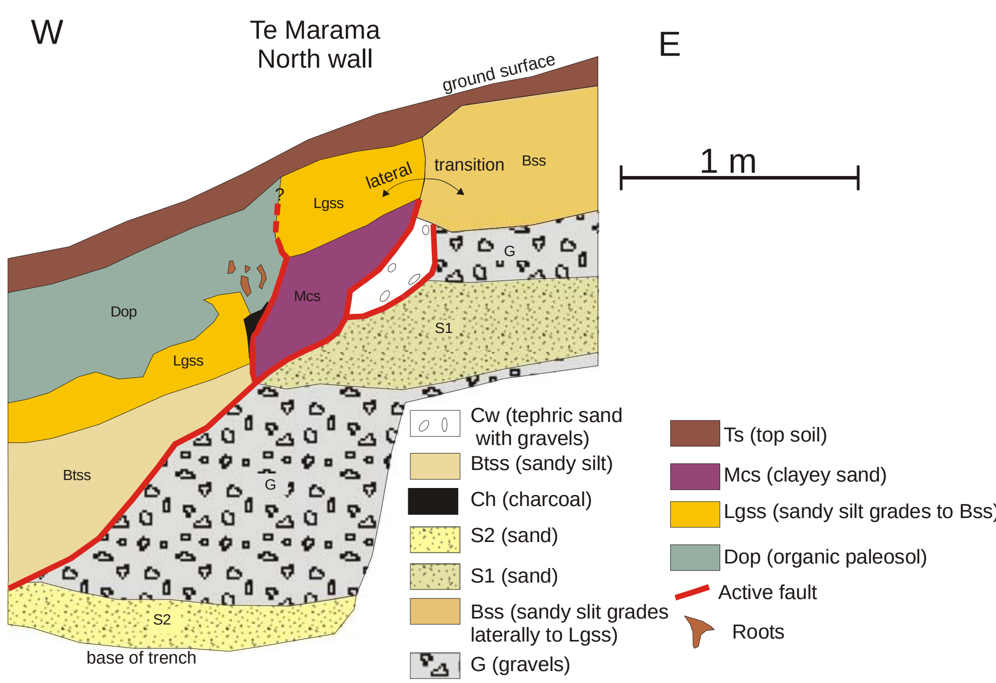

Fig. 4.14b The north wall of Te Marama Trench on the Whakatane Fault at Wharepora. For detailed description of the units see Appendix II.

4.4.6 Ruatoki North

The name of this trench is "Te Whetu" (=the star).
Tuhoe, the Maori people that have inhabited this forest for centuries now, know that the Wairua (soul) of each of their ancestors lives in Nga Whetu (the stars). Every night they return, through the glimmering celestial light, to reveal the past. They whisper old Karakia (prayers) for battles that once were won, for trips that once were pursued, for values that once were honoured…

Our trench, Te Whetu, is also alive. Her Wairua murmured to us pieces of Ruatoki's earthquake history. Her words are now going to stay with us forever. And will be passed on from generation to generation…

How many Whetu, with Wairua full of wisdom, are we encountering in our everyday life…? It is when we learn to recognize, listen and interpret them that the world around us will start turning into a Miracle…

4.4.6.1 Site and trench descriptions

Ruatoki North settlement, where Te Whetu Trench was excavated, is located in the Taneatua Basin (Map G in Appendix I). The lens-shaped Taneatua Basin is c. 20 km long, and up to 7 km wide and is thought to have formed in response to a northward increase in the normal (down to the west) component on the Whakatane Fault. The Whakatane Fault bounds the eastern margin of the basin, striking mainly N-S (e.g. 355-010°) and dipping consistently to the west at an average dip of c. 70°. The fault at this site is dextral – normal, with typical H:V slip ratios of c. 0.9 (Table 2.1 in Chapter 2).

Te Whetu Trench was excavated c. 500 m to the east of Ruatoki North Valley Road (W16/619327) across a linear fault scarp which extends continuously for over 1 km (site 25 in Map G, Appendix I). Te Whetu Trench was located only c. 300 m to the south of Beanland's (1989b) trench site (see site 25a in Map G, Appendix I). At the locality where Te Whetu was excavated, the fault traverses a river terrace, which contains Rotoehu Tephra (c. 50 kyr BP) above its basal gravels, and forms a west facing scarp of at least 6 m height. This alluvial terrace is locally buried beneath younger fan deposits formed by active streams that run from the ranges east of the fault. Te Whetu Trench was located in between such two fan surfaces (Fig. 33 in Appendix I).

4.4.6.2 Stratigraphy and Age control

Taneatua Basin is a depression formed by faulting during the last 600±30 kyr (Fleming, 1955; Nairn & Beanland, 1989; Beu, 2004). The greywacke basement is downthrown to the west of the Whakatane Fault by 500±100 m (see Chapter 6 for further details) forming the basin, which has subsequently been filled in by a succession of volcanic and sedimentary deposits. The Whakatane River traverses the basin in a N-S orientation and forms successive fluvial terrace surfaces that are today elevated (abandoned) above the modern river bed. Typical ages of these preserved terraces in the Taneatua Basin are c. 18 and c. 50 kyr BP (inferred from the Rerewhakaaitu and Rotoehu tephras; Tables 22 & 28 in Appendix III).

Figure 4.15 illustrates, in a schematic way, the evolution of the landscape in the northern Bay of Plenty during the last >50 kyr in conjunction with regional climatic changes. Prior to 50 kyr BP the region was dominated by cold climate and the rivers were aggrading through the deposition of silts and loess. At about 50 kyr ago, the big eruption of Rotoiti caldera resulted in abundance of Rotoehu airfall ash (Jurado-Chichay & Walker, 2000). This ash mantled the aggrading river terraces (Fig. 4.15a). Subsequently, the climate became warmer and wetter (interstadial period) and the rivers started to incise, resulting in the abandonment of the former aggradational terrace at c. 50-40 kyr BP (equivalent to T3 Terrace of Litchfield & Berryman, 2005) (Fig. 4.15b). The widespread occurrence throughout the central and east North Island of younger aggradational terraces formed during the period of c. 40-30 kyr BP, (Rata Terrace in Litchfield & Berryman, 2005) indicates a transition towards a colder period which was associated with loess deposition (Kennedy, 1998). The latter terrace (Rata Terrace) is not recognised in the study area, either because it was never deposited or because it is not preserved today. Instead, air fall tephras of the Mangaone subgroup (c. 30 kyr) rest horizontally on the loess that overlies the Rotoehu Tephra on the 70-50 kyr old T3 Terrace (Fig. 4.15c). Between 30 and 25 kyr BP, when the region was dominated again by cold climatic conditions, a new aggradational terrace commences gradually to form

(Ohakean Terrace) while Kawakawa (27 kyr BP) and Te Rere (25 kyr BP) tephras were deposited, together with loess, on top of the Mangaone subgroup tephras (although not on the younger Ohakean Terrace sill swept by alluvial processes) (Fig. 4.15d).

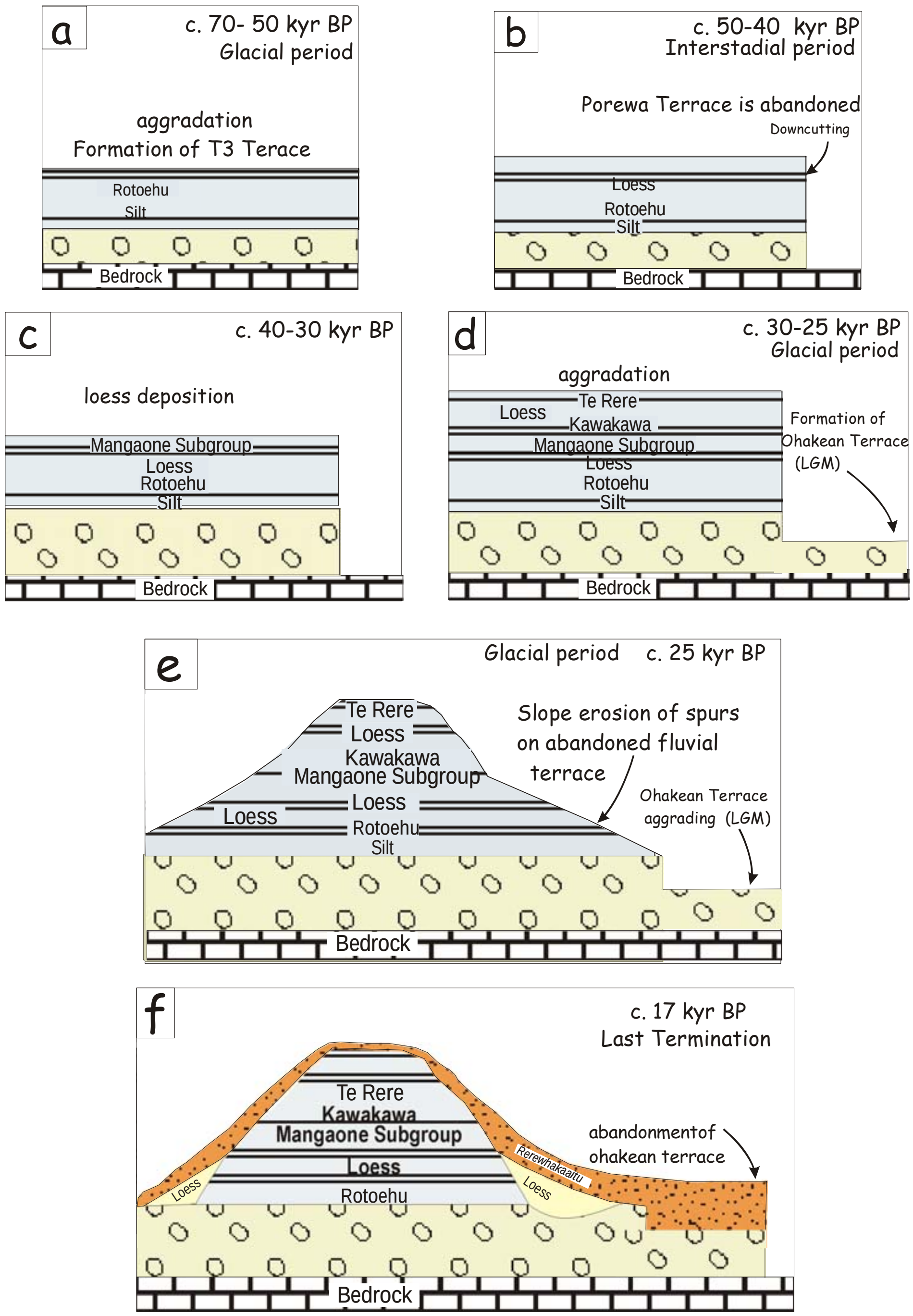

Fig. 4.15 Schematic diagram illustrating the interrelationship between the evolution of the landscape and the climatic changes in the broader northern Bay of Plenty region.

After the deposition of Te Rere Tephra (c. 25 kyr BP), periglacial processes during the Last Glacial Maximum resulted in slope erosion of the abandoned T3 Terrace (Kennedy, 1994) (Fig. 4.15e), forming ridge-spurs widely documented in this thesis for the region of northern Bay of Plenty, and which have subsequently been displaced by the faults. At the same time, river aggradation was depositing the gravels that later became the Ohakean Terrace (Fig. 4.15e).

The transition into the present interglacial period terminated the aggradation of the Ohakean Terrace at c. 18 kyr. The Rerewhakaaitu eruption (17.6 kyr BP) that followed, mantles the Ohakean Terraces with ash but also mantles unconformably the abandoned and incised older aggradational surfaces in the area (e.g. T3 Terraces, c. 50 kyr) (Fig. 4.15f).

Evidence for the two aggradational terraces occur, for example, at site 26 in Taneatua Basin (Map G and Fig. 32 in Appendix I) where both the higher (older / c. 70-50 kyr BP) and lower (younger / c. 30-17.6 kyr BP) terraces are recorded. At site 26 the older (c. 70-50 kyr BP) has been displaced by the Whakatane Fault (Table 2.1 in Chapter 2 and Tables 20-22 in Appendix III). Rerewhakaaitu Tephra is deposited directly on the basal terrace aggradation gravels of the lower terrace and exceeds 3 m in thickness. The most recent fluvial surface in the region is today's active floodplain of the Whakatane River (Fig. 32 in Appendix I).

Te Whetu Trench was located upon the oldest aggradational terrace as Rotoehu Tephra (c. 50 kyr BP) rests directly on the basal gravels (Table 28 in Appendix III). Additional tephras present in the trench on top of the Rotoehu Tephra include Mangaone Subgroup (c. 30 kyr BP), Waiohau (13.8 kyr BP), Rotoma (9.5 kyr BP) and reworked Whakatane (< 5.6 kyr BP) and Taupo (1.8 kyr BP) tephras (Tables 29-35 in Appendix III). The age of the alluvial fan that partially buries the older (70-50 kyr BP) aggradational surface is constrained by the radiocarbon dating of wood and peats that are exposed on the western part of the south wall (samples RT-A / NZA 22386 and RT-G / NZA 22388 in Table 4.2) to be < 0.8 kyr BP (Table 4.2 and Fig. 4.16). The fault does not appear to disrupt the young fan, although the relationship between faulting and the young fan is not clear.

Sample Number (*AMS date)	Method used to claim sample	Sample Description	Grid Reference	Radiocarbon Age		
				Conventional years B.P.	Calibrated years B.P.	Calendar years (calibrated)
NZA 22455 (RT-H)	Trenching	organic paleosol	W16/619327	4258 ± 35 BP	4849 - 4583 BP	2900 - 2634 BC
NZA 22530 (RT-F)	Trenching	organic paleosol	W16/619327	535 ± 35 BP	551 - 496 BP	1399 -1454 AD
NZA 22386 (RT-A)	Trenching	peat	W16/619327	708 ± 30 BP	708 ± 30 BP	1264 - 1300 AD
NZA 22387 (RT-E)	Trenching	organic paleosol	W16/619327	-1114 ± 30 BP	modern age	modern age
NZA 22388 (RT-G)	Trenching	tree root	W16/619327	402 ± 30 BP	512 - 432 BP	1438 - 1518 AD

Table 4.2 Summary of radiocarbon samples and dates collected from Te Whetu Trench in Ruatoki North.

4.4.6.3 Fault Geometries

The geometry of the fault within the trench typifies that of normal faults (Fig. 4.16). Faulting is distributed over at least 6 m through nine principal and several secondary, antithetic and synthetic, displacement surfaces (fault strands are numbered in Fig. 4.16). The main fault surface (strand 1) strikes 010° and dips 68° to the west. Most of the displaced units can be followed and matched across the fault strands. Significant faulting is exposed at the corner between the south and the east wall, however, stability issues (the height of the wall at this point exceeded 6 m) prevented us from extending the excavation further into the steep fault scarp. For this reason it is inferred that the trench-log samples an incomplete record of the total fault splays and past earthquake activity on this part of the Whakatane Fault.

4.4.6.4 Timing of paleoearthquakes on Whakatane Fault at Ruatoki North

<u>Te Whetu / South Wall (Fig. 4.16):</u>

- 1st event (most recent): Slip on strand 1 during this earthquake displaces the unit Z (sand mixed with soil) which is of 4716±133 yrs BP age (NZA 22455 / RT-H in Table 4.2), but does not displace the unit M (mixed tephric paleosol) on strand 7. Unit M is dated 523±27 yrs BP (NZA 22530 / RT-F in Table 4.2). The last event recorded in this trench, therefore, appears to have occurred between 4716±133 and 523±27 yrs BP. Beanland (1989b) better constrained the last event on the Whakatane Fault (which is associated with 1.9 m of vertical separation), 300 m north of Te Whetu Trench at between 627±94 and 620±410 yrs BP. Beanland's (1989b) timing for the last event is adapted here.

- 2nd event: Slip during this event offsets the unit R (tephric sand) by at least 35 cm (slip accrued on strands 2, 7 & 9). The unit R post-dates deposition of Rotoma Tephra (9.5 kyr BP) but pre-dates deposition of the unit Z (4716±133 yrs BP / NZA 22455 in Table 4.2). As there are three upper terminations of fault ruptures (strands 2, 7 & 9) within the unit R, this earthquake is inferred to have occurred during deposition of unit R (9.5>R>4.715 kyr BP).
- 3rd event: The base of the Waiohau Tephra (c. 13.8 kyr BP), is displaced vertically across the 9 main strands of the fault zone by 3.3 m while the bottom of Rotoma (9.5 kyr BP) is offset only by 2.4 m (across fault-strands 1-8). This throw difference suggests that one event occurred in the time interval between the deposition of these two tephras. Therefore, this event is bracketed between 13.8 – 9.5 kyr BP.
- 4th event: Given that the base of the Mangaone Subgroup (c. 30 kyr BP), is displaced vertically across the fault zone by 4.3 m whereas the bottom of Waiohau Tephra (13.8 kyr BP) is offset only by 3.35 m, there is at least one earthquake event that occurred in the time span between the deposition of the two tephras. Therefore, this event(s) is bracketed between 30 – 13.8 kyr BP.
- 5th event (oldest): The top of the gravels, at the base of Rotoehu Tephra, is displaced vertically across the fault zone by 5.6 m whereas the bottom of Mangaone Subgroup (c. 30 kyr BP) is offset only by 4.3 m. Therefore, there is at least one event occurred in the time interval between the deposition of the two tephras. This event(s) is bracketed between 50 – 30 kyr BP.

There are almost certainly a number of events not recognised in this list of earthquakes, particularly prior to 13.8 kyr, due to depositional breaks in the Te Whetu Trench sequence. The Waiohau Tephra (13.8 kyr BP), for example, sits directly on Mangaone subgroup tephras (c. 30 kyr BP) and approximately 16 kyr are absent from the record.

Furthermore, by dividing the cumulative displacement on key volcanic horizons across the exposed fault strands (e.g. Rotoehu, Mangaone, Waiohau and Rotoma) by their depositional age, the slip rates derived (0.3-0.4 mm/yr) are significantly less than the minimum slip rate estimated on the Whakatane Fault in Taneatua Basin from offset geomorphic features (c. 1.5 mm/yr) (see sites 23 & 26 from Table 2.1 in Chapter 2). Te Whetu Trench is therefore inferred to have spanned perhaps only about one third of the total fault zone width. Additional trenching may help constrain further the kinematics and the earthquake activity on the fault.

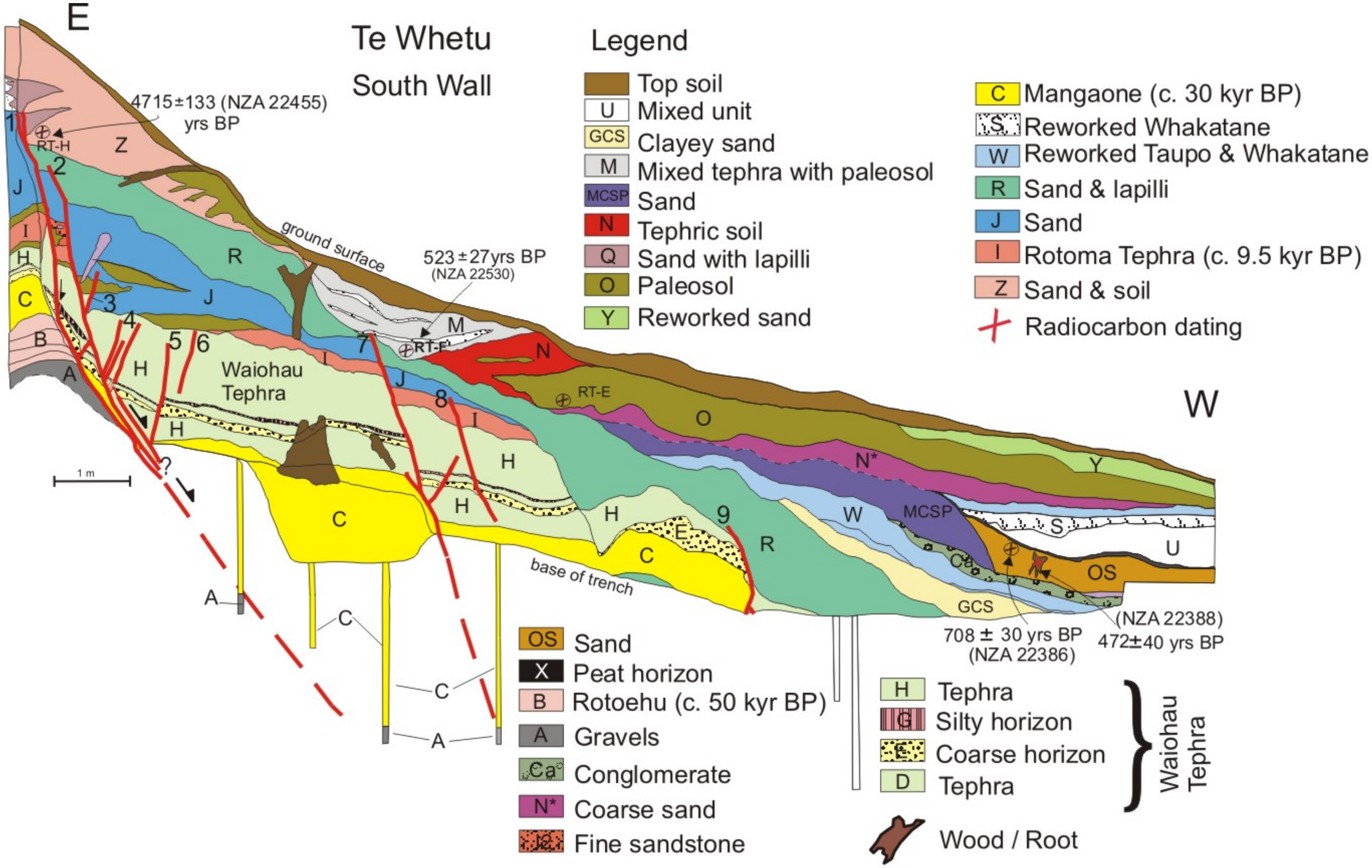

Fig. 4.16 The geometry of the fault on the south wall of Te Whetu Trench reveals its principally normal nature. At least 5 earthquakes are identified. Slip surfaces are numbered (e.g. 1-9). For further details on the description of the units see Appendix II.

4.4.7 Timing of paleoearthquakes on the Whakatane-Mohaka Fault

Figure 4.17 summarises the temporal and spatial distribution of late Quaternary earthquakes along the northernmost 200 km of the Whakatane-Mohaka Fault. Trench data, deriving from six different localities along the fault, indicate that the southern and northern sections of the Whakatane-Mohaka Fault (i.e. at Te Hoe and Ruatoki North), have ruptured more recently (at least once within the last 800 years) than the section of the fault near Ruatahuna (i.e. located in between Te Hoe and Ruatoki North) which does not appear to have ruptured during the same time interval.

Furthermore, the ultimate and penultimate events that have been recorded at the Ruatahuna trench sites do not appear to have ruptured through the Wharepora and Ruatoki North trench sites (northern section of the Whakatane-Mohaka Fault). In fact, at least 80 % of the total Holocene earthquakes recorded along the northernmost 70 km of the Whakatane Fault appear to have ruptured the southern (Ruatahuna trenches) and northern (Wharepora and Te Whetu trenches) sections of the fault at different times. Trench data, therefore, suggest that the earthquake activity is not distributed uniformly along the length of the fault. This non-uniform spatial distribution of paleoearthquakes appears to indicate the presence of earthquake segment boundaries along the northernmost 200 km of the fault. The details of this potential earthquake segmentation are discussed in detail in Chapter 5.

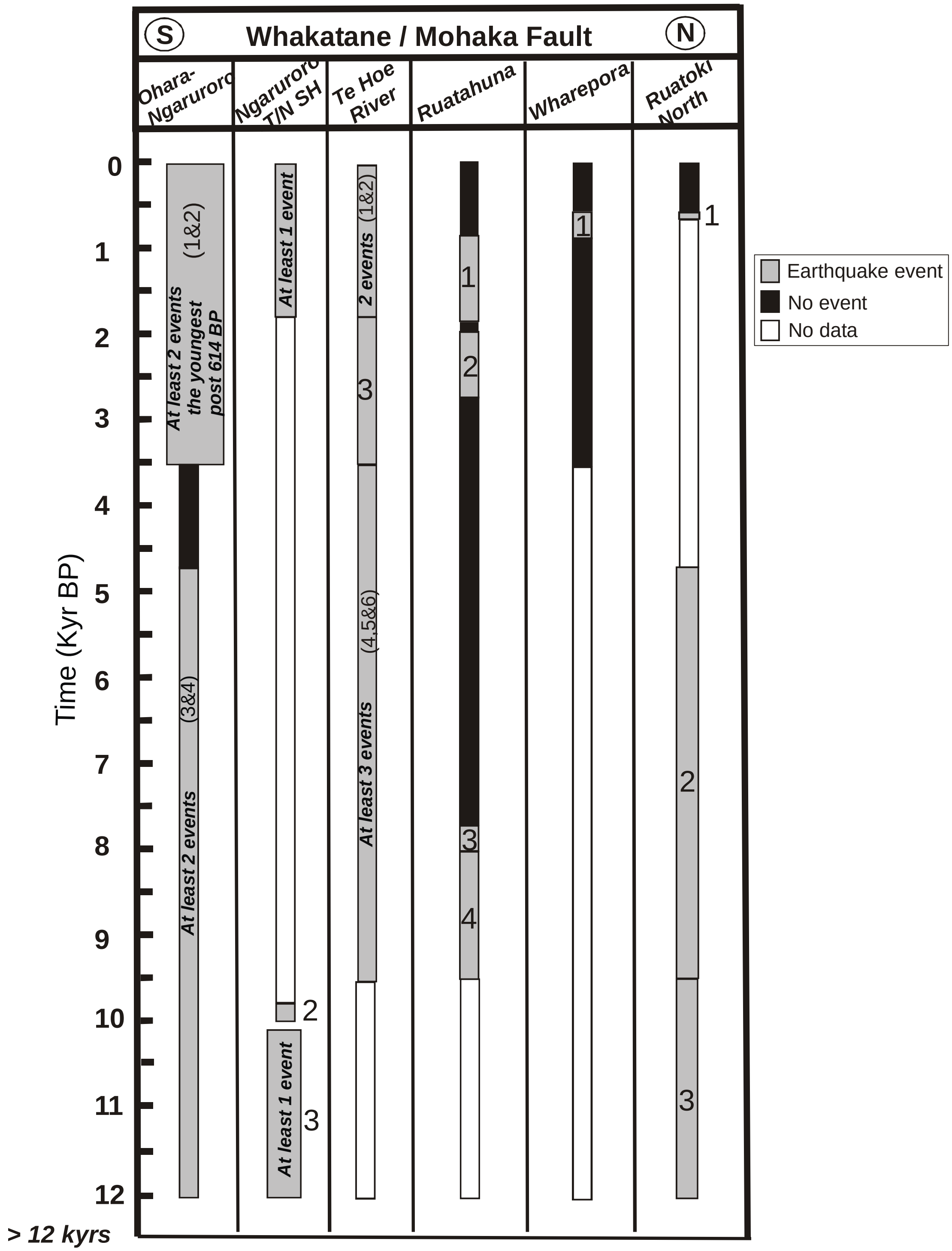

Fig. 4.17 Summary of the late Quaternary paleoearthquake history on the northernmost 200 km of the Whakatane-Mohaka Fault. Consecutive numbering of events within the grey polygons is shown. Black lines that bound the grey polygons represent minimum and maximum age for each event, respectively.

4.3 Waimana Fault

4.5.1 Te Ahirau*

4.5.1.1 Site and trench descriptions

Te Ahirau site is located c. 30 km to the south of the Bay of Plenty coast, within Te Urewera Forest (W16/705161) (Maps J & A in Appendix I). The Waimana Fault at Te Ahirau is a predominantly strike-slip fault, striking c. N-S and dipping steeply (>80°) forming prominent west or east facing scarps. Approximately 500 m to the east of the Matahi Valley Road, across the Waimana River from the Whakarae Marae, a series of closely spaced sites provide data on the kinematics of the fault over the last c. 15 kyr (Map J in Appendix I). Here the fault traverses a diachronous landscape with landforms ranging in age from <5.6 to 13.8 kyr BP. The fault offsets these landforms right-laterally, including stream channels, river terraces and ridge spurs (Fig. 4.18). Within a south to north strike distance of c. 3 km, the Waimana Fault displaces right-laterally a 5.6 kyr river terrace riser by c. 5.5 m (site 79 in Map J, Appendix I), a stream incised onto a 13.8 kyr surface by c. 10 m (site 75 in Map J, Appendix I), a ridge-spur by c. 18 m (site 78 in Map J, Appendix I) and a 13.8 kyr river margin by c. 13 m (site 73 in Map J, Appendix I). All displaced features are linked by a continuous fault trace.

At this locality three trenches were excavated. The Ahirau 1 & Ahirau 2 trenches (sites 76 & 77 in Table 2.1, Chapter 2) were excavated across the fault where an uphill (east) facing scarp ponds a small swamp behind it (Map J and Fig. 46 in Appendix I) (W16/705161). The Ahirau 4 Trench (site 75 in Table 2.1, Chapter 2) was excavated across an offset channel (Map J and Fig. 43 in Appendix I) (W16705158). Trenching across the fault provided data on the past earthquake activity on this section of the Waimana Fault while trenching across the stream channel and parallel to the fault provided information on the slip-rate on the Waimana Fault.

* 'Te Ahirau' means 'Hundred Fires' in Maori.

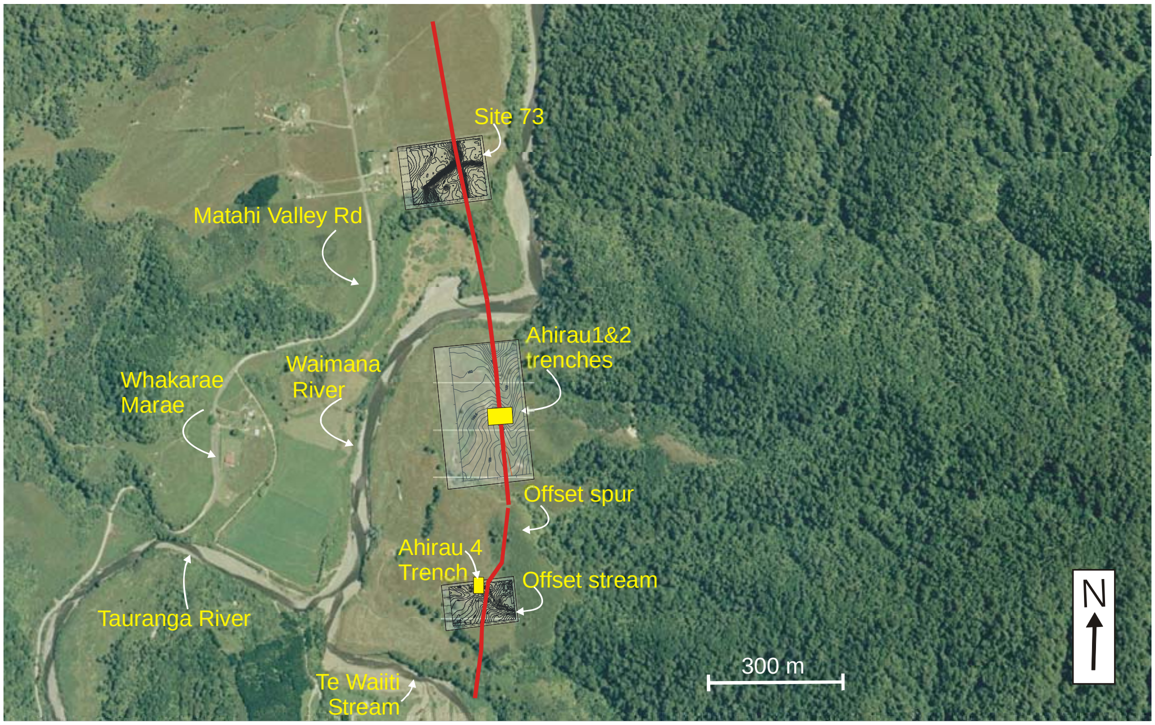

Fig. 4.18 Vertical aerial photograph of Te Ahirau site, Te Urewera Forest. The Waimana Fault is indicated by the red line and the location of the trenches by the yellow polygons. Detail topographic maps overlay aerial views where available.

4.5.1.2 Stratigraphy and Age control

At this location, the Waimana Fault runs sub-parallel to the Waimana River. The Waimana River at Te Ahirau, like the Whakatane River in Taneatua, has deposited aggradational terraces that today lie above the elevation of the modern river bed. These gravel terrace surfaces, mantled by loess and tephric layers derived from the Okataina and Taupo volcanic centers, have been sequentially displaced by the fault.

At Te Ahirau the 5.6 and 13.8 kyr BP Whakatane and Waiohau tephras, respectively, lie on terrace gravels and date the abandonment of two of these terraces (Tables 45, 47 & 48 in Appendix III). Additional tephras encountered within the trenches include Rotoma (9.5 kyr BP), Mamaku (c. 8 kyr BP) and Taupo (1.8 kyr BP) tephras (Tables 46 and 49-53 in Appendix III). All the displaced landforms discussed in this section are located on a single aggradational terrace that characteristically includes the Waiohau Tephra (c. 13.8 kyr BP) on top of the river gravels. Additional control on the timing of the past earthquakes and the slip rate on the Waimana Fault is provided by radiocarbon dating. Table 4.3 summarizes the details of these samples.

Sample Number (*AMS date)	Method used to claim sample	Sample Description	Grid Reference	Radiocarbon Age			Data on
				Conventional years B.P.	Calibrated years B.P.	Calendar years (calibrated)	
NZA 21342 * (Ahirau1-4)	Trenching	Peaty paleosol	W16/ 705161	2873 ± 35 BP	3078 - 2873 BP	1129 - 924 BC	timing of event in Ahirau1
NZA 21341 * (Ahirau1-1)	Trenching	Peat	W16/ 705161	8566 ± 45 BP	9557-9483 BP	7608 - 7534 BC	oldest event in Ahirau1
NZA 21343 * (Ahirau1-9)	Trenching	Peat	W16/ 705161	2801 ± 35 BP	2977- 2788 BP	973 - 784 BC	tephra ID

Table 4.3 Summary of radiocarbon samples and dates collected in the Ahirau-1 Trench.

Slip Rate on Waimana Fault at Te Ahirau

Two right-laterally displaced features, a channel and a river riser, were used to estimate the late Quaternary slip-rate on this part of the Waimana Fault (sites 75 & 73, respectively in Table 2.1 of Chapter 2; Map J in Appendix I). Trenching of the displaced channel Ahirau 4 (site 75) provided data on the age of the formation of the stream and therefore the time interval during which the corresponding right-lateral displacement (10±5 m) accumulated on the fault (Fig. 4.19a & b). Trenching across the axis of the channel indicates that the youngest deposit pre-dating incision is c. 13.8 kyr (Waiohau Tephra) (Table 50 in Appendix III). The Mamaku Tephra (c. 8 kyr BP) is the oldest of the infill deposits and post dates stream-channel incision (Table 49 in Appendix III) (Fig. 4.19b). Combining these ages with the 10±5m horizontal displacement of the channel (Fig. 4.19a) suggests a horizontal slip rate on the Waimana Fault of 1.1±0.5 mm/yr. The vertical displacement measured on the same surface (site 76) is 2±1 suggesting a horizontal to vertical slip ratio (H:V) of c. 5.

Similarly, the study of a displaced terrace riser (site 73 in Map J and Fig. 44 in Appendix I) located approximately 500 m north of Ahirau 1 Trench (W16/704170), provides further constraint on the slip rate of the Waimana Fault. At this site, the Waimana Fault displaces two successively abandoned river terraces, T1 and T2 (Fig. 4.20), forming an east-facing scarp of c. 5 and 2 m height on each terrace, respectively (sites 73 & 74 in Table 2.1, Chapter 2). The difference in height of the fault-scarps formed on the two terraces implies that each of these terraces has accommodated a different number of events. Augering on the younger (lower) T2 terrace shows that Waiohau Tephra (13.8 kyr BP) (Table 48 in Appendix III) sits directly on river gravels. The river, therefore, abandoned the T2 terrace just prior to c. 13.8 kyr BP, and the displacement of this terrace accrued since then. The horizontal (dextral) and vertical displacements of the T1/T2 terrace riser measured on the fault are 13±4 and 2±1 m, respectively. This data provide a (minimum) dextral slip rate of c. 1±0.4 mm/yr, and horizontal to vertical slip ratio at this location of c. 5.

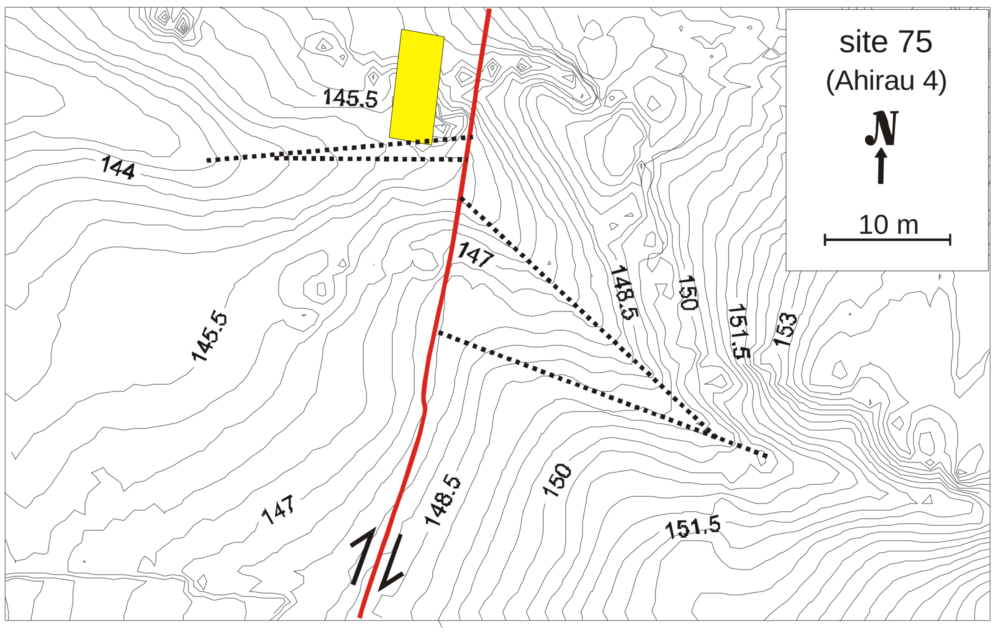

Fig. 4.19a Detailed contour map created by GPS-RTK illustrates the offset stream at site 75. The ‘Ahirau 4’ trench is indicated by the yellow polygon and the Waimana Fault by the red line. Dashed lines represent offset piercing points.

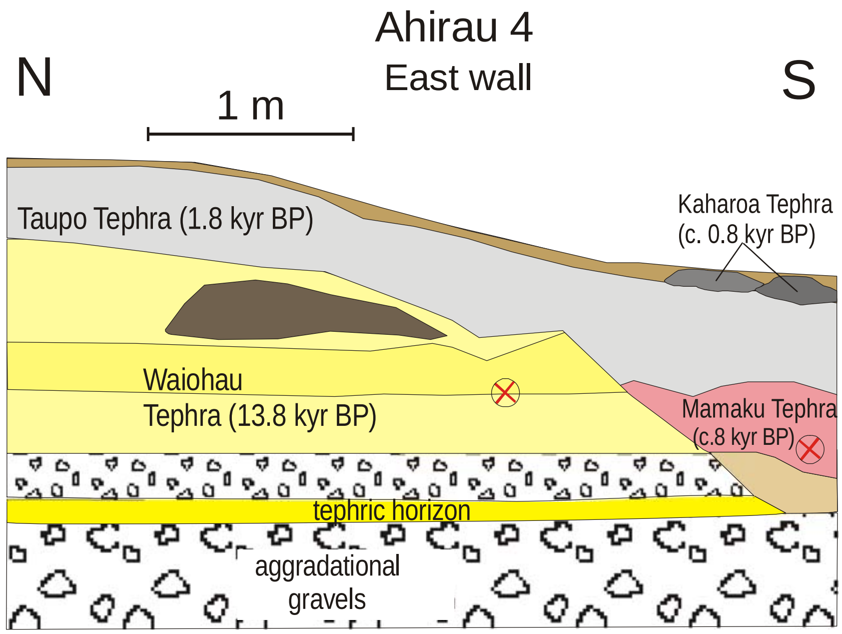

Fig. 4.19b Sketch of the east wall of the trenched channel 'Ahirau 4' at site 75.

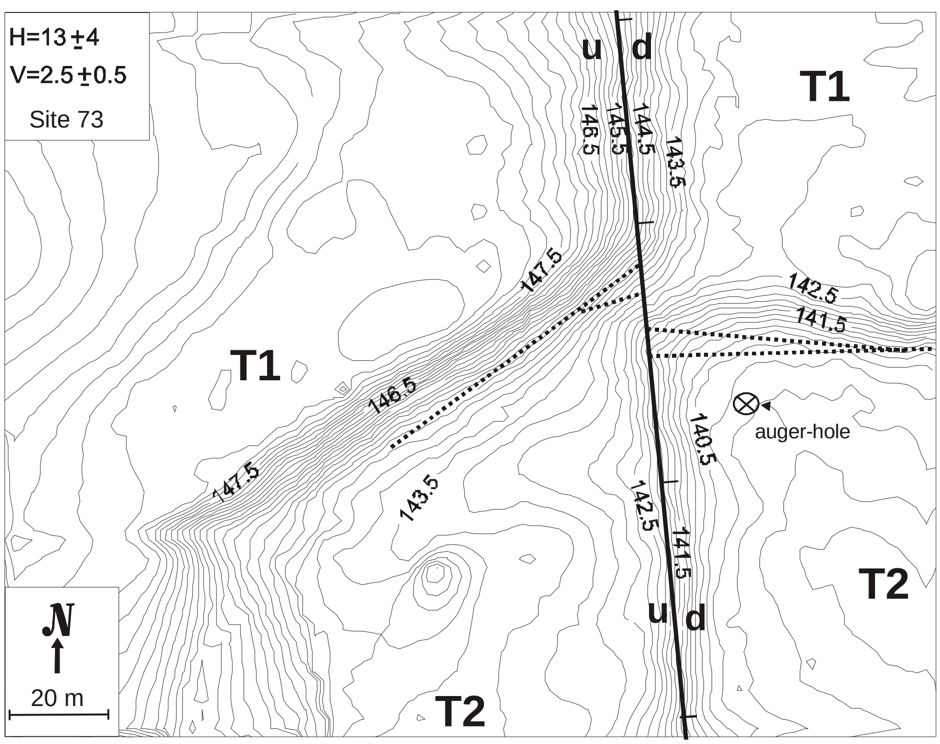

Fig. 4.20 The Waimana Fault at site 73 traverses and displaces dextrally an abandoned river terrace riser. Detailed contour map created by GPS-RTK illustrates the offset feature. Dashed lines represent offset piercing points. T2 is the terrace where Waiohau Tephra rests directly on river gravels while T1 surface indicates an older aggradational terrace.

4.5.1.3 Fault Geometries

The Waimana Fault in Ahirau 1 Trench has an average strike of 008° and dips 82° to the east. Faulting in the south wall is typically confined to a 15-20 cm wide zone (slip surfaces 1-5 in Fig. 4.21). At the bottom of the south wall the main displacement surface dips sub-vertically and juxtaposes dissimilar stratigraphic units (Fig. 4.21). This slip surface splays upwards into several smaller slip surfaces. Faulting in the north wall is distributed, over a 2-3 m wide zone, across a series of independent strands (e.g. slip surfaces 7-18 in Fig. 4.22). The fault-strand 18 on the north wall carries the largest apparent vertical offset (Fig. 4.22).

The average strike of the fault in Ahirau 2 is 352° with a dip of 70° to the east (Fig. 4.23). It is inferred that the shallow dip of the fault here, is probably a near surface feature which does not reflect the average dip of the strike-slip Waimana Fault (> 80°, see also Ahirau 1). The faulting on the north wall of Ahirau 2 Trench (the only one logged) is distributed over a c. 3 m wide zone and has three main slip surfaces (fault strands 1-4, 6 & 7 in Fig. 4.23). The two eastern strands extend upwards as single slip surfaces while the westermonst bifurcates into secondary splays (Fig. 4.23).

4.5.1.4 Timing of paleoearthquakes on Waimana Fault at Te Ahirau

<u>Ahirau 1 Trench (Figs. 4.21 & 4.22):</u>

- 1st event (most recent): The upper terminations of the eastern fault splays in the south wall log (strands 2, 3 & 4 in Fig. 4.21) and of the eastern and long central faults in the north wall log (strands 13 & 18 in Fig. 4.22) represent the most recent rupture event. In the north wall log, Taupo Tephra (1.8 kyr BP) lies undisplaced across the top of the faults. In the south wall log the paleosol (unit E) overlying the reworked Whakatane Tephra (unit F) and immediately underlying Taupo Tephra, is not displaced by all fault strands. This paleosol (unit E) that pre-dates Taupo Tephra indicates a likely time gap between cessation of deposition of the reworked tephra and accumulation of Taupo Tephra. The minimum age of rupture is 1.8 kyr BP. The uppermost displaced units in the logs are the horizons of reworked Whakatane Tephra (unit F in both walls). Displacement of unit F, that contains reworked Whakatane eruptive material, indicates a rupture age of less than 5.6 kyr BP. Unit F in the south wall is underlain by peat (Unit H) that yielded a radiometric age of 2882±95 yrs BP (NZA 21343). The maximum age of the rupture event is c. 2.88 kyr BP.

The most recent rupture event occurred between 2.88 kyr BP and 1.8 kyr BP.

- 2nd event: Slip during this event resulted in the upward terminations of the fault-strands 1 and 6, in the south wall log (Fig. 4.21), and of the fault-strands 7-12, 15, 16 & 17 in the north wall log (Fig. 4.22), within or close to the top of the equivalent units P, T, BW and MW (reworked Waiohau Tephra) (Fig. 4.21). In the south wall log, fault strand 1 terminates beneath unit O (paleosol), whereas fault strand 6 terminates beneath the unit Q (medium sand).

  The coarse nature and high energy depositional environment of units P, T, BW and MW (reworked Waiohau Tephra) indicate rapid deposition and, although relatively thick, they are unlikely to represent a long period of time. A radiocarbon age from carbonaceous material in unit O in the south wall (undisplaced by this event) provides a minimum age for this rupture of 2975±102 yrs BP (NZA21342). The base of unit O probably represents a substantial break in deposition in the sequence expressed in this wall.

  Units P and T comprise mostly material reworked from Waiohau Tephra (13.8 kyr BP), so this rupture event must post-date 13.8 kyr BP. A radiometric age (NZA 21341; 9520±37 yrs BP; South wall; Unit V) from peat underlying unit T, the reworked Waiohau Tephra, is displaced by this event and provides a maximum age.

  The age of the second rupture event distinguishable in Ahirau 1 is bracketed by these dates at c.9.5-c.3 kyr BP.

- 3rd event (oldest): Thickening of peat unit V on the eastern side of the fault in the south wall log suggests proximity to a fault scarp. If so, the event that resulted in the space represented by this thickening must have pre-dated deposition of the peat (c.9.5 kyr BP). Otherwise its age is unconstrained.

Summary of paleoearthquakes in Ahirau 1 Trench:

- 1st earthquake event: Post-2.88 kyr BP
- 2nd earthquake event: post-dates c.9.5 kyr BP and pre-dates c.2.98 kyr BP.
- 3rd earthquake event: pre-dates c.9.5 kyr BP.

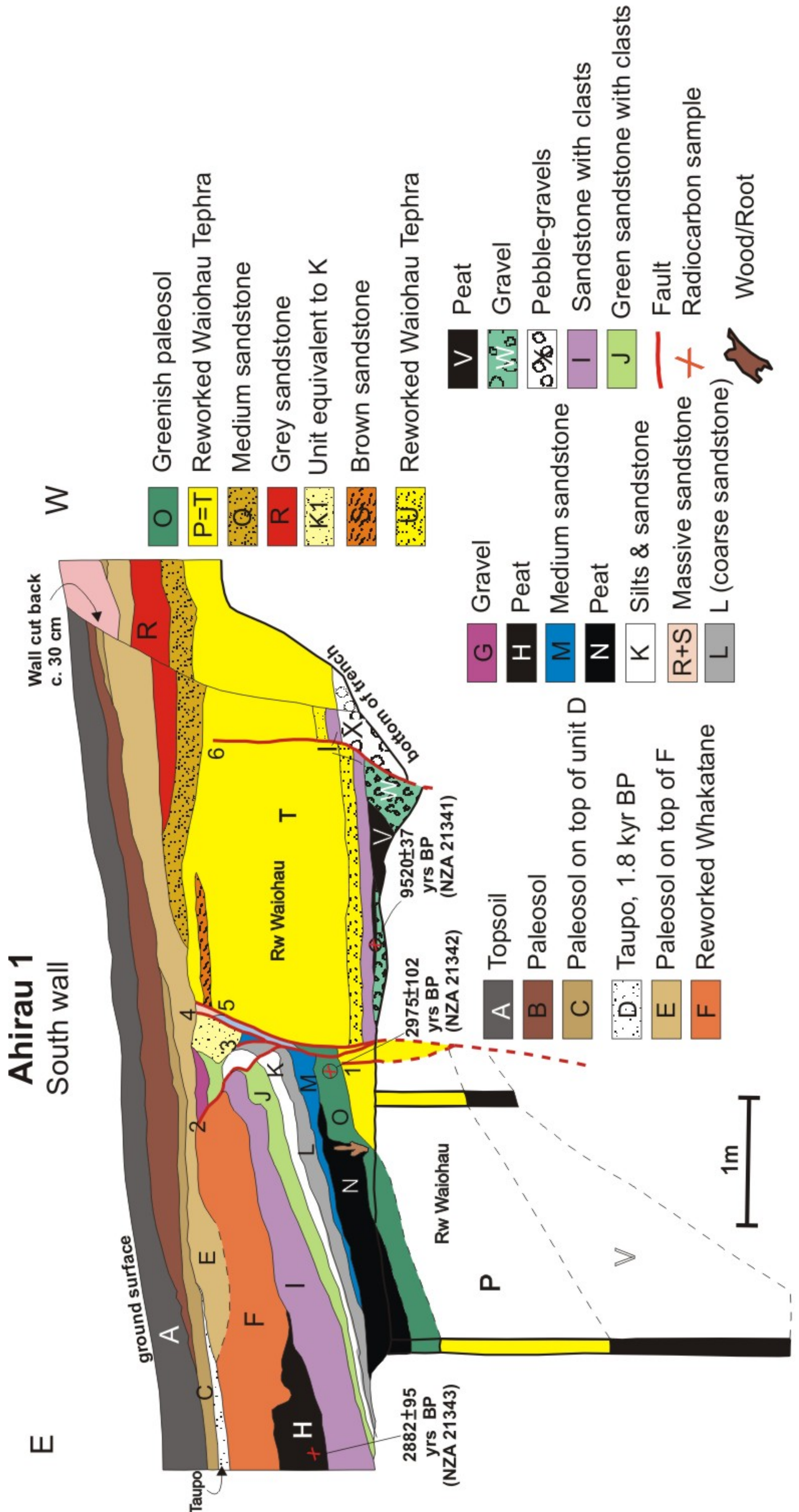

Fig. 4.21 South wall of Ahirau 1 Trench. Slip surfaces are numbered (e.g. 1-6). For further details on the description of the units see Appendix II.

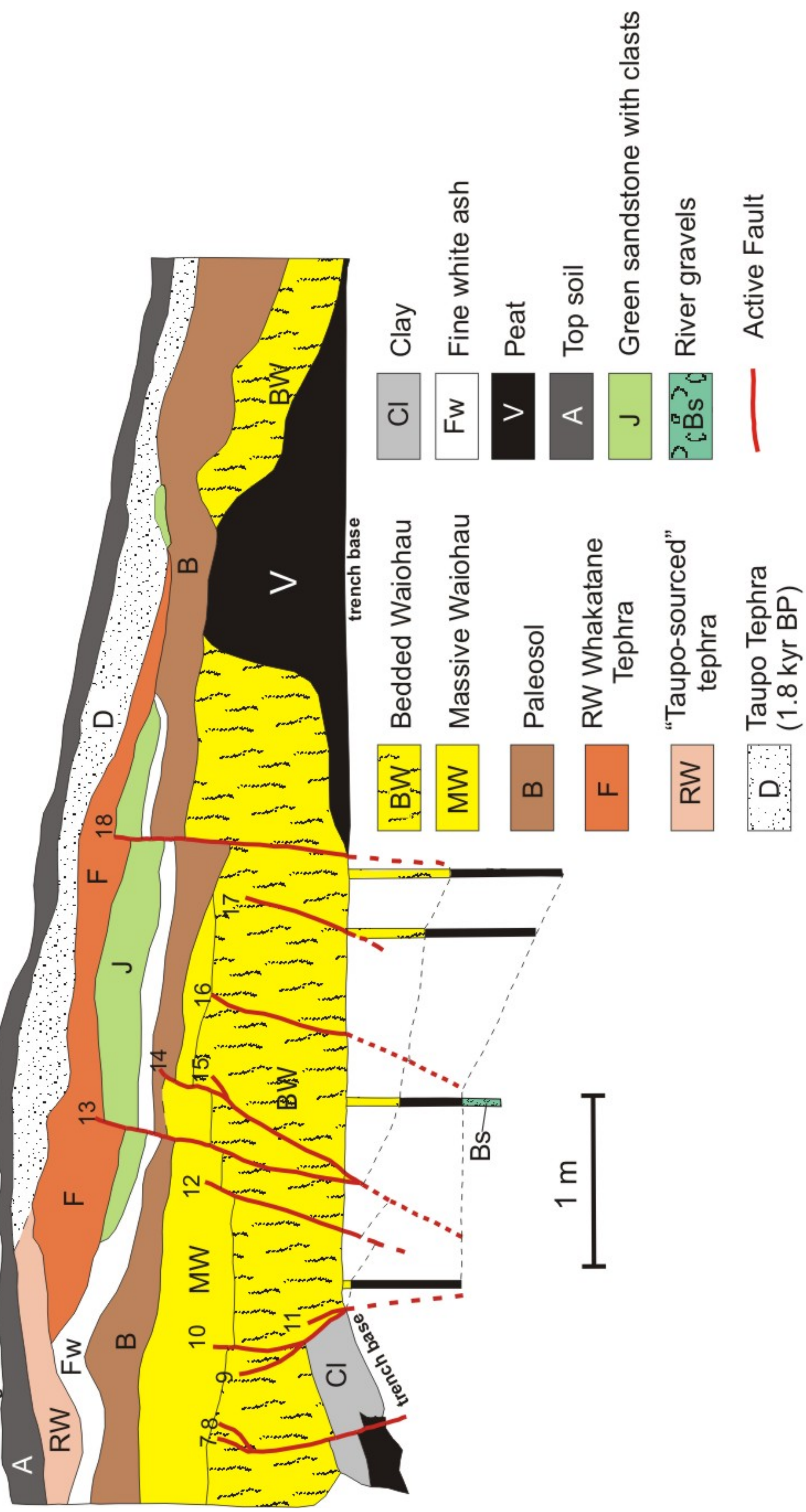

Fig. 4.22 North wall of Ahirau 1 Trench. Slip surfaces are numbered (e.g. 7-18). For further details on the description of the units see Appendix II

Ahirau 2 / North Wall (Fig. 4.23):

- 1st event (most recent): The unit E which contains Reworked Whakatane Tephra (<5.6 kyr BP) (Table 54 in Appendix III) is the youngest displaced deposit, ruptured by fault strand 7 (Fig. 4.23). The overlying paleosol (unit B), which underlies reworked Taupo Tephra (<1.8 kyr BP), is undisplaced and probably represents a long period of time, or hosts a cryptic unconformity. This event is interpreted to be the same as the first event at Ahirau 1 (bracketed between 2882 ± 95 and 1800 yrs BP).
- 2nd event: Slip during this event on fault-strand 5 displaces unit W (colluvial wedge) whereas slip (during the same event) on fault strands 2-4 & 6 offset the unit P (reworked Waiohau). However, neither unit B (paleosol), which overlies the unit P (reworked Waiohau), nor unit C (mixed Taupo-sourced tephras) (3.5 and 1.8 kyr BP) are displaced. Several fault strands (e.g. 2, 3, 4 & 6 in Fig. 4.23) terminate upwards within the unit of reworked Waiohau suggesting that this event occurred contemporaneously with deposition of that unit. The reworked Waiohau unit is similar in style to that in the Ahirau 1 Trench and the faulting relationships appear similar, so this event is probably equivalent to the second earthquake recorded at Ahirau 1 Trench (bracketed between 9.5 and 2.98 kyr BP).
- 3rd event (oldest): The presence of a colluvial wedge (unit W) beneath the reworked Waiohau (unit P) reflects the existence of a fault scarp prior to blanketing by that deposit. Slip during this earthquake is inferred to have formed this fault scarp.

Summary of paleoearthquakes at Te Ahirau site (Ahirau 1 & 2 trenches)

1st event: Occurred between 2882 ± 95 and 1800 yrs BP.
2nd event: Occurred synchronously with the deposition of the unit P which contains reworked Waiohau Tephra, post 9.5 and pre-2.98 kyr BP.
3rd event: Occurred prior to 9.5 kyr BP.

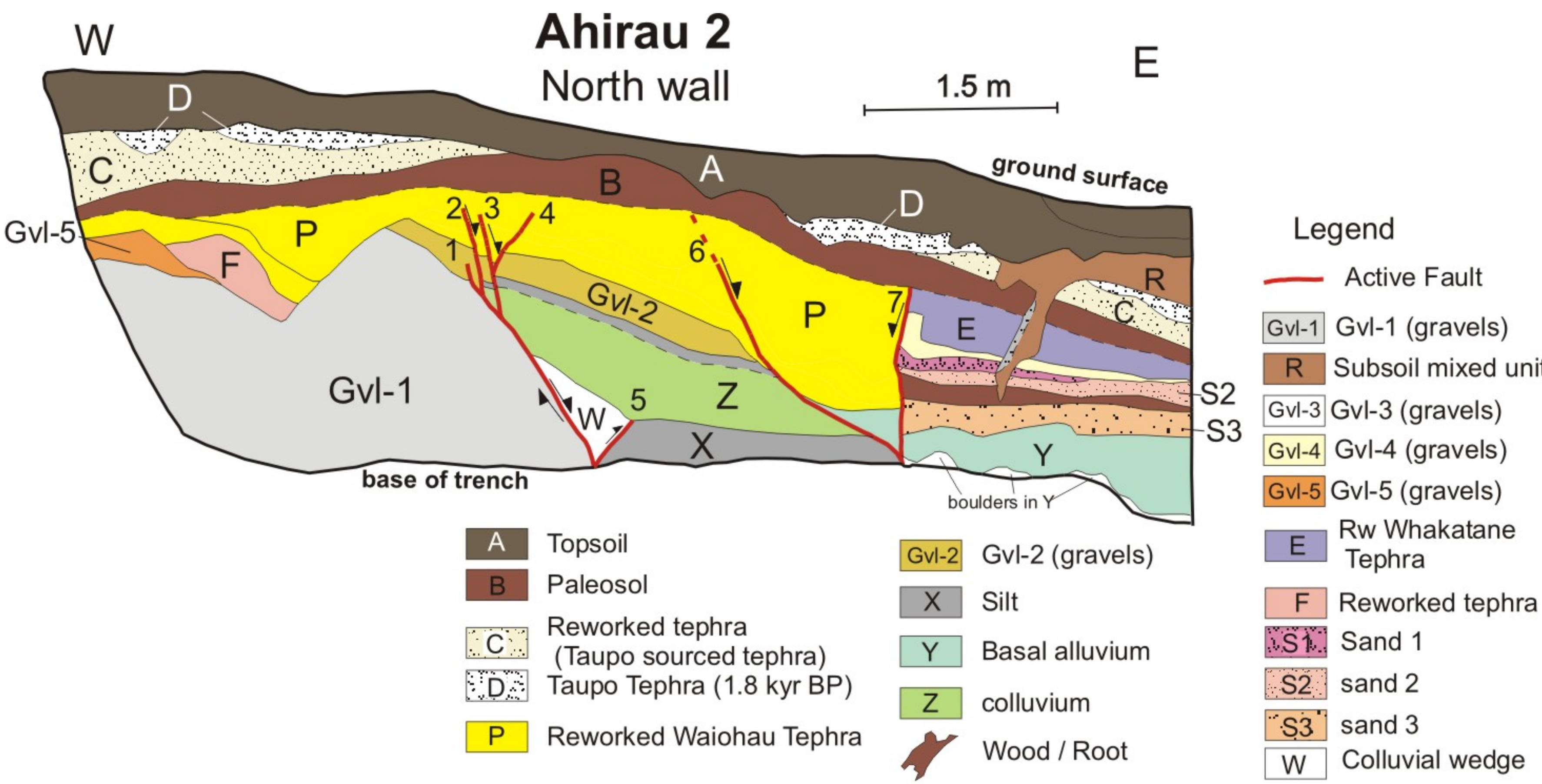

Fig. 4.23 North wall of Ahirau 2 Trench. Slip surfaces are numbered (e.g. 1-7). For further details on the description of the units see Appendix II.

4.5.2 Nukuhou North

4.5.2.1 Site and trench descriptions

Nukuhou North settlement is located c. 11 km south of the Bay of Plenty coastline, adjacent to the State Highway 2 (Map L in Appendix I). The Waimana Fault at Nukuhou North strikes c. N-S, dips steeply (i.e. >80°) to the west and is chiefly a right-lateral strike-slip fault. Its trace is continuous for over 300 m near the trench sites (Fig. 4.24). The fault traverses a diachronous landscape, which spans in age from <1.8 to c. 50 kyr BP, displacing right-laterally several geomorphic features, such as stream channels, terrace risers and ridge spurs (Fig. 4.24).

Fig. 4.24 Vertical aerial photograph of the Nukuhou North site. The Waimana Fault is indicated by the red line. The locations of the two trench sites, Moana and Moana-Iti, are indicated by the yellow polygons. The displaced stream at site 62 is also indicated. Microtopographic maps, created by GPS-RTK survey, overlay the aerial photograph where available.

Two trenches (Moana and Moana-Iti) were excavated some 250 m to the west of the State Highway 2, where the Waimana Fault displaces an abandoned stream channel right-laterally by 20±3 m (W16/725379) (Fig. 4.25 in this chapter and Fig. 51 in

Appendix I). The Moana Trench was excavated perpendicularly across the fault to provide information on the paleoearthquake history of the fault. A second trench, Moana-Iti, was opened perpendicular to the stream axis, and also across part of the fault, chiefly to constrain the age of the offset stream and thus, the slip rate on the fault (Fig. 4.25).

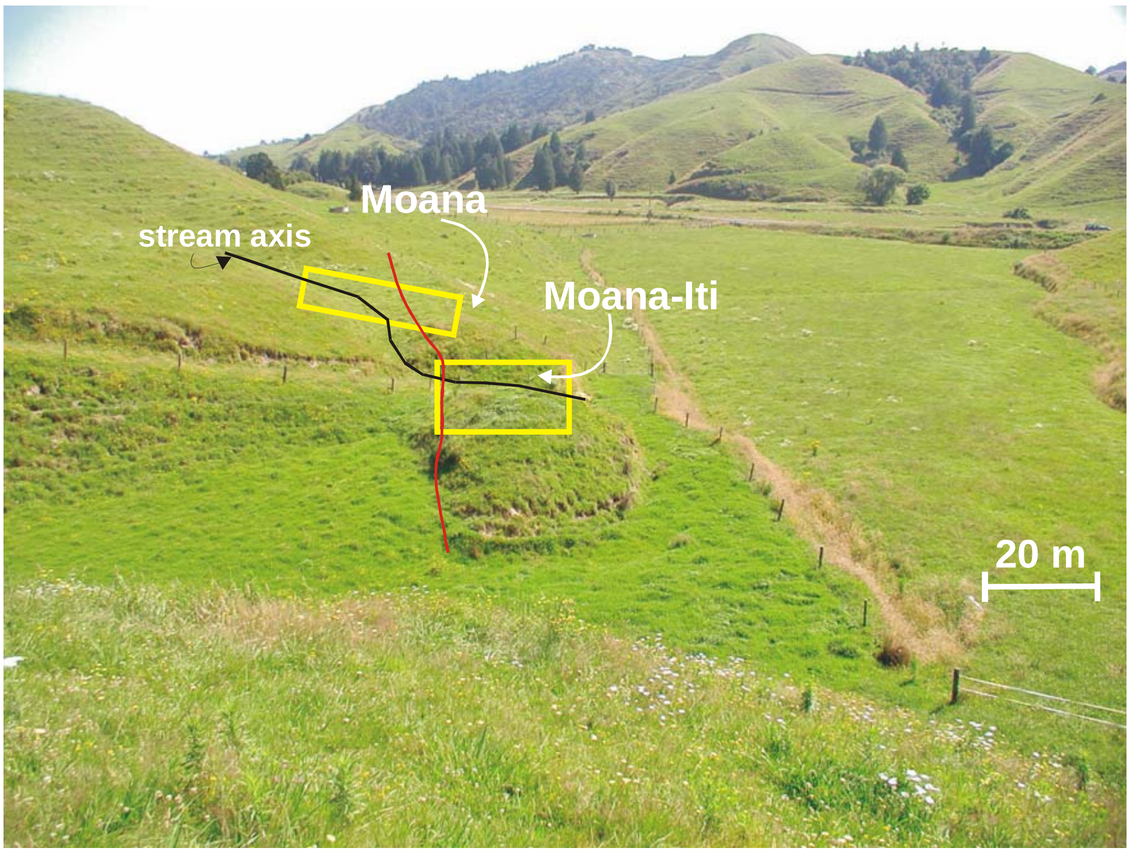

Fig. 4.25 Photograph showing the location of the two trenches at Nukuhou North (sites 64 & 65). Trench sites are indicated by yellow rectangles. Views are towards the northeast.

Approximately 150 m to the south of Moana-Iti Trench, at site 62, the Waimana Fault displaces right-laterally an active stream by c. 24±15 m (Fig. 4.26 and Fig. 50 in Appendix I). Augering of the channel deposits provided data related to the stratigraphy which, in combination with trenching and radiocarbon dating, helped constrain the horizontal slip rate on this section of the Waimana Fault (see next section 4.5.2.2).

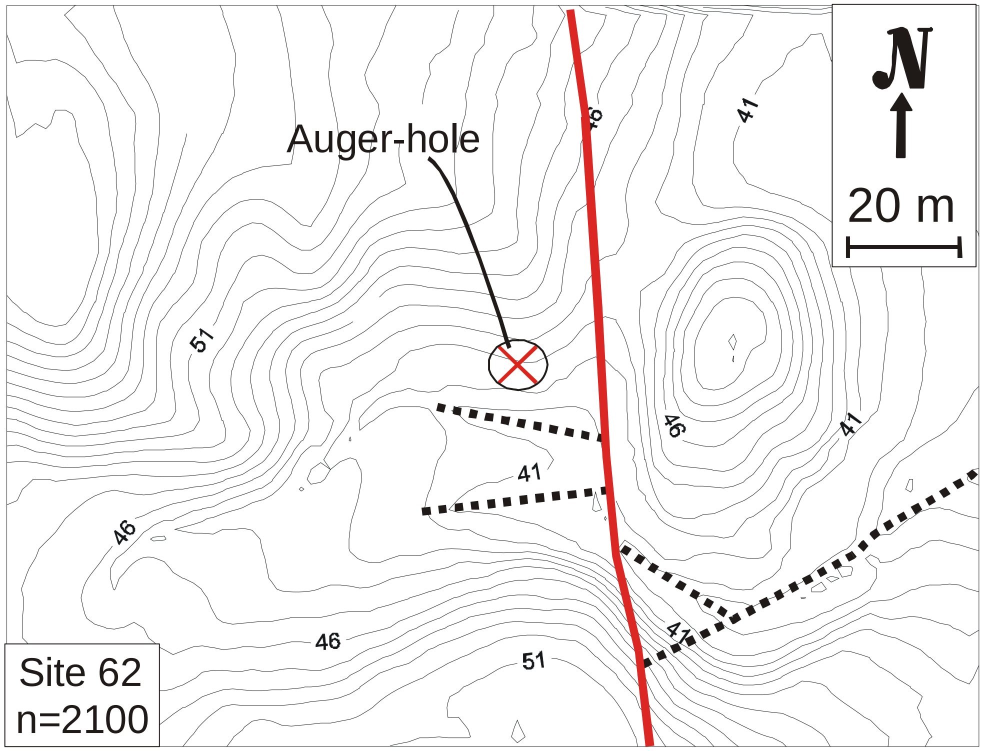

Fig. 4.26 Detailed contour map created by GPS-RTK illustrates the offset stream at site 62. The location of the auger-hole is indicated (see also Fig. 4.27). Dashed lines represent the stream-channel axis on each side of the fault and indicate offset. n=number of topographic measurements.

4.5.2.2 Stratigraphy and Age control

In this region, basement rocks (Mesozoic greywacke) are covered by Castlecliffian mudstone which is, in turn, mantled by aggradational terraces (Edbrooke, 1977). The Waimana Fault commonly traverses and displaces these terrace surfaces. At Nukuhou North both trenches were excavated into an aggradational terrace that consists of fluvial gravels overlain by loess, silts and volcanic layers. Trenching, augering and radiocarbon dating of key stratigraphic horizons overlying the terrace gravels helped constrain the landscape evolution, the timing of large surface rupturing earthquakes and the slip rate on the Waimana Fault. Tephra horizons in the trenches were identified using micro-probe analysis and radiocarbon dating of adjacent organic layers. A summary of radiocarbon samples and dates are presented in Table 4.4.

The fluvial gravels beneath the trenched terrace surface are exposed in a road-cut on the west side of State Highway 2, some 250 m to the east of the trenches. These gravels are overlain by a thin (c. 10-15 cm) layer of silt and a thick (over 3 m) deposit of airfall Rotoehu Tephra (c. 50 kyr old) (Table 59 in Appendix III, Fig. 4.27). The presence of Rotoehu Tephra suggests that the terrace was abandoned by the river at c. 50 kyr BP. Loess, up to 1 m thick, sits on top of Rotoehu (c. 50 kyr BP) while Mangaone Subgroup airfall tephras (c. 30 kyr BP) overlay the loess (Fig. 4.27). The thickness of the Mangaone subgroup tephras, in places, exceeds 5 m.

Augering of the surface at site 62 (Figs. 4.26 & 4.27), provided constraints on younger stratigraphic horizons that sit stratigraphically above the Mangaone Subgroup on this terrace. Kawakawa Tephra (27 kyr BP) was found at the base of the 5.2 m-deep auger-hole, and Rerewhakaaitu Tephra (17.6 kyr BP) at c. 3.5 m depth (Tables 61 & 62 in Appendix III). A mixture of reworked Okataina and Taupo-sourced tephra rest at c. 0.5-1 m depth (Table 60 in Appendix III) (Fig. 4.27).

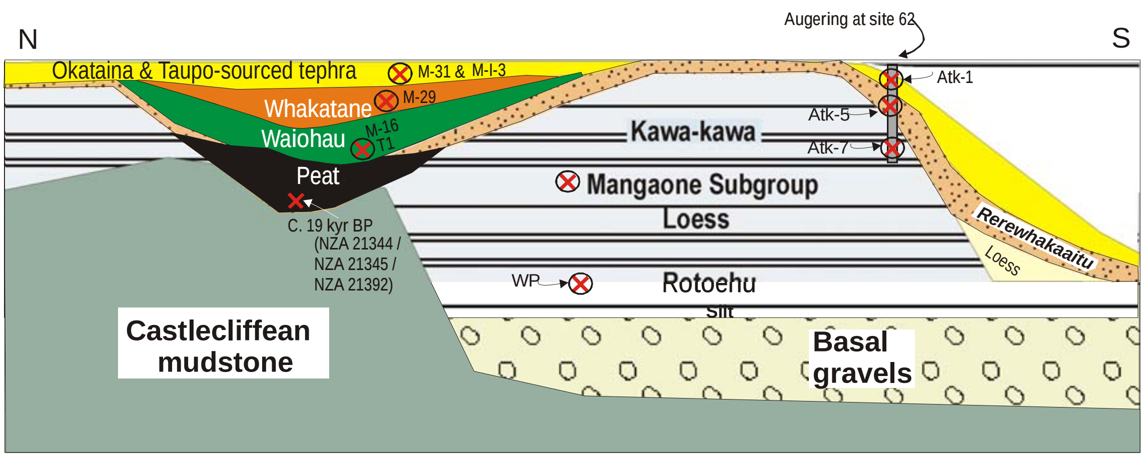

Fig. 4.27 This schematic cartoon combines data produced by augering (site 62) and trenching (sites 64 & 65), and illustrates the inferred stratigraphic relationships between the basement Castlecliffean mudstone, the aggradational terrace, the younger mantling tephras and the trenched channel. Note that the cartoon is simplified and tephra-centric (i.e. paleosols often developed between volcanic layers are not included).

Trenching where the Waimana Fault displaces right-laterally the channel of Moana stream (immediately to the north of site 62) provides additional control on the stratigraphy of the area. Peat found at the bottom of the trench lies directly on Castlecliffean mudstone (Fig. 18 in Appendix II) and has an average age of 19±4 kyr BP (samples NZA 21344, NZA 21345 and NZA 21392 in Table 4.4). Primary and reworked Waiohau Tephra (13.8 kyr BP) rests above the peat (Tables 65 & 70 in Appendix III, Fig. 4.27) whereas primary and reworked Whakatane (5.6 kyr BP) (Tables 66-68 in

Appendix III) and a mixture of reworked Whakatane and Taupo-sourced tephras (Tables 63, 69-71 in Appendix III) occur at higher stratigraphic layers.

Sample Number (*AMS date)	Method used to claim sample	Sample Description	Grid Reference	Radiocarbon Age			Data on
				Conventional years B.P.	Calibrated years B.P.	Calendar years (calibrated)	
NZA 21344 * (Moana-P1)	Trenching	Peat	W17/725379	12433 ± 50 BP	15512-14153 BP	13508 BC - 12141 BC	slip rate
NZA 21345 * (Moana-P2)	Trenching	Peat	W17/725379	12336± 45 BP	15469-14122 BP	13520 - 12173 BC	slip rate
NZA 21346 * (Moana-M28)	Trenching	Peat	W17/725379	6803± 35 BP	7683-7580 BP	5734 - 5631 BC	oldest event on south wall of Moana
NZA 21392 * (Moana-Iti-4)	Trenching	Peat	W17/725379	23080± 160 BP			slip rate
NZA 21389 * (Moana-Iti-5)	Trenching	Organic paleosol	W17/725379	3139± 30 BP	3402-3325 BP	1455 - 1376 BC	1st event at Moana Iti
NZA 21391 * (Moana-Iti-6)	Trenching	Organic soil	W17/725379	2039± 30 BP	2063-1917 BP	114 BC - 33 AD	slip rate

Table 4.4 Summary of radiocarbon samples and dates collected from Moana and Moana-Iti trenches.

Slip Rate on the Waimana Fault at Nukuhou North

The age of the peat at the base of the infill deposits in the channel (average of Moana-P1 / NZA 21344, Moana-P2 / NZA 21345 & Moana-Iti-4 / NZA 21392 in Table 4.4), indicates that stream incision ceased (transition from its erosional to depositional phase) 19±4 kyr ago. Right-lateral displacement of the channel during this time amounts to 20±3 m (Fig. 51 in Appendix I) providing a maximum strike-slip rate of 1.2±0.5 mm/yr on the Waimana Fault. This maximum slip rate is comparable with the average slip rates that derived from offset landforms approximately 10 and 20 km to the south (sites 71-73 & 75 in Table 2.1, Chapter 2). The horizontal to vertical (H:V) slip ratio is c. 10 indicating a predominantly strike-slip sense of displacement on the fault at this locality.

4.5.2.3 Fault geometries

The Waimana Fault on the north wall of the Moana Trench strikes 357° and has a dip of 47° to the west (Fig. 4.28). This low dip is probably a shallow feature and does not represent the average dip of the Waimana Fault in this region which is inferred from gravity data to be near vertical (i.e. >80°) (Fig. 6.4b in Chapter 6). The faulting is mainly restricted to the eastern section of the north wall (strands 1-6 in Fig. 4.28) where it extends across a 3.5 m wide zone. The principal slip surface, strand 3, has a shallow dip (i.e. 47° W) and juxtaposes Castlecliffean mudstone to the east, against younger volcanic and sedimentary deposits, to the west. There are at least three splays that bifurcate upwards from the main slip surface (strands 4, 5 & 6 in Fig. 4.28). These splays dip steeply. Approximately 5.5 m to the west of the main fault zone the isolated fault strand 7 dips steeply and bifurcates upwards into smaller slip surfaces (Fig. 4.28).

The Waimana Fault on the south wall of Moana strikes 010° and dips 53° W (Fig. 4.29). As is the case on the north wall, this dip probably underestimates the average dip at depth (i.e. >80°). Faulting here is confined to a west dipping slip surface which is < 5 cm wide at the bottom of the trench but splays upwards into numerous secondary slip surfaces that extend across a zone c.1.5 m wide (fault strands 8-14 in Fig. 4.29). Several slickenside striations were measured on the main slip surface of the south wall revealing a dominantly strike-slip sense of motion on the fault at this locality: 008/04, 010/02, 353/17, 011/01, 009/06, 008/20, 010/18, 009/17.

The fault on the north wall of Moana-Iti Trench strikes 360° and its dip is near vertical (i.e. 88°). Here, the fault zone is c. 30 cm wide and comprises three steeply dipping strands (splays 1-3 in Fig. 4.30). The units juxtaposed between the strands cannot be correlated across the faults indicating significant strike-slip movement on the fault.

4.5.2.3 Timing of paleoearthquakes on Waimana Fault at Nukuhou North

Moana Trench / North wall (Fig. 4.28):

- 1st (most recent) event: Slip during this event on strand 3, displaces unit F which consists of reworked Whakatane and Taupo-sourced tephras (<5.6 ky BP) and the colluvial wedge (unit W). However, strand 3 does not appear to displace either the Taupo Tephra (1.8 kyr BP) (unit Bz) or the top soil (unit A).
- 2nd event: Slip during this event displaces the unit C3 which consists of Whakatane Tephra (5.6 kyr BP) on fault strand 7 (west part of the north wall), and also accounts for the formation of the colluvial wedge (unit W). This rupture

does not appear to propagate either through unit F (reworked Whakatane and 'Taupo sourced' tephras) or its paleosol (unit C1). In the absence of a paleosol between units F (reworked Whakatane and 'Taupo sourced' tephras) and C3 (Whakatane Tephra), it is inferred that the time interval between deposition of the two units is small. This earthquake is inferred to have occurred soon after the deposition of Whakatane Tephra (5.6 kyr BP).

- 3rd event: This earthquake is represented by fault strands 4, 5 & 6 that terminate within unit D (volcanic horizon that contains reworked Waiohau Tephra, dated as 7683-7580 cal yrs BP on the south wall of Moana / NZA 21346). Whakatane Tephra (5.6 kyr BP) (unit C3) is not displaced by this earthquake. The rupture occurred during deposition of reworked Waiohau (unit D) at c. 7631± 51 cal. yrs BP.
- 4th event (oldest): This event formed a scarp on which the units J (clay) and D (reworked Waiohau) are deposited and thicken against the fault. Units J and D are therefore deposited on a pre-existing inclined surface that was formed during this earthquake. This suggests that there is at least one earthquake of uncertain age that pre dates the formation of the units J and D (c. 7631± 51 cal. yrs BP).

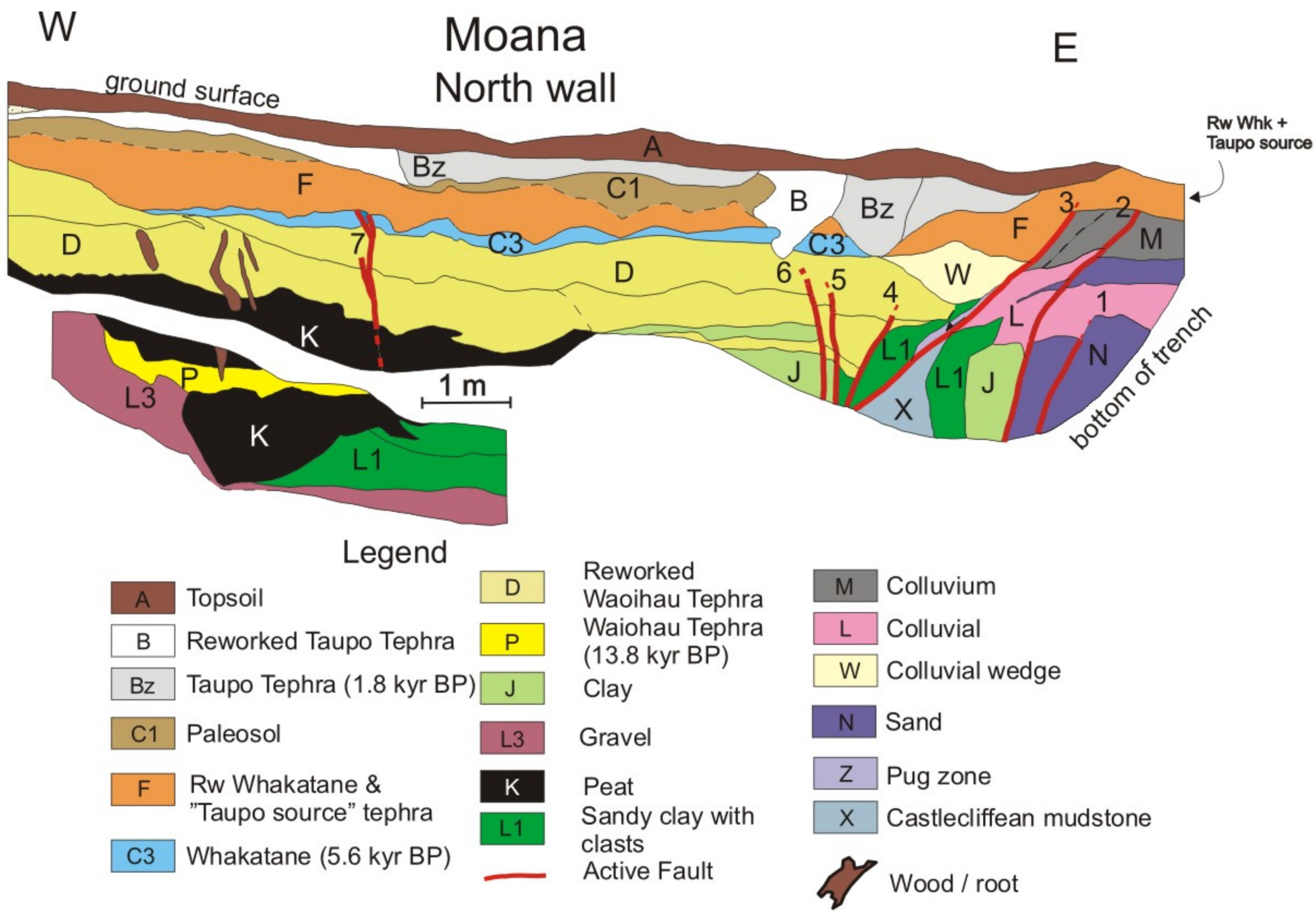

Fig. 4.28 The north wall of Moana Trench. Slip surfaces are numbered (e.g. 1-7). For further details on the description of the units see Appendix II.

Moana / South wall (Fig. 4.29):

- 1st event (most recent): Slip during this earthquake produced fault strands 8-11, which offset unit W (colluvial wedge) and unit RT (reworked Whakatane Tephra). The same earthquake produced slip on the secondary antithetic strands 13 & 14 (Fig. 4.29). Rupture of strands 8-11 and 13-14 do not appear to displace the Taupo Tephra (1.8 kyr BP) or the top soil (unit A). Therefore, this event is bracketed between 5.6 and 1.8 ky BP.
- 2nd event (oldest): Slip during this earthquake on fault strand 12 displaces unit C3 that contains primary Whakatane Tephra (5.6 kyr BP) and accounts for the formation of the colluvial wedge (unit W). This event does not, however, appear to displace unit RT (reworked Whakatane Tephra). The paleosol that develops between the units of lower RT (reworked Whakatane Tephra) and C3 (primary Whakatane) is very weak and thin and may indicates a small time interval between their deposition.

Here should be noted that the antithetic faulting on strands 13 & 14 (Fig. 4.29), attributed to the most recent event, could instead have been formed during a separate earthquake event that precedes the last earthquake. The antithetic faulting that displaces units W (colluvial wedge) and RT (reworked Whakatane Tephra) may have occurred between deposition of the lower and upper RT (reworked Whakatane) units. However, based on the average recurrence interval, estimated by the single event displacement and the slip rate on the fault at this locality (4.2±1.9 kyr) (see section 4.6 in this chapter) it is suggested that this scenario is less likely than the preferred interpretation.

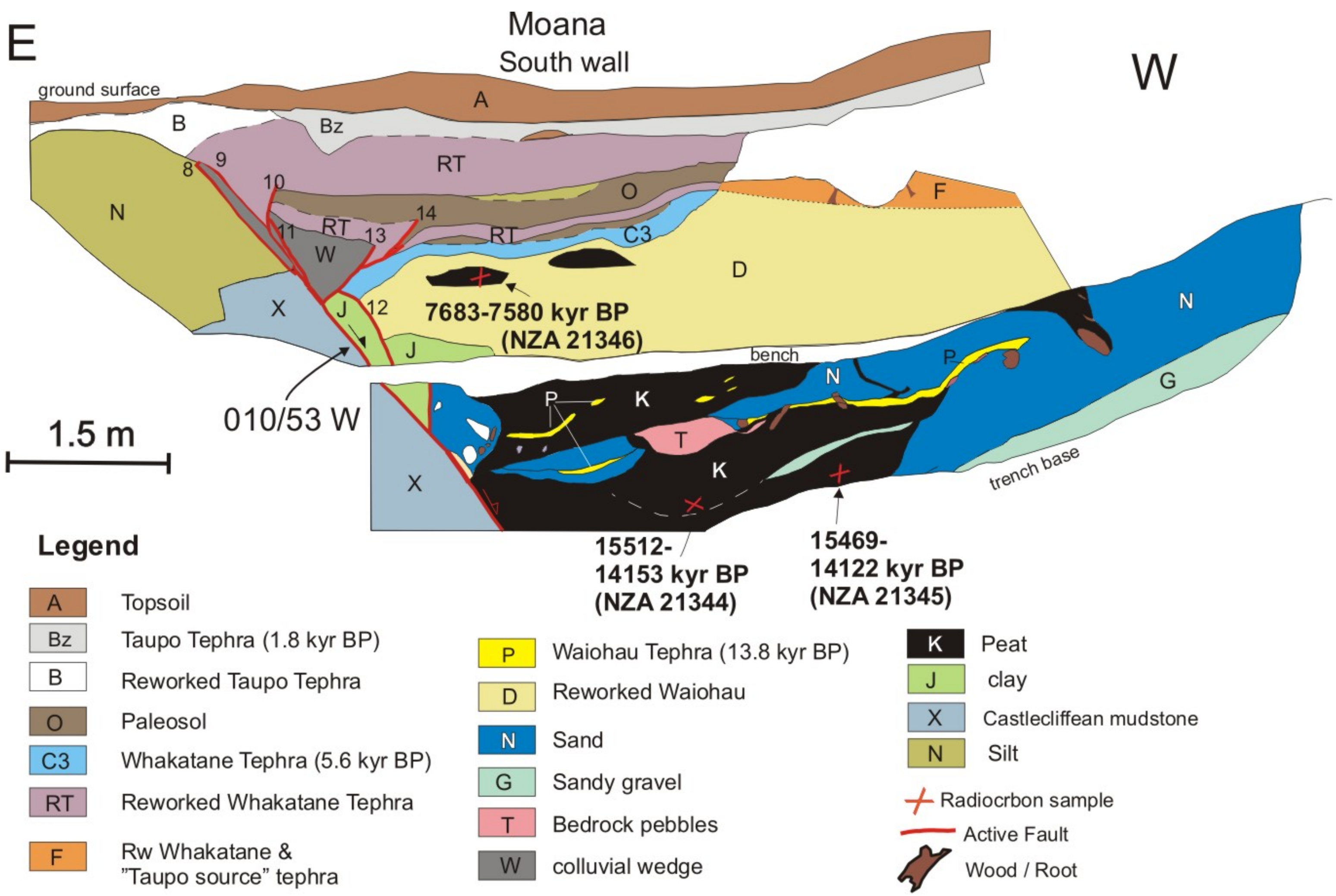

Fig. 4.29 The south wall of Moana Trench at Nukuhou North. Slip surfaces are numbered (e. g. 8-14). For further details on the description of the units see Appendix II.

Moana-Iti (Fig. 4.30):

- 1st earthquake event: Slip on strand 1 during this earthquake disrupts both the unit Toru (sandy mustone), which is radiocarbon dated as of 3364 ± 38 kyr BP (NZA 21389 / Table 4.4), and the unit Tahi (reworked Whakatane & a Taupo-sourced tephra, Table 71 in Appendix III), but does not displace the Taupo Tephra (1.8 kyr BP) (unit Whetu) or the top soil (unit S). Therefore the last earthquake is bracketed between 3364 ± 38 and 1800 yrs BP.
- 2nd earthquake event(s) (oldest): Slip on strands 2 & 3 during this earthquake disrupts the units Rua (peat) and Wha (tephric sand) without, however, displacing the unit Toru (sandy mudstone). It is not possible to discriminate whether fault strands 2 & 3 were produced by slip during one or two separate events. Radiocarbon dating of the peat within unit Rua returned a 23080 ± 160 yrs BP (NZA 21392) age. Therefore, the oldest event(s) recorded within Moana-Iti is bracketed between 23080 ± 160 and 3364 ± 38 kyr BP.

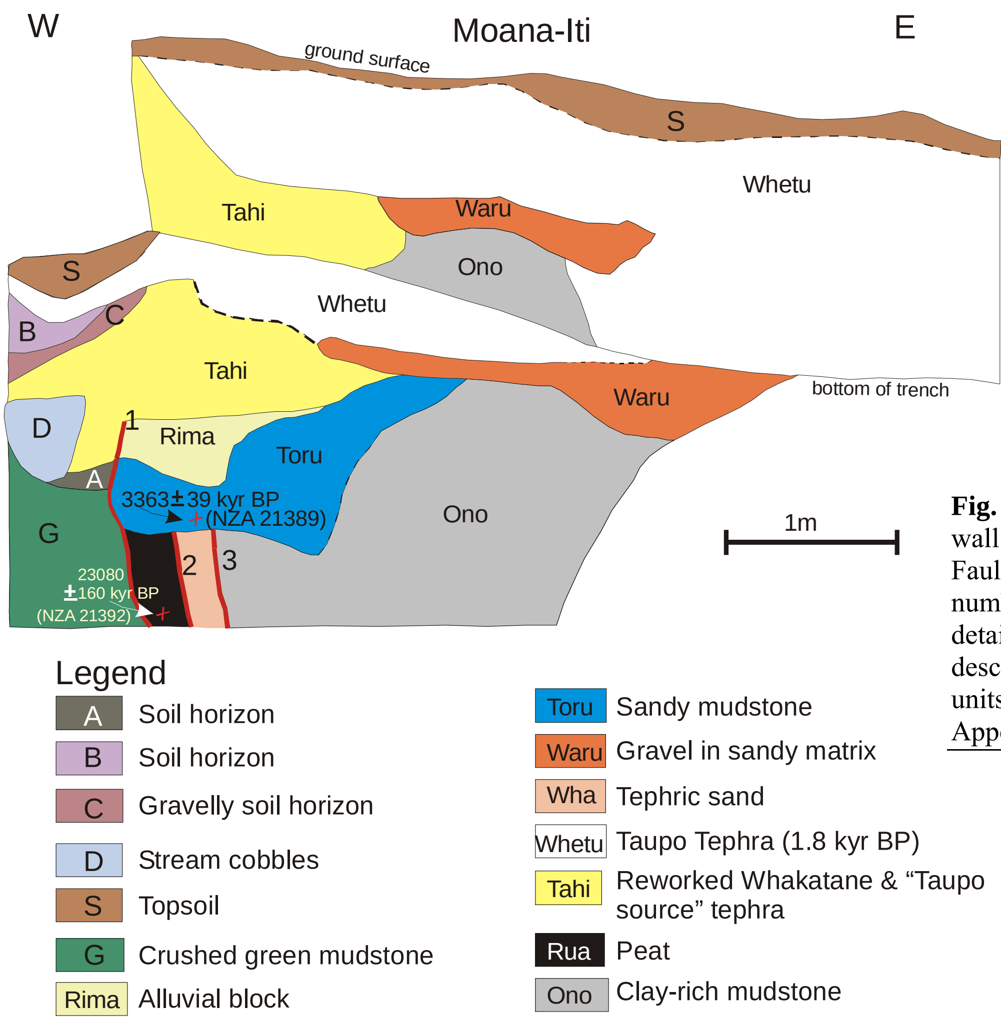

Fig. 4.30 The north wall of Moana-Iti. Fault strands are numbered. For further details on the description of the units see the Appendix II.

<u>Summary of paleoearthquakes in Nukuhou North:</u>

- 1st event (most recent): Postdates deposition of unit RT (reworked Whakatane Tephra) but pre-dates deposition of Taupo Tephra (constrained on both walls of Moana) and accounts for the antithetic faulting on strands 13 & 14 in the south wall. This event is constraint in Moana-Iti to have occurred between 3364 ± 38 and 1800 yrs BP.
- 2nd event: Occurred soon after the deposition of the unit C3 (primary Whakatane Tephra, 5.6 ky BP) (constrained on both walls of Moana).
- 3rd event: This earthquake appears to be synchronous with deposition of unit D (reworked Waiohau Tephra) which is dated as c. 7631± 51 yrs BP (constrained on the north wall of Moana).
- 4th event (oldest): Predates deposition of the unit that contains reworked Waiohau tephra (c. 7631± 51 cal. yrs BP) (constrained on the north wall of Moana), but is of unknown age.

4.5.3.1 Timing of paleoearthquakes on the Waimana Fault

Figure 4.31 summarises the late Quaternary earthquake history on the Waimana Fault at two different localities. At both localities there is no surface rupturing event during the last 1800 years. Instead, the most recent earthquake is constrained to have occurred between 1800 and 2882 ± 95 yrs BP at Te Ahirau and between 1800 and 3364 ± 38 yrs BP at Nukuhou North. The penultimate event recorded at Nukuhou North is inferred to have slightly post-dated deposition of Whakatane Tephra, c. 5.6 kyr BP. This earthquake may also have ruptured through the group of southern trenches (Ahirau 1 & 2), however, present data cannot confirm this. A third event appears to have ruptured the Nukuhou North site synchronously with the deposition of reworked Waiohau unit that is dated as of c. 7631± 51 cal. yrs BP (south wall of Moana). This syn-reworked Waiohau event is also present in both trenches at the Te Ahirau site (2nd event in Ahirau 1 & 2 trenches) where numerous fault strands terminate within the unit that contains reworked Waiohau Tephra. Fault rupture during this earthquake probably extended continuously between the two sites. The oldest event recorded in Nukuhou North (Moana Trench) predates the deposition of reworked Waiohau Tephra (c. 7.6 kyr). Similarly, the oldest event recorded to have ruptured through the southern sites, predates 9.5 kyr BP. Data therefore suggest that most (or all) earthquakes could have ruptured the Nukuhou North and Te Ahirau sites contemporaneously.

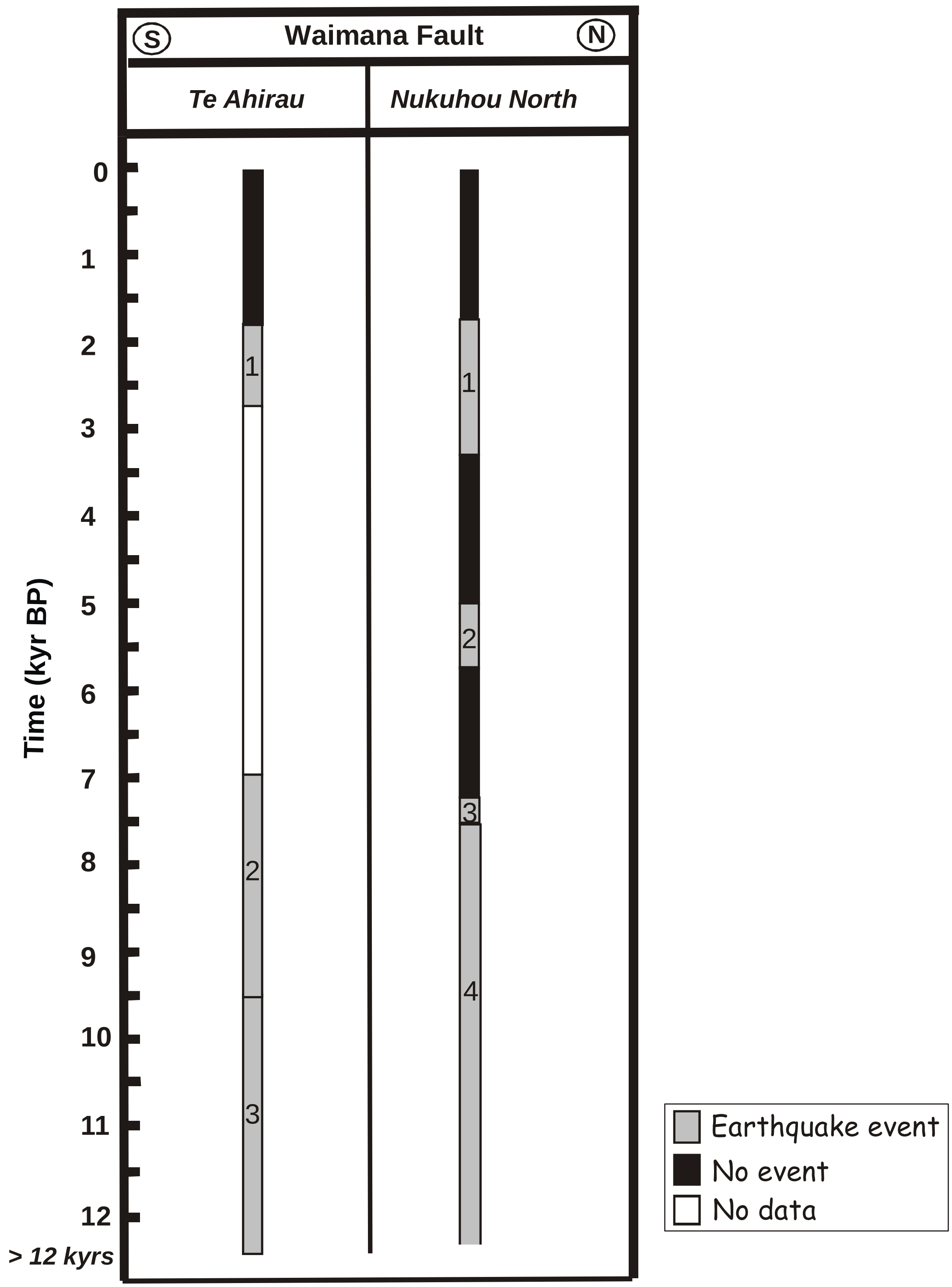

Fig. 4.31 Summary of late Quaternary paleoearthquake history on the northernmost 35 km of the Waimana Fault. Consecutive numbering of events within the grey polygons is shown. Black lines that bound the grey polygons represent minimum and maximum age for each event, respectively.

4.6 Earthquake Hazards

4.6.1 Earthquake Recurrence Interval in the northern NIFS

The earthquake recurrence interval (RI) is the period of time between large magnitude events on an individual fault (McCalpin, 1996). The RI can be estimated using two different methods: 1) directly from the earthquakes observed in trenches (observed RI) or 2) calculated from the mean single event displacement (SED) and the slip rate on the fault (estimated average RI for the time interval of slip rate measurement). The methods are independent from one another and collectively provide a powerful means of estimating recurrence intervals and their variability.

Estimates of recurrence interval by numerical dating of paleoearthquakes recorded in trenches, was introduced by workers in the 1970's (e.g. Sieh, 1978). This method relies on the stratigraphy within the trench being complete and can incorporate significant uncertainty because: a) the precise dating of individual earthquakes is difficult (instead events are often constrained by numerical ages that postdate and/or predate the fault movement) and, b) the stratigraphic record in many trenches is incomplete (particularly on strike-slip faults) and earthquakes may be missed.

The value of "estimated average recurrence interval" was first proposed by Wallace (1970) and is based on the cumulative displacement of a dated feature that has been offset by multiple earthquakes. The slip per event is typically estimated from the maximum or average slip documented during single earthquakes. Average RI = $D\Delta t$ / (S-C), where RI = average recurrence interval, D = displacement per event, S and C are cumulative displacements produced by earthquakes and creep (which is assumed to be zero here), respectively, and Δt is the time interval over which they have accumulated. Uncertainties in the calculated average RI's arise from two sources: a) the uncertainty in the age and displacement of the offset feature and b) the uncertainty associated with the estimate of mean single event displacement. The errors are asymmetric and treated using the division rule for values with unequal standard deviations (Geyh and Schliecher, 1990).

Table 4.5 presents both, the observed and calculated recurrence intervals for each site of the Waiohau-Ruahine, Whakatane-Mohaka and Waimana faults. For cases in which the slip per event at the site trenched is not constrained, the nearest available slip per event measurement is used derived from the section of the fault that has similar kinematics to the site studied.

Fault	Site *	Net SED (m)	Net Slip Rate (mm/yr)	Time interval over which slip rate is calculated (kyr)	Calculated RI (kyr) †	Observed RI (kyr) ‡	Time interval over which events in trenches are recorded (kyr)	Reference
Waiohau/Ruahine	Kaweka Forest	3.5±1.5	1.5±0.5	5	2.3±1.3	2.8	13.8	1,2
Waiohau/Ruahine	Galatea Basin	3.4±0.2	0.7±0.2	17.6	5±1.3	7.3 ±1.5	17.6	3,5
Waiohau/Ruahine	Waiohau Basin	2.5±0.5	0.7±0.2	13.8	3.6±1.2	3.9±0.5	13.8	3,4,5
Whakatane/Mohaka	Ohara /Ngaruroro	4±1^	4.2±0.5	16.8±0.5	1±0.3	2	16.8±0.5	2
Whakatane/Mohaka	Ngaruroro/TN-SH	4±1^	4.2±0.5^	10	1±0.3	4.9±0.2	10	2
Whakatane/Mohaka	Te Hoe	4±1	3.5±0.8	10	1.1±0.4	1.6	9.5	6
Whakatane/Mohaka	Ruatahuna	5.5±1	3.1±1	8±2	1.8±0.6	2.4	9.5	5
Whakatane/Mohaka	Ruatoki North	2.8±0.2	2.2±0.9	30	1.3±0.6	3.1	9.5	5,3
Waimana	Te Ahirau	5.5±2	1.2±0.8	13.8	5±2.7	4.6	13.8	5
Waimana	Nukuhou North	5.5±2^	1.2±0.5	19±4	4.6±2.5	2.5±0.02	7.7±0.05	5
Whakatane	Wharepora	1.7±0.5	2.2±0.9		0.8±0.4			5

* See Table 5.1 in Chapter 5 for grid references.
† Calculated from SED and slip rate (over the time period indicated by kyr) based on the relation: RI= D / (S-C), where C is zero, because no evidence for fault creep has been found on these faults.
‡ Observed in trenches over the time period indicated by kyr.
^ extrapolated value.

Table 4.5 Estimation of earthquake recurrence interval in the northern NIFS. 1=Beanland & Berryman (1987), 2=Hanson (1998), 3=Beanland (1989b), 4=Woodward-Clyde (1998), 5=This study (Table 2.1, Appendix I), 6=Hull (1983). Note that localities on each fault are arranged in sequence from south to north.

Table 4.5 shows that while recurrence intervals along the Waiohau-Ruahine Fault vary significantly between sites, at any given site the calculated and observed recurrence intervals are typically compatible (they plot near the 1:1 line in Figure 4.32), and often within the margin of error. The proximity of points to the 1:1 line indicates that these independent methods produce comparable first order estimates of recurrence interval.

Along strike variation in RI’s is demonstrated on the Waiohau-Ruahine Fault. The Galatea site, for example, appears to have an average RI of c. 6 kyr while the sections to the north and south are characterized by average recurrence intervals of c. 3.7 and 2.5 kyr, respectively. The variability in recurrence intervals along the northernmost 150 km of the Waiohau-Ruahine Fault raises the possibility of two earthquake rupture boundaries: one between the Kaweka Forest and Galatea Basin and another between Galatea and Waiohau basins (see Chapter 5 for further discussion).

The recurrence interval on the Whakatane Fault is estimated at five different localities where more than one earthquake has been identified by trenching (Table 4.5). For the two southernmost sites (Ohara-Ngaruroro and Ngaruroro-Taupo Napier SH) the calculated RI appears to be comparable (c. 1 kyr) while the observed at Ngaruroro-

Taupo SH RI (c. 4.9 kyr) differs significantly. The observed RI on the Whakatane-Mohaka Fault increases to the north (1.6 kyr at Te Hoe and 2.4 at Ruatahuna). The observed RI (3.1 kyr) at Ruatoki North is significantly higher than the calculated average RI (1.3±0.6 kyr). This discrepancy may arise either because a number of paleoearthquakes were not represented in the Te Whetu Trench (and were therefore missing), or because earthquakes on this section of the fault were clustered in time with relatively few events during Holocene.

The recurrence interval on the Waimana Fault is estimated at two different localities (Te Ahirau and Nukuhou North). The calculated recurrence interval appears to be comparable at both sites (i.e. 5±2.7 kyr at Te Ahirau and 4.6±2.5 kyr at Nukuhou North). The RI observed within Te Ahirau trenches for a time interval of c. 13.8 kyr appears to be comparable to the calculated RI (i.e. 4.6 kyr) for the same time interval. This is consistent with trench data which suggest that at least three out of four earthquake events recorded at the northern sites (Nukuhou North) ruptured through the southern sites (Te Ahirau). In contrast, the RI observed within the Nukuhou North trenches over a time interval of c. 7.7 kyr is c. 2 kyr less than the calculated over the last 19±4 kyr (Table 4.5 & Fig. 4.32). The variation between the calculated and observed RI on the Waimana Fault at Nukuhou North may arise due to more frequent events (earthquake clustering) during the last c. 7.7 kyr.

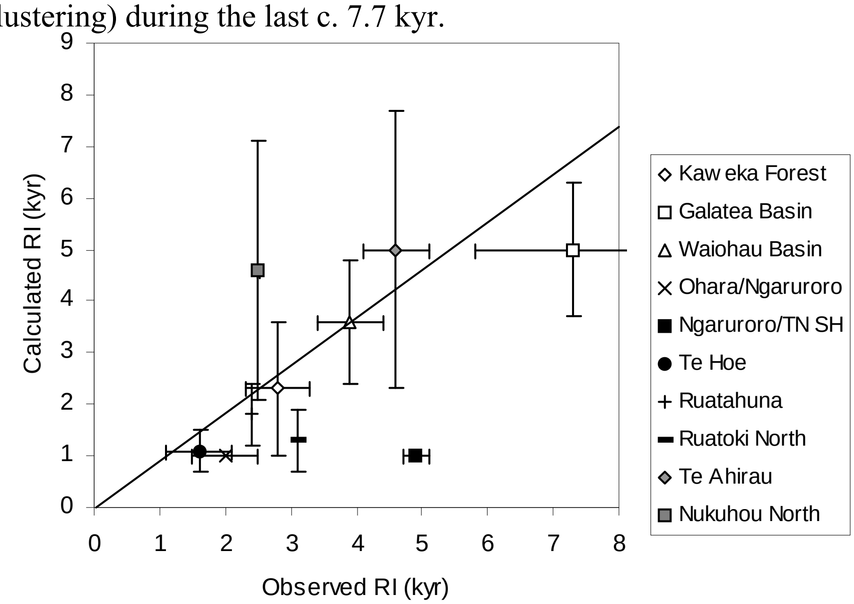

Fig. 4.32 Plot shows the relationship between recurrence intervals estimated from single event displacement and slip rate (see Table 4.5) versus those observed in the trenches. Note that the bulk of the data plot near to 1:1 line.

4.6.2 Paleoearthquake Magnitude in the northern NIFS

Earthquake magnitudes for prehistoric events can be estimated if information is available on the dimensions of the rupture surface, the amount of slip/event and the shear modulus of the rock volume enclosing the fault. Presently the most widely utilised magnitude scale is that of the Moment Magnitude (M_w) (Kanamori, 1977; Hanks and Kanamori, 1979). The formula used to determine the M_w proposed by Hanks and Kanamori (1979) is:

$$M_{(HK)} = 2/3 \log M_o - 10.7 \qquad (1)$$

where M_o is the seismic moment, and $M_o = D\ A\ \mu$. D (cm) is the average displacement per event on the fault surface; A (cm^2) the rupture area and μ is the shear modulus (3×10^{11} dyne/cm^2 or 30,000N/m^2). A is the product of the fault rupture length at the ground surface and the thickness of the seismogenic crust (in this case 15 km, for further information see Stirling et al., 2002).

Empirical relations from a global historical earthquake database may also be used to estimate the magnitudes of prehistoric events. The empirical relationship between magnitude and rupture area from Wells and Coppersmith (1994) is used here:

$$M_{(WK)} = 3.98+1.02 \log A \qquad (2)$$

again A is the rupture area (i.e. product of the fault rupture length at the ground surface and the thickness of the seismogenic crust, in this case 15 km. For further information see Stirling et al., 2002).

Trench data presented in this chapter, suggest that although the total length of the Waiohau-Ruahine and Whakatane-Mohaka faults studied is 150 and 200 km respectively, they are segmented so that most (or all) times the northernmost c. 30 km of the Waiohau Fault and the northernmost 50 km of the Whakatane Fault, rupture during separate events from their southern sections. Table 4.6 shows an estimated range of earthquake magnitudes of 6.6–7.7 for a range of ruptures on the northern NIFS. While the possible range of rupture lengths are likely to be captured in Table 4.6, the data constraining the average slip/event are sparse and these numbers (and the resultant magnitudes) may require revision as more information becomes available.

The rupture lengths assigned for the Waiohau-Ruahine Fault, from north to south, are: 30 km for the *northern Waiohau-Ruahine* section (WR_N = south of Waiohau Basin to the intersection with the Taupo Rift), 30 km for the *Galatea Basin section* of the Waiohau-Ruahine Fault (WR_G = south of Waiohau Basin to south of Galatea Basin), 60 km for a single rupture through WR_N and WR_G sections (e.g. south of Galatea Basin to the intersection with the Taupo Rift), a minimum length of 85 km for the *southern Waiohau-Ruahine* section (WR_S = south of Galatea Basin to Kaweka Forest), and 150 km for the entire fault-length studied (Fig. 4.33).

Similarly, for the Whakatane-Mohaka Fault the assigned rupture lengths, from north to south, are: 50 km for the *northern Whakatane-Mohaka* section (WM_N = south of Wharepora to the intersection with the Taupo Rift), 70 km for the *Ruatahuna section* of the Whakatane-Mohaka Fault (WM_R = south of Wharepora to north of Te Hoe River), 120 km for a combined rupture through the WM_N and WM_R sections of the Whakatane-Mohaka Fault (e.g. north of Te Hoe River to the intersection with the Taupo Rift) and 200 km for the entire fault-length studied (including the two southernmost sections: *Te Hoe section* (WM_T), and *Ngaruroro section* (WM_{Ng})) (Fig. 4.33).

The Waimana Fault, similar to the Waiohau/Ruahine and Whakatane/Mohaka faults, is not expected to rupture in its entirety (length of c. 150 km). Available gravity and seismic-reflection data (Davey et al., 1995; Chapter 6 in this study) indicate that the fault kinematics and geometry change offshore. These changes are thought to be associated with a rupture arrest similar to that observed on the Waiohau-Ruahine and Whakatane-Mohaka faults. Therefore, it is assumed that most, or all, of the earthquake ruptures recorded in the trenches at the two studied sites on the Waimana Fault may not have propagated offshore where the fault-dip is shallower and the sense of displacement is normal dip-slip as opposed to mainly strike-slip (see next Chapter 5 for further discussion). The rupture length assigned on the *northern (onshore) section of the Waimana Fault* that includes the two studied sites (Nukuhou North and Te Ahirau) is c. 60 km (W_N = north of Nukuhou North to the intersection between the Waimana - Waiotahi faults) (Fig. 4.33).

In summary the changing fault kinematics in the northern NIFS and the common occurrence of fault intersections provide significant potential for rupture arrest and it seems unlikely that the fault system would rupture in a single event along its entire length. An average magnitude for the northern NIFS of about 7 may represent a reasonable first-order estimate at this time. This estimate is notably different to the M 7.4-7.6 of Stirling et al. (2002), whose data underpin the New Zealand National Seismic Hazard Model. This difference is attributable to earthquake rupture segmentation which reduces the rupture dimensions and results in a decrease of the perceived seismic hazard in the area.

	Fault	Section description	Rupture Length (km)	Single Event Displacement (m)	Moment Magnitude (M_{HK})*	Magnitude (M_{WK})#
Fault sections	Waiohau	WR_N	c. 30	2.5±0.5	7.0	6.6
	Waiohau	WR_G	c. 30	3.4±0.2	7.0	6.7
	Ruahine	WR_S	85 (min)	3.5±1.5	7.4	7.1
	Whakatane	WM_N	c. 50	2.8±0.2	7.2	6.9
	Whakatane-Mohaka	WM_R	70	4.7±0.7	7.4	7.1
Total fault length	Waiohau - Ruahine	$WR_N+WR_G+WR_S$	c. 150	3.5±1.5	7.5	7.4
	Whakatane - Mohaka	$WM_N+WM_R+WM_T+WM_{Ng}$	200	5±1	7.7	7.5

Table 4.6 Magnitude estimates based on Hanks and Kanamori (1979) (M_{HK})* & Wells and Coppersmith (1994) (M_{WK})# regression equations for possible earthquake rupture lengths on the Waiohau-Ruahine, Whakatane-Mohaka and Waimana faults in northern NIFS. Rupture lengths represent a range of potential values and do not include all possible fault segments.

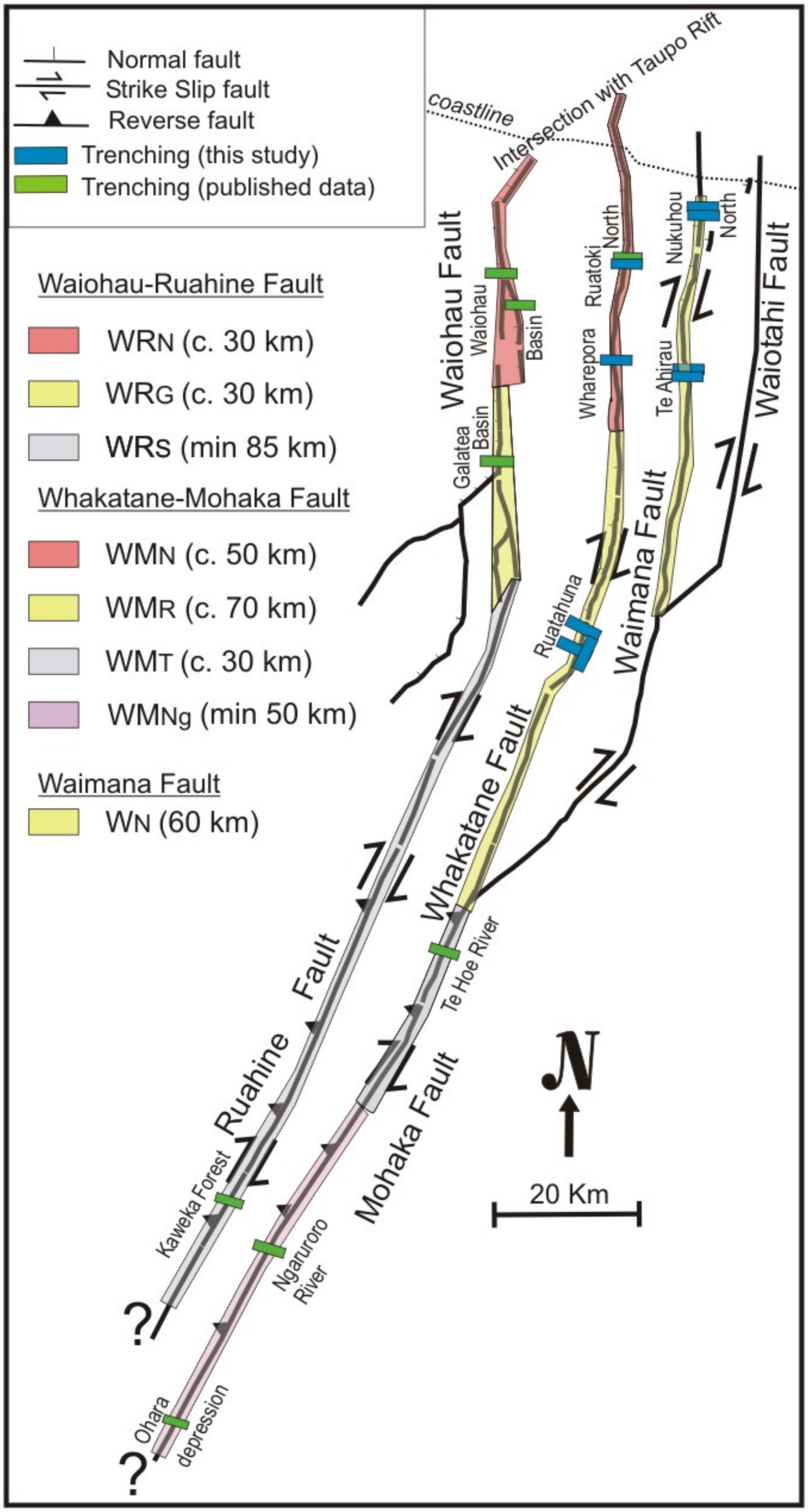

Fig. 4.33 Rupture lengths (km) assigned for the northern NIFS. Note that these rupture lengths represent a range of potential values and do not include all possible fault segments. See text for names of sections (e.g. WM_R= Ruatahuna section of Whakatane-Mohaka Fault).

4.7 Conclusions

Data from 16 trenches on the Waiohau-Ruahine, Whakatane-Mohaka and Waimana faults in the northern NIFS suggest that these faults generated large, surface rupturing, earthquakes during the Holocene. Most large-magnitude earthquakes appear to have ruptured fault lengths of c. 25 to 85 km. Rupture arrest typically occurred within the kinematic transition zone between strike-slip and oblique-normal slip where fault dips decrease by c. 30°. For the inferred rupture lengths average earthquake magnitudes in the northern NIFS were c. 7, while recurrence intervals range from < 2 kyr (Whakatane Fault) to > 7 kyr (Waiohau Fault). These estimates of earthquake magnitudes are lower than the M 7.4-7.6 estimated in the national seismic hazard model for faults in the northern NIFS (Stirling et al., 2002). A decrease in the average magnitudes of surface-rupturing earthquakes in the NIFS may decrease the seismic hazard in the eastern Bay of Plenty.

Acknowledgments: I am grateful to I. Nairn and J. Patterson for their invaluable help in tephra identification and A. Nicol, T. Little, D. Beetham, H. Seebeck, K. Berryman, R. Langridge, P. Villamor, D. Heron, B. Lukovic, P. Tamiana, G. Hughes, S. Toulmin, B. Savage and H. Brown for assisting in trenching and its interpretation. J. Begg is thanked for augering at the Wharepora site, for reviewing this chapter and helpful discussions. Special thanks go to the tangata whenua of Rahiri Marae in Waimana Valley and Noti Teepa for they taught us how poor people can be so "rich".

References

Beanland, S. & Berryman, K.R., 1987. Ruahine Fault reconnaissance. Geological Survey Report, EDS 109.

Beanland, S., 1989b. Detailed mapping in the Matahina Dam region. New Zealand. Geological Survey Client Report, 89/8, 45pp.

Beanland, S., 1995. The North Island Dextral Fault Belt, Hikurangi Subduction margin, New Zealand. PhD Thesis, Victoria University of Wellington, New Zealand.

Beu, A.G., 2004. Marine mollusca of oxygen isotope stages of the last 2 million years in New Zealand. Part 1: Revised generic positions and recognition of warm-water and cool-water migrants. Journal of the Royal Society of New Zealand, 32, 111-265.

Davey, F.J., Henrys, S. and Lodolo, E., 1995. Asymetric rifting in a continental back-arc environment, North Island, New Zealand. Journal of Volcanology and Geothermal Research, 68, 209-238.

Edbrooke, S.W., 1977. The geology of the marine Castlecliffean strata in the Whakatane – Ohope beach area, Eastern Bay of Plenty. M.Sc. Thesis, University of Auckland, New Zealand.

Fleming, C.A., 1955. Castlecliffian fossils from Ohope Beach, Whakatane (N69). New Zealand Journal of Science and Technology Section, B36, 511-522.

Francis, D.A., Beanland, S. and Berryman K.R., 1988. Preliminary work on Ruatahuna outliner and Tuatahuna Fault, Urewera Country, 30 August – 1 September 1988. New Zealand Geological Survey Report, EDS, 88/11.

Geyh, A.A. & Schliecher, H., 1990. Absolute age determination. Springer-Verlag, Berlin.

Hanks T.C. & Kanamori H., 1979. A moment magnitude scale. Journal of Geophysical Research 84, B5, 2348-50.

Hanson, J.A., 1998. The neotectonics of the Wellington and Ruahine faults between the Manawatu gorge and Puketitiri, North Island, New Zealand. PhD Thesis, Massey University, New Zealand.

Hull., A.G., 1983. Trenching of the Mohaka Fault near Hautapu River, Hawkes Bay. New Zealand Geological Survey report, file 831/26.

Jurado-Chichay, Z. & Walker, G.P.L., 2000. Stratigraphy and dispersal of the Mangaone Subgroup pyroclastic deposits, Okataina Volcanic Centre, New Zealand. Journal of Volcanology and Geothermal Research, 104, 319-383.

Kanamori, H., 1977. “Energy-release in great earthquakes”. Transactions of the American Geophysical Union, 58, 438-438.

Kennedy, N., 1994. New Zealand tephro-chronology as a tool in geomorphic history of the c.140 ka Mamaku Ignimbrite Plateau and in relating oxygen isotope stages. Geomorphology, 9, 95-115.

Kennedy, N., 1998. Late Quaternary loess associated with the Mamaku Plateau, North Island, New Zealand. In: Loess: its distribution, geology and soils, Eden D.N & Furkert R.J. (eds), Balkema, Rotterdam, 71-80.

Litchfield, N.J. & Berryman K.R., 2005. Correlation of fluvial terraces within the Hikurangi Margin, New Zealand: implications for climate and baselevel controls. Geomorphology, 68, 291-313.

McCalpin, J.P., 1996. Paleoseismology. International Geophysical Series, 62, 1-588.

McMorran, T. & Berryman, K., 2001. Late Quaternary faulting beneath Matahina Dam. p. 185 -193 in the proceedings of the New Zealand Geotechnical Society Symposium - "Development and Engineering in Hazardous Terrain" Christchurch.

Nairn, I.A. & Beanland, S., 1989. Geological setting of the 1987 Edgecumbe earthquake, New Zealand. New Zealand Journal of Geology and Geophysics, 32, 1-13.

Sieh, K., 1978. Slip on the San Andreas fault associated with the great 1857 earthquakes. Seismological Society of America Bulletin, 67, 1421–1428.

Stirling, M.W., McVerry, G.H. and Berryman, K.R., 2002. A new seismic hazard model for New Zealand. Bulletin of the Seismological Society of America, 92, 1878-1903.

Wallace, R.E., 1970. Earthquake recurrence intervals on the San Andreas fault. Geological Society of America Bulletin, 81, 2875-2890.

Wells, D.L. & Coppersmith, K.J., 1994. New empirical relationships among magnitude, rupture length, rupture width, rupture area and surface displacement. Bulletin of the Seismological Society of America, 8, 974-1002.

Woodward-Clyde, 1998. Matahina Dam strengthening project. Geological completion report to Electricity Corporation of New Zealand.

Zachariasen, J. & Van Dissen, R., 2001. Paleoseismicity of the northern Horohoro Fault, Taupo Volcanic Zone, New Zealand. New Zealand Journal of Geology and Geophysics, 44, 391-401.

CHAPTER FIVE

PALEOEARTHQUAKE SURFACE RUPTURE IN A TRANSITION ZONE FROM STRIKE-SLIP TO OBLIQUE-NORMAL SLIP, NORTH ISLAND FAULT SYSTEM, NEW ZEALAND

Abstract

The North Island Fault System (NIFS) is the longest and highest slip-rate strike-slip fault system within the Hikurangi subduction margin in New Zealand, accommodating up to 10 mm/yr of the margin-parallel plate motion. Displacement of landforms over the last c. 30 kyr indicates a gradual northward change in the slip kinematics of faults in the northern NIFS, from right-lateral strike-slip to oblique-normal slip. This change is expressed by a c. 60° increase in the pitch of the slip vector on these faults in proximity to their northward intersection with the active Taupo Rift. The oblique-normal motion in the northern NIFS reflects an accommodation of NW-SE extension that is distributed outside the main boundary of the Taupo Rift. This chapter explores whether these changes in late Quaternary fault kinematics principally arise due to earthquake rupture segmentation and/or variations in slip vector pitch during individual earthquakes. Fault data from 20 trenches located within the northern NIFS and Taupo Rift are used to chart the spatial and temporal distribution of paleoearthquakes over the last 10-13 kyr. Results show that earthquake rupture segmentation occurs along the strike of the NIFS with, at least 80% of all events during the last 10-13 kyr terminating across the zone of late Quaternary (c. 30 kyr) kinematic transition from strike-slip to oblique-normal slip. The strike of the faults across the kinematic transition is unchanged, and it is suggested that rupture arrest occurs due to a 20-30° shallowing of the fault-dip northward, across this transition zone. Simple kinematic earthquake-slip models indicate that, the pattern of individual earthquake-ruptures most likely to have produced the late Quaternary displacement vectors comprises oblique-slip events, north of the kinematic transition zone, with variable slip-vector pitches during individual earthquakes. Strike-slip earthquakes, which are principally confined to the NIFS south of the transition zone, will also have variable coseismic slip vector orientations when they intermittently rupture through this zone. Changes in coseismic slip vectors during individual earthquakes may arise due to the northward decrease in fault-dip and associated steepening of the principal compressive stress axis (σ_1) which, in turn, is due to fault interactions between the NIFS and the adjacent active Taupo Rift.

5.1 Introduction

Some strike-slip earthquake ruptures are characterized by slip vectors that change their pitch significantly along strike to include oblique motion (e.g. Yoshida et al., 1996; Eberhart-Phillips et al., 2003; Muller & Aydin, 2004). In many cases these changes appear to correlate with corresponding changes in the strike of the fault plane as occurs, for example, across fault bends or step-overs (i.e. Barka & Kandinsky-Cade, 1988; Baljinnyan et al., 1993; Wald & Heaton, 1994; Aydin & Du, 1995; Muller & Aydin, 2004) (Fig. 5.1a), or where large strike-slip faults terminate against reverse or normal faults (Bayasgalan et al., 1999; Hreinsdottir et al., 2003) (Fig. 5.1b). Changes in the slip vector pitch along a fault or fault system may also accompany along strike partitioning of the strike-slip and dip-slip components across a fault system (Begg & Johnston, 2000) (Fig. 5.1c) or up-dip partitioning along a single fault (Ide et al., 1996; Nicol & Van Dissen, 2002). This chapter examines how slip in individual earthquake ruptures may accrue to produce late-Quaternary spatial changes in the pitch of slip vectors, along fault systems that neither change in strike nor partition their co-seismic slip into strike-slip and dip-slip.

Some faults globally change their kinematics along strike yet do not vary in strike significantly (e.g. Beroza, 1991; Johnson & Segall, 2004; Oglesby, 2005). These changes presumably reflect regional variations in the orientations and/or the magnitudes of the principal stress axes. These along strike changes in stress regime either require that: 1) earthquakes rupture through the transition zone and undergo a change in their slip-vector pitch (Figs 5.1d & 5.2a) or, 2) separate earthquakes have different slip vectors either side of the transition zone into which they terminate (Knuepfer, 1989) (Fig. 5.2c). Finally, a combination of the two slip rupture models, with a number (but not all) of earthquakes being arrested within the kinematic transition zone (Fig. 5.2b), might also account for the changing fault kinematics.

Support for the first model (Fig. 5.2a) is provided by the 1989 Loma Prieta and 1999 Chi-chi earthquakes where the rake of coseismic slip changed by up to 70° along sections of the faults with relatively uniform strike (Beroza, 1991; Oglesby & Day, 2001). These two cases, which are associated with extreme changes in slip vector orientations, are thought to have resulted from a combination of geometric (i.e. change in the fault-dip) and static (spatial variations in the pre-earthquake magnitudes and orientations of the principal stress axes) effects (Árnadóttir & Segall, 1994; Guatteri & Cocco, 1996; Oglesby & Day, 2001).

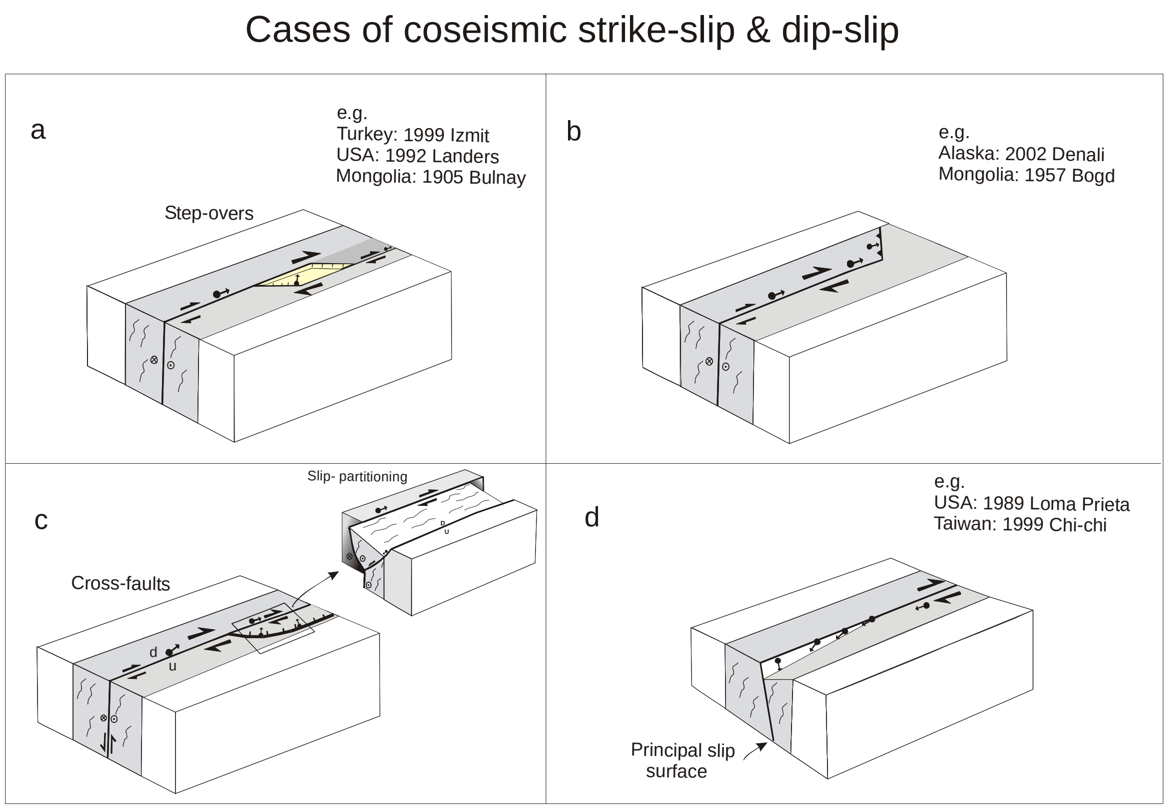

Fig. 5.1 Schematic block diagrams illustrating cases in which strike-slip and dip-slip faulting is produced co-seismically: **a)** where the strike of a strike-slip fault swings and coseismic slip propagates through fault bends and/or step-overs (i.e. 1905 Bulnay; 1992 Landers; 1999 Izmit earthquakes), **b)** where coseismic slip on strike-slip faults terminates at high angle reverse or normal faults (1957 Bogd; 2002 Denali earthquakes), **c)** where slip is partitioned along the strike of the fault into strike-slip and dip-slip components (1855 Wairarapa earthquake, dextral and reverse-slip), and **d)** where the coseismic slip vector pitch changes spatially along strike (1989 Loma Prieta; 1999 Chi-chi earthquakes).

Displacements of ≤ 30 kyr old landforms by the North Island Fault System (NIFS), New Zealand, suggest that the kinematics of the 500 km long strike-slip fault system change from dominantly strike-slip (horizontal to vertical ratio 10:1) to dominantly oblique-normal slip (horizontal to vertical ratio c. 0.8) near its northern termination against the Taupo Rift. Fault strike across this kinematic transition zone remains relatively uniform. The question addressed in this chapter is whether, in the case of the NIFS, changes in fault kinematics along the system arise due to variable slip-vector pitch during individual earthquakes (model 1) or to fault-rupture segmentation (model 2). Fault-trench data from a total of twenty excavations are compiled to characterize the paleoearthquake history, during the last 10-13 kyr, on faults either side of the kinematic transition zone. Estimates of the timing of past earthquakes and of their co-seismic slip vectors provide a means of testing the two concepts. I investigate the way individual earthquakes, with either a uniform or variably oriented coseismic slip vector, aggregate to account for the late Quaternary (c. 30 kyr) finite slip vector orientations in northern NIFS (Figs 5.2 & 5.3).

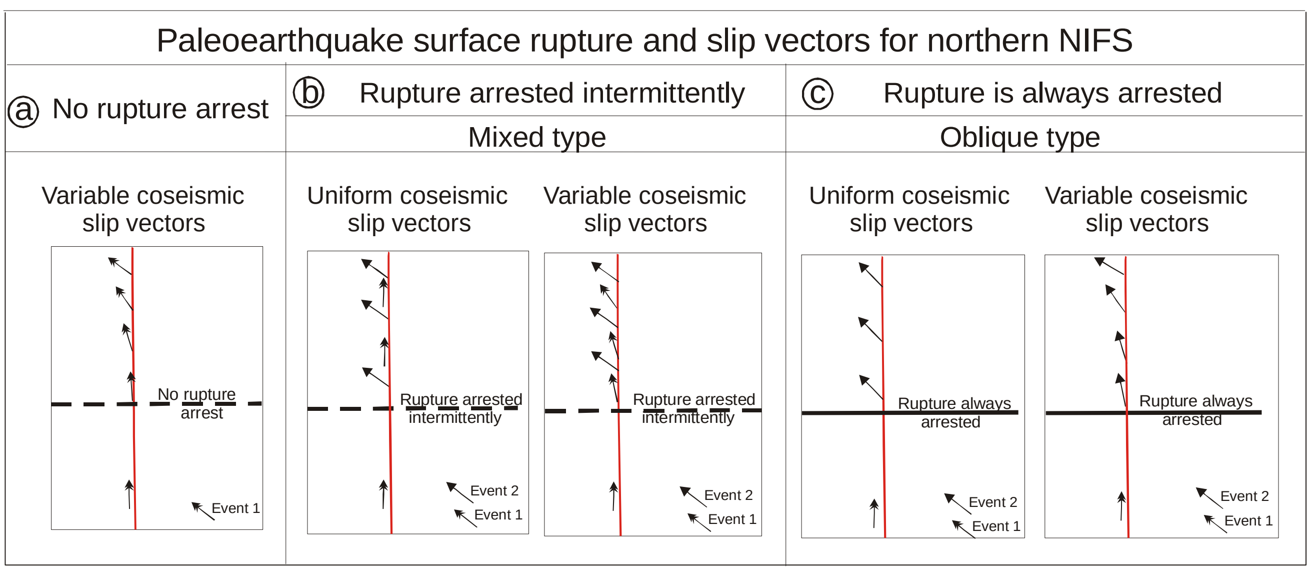

Fig. 5.2 End member models of earthquake surface rupture propagation for the northern NIFS with respect to the kinematic transition from strike-slip to oblique-normal faulting (thick dashed and solid lines): **a)** there is no arrest of surface-rupturing earthquake across the transition zone, **b)** the kinematic transition zone arrests all oblique-slip but not all strike-slip earthquakes, which intermittently rupture through the transition zone, resulting in a mixture of strike-slip and oblique-slip earthquake ruptures north of the transition zone, and **c)** strike-slip and oblique-slip earthquake ruptures are always arrested within the kinematic transition zone. For all scenarios the possibility that earthquakes rupture with either spatially variable or stable slip-vector pitch is considered. To simplify the model, the segment boundary is drawn as a line although it represents a zone.

The NIFS in New Zealand provides an excellent opportunity to conduct this study as the change in the kinematics of these faults is well documented (Beanland, 1995; Wallace et al., 2004; Chapter 2, this study), there are numerous trenches along the fault system and across the kinematic transition zone and also because tephra layers in the trenches provide, together with radiocarbon dating, excellent age control on the timing of past earthquakes (Manning, 1995; Chapter 2, this study). Collectively these data suggest that the late Quaternary change in the kinematics along strike in the NIFS arises due to a combination of earthquake segmentation and variations in the orientation of the coseismic slip vectors. Earthquake segmentation may arise due to a 20-30° shallowing of fault-dips across the kinematic transition zone while spatial variations in the pitch of the earthquake vectors, may reflect a regional northward steepening of the principal stress axis (σ_1) with increasing proximity to the Taupo Rift.

5.2 Definition of kinematic zones in the NIFS

Along the Hikurangi margin in the North Island of New Zealand the Pacific Plate is being subducted beneath the Australian Plate (Ballance, 1975; Walcott, 1978; 1984; Rait et al., 1991; Beaven & Haines, 2001). The relative motion between the two plates is oblique with > 80 % of the margin-normal motion accommodated on the plate interface itself and > 50 % of the margin-parallel motion (i.e. strike-slip and vertical axis fault-block rotations) accommodated in the upper plate (Nicol & Beaven, 2003; Wallace et al., 2004; Nicol & Wallace, in review).

The North Island Fault System is the principal strike-slip fault system in the upper plate of the Hikurangi margin and comprises two main strands, which are typically referred to as the western and the eastern strands (inset in Fig. 5.3). This study focuses on the western strand of this fault system which hereafter is referred to as the NIFS.

The NIFS is c. 500 km long and traverses the entire North Island, from Wellington to Bay of Plenty, with an average strike of NE-SW (i.e. 30°) and mainly dips steeply (i.e. >80°) either to the east or west (Fig. 5.3, inset). The rate of strike-slip in the NIFS increases in a southward direction, from c. 4 to 10 mm/yr, and accommodates up to about 30 % of the margin-parallel relative plate motion near Wellington (Beanland, 1995; Chapter 2, this study; Nicol & Wallace, in review). The NIFS comprises two principal splays, the Wellington-Mohaka and Ruahine faults. The Wellington-Mohaka Fault bifurcates northwards into the Patoka-Rangiora, Whakatane, Waimana, Waiotahi and Waioeka faults, whilst the Ruahine Fault becomes the Waiohau Fault which has several secondary fault splays (e.g. Wheo Fault) (Fig. 5.3). Near the Bay of Plenty coast, where the faults in the NIFS are oblique-normal faults, the NIFS is intersected by the NE-striking active Taupo Rift (Fig. 5.3).

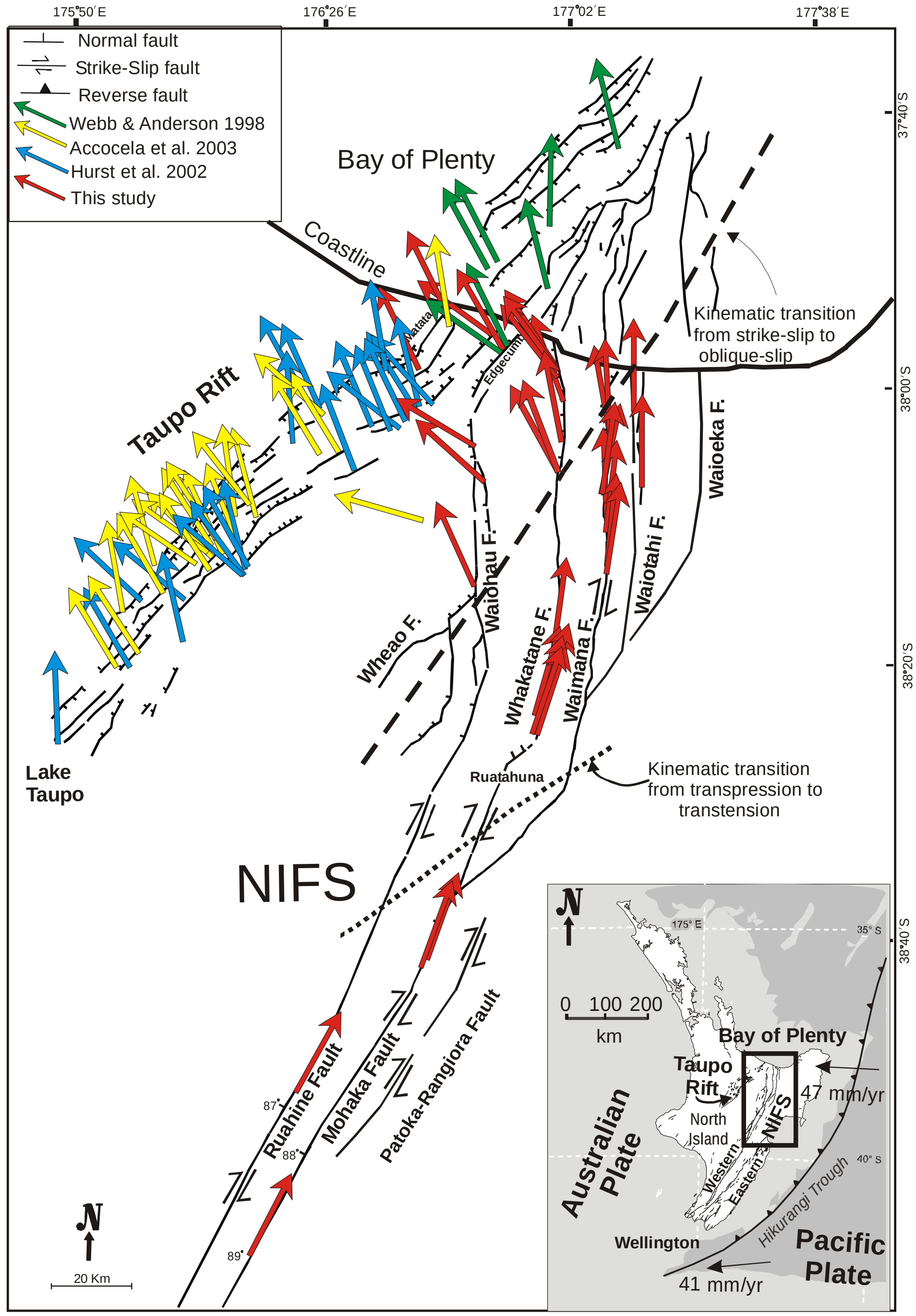

Fig. 5.3 Map of the NIFS – Taupo Rift fault intersection showing the location of the main active faults. The azimuths of the net-slip vectors on the faults, which derive from a combination of outcrop geology and focal mechanism solutions (Webb & Anderson, 1998; Hurst et al., 2002; Acocella et al., 2003; Chapter 2, this study) and the two kinematic transition zones across the northern NIFS (dashed lines) are indicated. These transition zones are drawn as lines although they represent zones (of uncertain width). The overall kinematic pattern mirrors the way displacement vectors on the faults in the NIFS deflect gradually anticlockwise to accommodate some of the NW-SE-oriented extension which is distributed outside the main Taupo Rift. Displacement vectors in the NIFS represent a number of cumulative earthquakes, ranging from 1-17 events, during the last c. 30 kyr. Inset: The NIFS, on the upper plate of the Hikurangi Margin, accommodates the margin parallel component of the westward oblique subduction of the Pacific Plate beneath the Australian Plate. Rates of relative plate motion from De Mets et al. (1994).

The geometry of the faults in the NIFS varies along strike. The NIFS has a constant NE-SW strike along its southern 400 km and swings abruptly 25° anticlockwise to a N-S strike about 100 km south of the Bay of Plenty coast (Fig. 5.3). This northward change in strike is accompanied by splaying of the main strands into numerous secondary faults and by a reduction of fault-dip, from almost vertical to the south to c. 60° W to the north (Chapter 2, this study). Still further north, some 10-15 km south of their intersection with the Taupo Rift, the N-S striking faults of the NIFS swing clockwise their mean strike by 20-25° (Fig. 5.3).

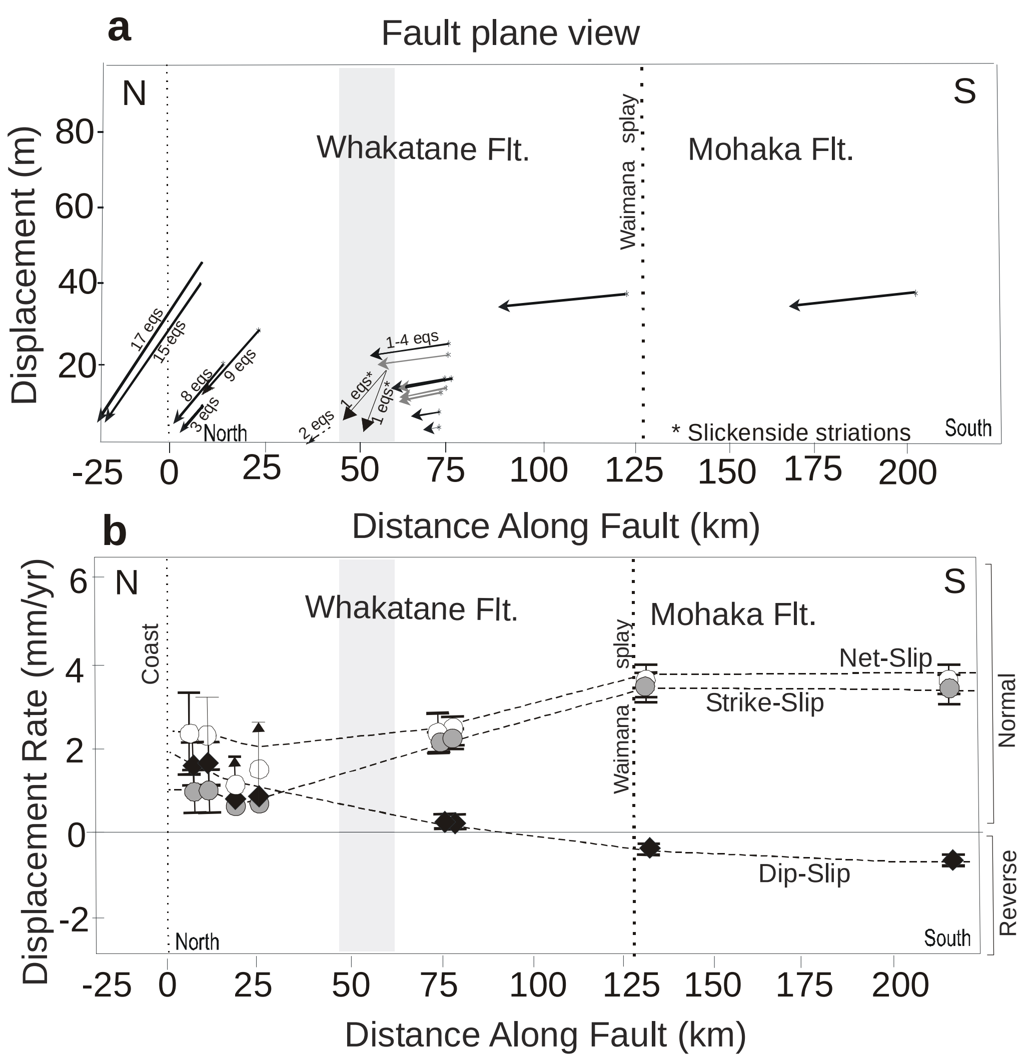

Fig. 5.4 a) Fault plane view illustrating the pitch of the slip vectors along the length of the Whakatane-Mohaka Fault. Length of arrows is proportional to the magnitude and time period over which the slip was measured. Black arrows indicate slip down to the NW while grey arrows indicate slip down to the NE. b) The three components of slip (i.e. dip-slip, strike-slip and net-slip) of the Whakatane-Mohaka Fault are plotted against distance along the strike of the fault. Data are consistent with a kinematic transition from strike-slip to oblique-slip northwards as the Whakatane Fault approaches the Taupo Rift. In both diagrams, the kinematic transition zone is shaded grey.

In conjunction with the observed strike and dip changes, faults in the NIFS experience significant along strike changes in their slip kinematics. In the south, where the faults dip steeply (> 80°), they function chiefly as strike-slip faults with typical slip vector pitch angles of 0-10° (Fig. 5.4a). Along this steeply dipping section of the NIFS, the slip azimuth is approximately constant and parallel to fault strike, although the downthrown side of the faults changes northwards, from east to west, to produce a gradual transition from minor transpression to minor transtension (Figs 5.3 and 5.4b). Approximately 50-60 km south of the Bay of Plenty coast, the late-Quaternary rate of normal-slip in the NIFS begins to increase significantly, while the corresponding rate of strike-slip on the same faults decreases (Fig. 5.4a & b). These changes in the rates of strike- and dip-slip are expressed by a gradual northward steepening (up to 60°) of the slip vector (Fig. 5.4a) and thus, an anticlockwise rotation in the trend of the slip azimuth (Fig. 5.3) (Chapter 2, this study). The ratio of horizontal to vertical slip decreases northwards from c. 10 to < 1. At the northern end of the NIFS, slip vector orientations on faults in the NIFS are comparable to those on faults in the Taupo Rift and sub-parallel to the lines of intersection between the two fault systems (Fig. 5.3) (Chapter 2, this study).

5.3 Temporal and spatial distribution of surface rupturing earthquakes

To test whether the observed changes in late Quaternary fault kinematics could be achieved by fault rupture segmentation and associated surface rupture arrest across, or within, the kinematic transition zone, the timing of paleoearthquakes from 16 trenches excavated across faults in the NIFS is estimated (Fig. 5.5). The trenches are distributed along three of the main strands of the NIFS (Waiohau-Ruahine, Whakatane-Mohaka and Waimana faults) and record large magnitude surface rupturing earthquakes during the past c. 10-13 kyr (Figs 5.5 & 5.6, Table 5.1). To complement these data and to examine the possible interrelationship between paleoearthquakes in the northern NIFS and the Taupo Rift I draw on published paleoearthquake information from trenching on the four principal faults of the northern Taupo Rift (Edgecumbe, Rotoitipakau, Braemar and Matata faults) (Fig. 5.5, Table 5.1). This section, examines the spatial relationships

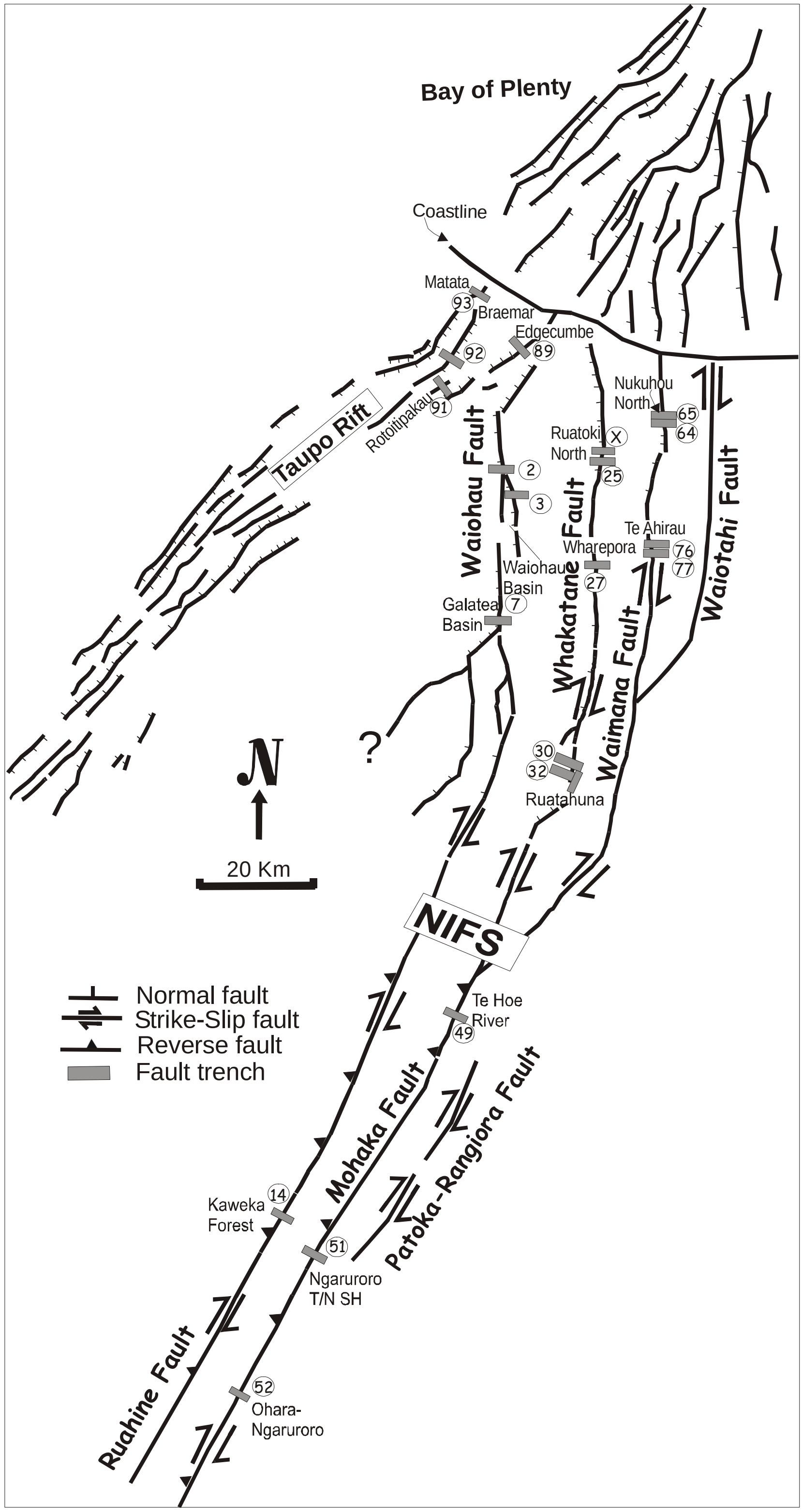

Fig. 5.5 Fault map showing the location of the 20 fault trenches across the northern NIFS (n=16) and Taupo Rift (n=4). The details of each trench are summarized in Table 5.1.

Trenches in the northern NIFS and Taupo Rift								
Site_No	**Trench name**	**Grid reference**	**Which fault**	**Site location**	**Last ethq recorded (kyr BP)***	**Oldest ethq recorded (kyr BP)***	**Net SR (mm/yr)#**	**References**
2	Tasman	V16/453298	Waiohau	Waiohau Basin	1.8<ethq<5.6	<17.6	0.7±0.2	Woodward-Clyde, 1998†
3	Cornes	V16/472252	Waiohau	Waiohau Basin	>8.050	9.5<ethq< 13.8	0.7±0.2	Woodward-Clyde, 1998
7	Troutebeck	V17/446057	Waiohau	Galatea Basin	1.8<ethq<9.5	13.8<ethq<17.6	0.7±0.2	Beanland, 1989b
14	Davis	V20/092077	Ruahine	Kaweka Forest	<1.8	>13.8	-	Hanson, 1998†
x	Ruatoki/Sarah	W16/620330	Whakatane	Ruatoki North	0.62±0.12<ethq<0.627±0.94	-	-	Beanland, 1989b
25	Te Whetu	W16/619327	Whakatane	Ruatoki North	0.52±0.2<ethq<4.7±0.13	< 50	1.5 (min)	Chapter 4, This study
27	Te Marama	W16/603193	Whakatane	Wharepora	< 0.794±126	-	-	Chapter 4, This study
30	Armyra	W17/556802	Whakatane	Ruatahuna	<1.8	<3.5	3±1.1	Chapter 4, This study
32	Thalassa/Helios	W17/555802	Whakatane	Ruatahuna	0.93<ethq<1.8	8.050<ethq<9.550	3±1	Chapter 4, This study
49	Te Hoe	V19/379395	Mohaka	Te Hoe River	< 0.8	< 9.550	3.5±0.8	Hull, 1983
51	Syme	V20/137986	Mohaka	Ngaruroro-T/N SH	<1.8	23±0.16<ethq<3.36±0.38	c. 6.5	Hanson, 1998
52	McCool	U21/010746	Mohaka	Ohara-Ngaruroro	< 1.8 or 0.6	>14	c. 4-5	Hanson, 1998†
65	Moana	W16/725379	Waimana	Nukuhou North	1.8<ethq<5.6	c.13.8	1.2±0.5 (max)	Chapter 4, This study
64	Moana-Iti	W16/725379	Waimana	Nukuhou North	1.8<ethq<3.36±0.38	>10,1	1.2±0.5 (max)	Chapter 4, This study
76	Ahirau1	W16/705161	Waimana	Te Ahirau	1.8<ethq<2.88±0.94	9.5<ethq< 13.8	1.1±0.6	Chapter 4, This study
77	Ahirau2	W16/705161	Waimana	Te Ahirau	1.8<	< 13.8	1.1±0.6	Chapter 4, This study
89	Edgecumbe	V15/477502	Edgecumbe	Edgecumbe	1987 AD	-	2.6±1.4	Beanland et al., 1989
91	Rotoitipakau	V15/345436	Rotoitipakau	Rotoitipakau	1987 AD	<9.5	2.2±0.25	Berryman et al., 1998
92	Braemar	V15/358480	Braemar	Braemar	<5.6	<9.5	0.7±0.3	Beanland, 1989b
93	Matata	V15/414602	Matata	Matata	200 yr BP	<5.6	1.8±0.2	Ota et al.,1988

Table 5.1 Summary of paleoearthquake data from 20 trenches across the northern NIFS and Taupo Rift. *Calibrated age, #Average slip-rate of the segment trenched, †Re-interpreted data.

between paleoearthquakes in the NIFS and the locations of kinematic transition zones on the faults (see previous section).

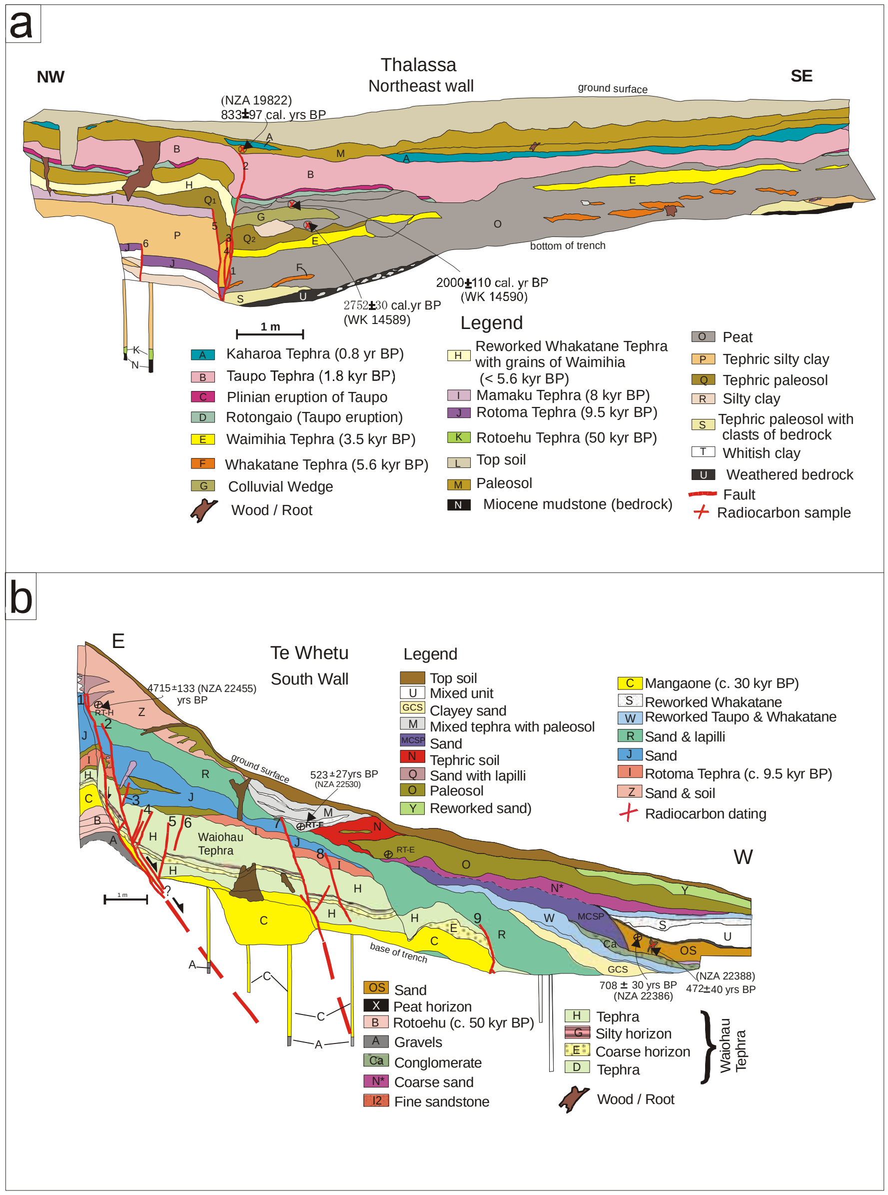

Fig. 5.6 Two trench-logs that derive from sections of the Whakatane Fault that most often ruptured during different earthquakes. The northeast wall of Thalassa, at Ruatahuna, is characterized by confined faulting on a vertically dipping fault plane that juxtaposes dissimilar stratigraphic units **(a)**. In contrast, displaced horizons can be correlated across the main, low angle (68°), distributed slip surfaces on the south wall of Te Whetu (c. 50 km north of Ruatahuna) **(b)**.

Individual strike-slip earthquakes are identified in trenches where stratigraphic horizons are truncated or deformed against the fault, where colluvial scarp-derived wedges abut the fault, or where specific ruptures terminated upwards against younger less deformed units (Fig. 5.6a). In the case of oblique-slip paleoearthquakes, offset stratigraphic units may be correlated across the fault and, in such cases, the timing of successive earthquakes can be constrained by downward increases in dip-separation (Fig. 5.6b). In most trenches, surface rupture earthquakes with displacements < 0.1 m cannot be reliably resolved. The timing of the earthquakes was determined by a combination of tephrochronology (analysis of glass chemistry) and radiocarbon dating of selected organic-rich layers.

The temporal resolution provided by the available dating techniques does not allow discrimination of earthquakes that occurred closely in time (e.g. < 500-1500 years). Thus, when the timing of fault rupture in two neighbouring trenches is approximately the same (e.g. 8-9 kyr BP), we cannot differentiate whether the fault ruptured in each trench during one event, or in two events very closely spaced in time (e.g. <10 years) or in two events separated by 500-1000 years. Based on trench data, therefore, the occurrence of mechanical segment boundaries cannot be excluded even where surface rupturing events appear to occur at about the same time in both sides of that putative boundary. By contrast, when events of the same age are not observed in contiguous trenches, it can be inferred that a rupture was arrested between those two sites.

The details of each trench, including source of data, grid reference, timing of the most recent event, etc, are summarized in Table 5.1. The timing of the paleoearthquakes revealed by the trenches of Table 5.1 are plotted in Figure 5.7, which summarizes the temporal and spatial distribution of surface rupturing paleoearthquakes for the northern c. 200 km of the NIFS over the last 10-13 kyr. The black circles, located between trench sites, indicate the inferred locations of surface rupture terminations or indicate mismatches in the number of paleoearthquakes recorded in neighbouring trenches for the same time span. The solid black line attached to each black circle shows the part of the fault that is inferred to have ruptured during each event, and points away from the location of inferred arrest (Fig. 5.7). To avoid biasing in favour of the notion of earthquake surface rupture segmentation at specific localities, it is always assumed that a nearby rupture propagated through trench sites for which there is no available temporal paleoearthquake information of the same age (indicated by white boxes). Moreover, where the number of earthquake ruptures in a single site in uncertain (i.e. one or possibly

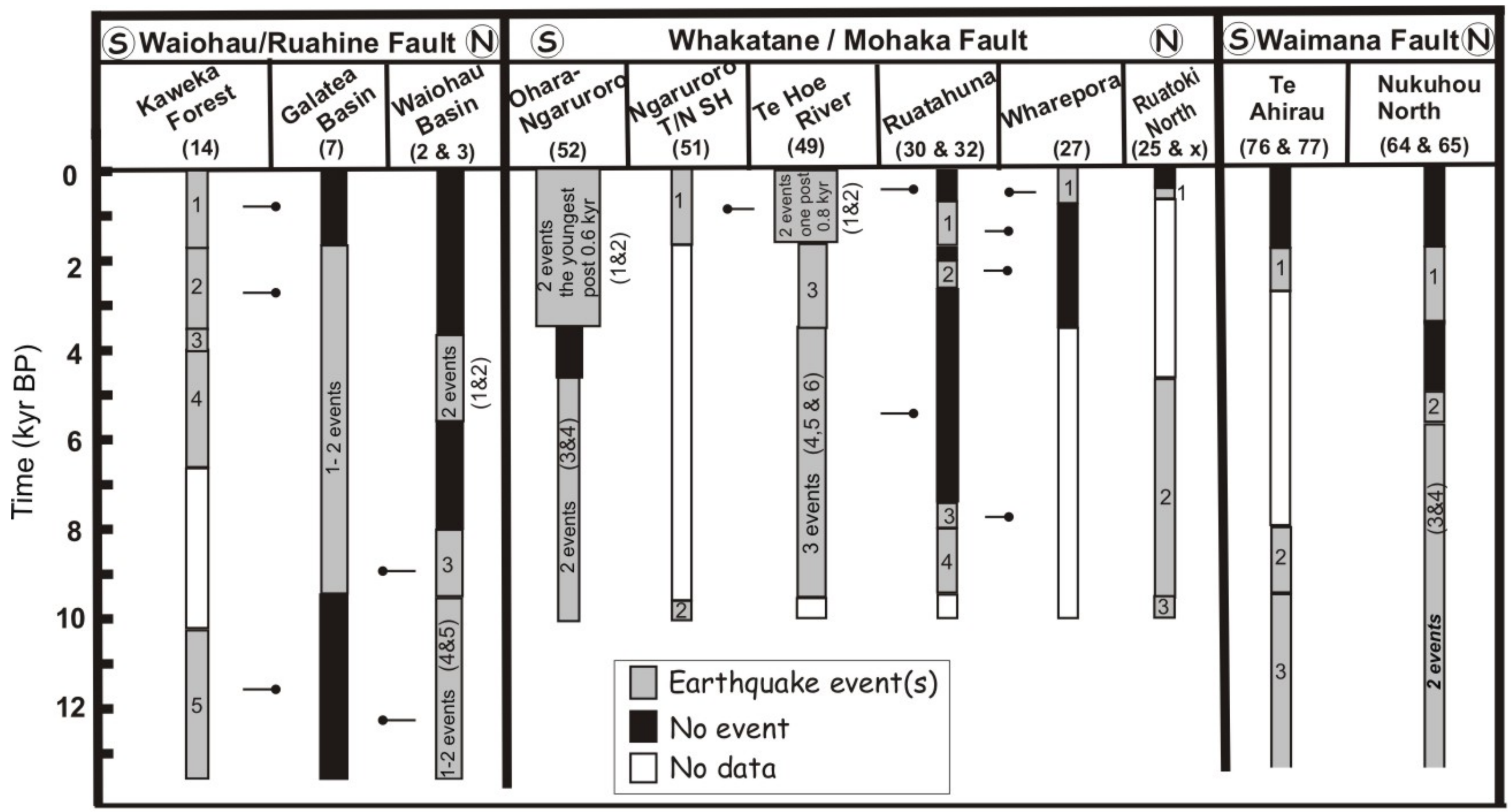

Fig. 5.7 Time distance plot summarizing the timing of the paleoearthquakes revealed by trenches along the northernmost 200 km of the NIFS during the last c. 10-13 kyr. Faults are presented from west to east, and localities on each fault from south to north. The numbers in parentheses below each site correspond to trenches listed in Table 5.1 and Figure 5.5. Numbers within (or adjacent) each grey box represent consecutive earthquakes. Lower and upper boundaries on each grey box represent maximum and minimum age for the earthquake, respectively. The timing of most earthquakes is constrained by tephrachronology. Black circles located between trench sites indicate the inferred locations of surface rupture terminations or indicate mismatches in the number of paleoearthquakes recorded in neighbouring trenches for the same time span. Locations of repeated earthquake arrest are inferred on the Waiohau and Whakatane faults where neighbouring trenches appear to record different earthquake histories. Note that although the position of the rupture tips (black solid lines) in some cases is non-unique, the number of rupture tips between sites at given time intervals is unique.

two events), the maximum number of events is adopted, again to avoid biasing the data towards rupture segmentation. The number of rupture tips indicated on Figure 5.7 is therefore the minimum required to account for the available data. For the data underpinning the timing of each earthquake event presented in Figure 5.7 refer to Chapter 4 of this study.

5.3.1 Waiohau-Ruahine Fault

Figure 5.7 (left-hand panel) summarizes the temporal and spatial distribution of paleoearthquakes recorded along the northernmost 150 km of the Waiohau-Ruahine Fault during the past c. 13 kyr. These paleoearthquakes were revealed by trenches at three locations along the Waiohau-Ruahine Fault (Fig. 5.5). During the last 13 kyr the fault appears to have ruptured most recently and more frequently at the Kaweka Forest and Waiohau Basin sites than the Galatea Basin site (Fig. 5.7). The section of the fault at Kaweka Forest appears to have ruptured at least once within the last 1.8 kyr whilst the section immediately to the north in the Galatea Basin did not accommodate any surface rupturing earthquake during this period. The southern Kaweka Forest section has ruptured at least five times during the last c. 13 kyr while the Galatea Basin section appears to have ruptured one or possibly two times during the same time interval (Fig. 5.7). A maximum of two events could have ruptured the entire fault between the Kaweka Forest and Waiohau Basin, while a minimum of three paleoearthquakes ruptured the Kaweka Forest section of the fault but terminated before reaching the Galatea Basin site (trenches 7 & 14 in Figs 5.5 & 5.7 and Table 5.1).

The timing of paleoearthquakes is also different on the two sections of the Ruahine-Waiohau Fault at Galatea Basin and Waiohau Basin further to the north of Kaweka Forest (sites 2, 3 & 7 in Figs 5.5 & 5.7 and Table 5.1). During the last 13 kyr, at least two earthquakes that ruptured the Waiohau Basin section of the fault did not extend as far south as the Galatea Basin (Fig. 5.7). The section of the fault in the Waiohau Basin appears to be overall more active, with a minimum of four paleoearthquakes during the last c. 13 kyr, than the Galatea Basin section, which has accommodated a maximum of two paleoearthquakes during the same time interval.

The non-uniform spatial and temporal distribution of paleoearthquakes along the Waiohau-Ruahine Fault is consistent with the presence of two localities where paleoearthquakes were repeatedly arrested. The southern arrest site occurs along the c. 100 km of the fault between the Kaweka Forest and Galatea Basin trench sites (Fig. 5.5 and Table 5.1) and is associated with a c. 20° change in the dip of the fault, a 25° change in the fault strike immediately south of the Galatea Basin and a northward anticlockwise rotation of the fault-slip azimuth on the faults (Figs 5.3 & 5.4). The northern arrest site occurs along the 25 km between the Galatea and Waiohau basins (Fig. 5.5, Table 5.1) where the fault trace is almost linear but the dip of the fault decreases northwards from 70° to 60°. The decrease in fault dip is accompanied by an increase in the dip-slip component on the fault (Chapter 2, this study).

Additional support for earthquake rupture segmentation along the Waiohau-Ruahine Fault is provided by the recurrence intervals as estimated (independently of paleoearthquake timing from the trenches) by the single event displacement and the slip rate at given points along the strike of the fault (Chapter 2, this study). The recurrence intervals that typify the Kaweka Forest, Galatea Basin and Waiohau Basin sections of the fault are 2.3±1.3 kyr BP, 5±1.3 kyr BP and 3.6±1.2 kyr BP, respectively, and suggest different return periods for each section of the fault (Chapter 4, this study).

5.3.2 Whakatane-Mohaka Fault

Figure 5.7 (middle panel) summarizes the earthquake events recorded by trenches at six localities along the northernmost 200 km of the Whakatane-Mohaka Fault. Similar to the Waiohau-Ruahine Fault, the timing of paleoearthquakes was not uniform along the Whakatane-Mohaka Fault (Fig. 5.7). In the southern (sites 49, 51 & 52, Fig. 5.5) and northern (sites 25, 27 & x, Fig. 5.5) sections of the fault, for example, the most recent earthquake appears to have occurred within the last 800 years whereas at Ruatahuna (sites 30 & 32, Fig. 5.5), in between the southern and northern sections, the last earthquake is bracketed between c. 1.8 – 0.83 kyr BP with no rupture during the last c. 770 years (Fig. 5.7).

In the southern section of the fault, between Ohara and Te Hoe River, the timing of paleoearthquakes was comparable between sites (Fig. 5.7). Only one of the six Holocene paleoearthquakes identified at Te Hoe River could not be correlated (within the temporal resolution of the data) with events at the Ohara-Ngaruroro and Ngaruroro-T/N SH sites further south (sites 51 & 52 in Fig. 5.5, Fig. 5.7). In addition, along the section of the fault between Te Hoe River and Ruatahuna (Fig. 5.5), where the fault kinematics change from minor transpression to minor transtension, four of the six paleoearthquakes recorded in the Te Hoe Trench can be correlated with paleoearthquakes identified in the trenches at Ruatahuna (Fig. 5.7). The termination of some Holocene paleoearthquakes between Te Hoe River and Ruatahuna may have been related to the eastward bifurcation of the Whakatane-Mohaka Fault into the Waimana Fault, to the presence of a c. 1.5 km wide releasing bend at Ruatahuna and/or to the change from slight tranpression to slight transtension (Figs 5.3, 5.4b & 5.5).

Within the northern section of the fault, between Ruatahuna and Ruatoki North, the timing of paleoearthquakes is often different. The northern end of the fault, at Ruatoki North and at Wharepora sites, (site 25 & 27 in Fig. 5.5 and Table 5.1) appears to have ruptured at least once within the last 800 years in contrast to the southern end of this section, at Ruatahuna, which has not accommodated a surface rupturing earthquake during that period (sites 30 & 32, Figs 5.5 & 5.7). Furthermore, the ultimate (1.8 – 0.83 kyr BP) and penultimate (2.7-2 kyr BP) earthquakes recorded at Ruatahuna, do not appear to have ruptured the section of the fault immediately to the north, at Wharepora (site 27 in Figs 5.5 & 5.7). At least 80 %, and possibly all, of the Holocene earthquakes recorded along the northernmost 70 km of the Whakatane Fault ruptured the Ruatoki North-Wharepora and Ruatahuna sections at different times. It is inferred, therefore, that most (if not all) fault rupture events terminated between the Wharepora and Ruatahuna sites (sites 27, 30 & 32 in Fig. 5.5 and Table 5.1).

In summary, none of the paleoearthquakes inferred from the trenches can be shown to have ruptured the entire 200 km sample length of the Mohaka-Whakatane Fault. Within the temporal resolution of the data, two paleoearthquakes terminated somewhere within the kinematic transition zone from transtension (to the north) to transpression (to the south). By contrast, at least four (and perhaps all) paleoearthquakes were arrested within the northern kinematic transition zone from strike-slip faulting to oblique-normal faulting. The presence of the latter transition zone is also indicated by the different fault geometries revealed in trenches located across the kinematic transition (Chapter 4, this study). The near-vertical strike-slip fault at Ruatahuna (Fig. 5.6a), for example, becomes a zone of distributed, predominantly normal faulting on a shallow (60-70°) dipping plane in Ruatoki North (Fig. 5.6b).

5.3.3 Waimana Fault

The Waimana Fault does not show significant variability in the timing of its Holocene paleoearthquakes at two localities along its northernmost 35 km (sites 64&65 and 76&77 in Fig. 5.5 & Fig. 5.7). The most recent earthquake, for example, is constrained at both localities to have ruptured between c. 1.8 kyr and 3.3 kyr BP. The penultimate earthquake event ruptured through the northern locality, at Nukuhou North, at c. 5.6 kyr BP and no data can exclude its coeval rupturing through the southern locality, at Te Ahirau (Fig. 5.7, sites 64&65 and 76&77 in Fig. 5.5 and Table 5.1). A third event appears to have ruptured both trench locations at approximately c. 7.5 kyr BP (Fig. 5.7). The poorly dated oldest event at the northern locality (site 65 in Fig. 5.5 and Table 5.1) predated 7.5 kyr BP, while a similarly poorly constrained event at the southern sites occurred prior to 9.5 kyr BP.

Most (or all) of the paleoearthquakes recorded at Nukuhou North therefore, appear to have ruptured through the trenches located some 20 km to the south, at Te Ahirau (Figs 5.5 & 5.7, Table 5.1). The lack of evidence for rupture termination along the Waimana Fault is significant because neither the kinematics nor the geometries change considerably from Nukuhou North to Te Ahirau (Fig. 5.3) (Chapter 2, this study). It is anticipated, however, that the abrupt change in the fault's kinematics that occurs close to the coastline, some 10 km north of the Nukuhou North locality (Chapter 2, this study), may be accompanied by rupture arrest, similar to that inferred for the Whakatane and Waiohau faults.

5.4 Earthquake Rupture Models

Rupture segmentation at the surface during the last 10-13 kyr has been inferred for the Waiohau-Ruahine and Whakatane-Mohaka faults using fault trench data. Collectively, trench data suggest that large magnitude earthquakes of these two faults have often terminated within the kinematic transition zone between strike-slip faulting and oblique-normal faulting. The fault-rupture model in which all paleoearthquakes typically propagate through the kinematic transition zone (Fig. 5.2a) is therefore inconsistent with the data for the northern NIFS.

To explore how the cumulative late Quaternary displacements might accrue in the northern NIFS during individual earthquakes (or earthquake cycles), each of the two remaining possible scenarios of paleoearthquake surface rupture is tested: i) mixed strike-slip and oblique-slip events with the former intermittently rupturing, northwards, through the kinematic transition either with uniform (section 5.4.1) or variable slip vector pitch along strike (section 5.4.2) (Fig. 5.2b) and, ii) oblique-slip events confined to fault segments north of the kinematic transition and strike-slip events confined to segments south of the zone (section 5.4.2) (Fig. 5.2c). Given that faults north of the transition zone are associated with a gradual (10°/15 km) northward steepening in the pitch of the late Quaternary slip vectors, oblique-slip vectors in scenario depicted in Fig. 5.2c must also involve a steepening in the pitch of the coseismic slip vectors in a northward direction along strike.

Slickenside striations are likely to indicate single event slip vectors north of the kinematic transition zone and help to differentiate between these two possible rupture scenarios (i & ii). Two sets of slickenside striations were observed at a single site on the Whakatane Fault north of the transition zone (site 29 in Table 2.1 of Chapter 2, this study), indicating oblique-slip motion (50° & 70°). Although these striations confirm that the faults north of the kinematic transition are oblique-normal slip, they do not exclude the possibility that large strike-slip events have also ruptured through the kinematic transition zone.

As we could not differentiate by first order observations the manner in which the northern NIFS ruptures to produce its distinctive late Quaternary kinematic pattern which varies along strike (Figs 5.3 & 5.4a), available earthquake data were utilized to model earthquake cycles in order to explore which earthquake rupture model may account for this kinematic transition. The following two sections, 5.4.1 and 5.4.2, discuss earthquake rupture models that involve uniform or variable coseismic slip vector pitches, respectively. Intra-seismic variations in the pitch of the coseismic slip at given points on the faults (e.g. curved slickensides formed during single earthquakes), as introduced by Spudich et al. (1998) and Guaterri & Spudich (1998) are not considered in this chapter.

5.4.1 Mixed strike-slip and oblique-slip ruptures with uniform slip vector pitches

In the absence of data on the distribution of slip-vector orientations for individual earthquakes in the NIFS I use available data on the incremental slip on earthquake ruptures, horizontal to vertical slip ratios and number of earthquakes during the last 10-13 kyr to model slip accumulation on the Waiohau and Whakatane faults. As faults south of the transition zone are predominantly strike-slip (Chapter 2, this study), it is inferred that no oblique-slip events rupture this part of the fault. Earthquakes that nucleate in the south, where the length of inferred fault ruptures are generally larger (i.e. > 50 km) than those in the north (i.e. ≤ 50 km), are likely to have larger earthquake magnitudes and therefore may have greater potential to propagate through any mechanical barrier in its path (Aki, 1979). Therefore, it is argued that paleoearthquakes which may occasionally rupture the transition zone (Fig. 5.7) are more likely to originate in the south, where the fault is predominantly strike-slip, and to propagate northwards.

Moreover, it is assumed that each event typically ruptures the entire fault north of the transition zone to be arrested at the fault's intersection with the Taupo Rift. The latter assumption is supported by Figures 5.7 & 5.8 which show the temporal relationships between the timing of the earthquakes in Taupo Rift and in the northern NIFS. Holocene paleoearthquakes in the northern onshore Taupo Rift revealed by trenches across four faults (Edgecumbe, Rotoitipakau, Braemar and Matata faults; for references see Table 5.1) show that most of these faults have ruptured three or more times during the last 1.8 kyr (Fig. 5.8, Table 5.1), while the faults in the northern section of the NIFS have ruptured only once (Whakatane Fault) or not at all (Waiohau and Waimana faults) during the same period (Fig. 5.7). Thus, the NIFS – Taupo Rift fault junction appears to act as a barrier to rupture propagation during surface rupturing earthquakes.

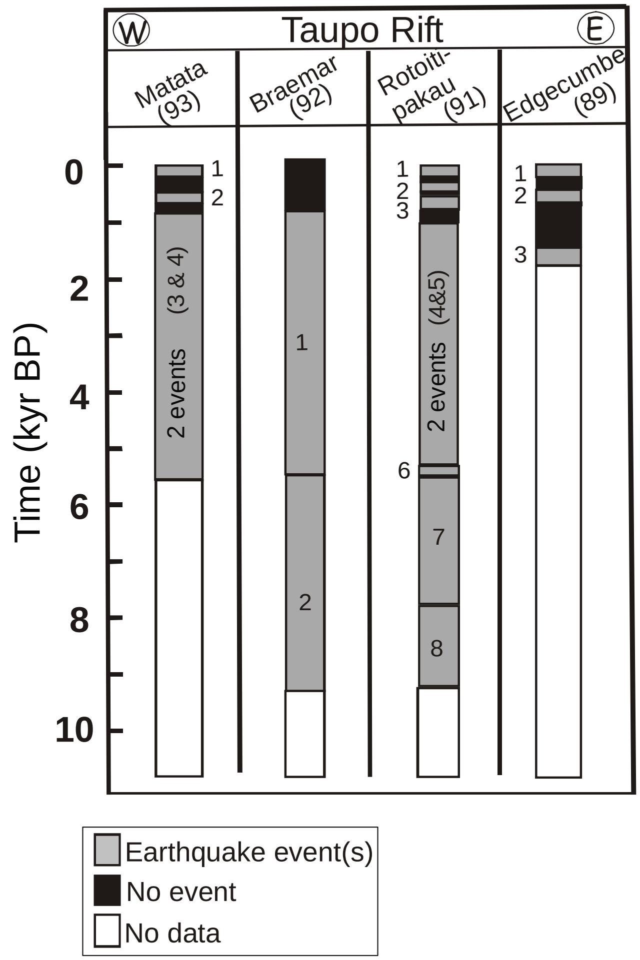

Fig. 5.8 Time - distance plot summarising the spatial and temporal distribution of paleoearthquakes in the northern Taupo Rift. Note that most of the faults have ruptured several times within the last 2 kyr. The numbers in parentheses below each site correspond to trenches listed in Table 5.1 and Figure 5.5. Numbers within (or adjacent) each grey box represent consecutive earthquakes during given time period. Lower and upper boundaries on each grey box represent maximum and minimum age for the earthquake, respectively. The timing of most earthquakes is constrained by tephrochronology.

The analysis in this model is therefore focused on the NIFS north of the kinematic transition zone and south of the NIFS – Taupo Rift intersection. Furthermore, it is assumed that strike-slip paleoearthquakes with uniformly pitching coseismic slip-vector orientations may sporadically rupture northwards, through the kinematic transition zone. These strike-slip events are aggregated with oblique-slip events and the resulting model-derived cumulative net-slip pitch directly compared to (cumulative) net-slip pitch measured from displaced late Quaternary landforms along the faults in the NIFS (Chapter 2, this study).

Fault-trench data show that the Waiohau and Whakatane faults have ruptured five times during the last 13-10 kyr with up to two of these paleoearthquakes (20-40 % of the total earthquakes) also having possibly propagated through the kinematic transition zone (Fig. 5.7). Accordingly in these models, paleoearthquakes that ruptured through the kinematic transition zone are inferred to be large strike-slip events (pitch ≈ 0) nucleating south of the transition, with coseismic slip decreasing northwards, at an average rate of decrease of c. 1 m/20 km, i.e. from c. 5.5 to 3 m and 3.5 to 1.5 m between the transition zone (> 60 km south of the coast) and the northern tips of the Whakatane and Waiohau faults, respectively (single event displacements from Chapter 4, this study) (Table 5.2, Fig. 5.9). Paleoearthquakes restricted to the northern c. 50 km long sections of the faults, north of the kinematic transition zone, carry oblique-slip in the models with no change in slip magnitude during individual events (Fig. 5.9, Table 5.2). This is supported by the single event displacement (throw) recorded at two sites along the Whakatane Fault (Ruatoki North and Wharepora) which are located c. 20 km apart from one another, and which show a similar value of coseismic slip (1.7-1.9 m) (Chapter 4, this study). The coseismic slip-vector orientations, however, may range in pitch orientations between 40° and 90° during successive events (but not during single events). All the input data used to model the earthquake cycles are summarised in Table 5.2.

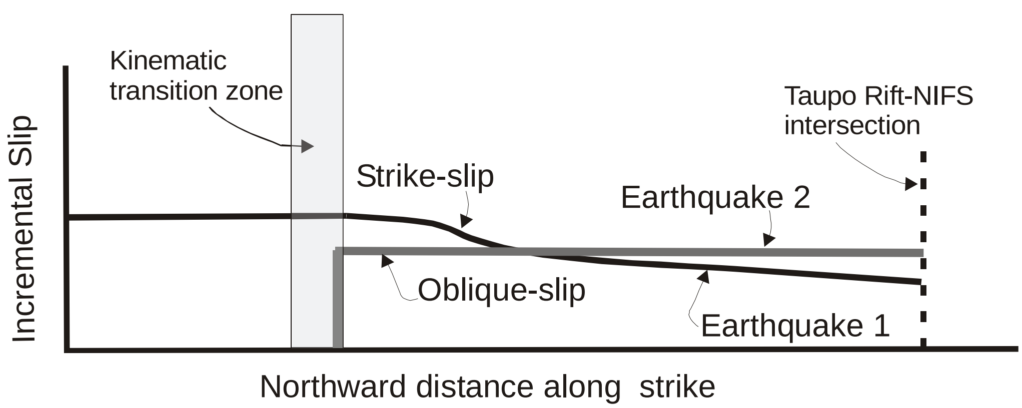

Fig. 5.9 Schematic diagram showing the distribution of the incremental co-seismic slip along the northern NIFS with respect to the inferred zone of earthquake rupture arrest for distinct oblique-normal slip and strike-slip events. The oblique-slip events that rupture only the northern section of the fault (north of the kinematic transition zone) are assumed to have uniform slip as opposed to the strike-slip events that originate in the south and which reduce their coseismic-slip magnitude northwards from the transition zone.

Figure 5.10 shows the simulation of the cumulative net-slip vector pitch on the Waiohau and Whakatane faults for two hypothetical earthquake cycles each of which comprises one (minimum) or two (maximum) strike-slip events aggregated with four and three oblique-slip earthquakes, respectively (see Table 5.2). In cases where the cumulative strike-slip is a maximum (i.e. two strike-slip events have ruptured through the kinematic transition zone during the last 10-13 kyr), the pitch of each of the oblique-slip events must range between c. 80-90° (Whakatane Fault) (Fig. 5.10a) or ≥ 90° (Waiohau Fault) (Fig. 5.10b) in order to match the pattern of cumulative net slip-vector pitch along strike (Fig. 5.3). I believe that pure dip-slip events (i.e. ≥ 80°) are unlikely given the obliquity of the observed (albeit sparse) slickensides (Chapter 2, this study) and the oblique-slip (pitches of 34-45°) measured from offset landforms (sites 19 & 28, Table 2.1 in Chapter 2, this study) which may have accrued in 2 or 3 events. Therefore, at present there is no evidence in support of pure dip-slip rupturing. For cases in which the cumulative strike-slip is a minimum (i.e. one strike-slip event has ruptured through the kinematic transition zone during the last 10-13 kyr), the cumulative net slip-vector pitches from displaced landforms can be reproduced when the modelled oblique-slip pitch, during successive repeated earthquakes, ranges between c. 75-80° and 55-70° for the Waiohau and Whakatane faults, respectively (Fig. 5.10c & d). On the Whakatane Fault, an oblique-slip pitch of 55-70° during successive earthquakes requires either a non-uniform oblique-slip magnitude (which is not supported by the measured data) or a non-uniform slip vector patterns during each event (coseismic rotation of the slip-vector pitch) to reproduce the late Quaternary northward gradient in net slip-vector pitch of 10°/15 km (Fig. 5.10c). The potential for rotation of slip vectors during single earthquakes is discussed in the following section.

Waiohau Fault (Earthquake cycle: 2 strike-slip and 3 oblique-slip events)					
Input				output	Real data
Distance (km)	Strike-slip earthquake (m)	Oblique-slip earthquake (m)	Pitch (°)	Cum. net-slip pitch (°)	Long-term net-slip pitch (°)
50	7	10	90	55	63
30	5	10	90	63	69
10	3	10	90	73	71
50	7	10	80	48	63
30	5	10	80	56	69
10	3	10	80	64	71
50	7	10	70	42	63
30	5	10	70	48	69
10	3	10	70	56	71
50	7	10	60	36	63
30	5	10	60	41	69
10	3	10	60	47	71
50	7	10	50	30	63
30	5	10	50	34	69
10	3	10	50	39	71
50	7	10	40	24	63
30	5	10	40	27	69
10	3	10	40	31	71

Waiohau Fault (Earthquake cycle: 1 strike-slip and 4 oblique-slip events)					
Input				output	Real data
Distance (km)	Strike-slip earthquake (m)	Oblique-slip earthquake (m)	Pitch (°)	Cum. net-slip pitch (°)	Long-term net-slip pitch (°)
50	3.5	12.5	90	74	63
30	2.5	12.5	90	79	69
10	2	12.5	90	81	71
50	3.5	12.5	80	65	63
30	2.5	12.5	80	69	69
10	2	12.5	80	71	71
50	3.5	12.5	70	56	63
30	2.5	12.5	70	60	69
10	2	12.5	70	62	71
50	3.5	12.5	60	48	63
30	2.5	12.5	60	51	69
10	2	12.5	60	53	71
50	3.5	12.5	50	40	63
30	2.5	12.5	50	42	69
10	2	12.5	50	44	71
50	3.5	12.5	40	32	63
30	2.5	12.5	40	34	69
10	2	12.5	40	35	71

Whakatane Fault (Earthquake cycle: 2 strike-slip and 3 oblique-slip events)					
Input				output	Real data
Distance (km)	Strike-slip earthquake (m)	Oblique-slip earthquake (m)	Pitch (°)	Cum. net-slip pitch (°)	Long-term net-slip pitch (°)
50	11	9	90	39	34
30	8	9	90	48	47
10	6	9	90	56	51
50	11	9	80	35	34
30	8	9	80	43	47
10	6	9	80	50	51
50	11	9	70	31	34
30	8	9	70	37	47
10	6	9	70	43	51
50	11	9	50	22	34
30	8	9	50	27	47
10	6	9	50	30	51
50	11	9	40	18	34
30	8	9	40	21	47
10	6	9	40	24	51

Whakatane Fault (Earthquake cycle: 1 strike-slip and 4 oblique-slip events)					
Input				output	Real data
Distance (km)	Strike-slip earthquake (m)	Oblique-slip earthquake (m)	Pitch (°)	Cum. net-slip pitch (°)	Long-term net-slip pitch (°)
50	5.5	12	80	57	34
30	4	12	80	63	47
10	3	12	80	67	51
50	5.5	12	70	50	34
30	4	12	70	54	47
10	3	12	70	58	51
50	5.5	12	60	42	34
30	4	12	60	46	47
10	3	12	60	49	51
50	5.5	12	50	35	34
30	4	12	50	38	47
10	3	12	50	41	51
50	5.5	12	40	28	34
30	4	12	40	30	47
10	3	12	40	32	51
50	5.5	12	30	21	34
30	4	12	30	23	47
10	3	12	30	24	51

Table 5.2 Input data used to simulate earthquake cycles on the Waiohau and Whakatane faults. Output data (model-derived) values of cumulative net slip-vector pitches are plotted in Figure 5.10 together with real (measured) data of cumulative net slip-vector pitches.

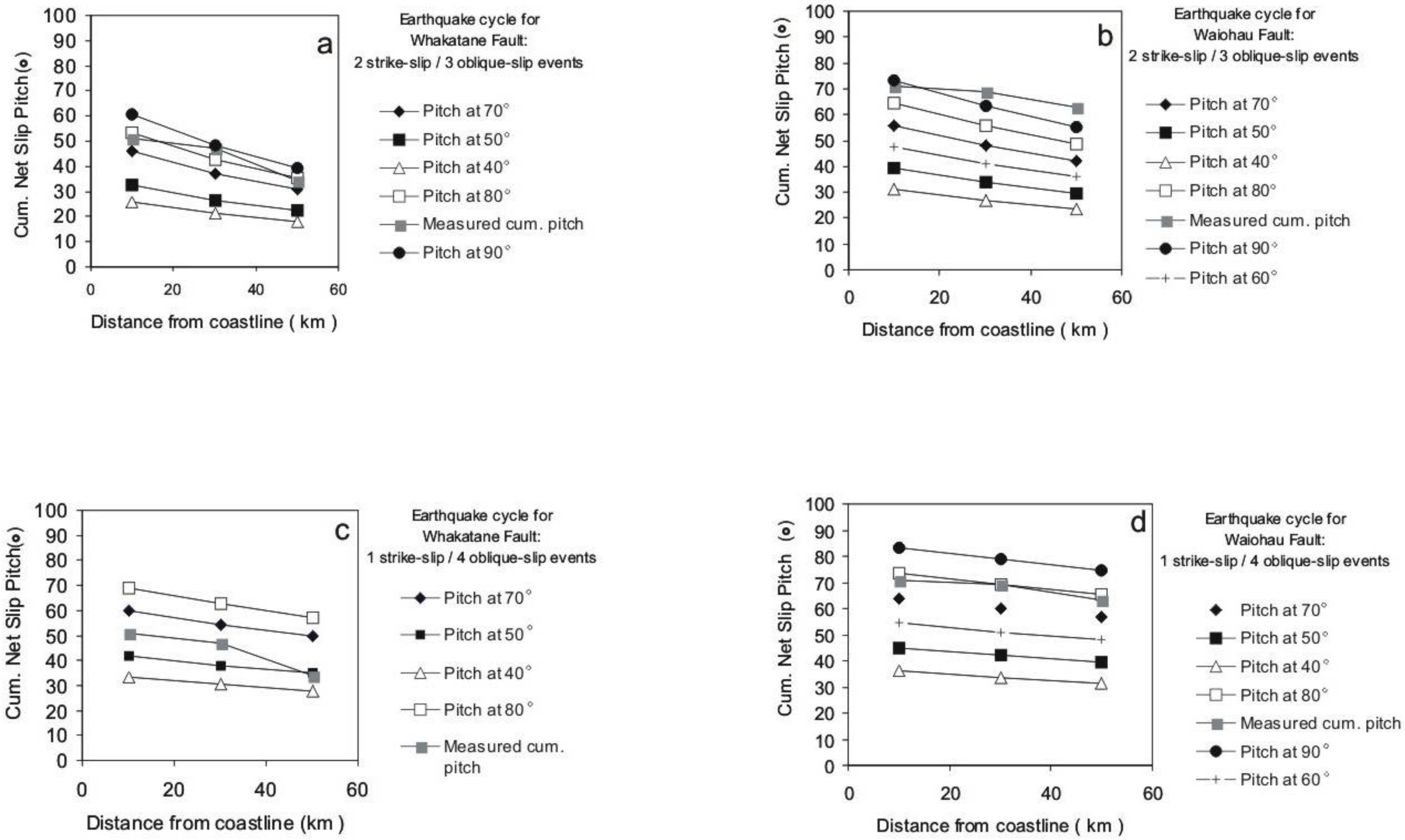

Fig. 5.10 Cumulative net slip-vector pitches reproduced by simulation of Holocene paleoearthquakes that have ruptured the northern sections of the Whakatane and Waiohau faults plotted against northward distance from the kinematic transition zone. Holocene earthquakes for both the Whakatane and the Waiohau faults comprise five events, each of which involves one (minimum) or two (maximum) strike-slip events aggregated with four and three oblique-slip earthquakes, respectively. The pitch on the oblique-normal slip events ranges, during successive earthquakes, between 40-90° while the pitch of the coseismic slip vector remains stable. The results are compared to observed cumulative net slip-vector pitches (grey squares) from offset late Quaternary landforms. See text for discussion.

5.4.2 Mixed strike-slip and oblique-slip ruptures with variable slip vector pitch

An efficient means of achieving the observed late Quaternary along strike gradient in slip vector orientations, is to allow the pitch of the slip vector to change along strike during individual earthquake ruptures. Review of the literature of large magnitude historic earthquakes supports the notion that slip vector orientations can change significantly during individual events along a fault that does not change strike (Olson & Apsel, 1982; Beroza, 1991; Yoshida et al., 1996; Johnson & Segall, 2004).

This section explores possible rupture combinations in which slip vector pitches are permitted to change spatially along strike during a single earthquake. For the scenario depicted in Fig. 5.2b (right diagram), where earthquake events are mostly, but not always, arrested in the kinematic transition zone, the section of the fault to the north of this zone experiences some strike-slip earthquakes with variable slip vector pitches in addition to the oblique-slip earthquake ruptures. In the scenario in Fig. 5.2c (right diagram) where earthquake events are always arrested within the kinematic transition zone, coseismic slip vectors are permitted to vary in pitch during individual oblique-slip earthquakes to the north of the transition zone. Either scenario can be considered consistent with observed late Quaternary data if individual earthquakes carry a gradient in the coseismic slip vector pitch of about 30°/10 km for scenario in Fig. 5.2b and 10°/15 km for scenario in Fig. 5.2c. These values are less than the 70°/13 km observed during the 1989 Loma Prieta earthquake (Beroza, 1991; Guatteri & Cocco, 1996). For these models, the slip vector pitches during individual earthquakes could be comparable to those of the cumulative late Quaternary vectors at each point on a fault trace. The fact that late Quaternary slip vectors are mainly parallel and independent of the number of events (Fig. 5.4a) is consistent with the notion of parallel finite and incremental slip vectors.

Spatial changes in co-seismic slip vector rake angles of > 50° are thought to result from a combination of geometric and static effects (Oglesby & Day, 2001). Geometric effects are usually associated with changes of the dip of the fault (Árnadóttir & Segall, 1994), while the static effects are attributed to non uniform pre-stress conditions proximal to the section of the fault that undergoes the spatial rake rotations (e.g. due to fault interactions) (Guatteri & Cocco, 1996). Knowing that the mean dip of the faults in the northern NIFS changes by 20-30° in a northward direction across the kinematic transition zone (Chapter 2, this study), it is suggested that variable coseismic slip-vector pitches could arise on single earthquake ruptures to account for the corresponding along strike gradient in the late Quaternary slip vectors in this part of the fault system (Fig. 5.3).

5.5 Discussion and conclusions

The northern NIFS is characterized by northward changes in slip-vector pitch and azimuth by up to 60° (Figs 5.3 & 5.4). This northward main kinematic transition from strike-slip to oblique-normal faulting occurs along faults that maintain a nearly uniform strike. These variations in slip vector orientations arise due to regional changes in the kinematics of the North Island, from margin-parallel dominated strike-slip in the south to oblique extension in the north within, and adjacent to, the Taupo Rift (Wallace et al., 2004). The observed late Quaternary changes in fault kinematics along strike are accomplished by superimposition of earthquakes, involving a combination of segmentation and rotation of the coseismic slip-vector pitch.

Differences in the timing of paleoearthquakes either side of the main kinematic transition zone indicate fault rupture arrest in at least 80 % of events during the last 10-13 kyr BP. Paleoearthquake rupture segmentation may contribute to the observed late Quaternary pattern of slip vectors by permitting faults north and south of the kinematic transition zone to rupture in separate events with different slip vector orientations (i.e. strike-slip in the south and oblique-slip in the north).

There is no apparent change in the strike of faults in the NIFS across the segment boundary zone and it is suggested that changes in the dip of the fault, from approximately 90° in the south to c. 60° W in the north (Fig. 5.11), contribute to a mechanical arrest of dynamic rupture propagation on the Waiohau and Whakatane faults. The gradual northward decrease in the fault-dips is interpreted to be <1 Ma old and to have formed in response to the increase in NW-SE extension proximal to the Taupo Rift (Fig. 5.11) (Chapter 2, this study).

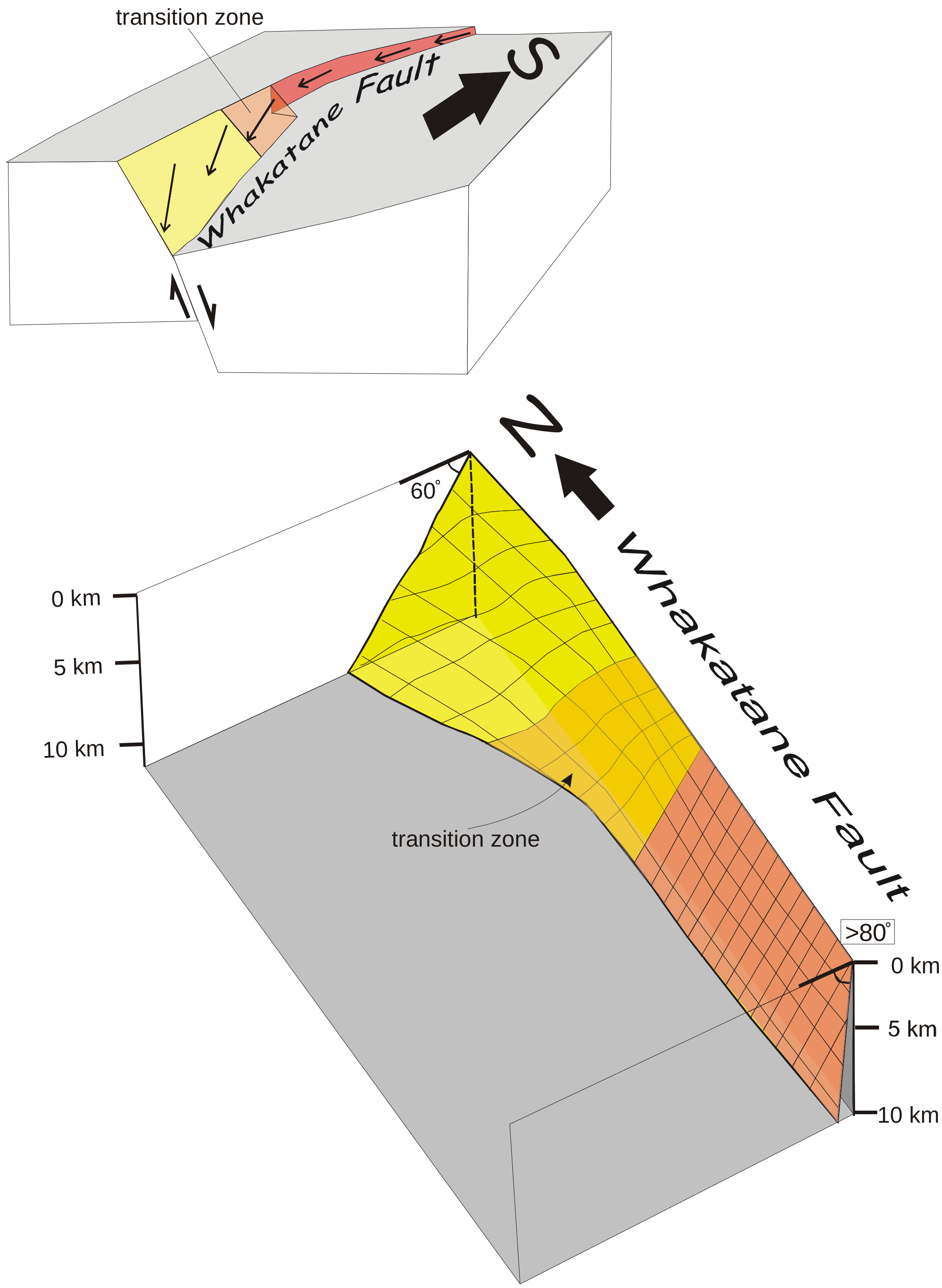

Fig. 5.11 Schematic diagram illustrating the gradual change in the fault-dip on the Whakatane-Mohaka Fault, from near vertical in the south to c. 60° W in the north. The change in the fault-dip may produce geometric and kinematic changes during rupture which result in rupture arrest.

Data from this study do not preclude the possibility that occasional large strike-slip events rupture through the kinematic transition zone from south to north. Simple kinematic modelling indicates that strike-slip events which may rupture through the transition zone with uniform (non-variable pitch) coseismic slip vectors, cannot produce the observed c. 10°/15 km change of the slip vector pitch (and slip azimuth) indicated by the offset landforms (see section 5.4.1). Therefore, in addition to segmentation, the gradual northward steepening of the pitch on the late-Quaternary slip vectors also requires that slip vectors vary during single earthquakes across, and north of, the main transition zone (see sections 5.4.2).

Historical earthquakes provide support for variations in slip vector orientation during individual events. During the 1989 Loma Prieta earthquake, for example, rupture initiated as right-lateral strike-slip and the slip vector rake rotated up to 70° to become reverse dip-slip over a fault strike distance of 13 km (Beroza, 1991; Guatteri & Cocco, 1996). Similarly, during the 1999 Chi-chi earthquake, reverse dip-slip rotated more than 50° towards the horizontal to become oblique left-lateral at the rupture termination (Oglesby & Day, 2001).

Non-uniform distribution of strength over a fault plane can cause a complex rupture process, including rotations of the coseismic slip vector (Mikumo & Miyatake, 1978; Aki, 1979). At the northern end of the NIFS the presence of the seismically active, rapidly extending (c. 10 - 15 mm/yr) Taupo Rift may locally impact on static stresses. Changes in coseismic slip vectors in the NIFS may arise due to the northward decrease in fault dip and associated steepening of the principal compressive stress axis (σ_1) approaching the active rift.

Acknowledgments: A. Nicol, T. Little and J. Begg are thanked for reviewing this chapter and contributing helpful comments.

References

Acocella, V., Spinks, K., Cole, J. and Nicol, A., 2003. Oblique back arc rifting of Taupo Volcanic Zone, New Zealand. Tectonics, 22, 4, 1045, doi:10.1029/2002TC001447.

Aki, K., 1979. Characterization of barriers on an earthquake fault. Journal of Geophysical Research, 84, 6140-6148.

Árnadóttir, T. & Segall, P., 1994. The 1989 Loma Prieta earthquake imaged from inversion of geodetic data. Journal of Geophysical Research, 99, B11, 21,835-21,855.

Aydin, A. & Du, Y., 1995. Surface rupture at a fault bend: the 28 June 1992 Landers, California earthquake. Bulletin of the Seismological Society of America, 85, 111-128.

Ballance, P.F., 1975. Evolution of the India-Pacific plate boundary in North Island, New Zealand. Bulletin of the Australian Society of Exploration Geophysicists, 6, 2/3, 58-59.

Baljinnyan, I. et al., 1993. Ruptures of major earthquakes and active deformation in Mongolia and its surroundings. Memoirs of Geological Society of America, 181, 62pp.

Bayasgalan, A., Jackson, J., Ritz, J.F. and Carretier, S., 1999. Field examples of strike-slip fault terminations in Mongolia and their tectonic significance, Tectonics, 18, 394–411.

Beanland, S., Berryman, K.R. and Blick, G.H., 1989. Geological investigations of the 1987 Edgecumbe earthquake. New Zealand Journal of Geology and Geophysics, 32, 73-91.

Barka, A.A. & Kadinsky-Cade, K., 1988. Strike-slip fault geometry in Turkey and its influence on earthquake activity. Tectonics, 7, 3, 663-684.

Beanland, S., 1989b. Detailed mapping in the Matahina Dam region. New Zealand. Geological Survey Client Report 89/8: 45pp.

Beanland, S. 1995. The North Island Dextral Fault Belt, Hikurangi Subduction margin, New Zealand. PhD Thesis, Victoria University of Wellington, New Zealand.

Berryman, K.R., Beanland, S. and Wesnousky, S., 1998. Paleoseismicity of the Rotoitipakau Fault Zone, a complex normal fault in the Taupo Volcanic Zone, New Zealand. New Zealand Journal of Geology and Geophysics, 41, 449-465.

Begg, J.G. & Johnston, M.R., 2000. Geology of the Wellington area: scale 1:250,000. Lower Hutt: Institute of Geological & Nuclear Sciences. Institute of Geological & Nuclear Sciences 1:250,000 geological map 10. 64p.

Beroza, G.C., 1991. Near-source modelling of the Loma Prieta earthquake: evidence for heterogeneous slip and implications for earthquake hazard. Bulletin of the Seismological Society of America, 81, 5, 1603-1621.

Beavan, R.J. & Haines, J., 2001. Contemporary horizontal velocity and strain rate fields of the Pacific-Australian plate boundary zone through New Zealand. Journal of Geophysical Research, Solid Earth, 106, B1, 741-770.

De Mets, C.R., Gordon, R.G., Argus, D. and Stein, S., 1994. Effect of recent revisions to the geomagnetic reversal time scale on estimates of current plate motions. Geophysical Research Letters, 21, 2191-2194.

Guatteri, M. & Cocco, M., 1996. On the variation of the slip direction during earthquake rupture: supporting and conflicting evidence from the 1989 Loma Prieta earthquake. Bulletin of the Seismological Society of America, 86, 6, 1935-1951.

Guatteri, M & Spudich, P., 1998. Coseismic temporal changes of slip direction: the effect of absolute stress on dynamic rupture. Bulletin of the Seismological Society of America, 88, 777-789.

Eberhart-Phillips, D., Haeussler, P.J., Freymueller, J.T., Frankel, A.D., Rubin, C.M., Craw, P., Ratchkovski, N.A., Anderson, G., Crone, A.J., Dawson, T.E., Fletcher, H., Hansen, R., Harp, E.L., Harris, R.A., Hill, D.P., Hreinsdottir, S., Jibson, R.W., Jones, L.M., Keefer, D.K., Larsen, C.F., Moran, S.C., Personlus, S.F., Plafker, G., Sherrod, B., Sieh, K. and Wallace W.K., 2003. The 2002 Denali Fault earthquake, Alaska: A large magnitude, slip-partitioned event. Science, 300, 1113-1118.

Hanson, J.A., 1998. The neotectonics of the Wellington and Ruahine Faults between the Manawatu gorge and Puketitiri, North Island, New Zealand. PhD Thesis, Massey University, New Zealand.

Hreinsdottir, S., Freymueller, J.T., Fletcher, H.J., Larsen, C.F. and Burgmann, R., 2003. Coseismic slip distribution of the 2002 M_W 7.9 Denali fault earthquake, Alaska, determined from GPS measurements. Geophysical Research Letters, 30, 13, 1670, doi:10.1029/2003GL017447.

Hull, A.G., 1983. Trenching of the Mohaka Fault near Hautapu River, Hawkes Bay. New Zealand Geological Survey Report, file, 831/26.

Hurst, W.A., Bibby, H.M. and Robinson, R.R., 2002. Earthquake focal mechanism in the Central Volcanic Zone and their relation to faulting and deformation. New Zealand Journal of Geology and Geophysics, 45, 527-536.

Johnson, K.M. & Segall, P., 2004. Imaging the ramp-decollement geometry of the Chelungpu fault using coseismic GPS displacements from the 1999 Chi-chi, Taiwan Earthquake. Tectonophysics, 378, 123-139.

Ide, S., Takeo, M. and Yoshida, Y., 1996. Source process of the 1995 Kobe Earthquake: determination of spatio-temporal slip distribution by Bayesian modeling. Bulletin of the Seismological Society of America, 86, 3, 547-566.

Knuepfer, P.L.K., 1989. Implications of the characteristics of end-points of historical surface fault ruptures for the nature of fault segmentation. In Fault segmentation and controls of rupture initiation and termination (D.P. Schwartz, D.P. and R.H. Sibson, eds.), U.S. Geological Survey Open File Report, 89-315, 193-228.

Manning, D.A., 1995. Late Pleistocene tephrostratigraphy of the eastern Bay of Plenty, North Island, New Zealand. PhD Thesis, Victoria University of Wellington, Wellington, New Zealand.

Mikumo, T. & Miyatake, T., 1978. Dynamic rupture process on a three-dimensional fault with non-uniform frictions and near-field seismic waves. Geophysical Journal of Royal Astronomical Society, 54, 417-438.

Muller, J.R. & Aydin, A., 2004. Rupture progression along discontinuous oblique fault sets: implications for the Karadere rupture segment of the 1999 Izmit earthquake, and future rupture in the Sea of Marmara. Tectonophysics, 391, 283-302.

Nicol, A. & Beavan, R.J., 2003. Shortening of an overriding plate and its implications for slip on a subduction thrust, central Hikurangi Margin, New Zealand. Tectonics, 22, 6, 1070, doi:10.1029/2003TC001521.

Nicol, A. & Van Dissen, R., 2002. Up dip partitioning of displacement components on the oblique slip Clarence fault. Journal of Structural Geology, 24, 1521-1535.

Nicol, A. & Wallace, L., in review. Temporal stability of deformation rates estimated by comparison of geological and geodetic data, Hikurangi Margin, New Zealand. Submitted to Tectonics.

Oglesby, D.D. & Day, S.M., 2001. Fault geometry and the dynamics of the 1999 Chi-chi (Taiwan) earthquake. Bulletin of the Seismological Society of America, 91, 5, 1099-1111.

Oglesby, D.D., 2005. The dynamics of strike-slip step-overs with linking dip-slip faults. Bulletin of the Seismological Society of America, 95, 5, 1604-1622.

Olson, A.H. & Apsel, R.J., 1982. Finite faults and inverse theory with applications to the 1979 Imperial Valley Earthquake. Bulletin of the Seismological Society of America, 72, 6, 1969-2001.

Ota, Y., Beanland, S., Berryman, K.R. and Nairn, I.A., 1988. The Matata Fault: active faulting at the north-western margin of the Whakatane graben, eastern Bay of Plenty. New Zealand Geological Survey record, 35, 6-13.

Rait, G., Chanier, F. and Waters, D.W., 1991. Landward- and seaward-directed thrusting accompanying the onset of subduction beneath New Zealand. Geology, 19, 230-233.

Spudich, P., Guatteri, M., Otsuki, K. and Minagawa, J., 1998. Use of fault striations and dislocation models to infer tectonic shear stress during the 1995 Hyogo-ken Nanbu (Kobe) earthquake. Bulletin of the Seismological Society of America, 88, 2, 413-427.

Wallace, L.M., Beaven, J., McCaffrey, R. and Darby, D., 2004. Subduction zone coupling and tectonic block rotations in the North Island, New Zealand. Journal of Geophysical Research, 109, B12, 2406, doi:10.1029/2004JB003241.

Walcott, R.I., 1978. Present tectonics and Late Cenozoic evolution of New Zealand. Geophysical Journal of the Royal Astronomical Society, 52, 1, 137-164.

Walcott, R.I., 1984. An introduction to the recent crustal movements of New Zealand. Royal Society of New Zealand, Miscellaneous series, 7, 1-108.

Wald, D. J. & Heaton, T. H., 1994. Spatial and temporal distribution of slip for the 1992 Landers, California, earthquake. Bulletin of the Seismological Society of America, 84, 3, 668-691.

Webb, T. & Anderson, H., 1998. Focal mechanisms of large earthquakes in the North Island of New Zealand: slip partitioning at an oblique active margin. Geophysical Journal International, 134, 40-86.

Woodward-Clyde, 1998. Matahina Dam strengthening project. Geological completion report to Electricity Corporation of New Zealand.

Yoshida, S., Koketsu, K., Shibazaki, B., Sagiya, T., Kato, T. and Yashida, Y., 1996. Joint inversion of near- and far-field waveforms and geodetic data for the rupture process of the 1995 Kobe earthquake. Journal of Physics of the Earth, 44, 437-454.

CHAPTER SIX

QUATERNARY TEMPORAL STABILITY OF A STRIKE-SLIP AND NORMAL FAULT INTERSECTION, NORTH ISLAND, NEW ZEALAND

Abstract

The strike-slip North Island Fault System, North Island, New Zealand, obliquely intersects (c. 45°) the Taupo Rift and terminates. The temporal stability of a strike-slip and normal fault intersection over timescales of 10 to 1500 kyr is examined. Analysis of gravity, seismic-reflection, drillhole and outcrop data shows that throws on the 280 kyr Matahina ignimbrite and the top-basement surface (600-1500 kyr in age) generally increase northwards on each of the faults in the NIFS as they approach the Taupo Rift. Short-intermediate (≤ 280 kyr) and long-term (≥ 600 kyr) throws on the fault that bounds the eastern margin of the rift, decrease near its intersection with each of the strike-slip faults of the NIFS. This decrease in throw is equal to the increase in throw on the intersecting fault of the NIFS. Therefore, the total throw across each strike-slip and normal fault intersection is constant and equal to the throw accommodated by the rift alone away from the intersection zone. Interdependence of fault-throws (or throw rates) between the NIFS and Taupo Rift suggests that the intersection of the two fault systems has functioned coherently for much of the last 600-1500 kyr. Throw rates in the rift, and on those faults in the NIFS that accommodate a component of normal displacement, increased by up to a factor of 3 about 300 kyr ago. This acceleration of rifting may be due to an eastward migration of extension. Therefore, the rates of faulting and the orientations (pitch and azimuth) of slip vectors that typify the contemporary kinematics of the intersection zone, and which have persisted in the late Quaternary (e.g. 30 kyr), may have only been stable for the last c. 300 kyr.

6.1 Introduction

The North Island Fault System (NIFS) is the longest and the highest slip-rate active fault system in the upper plate of the Hikurangi margin, New Zealand. At its northern termination the NIFS intersects the active Taupo Rift at c. 45º and terminates (Fig. 6.1). The late Quaternary (c. 30 kyr) geometries and kinematics of faults in the NIFS change conspicuously with spatial proximity to the Taupo Rift (Chapter 2). Approximately 50-60 km south of their termination, the dips on the faults in the NIFS begin to decrease gradually, from c. 90° to c. 60° W, northwards near the intersection. Along the same section of the NIFS, the corresponding slip vectors on the faults steepen northward from strike-parallel (horizontal), to the south, to 60° NW, to the north, adjacent to the rift margin. These changes, which result from the superimposition of NW-SE distributed extension onto the northern section of the NIFS, generate a gradual anticlockwise rotation of the mean net-slip azimuth of the faults in the NIFS, as they approach the Taupo Rift from the south (Fig. 6.1). As a consequence of these changes, at the point of fault intersection, slip vectors on the two mutually active fault systems are sub-parallel to one another and to their plunging intersection line (in 3D). This parallelism allows the strike-slip component of slip in the NIFS to be transferred into the rift without the margin of the rift being obviously offset and with the overall geometry of the junction being unchanged (Fig. 6.1) (Chapter 2). Therefore, the along strike kinematic changes that have characterized the last 30 kyr of activity on these two fault systems accomplish a kinematically coherent interaction at the point where they intersect one another, and across which their displacements are transferred. Similar kinematic coherence has been demonstrated for normal faults (e.g. Walsh and Watterson, 1991; Nicol et al., 2006) but has not been widely documented for synchronously intersecting strike-slip and normal fault systems (Chapter 3). This chapter addresses; 1) how geometries and kinematics of fault systems locally adjust to accommodate displacement transfer between the intersecting NIFS and Taupo Rift; and, 2) how long-lived this kinematically stable intersection zone has been.

To answer these questions, seismic-reflection, gravity, drill-hole and outcrop data are utilized to chart the vertical displacement accumulation on both fault systems, proximal to their intersection, over timescales of thousands to millions of years (i.e. 0-10, 0-18, 0-280, 0-600, 0-1000, 0-1500 kyr BP). This chapter examines the geometry and kinematics of the Waiohau-Edgecumbe fault intersection, the only such junction that is exposed onshore, to determine how the faults locally accommodate displacement transfer. To estimate the longevity of the currently

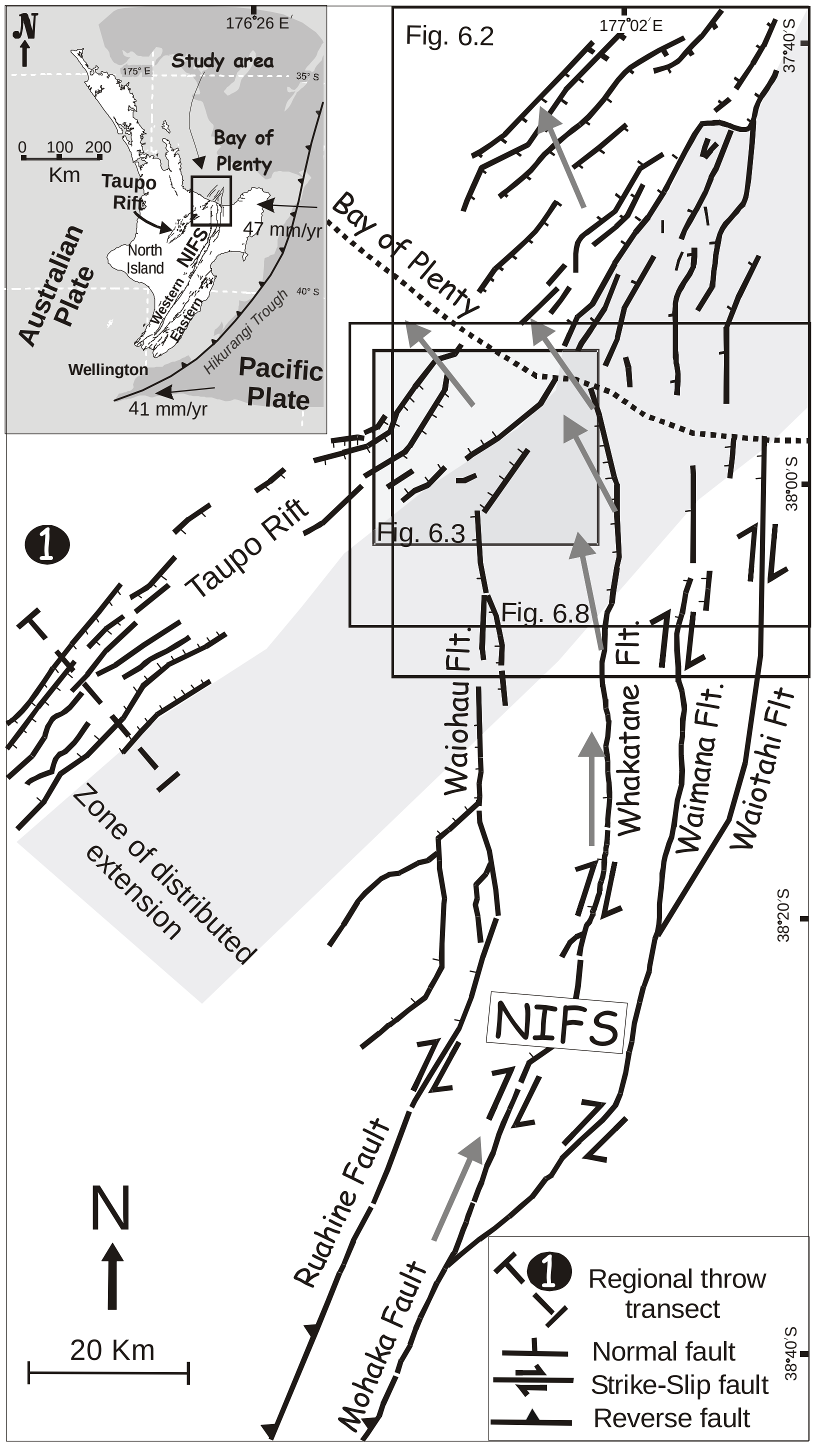

Fig. 6.1 Regional fault map shows the northern North Island Fault System (NIFS) intersecting and terminating against the Taupo Rift. Grey arrows along the two fault systems represent average net-slip azimuths (see Chapter 2). Zone of distributed extension outside the main rift is shaded grey. Dashed line indicates approximate location of regional throw transect-1. Inset: The North Island, New Zealand, where the Pacific Plate is being obliquely subducted beneath the Australian Plate. Relative plate motion vectors are from De Mets et al. (1994).

kinematically coherent fault junction between the NIFS and the Taupo Rift, the short-intermediate (≤ 280 kyr) throw rates are compared to the long-term (≥ 600 kyr) throw rates on individual faults in both fault systems.

Data suggest that the intersection of the two fault systems has operated as kinematically coherent fault array for at least the last million years with individual faults within this array accumulating displacement interdependently. In addition, comparison of short, intermediate and long-term throw rates on individual faults within the NIFS shows that the majority of these faults have moved faster during the last 300 kyr, perhaps in response to an eastward migration of extension within the adjacent Taupo Rift. Therefore, the geometry and kinematics of the intersecting fault systems recorded for the last 30 kyr may only apply for the last 300 kyr.

6.2 Geological setting and data

The strike-slip NIFS and the extensional Taupo Rift have formed in response to the westward oblique subduction of the oceanic Pacific Plate beneath the continental Australian Plate (inset of Fig. 6.1) (Ballance, 1975; Rait et al., 1991; Beaven & Haines, 2001).

The NIFS (Wellington-Mohaka Fault and its northern splays) is c. 500 km long, strikes parallel to the Hikurangi margin (NE-SW) and dips steeply (>80°) along most of its length (Beanland, 1995; Chapter 2 in this study). The strike-slip rate in the NIFS increases southwards, from c. 4 mm/yr in the Bay of Plenty to 10 mm/yr near Wellington, and accommodates up to 30% of the margin parallel component of the relative Australian-Pacific plate motion (Nicol & Wallace, in review).

The Taupo Rift is c. 200 km long and up to 40 km wide (Rowland & Sibson, 2001). The average strike of the normal faults within the rift is NE-SW while their average dip is 60° to either the SE or to NW (Villamor & Berryman, 2001). The cumulative extension rate across the rift ranges from < 4 mm/yr in the south (Villamor & Berryman, 2006) to c. 10-15 mm/yr in the north (Davey et al., 1995; Wallace et al., 2004). Near the Bay of Plenty coast (Fig. 6.1), where the NIFS intersects obliquely the Taupo Rift, the two fault systems carry c. 4 and 10 mm/yr of strike-slip and extension rate, respectively.

In the northeastern North Island of New Zealand, basement bedrock primarily consists of Mesozoic Torlesse supergroup greywacke (Mortimer, 1994). Basement rocks are unconformably overlain by sedimentary strata, unconsolidated sediments and volcanics which range in age from Cretaceous to Holocene (Nairn & Beanland, 1989). Both, the NIFS and the eastern Taupo Rift are 'rooted' within Torlesse greywacke which crops out extensively in the inland areas of the Bay of Plenty. Approaching the Taupo Rift, along the NIFS, the greywacke basement becomes progressively buried. Near the intersection of the two fault systems, the basement greywacke is buried by a thick sequence (≤ 3 km) of marine, non-marine and volcanic sediments (Nairn & Beanland, 1989; Bailey & Carr, 1994).

The age of the deposits on top of the greywacke basement varies along and across the Taupo Rift and NIFS fault intersection. On the northwestern margin of the rift, a K-Ar age of 620±30 kyr BP from c. 400 m above the top-basement unconformity suggests that the latter contact is significantly older than 600 kyr in age (Nairn & Beanland, 1989). If sedimentation rates onshore were similar to the c. 1 mm/yr inferred offshore (Taylor et al., 2004), then the marine sediments immediately overlying basement would be approximately 1000 kyr in age. Existing seismic-reflection lines from within, and east of, the rift, and in the hangingwall of the Waiohau Fault reveal strata that indicate normal-fault growth which is at least 1000 kyr older than Matahina ignimbrite (280 kyr BP) or correlative horizons (Woodward, 1988, 1989; O'connor, 1988; Davey et al., 1995; Woodward-Clyde, 1998; Taylor et al., 2004; Lamarche et al., 2006; Nicol et al., Unpubl. data). Collectively, these data are consistent with Wilson et al.'s (1995) suggestion that rifting initiated c. 1-2 Ma BP. Therefore the age of the oldest sediments on the top-basement unconformity within the rift is dated c. 1500±500 kyr BP.

On the eastern shoulder of the rift, on the footwall and hangingwall of the Whakatane Fault and the hangingwall of the Waiohau Fault, Castlecliffean Ohope marine beds (which are dated as c. 600±30 kyr BP, Fleming, 1955; Beu, 2004) and Lukes Farm Formation (a non-marine equivalent to the Ohope beds; Healy et al.,

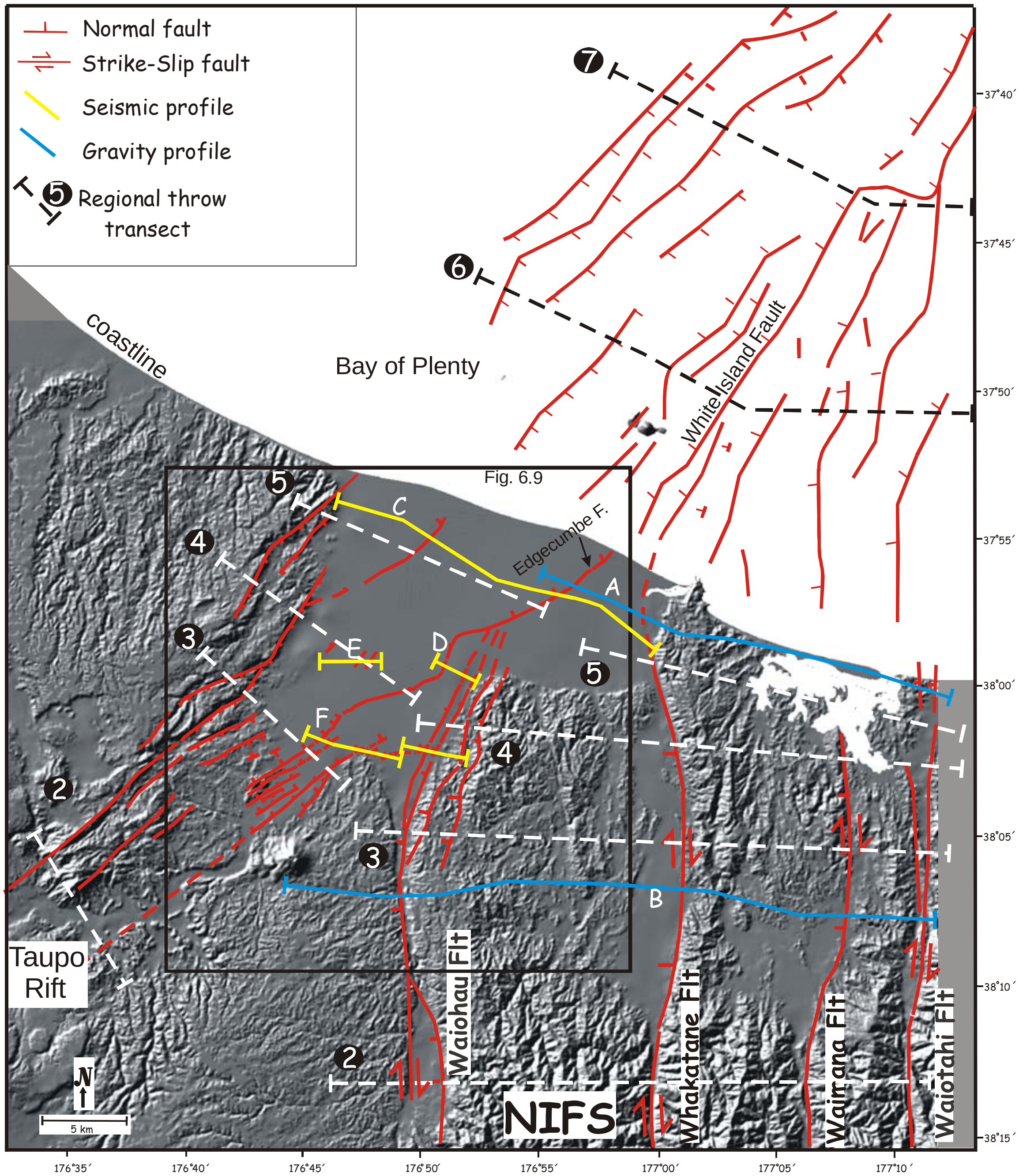

Fig. 6.2 Digital elevation model showing the intersection zone between the northern NIFS and Taupo Rift. Regional throw transects (2-7) are indicated by dashed white (onshore) and black (offshore) lines (see Fig. 6.1 for location of transect-1). Regional gravity profiles (A & B) are indicated by blue lines (this study). Seismic-reflection profiles are indicated by yellow lines (line C from Nicol et al., Unpubl. data; lines D, E & F from Woodward, 1988 and O'Connor, 1988). Offshore faults are from Davey et al. (1995), Taylor et al. (2004), Lamarche et al. (2006).

1964), respectively, rests on basement. On the hangingwall of the Waiohau Fault, a c. 400-500 m thick sequence of older ignimbrites and sediments rest beneath the

Lukes Farm Formation (Nairn, 2002; this study). Therefore, the age of the oldest sediments on the top-basement unconformity on the hangingwall of the Waiohau Fault is estimated to be c. 1000±400 kyr BP.

A sequence of ignimbrites, tuffs and other volcanics rest on the Lukes Farm Formation (Bailey & Carr, 1994). The Matahina ignimbrite is the most widespread of these volcanics in the northern part of the Taupo Rift and northern NIFS. Fission-track dating, from zircons within the pumice, indicates an age of 280±30 kyr BP for the Matahina ignimbrite (Bailey & Carr, 1994).

Gravity, seismic-reflection, drill-hole and outcrop data (Figs 6.2 & 6.3) have been used to constrain the vertical components of displacement on the top of greywacke basement and the Matahina ignimbrite in the eastern Bay of Plenty along and across the intersection between the NIFS and the Taupo Rift.

Two E-W oriented gravity profiles, each 35-40 km long, were collected as part of this study (Figs 6.2, 6.3 & 6.4). These profiles extend across four major faults in the NIFS (Waiohau, Whakatane, Waimana and Waiotahi faults) and the Edgecumbe Fault, which bounds the eastern margin of the Taupo Rift, and record displacements accrued on the top of greywacke basement (Fig. 6.4). Gravity data were obtained using a LaCoste and Romberg gravimeter. The location and height of each observation was established with Real Time Kinematic (RTK) GPS equipment. Residual gravity anomaly data along lines were projected onto a plane for modelling. For more details on the processing and modelling of gravity data refer to the Appendix IV (this study).

Seismic-reflection lines have been collected across the onshore and offshore Taupo Rift and the Waiohau and Whakatane faults in the NIFS (Woodward, 1988; O'Connor, 1988; Davey et al., 1995; Woodward-Clyde, 1998; Taylor et al., 2004; Lamarche et al., 2006; Nicol et al., Unpubl. data) (Figs. 6.2, 6.3, 6.5, 6.6 & 6.7). The onshore multichannel seismic reflection profiles are migrated with reflectors down to two-way travel times (TWT) of 2 seconds (Woodward, 1988; O'Connor, 1988; Woodward-Clyde, 1998; Nicol et al., Unpubl. data). The bulk of the offshore

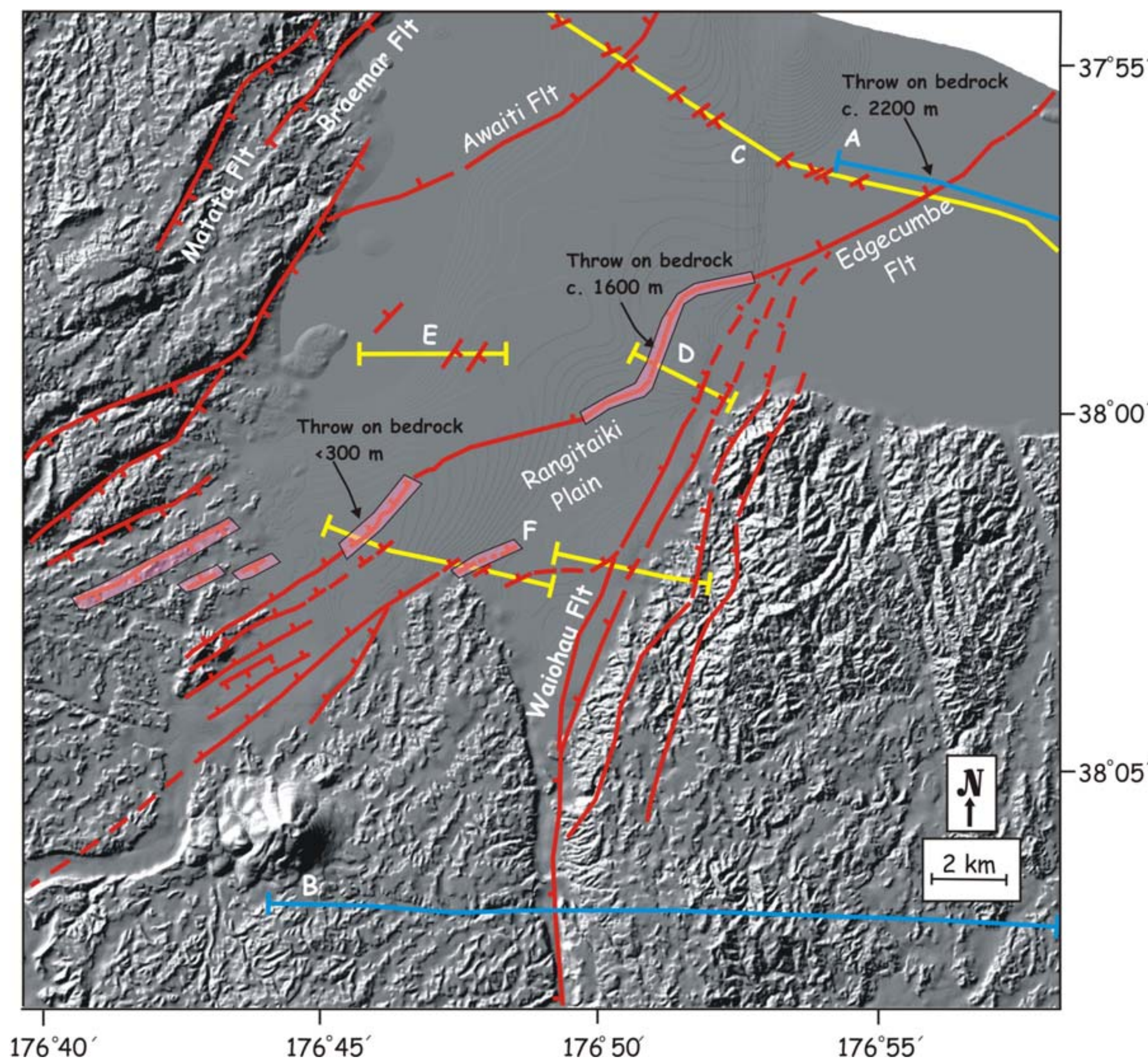

Fig. 6.3 Digital elevation model illustrates the fault intersection between the northern strands of the Waiohau Fault (NIFS) and the Edgecumbe Fault (Taupo Rift). The pink polygons along the Edgecumbe Fault indicate the distribution of the surface rupture during the Mw 6.6 1987 Edgecumbe earthquake (Beanland et al., 1989). See key of Figure 6.2 for further details.

seismic data consist of 3.5 kHz and migrated multi-channel seismic (MCS) reflection profiles which provide data down to 0.04 and 1.5 seconds, respectively (Davey et al., 1995; Lamarche et al., 2006). In this study, I have reinterpreted onshore seismic lines (Woodward, 1988; O'Connor, 1988) and some offshore data (Davey, 1995). The quality of the onshore seismic data is variable, with most fault throws of 50 to 2200 m, being resolvable and occurring on westward dipping faults with a clear component of normal displacement.

Additional control on the depth of basement greywacke and the Matahina ignimbrite is provided by drill-hole data (Woodward, 1988; Woodward-Clyde, 1998; Nairn & Beanland, 1989) (Figs 6.7, 6.8 & 6.9). Most of these holes were drilled for groundwater or geothermal energy at Kawerau and do not provide detailed records of the subsurface rock record.

6.3 Regional fault displacements within the intersection zone

The regional patterns of vertical displacements, since deposition of the Matahina ignimbrite and commencement of deposition on the unconformity at the top-basement, provide a means of assessing the long-term kinematics of the intersection zone of the NIFS and Taupo Rift. Gravity models and seismic data suggest that vertical fault displacements on the top of greywacke basement are consistently down to the west and increase northwards and westwards along and across the strike of the faults in the NIFS respectively, with increasing proximity to the active Taupo Rift (Fig. 6.8). The throw on the top-basement across the onshore northern NIFS, for example, ranges from c. 300 m on the easternmost fault (Waiotahi Fault) (Fig. 6.4a) to c. 700 m on the Waiohau Fault proximal to its intersection with the rift (Fig. 6.4b). Accordingly, near the coast, the Whakatane and Waimana faults, which are located between the Waiohau and Waiotahi faults, carry average vertical displacements of c. 600 and 500 m, respectively (Figs 6.4a, 6.5 & 6.8).

Throws on top-basement in the northern NIFS, also increase northwards along strike for the Waiohau, Whakatane, Waimana and Waiotahi faults. Approximately 25 km south of the coast, for example, the throws on the Waiohau and Whakatane faults are 700 and 500 m, respectively (Fig. 6.4b, 6.8), while near the coast, these throws have increased to c. 900 and 650 m respectively (Figs 6.4a, 6.5, 6.6 & 6.8) (Woodward, 1988; O'Connor, 1988; this study). Similarly, throws on the Waimana and Waiotahi faults increase from zero, 25 km south of the coast, to 500 and 300 m at the coast, respectively (Figs. 6.4a, 6.5, 6.6 & 6.8).

The northward increase of throws on top basement within the NIFS is supported

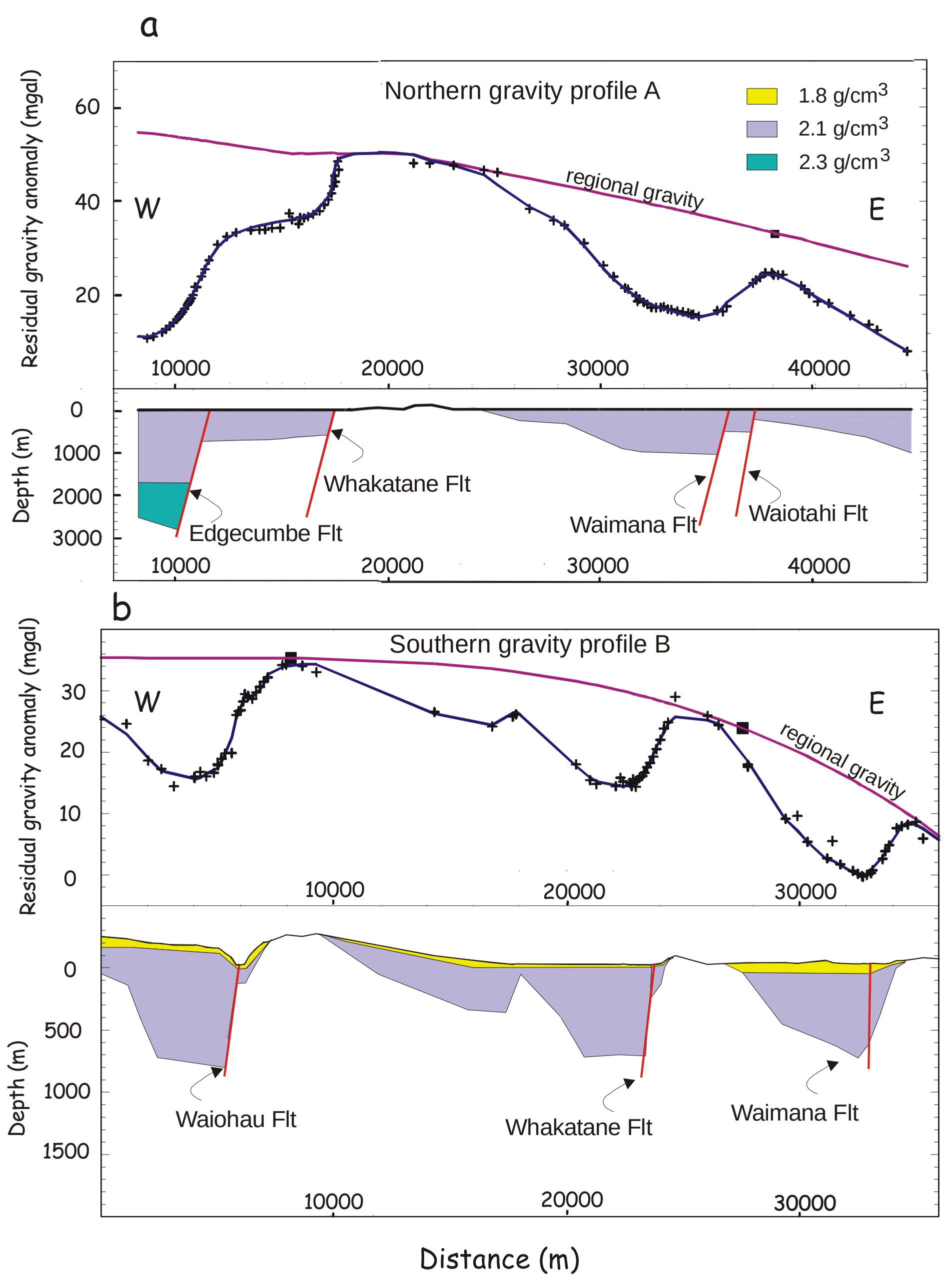

Fig. 6.4 Two dimensional residual gravity profiles for two regional sample lines (A and B). Densities used for modelling range from 1.8 to 2.3 g/cm^3 (description of the modelling is given in Appendix IV): (a) Northern gravity profile (A) across the Edgecumbe, Whakatane, Waimana and Waiotahi faults shows the westward increase in throw on the faults in the NIFS as the intersection with the Taupo Rift in approached. (b) Southern gravity profile (B) shows the Waiohau and Whakatane faults carrying a westwardly increasing throw as opposed to the Waimana Fault which is principally strike-slip. See Fig. 6.2 for locations of the gravity profiles.

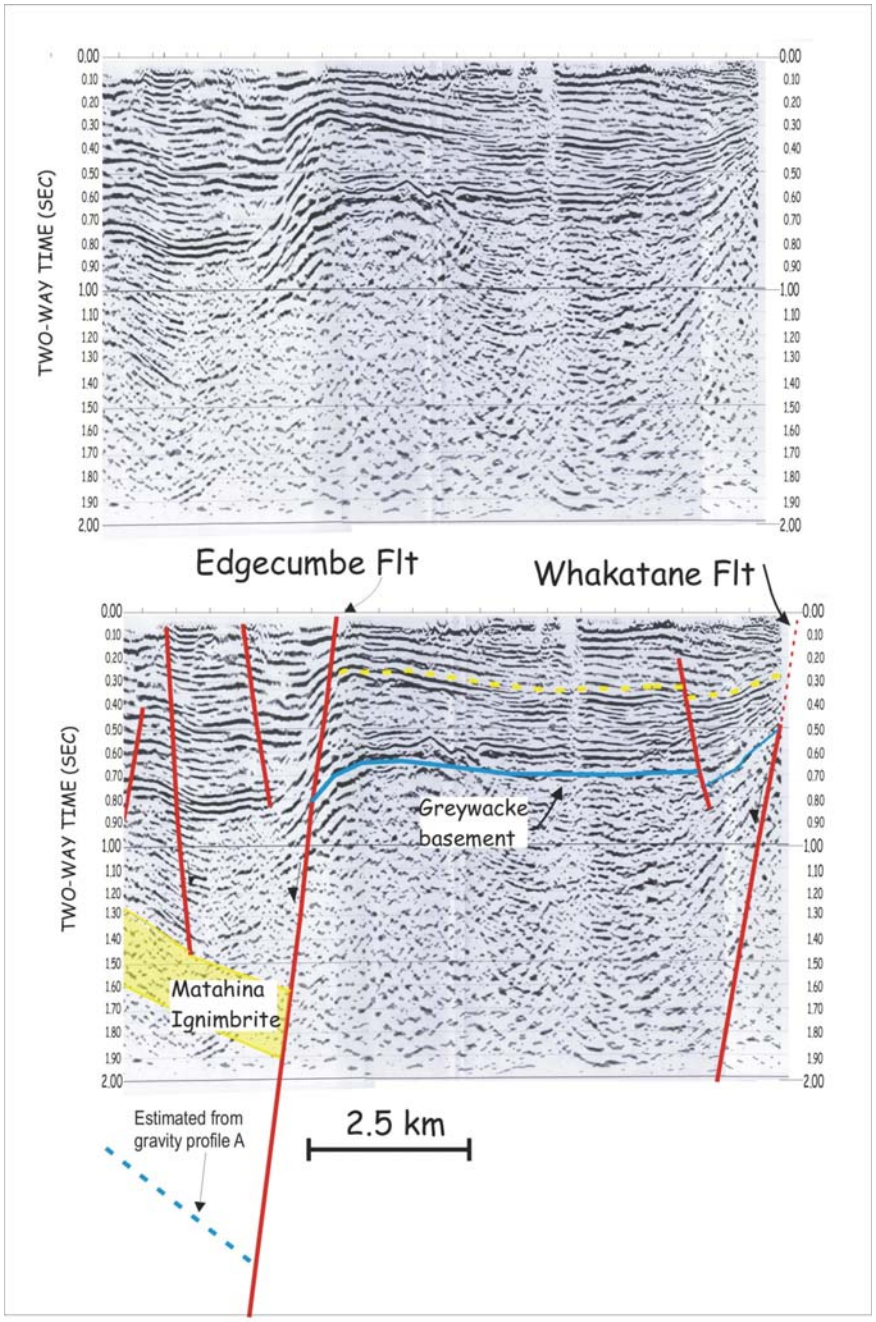

Fig. 6.5 Seismic-reflection profile C is part of an unpublished line (Nicol et al., Unpublished data) which crosses the Rangitaiki Plains (see Fig. 6.2 for location). The portion of the line presented here crosses the eastern margin of the Taupo Rift and the Whakatane Fault. The position of the top of the greywacke basement (blue line) is estimated from the northern gravity profile (A) in Figure 6.4. The location of the Matahina ignimbrite (yellow dashed line and shading) is estimated by projecting outcropping Matahina ignimbrite at the western end of the seismic line onto the western margin of the Taupo Rift and tracing the reflector inferred to correspond with the Matahina ignimbrite to the Edgecumbe Fault. Vertical exaggeration x 5.

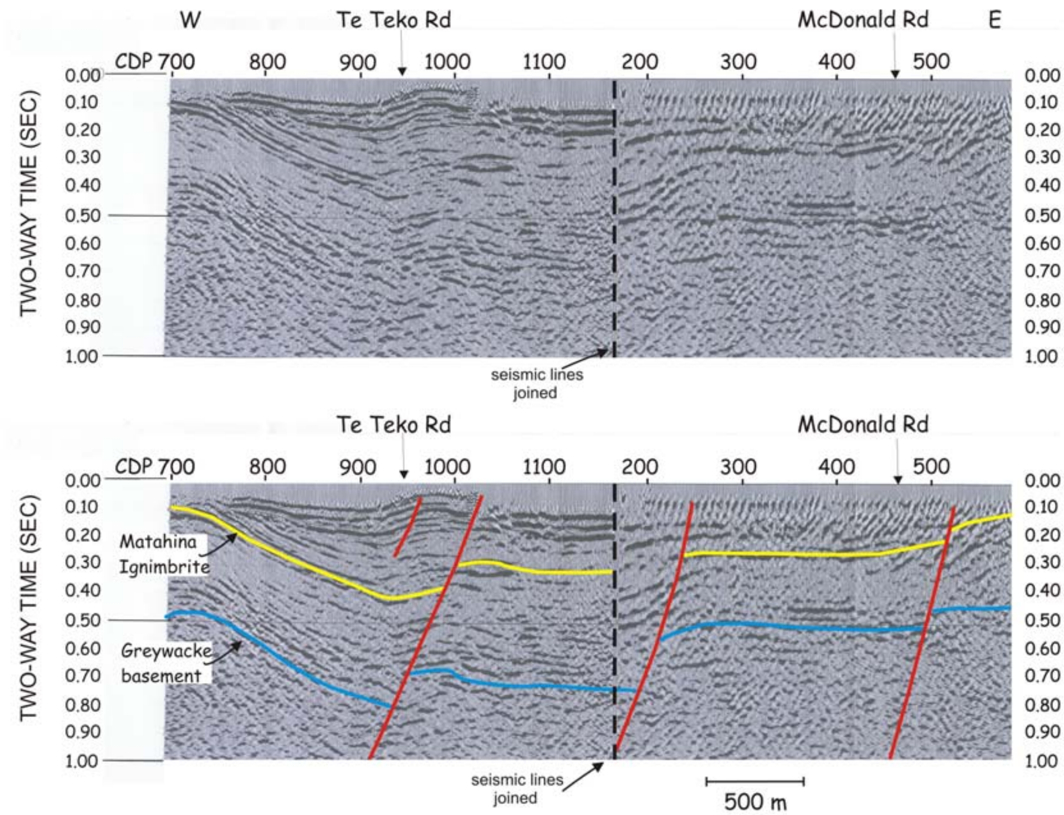

Fig. 6.6 Seismic line F. The easternmost section of the composite seismic-reflection profile, comprising components of lines 103 and 6 from Woodward (1988) and O'Connor (1988) and reprocessed by Woodward-Clyde (1998). The top of greywacke basement (1000-2000 kyr) (blue line) and Matahina ignimbrite (280 kyr) (yellow line) are shown to be displaced by strands of the Waiohau Fault. The entire seismic line extends further west across the eastern margin of the Taupo Rift (Edgecumbe Fault). See Fig. 6.2 for location of the seismic profile F.

by topographic data (Fig. 6.10). Along the Whakatane Fault, for example, basement crops out at the same elevations either side of the fault 35-60 km south of the coast, while further north the topography is higher on the footwall than on the hangingwall (Fig. 6.10). The northward increase in vertical displacement on, and topographic separation across, faults in the NIFS is consistent with the northward increase in dip-slip indicated by displaced landforms up to 30 kyr in age (Chapter 2).

Throws on the top Matahina ignimbrite on faults within the intersection zone are available for the Waiohau Fault (NIFS) and Edgecumbe Fault (Taupo Rift). The throw on top Matahina ignimbrite increases northwards along the Waiohau Fault from 200 to 400 m over a strike distance of c. 5 km towards its intersection with the

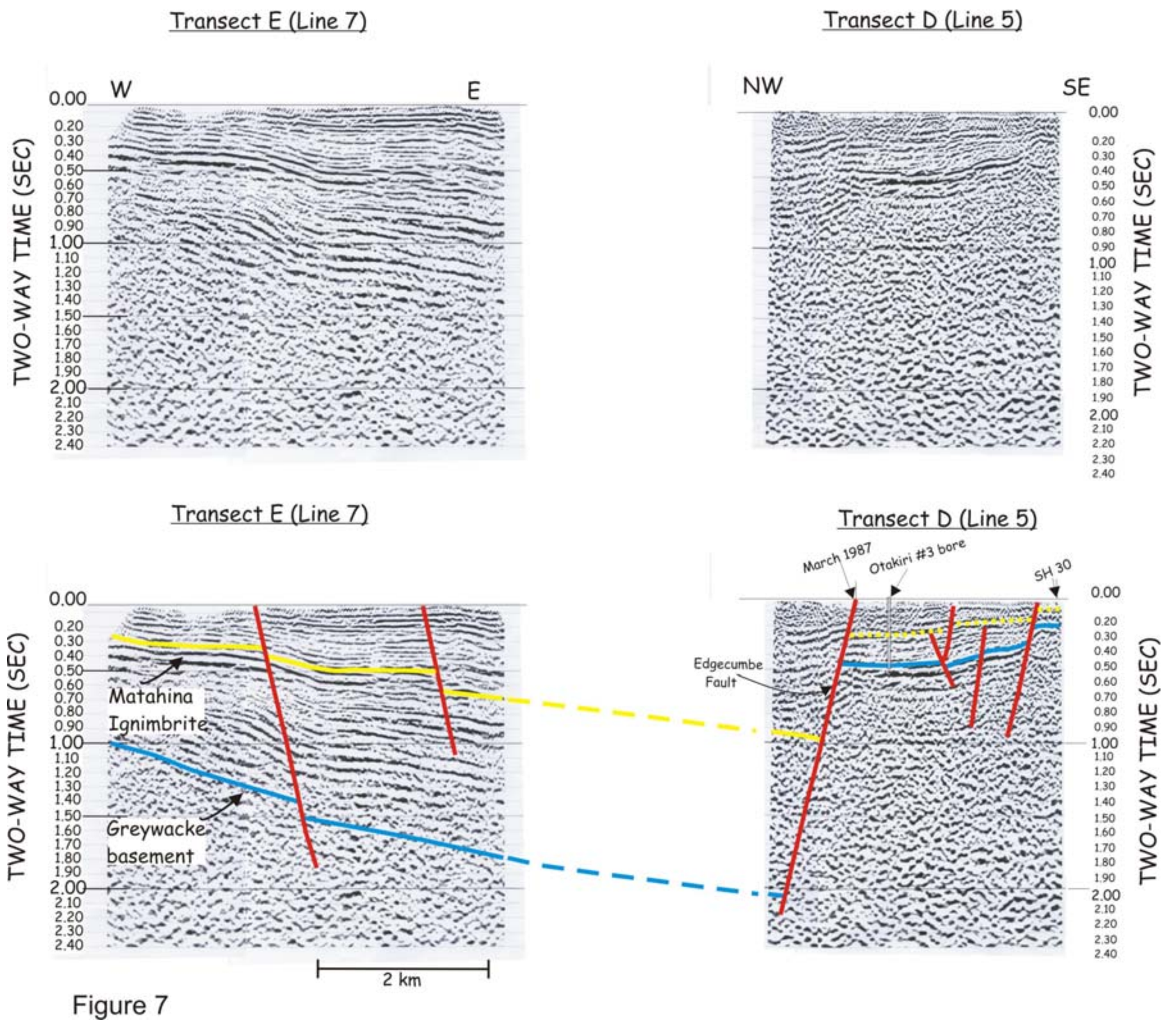

Fig. 6.7 Seismic reflection profiles D and E across the intersection of Edgecumbe-Waiohau Fault and central section of the Taupo Rift, respectively. The top of the greywacke basement (1000 to 2000 kyr) and Matahina ignimbrite (c. 280 kyr) are indicated by blue and yellow lines, respectively. Seismic lines are from Woodward (1988) and were reprocessed by J. Ravens in 2004. Drill-hole located on profile D is from Woodward (1988). For location refer to Figure 6.2.

Edgecumbe Fault, while throws on the Edgecumbe Fault decrease southwards from 1350 to < 100 m across its intersection with the Waiohau Fault (Fig. 6.9).

The northward increase in throw expressed on top-basement and top-Matahina surfaces, are consistent with each other and with changes in the vertical displacement rates on faults in the NIFS during the late Quaternary. The late Quaternary throw rates appear also to increase northwards and westwards along and

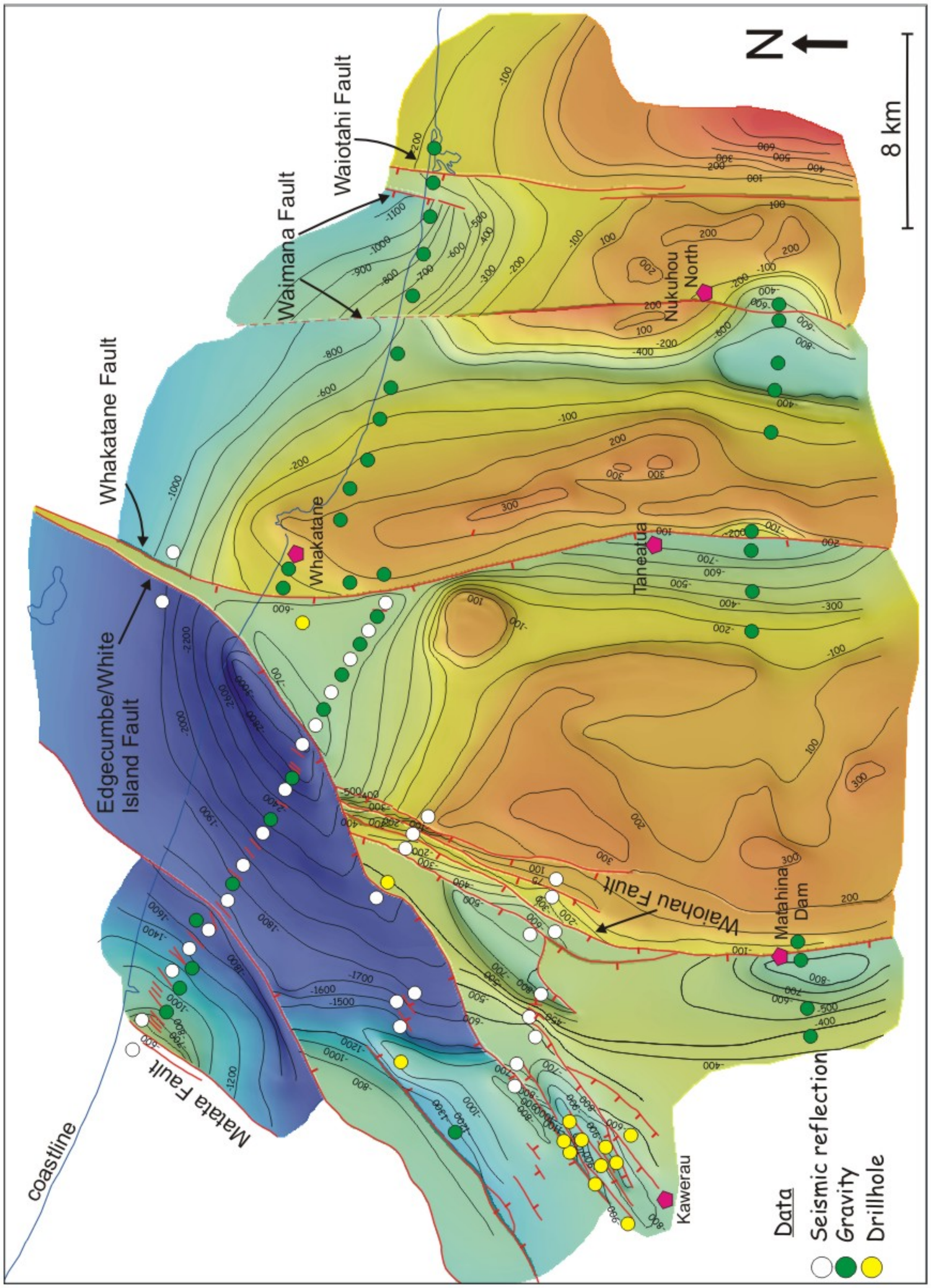

Fig. 6.8 Structure contour map for the top of greywacke basement in the region where the NIFS and Taupo Rift intersect (for location see Fig. 6.1). Contours are in metres above or below sea level. Data are from seismic-reflection and gravity profiles, drilling and outcrop geology (contours above zero are primarily controlled by outcrop of basement). Offshore contours are estimated from offshore residual gravity anomalies (Stagpoole & Bibby, 1999). Locations of data used to construct the contours are shown. Warm and cold colours indicate high and low altitudes, respectively. The coastline and major townships are indicated.

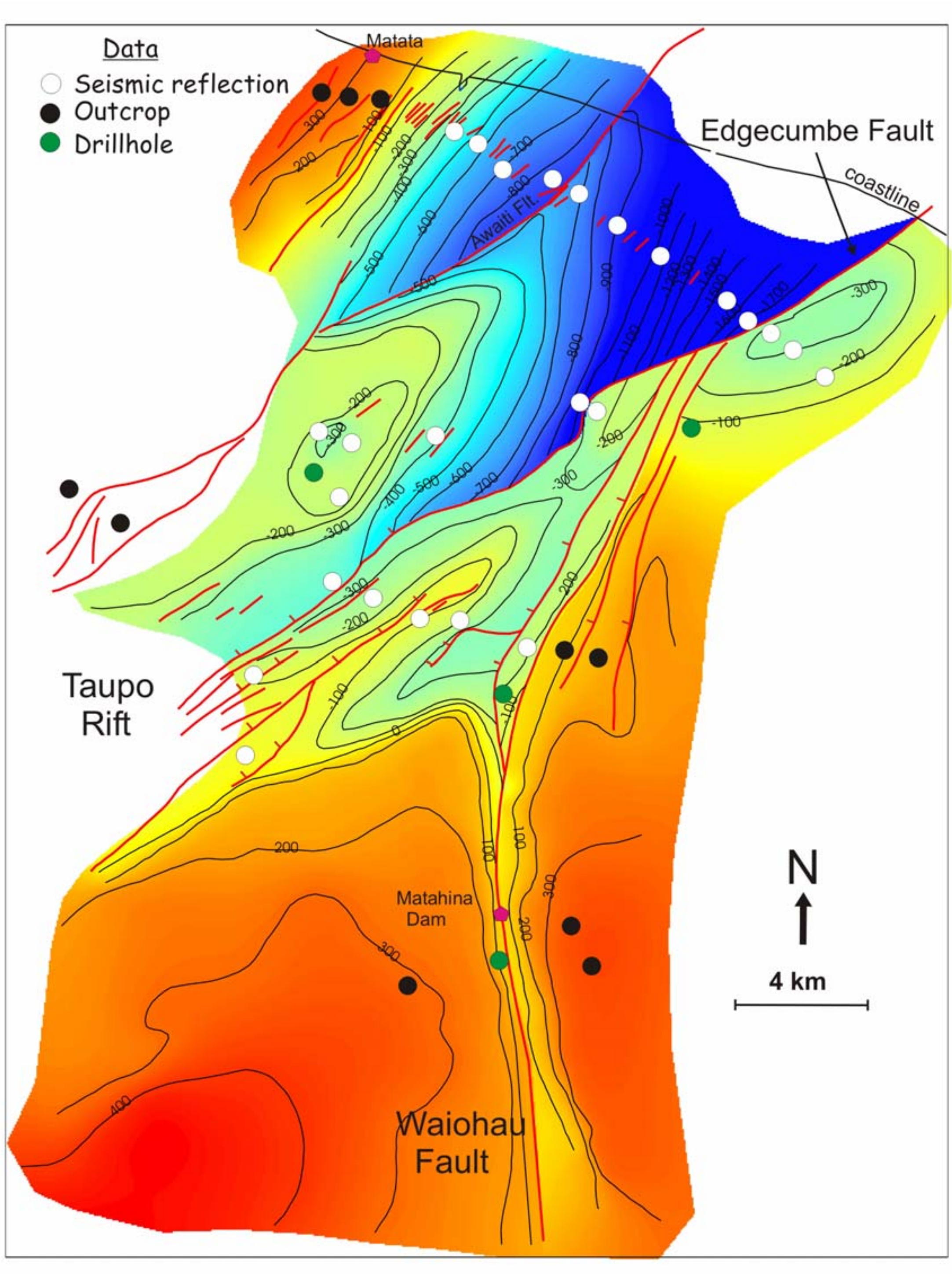

Fig. 6.9 Structure contour map for the top of Matahina ignimbrite proximal to the intersection of the Waiohau Fault - Taupo Rift (for location see Fig. 6.2). Contours are in metres above or below sea level. Data are from a combination of seismic-reflection profiles, drill-holes and outcrop geology. Locations of data used to construct the contours are shown. Warm and cold colours indicate high and low elevations, respectively. The coastline and major townships are indicated.

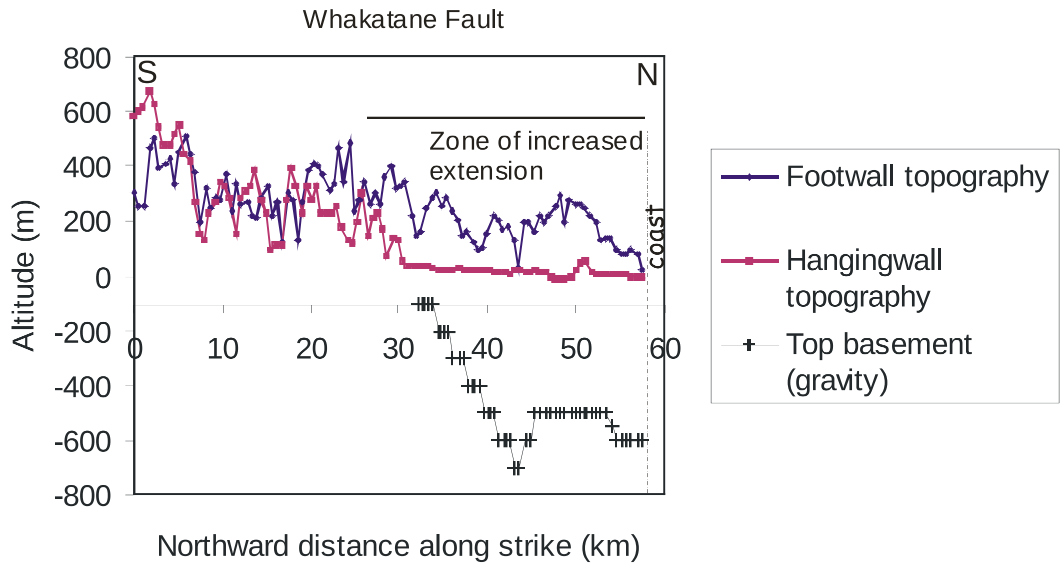

Fig. 6.10 Footwall and hangingwall separation diagram for topography and top basement along the onshore northernmost 60 km of the Whakatane Fault. The sub-surface location of top basement was estimated from gravity data (this study). Note that the separation between footwall and hangingwall increases northwards.

across the strike of the Whakatane, Waimana and Waiotahi faults (Davey et al., 1995; Lamarche et al., 2006; Chapter 2, this study). Late Quaternary throw rates on the Whakatane Fault, for example, increase northwards along a strike distance of c. 10 km, from c. 1.3 to 2.3 mm/yr (Fig. 6.11b), whereas, over the same distance, throw rates on the Waimana and Waiotahi faults increase from c. 0.2 and 0.1 to c. 1.1 and 0.7 mm/yr respectively (Davey et al., 1995; Lamarche et al., 2006; Chapter 2 in this study). The vertical slip rate at two different localities, c. 20 km apart, along the Waiohau Fault during the last 18 kyr appears to be uniform at 0.6 mm/yr (Chapter 2). The general compatibility of the displacements accrued on the top basement and younger landforms (i.e. 30 kyr BP) suggest that the slip vectors derived from the last 30 kyr may also apply for longer periods of time (e.g. 100's kyr).

To address the long-term regional kinematics of the intersection zone the total throw of the top-basement surface across the entire rift and the northern NIFS is estimated on seven regional transects (see Figs 6.1 & 6.2 for location of the

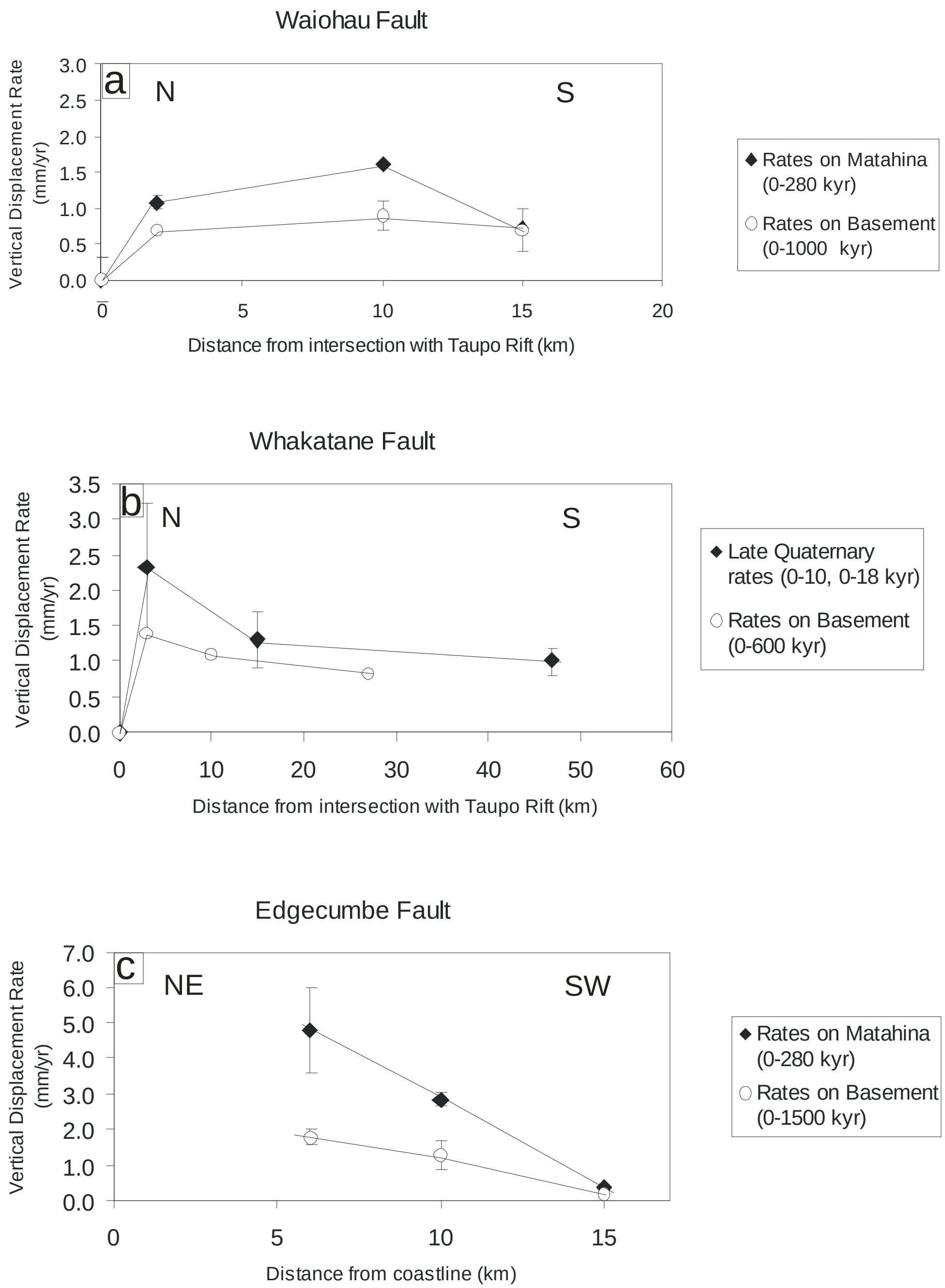

Fig. 6.11 Vertical displacement rates for the Waiohau (a), Whakatane (b) and Edgecumbe (c) faults plotted against southward distance from their intersection with the Taupo Rift (a & b) or the coastline (c). Throw rates on the Waiohau and Edgecumbe faults are calculated on top-basement (1000-1500 kyr) and Matahina ignimbrite (280 kyr) while on the Whakatane Fault on top-basement (0-600 kyr) and late Quaternary landforms (0-18 kyr). Note that for all faults, rates measured on younger horizons are higher. Note that for the Waiohau and Whakatane faults throw rates increase northwards as the intersection with the rift is approached while for the Edgecumbe Fault, throw rates decrease southwards (as its intersection with the Waiohau Fault is approached).

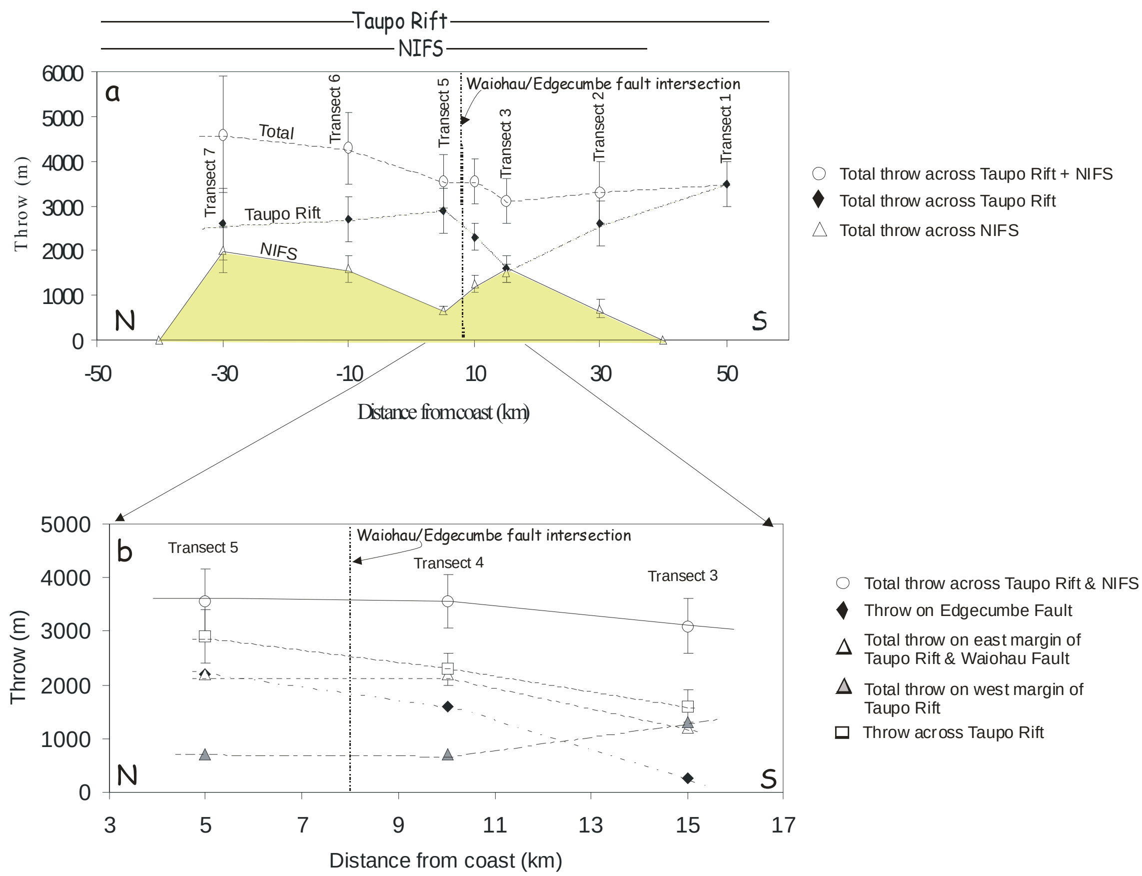

Fig. 6.12 (a) Throw accrued on the top basement across the Taupo Rift (black rhomb), the NIFS (open triangle) and their intersection (open circle) plotted against distance from the Bay of Plenty coastline. For location of the regional throw transects refer to Figs 6.1 & 6.2, **(b)** Throw on the top-basement across the NIFS and Taupo Rift at the latitude of the Edgecumbe-Waiohau fault intersection (transects 3-5 in Fig. 6.2). Data points for each transect derive from a combination of gravity and seismic-reflection profiles and outcrop geology (Rogan, 1982; Woodward, 1988; O'Connor, 1988; Nairn & Beanland, 1989; Davey, 1995; Woodward-Clyde, 1998; Lamarche, 2006; this study; Nicol et al., Unpublished data).

transects). The number of faults in the NIFS which are included within each transect decreases to the north as progressively more of these faults terminate against the Taupo Rift (Figs 6.1 & 6.2). Collectively these regional throw profiles suggest that the total throw accrued on top-basement surface across the intersection of the two fault systems increases gradually northwards, from 3500 m to 4600 m, over a distance of c. 80 km (transects 1-7 in Figs 6.1 & 6.2) (Fig. 6.12a). This increase in cumulative throw is mainly due to an increase of throw on the faults in the NIFS (i.e. from zero to 2000 m), while the throw accommodated by the rift decreases (i.e.

from 3500 m to 2600 m). Therefore, a significant amount of the throw accommodated by the rift south of the intersection zone, is distributed outside the rift and accommodated by the NIFS in the region where the two fault systems intersect. North of the northernmost NIFS-Taupo Rift intersection, it is expected that the total throw within the rift will increase, as displacement is transferred into the rift from the NIFS. The northward increase in cumulative throw across the intersection zone is consistent with the results of GPS modelling (Wallace et al., 2004). The interrelation of throws between the rift and the NIFS supports the view that these fault systems are kinematically coherent. This view is further supported by the approximately equal and opposite changes of the throw in NIFS and Taupo Rift across the intersection of the Waiohau and Edgecumbe faults (see next section for further discussion).

6.4 Displacements and geometries at the Waiohau-Edgecumbe fault intersection

The kinematic relationships between the NIFS and the Taupo Rift are examined across the intersection of the Waiohau and Edgecumbe faults, the only such intersection exposed onshore (Figs 6.2 & 6.3). The Waiohau Fault (NIFS) intersects, and terminates against, the rift-bounding Edgecumbe Fault c. 8 km south of the Bay of Plenty coast (Figs 6.2 & 6.3). The active Edgecumbe Fault bounds the eastern margin of the Taupo Rift near the Bay of Plenty coast (Fig. 6.1) and accommodated the largest (Mw 6.6) historic earthquake (i.e. during the last c. 160 years) in the rift in March 1987 (Fig. 6.3) (Beanland et al., 1989). The Edgecumbe Fault is at least 20 km in length onshore while offshore, it is referred to as the White Island Fault which is > 30 km long (Fig. 6.2).

The resolution of seismic-reflection and gravity data proximal to the Edgecumbe / Waiohau fault intersection constrains the geometries and kinematics of faults in this region (Fig. 6.12b). Proximal to this junction (< 10 km), the Waiohau Fault swings its strike from N-S to NE-SW, to become parallel to the strike of the Edgecumbe Fault, and bifurcates into four sub-parallel splays (Fig.

6.3). Each of these splays accommodates a throw on the top-basement surface that increases northwards as its intersection with the Edgecumbe Fault is approached. Similarly, the throw on the top-basement across the Edgecumbe Fault decreases southwards across the intersection with the Waiohau Fault, at a near-linear rate, from c. 2200 m near the coast (Figs 6.3, 6.4a, 6.5 & 6.8), to < 100 m (Fig. 6.8) 20 km south of the coast (Woodward, 1988; O'Connor, 1988; Nicol et al., Unpubl. data). Approximately 600 m of this decrease in throw occurs across the intersection between the Edgecumbe and the Waiohau faults (c. 8 km south of the coast) and may indicate displacement transfer between the two faults (Fig 6.12b).

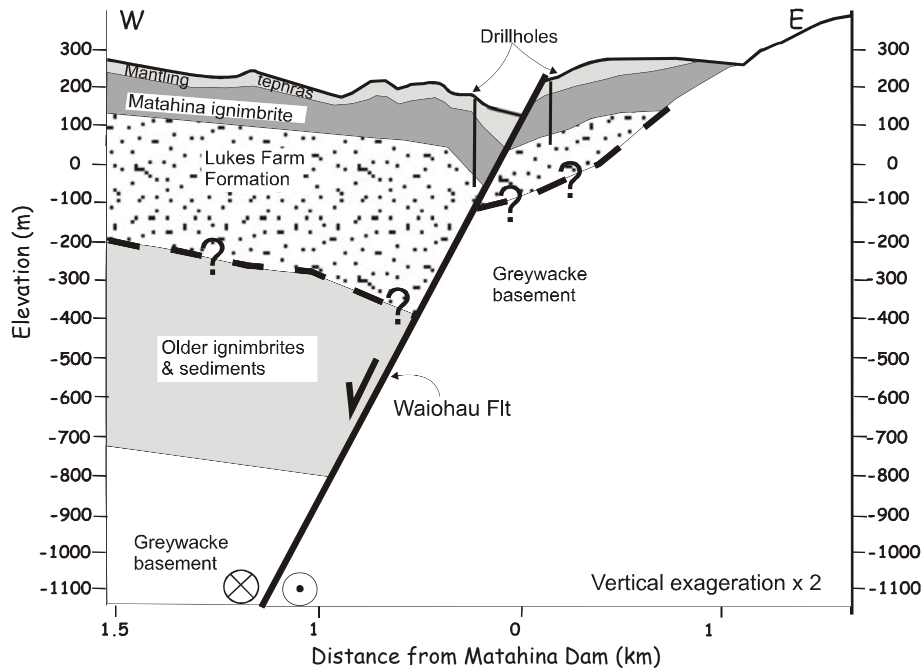

Fig. 6.13 Cross section showing the geology proximal to the Matahina Dam and across the Waiohau Fault. Cross section was constructed from gravity (this study), seismic (Woodward-Clyde, 1998), drill-hole (Woodward-Clyde, 1998) and outcrop information (Nairn, 2002).

Fault displacements on the top of the Matahina ignimbrite provide an additional control on the kinematics of the Waiohau – Edgecumbe fault intersection. On the Waiohau Fault, c. 15 km south of its intersection with the Edgecumbe Fault, the throw is c. 200 m (Figs 6.9 & 6.13) (Woodward-Clyde, 1998), while 10 and < 5 km south of the intersection the throws are c. 450 and 300 m, respectively (Figs 6.6, 6.7 & 6.11) (Woodward, 1988; O'Connor, 1988). This northward increase in displacement measurement is consistent with that on the top basement and suggests a northward increase in the post-280 kyr throw rates on the Waiohau Fault from c. 0.8 to 1.6 mm/yr over < 5 km (Figs 6.11a). The southward decrease of throw on the Edgecumbe Fault since the emplacement of the Matahina ignimbrite (280 kyr BP) is also broadly similar to changes in relative throws on top basement, decreasing southwards at a near-constant rate from c. 1350±350 m to < 100 m across its intersection with the Waiohau Fault (Figs 6.5 & 6.9) (Woodward, 1988; O'Connor, 1988; Nicol et al., Unpubl. data). This decrease in throw corresponds to a southward decrease in estimated post-280 kyr throw rates along the Edgecumbe Fault from c. 4.8 mm/yr, near the coast, to 0.4 mm/yr, c. 15 km south of the coast (Fig. 6.11c).

The sum of displacement for the top-Matahina ignimbrite and the top-basement horizons on the Waiohau and Edgecumbe faults immediately to the south of their intersection is approximately equal to displacement on the Edgecumbe Fault alone, immediately north of their junction (Fig. 6.14a). The relations between displacements on the two faults suggest that they interact, with displacements being transferred from the Waiohau Fault to the Edgecumbe Fault.

Throw on the Edgecumbe Fault is also influenced by the accumulation of displacements on other faults within the rift. The southward decrease in the throw on the Edgecumbe Fault arises not only because some of this throw is accommodated by the Waiohau Fault, but also because displacement is transferred from the Edgecumbe Fault to the fault on the west margin of the rift, which increases in throw on top-basement southwards, from c. 700 to 1200 m (Fig. 6.12b). This displacement transfer is associated with a change in the polarity of the rift, which is dominated by a west dipping eastern marginal fault in the north (i.e. near the coast) and an east dipping west marginal fault in the south (i.e. 15 km south of the coast). The aggregated throw for the rift and the Waiohau Fault across the intersection of the two fault systems along transects 3-5 remains approximately constant due to the fault interaction and associated displacement transfer (Fig. 6.12b). The near constant throw across the rift and on the Waiohau Fault in the area where it intersects with the Edgecumbe Fault suggests that all of these faults are kinematically interdependent.

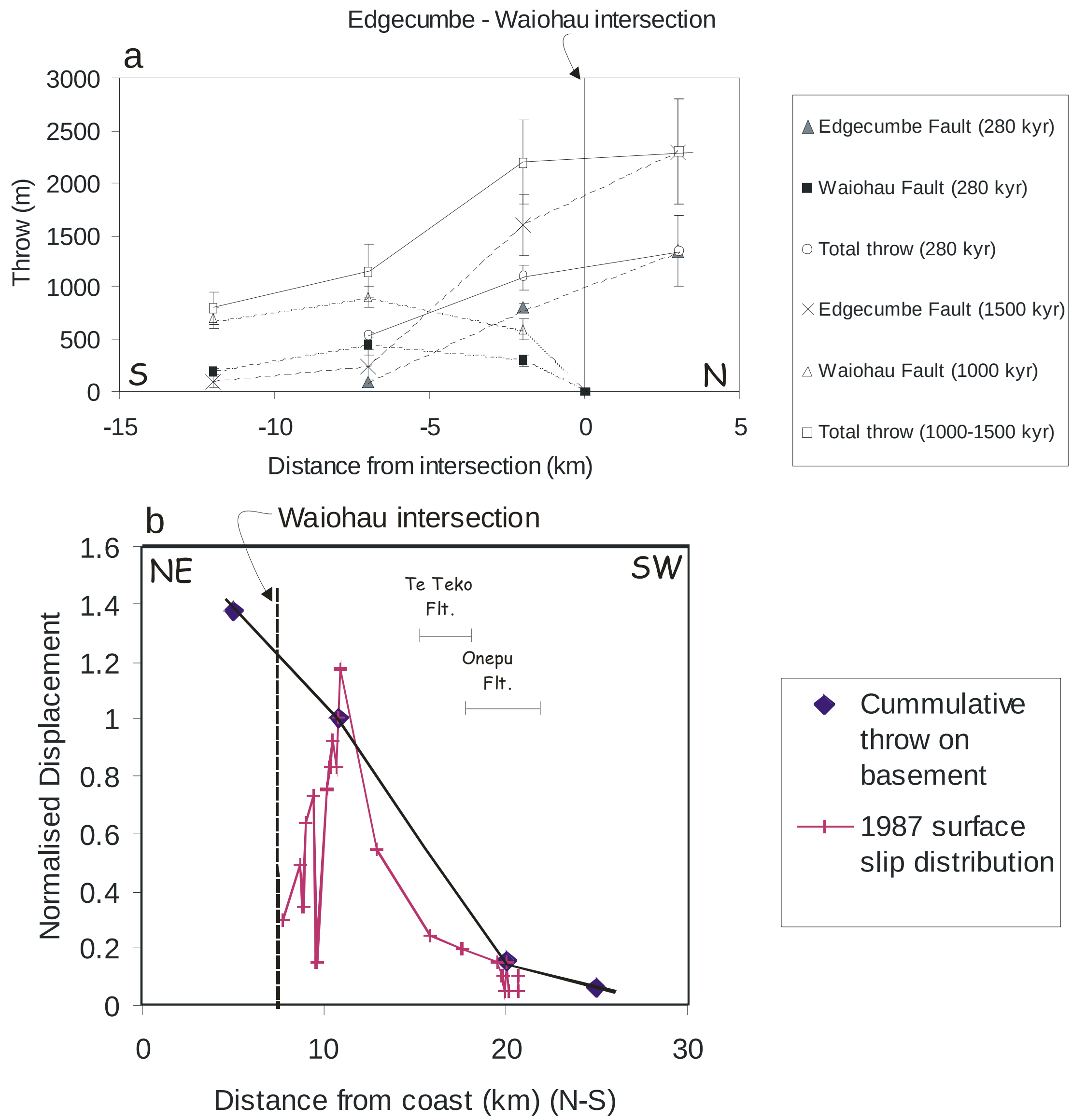

Fig. 6.14 (a) Plot shows the accumulation of throw for two different time intervals on the Waiohau (0-280 and 0-1000 kyr) and Edgecumbe (0-280 and 0-1500 kyr) faults across their intersection. **(b)** Normalised throws accrued on top basement for the Edgecumbe Fault during the last 1500 kyr, and the slip distribution at the surface for Mw 6.6 1987 Edgecumbe earthquake, plotted against distance along the fault from the Bay of Plenty coastline.

Further constraints on the kinematics of the intersection between the Waiohau and Edgecumbe faults are provided by the surface slip profile for the 1987 Mw 6.6 Edgecumbe earthquake. Geological and seismological data indicate that the fault rupture propagated southwards for a strike distance of c. 14 km (Beanland et al., 1989; Anderson & Webb, 1989) (Figs 6.3, 6.14b). Structural mapping conducted in this study, suggests that the rupture initiated at the intersection of the Waiohau and Edgecumbe faults and propagated to the southern tip of the fault (Fig. 6.3). Normalised displacements for the top-basement surface on the section of fault that ruptured in 1987 are comparable to slip during the Edgecumbe earthquake from the location of maximum earthquake slip southwards (Fig. 6.14b) (this study).

The proximity of the northern tip of the 1987 rupture to the Edgecumbe-Waiohau fault intersection suggests that rupture initiation at this locality may have been controlled by changes in the local stresses and/or in the Edgecumbe Fault geometry induced by the Waiohau Fault. The similarity in the shape of normalised displacement profiles for the 1987 earthquake and for the top-basement along the southern c. 14 km of the fault may indicate that many large magnitude earthquakes on the southern segment of the Edgecumbe Fault carried slip profiles comparable to the 1987 Edgecumbe earthquake (Fig. 6.14b).

In addition to Edgecumbe type earthquakes, the long-term displacement profile is probably the result of earthquakes that have mainly ruptured the Edgecumbe Fault at localities to the north of its intersection with the Waiohau Fault. Furthermore, recurrence intervals on the Waiohau Fault (3.6±1.2 kyr) are a factor of 4 to 8 times longer than those on the Edgecumbe Fault (c. 0.6 kyr) and, therefore, it seems unlikely that slip on the Edgecumbe Fault always triggers movements on the Waiohau Fault (or visa versa) (Chapter 4). Therefore, the interdependent displacements of the Edgecumbe and Waiohau faults probably arise partly due to earthquakes that do not rupture through the fault intersection. It is speculated that the interdependence of fault displacements occurs because earthquakes locally increase or decrease static stress which enhance or depress, respectively, the probability of future earthquakes on faults at the intersection.

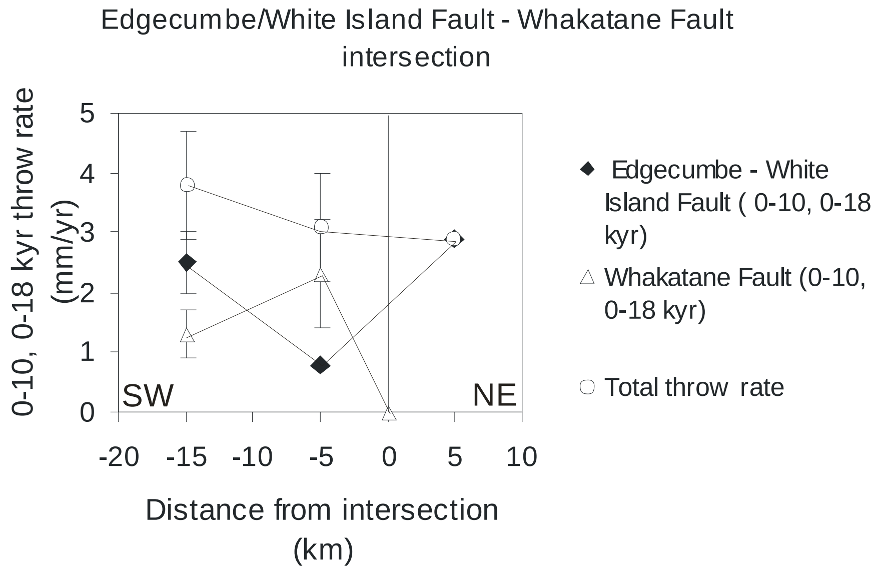

Fig. 6.15 Late Quaternary (0-18 kyr) throw rates for the Whakatane and Edgecumbe-White Island faults across their intersection plotted against distance from their intersection.

The kinematic coherence between individual NIFS and Taupo Rift fault intersections can be further demonstrated by comparing the results from the Waiohau-Edgecumbe fault intersection with those of the Whakatane-White Island fault intersection further north (the latter is the offshore extension of the Edgecumbe Fault) (Figs 6.2 & 6.15). The ≤ 10 kyr throw rate on the Edgecumbe-White Island Fault appears to decrease northwards, from c. 2.5±0.5 mm/yr onshore (Beanland et al., 1989) to c. 0.65±0.15 mm/yr offshore, proximal to its intersection with the Whakatane Fault (Fig. 6.15), while north of the intersection the throw rate on the White-Island Fault increases again to c. 2.9 mm/yr (Lamarche et al., 2006). The late Quaternary (0-18 kyr) throw rate on the Whakatane Fault increases northwards, from c. 1.3±0.4 mm/yr onshore (Chapter 2) to c. 2.3±0.9 mm/yr offshore (Lamarche et al., 2006) proximal to its termination against the White Island Fault (Fig. 6.15). Therefore, as is the case for across the intersection of the Edgecumbe and Waiohau faults, the sum of throw on the White Island and Whakatane faults is maintained across their intersection. A similar local decrease on the throw on the rift-bounding White-Island Fault it is anticipated to also occur further north, where it is intersected by the Waimana and Waiotahi faults.

6.5 Temporal stability of fault kinematics

In this section, the temporal stability of fault kinematics is examined by comparing vertical displacement rates on individual faults over time periods ranging from <10 kyr to 1500 kyr.

The slowest displacement rates are generally those calculated from the top-basement surface (Figs 6.16 & 6.17). In Figure 6.17 vertical displacement rates for the Edgecumbe, Whakatane, and Waiohau (0-280 kyr) faults plot clearly below the line of 1:1 slope suggesting that rates have been higher on these faults in the last ≤ 280 kyr than prior to this time. The increase in vertical displacement rates on the Edgecumbe Fault from 1.8±0.9 mm/yr averaged since 1500 kyr to 4.8±1.2 mm/yr for the last 280 kyr is consistent with an overall acceleration of rifting over that latter period (Figs 6.16 & 6.17). This suggestion is supported by Figure 6.18 which shows the spatial and temporal distribution of throw within the northernmost 15 km of the onshore Taupo Rift (transects 3 & 5 in Fig. 6.2). The throw rate across the entire rift appears to have increased from c. 1 to c. 3 mm/yr (transect 3 in Fig. 6.2) and from c. 2 to c. 5 mm/yr (transect 5 in Fig. 6.2) during the last 1500 and 280 kyr, respectively (Fig. 6.18).

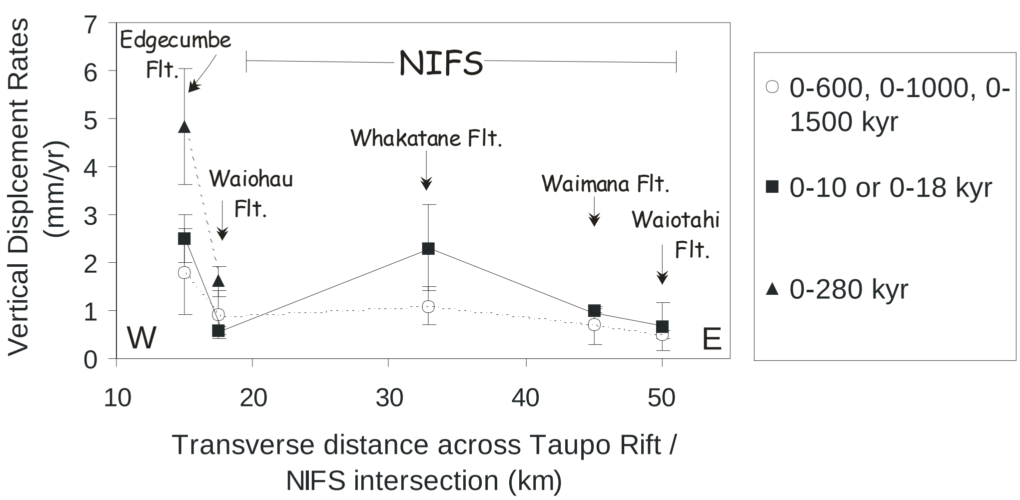

Fig. 6.16 Vertical displacement rates, for each of the faults in the NIFS and for the Edgecumbe Fault, plotted against transverse (W-E) distance across the fault systems. Rates are calculated over 0-10, 0-18, 0-280, 0-600, 0-1000 and 0-1500 time intervals.

Davey et al. (1995) recognised a similar acceleration of displacement rates within the active portion of the rift offshore and suggested that this was due to an eastward migration of the locus of NW-SE extension. I suggest that this migration of extension also produced an increase in the throw rate on the Whakatane and Waiohau faults during the last 280 kyr where they accommodate a component of rift-related extension (Figs 6.16 & 6.17). In contrast, vertical displacement rates on the Waimana and Waiotahi faults do not appear to have changed significantly over the last 600 kyr. The uniformity of these rates may arise because the sections of the Waimana and Waiotahi faults sampled accrued little, if any, extension in association with rifting. Therefore, throw rates on these faults were not significantly influenced by eastward migration of the rift.

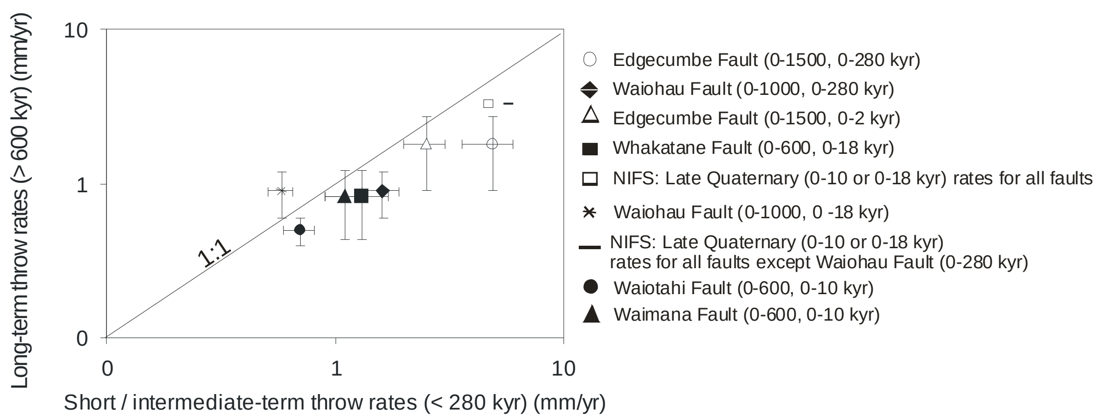

Fig. 6.17 Log-log plot showing the relations between vertical displacement rates calculated for the top-basement and rates derived for the 280 kyr or younger horizons for each of the fault in the NIFS and for the Edgecumbe Fault in the Taupo Rift.

Rift acceleration near the intersection zone is constrained here between 600 kyr (the youngest age of the deposits above the top-basement unconformity) and 280 kyr (top of Matahina ignimbrite). As the rates of throw vary significantly for the last 280 and 600 kyr, it is inferred that the increase occurred closer to 280 kyr than 600 kyr. Villamor & Berryman (2006) also suggest that significant faulting within the southern Taupo Rift, some 200 km south of the present study area, initiated post 400 kyr BP. Collectively data from this study, Davey et al. (1995) and Villamor &

Berryman (2006) indicate a change in geometries and the kinematics of the Taupo Rift along its entire length about 300 kyr ago. Villamor & Berryman (2006) attributed this change in rifting to a major rhyolitic eruptive episode c. 340 kyr ago, however, it is possible that this eruption, and a period of major ignimbrite eruptions (240-340 kyr ago), could have been induced by a migration and focusing of the active rift (Davey et al., 1995; this study).

Late Quaternary (c. 30 kyr BP) slip vectors in the NIFS adjacent to the rift have approximately equal amounts of dip-slip and strike-slip (Chapter 2). Acceleration of rifting in the last 300 kyr was associated with increase in the rates of dip-slip in the NIFS. Therefore, the kinematics of the NIFS near its intersection with the rift changed about 300 kyr ago. This kinematic change may have taken one of two forms: If rates of strike-slip in the northern NIFS prior to 300 kyr were comparable to today's rates (i.e. c. 4 mm/yr), then the increase in dip-slip rates would have resulted in steepening of the slip vectors on the faults in the NIFS. Alternatively, if both the dip-slip and the strike-slip rates increased at 300 kyr, then slip in the NIFS began to accumulate more rapidly at this time but the pitch of the slip vectors of these faults need not have changed. Strike-slip rates in the northern NIFS prior to 30 kyr are poorly constrained. Displaced basement terranes near Wellington, however, indicate a minimum dextral displacement of 10-12 km (Begg & Mazengarb, 1996). At the current rates of about 7 mm/yr (Wellington Fault, Van Dissen & Berryman, 1996) this displacement could be produced in about 1500 kyr. These data are consistent with the view that the present strike-slip rates in the NIFS predate 300 kyr. Therefore, the preferred model is that late Quaternary slip vectors and displacement rates in the NIFS and the displacement rates in the rift were established approximately 300 kyr ago, when rifting accelerated and the dip-slip rate on the faults in the NIFS increased. The kinematics of the rift-NIFS intersection is, in geological timescale, relatively short lived. The late Quaternary geometries of the intersection may also have been relatively short lived, with possible low pitch slip vectors prior to 300 kyr, which are likely to have resulted in offset of the south-eastern margin of the rift.

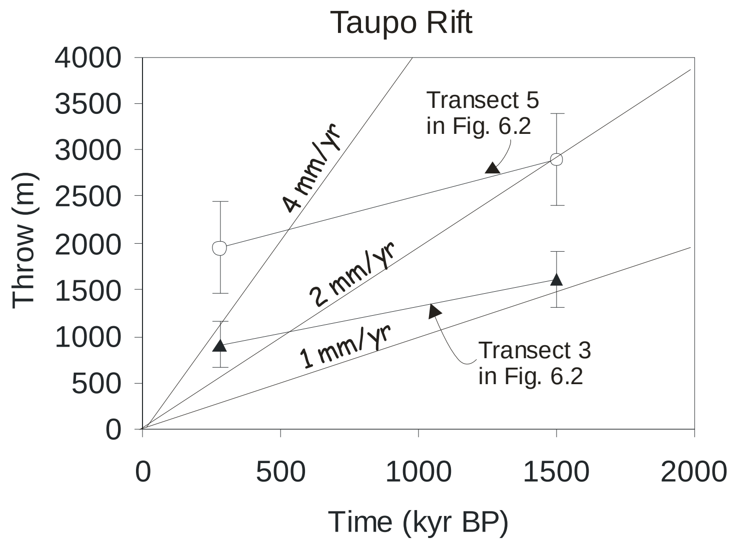

Fig. 6.18 Accumulation of throw through time across the Taupo Rift at two different transects (see Fig. 6.2 for location of transects).

6.6 Conclusions

Seismic-reflection, gravity, drill-hole and outcrop data were used to chart accumulation of vertical displacements proximal to the intersection of the strike-slip NIFS and the Taupo Rift, New Zealand, over timescales of thousand to millions of years.

The intersection of the two fault systems has operated as a kinematically coherent fault array for at least the last 1000 kyr. Short-intermediate (≤ 280 kyr) and long-term (≥ 600 kyr) throws generally increase northwards along each of the faults in the NIFS approaching the Taupo Rift. Throws for the same time interval on the fault that bounds the eastern margin of the rift, decrease where it is intersected by the strike-slip faults of the NIFS. The faults in the NIFS and the rift interact at their intersection zone with the total throw across each strike-slip and normal fault intersection constant and equal to the throw accommodated by the rift alone away from the intersection zone. Interdependence of fault-throws (or throw rates) between the NIFS and Taupo Rift suggests that the intersection of the two fault systems has functioned coherently for much of the last 600-1500 kyr. Throw rates in the rift and for those faults in the NIFS that accommodate NW-SE distributed extension were up to a factor of 3 higher during the last 300 kyr than average rates since 1500 kyr. This acceleration of rifting may be due to the eastward migration of rifting axis about 300 kyr. The rates of faulting and the orientations (pitch and azimuth) of slip vectors that typify the kinematics of the intersection zone in the late Quaternary (e.g. 30 kyr), may have been stable for only the last c. 300 kyr.

Acknowledgments: I am grateful to Vaughan Stagpoole and Derek Woodward for assistance in the process of the gravity data, to Dave Heron for 'building' the Digital Elevation Model for the structural contour maps presented in Figures 6.8 & 6.9 and to A. Nicol, T. Little and J. Begg for helpful reviews.

References

Anderson, H. & Webb, T., 1989. The rupture process of the Edgecumbe earthquake, New Zealand. New Zealand Journal of Geology and Geophysics, 32, 43-53.

Bailey, R.A. & Carr, R.G., 1994. Physical geology and eruptive history of the Matahina Ignimbrite, Taupo Volcanic Zone, North Island, New Zealand. New Zealand Journal of Geology and Geophysics, 36, 319-344.

Ballance, P.F., 1975. Evolution of the India-Pacific plate boundary in North Island, New Zealand. Bulletin of the Australian Society of Exploration Geophysicists, 6, 2/3, 58-59.

Beanland, S., Berryman, K.R. and Blick, G.H., 1989. Geological investigations of the 1987 Edgecumbe earthquake. New Zealand Journal of Geology and Geophysics, 32, 73-91.

Beanland, S., 1995. The North Island Dextral Fault Belt, Hikurangi Subduction margin, New Zealand. PhD Thesis, Victoria University of Wellington, New Zealand.

Beavan, R.J. & Haines, J., 2001. Contemporary horizontal velocity and strain rate fields of the Pacific-Australian plate boundary zone through New Zealand. Journal of Geophysical Research, 106, B1, 741-770.

Begg, J.G. & Mazengarb, C., 1996. Geology of the Wellington area, scale 1:50 000. Institute of Geological & Nuclear Sciences geological map 22. 1 sheet + 128 p. Lower Hutt, New Zealand: Institute of Geological and Nuclear Sciences Limited.

Beu, A.G., 2004. Marine mollusca of oxygen isotope stages of the last 2 million years in New Zealand. Part 1: Revised generic positions and recognition of warm-water and cool-water migrants. Journal of the Royal Society of New Zealand, 32, 2, 111-265.

Davey, F.J., Henrys, S. and Lodolo, E., 1995. Asymmetric rifting in a continental back-arc environment, North Island, New Zealand. Journal of Volcanology and Geothermal Research, 68, 209-238.

De Mets, C.R., Gordon, R.G., Argus, D. and Stein, S. 1994. Effect of recent revisions to the geomagnetic reversal time scale on estimates of current plate motions. Geophysical Research Letters, 21, 2191-2194.

Fleming, C.A., 1955. Castlecliffian fossils from Ohope Beach, Whakatane (N69). New Zealand Journal of Science and Technology Section, B36, 511-522.

Healy, J., Schofield, J.C. and Thompson, B.N., 1964. Sheet 5, Rotorua (1st Ed.). Geological map of New Zealand. 1:250, 000. Department of Scientific and Industrial Research, Wellington, New Zealand.

Lamarche, G., Barnes, P.M. and Bull, J.M., 2006 (in press). Faulting and extension rate over the last 20,000 years in the offshore Whakatane Graben, New Zealand continental shelf, Tectonics.

Mortimer, N. 1994. Origin of the Torlesse Terrane and coeval rocks, North Island, New Zealand. International Geology Review, 36, 891-910.

Nairn, I.A. & Beanland, S., 1989. Geological setting of the 1987 Edgecumbe earthquake, New Zealand. New Zealand Journal of Geology and Geophysics, 32, 1, 1-13.

Nairn, I.A., 2002. Geology of the Okataina Volcanic Center, scale 1:50 000. Institute of Geological & Nuclear Sciences, Lower Hutt, New Zealand: Institute of Geological & Nuclear Sciences Limited.

Nicol, A., Walsh, J.J., Berryman, K. & Villamor, P., 2006. Interdependence of fault displacement rates and paleoearthquakes in an active rift. Geology, 34, 10, 865-869.

Nicol, A. & Wallace, L., in review. Temporal stability of deformation rates estimated by comparison of geological and geodetic data, Hikurangi Margin, New Zealand. Submitted in Tectonics.

O'Connor, R.M., 1988. Seismic reflection investigations near the Matahina Dam. DSIR contract report, No. 84.

Rait, G., Chanier, F. and Waters, D.W., 1991. Landward- and seaward-directed thrusting accompanying the onset of subduction beneath New Zealand. Geology, 19, 230-233.

Rogan, M., 1982. A geophysical study of the Taupo Volcanic Zone, New Zealand. Journal of Geophysical Research, 87, B5, 4073-4088.

Rowland, J.V. & Sibson, R.H., 2001. Extensional fault kinematics within the Taupo Volcanic Zone, New Zealand: soft-linked segmentation of a continental rift system. New Zealand Journal of Geology and Geophysics, 44, 271-283.

Stagpoole V. M. & Bibby H. M., 1999. Residual gravity anomaly map of the Taupo Volcanic Zone, New Zealand, 1:250 000. Institute of Geological & Nuclear Sciences. Geophysical map 13. Institute of Geological and Nuclear Sciences, Lower Hutt.

Taylor, S.K., Bull, J.M., Lamarche, G. and Barnes, P.M., 2004. Normal fault growth and linkage in the Whakatane Graben, New Zealand, during the last 1.3 Myr. Journal of Geophysical Research, 109, B2, B02408, doi:10.1029/2003JB002412.

Van Dissen, R.J. & Berryman, K.R. 1996. Surface rupture earthquakes over the last ~1000 years in the Wellington region, New Zealand, and implications for ground shaking hazard. Journal of Geophysical Research, 101, B3, 5999-6019.

Villamor, P. & Berryman, K.R., 2001. A Late Pleistocene extension rate in the Taupo Volcanic Zone, New Zealand, derived from fault slip data. New Zealand Journal of Geology and Geophysics, 44, 243-269.

Villamor P. & Berryman, K. R., 2006. Evolution of the southern termination of the Taupo Rift, New Zealand. New Zealand Journal of Geology & Geophysics, 49, 23–37.

Wallace, L.M., Beaven, J., McCaffrey, R. and Darby, D., 2004. Subduction zone coupling and tectonic block rotations in the North Island, New Zealand. Journal of Geophysical Research, 109, B12, 2406, doi:10.1029/2004JB003241.

Walsh, J.J. & Watterson, J., 1991. Geometric and kinematic coherence and scale effects in normal fault systems. In Roberts A.M., Yielding, G. and Freeman, B. (eds), 1991. The geometry of normal faults. Geological Society of London, Special Publication, 56, 193-203.

Wilson, C.J.N., Houghton, B.F., McWilliams, M.O., Lamphere, M.A., Weaver, S.D. and Briggs, R.M., 1995. Volcanic and structural evolution of Taupo Volcanic Zone, New Zealand: a review. Journal of Volcanology and Geothermal Research, 68,1-28.

Woodward, D.J., 1988. Seismic reflection survey on the Rangitaiki plains, eastern Bay of Plenty. Geophysics Division research report 218. Department of Scientific and Industrial Research, New Zealand.

Woodward, D.J., 1989. Geological structure of the Rangitaiki Plains near Edgecumbe, New Zealand, from seismic data. New Zealand Journal of Geology and Geophysics, 32, 15-16.

Woodward-Clyde, 1998. Matahina Dam strengthening project. Geological completion report to Electricity Corporation of New Zealand.

CHAPTER SEVEN

CONCLUSIONS

What is the purpose of this struggle? Why did you fight behind phenomena to track down the Invisible? What was the purpose of all your warlike, your erotic march?

"I felt all the powers of the universe whirling within me. Before they crush me, I wanted to open my eyes for a moment, to see them all. I set my life no other purpose."

N. Kazantzakis, 1883-1957

(from Askitiki)

1. The faults within the northern North Island Fault System (NIFS) are active. The late Quaternary kinematics (c. 30 kyr) of the northern NIFS changes northward along strike. With increasing proximity to the Taupo Rift the slip vector pitch on each of the faults in the NIFS steepens gradually by up to 60°, while the mean fault-dip decreases by c. 30°. Due to these changes, the kinematics of the NIFS transition from strike-slip to oblique-normal faulting adjacent to the rift. Adjustments in the kinematics of the NIFS reflect the gradual accommodation of the NW-SE extension that is distributed outside the main boundary of the Taupo Rift (Chapter 2).

2. Sub-parallel slip vectors, fault-dips and fault-strikes on the faults at each intersection between the NIFS and the Taupo Rift allows the strike-slip component of slip to be transferred into the rift, accounting for a significant amount of the northeastward increase of extension along the rift (Chapter 2).

3. The steepening of the pitch of slip vectors towards the northern tip of the NIFS allows the kinematics and geometry of faulting to change efficiently, from strike-slip to normal faulting, providing an alternative mechanism to vertical axis rotations for terminating large strike-slip faults (Chapter 2).

4. Kinematic sub-parallelism at the intersection of two synchronously intersecting fault systems reduces potential space problems and facilitates the development of a three-plate quasi-stable configuration in the intersection region, which, in many cases, would not be possible for rigid-block translations (Chapter 3).

5. Analyses of other global examples of synchronous strike-slip and normal faults that intersect to form two or three plate configurations, within either oceanic or continental crust, suggest that displacement is similarly transferred between the fault systems. Thus, the NIFS - Taupo Rift fault intersection provides a key case study for a process that is global in its extent and applicability (Chapter 3).

6. The dimensions of the area over which the fault-strike and slip vectors of two intersecting strike-slip and normal faults change, is principally controlled by the extent to which displacements on the dominant of the two intersecting fault systems are confined to a single slip surface or distributed across a zone. The dimensions of the transition zone are larger for continental crust than for oceanic crust because oceanic crust is thinner, fault geometries in oceanic crust are simpler two-plate configurations and the slip vectors of the component intersecting fault systems are sub-parallel (Chapter 3).

7. At least 80% of all surface rupturing earthquakes on the Waiohau and Whakatane faults in the NIFS during the last 10-13 kyr appear to have terminated within the kinematic transition zone from strike-slip to oblique-normal slip. Fault segmentation results in a reduction of the magnitudes of large surface rupturing earthquakes in the northern NIFS from 7. 4 – 7.6 (Stirling et al., 2002) to 7 (Chapter 4).

8. The late Quaternary (c. 30 kyr) change in the kinematics of the northern NIFS along strike, from dominantly strike-slip to oblique-normal faulting, arises due to a combination of rupture arrest within the transition zone and along strike variations in the orientation of the coseismic slip vectors (Chapter 5).

9. Arrest of earthquake ruptures within the northern NIFS may arise due to a 20-30° shallowing of fault-dips across the kinematic transition zone while spatial variations in the pitch of the earthquake vectors, may reflect a regional northward steepening of the principal stress axis (σ_1) with increasing proximity to the Taupo Rift (Chapter 5).

10. The pattern of individual earthquake-ruptures most likely to have produced the late Quaternary (c. 30 kyr) displacement vectors comprises oblique-slip events, north of the kinematic transition zone, with variable slip-vector pitches during individual earthquakes. Strike-slip earthquakes, which are principally confined to the NIFS south of the transition zone, will also have variable coseismic slip vector orientations when they intermittently rupture through this zone (Chapter 5)

11. Interdependence of fault-throws (or throw rates) between the NIFS and Taupo Rift suggests that the intersection of the two fault systems has functioned coherently for much of the last 0.6-1.5 Myr (Chapter 6).

12. The majority of faults in the NIFS accommodated higher throw rates since 300 kyr than during the last 0.6-1.5 Myr. This increase in throw rates occurred in response to a regional acceleration of rifting and associated extension within the Taupo Rift (Chapter 6).

13. The rates of faulting and the orientations (pitch and azimuth) of slip vectors that typify the kinematics of the northern NIFS proximal to its intersection with the Taupo Rift, in the late Quaternary (e.g. 30 kyr), may have only been stable for the last c. 300 kyr (Chapter 6).

APPENDIX I

S I T E S   A N D   F A U L T   M E A S U R M E N T S

Organisation and analysis of data

In this Appendix locations, site descriptions and maps for sites of detailed fault studies are presented. Fault maps are presented on a fault by fault basis, starting from the westernmost fault (i.e. Waiohau Fault) and advancing eastwards (i.e. Whakatane Fault) while studied sites on each fault are presented from south to north. For each site, the exact location and a brief description are given. For additional information see Table 2.1 in Chapter 2. Microtopographic maps of displaced geomorphic landforms are presented where available. These maps show topographic contours in metres above mean sea level and were constructed using Real Time Kinematics Global Position System equipment (Leica SR530). Estimated errors are 5-6 and 2-3 cm for the height and location, respectively. On each map, piercing points (indicated by dashed lines) were identified and correlated across faults by constructing profiles parallel (and adjacent) to the fault in both footwall and hangingwall. The offset feature matched across the fault in each case is usually site-dependent. Where offsets are measured on stream-channels, the thalweg is often used as piercing point while on ridge-spurs either the ridge-crest or the flanks (or both) are matched across the fault. For offset terrace river risers, either the middle or the lower parts (the ‘rising’ section) of the risers may be matched across the fault. Where the displaced lineaments have been eroded or modified by deformation close to the fault, they have been projected as an inclined lineation to intersect the fault surface from both sides of the fault. Errors in slip estimates are chiefly due to projection uncertainties rather than measurement precision.

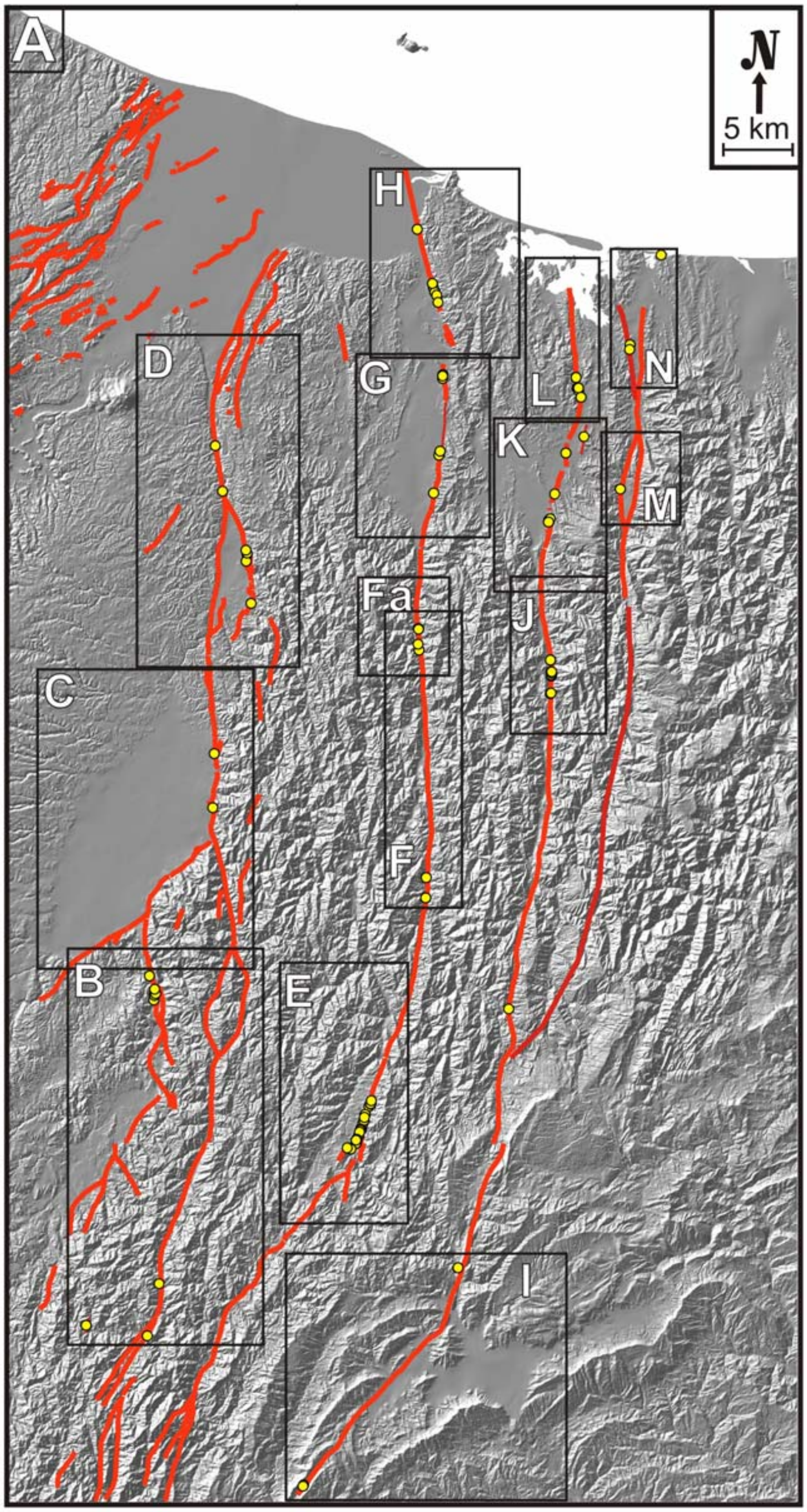

Map A: Index map shows the fault maps (B-N) presented in the Appendix I. Maps include active faults of the onshore northern North Island Fault System. Active faults are shown by red lines. Filled yellow circles indicate sites of detailed fault analysis.

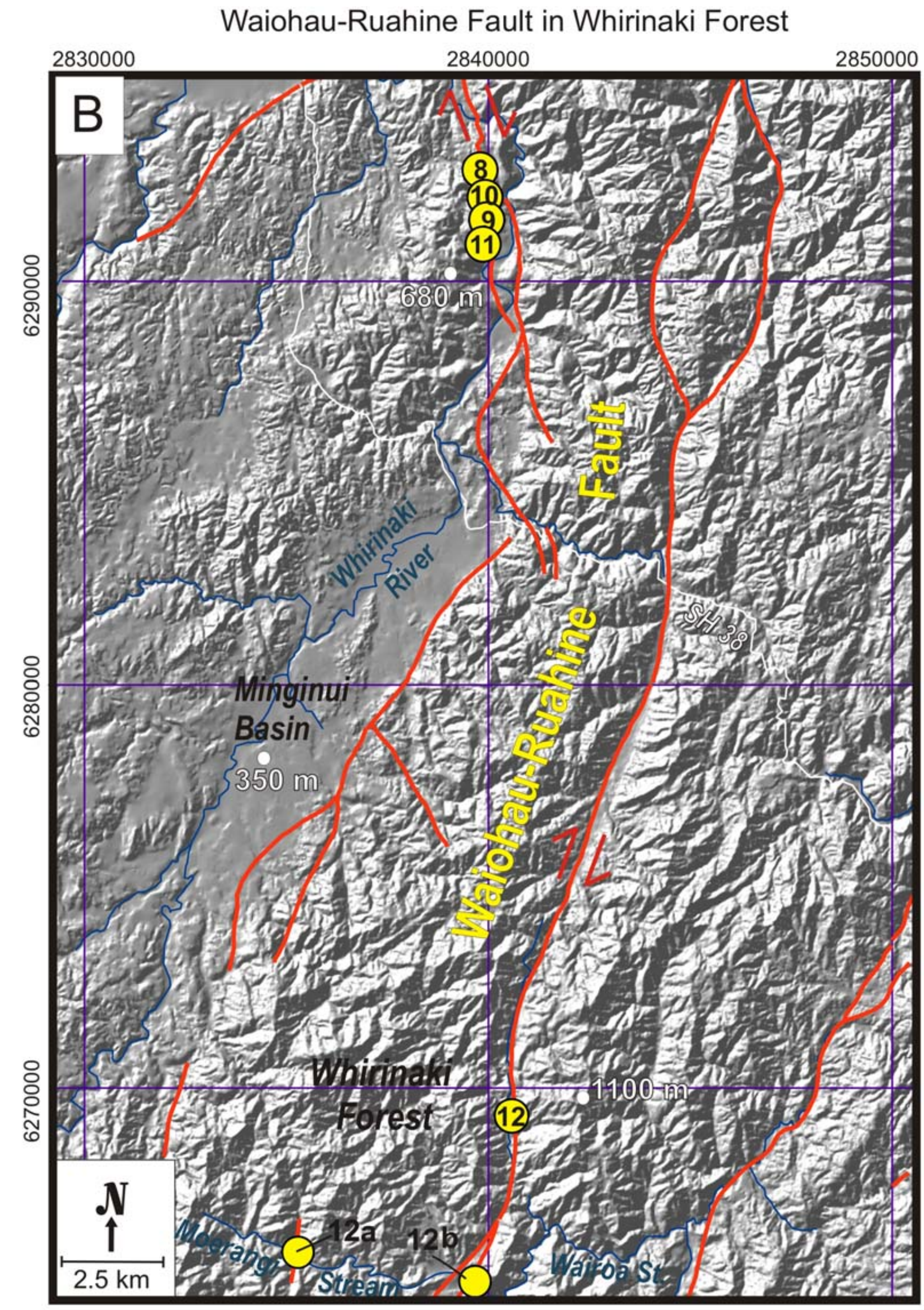

Map B: The Waiohau-Ruahine Fault in the Whirinaki Forest (red lines). Numbers in circles indicate studied sites (8-12b) (see also Table 2.1 in Chapter 2). White lines indicate main roads while blue lines show major rivers. Representative elevations are indicated (in meters).

WAIOHAU-RUAHINE FAULT

Site 12

Location: V18/404692

Brief description: Soft grey fault-gouge of centimeters to decimeter-wide bands was recorded. No slickenide striations were preserved.

Site 12a

Location: V18/349660

Brief description: Soft grey fault-gouge was recorded on a N-S striking fault in Moerangi stream.

Site 12b

Location: V18/396652

Brief description: At this locality the geomorphologic evidence of the fault is indirect. An antecedent stream of the Wairoa River has incised into greywacke bedrock (which has been uplifted by faulting) to form a narrow gorge (Map B). Greywacke bedrock is exposed to the east of the fault whereas to the west, bedrock is downthrown and mantled under young tephras of uncertain age.

Site 11

Location: V17/397928

Brief description: The fault displaces dextrally a spur by c. 24 m.

Site 10

Location: V17/402914

Brief description: The fault displaces dextrally a spur by c. 24 m.

Site 9

Location: V17/401913

Brief description: The fault displaces dextrally a spur by c. 38 m.

Site 8

Location: V17/401916

Brief description: The fault displaces dextrally a stream by c. 24 m.

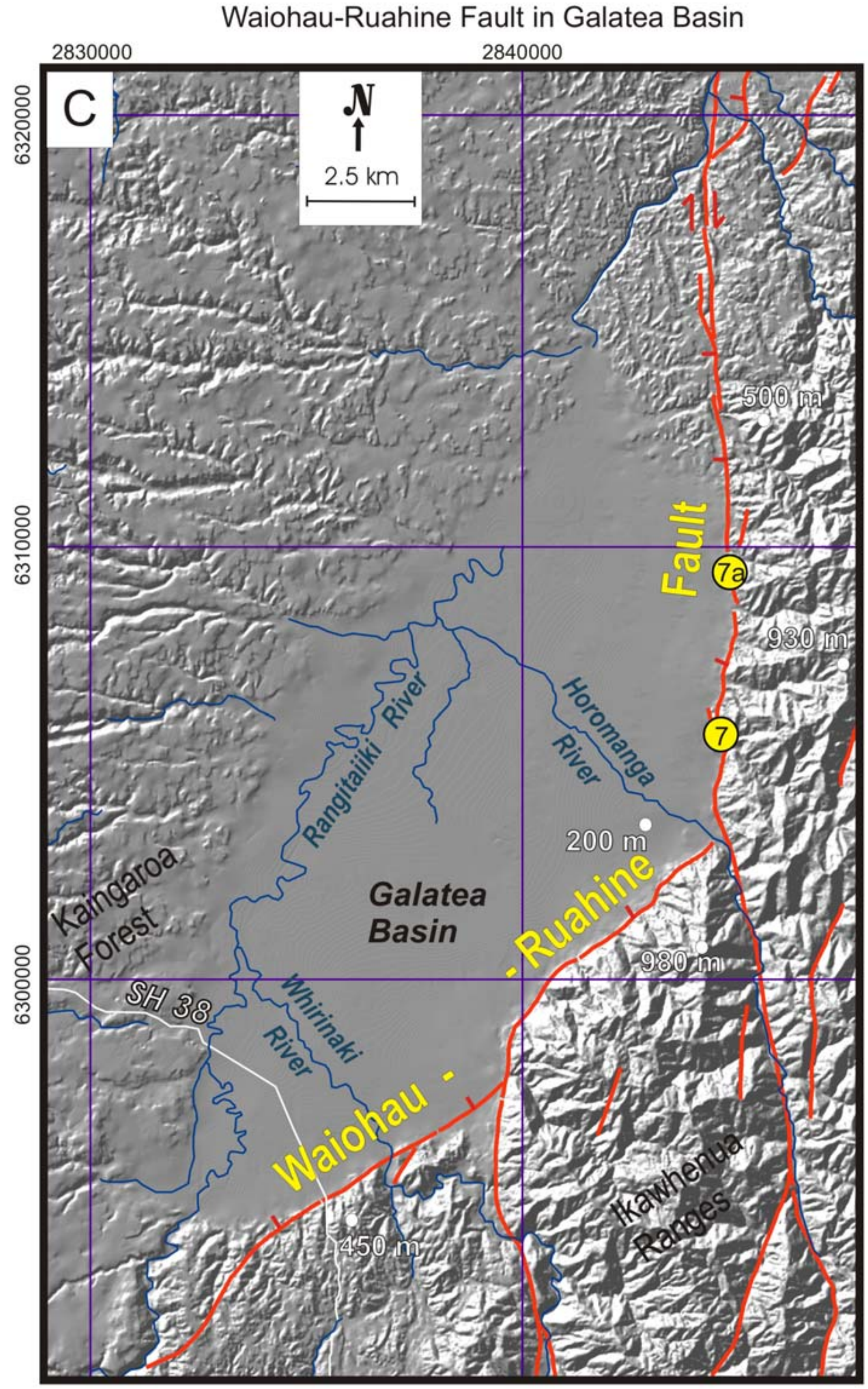

Map C: The Waiohau Fault in Galatea Basin (red lines). Numbers in circles indicate studied sites (7 and 7a) (see also Table 2.1 in Chapter 2). White lines indicate main roads while blue lines show major rivers. Representative elevations are indicated (in meters).

Figure 1: Panoramic views of the Ikawhenua Ranges in Galatea Basin. The principally dip-slip Waiohau-Ruahine Fault runs at the base of the ranges forming the triangular faceted spurs. View towards the southeast.

Site 7

Location: V17/446057

Brief description: The Troutebeck Trench was excavated here by Beanland (1989b). See Chapter 4, section 4.3.2 for details on the geomorphology of the site and data on the paleoearthquake activity.

Site 7a

Location: V17/447093

Brief description: A trench was excavated at this site by Beanland (1989b). Taupo (1.8 kyr BP) and Kaharoa (0.8 kyr BP) tephras were unfaulted. See Chapter 4, section 4.3.2 for further details.

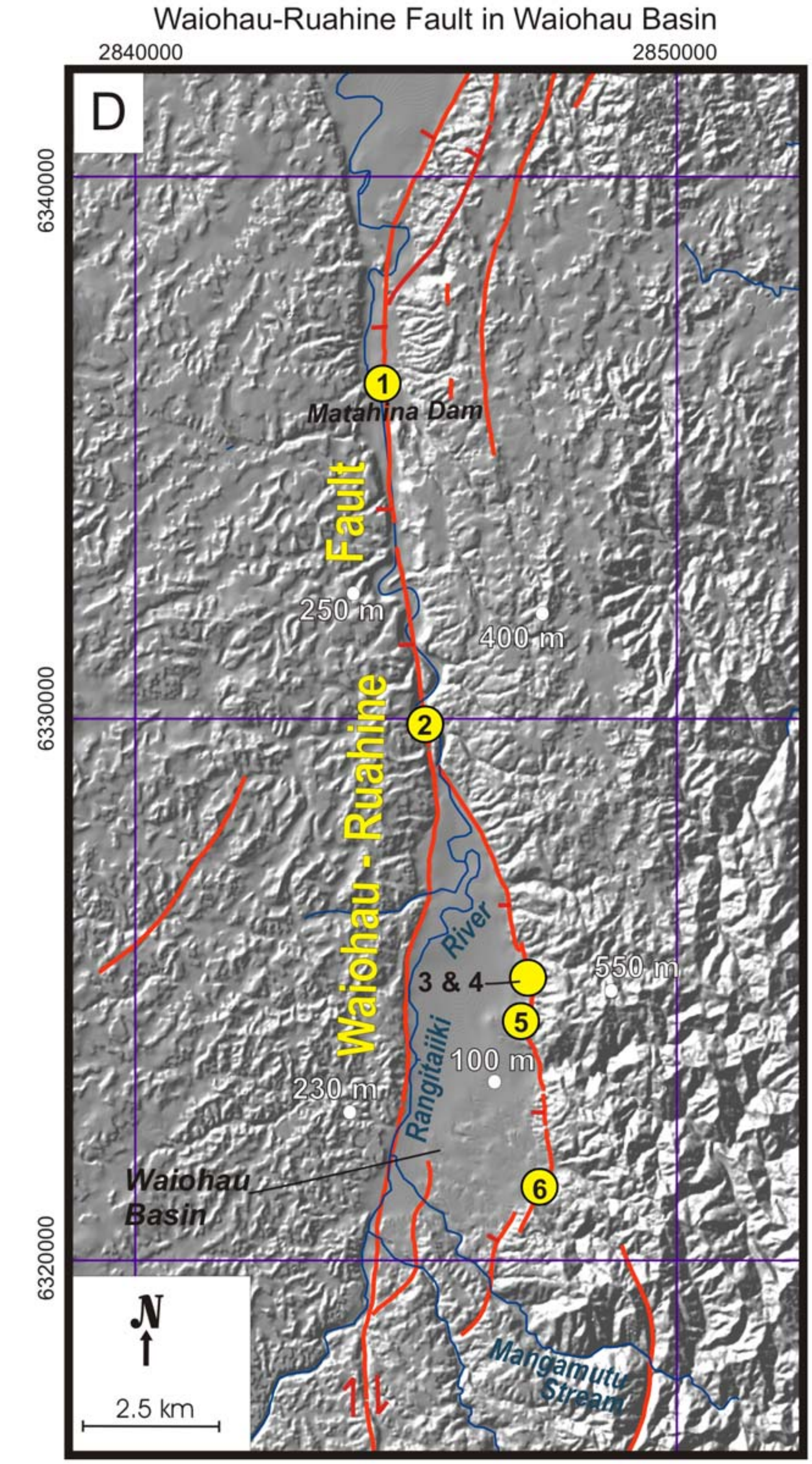

Map D: Waiohau Fault in Waiohau Basin (red lines). Numbers in circles indicate studied sites (1-6) (see also Table 2.1 in Chapter 2). Blue lines show major rivers. Representative elevations are indicated (in meters).

Site 6

Location: V16/475213

Brief description: The fault runs at the base of the low hills bounding the eastern margin of the Waiohau Basin. The trace is continuous for a strike distance of c. 200 m and forms triangular faceted scarps of 3-8 m height. No dextral displacement has been observed.

Site 5

Location: V16/471246

Brief description: An abandoned stream which is incised into an alluvial fan of uncertain age is obliquely displaced by the Waiohau Fault (3±2 m dextrally and 4±2 m vertically).

Site 4

Location: V16/472251

Brief description: A stream incised into a post 25 kyr old surface is obliquely displaced by the Waiohau Fault (8±1 m vertically and 3±1 m dextrally) (see Fig. 2.5c in Chapter 2 for a detailed microtopographic map of the site). The stratigraphy, and therefore the slip rate, at this site is constrained by data derived from the Cornes Trench which is located c. 100 m to the north of this offset stream.

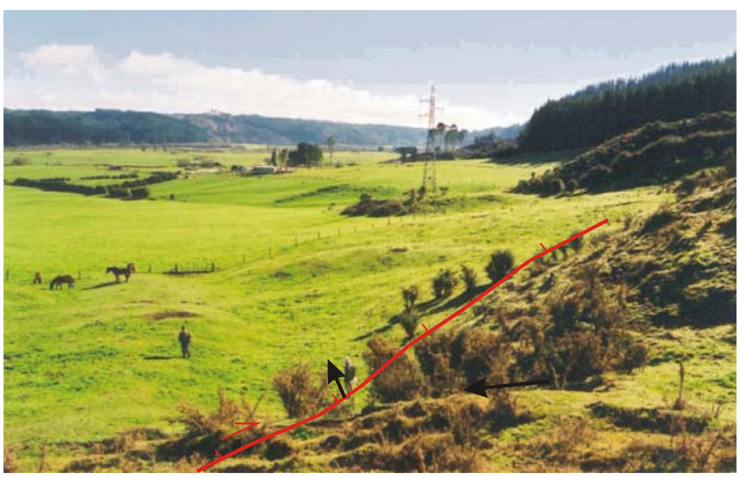

Figure 2: The Waiohau Fault at site 4 where it obliquely displaces a stream.

Site 3

Location: V16/472252

Brief description: Site of Cornes Trench excavated by Woodward-Clyde (1998). See Chapter 4, section 4.3.3 for details on the geomorphology of the site and data on the paleoearthquake activity.

Site 2

Location: V16/453298

Brief description: Tasman 1 Trench site, excavated by Woodward-Clyde (1998). See Chapter 4, section 4.3.3 for details on the geomorphology of the site and data on the paleoearthquake activity.

Site 1

Location: V16/453360

Brief description: Gravity data collected across the fault suggest that the Waiohau-Ruahine Fault has downthrown (to the west) the top of the greywacke basement by c. 700 m (Fig. 4b in Chapter 6). For details on the gravity survey see Chapter 6 and Appendix IV.

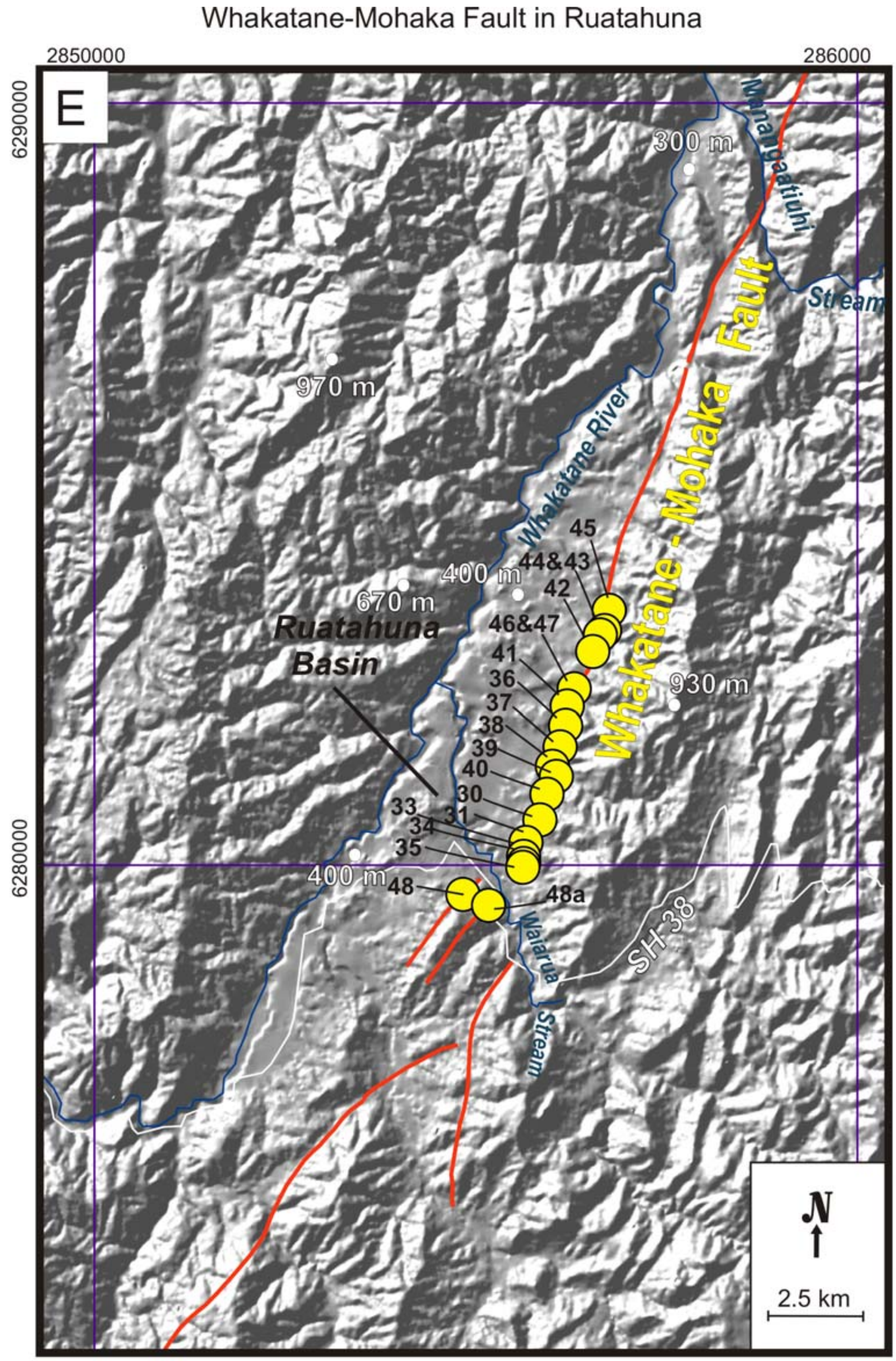

Map E: The Whakatane Fault at Ruatahuna Valley (red lines). Numbers in circles indicate studied sites (30-48) (see also Table 2.1 in Chapter 2). White lines indicate main roads while blue lines show major rivers. Representative elevations are indicated (in meters).

Figure 3: The Whakatane Fault (red line) in the Ruatahuna Valley. View towards the ESE, approximately normal to the NNE-SSW fault strike (photo by Lloyd Homer).

Site 48

Location: W17/551795

Brief description: The Whakatane Fault traverses the hills that bound the Ruatahuna Basin, forming uphill facing scarps (down to SE). Scarps are 2 - 3 m high and often block the drainage, forming swamps.

Figure 4: Whakatane Fault at site 48 (location marked by arrow) swings to a 050° strike and traverses the low ranges, forming uphill facing scarps. View towards the southwest.

Site 48a

Location: W17/554792

Brief description: Faulted contact between Miocene mudstone and Torlesse bedrock. The fault strikes 020° and dips to the west (apparent dip of c. 50° W). The Miocene rock consists of massive sandstone (dip 80°W) whereas the Torlesse consists of red/brown argillite (bedding: 50°/200° SW).

Figure 5: The Whakatane Fault is exposed on the road cut of State Highway 38 in Ruatahuna (Map E) where it forms the boundary between Miocene mudstone (greenish) and Cretaceous argillite (reddish). The apparent dip of the fault here is c. 50° W.

Site 35

Location: W17/555799

Brief description: Whakatane Fault offsets a spur by 17±7 m dextrally and 2±0.5 m vertically (Figs. 6a & 7).

Site 34

Location: W17/555799

Brief description: Whakatane Fault displaces a stream dextrally by 9.5±5 m (see Fig. 6a).

Site 33

Location: W17/555800

re 6: Microtopographic map constructed by Real Time Kinematics GPS y for a) the offset spur and stream at sites 34 & 35, respectively and, b) the t stream at site 33. Dotted lines indicate offset piercing points; the divergence otted lines [redacted] piercing point locations. n = number of graphic measurements.

Figure 7: At site 35 the Whakatane Fault displaces dextrally a spur by c. 13 m.

Site 31

Location: W17/555802

Brief description: Stream is displaced dextrally and vertically by 22±2 m and 2±0.5 m, respectively. The Thalassa and Helios trenches were excavated here (see Fig. 2.6 in Chapter 2 and Figs. 4.5a & b in Chapter 4).

Figure 8: The Whakatane Fault at sites 31/32 where it offsets dextrally a stream-channel. The locations of Thalassa and Helios trenches are indicated by the yellow and blue polygons, respectively.

Figure 9: The river terrace on which Thalassa, Helios and Armyra trenches were excavated (sites 30-32).

Site 30

Location: W17/556802

Brief description: Stream terrace margin offset by the Whakatane Fault. The dextral separation is 20±2 m and the vertical is 3±1 m. The uphill facing scarp (down to the east) forms a swamp. Armyra Trench (yellow box) was excavated at this locality across the fault and the margin of the swamp (Fig. 11 in this Appendix and Fig. 4.6 in Chapter 4).

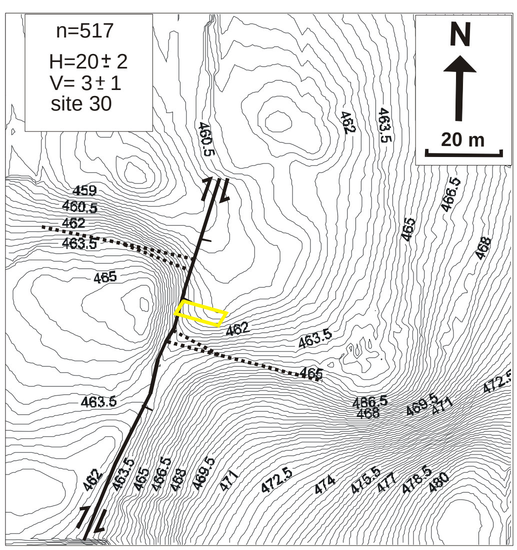

Figure 10: Microtopographic map of the offset stream terrace margin at site 30, constructed by RTK GPS survey. Dotted lines indicate offset piercing points; the divergence of dotted lines represents errors on the piercing point locations. n = number of topographic measurements.

Figure 11: The displaced stream terrace margin at site 30 where the Whakatane Fault forms an uphill facing scarp that blocks the drainage. The location of Armyra Trench is indicated by the yellow polygon. View towards the northwest.

Site 40

Location: W17/557805

Brief description: Stream is displaced dextrally by 14±1 m.

Site 39

Location: W17/558808

Brief description: Small spur is displaced dextrally and vertically by 5.5±1 and 1.2±0.3 m, respectively.

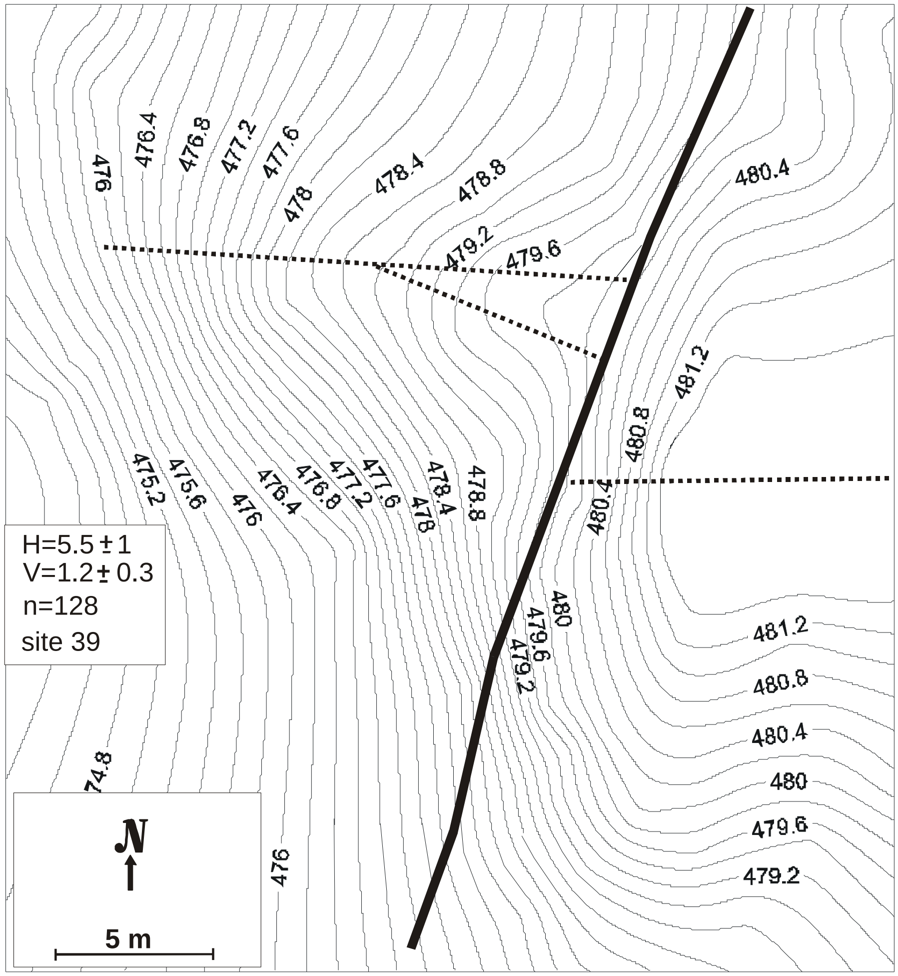

Figure 12: Microtopographic map of the offset spur at site 39, constructed by Real Time Kinematics GPS survey. Dotted lines indicate offset piercing points; the divergence of dotted lines represents errors on the piercing point locations. n = number of topographic measurements.

Site 38

Location: W17/558809

Brief description: Spur dextrally displaced by 15±5 m.

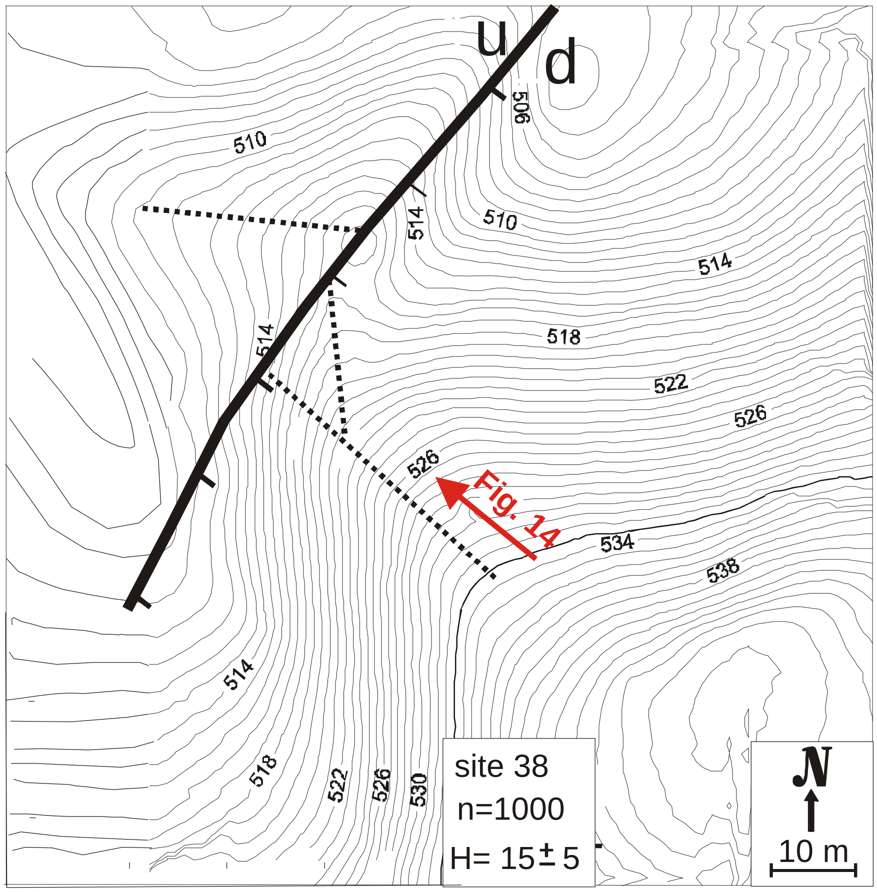

Figure 13: Microtopographic map of offset spur at site 38, constructed by Real Time Kinematics GPS survey. Dotted lines indicate offset piercing points; the divergence of dotted lines represents errors on the piercing point locations. n = number of topographic measurements.

Figure 14: Obliquely displaced spur at site 38 on the Whakatane Fault. View to the northwest.

Site 37

Location: W17/559810

Brief description: Whakatane Fault displaces a stream dextrally by 12±5 m.

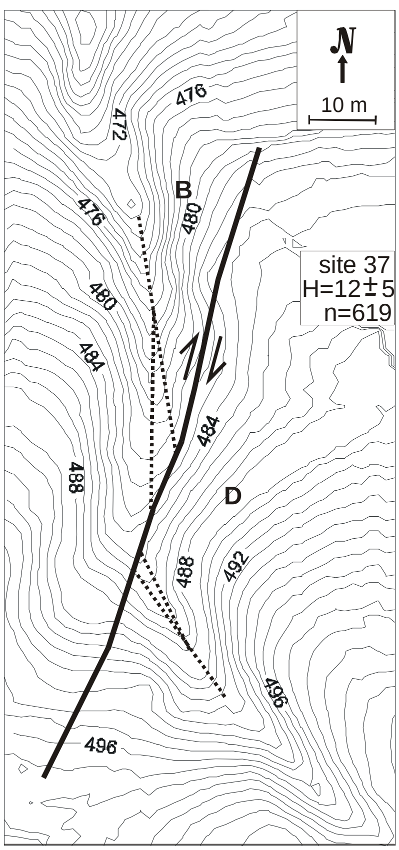

Figure 15: Microtopographic map of the offset stream at site 37, constructed by Real Time Kinematics GPS survey. Dotted lines indicate offset piercing points; the divergence of dotted lines represents errors on the piercing point locations. n = number of topographic measurements.

Site 36

Location: W17/559811

Brief description: Stream displaced dextrally and vertically by 15±2 and 2±0.5 m, respectively.

Site 41

Location: W17/561817

Brief description: Stream displaced dextrally by 11±5 m.

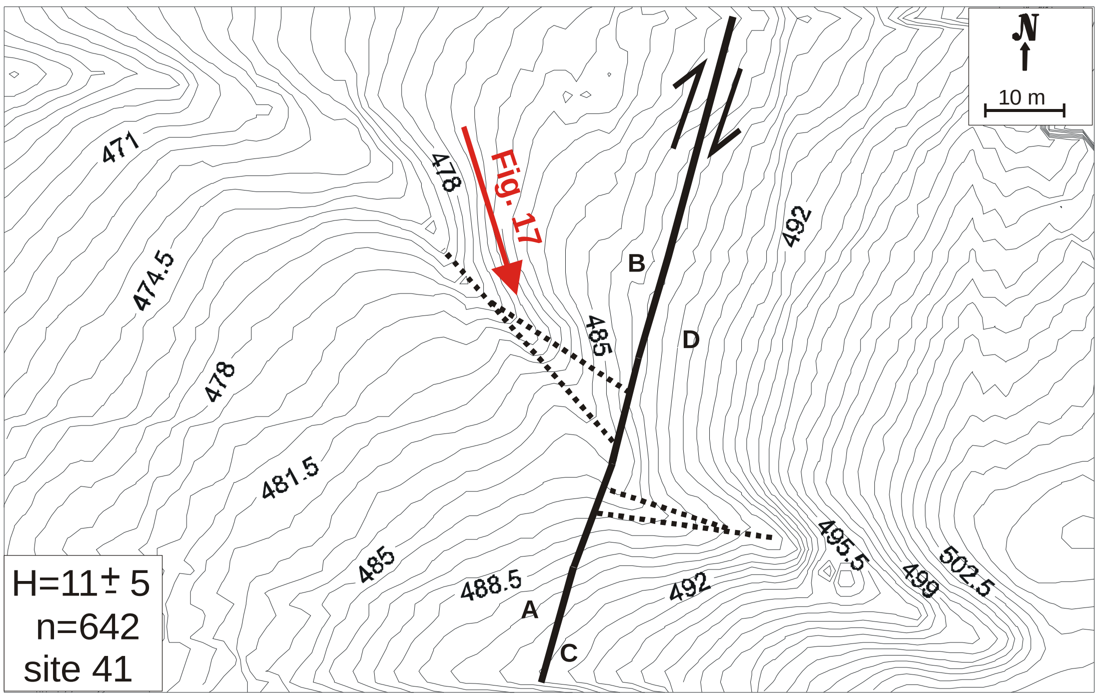

Figure 16: Microtopographic map of offset stream at site 41. Map is constructed by Real Time Kinematics GPS survey. Dotted lines indicate offset piercing points; the divergence of dotted lines represents errors on the piercing point locations. n = number of topographic measurements.

Figure 17: Whakatane Fault at site 41 displaces a stream dextrally by c. 11 m.

<u>Site 46</u>

Location: W17/562821

Brief description: Whakatane Fault traverses alluvial fan of uncertain age and forms a scarplet of 0.5±0.2 m height.

Figure 18: The west-dipping scarplet at site 46.

Site 47

Location: W17/562821

Brief description: Ancestral Opuhou stream appears to be beheaded and dextrally displaced, by 90±10 m, along the Whakatane Fault from the modern Opuhou stream (see Fig. 19).

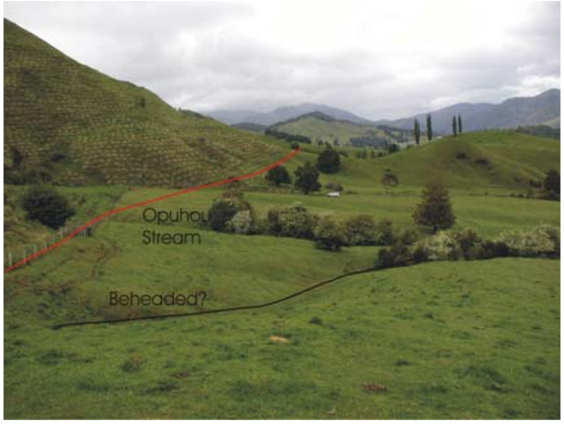

Figure 19: The Whakatane Fault at site 47 displaces the Opuhou stream by c. 90 m.

Site 42

Location: W17/565828

Brief description: Spur displaced dextrally and vertically by 15±8 and 2±1 m, respectively.

Figure 20: The Whakatane Fault at site 42 displaces dextrally a spur by c. 15 m. View to the south.

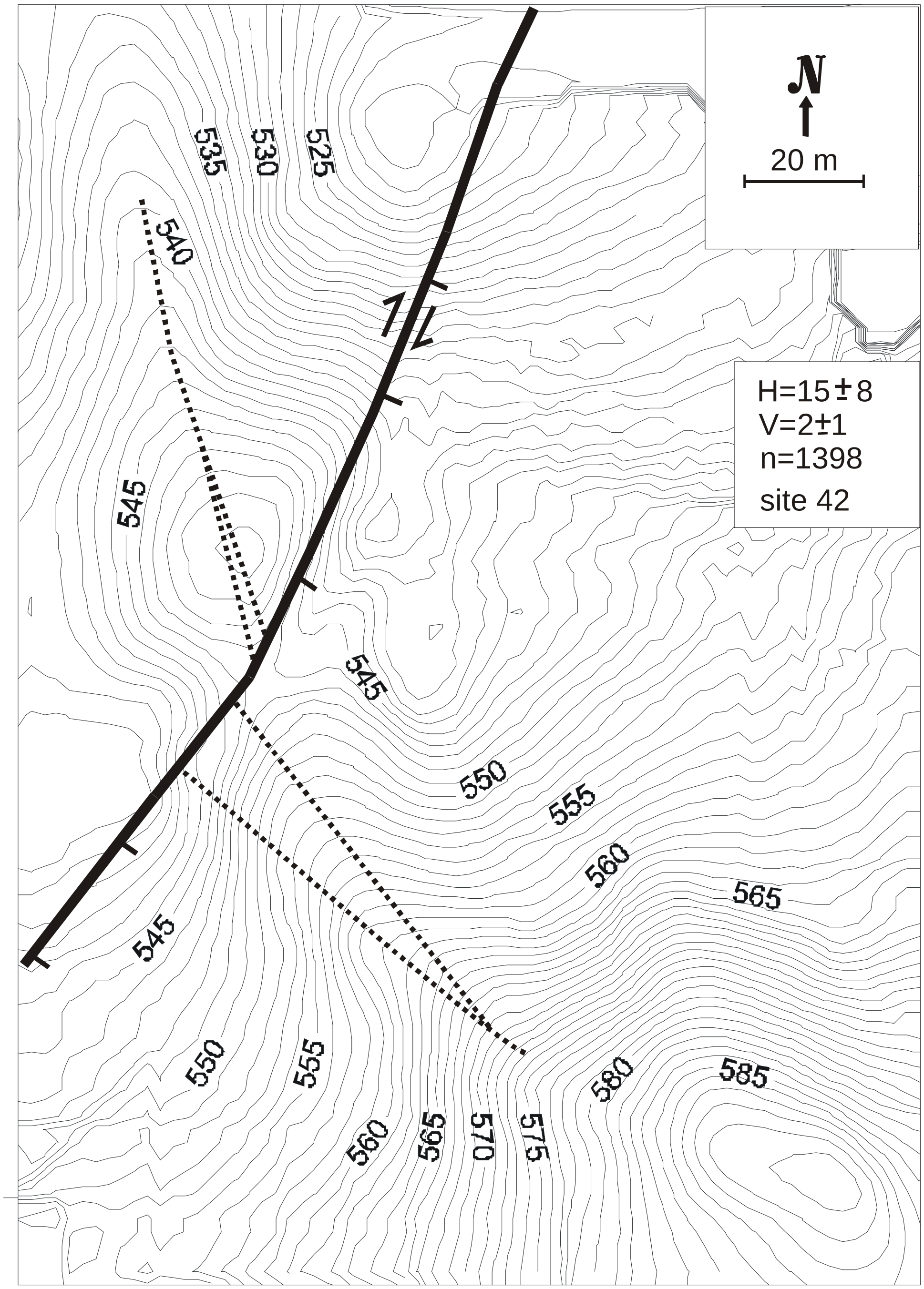

Figure 21: Microtopographic map of offset spur at site 42. Map is constructed by Real Time Kinematics GPS survey. Dotted lines indicate offset piercing points; the divergence of dotted lines represents errors on the piercing point locations. n = number of topographic measurements.

Site 44

Location: W17/566829

Brief description: Stream is displaced dextrally by 4.5±2.5 m.

Site 43

Location: W17/566829

Brief description: Whakatane Fault traverses alluvial fan and forms a scarp of 2±0.5 m height (see Fig. 22).

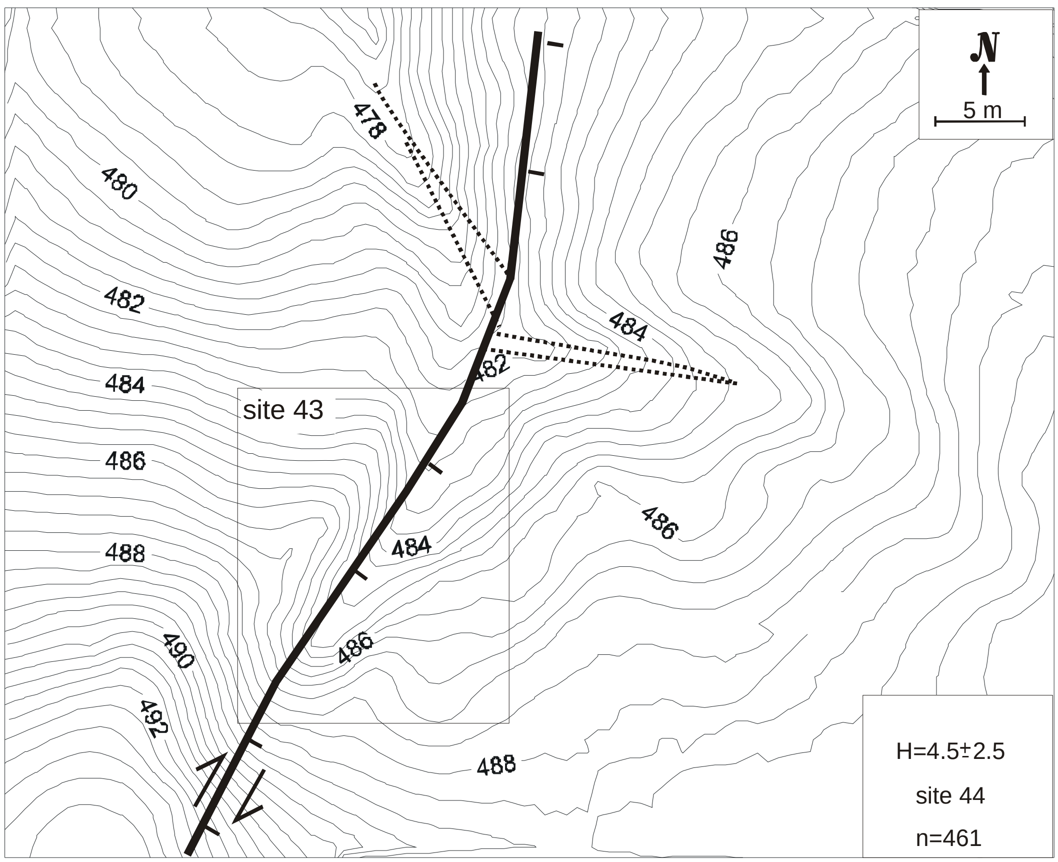

Figure 22: Microtopographic map of sites 43 (scarp) & 44 (offset stream) constructed by Real Time Kinematics GPS survey. Dotted lines indicate offset piercing points; the divergence of dotted lines represents errors on the piercing point locations. n = number of topographic measurements.

Site 45

Location: W17/567832

Brief description: Spur displaced dextrally and vertically by 15±5 and 3±1 m, respectively.

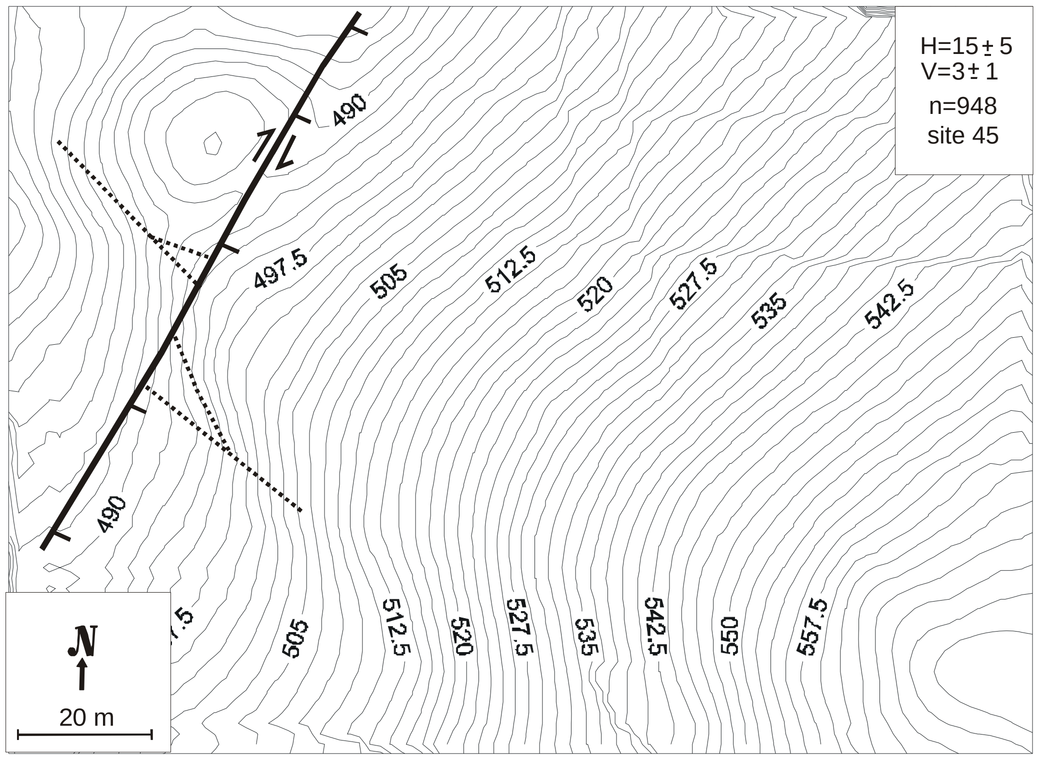

Figure 23: Microtopographic map of offset spur at site 45. Map is constructed by Real Time Kinematics GPS survey. Dotted lines indicate offset piercing points; the divergence of dotted lines represents errors on the piercing point locations. n = number of topographic measurements.

Figure 24: Whakatane Fault at site 45 displaces dextrally a spur by c. 12 m. View to the east. The fault north of this site, and for a strike distance of over 50 km, traverses rugged terrain of greywacke bedrock which is often heavily vegetated.

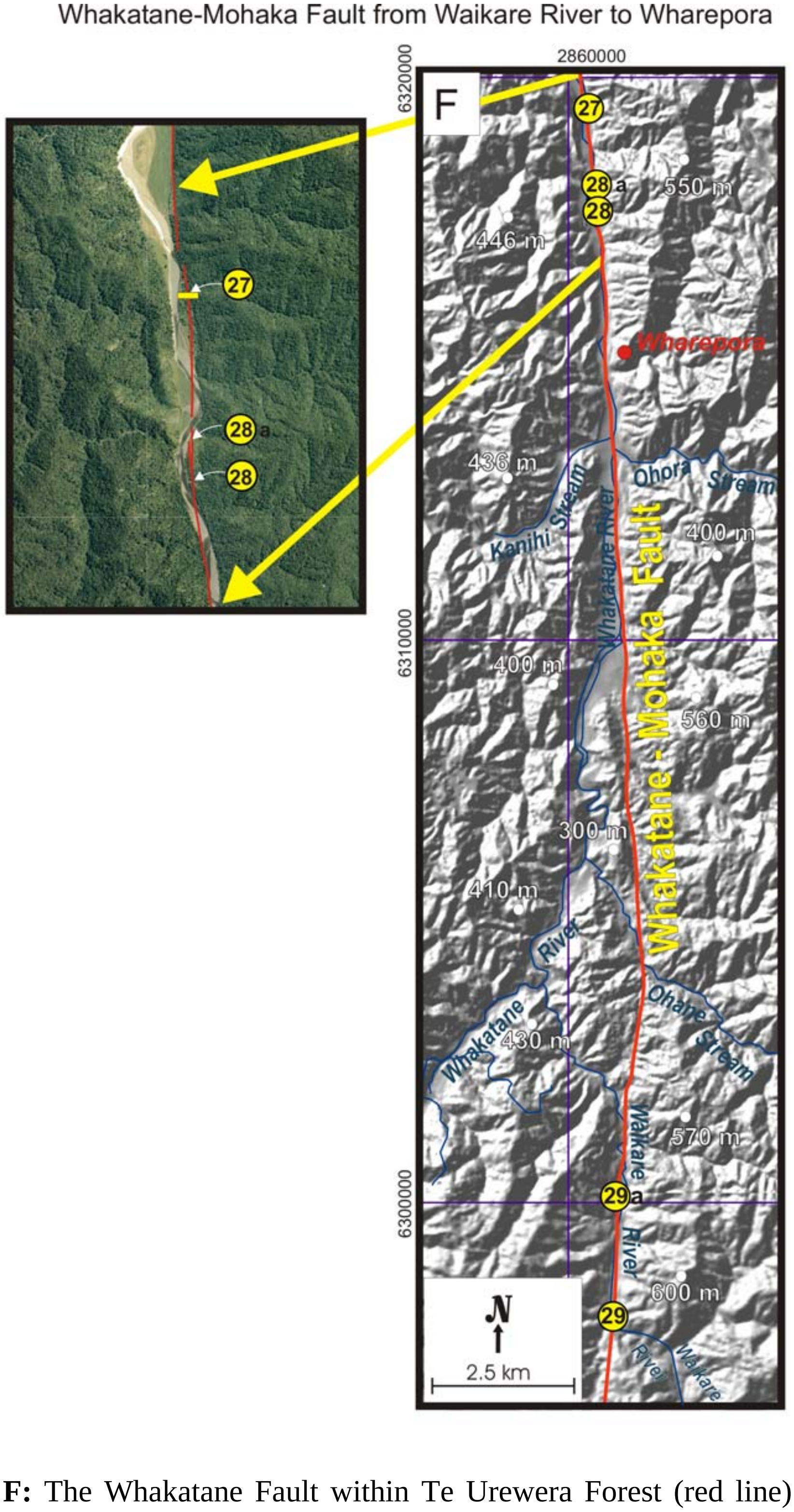

Map F: The Whakatane Fault within Te Urewera Forest (red line). Numbers in circles indicate studied sites (27-29) (see also Table 2.1 in Chapter 2). Blue lines show major rivers and streams. Representative elevations are indicated (in meters).

Site 29

Location: W17/608984

Brief description: Whakatane Fault runs parallel to the Waikare River, Te Urewera Forest, within Torlesse greywacke. Fault attitude: 009°/65°W. Fault zone comprises 50 cm-wide zone of soft-grey fault-gouge with clasts, and a 50-cm wide zone of whitish, more consolidated, tectonised rock. Two sets of slickenline striations were recorded on the bedrock: 70° NW (prominent) and 50° NW.

Figure 25: The Whakatane Fault at Waikare River (site 29) where two sets of slickenline striations were recorded (pitch: 50° & 70° NW).

Site 29a

Location: W17/609003

Brief description: Whakatane Fault runs parallel to the Waikare River and through a degradational terrace. It forms a scarp of < 3 m which in places is buried by alluvial fans. The scarp is downthrown to the east. No dextral displacement is recorded.

Site 28

Location: W16/603177

Brief description: Stream is displaced by 4±0.5 m. The ‘upstream’ side of the fault is deeply incised (c. 2 m) whereas the ‘downstream’ side is incised less. Fault scarp of 2.7±0.5 m in height is preserved < 100 m north of the displaced stream.

Site 28a

Location: W16/604184

Brief description: The Whakatane Fault splays into two sub-parallel strands and downthrows to the west by c. 1.5 m (net slip across two strands) a river terrace that contains Taupo Tephra (1.8 kyr BP). Three auger-holes were drilled at this locality. For details on the stratigraphy and geomorphology of this site see Chapter 4, section 4.4.5.

Figure 26: Airfall Taupo Tephra (1.8 kyr BP) within the degradational terrace at site 28a.

Figure 27: The Whakatane Fault at site 28a where it splays into two sub-parallel strands (red dashed lines).

Site 27

Location: W16/603193

Brief description: 1 km north of site 28a, the Whakatane Fault traverses the immediately younger terrace from that at site 28a and forms a scarp of 1.7 m. Te Marama Trench was excavated at this locality. No dextral displacement was observed. See Chapter 4, section 4.4.5 for further details.

Figure 28: The Whakatane Fault at site 27 where it forms a scarp of c. 1.7 m.

Figure 29: Successive degradational terraces on the western bank of the Whakatane River in Te Urewera Forest. View to the west.

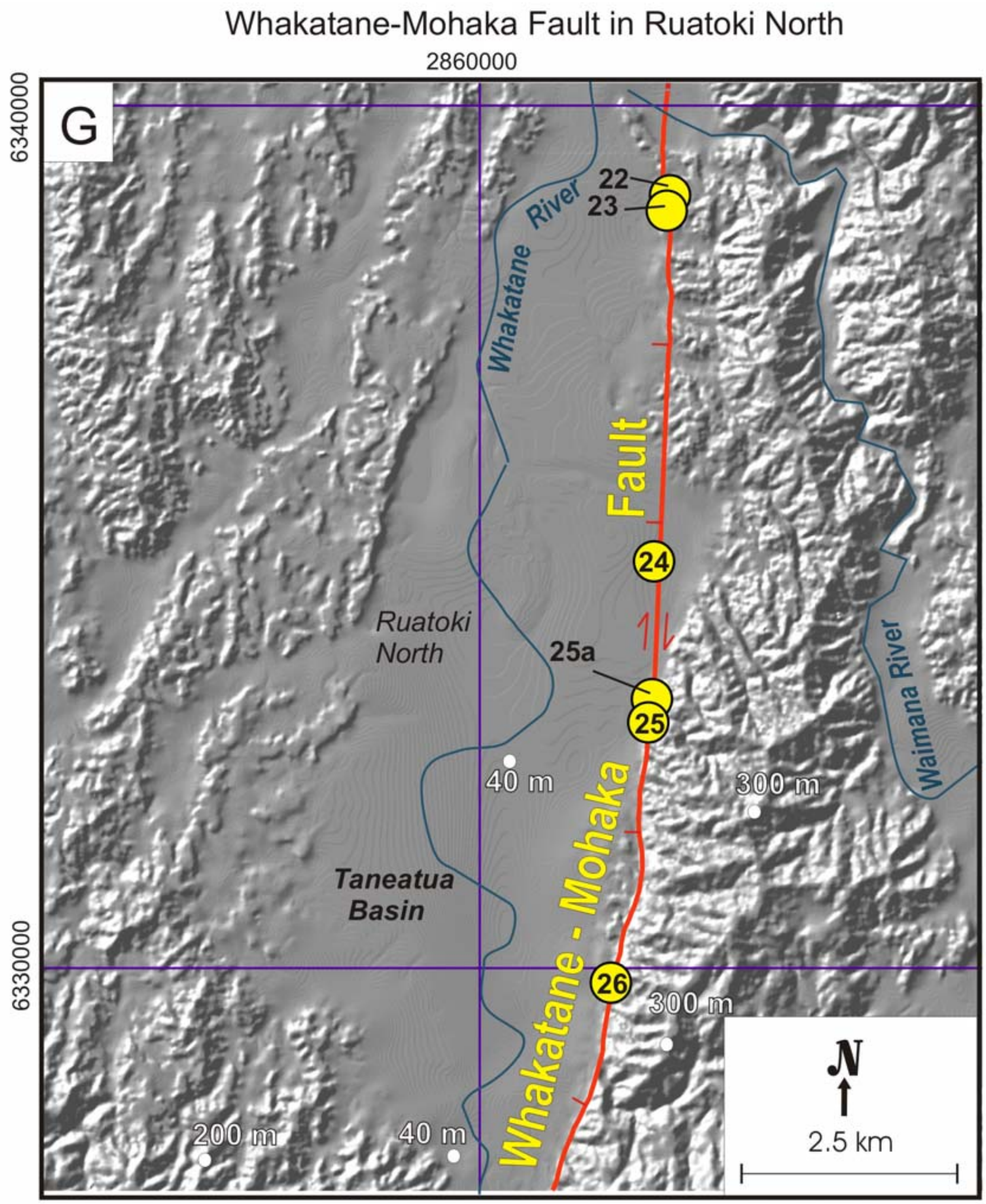

Map G: The Whakatane Fault at Ruatoki North (red line). Numbers in circles indicate studied sites (22-26) (see also Table 2.1 in Chapter 2). Blue lines indicate major rivers. Representative elevations are indicated (in meters).

Site 26

Location: W16/615298

Brief description: The Whakatane Fault traverses a terrace that contains Rotoehu Tephra near its basal aggradational gravels and displaces obliquely a spur (15±7 m dextrally and a minimum of 15.5 m vertically – down to the west). Te Rere Tephra (c. 25 kyr BP) is identified after augering (Table 21 in Appendix III) to rest at 2.5 m depth (from the terrace surface) on the downthrown side of the spur whereas tephra that belongs in the Mangaone Subgroup (c. 30 kyr BP) (see Table 20 in Appendix III) is recorded on the upthrown side. Te Rere Tephra is eroded from the upthrown side. Therefore, the vertically offset piercing point provided by those two layers is only a minimum.

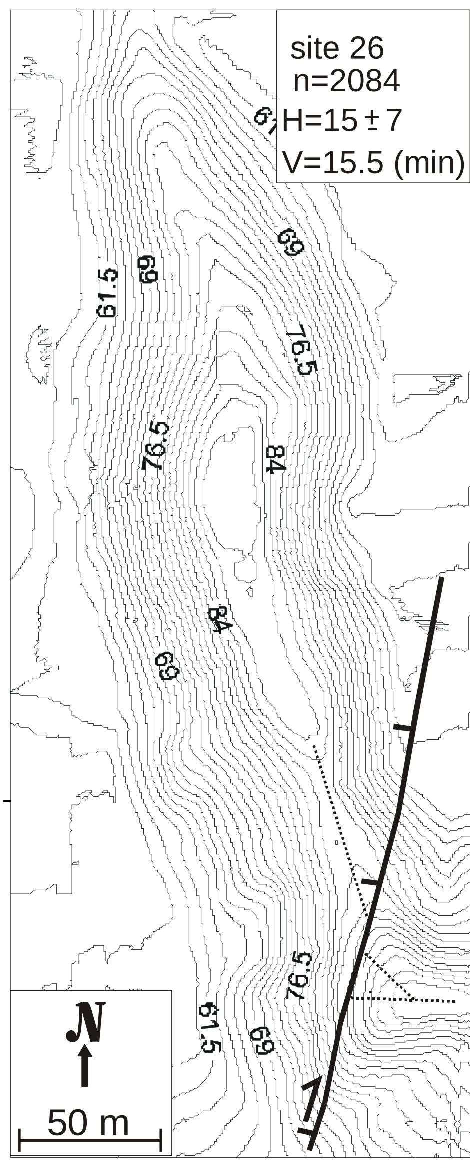

Figure 30: Microtopographic map of offset spur at site 26. Map is constructed by Real Time Kinematics GPS survey. Dotted lines indicate offset piercing points; the divergence of dotted lines represents errors on the piercing point locations. n = number of topographic measurements.

Figure 31: The Whakatane Fault at site 26 displaces obliquely a spur.

Figure 32: At site 26 three successive surfaces (c. 70-50 kyr BP, c. 30-17.6 kyr BP and the currently active floodplain) have been formed by the Whakatane River. The Whakatane Fault here traverses the oldest (c. 70-50 kyr) aggradational river terrace.

Site 25

Location: W16/619327

Brief description: Whakatane Fault bounds the eastern margin of the Taneatua Basin forming a scarp of 10±1 m. Te Whetu Trench was excavated here (located by red arrow, see photograph below). See Chapter 4, section 4.4.6 for further details.

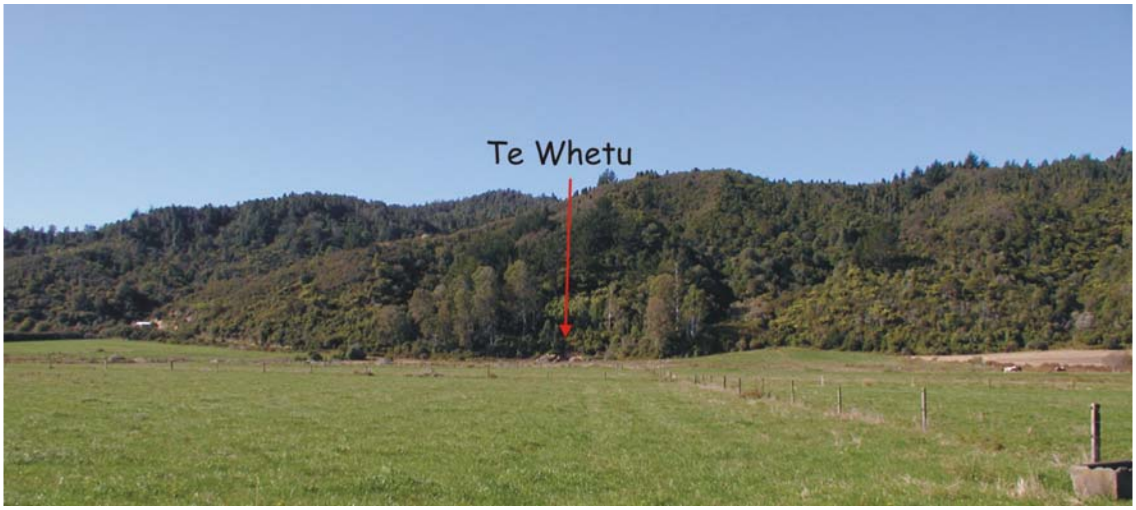

Figure 33: Te Whetu Trench site is located in between two alluvial fans. Note the triangular facets formed by the dip-slip component of motion on the Whakatane Fault.

Site 25a

Location: W16/620330

Brief description: Fault traverses young (< 800 kyr old) alluvial fan. A trench was excavated at this locality by Beanland (1989b).

Site 24

Location: W16/622346

Brief description: Gravity data across the fault suggest that the Whakatane Fault has downthrown (to the west) the top of the greywacke basement by 500±100 m (Fig. 4b in Chapter 6). For details on the gravity survey see Chapter 6 and Appendix IV.

Site 23

Location: W16/621388

Brief description: Whakatane Fault traverses a terrace that contains Rotoehu Tephra near its aggradational gravels and displaces obliquely a spur (14±6 dextrally and 13±2 m vertically).

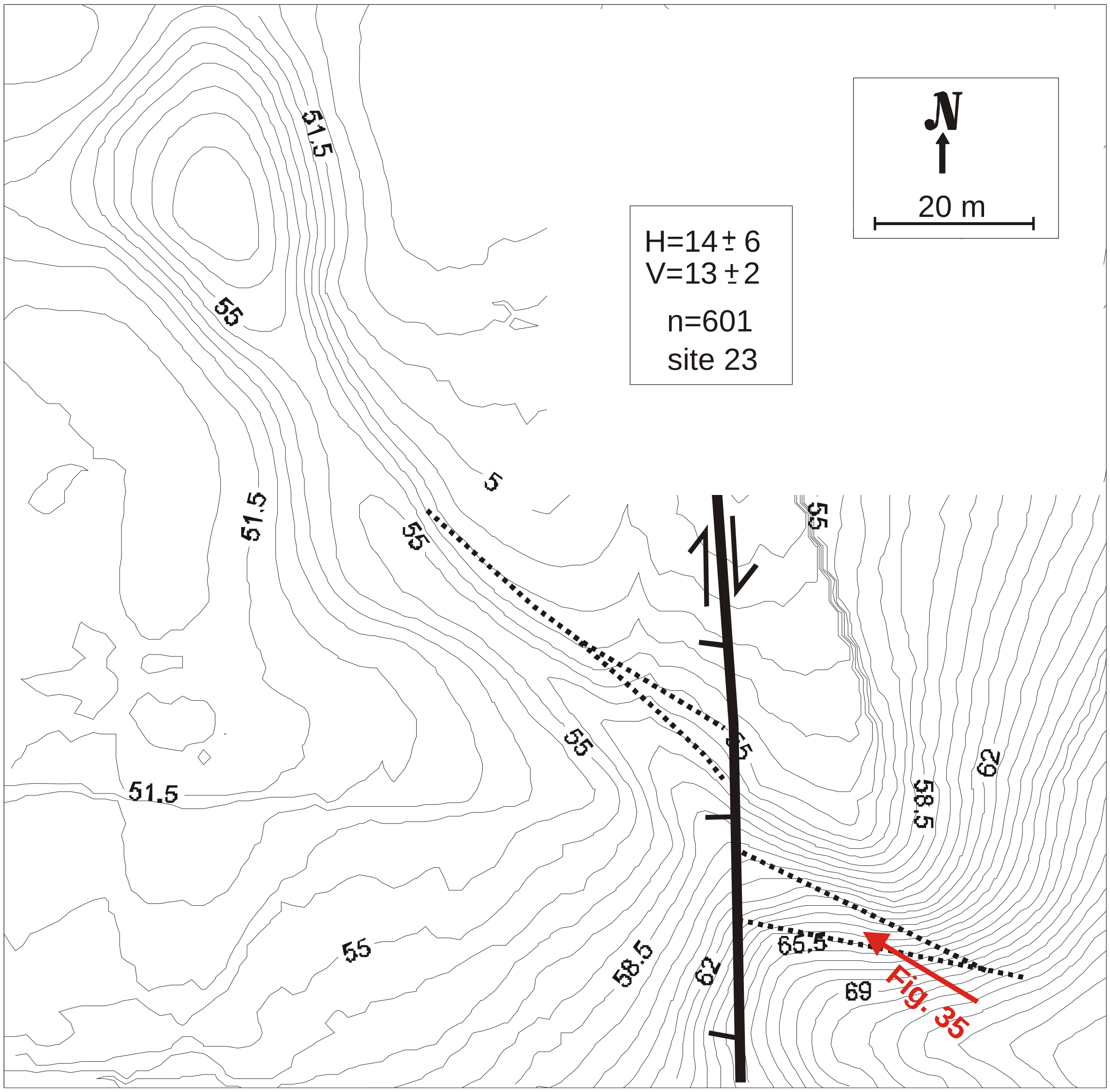

Figure 34: Microtopographic map of the offset spur at site 23 constructed by Real Time Kinematics GPS survey. Dotted lines indicate offset piercing points; the divergence of dotted lines represents errors on the piercing point locations. n = number of topographic measurements.

Figure 35: The Whakatane Fault at site 23 where it obliquely displaces a spur.

Site 22

Location: W16/622389

Brief description: Stream dextrally displaced by the Whakatane Fault (5±3 m).

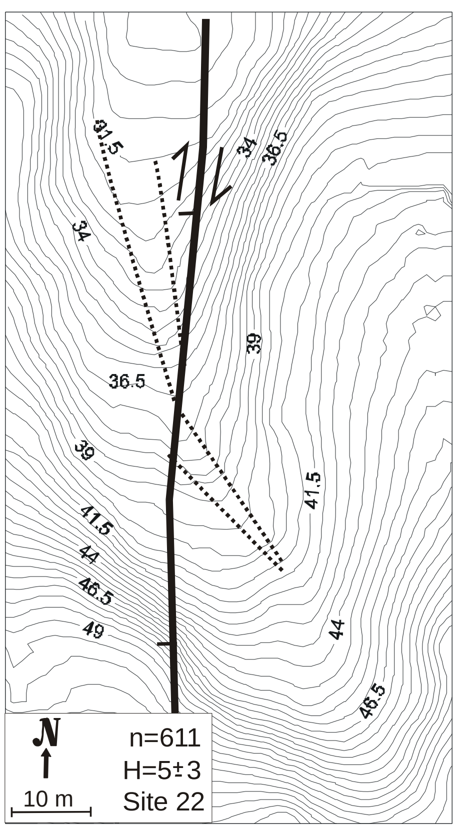

Figure 36: Microtopographic map of offset stream at site 22. Map is constructed by Real Time Kinematics GPS survey. Dotted lines indicate offset piercing points; the divergence of dotted lines represents errors on the piercing point locations. n = number of topographic measurements.

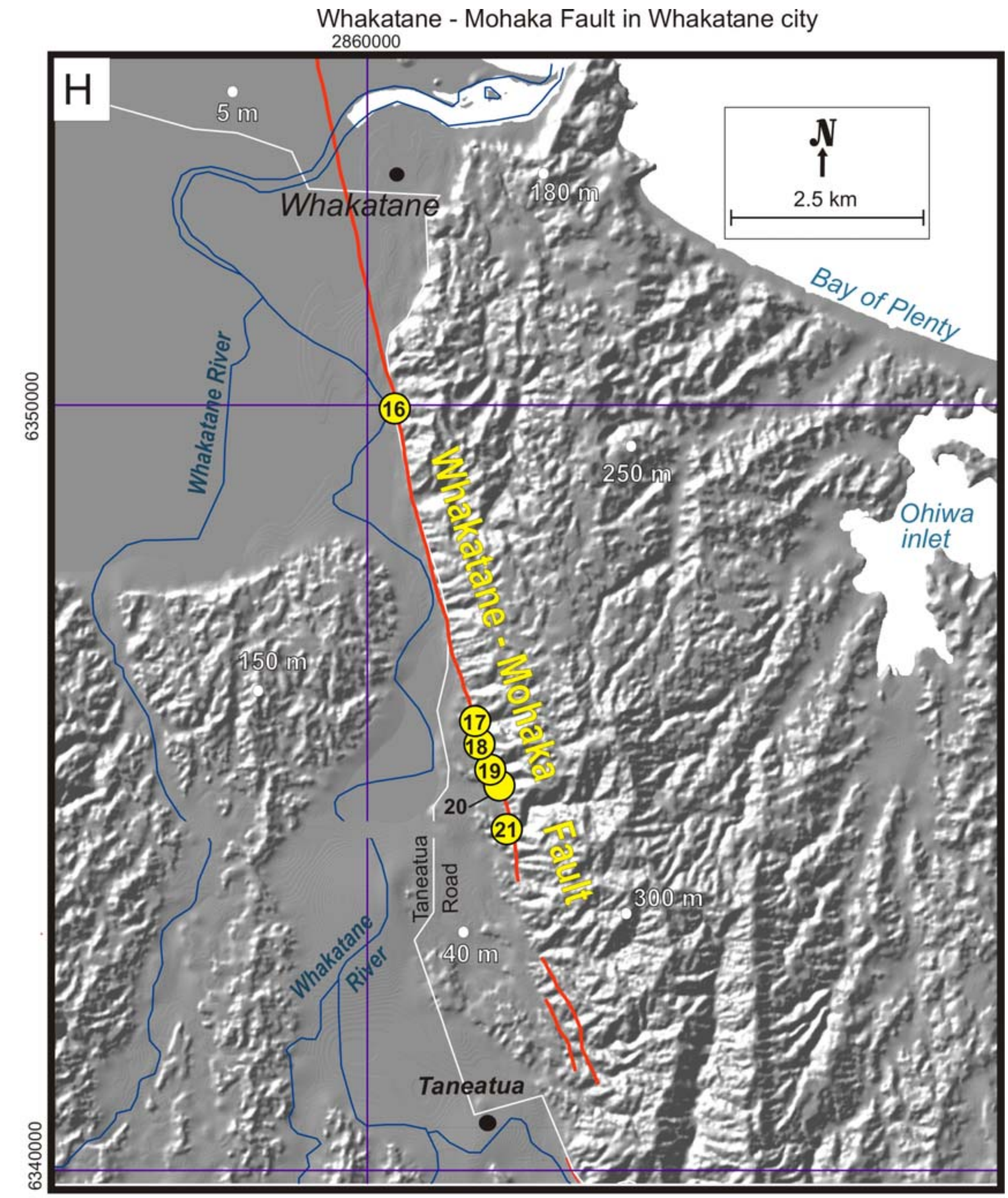

Map H: The coastal section of the Whakatane Fault (red line) near Whakatane city. Numbers in circles indicate studied sites (15-21) (see also Table 2.1 in Chapter 2). White lines indicate main roads while blue lines show major rivers. Representative elevations are indicated (in meters).

Site 21

Location: W15/618444

Brief description: Spur, formed on an aggradational terrace that contains Rotoehu Tephra (c. 50 kyr BP) near its river gravels, is displaced dextrally by 25±5.

Site 20

Location: W15/617450

Brief description: The 'Tophouse' spur, formed on an aggradational terrace that contains Rotoehu Tephra (c. 50 kyr BP) near its river gravels, is displaced dextrally and vertically by 22±5 and 30±2 m, respectively. See Figure 2.5b in Chapter 2 for a detailed topographic map of the site.

Site 19

Location: W15/615452

Brief description: The 'Galini' spur is displaced dextrally and vertically by 5±4 and 5±1 m, respectively.

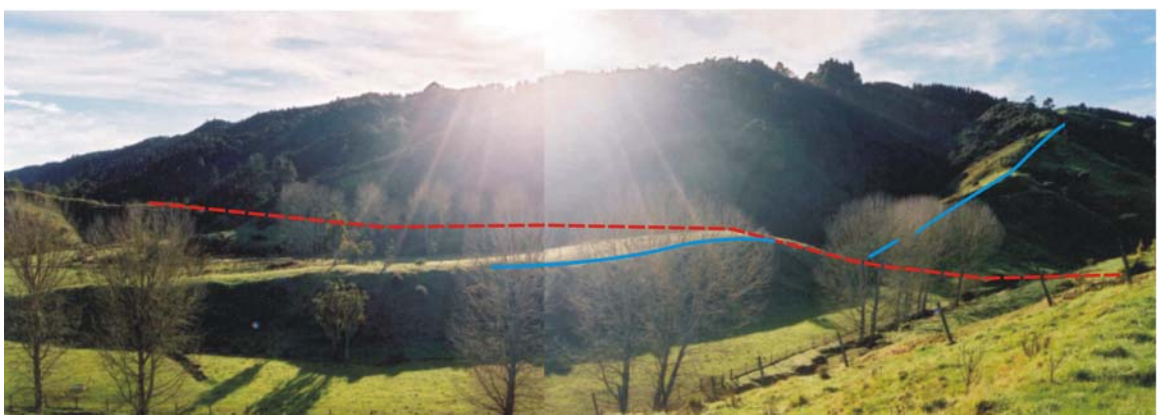

Figure 37: The Whakatane Fault (red dashed line) at site 19 displaces obliquely the crest of the 'Galini' spur (blue line).

Site 18

Location: W15/614455

Brief description: The 'Anemos' spur, formed on an aggradational terrace that contains Rotoehu Tephra (c. 50 kyr BP) near its river gravels, is displaced dextrally by the fault by 23±5 m.

Site 17

Location: W15/614459

Brief description: The ‘Pukehoko’ spur, formed on an aggradational terrace that contains Rotoehu Tephra (c. 50 kyr BP) near its river gravels, is displaced dextrally and vertically by the fault by 26±5 and 32±2 m, respectively.

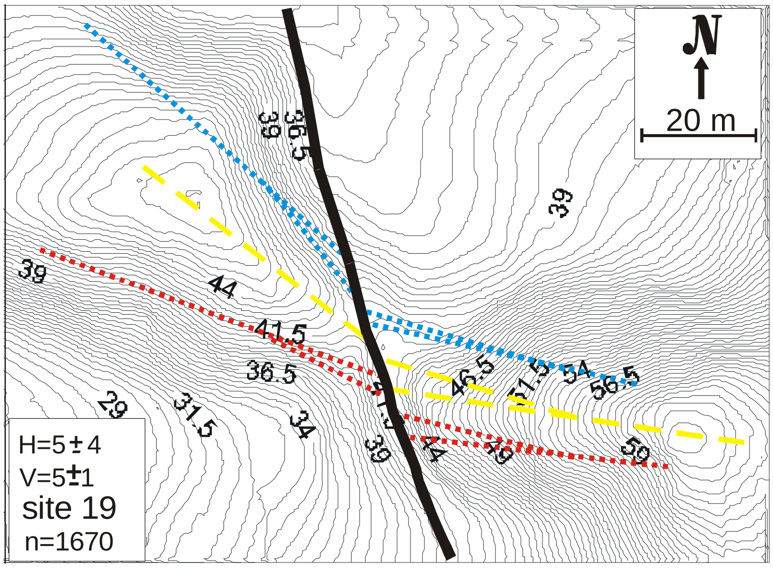

Figure 38: Microtopographic map of offset spur at site 19. Map is constructed by Real Time Kinematics GPS survey. Dotted lines indicate offset piercing points; the divergence of dotted lines represents errors on the piercing point locations. n = number of topographic measurements.

Figure 39: The Whakatane Fault at sites 17-20 where it obliquely displaces four spurs. Views towards the northwest.

Site 16

Location: W15/599532

Brief description: Gravity data across the fault at this locality suggest that the Whakatane Fault has downthrown (to the west) the top of greywacke basement by c. 660±100 m (Fig. 6.4a in Chapter 6). For details on the gravity survey see Chapter 6 and Appendix IV.

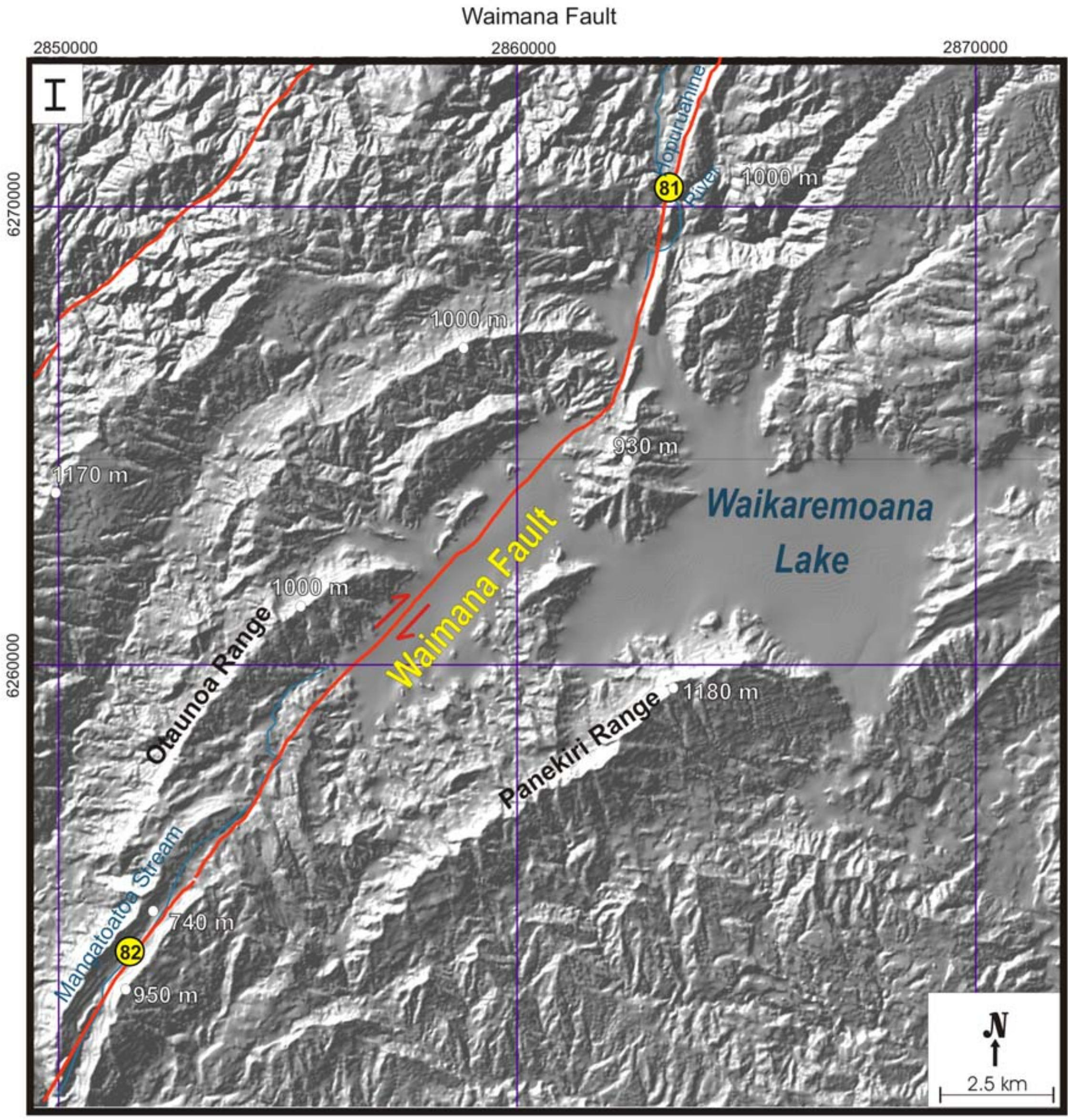

Map I: The Waimana Fault (red line) around Waikaremoana Lake. Numbers in circles indicate studied sites (81-82) (see also Table 2.1 in Chapter 2). Blue lines show major rivers. Representative elevations are indicated (in meters).

Site 82

Location: W18/515537

Brief description: Waimana Fault traverses Miocene bedrock, which consists of massive siltstone/sandstone (254°/20° SE), forming a west-facing scarp of 5±2 m.

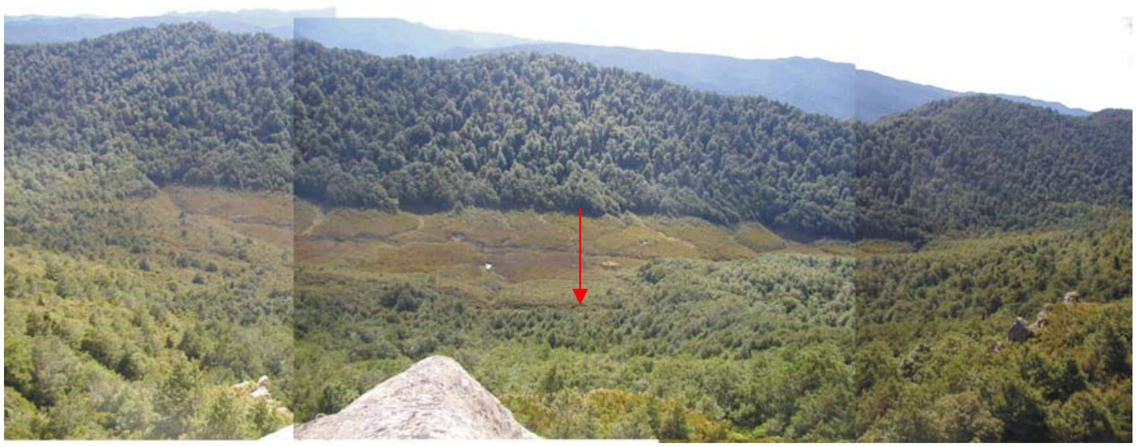

Figure 40: The Waimana Fault (in the foreground and marked by the arrow) at site 82 traverses rugged heavily vegetated topographic terrain, and forms a west-facing scarp. The Mangatoatoa stream (in the background) strikes parallel to the fault (NE-SW). Views are towards northwest.

Site 81

Location: W18/632701

Brief description: Waimana Fault forms the boundary between Miocene (calcareous sandstone) and Torlesse greywacke. The fault zone is c. 80 m wide. Soft grey fault gouge and fault breccias form the fault zone.

Site 80

Location: W18/672902

Brief description: Waimana Fault traverses Torlesse greywacke and displaces the Panoanoa stream by 330±50 m (airphoto analysis). The site was visited and fault gouge was found in places along the Panoanoa stream.

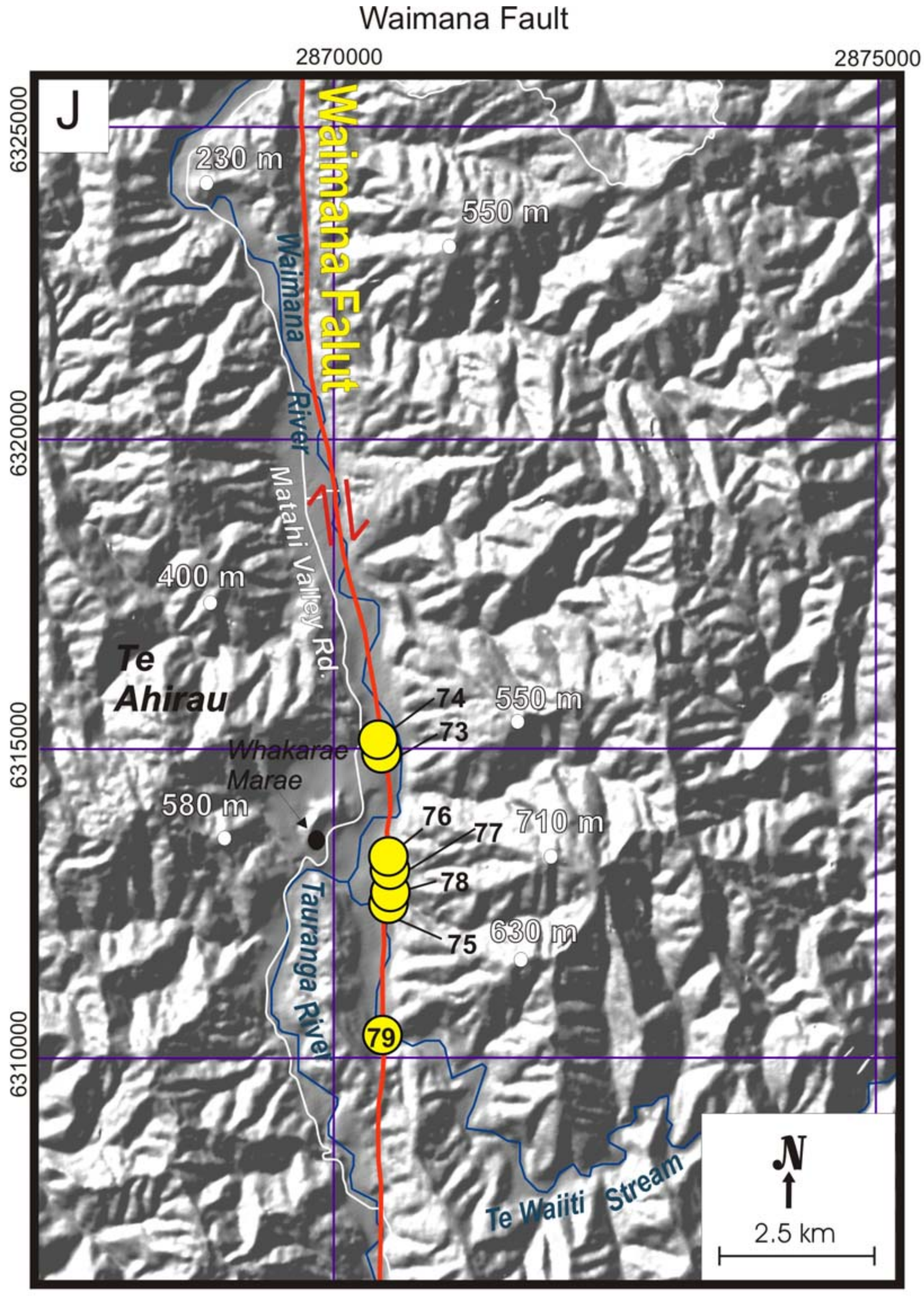

Map J: The Waimana Fault (red line) at Te Ahirau. Numbers in circles indicate studied sites (73-79) (see also Table 2.1 in Chapter 2). White lines indicate main roads while blue lines show major rivers. Representative elevations are indicated (in meters).

Site 79

Location: W16/704145

Brief description: Waimana Fault runs across the Waiiti stream (Fig. 41) and traverses a river terrace that contains Whakatane Tephra (5.6 kyr BP) on its river gravels (Table 47 in Appendix III). The margin of the terrace is displaced dextrally and vertically by 5.5±2 and 2.5±0.5 m, respectively (Fig. 42).

Figure 41: Fault gouge within the Waiiti stream, Waimana Valley, at site 79.

Figure 42: The Waimana Fault at site 79 dextrally displaces a river terrace.

Site 75

Location: W16/705158

Brief description: Stream incised into aggradational terrace that contains Waiohau Tephra (13.8 kyr BP) on its river gravels, is displaced dextrally and vertically by 10±2 and 2±1 m, respectively. For detailed microtopographic map of the offset stream see Figure 4.19b in Chapter 4.

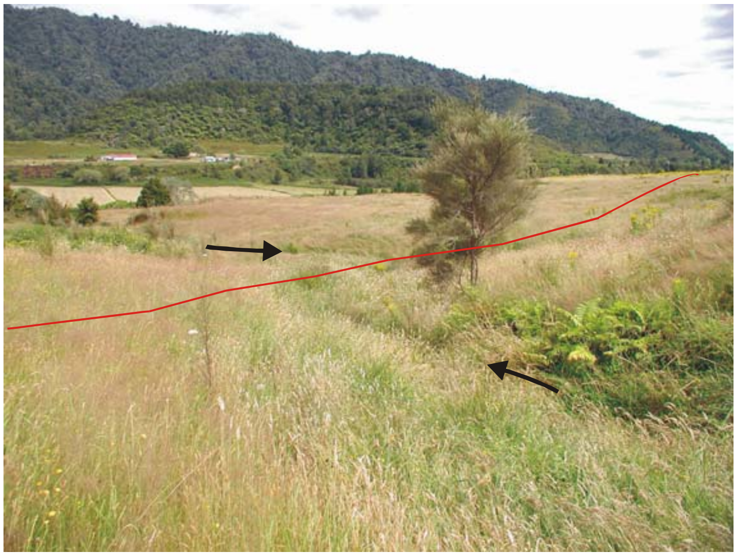

Figure 43: The Waimana Fault at site 75 where it dextrally displaces a stream by c. 10 m. Note the "S" shape of the channel caused by cumulative displacement. View towards the west.

Site 78

Location: W16/705160

Brief description: Spur, located in between sites 75 and 77, is displaced dextrally by 18±2 (Map J).

Site 77

Location: W16/705161

Brief description: At this locality the Waimana Fault traverses aggradational terrace that contains Waiohau Tephra (13.8 kyr BP) onto its river gravels, forming an east-facing scarp (c. 2 m high). The Ahirau 2 Trench was excavated here.

Site 76

Location: W16/705161

Brief description: Waimana Fault traverses aggradational terrace that contains Waiohau Tephra (13.8 kyr BP) onto its basal gravels, and forms an east-facing scarp (c. 2 m high). The scarp blocks the drainage forming a swamp. The Ahirau 1 Trench was excavated across the fault and the swamp.

Site 73

Location: W16/704170

Brief description: Waimana Fault traverses aggradational terrace that contains Waiohau Tephra (13.8 kyr BP) onto its river gravels, and displaces obliquely a river riser by 13±4 m (dextral) and 2.5±0.5 m (vertical).

Figure 44: The Waimana Fault at sites 73 where it displaces obliquely a river riser. Views are towards east.

Site 74

Location: W16/704180

Brief description: Waimana Fault strikes N-S forming an east-facing scarp of 5±1 m.

Figure 45: The Waimana Fault at site 74 where it strikes N-S and traverses the post 13.8 kyr old aggradational terrace forming a scarp of c. 5 m.

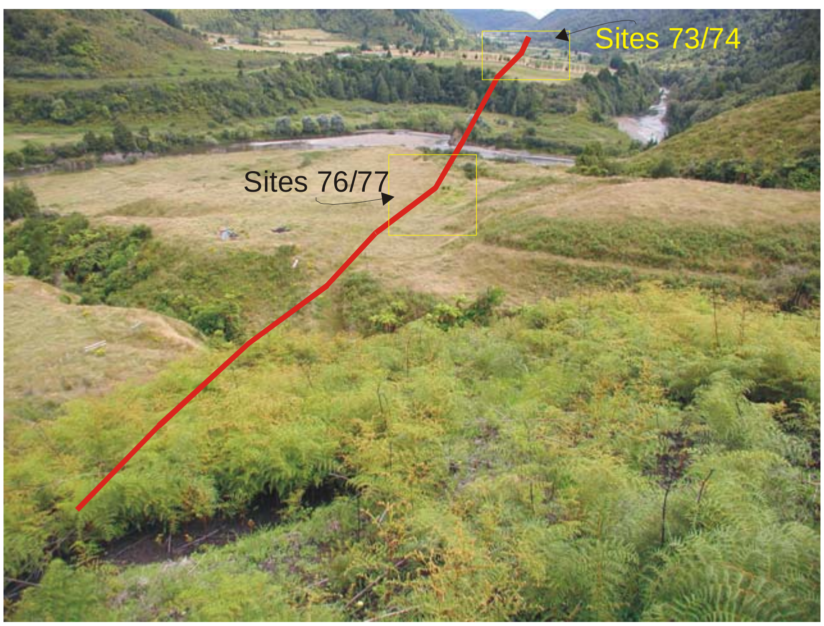

Figure 46: Photograph is taken from site 78 (offset spur). View towards the north (sites 73, 74, 76 and 77).

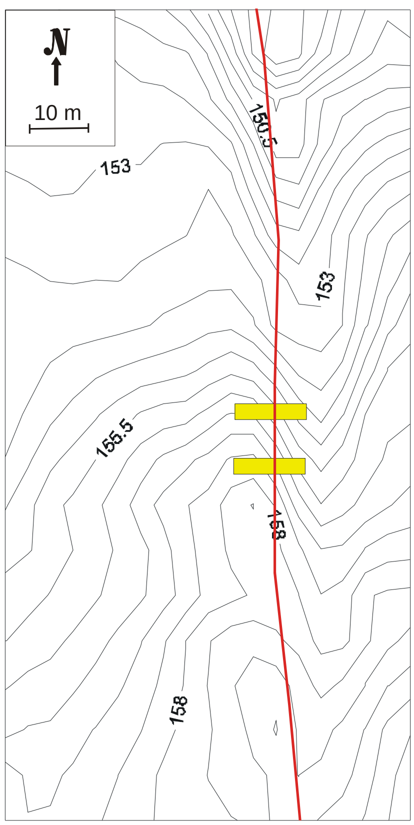

Figure 47: a) Panoramic views of Te Ahirau site where the Waimana Fault traverses an aggradational terrace on the gravels of which rests Waiohau Tephra (13.8 kyr BP). The locations of the Ahirau 1 & 2 trenches are indicated on the left-hand side of the figure. The location of the offset stream Ahirau 4 is also indicated. View towards the east. **b)** Microtopographic map constructed by GPS-RTK showing the location of Ahirau 1 & 2 trenches.

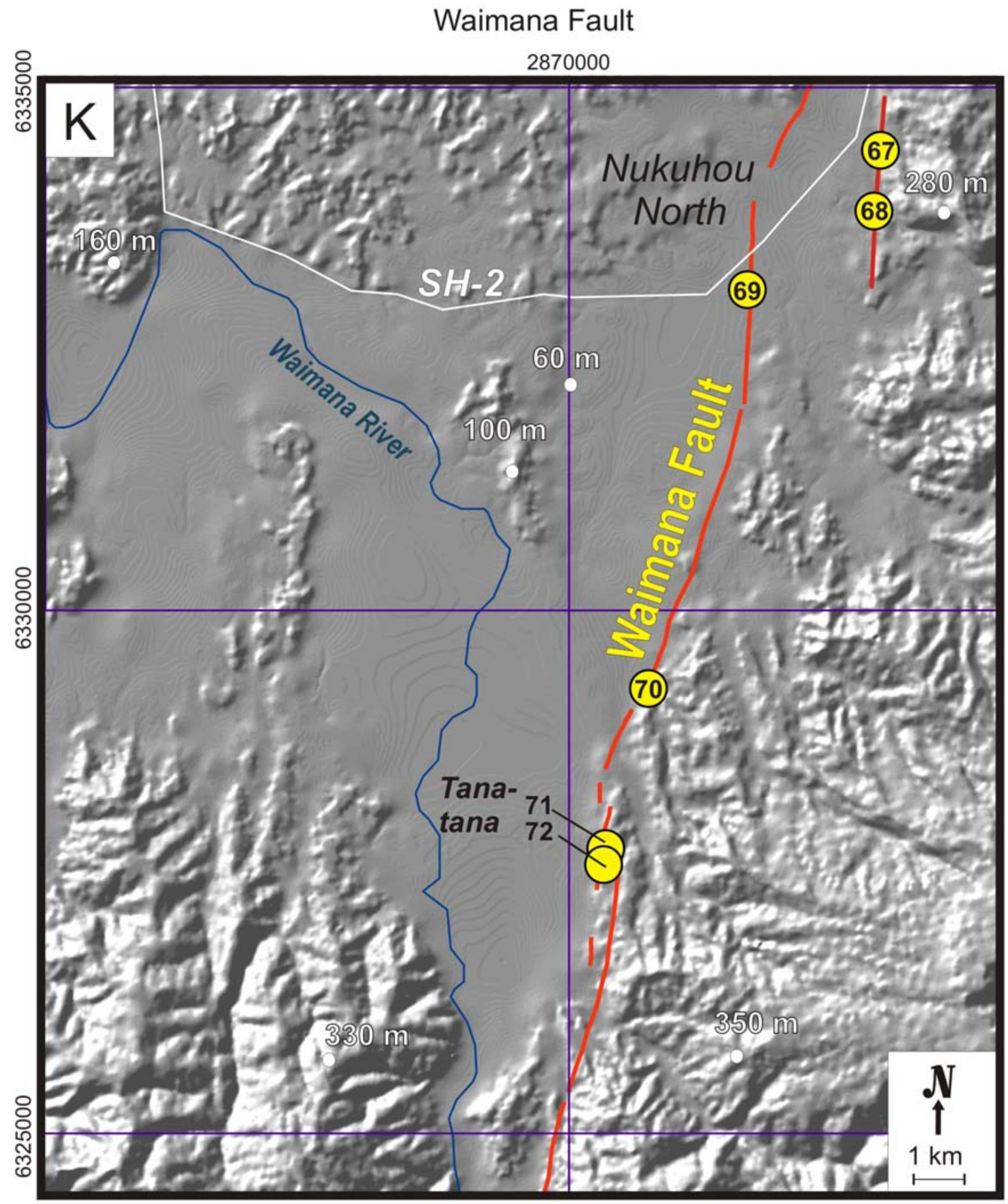

Map K: The Waimana Fault (red line) at Tana-tana. Numbers in circles indicate studied sites (67-72) (see also Table 2.1 in Chapter 2). White lines indicate main roads while blue lines show major rivers. Representative elevations are indicated (in meters).

Site 72

Location: W16/702276

Brief description: Fault traverses aggradational terrace that contains Rotoehu Tephra onto its river gravels (c. 50 kyr BP) and displaces obliquely a spur by 12±6 m (dextral) and 2±1 m (vertical).

Site 71

Location: W16/703278

Brief description: Fault traverses aggradational terrace that contains Rotoehu Tephra onto its river gravels (c. 50 kyr BP) and displaces obliquely a spur by 13±7 m (dextral) and 2±1 m (vertical).

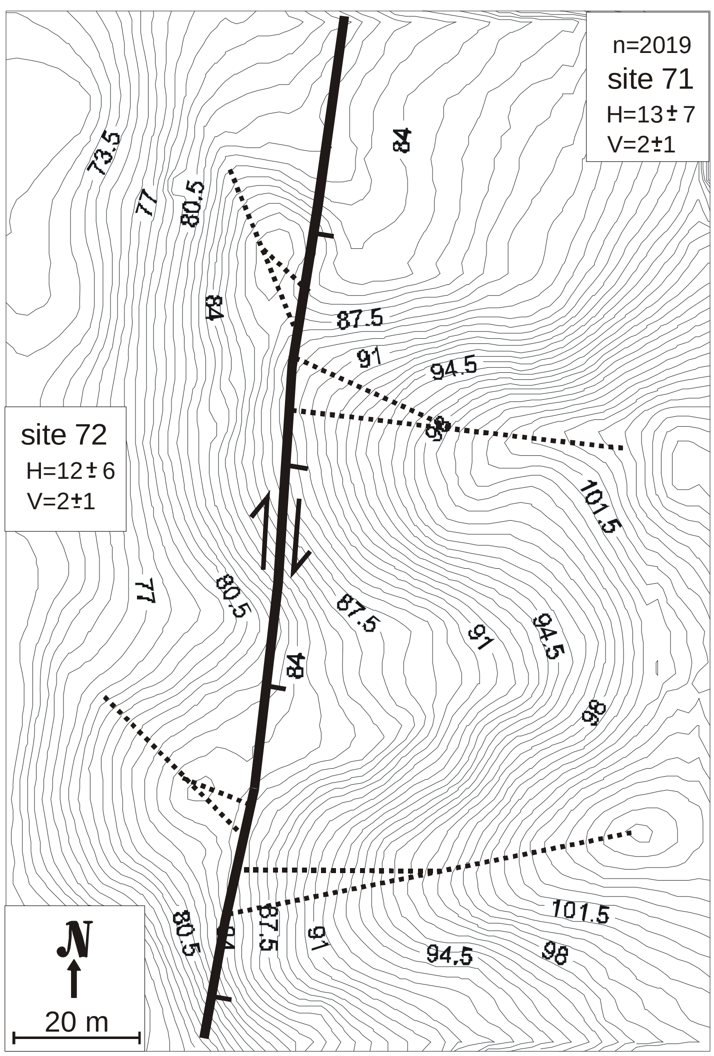

Figure 48: Microtopographic map of sites 71 & 72. Map is constructed by Real Time Kinematics GPS survey. Dotted lines indicate offset piercing points; the divergence of dotted lines represents errors on the piercing point locations. n = number of topographic measurements.

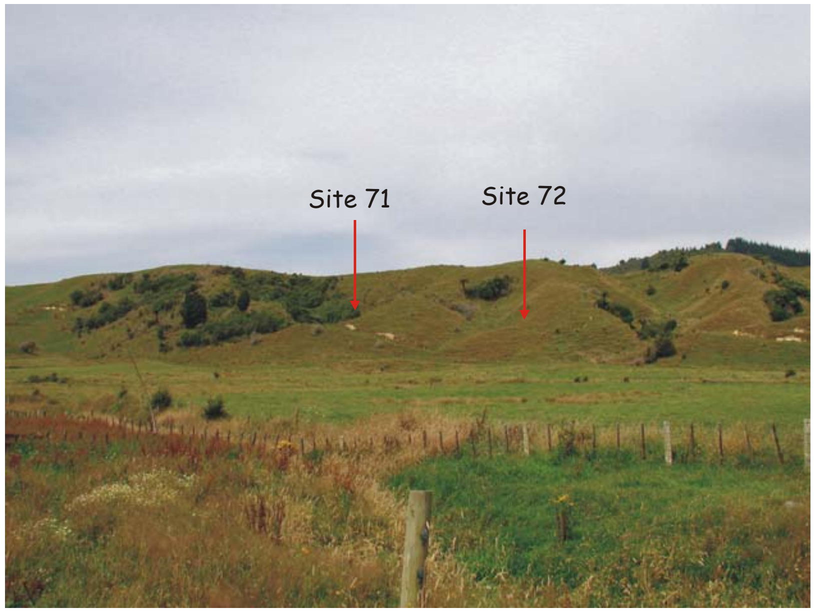

Figure 49: At Tana-tana settlement, where the Waimana Fault displaces dextrally two spurs (sites 71 & 72).

Site 70

Location: W16/707293

Brief description: Fault traverses and displaces dextrally a spur by 20±5 m.

Site 69

Location: W16/716329

Brief description: Fault traverses an alluvial fan and forms a west-facing scarp of 4±1 m.

Site 67

Location: W16/728342

Brief description: Fault traverses an alluvial fan and displaces dextrally a stream by 20±2.5 m.

Site 68

Location: W16/724328

Brief description: Gravity data collected across the Waimana Fault suggest that the displacement accrued on top of the greywacke basement is insignificant (Fig. 6.4b in Chapter 6). The fault at this locality is principally strike-slip. For details on the gravity survey see Chapter 6 and Appendix IV.

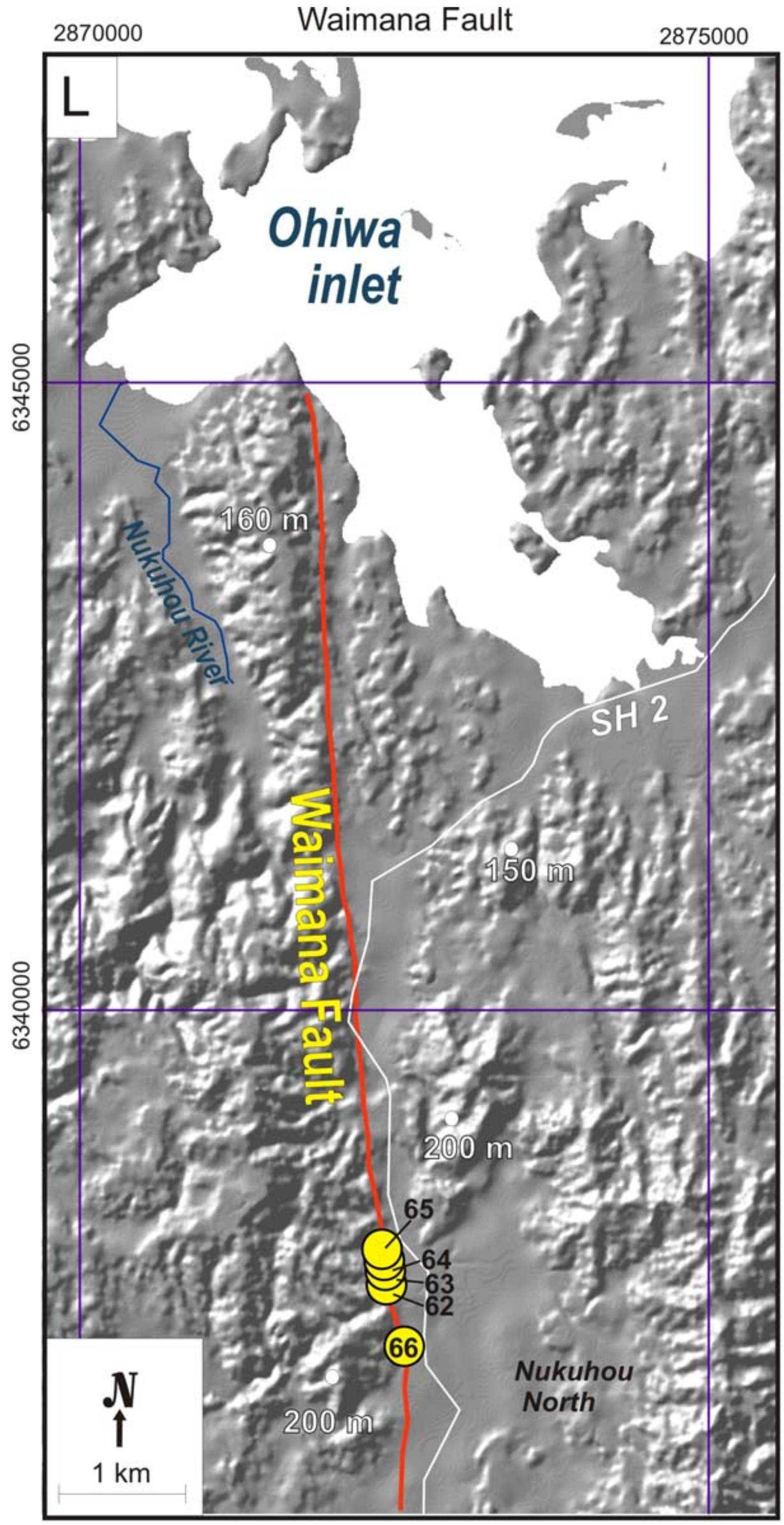

Map L: The Waimana Fault at Nukuhou North. Numbers in circles indicate studied sites (62-66) (see also Table 2.1 in Chapter 2). White lines indicate main roads while blue lines show major rivers. Representative elevations are indicated (in meters).

Site 66

Location: W16/727371

Brief description: Fault displaces dextrally an active stream by 19±2 m.

Site 62

Location: W16/725377

Brief description: Fault displaces dextrally an active stream by 24±15 m. For detail topographic map of the offset stream see Figure 4.27 in Chapter 4 whereas for details on the stratigraphy of the site see section 4.5.2.2. in Chapter 4.

Figure 50: Offset stream Don-1 at Nukuhou North (site 62). View towards the east.

Site 63

Location: W16/725379

Brief description: Fault traverses an aggradational terrace which contains Rotoehu Tephra (c. 50 kyr BP) near its river gravels and displaces obliquely a stream margin by 13.5±1 m (dextral) and 2±0.5 m (vertical) (Fig. 52).

Site 64

Location: W16/725379

Brief description: Fault displaces obliquely a stream-channel by 20±3 m (dextral) and 2±1 m (vertical). Moana-Iti Trench was excavated at this locality, across the stream axis and across the fault (Fig. 4.26 in Chapter 4).

Site 65

Location: W16/725379

Brief description: Fault displaces obliquely a stream-channel by 20±3 m (dextral) and 2±1 m (vertical). Moana Trench was excavated at this locality (Fig. 4.26 in Chapter 4).

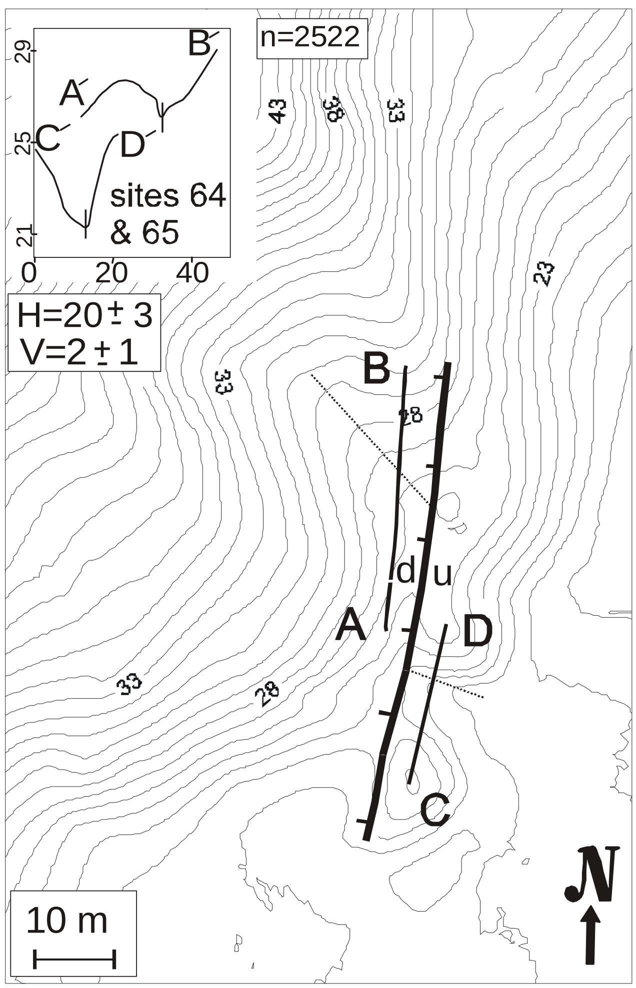

Figure 51: Microtopographic map of the offset stream at sites 64 & 65, constructed by Real Time Kinematics GPS survey and associated displacement profiles across the offset features. n = number of topographic measurements.

Figure 52: At sites 63-65 the Waimana Fault strikes N-S and displaces a stream margin and a stream-channel. Moana and Moana-Iti trenches were excavated at this locality (see Chapter 4, Figure 4.26). View towards the north.

Figure 53: Faulted topography at Nukuhou North (sites 62-65). View from site 65 towards the south.

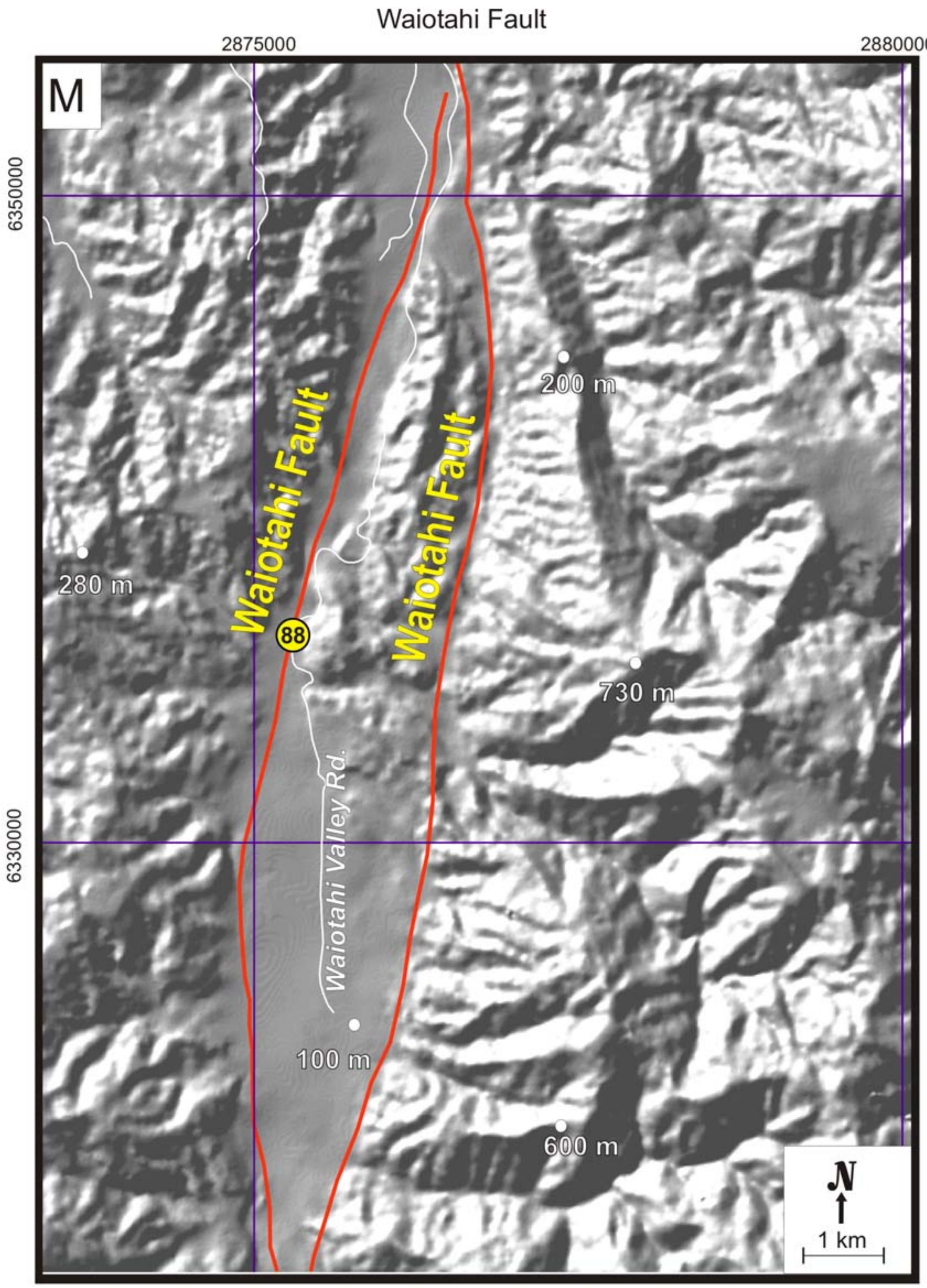

Map M: The Waiotahi Fault (red lines) at the southern end of the Waiotahi Valley Road, Waiotahi Valley. Number in circles indicates studied site (88) (see also Table 2.1 in Chapter 2). White lines indicate main roads. Representative elevations are indicated (in meters).

Site 88

Location: W16/761308

Brief description: Waiotahi Fault runs parallel to the Waiotahi Valley Road and displaces dextrally a stream by 17±3 m. A small scarp 2±0.5 m is preserved c. 100 m south of the stream.

Figure 54: Beheaded stream at site 88. At this locality the Waiotahi Fault runs parallel to the road and truncates dextrally the stream by c. 17 m. The two sections of the offset stream are indicated, as is the fault. View towards the east.

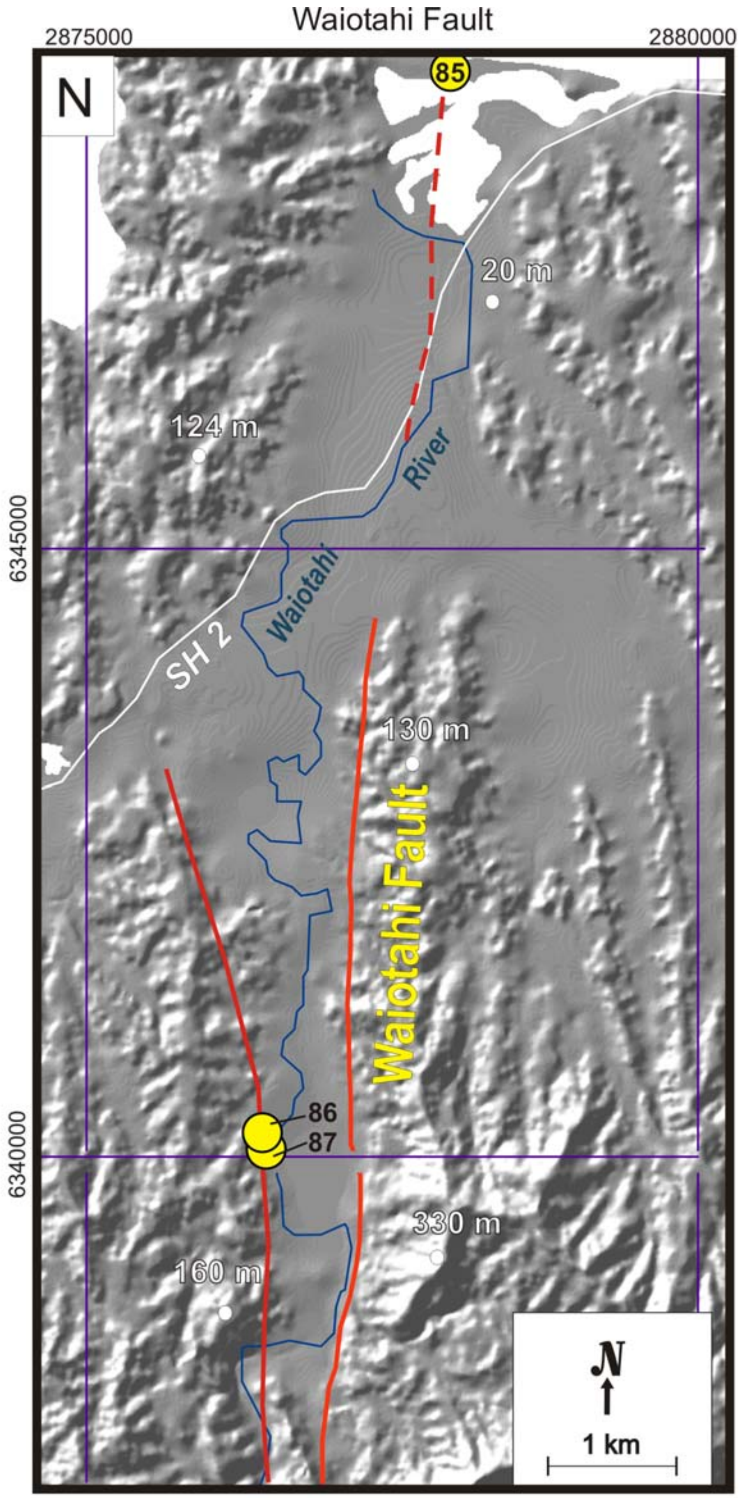

Map N: The coastal section of the Waiotahi Fault (red lines). Numbers in circles indicate studied sites (85-87) (see also Table 2.1 in Chapter 2). White lines indicate main roads. Blue lines show major rivers. Representative elevations are indicated (in meters).

Site 87

Location: W16/767396

Brief description: Waiotahi Fault forms a west-dipping scarp of 5±1 m which is continuous for a strike distance of c. 300 m.

Site 86

Location: W16/766397

Brief description: Waiotahi Fault traverses aggradational terrace that contains Rerewhakaaitu Tephra onto its basal gravels (c. 17.6 kyr BP) and displaces obliquely a stream by 16±1 m (dextral) and 2±0.5 m (vertical).

Figure 55: Waiotahi Fault at site 86 displaces dextrally a stream by c. 16 m. Views are towards east.

Site 85

Location: W15/775485

Brief description: Gravity data collected across the fault at this locality suggest that the Waiotahi Fault has downthrown (to the west) the top of the greywacke basement by c. 300±50 m (Fig. 6.4a in Chapter 6). For details on the gravity survey see Chapter 6 and Appendix IV.

APPENDIX II

DESCRIPTION OF UNITS ENCOUNTERED IN THE TRENCHES

WHAKATANE FAULT

THALASSA TRENCH

Northeast wall

A: Kaharoa Tephra (0.8 yr BP). Fine sugary ash deposited discontinuously or in lenses.

B: Taupo Tephra (1.8 kyr BP). Cream-coloured layer of pumiceous coarse ash below an orange fine lapilli.

C: Plinian eruption of Taupo. Coarse pumice that overlies sharply the Rotongaio Tephra.

D: Rotongaio Tephra (Taupo eruption). Dark grey dense phreatoplinian ash, up to few millimetres in size (but most of the deposits consists of sub-milimetre material).

E: Waimihia Tephra (3.5 kyr BP). Low density orange-whitish pumice with clasts size up to 2-3 cm.

F: Whakatane Tephra (5.6 kyr BP). It comprises a mottled brown to yellow-brown pumice lapilli. It is well sorted with an average clast size of 5-10 mm.

G: Colluvial wedge. Mixed unit of paleosol, silty-sand and clasts up to few mm size.

H: Reworked Whakatane Tephra with grains of Waimihia (< 5.6 kyr BP).

I: Mamaku Tephra (8 kyr BP). Medium to fine whitish ash.

J: Rotoma Tephra (9.5 kyr BP). Pale yellow to brown weathered fine ash that forms grey ‘cream cakes’ in places.

K: Rotoehu Tephra (50 kyr BP). Fine whitish ash that contains cummingtonite.

L: Organic dark brown top soil.

M: Light to dark brown organic horizon (paleosol)

N: Miocene mudstone (Bedrock).

O: Peat. Organic horizon very dark, nearly black.

P: Tephric silty clay with pumice clasts up to 3 mm in size.

Q: Tephric paleosol that contains lapilli up to 2 mm in size (Q_1= Paleosol that develops on top of unit I, Q_2=Paleosol that develops on top of unit E)

R: Silty clay.

S: Tephric paleosol with clasts of bedrock.

T: Whitish fine clay, very dense.

U: Weathered Miocene mudstone (bedrock).

Figure 1: The northeast wall of Thalassa Trench, Whakatane Fault, Ruatahuna.

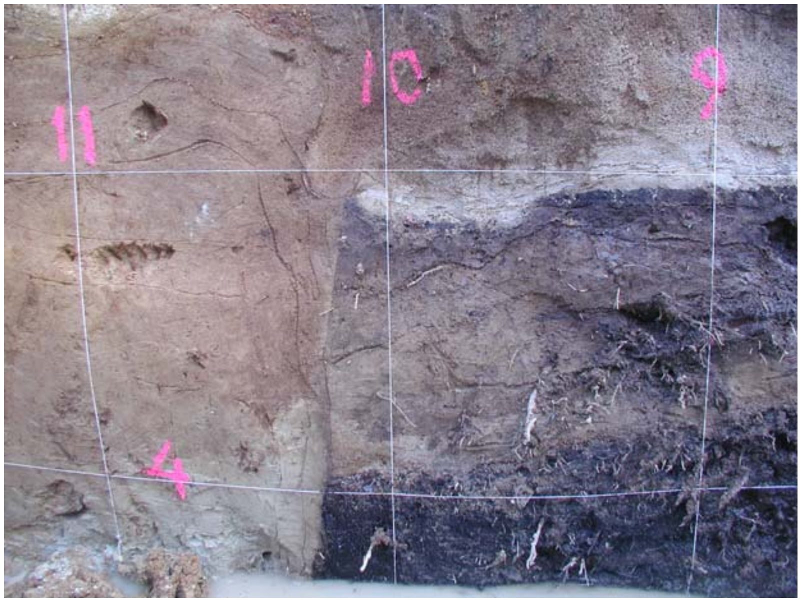

Figure 1: The principal slip surface of the Whakatane Fault, northeast wall of Thalassa Trench, Ruatahuna.

Southwest wall

B: Taupo Tephra (1.8 kyr BP). It comprises a cream-coloured layer of pumiceous coarse ash.

D: Rotongaio (Taupo eruption). Dark grey dense phreatoplinian ash, up to few millimetres in size (but most of the deposits consists of sub-milimetre material.

E: Waimihia Tephra (3.5 kyr BP). Low density orange-whitish pumice with clasts size up to 2-3 cm.

F: Whakatane Tephra (5.6 kyr BP). It comprises a mottled brown to yellow brown pumice lapilli. It is well sorted with an average clast size of 5-10 mm.

I: Mamaku Tephra (8 kyr BP). Medium to fine whitish ash.

J: Rotoma Tephra (9.5 kyr BP). Pale yellow to brown weathered fine ash that forms grey 'cream cakes' in places.

Z: Mangaone Subgroup (30 kyr BP). Coarse whitish lapilli.

M: Light to dark brown organic horizon (paleosol).

X: Colluvial wedge (tephric silt).

Y: Clay silt, dense and fine grains.

L: Organic dark brown top soil.

W: Kawa Kawa (27 kyr BP). Orange-whitish, medium to coarse ash with bedding.

Gs: Green/grey silty fine sand.

Q: Paeosol (tephric silty sand).

U: Weathered Miocene mudstone (bedrock).

Rt: Reworked tephra of uncertain origin.

Mc: Mixed colluvium+ brown paleosol.

Pm: Tephric silt mixed with dark brown paleosol.

ARMYRA TRENCH

North wall

A: Kaharoa Tephra (0.8 yr BP). Fine sugary ash deposited discontinuously or in lenses.

Aa: Reworked Kaharoa

B: Taupo Tephra (1.8 kyr BP). It comprises a cream-coloured layer of pumiceous coarse ash.

C: Mixed colluvium wedge.

D: Peaty dark organic paleosol.

E: Waimihia Tephra (3.5 kyr BP). Low density orange-whitish pumice with clasts size up to 2-3 cm.

F: Mixed tephric peat. Lapilli size up to 2 mm.

H: Mixed bedrock clasts and mud.

I: Mixed tephra colluvium.

J: Mixed peat and medium sand.

K: Mixed medium to fine sand and tephra.

L: Organic dark brown top soil.

M: Light to dark brown organic horizon (paleosol).

N: Miocene mudstone (bedrock).

O: Peat. Organic horizon very dark, nearly black.

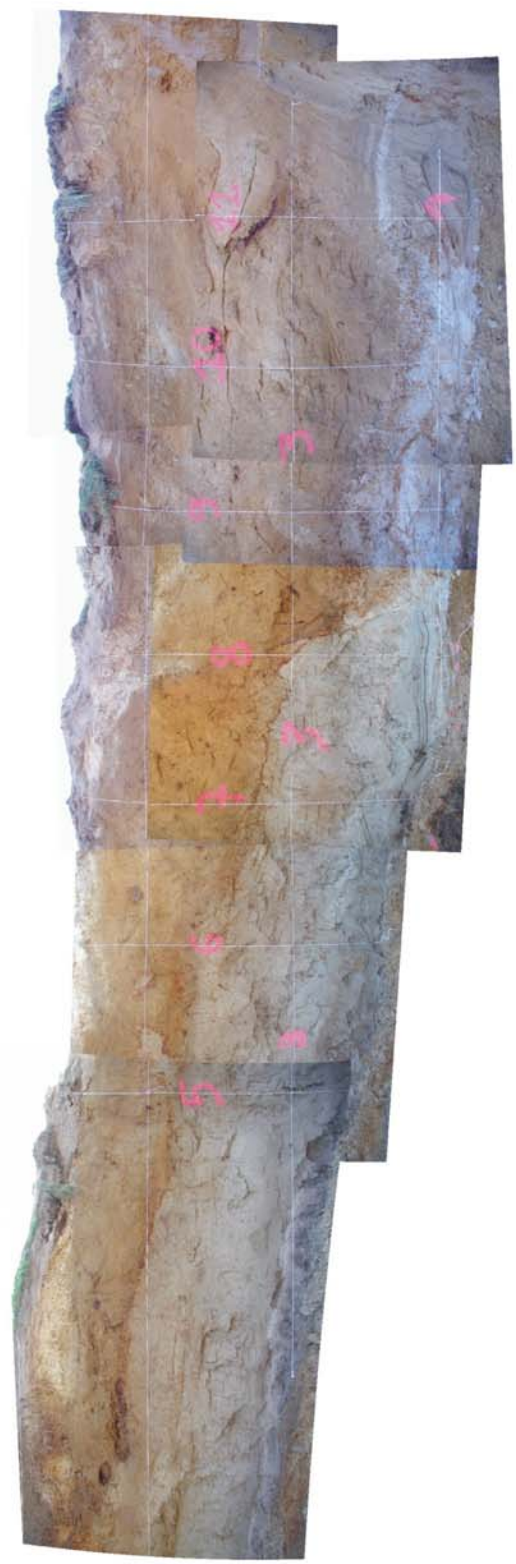

Figure 2: The southwest wall of Thalassa Trench, Whakatane Fault, Ruatahuna.

HELIOS TRENCH

Northwest wall

A: Kaharoa Tephra (0.8 yr BP). Fine sugary ash deposited discontinuously or in lenses.

B: Taupo Tephra (1.8 kyr BP). It comprises a cream-coloured layer of pumiceous coarse ash.

C: Plinian eruption of Taupo. Coarse pumice that overlies sharply the Rotongaio Tephra.

D: Rotongaio Tephra (Taupo eruption). Dark grey dense phreatoplinian ash, up to few millimetres in size (but most of the deposits consists of sub-milimetre material.

E: Waimihia Tephra (3.5 kyr BP). Low density orange-whitish pumice with clasts size up to 2-3 cm.

F: Whakatane Tephra (5.6 kyr BP). It comprises a mottled brown to yellow brown pumice lapilli. It is well sorted with an average clast size of 5-10 mm.

L: Organic dark brown top soil.

M: Light to dark brown organic horizon (paleosol).

N: Miocene mudstone (bedrock).

O: Peat. Organic horizon very dark, nearly black.

Q: Tephric paleosol with up to 2 mm size lapilli.

Z: Silty reworked tephra of uncertain origin.

X: Silty sandy weathered bedrock.

Figure 3: The northwest wall of Helios Trench at Ruatahuna

Figure 4: Thalassa (right-hand excavation) and Helios (left-hand excavation) trenches at Ruatahuna. View towards the southwest.

Figure 5: The northwest wall of Helios Trench at Ruatahuna in the foreground and the Thalassa Trench in the background. View towards the northwest.

Figure 6: The Armyra Trench at Ruatahuna Valley. View towards west.

TE MARAMA TRENCH

South wall

Ts: Top soil.

Mts: Mixed tephric sand.

Mcs: Mixed clayey sand.

Lts: Loose tephric sand with rounded gravels (up to 7 cm in diameter)

Dop: Dark organic mixed tephric paleosol with fragment of Taupo lapilli and rootlets.

Bss: Mixed brown sandy silt with rootlets.

Lgss: Light grey sandy silt with iron stain and dark organic lenses (MT1a-b) and roots.

Btss: Brown tephric sandy silt with roots.

Lmop: Loose mixed organic paleosol.

Sp: Sandy paleosol with rootlets.

Msc: Mixed sandy clay.

S1: Grey water-layered coarse to medium sand.

S2: Yellowish water-layered coarse to medium sand.

G: Rounded river gravels with coarse sand embedded within them.

Ch: Charcoal.

North wall

Ts: Top soil.

Tss: Mixed tephric silty sand with roots and charcoal in places. It forms a colluvial wedge.

Dop: Dark organic mixed tephric paleosol with fragment of Taupo lapili and rootlets.

Lgss: Light grey sandy silt with iron stain.

Bss: Lgss grades to a darker, more organic horizon of sandy silt with roots eastwards.

Btss: Brown tephric sandy silt with roots.

S1: Grey water-layered coarse to medium sand.

S2: Yellowish water-layered coarse to medium sand.

G: Rounded river gravels with coarse sand embedded within them.

CW: Mixed loose tephric sand, organic in places, with up to 2-3 cm rounded pebbles and angular gravels.

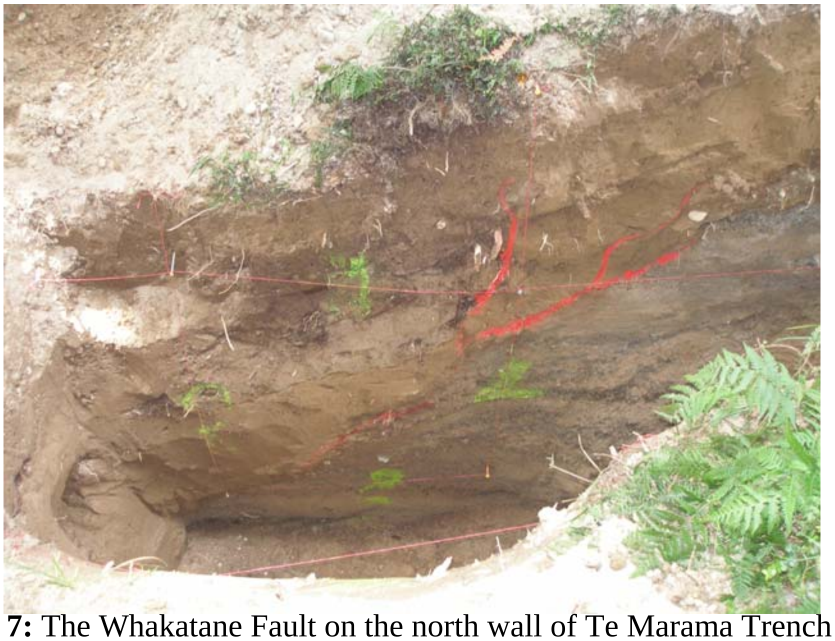

Figure 7: The Whakatane Fault on the north wall of Te Marama Trench at Wharepora.

Figure 8: The Whakatane Fault on the south wall of Te Marama Trench, Wharepora.

TE WHETU TRENCH
South walll

A: Conglomerate consisted of rounded river gravels up to 10 cm.

B: Rotoehu tephra (c. 50 kyr BP): 60-70 cm thick, whitish-pinkish coarse tephra.

C: Coarse lapilli within light brown clayey medium. This tephric unit belongs to Mangaone subgroup (c. 30 kyr BP).

D: Waiohu Tephra (13.8 kyr BP).

E: Waiohau Tephra (coarse lithic bed).

G: Pink clayey horizon up to 5cm thick within Waiohau Tephra.

H: Waiohau Tephra (creamy pumiceous coarse sand).

The (above) layers D-H represent the primary Waiohau airfall deposition (13.8 kyr BP).

I: Rotoma Tephra (9.5 kyr BP) consisted of brown coarse lapilli.

J: Brown medium to fine sandy horizon.

MCSP: Red brown medium to coarse grained pumicious massive sand.

L: Reworked Taupo Tephra. Granular tephra with white pumice lumps up to 1cm.

M: Mixed sandy tephra with charcoal and paleosol.

N: Brown mixed tephric soil with occasional charcoal and lapilli.

N*: Reddish brown coarse sand, frequent scattered pieces of lapilli up to 2 cm and few gravel clasts up to 7 cm especially on top surface and grey mottling.

O: Mixed dark brown bio-turbated paleosol with abundant cm size pumice lumps and occasional charcoal.

P: Mixed coarse tephric layer with medium to fine sand.

Q: Sandy brown wedges with occasional lapilli.

R: Brown fine to medium sand with occasional fragments of lapilli.

I2: Fine white sandstone mixed with paleosol.

S: Light-grey massive medium sand with some fe-staining, rare pumice up to 1 cm, overlies 1-2 cm peat layer. This is reworked Whakatane Tephra (5.6 kyr BP).

U: Mixed unit, brown-white cream in colour. Finely laminated mud at the base (lentic), brown-clayey coarse sand (lentic), white tephritic sand (lentic), with rare organic lenses.

OS: Dark brown clayey organic-rich medium sand with numerous twigs and branches gradational contact with J, contains lenses of coarse to medium sand.

Y: Reworked yellow-brown colour, cream brown medium sand with pumice clasts up to 15mm. Sandstone clasts average 20 mm.

W (Reworked Taupo & Whakatane tephras): Creamy to rusty-brown granular coarse sand / lapilli, up to 5 mm.

Ca: Blue-grey conglomerate medium sand sub-rounded siltstone pebbles up to >1.5 cm and pumice lumps up to 3 cm.

GCS: Grey medium to coarse pumiceous clayey sand with roots, sticks, organic fragments, up to 3cm pebbles of sandstone lithics, up to 4 mm pumice fragments.

Z: dark brown sand mixed with soil.

X: Dark brown organic peaty horizon.

Top soil: Modern A horizon.

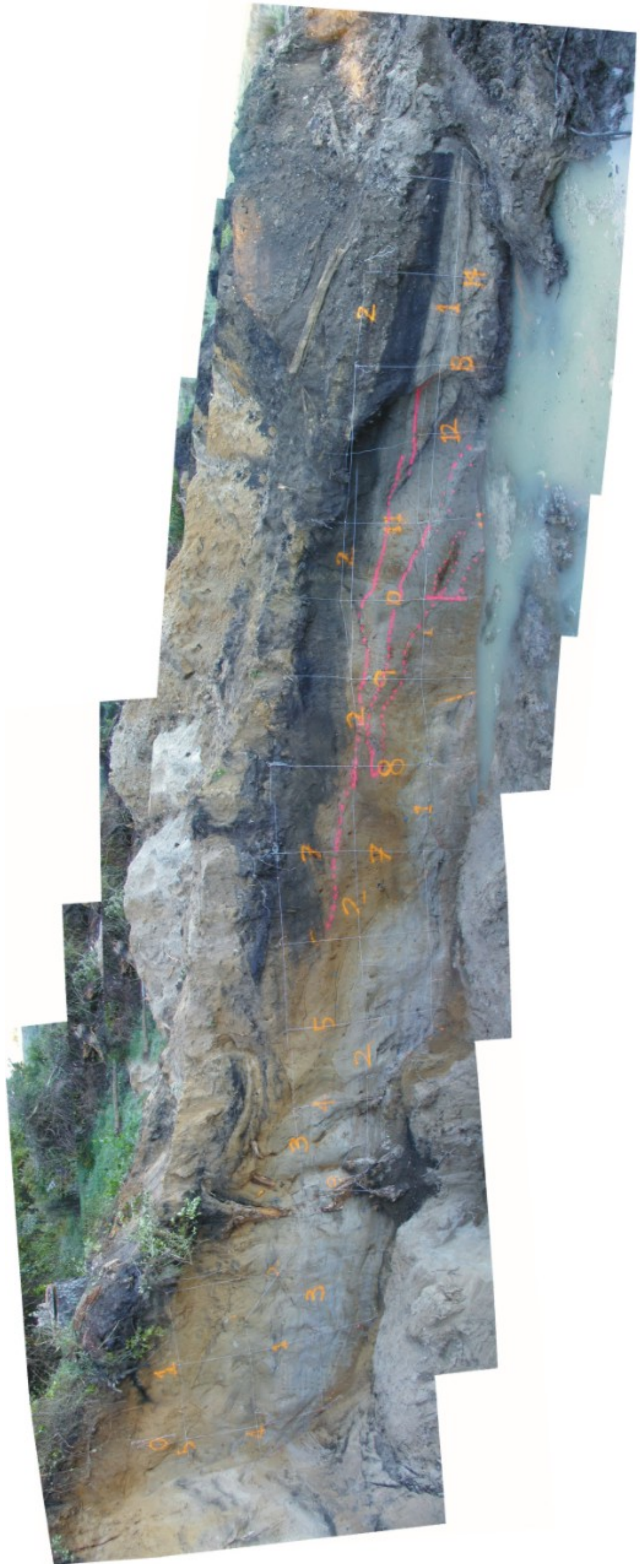

Figure 10: The Whakatane Fault on the south wall of Te Whetu Trench at Ruatoki North

WAIMANA FAULT

AHIRAU 1 TRENCH

South Wall

A: Black carbonaceous topsoil.

B: Paleosol below unit A (topsoil).

C: Paleosol on top of unit D. Contains coarse Taupo lapilli.

D: Coarse sand sized (lapilli) tephra – slightly oxidized. Taupo Tephra (1.8 kyr BP).

E: Paleosol on top of unit F. Light grey/brown. Base difficult to locate in places.

F: Light brown-white massive tephra.

G: Massive pebble/coble gravel – channel infill. Matrix fine-course sandstone.

H: Dark brown peat irregular top some modern roots.

I: Grey/green massive medium sandstone containing angular to rounded clasts up to pebble-small cobble size.

J: Grey/green massive pebble-coble gravel, angular to rounded clasts, medium sandstone matrix.

K: White to light grey well bedded (beds mm to cm thick) silt and fine sandstone.

K1: massive mixed unit equivalent to K.

L: Light grey/brown moderately bedded, coarse sandstone.

M: Grey/green/brown well sorted medium sandstone with some silt.

N: Dark brown peat some medium to fine sandstone.

O: Grey/green medium to coarse massive sandstone.

P: Brown/white coarse sandstone, well bedded. Bed dips 40-50°. Beds 1-4 mm thick. Waiohau Tephra (13.8 kyr BP).

Q: Light borwn, massive medium sandstone unit.

R: Light grey massive medium sandstone.

S: Dark brown/orange oxidized layer coarse well bedded sandstone.

T: Light grey/brown massive medium sandstone. Waiohau Tephra (13.8 kyr BP).

U: Light/grey well bedded coarse sandstone. Waiohau Tephra (13.8 kyr BP).

V: Dark brown peat discontinuous. Adjacent to fault zone contains angular to rounded clasts with sandstone matrix.

W: Dark/green massive pebble-cobble gravel, angular to rounded clasts with sandstone matrix.

X: Dark/grey massive pebble to boulder (clasts < 20 cm diameter) gravel (main alluvial gravel).

Figure 9: The Waimana Fault on the south wall of Ahirau 1 Trench, Te Ahirau.

North Wall

A: Black carbonaceous topsoil.

RW: Reworked "Taupo-sourced" tephra (Waimihia or Taupo).

F: Reworked Whakatane Tephra (5.6 kyr BP).

D: Taupo Tephra (1.8 kyr BP).

J: Grey/green massive pebble-coble gravel angular to rounded clasts, medium sandstone matrix (unit equivalent to unit J of south wall).

B: Brown paleosol, tephric in places.

MW: Massive reworked Waiohau Tephra (13.8 kyr BP).

BW: Bedded reworked Waiohau Tephra (13.8 kyr BP).

Cl: Massive clayey horizon.

Fw: Fine white ash.

Bs: River gravels up to 5 cm in size.

V: Dark brown peat organic horizon.

Figure 10: The main slip surface of the Waimana Fault on the north wall of Ahirau 1 Trench, Te Ahirau.

AHIRAU 2 TRENCH

North Wall

A: Massive blocky black fine sand with abundant roots and pods of yellow/brown reworked ‘subsoil’.

R: Subsoil-mixed unit. Massive weak brown coarse gritty sand with lapilli up to 5mm (possible of “Taupo Tephra” origin).

P: Reworked Waiohau. Dark yellow to yellow brown, massive-medium tephric poorly sorted sandstone/siltstone. Pumiceous grains (up to 5 mm) with angular quartzite clasts. Rusty spots, charcoal-bearing. At the base: Rusty weathered friable sandstone, well sorted, quartz rich, some coarse lapilli, massive = 10cm thick. Basal part of reworked Waiohau Tephra (13.8 kyr BP) includes pumice chips up to 5 mm in diameter.

D: Taupo Tephra (1.8 kyr BP). Massive loose yellow to pale yellow well sorted grit with lapilli, up to 5 mm.

C: Reworked Taupo-sourced tephra (possibly Waimihia - 3.5 kyr BP). Brown to yellow brown massive silty sand.

E: Reworked tephra. Pale yellow brown to yellow brown massive sand with some black staining along root channels.

F: Reworked tephra. Massive yellow brown silty tephric sand.

B: Paleosol. Grey to pale yellow brown slightly massive silty sand with few large greywacke angular clasts (up to 2cm) with some manganese.

S1: White to pale yellow blocky tephric fine sand.

S2: Pale yellow brown massive well sorted coarse sand.

S3: Grey to pale yellow coarse massive sand with sparse angular pebbles up to 3 cm.

X: Grey laminated silt ripples (2 mm), through cross bedding, light grey or brown mud lenses.

Gvl 1: Angular boulders and gravels up to 1 m diameter, beneath channel on west headwall on trench (E-W in axis). Silty sandstone matrix, clast massive colluvium.

Gvl-2: Grey-brown mottled sandy silt, contains angular greywacke clasts (up to 10 cm), massive in texture with tree roots.

Gvl-3: Poorly sorted gravel (cobbles 10 cm) and greywacke clasts within grey matrix of silty sand (poorly sorted).

Gvl-4: Matrix supported sub-angular pebble gravel within a pale yellow-brown matrix of tephric sand. Gravels at the base.

Gvl-5: Matrix supported pebble to small cobble gravel, sub-angular surrounded clasts (up to 6 cm). Matrix = pale yellow brown tephric sand.

Z: Angular gravels with grey silty matrix. Greywacke clasts (up to 10 cm). It also contains grey siltstone clasts capped by a 10 cm thick massive silt layer with gravel (fines upwards).

Y: Basal alluvium. Top: Matrix of grey to olive brown clayey silt with sparse sub-angular to sub-rounded pebbles up to 5 cm. Base: Sub-angular to sub-rounded greywacke boulders up to 15 cm.

W: Colluvial wedge. Mixed unit of gravels, sand, clay.

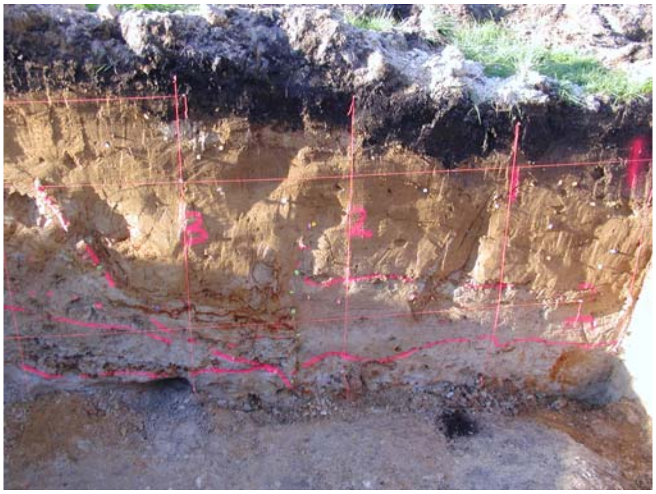

Figure 11: The Waimana Fault on the north wall of the Ahirau 2 Trench.

Figure 12: View of the Ahirau 1 (right-hand excavation) & Ahirau 2 (left-hand excavation) trenches at Te Ahirau. View towards the northwest.

MOANA TRENCH

North Wall

A: Organic topsoil.

Bz: Massive light brown coarse to medium lapilli extending laterally and below unit B (Taupo Tephra, 1.8 kyr BP).

B: Brown mid-coarse sand, some clay clasts (1cm) and pumice. Reworked Taupo Tephra.

F: Reworked Whakatane Tephra with few grains of a Taupo-sourced tephra - probably Waimihia. Coarse medium sand. Pale red brown tephritic clay-sand with some cream cakes. Laminated, becomes finer upwards, well bedded base, yellow to whitish layer with iron staining.

C3: Coarse whitish sand which contains grains of cummingtonite (Whakatane Tepha, 5.6 kyr BP).

D: Reworked Waiohau Tephra. Light yellow coarse sand well sorted that becomes coarser upwards. Horizontally stratified with some iron staining and with some charcoal. There is a white layer with cross bedding within this unit. In places contains bedrock clasts and becomes more clayey. Non-organic unit but becomes more organic towards the western section of the wall.

P: Primary Waiohau Tephra (13.8 kyr BP). Creamy white well sorted tephritic sand with grains up to 1-2 mm.

J: Green to whitish grayish clay (matrix) with some angular bedrock green pebbles (up to 4 cm).

L1: Gravely sandy clay, light brown to light grey. Bedrock mudstone and pumice clasts, poorly sorted mud flow. It becomes sandier and organic towards top.

K: Organic rich, peaty layer with dark brown to greenish grey poorly sorted gravel sand. Alternating coarse gravel-sand with clay. Upwards grades to fine sand.

L3: Clayey sandy gravel, greenish to grey, clasts up to 12 cm (most of them 1 cm), angular clasts very poorly sorted with some matrix supported.

M: Colluvium faulted in grain size. Sub-angular bedrock (up to 10 cm) pebbles. Sandy matrix, appears to be faulted against colluvium. It becomes more weathered towards the west.

L: Gritty colluvial – white grey clay matrix (pebbles up to 1 cm). Angular bedrock pebbles strongly mottled. Pebbles are iron coated.

W: Colluvial wedge. Light yellow brown sandy silt- fine sand mottling, iron stained with sparse bedrock clasts.

N: Light brownish to grey soft fine to medium massive sand.

X: Blue grey crushed Castlecliffean mustone with angular pebbles.

Figure 13: The main slip surface of the Waimana Fault on the north wall of Moana Trench.

South Wall

A: Organic topsoil.

Bz: Taupo Tephra (1.8 kyr BP). Compact massive yellow brown sandy ash with abundant yellow brown lapilli up to 4 mm.

B: Brown mid-coarse sand, some clay clasts (1cm) and pumice. Reworked Taupo Tephra.

O: Paleosol. Pale yellow brown, weak paleosol.

C3: Whakatane Tephra (5.6 kyr BP). A very pale brown-grey brown massive coarse sandy ash, with lapilli up to 2 mm.

RT: Reworked Whakatane Tephra. Pale yellow-brown sandy massive ash, loose in places, with a pale-brown clayey-silt at the base.

F: Whakatane Tephra reworked with few grains of a Taupo-sourced tephra - probably Waimihia. Pale red brown tephritic clay-sand with some cream cakes.

Coarse medium sand. Laminated, becomes finer upwards, well bedded base, yellow to whitish layer with iron staining.

P: Primary Waiohau Tephra (13.8 kyr BP). Creamy white coarse sandy layer laminated grains 1-2mm, well sorted. Contains charcoal and reworked wood.

D: Reworked Waiohau Tephra. Light yellow coarse sand, well sorted that becomes coarser upwards. Horizontally stratified with some iron staining and with some charcoal. There is a white layer with cross bedding within this unit. In places contains bedrock clasts and becomes more clayey. Non-organic unit but becomes more organic towards the western section of the wall.

K: Peaty soil. Dark reddish brown organic peaty mud with fibrous wood fragments, locally sandy and light in colour. Large local pebble gravel lenses (peat equivalent to that recorded in the unit K of north wall).

N: Light brownish/grey to yellowish coarse to fine sand. Fragments of detrital wood, rootlets with abandoned charcoal fragments and scattered bedrock pebbles.

G: Sandy gravel. Fluvial pebble gravel very poorly sorted, sub-angular pebbles in sand rich matrix.

T: Sub-angular bedrock pebble clasts less than 3 cm.

W: Tephric, sandy colluvium with clasts < 4 cm.

J: Medium grey clay with sparse sand and organics and bedrock clasts (weathered) up to 4 cm.

X: Crushed blue grey Castlecliffean mustone.

N: Intensely mottled clayey silt with sparse pods of rock clasts up to 5cm in bedrock relict fabric. Colour pale grey to dark yellow brown. Iron rich weathering.

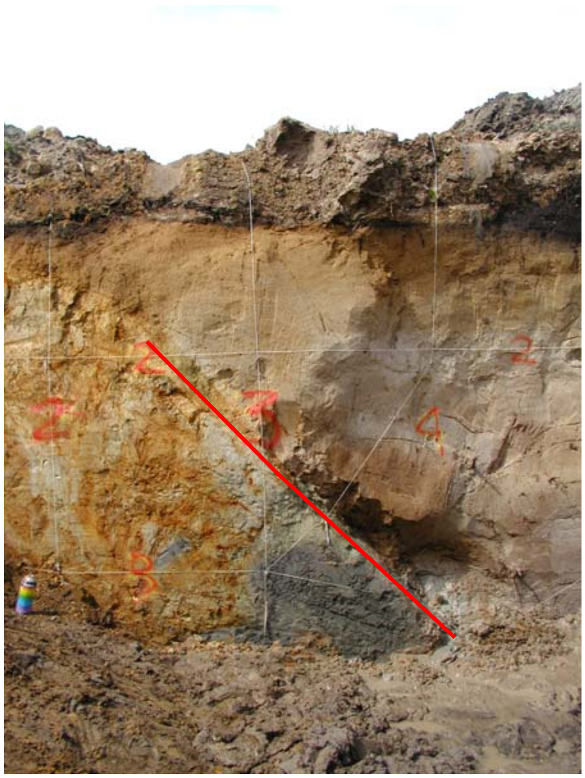

Figure 14: The main fault on the south wall of Moana Trench.

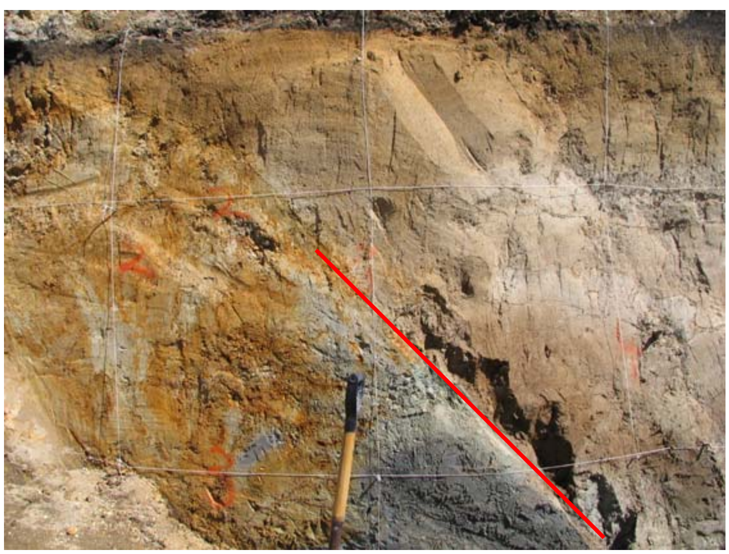

Figure 15: The main slip surface of the Waimna Fault on the south wall of Moana Trench.

Figure 16: Peat accumulated at the base of the Moana trench (south wall) against faulted Castlecliffean (green grey) mudstone (bottom left).

MOANA-ITI TRENCH

North Wall

S: Organic top soil.

A: Very dark-black soil horizon.

B: Grey brown to light brown with large clasts soil horizon.

C: Gravelly soil horizon with coarse sand and some clay and massive bedrock clasts. It is moderately dense.

D: Stream cobbles.

G: Crushed green Castlecliffean mudstone.

Tahi: Clayey sand with coarse pumiceous sand in it. Pinkish brown in colour.

Rua: Peat. Dark, reddish-brown ‘sheared-up’ peat.

Toru: Sandy mudstone, pale grey creamy in colour, very poorly sorted, possible debris flow with angular bedrock pebbles (<1cm) becoming clayey towards vertical 2.

Wha: White medium tephric sand.

Rima: Alluvial slump-block.

Ono: Very weathered clay rich Castlecliffean mudstone.

Whetu: Taupo Tephra (1.8 kyr BP).

Waru: Gravel layer, brown matrix supported medium sized gravel, clasts <10 cm, very angular. Matrix is sandy silt.

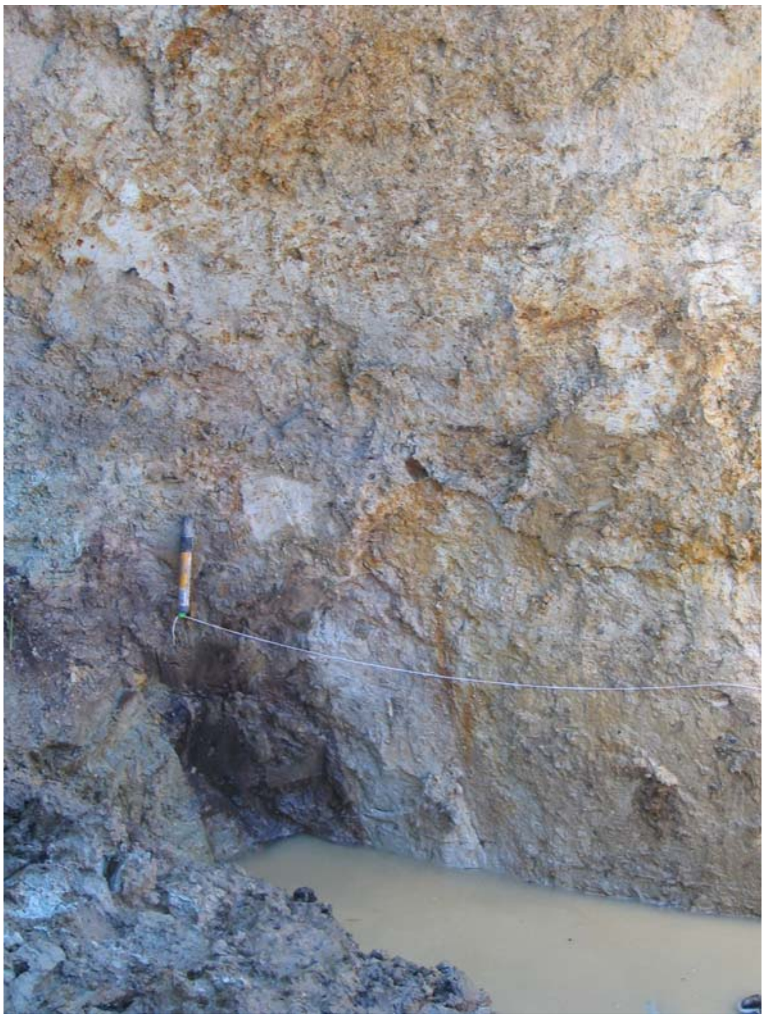

Figure 17: The Waimana Fault on the north wall of Moana-Iti Trench.

APPENDIX III

G L A S S   G E O C H E M I S T R Y   A N A L Y S E S

Representative electron microscope analyses of glass chemistry of late Quaternary tephras derived from the Okataina and Taupo volcanic centers, North Island, New Zealand are presented in this Appendix III. Analyses were conducted at Victoria University of Wellington, using the JEOL 733 SuperProbe (electron microprobe). The analytical facility has three wavelength dispersive X-ray spectrometers. An Electron Microprobe is a specialised Scanning Electron Microscope designed primarily for elemental analysis of polished surfaces such as rock and mineral thin sections. It does this by measuring the intensities and wavelengths of characteristic x-rays emitted from the point on the sample where the stationary electron beam is focused. A measured wavelength identifies the element, while the concentration is related to the x-ray intensity by a ZAF calculation. The finely focused electron beam can also be scanned over the sample to generate a corresponding magnified image on a high resolution screen.

The x-rays produced by the micro-probe are characterized by electromagnetic radiation of very short wavelength and high energy. They result from an incident primary electron ionising an inner shell electron in a sample atom. The excited atom relaxes when an outer electron fills the space. Energy is lost by emission of a characteristic x-ray. Secondary and backscattered electrons are also emitted and are detected separately for imaging purposes.

The Electron Microprobe is calibrated using standard minerals of known composition. For example Si and Ca are calibrated with a polished, carbon coated section of wollastonite. Some synthetic minerals, such as titanium dioxide and alumina, are also used to calibrate the micro-probe. A wide range of standards are mounted on a standards bar which resides inside the instrument. The bar is periodically repolished and re-coated with carbon.

A preliminary examination of the sample with an optical microscope is necessary. An incident light examination ensures that the region of interest is well polished and suitable for probing. The slide must be clean and needs to be coated with a carbon film of a standard 25nm thickness to make the surface conductive. This prevents the sample charging up and reducing the effective electron energy. The coating is deposited in a high vacuum chamber by electrically heating a narrow carbon rod. A polished brass plate is also coated. A royal blue interference colour on the plate corresponds to a coating thickness of 25 nm. The coating quality is important for successful analyses. For this reason coating should be done here as the thickness will be the same as on our standards. The coated sample is connected to the brass sample holder by a combination of metallised tape and a silver based paint. The typical program elements and probe conditions for tephras (settings depend on sample size and stability with the beam induced temperature rise) are:

- **TEPHRAS: Na Mg Al Si K Cl Ca Ti Cr Mn Fe Ni.**

Electron energy 15kV, beam current 6 to 8 nanoamps (recorded on printout), beam spot size from 10 micron up to 30 micron. Alkali elements are run first to reduce changes from electron beam heating during analysis.

For the analysis presented here 10 μm beam diameter was used. Analyses recalculated to 100% (volatile-free). Probe analyses are presented on a fault by fault basis, starting from the westernmost strand of the NIFS (i.e. Waiohau Fault) and continuing eastwards and, also, on a site by a site basis, starting from the south and advancing northwards. The number(s) of the site(s) that correspond to each analysis is indicated. For further details on the exact location, geometry and kinematics of the site associated with each analysis, refer to the Table 2.1 of Chapter 2 and to the Appendix I. Where no site is associated with the analysis the exact location (NZ Map Grid) of the sample is indicated.

The tephra correlations were made by plotting the following elements:

- K_2O against FeO
- CaO against FeO
- K2O against Cao

and comparing these values to a database of results, including: Froggatt & Solloway (1986); Lowe & Hogg (1986); Lowe (1988); Eden et al. (1993); Manning (and references therein) (1995); Newnham et al. (1995); Lowe et al. (1999); Wilmhurst et al. (1999); Shane & Hoverd (2002); Pillans & Wright (1992); Nairn et al. (2004).

WAIOHAU FAULT

Sample name: Waio; **Tephra ID:** Rerewhakaaitu; **Site(s) associated with the analysis:** 2

Table 1

	SiO2	Al2O3	TiO2	FeO	MnO	MgO	CaO	Na2O	K2O	Cl	TOTAL
1	74.50	11.99	0.13	0.86	0.07	0.10	0.71	4.02	3.77	0.14	96.30
2	73.02	11.48	0.08	0.94	0.11	0.07	0.64	3.56	4.03	0.15	94.09
3	73.60	11.66	0.06	0.72	0.09	0.06	0.62	3.53	3.66	0.16	94.15
4	75.11	11.63	0.12	0.81	0.10	0.10	0.72	3.46	3.74	0.14	95.93
5	74.01	11.52	0.15	0.77	0.09	0.11	0.70	3.53	3.98	0.19	95.03
6	74.74	11.62	0.09	0.82	0.00	0.10	0.83	3.56	3.97	0.24	95.97
7	74.94	11.79	0.09	0.71	0.03	0.10	0.69	3.64	4.47	0.10	96.55
8	75.41	11.61	0.10	0.92	0.04	0.09	0.76	3.72	4.09	0.17	96.92
9	74.12	11.77	0.06	0.77	0.05	0.13	0.72	3.42	3.75	0.13	94.91

Normalised	SiO2	Al2O3	TiO2	FeO	MnO	MgO	CaO	Na2O	K2O	Cl	TOTAL
1	77.36	12.45	0.13	0.89	0.07	0.10	0.74	4.17	3.91	0.15	100
2	77.61	12.20	0.09	1.00	0.12	0.07	0.68	3.78	4.28	0.16	100
3	78.17	12.38	0.06	0.76	0.10	0.06	0.66	3.75	3.89	0.17	100
4	78.30	12.12	0.13	0.84	0.10	0.10	0.75	3.61	3.90	0.15	100
5	77.88	12.12	0.16	0.81	0.09	0.12	0.74	3.71	4.19	0.20	100
6	77.88	12.11	0.09	0.85	0.00	0.10	0.86	3.71	4.14	0.25	100
7	77.62	12.21	0.09	0.74	0.03	0.10	0.71	3.77	4.63	0.10	100
8	77.81	11.98	0.10	0.95	0.04	0.09	0.78	3.84	4.22	0.18	100
9	78.10	12.40	0.06	0.81	0.05	0.14	0.76	3.60	3.95	0.14	100
Mean	77.86	12.22	0.10	0.85	0.07	0.10	0.74	3.77	4.12	0.17	100
St. Deviation	0.30	0.16	0.03	0.08	0.04	0.02	0.06	0.17	0.24	0.04	0

Sample name: Roto; **Tephra ID:** Waiohau; **Site(s) associated with the analysis:** 2

Table 2

	SiO2	Al2O3	TiO2	FeO	MnO	MgO	CaO	Na2O	K2O	Cl	TOTAL
1	75.02	11.79	0.08	0.74	0.07	0.12	0.74	4.20	3.48	0.13	96.36
2	76.20	11.85	0.14	0.89	0.03	0.11	0.78	4.17	3.31	0.23	97.72
3	74.27	11.73	0.14	0.71	0.03	0.09	0.86	4.03	3.27	0.22	95.35
4	77.39	12.09	0.16	0.87	0.03	0.10	0.79	4.12	3.37	0.20	99.13
5	76.76	12.16	0.15	0.66	0.07	0.13	0.79	4.23	3.53	0.16	98.65
6	75.91	12.17	0.11	0.80	0.14	0.08	0.66	4.32	3.41	0.19	97.78
7	74.17	11.61	0.10	0.90	0.00	0.10	0.68	4.24	3.46	0.21	95.47
8	74.28	11.61	0.12	1.01	0.05	0.14	0.75	4.04	3.36	0.16	95.52
9	76.87	11.95	0.11	1.10	0.08	0.12	0.82	4.27	3.36	0.15	98.84
10	77.17	12.08	0.08	0.82	0.15	0.09	0.83	4.19	3.30	0.26	98.97
11	74.72	11.66	0.17	0.67	0.00	0.07	0.83	4.08	3.32	0.11	95.64
12	74.05	11.56	0.20	0.73	0.07	0.16	0.83	3.98	3.01	0.14	94.74

Normalised	SiO2	Al2O3	TiO2	FeO	MnO	MgO	CaO	Na2O	K2O	Cl	TOTAL
1	77.85	12.24	0.08	0.77	0.07	0.12	0.77	4.36	3.61	0.13	100
2	77.98	12.13	0.14	0.91	0.03	0.11	0.80	4.27	3.39	0.24	100
3	77.89	12.30	0.15	0.74	0.03	0.09	0.90	4.23	3.43	0.23	100
4	78.07	12.20	0.16	0.88	0.03	0.10	0.80	4.16	3.40	0.20	100
5	77.81	12.33	0.15	0.67	0.07	0.13	0.80	4.29	3.58	0.16	100
6	77.63	12.45	0.11	0.82	0.14	0.08	0.67	4.42	3.49	0.19	100
7	77.69	12.16	0.10	0.94	0.00	0.10	0.71	4.44	3.62	0.22	100
8	77.76	12.15	0.13	1.06	0.05	0.15	0.79	4.23	3.52	0.17	100
9	77.77	12.09	0.11	1.11	0.08	0.12	0.83	4.32	3.40	0.15	100
10	77.97	12.21	0.08	0.83	0.15	0.09	0.84	4.23	3.33	0.26	100
11	78.13	12.19	0.18	0.70	0.00	0.07	0.87	4.27	3.47	0.12	100
12	78.16	12.20	0.21	0.77	0.07	0.17	0.88	4.20	3.18	0.15	100
Mean	77.89	12.22	0.13	0.85	0.06	0.11	0.80	4.28	3.45	0.19	100
St. Deviation	0.17	0.10	0.04	0.14	0.05	0.03	0.07	0.09	0.13	0.05	0

Sample name: Mam**; Tephra ID:** Mamaku; **Site(s) associated with the analysis:** 2

Table 3

	SiO2	Al2O3	TiO2	FeO	MnO	MgO	CaO	Na2O	K2O	Cl	TOTAL
1	76.50	11.97	0.14	0.79	0.00	0.09	0.80	4.23	3.37	0.16	98.05
2	77.20	12.24	0.14	0.72	0.08	0.12	0.78	4.21	3.44	0.12	99.06
3	72.28	11.55	0.10	0.72	0.00	0.13	0.67	3.15	2.85	0.24	91.70
4	76.27	11.92	0.13	0.81	0.09	0.11	0.69	4.11	3.51	0.16	97.79
5	75.88	11.91	0.08	0.85	0.08	0.12	0.81	4.21	3.24	0.15	97.33
6	77.41	12.11	0.10	0.82	0.06	0.16	1.07	4.20	3.23	0.14	99.29
7	76.09	11.91	0.15	1.03	0.04	0.11	0.85	4.26	3.22	0.20	97.85
8	71.44	11.25	0.12	0.71	0.18	0.08	0.69	3.99	2.91	0.20	91.57
9	74.90	11.81	0.12	0.64	0.10	0.15	0.75	4.23	3.44	0.16	96.31
10	71.54	11.39	0.08	0.60	0.15	0.09	0.59	4.06	3.18	0.08	91.77
11	76.93	12.29	0.20	0.76	0.11	0.14	0.73	3.95	3.23	0.21	98.56

Normalised	SiO2	Al2O3	TiO2	FeO	MnO	MgO	CaO	Na2O	K2O	Cl	TOTAL
1	78.02	12.21	0.14	0.81	0.00	0.09	0.82	4.31	3.44	0.16	100
2	77.93	12.36	0.14	0.73	0.08	0.12	0.79	4.25	3.47	0.12	100
3	78.82	12.60	0.11	0.79	0.00	0.14	0.73	3.44	3.11	0.26	100
4	77.99	12.19	0.13	0.83	0.09	0.11	0.71	4.20	3.59	0.16	100
5	77.96	12.24	0.08	0.87	0.08	0.12	0.83	4.33	3.33	0.15	100
6	77.96	12.20	0.10	0.83	0.06	0.16	1.08	4.23	3.25	0.14	100
7	77.76	12.17	0.15	1.05	0.04	0.11	0.87	4.35	3.29	0.20	100
8	78.02	12.29	0.13	0.78	0.20	0.09	0.75	4.36	3.18	0.22	100
9	77.77	12.26	0.12	0.66	0.10	0.16	0.78	4.39	3.57	0.17	100
10	77.96	12.41	0.09	0.65	0.16	0.10	0.64	4.42	3.47	0.09	100
11	78.05	12.47	0.20	0.77	0.11	0.14	0.74	4.01	3.28	0.21	100
Mean	78.02	12.31	0.13	0.80	0.08	0.12	0.79	4.21	3.36	0.17	100
St. Deviation	0.28	0.14	0.03	0.11	0.06	0.03	0.11	0.28	0.16	0.05	0

Sample name: Whak; **Tephra ID:** Whakatane; **Site(s) associated with the analysis:** 2

Table 4

	SiO2	Al2O3	TiO2	FeO	MnO	MgO	CaO	Na2O	K2O	Cl	TOTAL
1	75.35	11.79	0.10	1.04	0.06	0.06	0.57	3.89	4.14	0.17	97.15
2	74.10	11.89	0.08	0.68	0.19	0.12	0.57	3.54	3.77	0.13	95.09
3	73.18	11.69	0.13	0.75	0.16	0.10	0.59	3.86	3.80	0.13	94.39
4	76.79	12.17	0.05	1.05	0.17	0.08	0.72	4.12	3.29	0.19	98.63
5	73.44	11.55	0.14	0.66	0.19	0.08	0.56	3.76	3.36	0.15	93.88
6	74.91	11.81	0.06	0.75	0.06	0.08	0.67	4.08	3.58	0.14	96.14
7	70.44	11.23	0.04	0.69	0.06	0.06	0.64	3.69	3.35	0.37	90.57
8	73.92	11.61	0.09	0.81	0.07	0.12	0.61	3.96	3.46	0.15	94.80
9	74.87	11.92	0.14	0.82	0.00	0.04	0.64	3.98	3.28	0.22	95.92
10	76.64	12.02	0.08	0.82	0.12	0.13	0.68	4.10	3.85	0.14	98.58

Normalised	SiO2	Al2O3	TiO2	FeO	MnO	MgO	CaO	Na2O	K2O	Cl	TOTAL
1	77.56	12.14	0.10	1.07	0.06	0.06	0.59	4.00	4.26	0.17	100
2	77.93	12.50	0.08	0.72	0.20	0.13	0.60	3.72	3.96	0.14	100
3	77.53	12.38	0.14	0.79	0.17	0.11	0.63	4.09	4.03	0.14	100
4	77.86	12.34	0.05	1.06	0.17	0.08	0.73	4.18	3.34	0.19	100
5	78.23	12.30	0.15	0.70	0.20	0.09	0.60	4.01	3.58	0.16	100
6	77.92	12.28	0.06	0.78	0.06	0.08	0.70	4.24	3.72	0.15	100
7	77.77	12.40	0.04	0.76	0.07	0.07	0.71	4.07	3.70	0.41	100
8	77.97	12.25	0.09	0.85	0.07	0.13	0.64	4.18	3.65	0.16	100
9	78.05	12.43	0.15	0.85	0.00	0.04	0.67	4.15	3.42	0.23	100
10	77.74	12.19	0.08	0.83	0.12	0.13	0.69	4.16	3.91	0.14	100
Mean	77.86	12.32	0.10	0.84	0.11	0.09	0.65	4.08	3.76	0.19	100
St. Deviation	0.21	0.11	0.04	0.13	0.07	0.03	0.05	0.15	0.28	0.08	0

Sample name: Rere; **Tephra ID:** Okareka; **NZ Map Grid:** V16/449366

Table 5

	SiO2	Al2O3	TiO2	FeO	MnO	MgO	CaO	Na2O	K2O	Cl	TOTAL
1	73.16	11.35	0.12	0.83	0.10	0.08	0.72	3.56	3.57	0.15	93.65
2	77.21	12.18	0.16	0.90	0.02	0.09	0.85	4.07	3.57	0.15	99.20
3	74.15	11.79	0.16	1.01	0.11	0.07	0.78	3.60	4.57	0.19	96.42
4	76.51	11.87	0.12	1.04	0.03	0.15	0.94	3.30	3.52	0.15	97.63
5	74.41	12.01	0.11	0.93	0.12	0.14	0.79	3.25	3.30	0.19	95.25
6	74.01	11.68	0.16	0.96	0.02	0.18	1.04	2.47	3.47	0.19	94.19
7	75.41	11.66	0.18	0.94	0.09	0.11	0.93	3.59	3.16	0.18	96.25
8	72.63	11.80	0.18	1.11	0.17	0.18	0.92	1.06	3.20	0.15	91.40
9	76.54	11.96	0.13	1.04	0.00	0.14	0.89	3.92	3.00	0.14	97.75
10	72.32	11.42	0.14	0.99	0.00	0.07	0.78	2.33	4.20	0.17	92.43

Normalised	SiO2	Al2O3	TiO2	FeO	MnO	MgO	CaO	Na2O	K2O	Cl	TOTAL
1	78.12	12.12	0.13	0.89	0.11	0.09	0.77	3.80	3.81	0.16	100
2	77.83	12.28	0.16	0.91	0.02	0.09	0.86	4.10	3.60	0.15	100
3	76.90	12.23	0.17	1.05	0.11	0.07	0.81	3.73	4.74	0.20	100
4	78.37	12.16	0.12	1.07	0.03	0.15	0.96	3.38	3.61	0.15	100
5	78.12	12.61	0.12	0.98	0.13	0.15	0.83	3.41	3.46	0.20	100
6	78.58	12.40	0.17	1.02	0.02	0.19	1.10	2.62	3.68	0.20	100
7	78.35	12.11	0.19	0.98	0.09	0.11	0.97	3.73	3.28	0.19	100
8	79.46	12.91	0.20	1.21	0.19	0.20	1.01	1.16	3.50	0.16	100
9	78.30	12.24	0.13	1.06	0.00	0.14	0.91	4.01	3.07	0.14	100
10	78.24	12.36	0.15	1.07	0.00	0.08	0.84	2.52	4.54	0.18	100
Mean	78.23	12.34	0.15	1.02	0.07	0.13	0.91	3.25	3.73	0.17	100
St. Deviation	0.63	0.25	0.03	0.09	0.06	0.05	0.10	0.91	0.53	0.02	0

Sample name: Kawa; **Tephra ID:** Te Rere; **NZ Map Grid:** V16/449366

Table 6

	SiO2	Al2O3	TiO2	FeO	MnO	MgO	CaO	Na2O	K2O	Cl	TOTAL
1	75.97	11.72	0.12	1.36	0.20	0.16	0.96	3.42	3.03	0.23	97.16
2	75.19	11.86	0.22	1.24	0.02	0.12	1.01	3.36	2.83	0.19	96.04
3	74.33	11.90	0.12	1.11	0.06	0.11	1.00	3.95	2.49	0.16	95.23
4	76.27	12.26	0.13	1.47	0.08	0.11	1.01	3.60	3.36	0.18	98.47
5	73.34	11.73	0.11	1.11	0.03	0.12	0.91	3.42	2.93	0.17	93.87
6	75.24	11.98	0.20	1.24	0.01	0.11	1.07	3.54	2.97	0.22	96.58
7	74.55	11.93	0.16	1.32	0.00	0.15	1.03	3.42	2.90	0.20	95.65
8	75.11	11.77	0.16	1.14	0.04	0.13	0.84	3.78	3.63	0.17	96.78
9	75.22	11.42	0.10	1.04	0.07	0.11	1.15	3.93	3.15	0.10	96.30
10	73.54	11.85	0.03	1.06	0.10	0.14	1.10	3.86	2.71	0.24	94.62

Normalised	SiO2	Al2O3	TiO2	FeO	MnO	MgO	CaO	Na2O	K2O	Cl	TOTAL
1	78.19	12.06	0.12	1.40	0.21	0.16	0.99	3.52	3.12	0.24	100
2	78.29	12.35	0.23	1.29	0.02	0.12	1.05	3.50	2.95	0.20	100
3	78.05	12.50	0.13	1.17	0.06	0.12	1.05	4.15	2.61	0.17	100
4	77.46	12.45	0.13	1.49	0.08	0.11	1.03	3.66	3.41	0.18	100
5	78.13	12.50	0.12	1.18	0.03	0.13	0.97	3.64	3.12	0.18	100
6	77.90	12.40	0.21	1.28	0.01	0.11	1.11	3.67	3.08	0.23	100
7	77.94	12.47	0.17	1.38	0.00	0.16	1.08	3.58	3.03	0.21	100
8	77.61	12.16	0.17	1.18	0.04	0.13	0.87	3.91	3.75	0.18	100
9	78.11	11.86	0.10	1.08	0.07	0.11	1.19	4.08	3.27	0.10	100
10	77.72	12.52	0.03	1.12	0.11	0.15	1.16	4.08	2.86	0.25	100
Mean	77.94	12.33	0.14	1.26	0.06	0.13	1.05	3.78	3.12	0.19	100
St. Deviation	0.27	0.22	0.06	0.13	0.06	0.02	0.10	0.25	0.31	0.04	0

WHAKATANE FAULT

Ruatahuna

Sample name: Ru-1a; **Tephra ID:** Taupo; **Site(s) associated with the analysis:** 30-32

Table 7

	SiO2	Al2O3	TiO2	FeO	MnO	MgO	CaO	Na2O	K2O	Cl	TOTAL
1	73.66	13.23	0.26	1.88	0.13	0.19	1.27	4.68	2.67	0.16	98.12
2	74.43	13.51	0.20	1.73	0.22	0.13	1.39	4.21	2.81	0.12	98.76
3	75.61	13.35	0.21	1.98	0.16	0.20	1.58	4.58	2.91	0.15	100.73
4	75.35	13.39	0.26	1.93	0.32	0.10	1.43	4.45	2.72	0.14	100.09
5	72.91	13.17	0.18	2.05	0.10	0.30	1.42	3.94	2.75	0.17	96.99
6	73.11	13.17	0.23	1.82	0.11	0.25	1.45	4.27	2.75	0.20	97.37
7	74.69	13.26	0.29	2.07	0.06	0.34	1.48	4.47	2.68	0.17	99.52
8	73.84	13.22	0.14	1.83	0.06	0.25	1.38	4.26	2.82	0.16	97.96
9	77.08	13.39	0.22	1.85	0.04	0.25	1.35	3.80	2.87	0.17	101.01

Normalised	SiO2	Al2O3	TiO2	FeO	MnO	MgO	CaO	Na2O	K2O	Cl	TOTAL
1	75.07	13.48	0.26	1.92	0.13	0.19	1.29	4.77	2.72	0.16	100
2	75.36	13.68	0.20	1.75	0.22	0.13	1.41	4.26	2.85	0.12	100
3	75.06	13.25	0.21	1.97	0.16	0.20	1.57	4.55	2.89	0.15	100
4	75.28	13.38	0.26	1.93	0.32	0.10	1.43	4.45	2.72	0.14	100
5	75.17	13.58	0.19	2.11	0.10	0.31	1.46	4.06	2.84	0.18	100
6	75.08	13.53	0.24	1.87	0.11	0.26	1.49	4.39	2.82	0.21	100
7	75.05	13.32	0.29	2.08	0.06	0.34	1.49	4.49	2.69	0.17	100
8	75.38	13.50	0.14	1.87	0.06	0.26	1.41	4.35	2.88	0.16	100
9	76.31	13.26	0.22	1.83	0.04	0.25	1.34	3.76	2.84	0.17	100
Mean	75.31	13.44	0.22	1.92	0.13	0.23	1.43	4.34	2.81	0.16	100
St. Deviation	0.40	0.15	0.05	0.12	0.09	0.08	0.08	0.29	0.07	0.02	0

Sample name: Ru-Marae; **Tephra ID:** Kaharoa; **Sites associated with the analysis:** 30-32

Table 8

	SiO2	Al2O3	TiO2	FeO	MnO	MgO	CaO	Na2O	K2O	Cl	TOTAL
1	74.60	12.47	0.18	0.85	0.09	0.34	0.47	3.64	4.03	0.15	96.83
2	75.52	12.42	0.10	0.81	0.00	0.28	0.65	3.95	3.62	0.16	97.50
3	73.92	12.86	0.20	1.79	0.28	0.28	1.33	4.56	2.79	0.12	98.11
4	74.22	12.59	0.18	1.79	0.14	0.02	1.28	4.07	2.67	0.13	97.08
5	75.62	12.97	0.13	1.83	0.10	0.16	1.24	4.57	2.74	0.21	99.56
6	75.43	11.98	0.15	0.85	0.20	0.14	0.73	4.26	3.30	0.10	97.14
7	73.89	13.01	0.33	2.07	0.08	0.21	1.45	4.28	2.75	0.18	98.22
8	76.40	12.86	0.24	1.51	0.08	0.18	1.24	4.43	2.87	0.15	99.96

Normalised	SiO2	Al2O3	TiO2	FeO	MnO	MgO	CaO	Na2O	K2O	Cl	TOTAL
1	77.04	12.88	0.19	0.88	0.09	0.35	0.49	3.76	4.16	0.15	100
2	77.46	12.74	0.10	0.83	0.00	0.29	0.67	4.05	3.71	0.16	100
3	75.34	13.11	0.20	1.82	0.29	0.29	1.36	4.65	2.84	0.12	100
4	76.45	12.97	0.19	1.84	0.14	0.02	1.32	4.19	2.75	0.13	100
5	75.95	13.03	0.13	1.84	0.10	0.16	1.25	4.59	2.75	0.21	100
6	77.65	12.33	0.15	0.88	0.21	0.14	0.75	4.39	3.40	0.10	100
7	75.23	13.25	0.34	2.11	0.08	0.21	1.48	4.36	2.80	0.18	100
8	76.43	12.87	0.24	1.51	0.08	0.18	1.24	4.43	2.87	0.15	100
Mean	76.44	12.90	0.19	1.46	0.12	0.21	1.07	4.30	3.16	0.15	100
St. Deviation	0.91	0.28	0.07	0.52	0.09	0.10	0.37	0.29	0.54	0.03	0

Sample name: T1 (NWT); **Tephra ID:** Rotoma; **Sites associated with the analysis:** 30-32

Table 9

	SiO2	Al2O3	TiO2	FeO	MnO	MgO	CaO	Na2O	K2O	Cl	TOTAL
1	76.57	12.13	0.23	0.84	0.09	0.14	0.83	3.94	3.41	0.12	98.29
2	76.39	11.93	0.19	0.89	0.09	0.14	0.69	4.02	3.32	0.15	97.80
3	75.92	12.21	0.07	1.00	0.01	0.12	0.92	3.88	3.16	0.20	97.49
4	73.74	11.80	0.13	1.00	0.00	0.13	0.76	3.56	3.19	0.11	94.43
5	76.38	12.13	0.16	1.05	0.16	0.10	1.12	3.84	3.41	0.21	98.55
6	77.14	12.09	0.13	0.91	0.11	0.15	0.87	3.91	3.37	0.25	98.93
7	75.23	12.12	0.07	0.90	0.18	0.12	0.90	3.98	3.28	0.13	96.91
8	76.71	12.15	0.16	0.85	0.03	0.09	0.73	3.93	3.18	0.25	98.09

Normalised	SiO2	Al2O3	TiO2	FeO	MnO	MgO	CaO	Na2O	K2O	Cl	TOTAL
1	77.90	12.34	0.23	0.85	0.09	0.14	0.84	4.01	3.47	0.12	100
2	78.11	12.20	0.19	0.91	0.09	0.14	0.71	4.11	3.39	0.15	100
3	77.87	12.52	0.07	1.03	0.01	0.12	0.94	3.98	3.24	0.21	100
4	78.09	12.50	0.14	1.06	0.00	0.14	0.80	3.77	3.38	0.12	100
5	77.50	12.31	0.16	1.07	0.16	0.10	1.14	3.90	3.46	0.21	100
6	77.97	12.22	0.13	0.92	0.11	0.15	0.88	3.95	3.41	0.25	100
7	77.63	12.51	0.07	0.93	0.19	0.12	0.93	4.11	3.38	0.13	100
8	78.20	12.39	0.16	0.87	0.03	0.09	0.74	4.01	3.24	0.25	100
Mean	77.91	12.37	0.15	0.95	0.09	0.13	0.87	3.98	3.37	0.18	100
St. Deviation	0.24	0.13	0.06	0.08	0.07	0.02	0.14	0.11	0.09	0.06	0

Sample name: T2 (NWT); **Tephra ID:** Mamaku; **Sites associated with the analysis:** 30-32

Table 10

	SiO2	Al2O3	TiO2	FeO	MnO	MgO	CaO	Na2O	K2O	Cl	TOTAL
1	74.37	11.79	0.06	0.77	0.06	0.14	0.82	3.82	3.19	0.17	95.19
2	76.03	11.87	0.14	0.83	0.00	0.10	0.91	4.04	3.42	0.15	97.49
3	75.32	12.02	0.16	0.85	0.13	0.13	0.79	4.03	3.30	0.22	96.95
4	74.83	12.27	0.14	0.77	0.08	0.12	0.69	3.91	3.98	0.16	96.38
5	77.61	12.37	0.14	0.97	0.08	0.09	0.67	3.68	3.47	0.14	99.22
6	77.72	12.16	0.12	0.88	0.07	0.17	0.73	3.94	3.35	0.19	99.34
7	75.74	12.20	0.17	0.77	0.07	0.12	0.68	3.85	3.11	0.16	96.86
8	74.84	11.91	0.13	0.79	0.09	0.09	0.73	3.84	3.19	0.18	95.78

Normalised	SiO2	Al2O3	TiO2	FeO	MnO	MgO	CaO	Na2O	K2O	Cl	TOTAL
1	78.13	12.39	0.06	0.81	0.06	0.15	0.86	4.01	3.35	0.18	100
2	77.99	12.18	0.14	0.85	0.00	0.10	0.93	4.14	3.51	0.15	100
3	77.69	12.40	0.17	0.88	0.13	0.13	0.81	4.16	3.40	0.23	100
4	77.64	12.73	0.15	0.80	0.08	0.12	0.72	4.06	4.13	0.17	100
5	78.22	12.47	0.14	0.98	0.08	0.09	0.68	3.71	3.50	0.14	100
6	78.24	12.24	0.12	0.89	0.07	0.17	0.73	3.97	3.37	0.19	100
7	78.20	12.60	0.18	0.79	0.07	0.12	0.70	3.97	3.21	0.17	100
8	78.14	12.43	0.14	0.82	0.09	0.09	0.76	4.01	3.33	0.19	100
Mean	78.02	12.43	0.15	0.86	0.08	0.12	0.76	4.00	3.49	0.18	100
St. Deviation	0.25	0.19	0.02	0.06	0.04	0.03	0.09	0.15	0.30	0.03	0

Sample name: T3 (NWT); **Tephra ID:** Whakatane; **Sites associated with the analysis:** 30-32

Table 11

	SiO2	Al2O3	TiO2	FeO	MnO	MgO	CaO	Na2O	K2O	Cl	TOTAL
1	74.38	13.14	0.26	1.49	0.09	0.24	1.52	4.08	2.92	0.10	98.22
2	73.29	12.29	0.11	1.30	0.00	0.13	0.93	3.75	2.87	0.14	94.81
3	76.98	12.57	0.19	1.40	0.23	0.15	0.91	3.97	3.20	0.12	99.72
4	74.34	11.67	0.07	0.77	0.08	0.08	0.71	3.41	3.41	0.30	94.85
5	74.81	12.56	0.16	1.52	0.03	0.21	1.19	3.93	2.81	0.23	97.45
6	75.91	11.73	0.12	0.92	0.07	0.10	0.78	3.86	3.14	0.10	96.74
7	75.23	11.88	0.12	0.73	0.06	0.13	0.74	3.63	3.07	0.15	95.76
8	75.09	11.99	0.12	0.88	0.04	0.12	0.98	3.19	3.64	0.24	96.29
9	75.78	12.25	0.09	0.76	0.12	0.13	0.76	3.71	3.38	0.10	97.10
10	75.34	12.06	0.05	0.73	0.07	0.15	0.68	3.07	3.36	0.12	95.63

Normalised	SiO2	Al2O3	TiO2	FeO	MnO	MgO	CaO	Na2O	K2O	Cl	TOTAL
1	75.73	13.38	0.26	1.52	0.09	0.24	1.55	4.15	2.97	0.10	100
2	77.30	12.96	0.12	1.37	0.00	0.14	0.98	3.96	3.03	0.15	100
3	77.20	12.61	0.19	1.40	0.23	0.15	0.91	3.98	3.21	0.12	100
4	78.38	12.30	0.07	0.81	0.08	0.08	0.75	3.60	3.60	0.32	100
5	76.77	12.89	0.16	1.56	0.03	0.22	1.22	4.03	2.88	0.24	100
6	78.47	12.13	0.12	0.95	0.07	0.10	0.81	3.99	3.25	0.10	100
7	78.56	12.41	0.13	0.76	0.06	0.14	0.77	3.79	3.21	0.16	100
8	77.98	12.45	0.12	0.91	0.04	0.12	1.02	3.31	3.78	0.25	100
9	78.04	12.62	0.09	0.78	0.12	0.13	0.78	3.82	3.48	0.10	100
10	78.78	12.61	0.05	0.76	0.07	0.16	0.71	3.21	3.51	0.13	100
Mean	77.72	12.63	0.13	1.08	0.08	0.15	0.95	3.78	3.29	0.17	100
St. Deviation	0.96	0.36	0.06	0.34	0.06	0.05	0.26	0.32	0.29	0.07	0

Sample name: T1 (channel); **Tephra ID:** Whakatane; **Site(s) associated with the analysis:** 30-32

Table 12

	SiO2	Al2O3	TiO2	FeO	MnO	MgO	CaO	Na2O	K2O	Cl	TOTAL
1	71.76	11.60	0.10	0.89	0.06	0.04	0.65	3.31	3.48	0.20	92.09
2	75.72	12.18	0.09	0.76	0.02	0.12	0.75	4.01	3.30	0.13	97.06
3	74.21	11.81	0.08	0.65	0.01	0.12	0.54	3.52	3.70	0.16	94.79
4	76.16	12.27	0.08	0.78	0.05	0.11	0.65	3.67	3.76	0.20	97.74
5	75.18	12.01	0.15	0.74	0.06	0.05	0.63	3.54	3.71	0.12	96.22
6	74.86	11.73	0.15	0.86	0.05	0.11	0.64	3.72	3.63	0.17	95.92
7	75.40	12.09	0.09	0.89	0.14	0.09	0.66	3.48	3.63	0.13	96.59
8	74.70	11.88	0.04	0.77	0.00	0.07	0.62	3.57	3.87	0.22	95.75
9	74.56	11.74	0.17	0.86	0.00	0.08	0.61	3.54	3.62	0.18	95.34

Normalised	SiO2	Al2O3	TiO2	FeO	MnO	MgO	CaO	Na2O	K2O	Cl	TOTAL
1	77.92	12.60	0.11	0.97	0.07	0.04	0.71	3.59	3.78	0.22	100
2	78.01	12.55	0.09	0.78	0.02	0.12	0.77	4.13	3.40	0.13	100
3	78.29	12.46	0.08	0.69	0.01	0.13	0.57	3.71	3.90	0.17	100
4	77.92	12.55	0.08	0.80	0.05	0.11	0.67	3.75	3.85	0.20	100
5	78.13	12.48	0.16	0.77	0.06	0.05	0.65	3.68	3.86	0.12	100
6	78.04	12.23	0.16	0.90	0.05	0.11	0.67	3.88	3.78	0.18	100
7	78.06	12.52	0.09	0.92	0.14	0.09	0.68	3.60	3.76	0.13	100
8	78.02	12.41	0.04	0.80	0.00	0.07	0.65	3.73	4.04	0.23	100
9	78.20	12.31	0.18	0.90	0.00	0.08	0.64	3.71	3.80	0.19	100
Mean	78.07	12.46	0.11	0.84	0.05	0.09	0.67	3.76	3.80	0.18	100
St. Deviation	0.12	0.12	0.04	0.09	0.05	0.03	0.05	0.16	0.17	0.04	0

Sample name: T(-1); **Tephra ID:** Mangaone; **Site(s) associated with the analysis:** 30-32

Table 13

	SiO2	Al2O3	TiO2	FeO	MnO	MgO	CaO	Na2O	K2O	Cl	TOTAL
1	73.53	12.51	0.17	0.77	0.19	0.18	1.03	3.82	2.84	0.22	95.26
2	72.59	12.08	0.19	0.92	0.10	0.17	1.02	3.79	2.84	0.18	93.87
3	72.81	12.23	0.15	1.10	0.10	0.20	0.95	3.70	2.67	0.24	94.14
4	72.58	12.04	0.14	0.97	0.02	0.13	1.04	3.61	2.61	0.18	93.32
5	71.87	11.82	0.17	1.10	0.15	0.18	1.12	2.74	2.47	0.14	91.74
6	74.24	12.00	0.18	1.41	0.16	0.18	0.94	3.71	2.76	0.18	95.76
7	74.03	12.06	0.19	0.83	0.06	0.17	0.91	3.65	2.72	0.15	94.76
8	73.78	12.51	0.21	0.97	0.07	0.23	0.96	3.43	2.63	0.19	94.99
9	71.80	12.24	0.24	1.17	0.14	0.21	0.91	3.75	2.52	0.24	93.22

Normalised	SiO2	Al2O3	TiO2	FeO	MnO	MgO	CaO	Na2O	K2O	Cl	TOTAL
1	77.19	13.13	0.18	0.81	0.20	0.19	1.08	4.01	2.98	0.23	100
2	77.33	12.87	0.20	0.98	0.11	0.18	1.09	4.04	3.03	0.19	100
3	77.34	12.99	0.16	1.17	0.11	0.21	1.01	3.93	2.84	0.25	100
4	77.78	12.90	0.15	1.04	0.02	0.14	1.11	3.87	2.80	0.19	100
5	78.34	12.88	0.19	1.20	0.16	0.20	1.22	2.99	2.69	0.15	100
6	77.53	12.53	0.19	1.47	0.17	0.19	0.98	3.87	2.88	0.19	100
7	78.12	12.73	0.20	0.88	0.06	0.18	0.96	3.85	2.87	0.16	100
8	77.67	13.17	0.22	1.02	0.07	0.24	1.01	3.61	2.77	0.20	100
9	77.02	13.13	0.26	1.26	0.15	0.23	0.98	4.02	2.70	0.26	100
Mean	77.59	12.93	0.19	1.09	0.12	0.19	1.05	3.80	2.84	0.20	100
St. Deviation	0.43	0.21	0.03	0.20	0.06	0.03	0.08	0.33	0.11	0.04	0

Sample name: T3 (SWT); **Tephra ID:** Whakatane; **Site(s) associated with the analysis:** 30-32

Table 14

	SiO2	Al2O3	TiO2	FeO	MnO	MgO	CaO	Na2O	K2O	Cl	TOTAL
1	74.64	12.11	0.17	1.19	0.01	0.07	0.76	3.66	3.40	0.10	96.12
2	76.87	12.33	0.12	0.74	0.13	0.06	0.69	3.72	3.77	0.21	98.64
3	74.05	11.89	0.12	0.91	0.02	0.10	0.55	3.71	3.65	0.16	95.17
4	75.87	12.05	0.06	1.29	0.07	0.14	0.62	4.04	3.52	0.16	97.82
5	78.05	12.28	0.08	0.83	0.11	0.07	0.62	3.89	3.65	0.21	99.78
6	75.40	11.78	0.15	0.60	0.08	0.12	0.67	3.61	3.57	0.26	96.23
7	76.88	12.11	0.08	0.70	0.10	0.12	0.73	4.08	3.31	0.18	98.31
8	76.47	12.70	0.18	1.56	0.14	0.21	1.46	3.88	3.18	0.13	99.92
9	76.65	12.34	0.02	1.01	0.05	0.14	0.72	3.75	3.52	0.19	98.39
10	74.34	12.12	0.22	1.04	0.19	0.12	1.05	3.72	3.32	0.20	96.32

Normalised	SiO2	Al2O3	TiO2	FeO	MnO	MgO	CaO	Na2O	K2O	Cl	TOTAL
1	77.65	12.60	0.18	1.24	0.01	0.07	0.79	3.81	3.54	0.10	100
2	77.93	12.50	0.12	0.75	0.13	0.06	0.70	3.77	3.82	0.21	100
3	77.81	12.49	0.13	0.96	0.02	0.11	0.58	3.90	3.84	0.17	100
4	77.56	12.32	0.06	1.32	0.07	0.14	0.63	4.13	3.60	0.16	100
5	78.22	12.31	0.08	0.83	0.11	0.07	0.62	3.90	3.66	0.21	100
6	78.35	12.24	0.16	0.62	0.08	0.12	0.70	3.75	3.71	0.27	100
7	78.20	12.32	0.08	0.71	0.10	0.12	0.74	4.15	3.37	0.18	100
8	76.53	12.71	0.18	1.56	0.14	0.21	1.46	3.88	3.18	0.13	100
9	77.90	12.54	0.02	1.03	0.05	0.14	0.73	3.81	3.58	0.19	100
10	77.18	12.58	0.23	1.08	0.20	0.12	1.09	3.86	3.45	0.21	100
Mean	77.73	12.46	0.12	1.01	0.09	0.12	0.80	3.90	3.57	0.18	100
St. Deviation	0.55	0.16	0.06	0.30	0.06	0.04	0.27	0.14	0.20	0.05	0

Sample name: T(-2) Auger; **Tephra ID:** Rotoehu; **Site(s) associated with the analysis:** 30-32

Table 15

	SiO2	Al2O3	TiO2	FeO	MnO	MgO	CaO	Na2O	K2O	Cl	TOTAL
1	76.16	11.73	0.10	0.97	0.06	0.12	0.78	3.88	3.17	0.19	97.16
2	76.59	12.23	0.15	0.88	0.00	0.11	0.71	3.76	3.13	0.19	97.75
3	74.99	11.98	0.12	0.78	0.05	0.21	0.79	3.79	3.27	0.08	96.06
4	75.82	12.34	0.16	0.81	0.14	0.15	0.80	3.80	3.35	0.13	97.49
5	74.49	12.15	0.15	0.80	0.14	0.18	0.78	3.74	3.10	0.21	95.75
6	75.12	12.06	0.11	0.76	0.07	0.12	0.86	3.77	3.14	0.15	96.17
7	76.34	12.00	0.12	1.03	0.07	0.10	0.69	3.72	3.32	0.19	97.58
8	74.68	12.21	0.10	0.72	0.08	0.14	0.79	3.75	3.22	0.17	95.87
9	75.46	11.84	0.20	0.73	0.04	0.17	0.67	3.70	3.22	0.14	96.17
10	75.71	12.18	0.10	0.93	0.13	0.16	0.98	3.81	2.90	0.20	97.11

Normalised	SiO2	Al2O3	TiO2	FeO	MnO	MgO	CaO	Na2O	K2O	Cl	TOTAL
1	78.39	12.07	0.10	1.00	0.06	0.12	0.80	3.99	3.26	0.20	100
2	78.35	12.51	0.15	0.90	0.00	0.11	0.73	3.85	3.20	0.19	100
3	78.07	12.47	0.12	0.81	0.05	0.22	0.82	3.95	3.40	0.08	100
4	77.77	12.66	0.16	0.83	0.14	0.15	0.82	3.90	3.44	0.13	100
5	77.80	12.69	0.16	0.84	0.15	0.19	0.81	3.91	3.24	0.22	100
6	78.11	12.54	0.11	0.79	0.07	0.12	0.89	3.92	3.27	0.16	100
7	78.23	12.30	0.12	1.06	0.07	0.10	0.71	3.81	3.40	0.19	100
8	77.90	12.74	0.10	0.75	0.08	0.15	0.82	3.91	3.36	0.18	100
9	78.47	12.31	0.21	0.76	0.04	0.18	0.70	3.85	3.35	0.15	100
10	77.96	12.54	0.10	0.96	0.13	0.16	1.01	3.92	2.99	0.21	100
Mean	78.10	12.48	0.14	0.87	0.08	0.15	0.81	3.90	3.29	0.17	100
St. Deviation	0.25	0.20	0.03	0.10	0.05	0.04	0.09	0.05	0.13	0.04	0

Sample name: T(0); **Tephra ID:** Kawakawa; **Site(s) associated with the analysis:** 30-32

Table 16

	SiO2	Al2O3	TiO2	FeO	MnO	MgO	CaO	Na2O	K2O	Cl	TOTAL
1	73.34	11.43	0.12	1.15	0.03	0.15	1.19	1.69	2.47	0.11	91.68
2	73.15	11.21	0.09	1.23	0.07	0.12	0.97	3.50	2.91	0.18	93.43
3	72.96	11.19	0.15	1.26	0.10	0.09	1.08	3.75	3.03	0.21	93.83
4	73.61	11.23	0.10	0.98	0.14	0.07	0.94	3.01	3.13	0.15	93.36
5	73.90	11.69	0.08	1.06	0.14	0.13	1.24	3.62	2.79	0.12	94.80
6	72.98	11.68	0.17	1.22	0.00	0.08	0.94	3.64	2.77	0.19	93.67
7	73.58	11.69	0.15	1.13	0.09	0.12	0.97	3.78	2.79	0.23	94.53
8	73.97	11.64	0.16	0.91	0.06	0.16	0.98	3.53	3.02	0.13	94.55
9	73.89	11.81	0.15	1.01	0.09	0.09	0.93	3.77	3.09	0.17	95.00

Normalised	SiO2	Al2O3	TiO2	FeO	MnO	MgO	CaO	Na2O	K2O	Cl	TOTAL
1	80.00	12.47	0.13	1.25	0.03	0.16	1.30	1.84	2.69	0.12	100
2	78.29	12.00	0.10	1.32	0.07	0.13	1.04	3.75	3.11	0.19	100
3	77.76	11.93	0.16	1.34	0.11	0.10	1.15	4.00	3.23	0.22	100
4	78.85	12.03	0.11	1.05	0.15	0.07	1.01	3.22	3.35	0.16	100
5	77.95	12.33	0.08	1.12	0.15	0.14	1.31	3.82	2.94	0.13	100
6	77.91	12.47	0.18	1.30	0.00	0.09	1.00	3.89	2.96	0.20	100
7	77.84	12.37	0.16	1.20	0.10	0.13	1.03	4.00	2.95	0.24	100
8	78.23	12.31	0.17	0.96	0.06	0.17	1.04	3.73	3.19	0.14	100
9	77.78	12.43	0.16	1.06	0.09	0.09	0.98	3.97	3.25	0.18	100
Mean	78.29	12.26	0.14	1.18	0.09	0.12	1.09	3.58	3.08	0.18	100
St. Deviation	0.73	0.21	0.03	0.14	0.05	0.03	0.13	0.69	0.21	0.04	0

Sample name: T1 (SW_IN); **Tephra ID:** Rotoma; **Site(s) associated with the analysis:** 30-32

Table 17

	SiO2	Al2O3	TiO2	FeO	MnO	MgO	CaO	Na2O	K2O	Cl	TOTAL
1	74.04	12.02	0.11	0.98	0.12	0.08	0.72	3.78	3.53	0.15	95.53
2	75.97	12.28	0.08	0.86	0.00	0.15	0.83	4.06	3.21	0.16	97.59
3	76.31	12.27	0.15	0.94	0.07	0.20	0.85	4.41	3.17	0.13	98.50
4	77.93	12.21	0.18	0.83	0.08	0.16	0.87	4.21	3.05	0.11	99.63
5	74.26	11.78	0.18	0.67	0.15	0.09	0.65	3.72	3.70	0.16	95.37
6	75.60	11.92	0.14	0.86	0.00	0.08	0.63	3.90	3.63	0.17	96.94
7	77.68	12.45	0.15	0.72	0.09	0.14	0.95	4.24	3.25	0.21	99.86
8	75.18	11.73	0.09	0.85	0.05	0.04	0.60	1.67	3.85	0.18	94.25

Normalised	SiO2	Al2O3	TiO2	FeO	MnO	MgO	CaO	Na2O	K2O	Cl	TOTAL
1	77.50	12.58	0.12	1.03	0.13	0.08	0.75	3.96	3.70	0.16	100
2	77.85	12.58	0.08	0.88	0.00	0.15	0.85	4.16	3.29	0.16	100
3	77.47	12.46	0.15	0.95	0.07	0.20	0.86	4.48	3.22	0.13	100
4	78.22	12.26	0.18	0.83	0.08	0.16	0.87	4.23	3.06	0.11	100
5	77.87	12.35	0.19	0.70	0.16	0.09	0.68	3.90	3.88	0.17	100
6	77.99	12.30	0.14	0.89	0.00	0.08	0.65	4.02	3.74	0.18	100
7	77.79	12.47	0.15	0.72	0.09	0.14	0.95	4.25	3.25	0.21	100
8	79.77	12.45	0.10	0.90	0.05	0.04	0.64	1.77	4.08	0.19	100
Mean	78.06	12.43	0.14	0.86	0.07	0.12	0.78	3.85	3.53	0.16	100
St. Deviation	0.73	0.12	0.04	0.11	0.06	0.05	0.12	0.86	0.37	0.03	0

Sample name: T2 (SW); **Tephra ID:** Mamaku (2 grains from different tephra); **Site(s) associated with the analysis:** 30-32

Table 18

	SiO2	Al2O3	TiO2	FeO	MnO	MgO	CaO	Na2O	K2O	Cl	TOTAL
1	75.36	12.20	0.03	0.99	0.07	0.14	0.81	4.32	2.89	0.15	96.95
2	74.73	12.12	0.10	0.79	0.01	0.17	0.71	4.12	3.23	0.15	96.11
3	73.95	11.87	0.04	0.80	0.08	0.12	0.71	4.35	3.35	0.12	95.40
4	73.70	13.04	0.18	1.52	0.07	0.19	1.37	4.21	2.85	0.20	97.33
5	74.08	12.07	0.15	0.78	0.10	0.08	0.75	3.77	3.29	0.14	95.20
6	72.38	12.92	0.21	1.67	0.09	0.27	1.66	4.33	2.97	0.17	96.68
7	74.81	11.85	0.10	0.88	0.07	0.15	0.69	4.25	3.12	0.22	96.14
8	76.29	12.11	0.16	0.78	0.03	0.13	0.78	4.16	3.59	0.20	98.24

Normalised	SiO2	Al2O3	TiO2	FeO	MnO	MgO	CaO	Na2O	K2O	Cl	TOTAL
1	77.73	12.58	0.03	1.02	0.07	0.14	0.84	4.46	2.98	0.15	100
2	77.75	12.61	0.10	0.82	0.01	0.18	0.74	4.29	3.36	0.16	100
3	77.52	12.44	0.04	0.84	0.08	0.13	0.74	4.56	3.51	0.13	100
4	75.72	13.40	0.18	1.56	0.07	0.20	1.41	4.33	2.93	0.21	100
5	77.82	12.68	0.16	0.82	0.11	0.08	0.79	3.96	3.46	0.15	100
6	74.87	13.36	0.22	1.73	0.09	0.28	1.72	4.48	3.07	0.18	100
7	77.81	12.33	0.10	0.92	0.07	0.16	0.72	4.42	3.25	0.23	100
8	77.66	12.33	0.16	0.79	0.03	0.13	0.79	4.23	3.65	0.20	100
Mean	77.11	12.72	0.13	1.06	0.07	0.16	0.97	4.34	3.28	0.17	100
St. Deviation	1.15	0.43	0.07	0.37	0.03	0.06	0.38	0.19	0.26	0.04	0

Sample name: T2 (bsw_IN); **Tephra ID:** Rotoma; **Site(s) associated with the analysis:** 30-32

Table 19

	SiO2	Al2O3	TiO2	FeO	MnO	MgO	CaO	Na2O	K2O	Cl	TOTAL
1	74.72	11.88	0.12	0.85	0.09	0.15	0.90	3.68	3.08	0.16	95.62
2	76.88	12.22	0.09	1.02	0.10	0.10	0.90	4.00	3.50	0.17	98.99
3	74.01	12.05	0.16	0.94	0.09	0.11	0.84	3.84	3.16	0.15	95.34
4	75.15	11.76	0.08	1.00	0.12	0.14	0.91	3.92	2.93	0.09	96.09
5	75.48	12.00	0.19	1.17	0.14	0.15	0.84	3.80	3.19	0.16	97.13
6	74.73	11.72	0.09	1.06	0.05	0.19	0.85	3.78	3.72	0.18	96.39
7	75.05	11.74	0.13	0.90	0.11	0.12	0.76	3.88	3.12	0.15	95.95
8	73.12	11.89	0.15	1.03	0.07	0.11	0.97	3.49	3.05	0.15	94.04
9	75.69	12.52	0.22	0.75	0.07	0.12	0.84	3.92	3.28	0.13	97.56
10	74.70	12.38	0.10	0.85	0.05	0.19	0.87	3.87	3.12	0.19	96.33

Normalised	SiO2	Al2O3	TiO2	FeO	MnO	MgO	CaO	Na2O	K2O	Cl	TOTAL
1	78.14	12.42	0.13	0.89	0.09	0.16	0.94	3.85	3.22	0.17	100
2	77.66	12.34	0.09	1.03	0.10	0.10	0.91	4.04	3.54	0.17	100
3	77.63	12.64	0.17	0.99	0.09	0.12	0.88	4.03	3.31	0.16	100
4	78.21	12.24	0.08	1.04	0.12	0.15	0.95	4.08	3.05	0.09	100
5	77.71	12.35	0.20	1.20	0.14	0.15	0.86	3.91	3.28	0.16	100
6	77.53	12.16	0.09	1.10	0.05	0.20	0.88	3.92	3.86	0.19	100
7	78.22	12.24	0.14	0.94	0.11	0.13	0.79	4.04	3.25	0.16	100
8	77.75	12.64	0.16	1.10	0.07	0.12	1.03	3.71	3.24	0.16	100
9	77.58	12.83	0.23	0.77	0.07	0.12	0.86	4.02	3.36	0.13	100
10	77.55	12.85	0.10	0.88	0.05	0.20	0.90	4.02	3.24	0.20	100
Mean	77.80	12.47	0.14	0.99	0.09	0.14	0.90	3.96	3.34	0.16	100
St. Deviation	0.28	0.25	0.05	0.13	0.03	0.03	0.06	0.11	0.22	0.03	0

Taneatua Basin

Sample name: NF; **Tephra ID:** Mangaone subgroup; **Site(s) associated with the analysis:** 26

Table 20

	SiO2	Al2O3	TiO2	FeO	MnO	MgO	CaO	Na2O	K2O	Cl	TOTAL
1	74.22	12.50	0.15	1.30	0.05	0.07	0.95	4.10	2.86	0.15	96.35
2	72.54	12.45	0.18	1.03	0.16	0.24	1.07	4.26	2.98	0.16	95.07
3	72.82	12.54	0.15	1.05	0.19	0.25	1.11	4.50	2.62	0.12	95.34
4	71.80	12.72	0.18	1.13	0.02	0.47	1.05	4.28	2.71	0.16	94.51
5	71.94	12.07	0.09	1.19	0.15	0.27	1.04	4.30	2.67	0.21	93.93
6	71.45	12.70	0.15	1.00	0.13	0.13	0.99	4.29	2.64	0.24	93.72
7	74.23	12.47	0.19	0.96	0.18	0.16	1.04	4.40	2.71	0.21	96.56

Normalised	SiO2	Al2O3	TiO2	FeO	MnO	MgO	CaO	Na2O	K2O	Cl	TOTAL
1	77.03	12.97	0.16	1.35	0.05	0.07	0.99	4.26	2.97	0.16	100
2	76.30	13.10	0.19	1.08	0.17	0.25	1.13	4.48	3.13	0.17	100
3	76.38	13.15	0.16	1.10	0.20	0.26	1.16	4.72	2.75	0.13	100
4	75.97	13.46	0.19	1.20	0.02	0.50	1.11	4.53	2.87	0.17	100
5	76.59	12.85	0.10	1.27	0.16	0.29	1.11	4.58	2.84	0.22	100
6	76.24	13.55	0.16	1.07	0.14	0.14	1.06	4.58	2.82	0.26	100
7	76.87	12.91	0.20	0.99	0.19	0.17	1.08	4.56	2.81	0.22	100
Mean	76.48	13.14	0.16	1.15	0.13	0.24	1.09	4.53	2.88	0.19	100
St. Deviation	0.37	0.27	0.03	0.12	0.07	0.14	0.06	0.14	0.13	0.05	0

Sample name: Noti B; **Tephra ID:** Te Rere; **Site(s) associated with the analysis:** 26

Table 21

	SiO2	Al2O3	TiO2	FeO	MnO	MgO	CaO	Na2O	K2O	Cl	TOTAL
1	75.12	12.11	0.14	0.71	0.01	0.08	0.73	3.59	4.11	0.19	96.79
2	75.83	11.88	0.13	0.86	0.08	0.18	0.73	3.61	3.27	0.09	96.66
3	75.39	12.14	0.13	0.89	0.00	0.16	1.00	3.86	3.14	0.24	96.96
4	74.09	12.15	0.11	1.13	0.13	0.14	0.75	3.74	3.23	0.13	95.62
5	75.14	12.15	0.18	1.19	0.05	0.14	0.99	3.31	3.36	0.20	96.71
6	74.97	11.90	0.11	1.32	0.08	0.16	0.75	3.85	3.11	0.13	96.38
7	73.42	11.72	0.15	0.95	0.11	0.15	0.92	3.23	2.95	0.21	93.81
8	74.43	11.77	0.19	0.92	0.00	0.12	0.88	1.95	2.82	0.17	93.24
9	75.72	12.11	0.10	1.17	0.00	0.16	1.01	3.83	3.31	0.17	97.58
10	74.44	12.05	0.12	0.73	0.04	0.08	0.69	3.65	3.46	0.18	95.46

Normalised	SiO2	Al2O3	TiO2	FeO	MnO	MgO	CaO	Na2O	K2O	Cl	TOTAL
1	77.61	12.51	0.14	0.73	0.01	0.08	0.75	3.71	4.25	0.20	100
2	78.45	12.29	0.13	0.89	0.08	0.19	0.76	3.73	3.38	0.09	100
3	77.75	12.52	0.13	0.92	0.00	0.17	1.03	3.98	3.24	0.25	100
4	77.48	12.71	0.12	1.18	0.14	0.15	0.78	3.91	3.38	0.14	100
5	77.70	12.56	0.19	1.23	0.05	0.14	1.02	3.42	3.47	0.21	100
6	77.79	12.35	0.11	1.37	0.08	0.17	0.78	3.99	3.23	0.13	100
7	78.26	12.49	0.16	1.01	0.12	0.16	0.98	3.44	3.14	0.22	100
8	79.83	12.62	0.20	0.99	0.00	0.13	0.94	2.09	3.02	0.18	100
9	77.60	12.41	0.10	1.20	0.00	0.16	1.04	3.92	3.39	0.17	100
10	77.98	12.62	0.13	0.76	0.04	0.08	0.72	3.82	3.62	0.19	100
Mean	78.05	12.51	0.14	1.03	0.05	0.14	0.88	3.60	3.41	0.18	100
St. Deviation	0.70	0.13	0.03	0.21	0.05	0.03	0.13	0.57	0.34	0.05	0

Sample name: Ng; **Tephra ID:** Rerewhakaaitu; **Site(s) associated with the analysis:** 26

Table 22

	SiO2	Al2O3	TiO2	FeO	MnO	MgO	CaO	Na2O	K2O	Cl	TOTAL
1	73.96	12.50	0.17	0.77	0.17	0.03	0.70	3.66	4.13	0.14	96.24
2	77.34	12.48	0.11	1.00	0.13	0.40	0.90	4.22	3.46	0.17	100.22
3	75.47	12.14	0.10	0.78	0.04	0.03	0.81	3.71	4.32	0.16	97.55
4	76.15	12.60	0.08	0.87	0.10	0.10	0.76	3.73	4.15	0.20	98.74
5	76.15	12.23	0.14	0.87	0.05	0.21	0.84	4.03	3.14	0.14	97.80
6	77.38	12.37	0.16	0.85	0.03	0.14	0.73	3.91	4.59	0.13	100.28
7	77.09	12.23	0.16	0.80	0.14	0.24	0.96	4.09	3.46	0.15	99.33
8	74.50	11.90	0.14	0.84	0.00	0.29	0.83	3.85	3.27	0.15	95.76

Normalised	SiO2	Al2O3	TiO2	FeO	MnO	MgO	CaO	Na2O	K2O	Cl	TOTAL
1	76.85	12.99	0.18	0.80	0.18	0.03	0.73	3.80	4.29	0.15	100
2	77.17	12.45	0.11	1.00	0.13	0.40	0.90	4.21	3.45	0.17	100
3	77.37	12.44	0.10	0.80	0.04	0.03	0.83	3.80	4.43	0.16	100
4	77.12	12.76	0.08	0.88	0.10	0.10	0.77	3.78	4.20	0.20	100
5	77.86	12.51	0.14	0.89	0.05	0.21	0.86	4.12	3.21	0.14	100
6	77.16	12.34	0.16	0.85	0.03	0.14	0.73	3.90	4.58	0.13	100
7	77.61	12.31	0.16	0.81	0.14	0.24	0.97	4.12	3.48	0.15	100
8	77.80	12.43	0.15	0.88	0.00	0.30	0.87	4.02	3.41	0.16	100
Mean	77.37	12.53	0.13	0.86	0.08	0.18	0.83	3.97	3.88	0.16	100
St. Deviation	0.36	0.23	0.03	0.07	0.06	0.13	0.08	0.17	0.54	0.02	0

Sample name: Hine 2; **Tephra ID:** uncertain; **NZ Map Grid:** W16/640070.

Table 23

	SiO2	Al2O3	TiO2	FeO	MnO	MgO	CaO	Na2O	K2O	Cl	TOTAL
1	75.65	12.22	0.15	0.71	0.08	0.11	0.78	4.33	3.22	0.19	97.44
2	75.60	12.23	0.00	0.90	0.09	0.10	0.79	3.84	3.27	0.22	97.03
3	74.41	12.05	0.09	1.02	0.05	0.15	0.88	3.75	3.04	0.09	95.53
4	74.75	11.90	0.10	1.03	0.09	0.09	0.74	3.59	3.14	0.18	96.52
5	77.28	12.34	0.12	0.93	0.11	0.13	0.76	3.91	3.20	0.13	98.93
6	74.07	11.69	0.18	0.86	0.02	0.15	0.86	4.19	3.20	0.14	95.34
7	78.17	12.29	0.17	1.09	0.08	0.15	0.80	4.23	3.25	0.18	100.41
8	77.08	12.67	0.11	0.90	0.12	0.15	0.71	3.98	3.22	0.15	99.08
9	77.84	12.73	0.08	0.82	0.09	0.11	0.74	4.05	3.38	0.19	100.03
10	77.20	12.21	0.16	0.72	0.02	0.12	0.74	4.04	3.69	0.13	99.03

Normalised	SiO2	Al2O3	TiO2	FeO	MnO	MgO	CaO	Na2O	K2O	Cl	TOTAL
1	77.64	12.54	0.15	0.73	0.08	0.11	0.80	4.44	3.30	0.19	100
2	77.91	12.60	0.00	0.93	0.09	0.10	0.81	3.96	3.37	0.23	100
3	77.89	12.61	0.09	1.07	0.05	0.16	0.92	3.93	3.18	0.09	100
4	77.45	12.33	0.10	1.07	0.09	0.09	0.77	3.72	3.25	0.19	100
5	78.12	12.47	0.12	0.94	0.11	0.13	0.77	3.95	3.23	0.13	100
6	77.69	12.26	0.19	0.90	0.02	0.16	0.90	4.39	3.36	0.15	100
7	77.85	12.24	0.17	1.09	0.08	0.15	0.80	4.21	3.24	0.18	100
8	77.80	12.79	0.11	0.91	0.12	0.15	0.72	4.02	3.25	0.15	100
9	77.82	12.73	0.08	0.82	0.09	0.11	0.74	4.05	3.38	0.19	100
10	77.96	12.33	0.16	0.73	0.02	0.12	0.75	4.08	3.73	0.13	100
Mean	77.81	12.49	0.12	0.92	0.08	0.13	0.80	4.08	3.33	0.16	100
St. Deviation	0.19	0.19	0.05	0.13	0.03	0.02	0.07	0.22	0.15	0.04	0

Sample name: Hine 1; **Tephra ID:** uncertain; **NZ Map Grid:** W16/640070

Table 24

	SiO2	Al2O3	TiO2	FeO	MnO	MgO	CaO	Na2O	K2O	Cl	TOTAL
1	75.43	12.02	0.09	0.79	0.14	0.09	0.63	4.01	3.75	0.19	97.13
2	76.46	12.05	0.09	0.72	0.10	0.10	0.61	4.07	3.77	0.11	98.08
3	74.80	12.13	0.15	0.77	0.06	0.08	0.77	3.94	3.62	0.13	96.44
4	75.60	12.34	0.14	0.76	0.03	0.10	0.82	3.99	3.50	0.12	97.41
5	76.93	12.34	0.08	0.97	0.00	0.14	0.64	4.16	3.45	0.15	98.87
6	74.38	11.68	0.12	0.85	0.08	0.13	0.74	3.54	3.02	0.16	94.71
7	76.19	11.98	0.12	0.78	0.03	0.14	0.68	4.07	3.29	0.16	97.44
8	77.18	11.92	0.07	0.82	0.05	0.12	0.68	4.05	3.42	0.15	98.45
9	75.08	12.01	0.18	0.71	0.14	0.14	0.57	4.06	3.47	0.16	96.53
10	76.72	12.31	0.12	0.91	0.12	0.15	0.68	4.13	3.57	0.16	98.86

Normalised	SiO2	Al2O3	TiO2	FeO	MnO	MgO	CaO	Na2O	K2O	Cl	TOTAL
1	77.66	12.38	0.09	0.81	0.14	0.09	0.65	4.13	3.86	0.20	100
2	77.96	12.29	0.09	0.73	0.10	0.10	0.62	4.15	3.84	0.11	100
3	77.56	12.58	0.16	0.80	0.06	0.08	0.80	4.09	3.75	0.13	100
4	77.61	12.67	0.14	0.78	0.03	0.10	0.84	4.10	3.59	0.12	100
5	77.81	12.48	0.08	0.98	0.00	0.14	0.65	4.21	3.49	0.15	100
6	78.53	12.33	0.13	0.90	0.08	0.14	0.78	3.74	3.19	0.17	100
7	78.19	12.29	0.12	0.80	0.03	0.14	0.70	4.18	3.38	0.16	100
8	78.40	12.11	0.07	0.83	0.05	0.12	0.69	4.11	3.47	0.15	100
9	77.78	12.44	0.19	0.74	0.15	0.15	0.59	4.21	3.59	0.17	100
10	77.60	12.45	0.12	0.92	0.12	0.15	0.69	4.18	3.61	0.16	100
Mean	77.91	12.40	0.12	0.83	0.08	0.12	0.70	4.11	3.58	0.15	100
St. Deviation	0.35	0.16	0.04	0.08	0.05	0.03	0.08	0.14	0.21	0.02	0

Sample name: Awa 1; **Tephra ID:** uncertain; **Site(s) associated with the analysis:** 22 & 23

Table 25

	SiO2	Al2O3	TiO2	FeO	MnO	MgO	CaO	Na2O	K2O	Cl	TOTAL
1	74.36	12.86	0.19	1.44	0.10	0.17	1.26	3.92	2.83	0.18	97.32
2	74.59	11.92	0.15	0.87	0.00	0.08	0.67	3.65	3.71	0.17	95.82
3	73.60	12.21	0.15	1.25	0.23	0.14	0.94	3.99	2.98	0.18	95.66
4	75.45	12.30	0.23	1.27	0.13	0.11	0.95	3.95	3.03	0.13	97.55
5	74.86	11.79	0.18	0.73	0.06	0.19	0.91	3.69	3.15	0.15	95.71
6	75.74	12.05	0.20	1.13	0.00	0.15	0.92	3.56	3.25	0.12	97.12
7	76.10	11.91	0.12	0.70	0.08	0.15	0.75	3.70	3.38	0.18	97.08
8	76.65	12.15	0.11	0.75	0.06	0.14	0.64	3.84	3.50	0.11	97.94
9	75.57	11.73	0.18	1.12	0.01	0.15	0.87	3.52	3.30	0.11	96.56
10	76.10	11.80	0.08	1.40	0.09	0.14	0.81	2.38	3.36	0.16	96.32

Normalised	SiO2	Al2O3	TiO2	FeO	MnO	MgO	CaO	Na2O	K2O	Cl	TOTAL
1	76.41	13.21	0.20	1.48	0.10	0.17	1.29	4.03	2.91	0.18	100
2	77.84	12.44	0.16	0.91	0.00	0.08	0.70	3.81	3.87	0.18	100
3	76.94	12.76	0.16	1.31	0.24	0.15	0.98	4.17	3.12	0.19	100
4	77.34	12.61	0.24	1.30	0.13	0.11	0.97	4.05	3.11	0.13	100
5	78.22	12.32	0.19	0.76	0.06	0.20	0.95	3.86	3.29	0.16	100
6	77.99	12.41	0.21	1.16	0.00	0.15	0.95	3.67	3.35	0.12	100
7	78.39	12.27	0.12	0.72	0.08	0.15	0.77	3.81	3.48	0.19	100
8	78.26	12.41	0.11	0.77	0.06	0.14	0.65	3.92	3.57	0.11	100
9	78.26	12.15	0.19	1.16	0.01	0.16	0.90	3.65	3.42	0.11	100
10	79.01	12.25	0.08	1.45	0.09	0.15	0.84	2.47	3.49	0.17	100
Mean	77.87	12.48	0.16	1.10	0.08	0.15	0.90	3.74	3.36	0.15	100
St. Deviation	0.77	0.31	0.05	0.29	0.07	0.03	0.18	0.48	0.27	0.03	0

Sample name: Awa 2**; Tephra ID:** uncertain**; Sites associated with the analysis:** 22 & 23

Table 26

	SiO2	Al2O3	TiO2	FeO	MnO	MgO	CaO	Na2O	K2O	Cl	TOTAL
1	77.86	12.56	0.10	0.83	0.05	0.11	0.72	3.98	3.73	0.15	100.10
2	74.76	12.97	0.16	1.86	0.11	0.23	1.22	4.27	2.80	0.15	98.54
3	76.65	13.12	0.22	1.63	0.10	0.15	1.24	4.05	3.02	0.18	100.35
4	75.93	12.51	0.15	0.87	0.02	0.09	0.71	4.09	3.93	0.21	98.51
5	72.22	12.18	0.28	1.63	0.07	0.15	1.03	3.39	2.90	0.11	93.37
6	76.17	12.23	0.15	0.82	0.02	0.14	0.94	3.92	3.37	0.14	97.90
7	73.80	12.45	0.19	1.54	0.14	0.17	1.18	4.18	2.69	0.15	96.48
8	76.27	12.12	0.14	0.72	0.09	0.09	0.75	3.73	3.41	0.14	97.45
9	74.18	12.22	0.12	0.84	0.17	0.07	0.78	3.83	3.07	0.15	95.43
10	76.00	12.11	0.12	0.57	0.12	0.09	0.53	3.71	4.00	0.19	97.44

Normalised	SiO2	Al2O3	TiO2	FeO	MnO	MgO	CaO	Na2O	K2O	Cl	TOTAL
1	77.78	12.55	0.10	0.83	0.05	0.11	0.72	3.98	3.73	0.15	100
2	75.87	13.16	0.16	1.89	0.11	0.23	1.24	4.33	2.84	0.15	100
3	76.38	13.07	0.22	1.62	0.10	0.15	1.24	4.04	3.01	0.18	100
4	77.08	12.70	0.15	0.88	0.02	0.09	0.72	4.15	3.99	0.21	100
5	77.35	13.04	0.30	1.75	0.07	0.16	1.10	3.63	3.11	0.12	100
6	77.80	12.49	0.15	0.84	0.02	0.14	0.96	4.00	3.44	0.14	100
7	76.49	12.90	0.20	1.60	0.15	0.18	1.22	4.33	2.79	0.16	100
8	78.27	12.44	0.14	0.74	0.09	0.09	0.77	3.83	3.50	0.14	100
9	77.73	12.81	0.13	0.88	0.18	0.07	0.82	4.01	3.22	0.16	100
10	78.00	12.43	0.12	0.58	0.12	0.09	0.54	3.81	4.11	0.19	100
Mean	77.28	12.76	0.17	1.16	0.09	0.13	0.93	4.01	3.37	0.16	100
St. Deviation	0.79	0.28	0.06	0.49	0.05	0.05	0.25	0.22	0.46	0.03	0

Sample name: Awa Manga; **Tephra ID:** Mangaone; **Site(s) associated with the analysis:** 22&23

Table 27

	SiO2	Al2O3	TiO2	FeO	MnO	MgO	CaO	Na2O	K2O	Cl	TOTAL
1	73.40	12.48	0.14	0.93	0.06	0.14	1.03	3.79	2.72	0.15	94.84
2	73.83	12.45	0.12	1.18	0.02	0.16	0.94	3.79	2.78	0.14	95.41
3	73.53	12.62	0.17	0.79	0.10	0.21	1.05	4.00	2.74	0.19	95.40
4	72.32	12.66	0.16	0.90	0.14	0.17	0.91	3.95	2.89	0.20	94.30
5	72.69	12.60	0.10	1.09	0.11	0.18	1.00	3.91	2.82	0.14	94.64
6	73.82	12.65	0.19	1.01	0.15	0.21	0.96	3.71	2.77	0.12	95.60
7	73.40	11.93	0.23	0.96	0.15	0.16	0.90	4.02	2.70	0.22	94.67
8	74.71	12.47	0.15	0.82	0.03	0.18	0.98	3.65	2.78	0.17	95.93
9	72.96	12.34	0.19	1.23	0.00	0.19	0.91	3.86	2.81	0.19	94.69
10	74.78	12.54	0.11	1.24	0.02	0.20	0.98	3.79	2.74	0.13	96.54

Normalised	SiO2	Al2O3	TiO2	FeO	MnO	MgO	CaO	Na2O	K2O	Cl	TOTAL
1	77.39	13.16	0.15	0.98	0.06	0.15	1.09	4.00	2.87	0.16	100
2	77.38	13.05	0.13	1.24	0.02	0.17	0.99	3.97	2.91	0.15	100
3	77.08	13.23	0.18	0.83	0.10	0.22	1.10	4.19	2.87	0.20	100
4	76.69	13.43	0.17	0.95	0.15	0.18	0.97	4.19	3.06	0.21	100
5	76.81	13.31	0.11	1.15	0.12	0.19	1.06	4.13	2.98	0.15	100
6	77.22	13.23	0.20	1.06	0.16	0.22	1.00	3.88	2.90	0.13	100
7	77.53	12.60	0.24	1.01	0.16	0.17	0.95	4.25	2.85	0.23	100
8	77.88	13.00	0.16	0.85	0.03	0.19	1.02	3.80	2.90	0.18	100
9	77.05	13.03	0.20	1.30	0.00	0.20	0.96	4.08	2.97	0.20	100
10	77.46	12.99	0.11	1.28	0.02	0.21	1.02	3.93	2.84	0.13	100
Mean	77.25	13.10	0.16	1.07	0.08	0.19	1.01	4.04	2.92	0.17	100
St. Deviation	0.36	0.23	0.04	0.17	0.06	0.02	0.05	0.15	0.07	0.04	0

Sample name: RT-1 (TW); **Tephra ID:** Rotoehu; **Site(s) associated with the analysis:** 25

Table 28

	SiO2	Al2O3	TiO2	FeO	MnO	MgO	CaO	Na2O	K2O	Cl	TOTAL
1	72.55	11.79	0.14	0.78	0.07	0.11	0.71	2.89	3.81	0.17	93.03
2	74.82	11.98	0.07	0.72	0.16	0.18	0.88	3.65	3.51	0.10	96.07
3	74.07	11.69	0.08	0.74	0.03	0.07	0.75	3.12	3.73	0.16	94.43
4	73.49	11.86	0.07	0.75	0.07	0.07	0.72	3.45	3.74	0.19	94.42
5	74.62	12.00	0.07	0.87	0.03	0.10	0.75	3.39	4.03	0.17	96.03
6	75.59	12.34	0.07	0.86	0.04	0.08	0.73	3.49	4.23	0.22	97.64
7	74.01	11.71	0.13	0.85	0.04	0.11	0.80	3.30	3.60	0.15	94.69
8	75.13	11.44	0.10	1.03	0.00	0.09	0.90	3.62	3.09	0.10	95.51
9	74.33	11.85	0.07	0.98	0.08	0.12	0.75	3.35	3.94	0.13	95.61
10	73.86	11.73	0.11	0.78	0.04	0.07	0.78	3.36	3.78	0.17	94.68

Normalised	SiO2	Al2O3	TiO2	FeO	MnO	MgO	CaO	Na2O	K2O	Cl	TOTAL
1	77.99	12.67	0.15	0.84	0.08	0.12	0.76	3.11	4.10	0.18	100
2	77.88	12.47	0.07	0.75	0.17	0.19	0.92	3.80	3.65	0.10	100
3	78.44	12.38	0.08	0.78	0.03	0.07	0.79	3.30	3.95	0.17	100
4	77.83	12.56	0.07	0.79	0.07	0.07	0.76	3.65	3.96	0.20	100
5	77.70	12.50	0.07	0.91	0.03	0.10	0.78	3.53	4.20	0.18	100
6	77.42	12.64	0.07	0.88	0.04	0.08	0.75	3.57	4.33	0.23	100
7	78.16	12.37	0.14	0.90	0.04	0.12	0.84	3.49	3.80	0.16	100
8	78.66	11.98	0.10	1.08	0.00	0.09	0.94	3.79	3.24	0.10	100
9	77.74	12.39	0.07	1.02	0.08	0.13	0.78	3.50	4.12	0.14	100
10	78.01	12.39	0.12	0.82	0.04	0.07	0.82	3.55	3.99	0.18	100
Mean	77.98	12.43	0.10	0.88	0.06	0.10	0.82	3.53	3.93	0.16	100
St. Deviation	0.36	0.19	0.03	0.11	0.05	0.03	0.07	0.21	0.31	0.04	0

Sample name: RT-2 (TW); **Tephra ID:** Waiohau; **Site(s) associated with the analysis:** 25

Table 29

	SiO2	Al2O3	TiO2	FeO	MnO	MgO	CaO	Na2O	K2O	Cl	TOTAL
1	75.71	12.08	0.12	0.89	0.07	0.12	0.75	3.74	3.13	0.16	96.78
2	74.50	11.89	0.11	0.64	0.25	0.14	0.74	3.67	3.14	0.20	95.28
3	73.80	12.05	0.10	0.85	0.07	0.08	0.74	3.60	3.27	0.12	94.68
4	75.13	12.18	0.08	0.54	0.01	0.08	1.22	4.24	2.40	0.20	96.07
5	75.59	11.95	0.14	0.77	0.00	0.12	0.80	3.78	3.22	0.13	96.48
6	76.28	12.07	0.13	0.81	0.19	0.11	0.80	3.75	3.34	0.10	97.58
7	73.85	11.72	0.10	0.81	0.03	0.14	0.75	3.27	3.05	0.13	93.85
8	77.60	11.96	0.09	0.91	0.09	0.14	0.82	3.70	3.37	0.21	98.88
9	74.22	11.75	0.12	0.98	0.13	0.15	0.86	3.66	2.80	0.16	94.82
10	74.61	12.25	0.18	0.93	0.04	0.06	0.71	3.67	3.05	0.16	95.65

Normalised	SiO2	Al2O3	TiO2	FeO	MnO	MgO	CaO	Na2O	K2O	Cl	TOTAL
1	78.23	12.48	0.12	0.92	0.07	0.12	0.77	3.86	3.23	0.17	100
2	78.19	12.48	0.12	0.67	0.26	0.15	0.78	3.85	3.30	0.21	100
3	77.95	12.73	0.11	0.90	0.07	0.08	0.78	3.80	3.45	0.13	100
4	78.20	12.68	0.08	0.56	0.01	0.08	1.27	4.41	2.50	0.21	100
5	78.35	12.39	0.15	0.80	0.00	0.12	0.83	3.92	3.34	0.13	100
6	78.17	12.37	0.13	0.83	0.19	0.11	0.82	3.84	3.42	0.10	100
7	78.69	12.49	0.11	0.86	0.03	0.15	0.80	3.48	3.25	0.14	100
8	78.48	12.10	0.09	0.92	0.09	0.14	0.83	3.74	3.41	0.21	100
9	78.27	12.39	0.13	1.03	0.14	0.16	0.91	3.86	2.95	0.17	100
10	78.00	12.81	0.19	0.97	0.04	0.06	0.74	3.84	3.19	0.17	100
Mean	78.25	12.49	0.12	0.85	0.09	0.12	0.85	3.86	3.20	0.16	100
St. Deviation	0.22	0.21	0.03	0.14	0.08	0.03	0.15	0.23	0.29	0.04	0

Sample name: RT-9 (TW); **Tephra ID:** Whakatane (re-deposited); **Site(s) associated with the analysis:** 25

Table 30

	SiO2	Al2O3	TiO2	FeO	MnO	MgO	CaO	Na2O	K2O	Cl	TOTAL
1	73.67	11.69	0.12	0.71	0.07	0.13	0.72	3.46	3.24	0.18	93.98
2	74.26	11.87	0.11	1.01	0.17	0.08	0.86	3.51	3.25	0.15	95.26
3	74.03	12.04	0.10	0.91	0.07	0.12	0.71	3.75	3.21	0.14	95.09
4	77.30	11.97	0.10	0.83	0.08	0.07	0.77	3.60	3.63	0.14	98.49
5	75.00	12.03	0.09	0.99	0.06	0.11	0.89	3.09	3.09	0.11	95.46
6	75.77	12.05	0.15	0.75	0.04	0.14	0.95	3.68	3.13	0.09	96.75
7	73.82	11.70	0.14	0.83	0.09	0.13	0.92	3.56	3.20	0.16	94.54
8	74.71	11.95	0.08	1.06	0.13	0.13	1.00	3.62	3.25	0.17	96.09
9	73.23	11.83	0.06	0.92	0.08	0.10	0.78	3.15	3.38	0.09	93.63

Normalised	SiO2	Al2O3	TiO2	FeO	MnO	MgO	CaO	Na2O	K2O	Cl	TOTAL
1	78.39	12.44	0.13	0.76	0.07	0.14	0.77	3.68	3.45	0.19	100
2	77.96	12.46	0.12	1.06	0.18	0.08	0.90	3.68	3.41	0.16	100
3	77.85	12.66	0.11	0.96	0.07	0.13	0.75	3.94	3.38	0.15	100
4	78.49	12.15	0.10	0.84	0.08	0.07	0.78	3.66	3.69	0.14	100
5	78.57	12.60	0.09	1.04	0.06	0.12	0.93	3.24	3.24	0.12	100
6	78.32	12.45	0.16	0.78	0.04	0.14	0.98	3.80	3.24	0.09	100
7	78.08	12.38	0.15	0.88	0.10	0.14	0.97	3.77	3.38	0.17	100
8	77.75	12.44	0.08	1.10	0.14	0.14	1.04	3.77	3.38	0.18	100
9	78.21	12.63	0.06	0.98	0.09	0.11	0.83	3.36	3.61	0.10	100
Mean	78.18	12.47	0.11	0.93	0.09	0.12	0.88	3.66	3.42	0.14	100
St. Deviation	0.29	0.16	0.03	0.13	0.04	0.03	0.11	0.22	0.15	0.04	0

Sample name: RT-5 (TW); **Tephra ID:** Two populations, one Whakatane and one from a Taupo-sourced tephra; **Site(s) associated with the analysis:** 25

Table 31

	SiO2	Al2O3	TiO2	FeO	MnO	MgO	CaO	Na2O	K2O	Cl	TOTAL
1	74.47	11.71	0.07	0.82	0.03	0.13	0.54	3.55	3.57	0.22	95.10
2	74.98	12.83	0.16	1.59	0.07	0.14	1.43	3.54	2.65	0.23	97.62
3	75.56	12.85	0.20	1.60	0.18	0.15	1.20	3.49	2.86	0.18	98.28
4	76.21	12.16	0.10	0.96	0.04	0.15	0.61	3.53	3.73	0.15	97.63
5	73.99	11.55	0.10	0.69	0.04	0.11	0.66	3.67	3.69	0.15	94.65
6	73.92	11.94	0.06	0.67	0.02	0.14	0.67	3.37	3.71	0.14	94.64
7	73.41	12.89	0.21	1.81	0.08	0.27	1.47	3.68	2.62	0.16	96.61
8	71.73	12.02	0.26	1.62	0.15	0.11	1.15	3.16	2.98	0.19	93.39
9	73.06	12.84	0.25	2.10	0.13	0.28	1.46	3.92	2.70	0.09	96.83

Normalised	SiO2	Al2O3	TiO2	FeO	MnO	MgO	CaO	Na2O	K2O	Cl	TOTAL
1	78.31	12.31	0.07	0.86	0.03	0.14	0.57	3.73	3.75	0.23	100
2	76.81	13.14	0.16	1.63	0.07	0.14	1.46	3.63	2.71	0.24	100
3	76.88	13.07	0.20	1.63	0.18	0.15	1.22	3.55	2.91	0.18	100
4	78.06	12.46	0.10	0.98	0.04	0.15	0.62	3.62	3.82	0.15	100
5	78.17	12.20	0.11	0.73	0.04	0.12	0.70	3.88	3.90	0.16	100
6	78.11	12.62	0.06	0.71	0.02	0.15	0.71	3.56	3.92	0.15	100
7	75.99	13.34	0.22	1.87	0.08	0.28	1.52	3.81	2.71	0.17	100
8	76.81	12.87	0.28	1.73	0.16	0.12	1.23	3.38	3.19	0.20	100
9	75.45	13.26	0.26	2.17	0.13	0.29	1.51	4.05	2.79	0.09	100
Mean	77.18	12.81	0.16	1.37	0.09	0.17	1.06	3.69	3.30	0.17	100
St. Deviation	1.04	0.43	0.08	0.55	0.06	0.07	0.41	0.20	0.54	0.04	0

Sample name: RT-7 (TW); **Tephra ID:** Reworked Whakatane; **Site(s) associated with the analysis:** 25

Table 32

	SiO2	Al2O3	TiO2	FeO	MnO	MgO	CaO	Na2O	K2O	Cl	TOTAL
1	74.02	11.45	0.12	0.78	0.10	0.10	0.72	3.68	2.95	0.20	94.12
2	75.48	12.38	0.11	0.98	0.00	0.12	0.75	3.85	3.43	0.19	97.28
3	76.50	12.43	0.08	1.02	0.13	0.07	0.72	3.57	3.27	0.10	97.88
4	73.83	11.99	0.13	0.79	0.08	0.10	0.69	3.12	3.08	0.25	94.07
5	76.05	12.34	0.13	0.80	0.00	0.10	0.87	3.64	3.44	0.16	97.53
6	76.24	12.27	0.17	0.98	0.14	0.09	0.70	3.49	3.64	0.21	97.93
7	74.18	11.80	0.18	0.79	0.05	0.16	0.76	3.38	3.52	0.06	94.88
8	76.00	12.34	0.15	0.98	0.14	0.12	0.79	3.66	3.35	0.15	97.68
9	74.47	12.15	0.11	0.88	0.12	0.14	0.67	3.56	3.59	0.18	95.86
10	73.05	11.98	0.24	0.84	0.03	0.10	0.77	3.42	3.27	0.10	93.79

Normalised	SiO2	Al2O3	TiO2	FeO	MnO	MgO	CaO	Na2O	K2O	Cl	TOTAL
1	78.64	12.17	0.13	0.83	0.11	0.11	0.76	3.91	3.13	0.21	100
2	77.59	12.73	0.11	1.01	0.00	0.12	0.77	3.96	3.53	0.20	100
3	78.16	12.70	0.08	1.04	0.13	0.07	0.74	3.65	3.34	0.10	100
4	78.48	12.75	0.14	0.84	0.09	0.11	0.73	3.32	3.27	0.27	100
5	77.98	12.65	0.13	0.82	0.00	0.10	0.89	3.73	3.53	0.16	100
6	77.85	12.53	0.17	1.00	0.14	0.09	0.71	3.56	3.72	0.21	100
7	78.18	12.44	0.19	0.83	0.05	0.17	0.80	3.56	3.71	0.06	100
8	77.81	12.63	0.15	1.00	0.14	0.12	0.81	3.75	3.43	0.15	100
9	77.69	12.67	0.11	0.92	0.13	0.15	0.70	3.71	3.75	0.19	100
10	77.89	12.77	0.26	0.90	0.03	0.11	0.82	3.65	3.49	0.11	100
Mean	78.03	12.60	0.15	0.92	0.08	0.11	0.77	3.68	3.49	0.17	100
St. Deviation	0.34	0.18	0.05	0.09	0.06	0.03	0.06	0.18	0.20	0.06	0

Sample name: RT-8 (TW); **Tephra ID:** Reworked Whakatane; **Site(s) associated with the analysis:** 25

Table 33

	SiO2	Al2O3	TiO2	FeO	MnO	MgO	CaO	Na2O	K2O	Cl	TOTAL
1	75.96	12.34	0.15	1.08	0.06	0.12	0.87	3.56	3.09	0.11	97.34
2	73.95	12.05	0.03	0.71	0.11	0.00	0.59	3.46	4.13	0.14	95.16
3	76.15	12.53	0.07	0.91	0.15	0.16	0.89	3.57	3.37	0.17	97.97
4	74.25	12.13	0.16	0.86	0.15	0.11	0.80	3.40	3.30	0.15	95.31
5	76.06	12.33	0.13	0.96	0.08	0.13	0.69	3.39	3.38	0.22	97.38
6	76.55	12.23	0.09	0.93	0.17	0.12	0.89	3.43	3.34	0.11	97.87
7	74.84	12.21	0.12	0.98	0.14	0.13	0.89	3.58	3.02	0.12	96.03
8	76.15	11.92	0.04	0.89	0.10	0.14	0.77	3.24	2.92	0.17	96.33
9	77.88	12.13	0.12	0.99	0.10	0.13	0.80	3.27	3.38	0.11	98.91
10	74.33	11.98	0.17	1.01	0.08	0.11	0.83	3.60	3.26	0.15	95.52

Normalised	SiO2	Al2O3	TiO2	FeO	MnO	MgO	CaO	Na2O	K2O	Cl	TOTAL
1	78.04	12.68	0.15	1.11	0.06	0.12	0.89	3.66	3.17	0.11	100
2	77.71	12.66	0.03	0.75	0.12	0.00	0.62	3.64	4.34	0.15	100
3	77.73	12.79	0.07	0.93	0.15	0.16	0.91	3.64	3.44	0.17	100
4	77.90	12.73	0.17	0.90	0.16	0.12	0.84	3.57	3.46	0.16	100
5	78.11	12.66	0.13	0.99	0.08	0.13	0.71	3.48	3.47	0.23	100
6	78.22	12.50	0.09	0.95	0.17	0.12	0.91	3.50	3.41	0.11	100
7	77.93	12.71	0.12	1.02	0.15	0.14	0.93	3.73	3.14	0.12	100
8	79.05	12.37	0.04	0.92	0.10	0.15	0.80	3.36	3.03	0.18	100
9	78.74	12.26	0.12	1.00	0.10	0.13	0.81	3.31	3.42	0.11	100
10	77.82	12.54	0.18	1.06	0.08	0.12	0.87	3.77	3.41	0.16	100
Mean	78.12	12.59	0.11	0.96	0.12	0.12	0.83	3.57	3.43	0.15	100
St. Deviation	0.44	0.17	0.05	0.10	0.04	0.04	0.10	0.15	0.36	0.04	0

Sample name: RT-4 (TW); **Tephra ID:** Rotoma; **Site(s) associated with the analysis:** 25

Table 34

	SiO2	Al2O3	TiO2	FeO	MnO	MgO	CaO	Na2O	K2O	Cl	TOTAL
1	74.44	12.02	0.21	0.99	0.00	0.13	0.75	3.29	3.28	0.18	95.29
2	73.76	13.26	0.26	1.92	0.09	0.23	1.64	3.81	2.65	0.17	97.79
3	76.42	11.99	0.06	0.91	0.14	0.00	0.63	3.70	3.98	0.22	98.06
4	76.39	12.42	0.15	0.95	0.06	0.15	0.77	3.68	3.33	0.15	98.05
5	78.66	12.12	0.15	0.72	0.04	0.19	0.82	3.50	3.23	0.16	99.60
6	75.79	12.45	0.14	0.89	0.08	0.15	0.69	3.65	3.30	0.16	97.31
7	75.81	11.83	0.11	0.90	0.07	0.14	0.82	3.64	3.46	0.12	96.92
8	75.10	11.66	0.10	0.94	0.07	0.17	0.97	3.39	3.39	0.16	96.04
9	76.29	12.20	0.10	0.99	0.00	0.11	0.69	3.31	4.13	0.10	97.93

Normalised	SiO2	Al2O3	TiO2	FeO	MnO	MgO	CaO	Na2O	K2O	Cl	TOTAL
1	78.12	12.61	0.22	1.04	0.00	0.14	0.79	3.45	3.44	0.19	100
2	75.43	13.56	0.27	1.96	0.09	0.24	1.68	3.90	2.71	0.17	100
3	77.93	12.23	0.06	0.93	0.14	0.00	0.64	3.77	4.06	0.22	100
4	77.91	12.67	0.15	0.97	0.06	0.15	0.79	3.75	3.40	0.15	100
5	78.98	12.17	0.15	0.72	0.04	0.19	0.82	3.51	3.24	0.16	100
6	77.89	12.79	0.14	0.91	0.08	0.15	0.71	3.75	3.39	0.16	100
7	78.22	12.21	0.11	0.93	0.07	0.14	0.85	3.76	3.57	0.12	100
8	78.20	12.14	0.10	0.98	0.07	0.18	1.01	3.53	3.53	0.17	100
9	77.90	12.46	0.10	1.01	0.00	0.11	0.70	3.38	4.22	0.10	100
Mean	77.84	12.54	0.15	1.05	0.06	0.14	0.89	3.65	3.51	0.16	100
St. Deviation	0.97	0.45	0.06	0.35	0.05	0.06	0.31	0.18	0.44	0.04	0

Sample name: RT-10 (TW); **Tephra ID:** Two populations, one Whakatane and one from a Taupo sourced tephra; **Site(s) associated with the analysis:** 25

Table 35

	SiO2	Al2O3	TiO2	FeO	MnO	MgO	CaO	Na2O	K2O	Cl	TOTAL
1	75.16	11.99	0.19	0.87	0.08	0.11	0.82	3.63	3.09	0.13	96.06
2	73.62	13.32	0.27	2.01	0.05	0.26	1.41	3.57	3.14	0.11	97.76
3	75.82	12.27	0.16	0.83	0.09	0.06	0.65	3.59	3.94	0.14	97.54
4	72.12	12.86	0.20	1.65	0.08	0.23	1.28	3.10	2.71	0.17	94.39
5	72.05	12.58	0.32	1.95	0.19	0.23	1.63	3.43	2.56	0.15	95.09
6	74.36	13.29	0.31	1.75	0.15	0.28	1.32	3.72	2.72	0.15	98.06
7	76.02	12.48	0.20	0.82	0.02	0.12	0.60	3.59	3.32	0.14	97.32
8	74.66	12.11	0.12	0.82	0.08	0.14	0.82	3.53	3.18	0.14	95.59
9	75.46	12.26	0.12	0.97	0.07	0.12	1.03	3.32	3.40	0.19	96.94
10	74.27	12.06	0.08	0.84	0.03	0.14	0.66	3.27	3.43	0.16	94.93

Normalised	SiO2	Al2O3	TiO2	FeO	MnO	MgO	CaO	Na2O	K2O	Cl	TOTAL
1	78.24	12.48	0.20	0.91	0.08	0.11	0.85	3.78	3.22	0.14	100
2	75.31	13.63	0.28	2.06	0.05	0.27	1.44	3.65	3.21	0.11	100
3	77.73	12.58	0.16	0.85	0.09	0.06	0.67	3.68	4.04	0.14	100
4	76.41	13.62	0.21	1.75	0.08	0.24	1.36	3.28	2.87	0.18	100
5	75.77	13.23	0.34	2.05	0.20	0.24	1.71	3.61	2.69	0.16	100
6	75.83	13.55	0.32	1.78	0.15	0.29	1.35	3.79	2.77	0.15	100
7	78.11	12.82	0.21	0.84	0.02	0.12	0.62	3.69	3.41	0.14	100
8	78.10	12.67	0.13	0.86	0.08	0.15	0.86	3.69	3.33	0.15	100
9	77.84	12.65	0.12	1.00	0.07	0.12	1.06	3.42	3.51	0.20	100
10	78.24	12.70	0.08	0.88	0.03	0.15	0.70	3.44	3.61	0.17	100
Mean	77.16	12.99	0.20	1.30	0.09	0.18	1.06	3.60	3.27	0.15	100
St. Deviation	1.18	0.46	0.08	0.54	0.05	0.08	0.38	0.17	0.41	0.02	0

<u>Northern Whakatane area</u>

Sample name: Q1; **Tephra ID:** Mangaone Subgroup; **Site(s) associated with the analysis:** 17-21

Table 36

	SiO2	Al2O3	TiO2	FeO	MnO	MgO	CaO	Na2O	K2O	Cl	TOTAL
1	74.00	13.97	0.45	1.77	0.14	0.37	1.63	4.38	3.25	0.08	100.05
2	73.47	12.51	0.17	1.17	0.09	0.22	1.25	4.45	2.68	0.18	96.21
3	72.22	12.58	0.19	1.00	0.10	0.25	1.11	4.31	2.71	0.19	94.67
4	73.29	12.52	0.18	1.16	0.04	0.38	1.15	4.34	2.91	0.14	96.11
5	72.38	13.02	0.13	1.04	0.05	0.12	0.96	4.40	2.82	0.20	95.11
6	73.90	13.00	0.24	1.26	0.07	0.25	1.20	4.82	2.84	0.18	97.76
7	72.01	12.52	0.15	1.05	0.19	0.05	1.15	4.15	3.04	0.21	94.52
8	73.55	12.60	0.21	1.26	0.13	0.36	1.18	4.73	2.75	0.16	96.92

Normalised	SiO2	Al2O3	TiO2	FeO	MnO	MgO	CaO	Na2O	K2O	Cl	TOTAL
1	73.96	13.96	0.45	1.77	0.14	0.37	1.63	4.38	3.25	0.08	100
2	76.36	13.00	0.18	1.22	0.09	0.23	1.30	4.63	2.79	0.19	100
3	76.29	13.29	0.20	1.06	0.11	0.26	1.17	4.55	2.86	0.20	100
4	76.26	13.03	0.19	1.21	0.04	0.40	1.20	4.52	3.03	0.15	100
5	76.10	13.69	0.14	1.09	0.05	0.13	1.01	4.63	2.96	0.21	100
6	75.59	13.30	0.25	1.29	0.07	0.26	1.23	4.93	2.91	0.18	100
7	76.18	13.25	0.16	1.11	0.20	0.05	1.22	4.39	3.22	0.22	100
8	75.89	13.00	0.22	1.30	0.13	0.37	1.22	4.88	2.84	0.17	100
Mean	75.83	13.31	0.22	1.26	0.11	0.26	1.25	4.61	2.98	0.17	100
St. Deviation	0.79	0.35	0.10	0.23	0.05	0.12	0.18	0.20	0.17	0.05	0

Sample name: Q2; **Tephra ID:** uncertain (older ignimbrite?); **Site(s) associated with the analysis:** 17-21

Table 37

	SiO2	Al2O3	TiO2	FeO	MnO	MgO	CaO	Na2O	K2O	Cl	TOTAL
1	73.50	12.14	0.08	1.16	0.06	0.06	0.88	3.95	4.31	0.29	96.42
2	72.10	12.16	0.08	1.32	0.10	0.32	0.85	4.04	4.05	0.36	95.38
3	73.09	12.16	0.14	1.15	0.04	0.18	0.88	3.98	3.91	0.26	95.80
4	74.07	12.08	0.12	1.11	0.11	0.19	0.71	3.66	4.18	0.17	96.41
5	72.55	12.37	0.14	1.18	0.07	0.30	0.72	3.85	4.10	0.22	95.50
6	73.39	12.38	0.17	1.19	0.16	0.20	0.89	3.95	4.23	0.24	96.80
7	74.40	11.85	0.03	1.02	0.06	0.08	0.61	3.53	4.04	0.26	95.88
8	73.03	11.89	0.15	1.24	0.10	0.00	0.87	3.81	4.25	0.27	95.61
9	69.75	12.49	0.07	1.28	0.14	0.29	0.88	3.78	4.27	0.27	93.23
10	73.91	12.19	0.15	1.24	0.09	0.24	0.86	3.80	4.22	0.30	97.00

Normalised	SiO2	Al2O3	TiO2	FeO	MnO	MgO	CaO	Na2O	K2O	Cl	TOTAL
1	76.23	12.59	0.08	1.20	0.06	0.06	0.91	4.10	4.47	0.30	100
2	75.59	12.75	0.08	1.38	0.10	0.34	0.89	4.24	4.25	0.38	100
3	76.29	12.69	0.15	1.20	0.04	0.19	0.92	4.15	4.08	0.27	100
4	76.83	12.53	0.12	1.15	0.11	0.20	0.74	3.80	4.34	0.18	100
5	75.97	12.95	0.15	1.24	0.07	0.31	0.75	4.03	4.29	0.23	100
6	75.82	12.79	0.18	1.23	0.17	0.21	0.92	4.08	4.37	0.25	100
7	77.60	12.36	0.03	1.06	0.06	0.08	0.64	3.68	4.21	0.27	100
8	76.38	12.44	0.16	1.30	0.10	0.00	0.91	3.98	4.45	0.28	100
9	74.81	13.40	0.08	1.37	0.15	0.31	0.94	4.05	4.58	0.29	100
10	76.20	12.57	0.15	1.28	0.09	0.25	0.89	3.92	4.35	0.31	100
Mean	76.17	12.71	0.12	1.24	0.10	0.19	0.85	4.00	4.34	0.28	100
St. Deviation	0.74	0.30	0.05	0.10	0.04	0.11	0.10	0.17	0.14	0.05	0

Sample name: Pu-B; **Tephra ID:** Rotoehu; **Site(s) associated with the analysis:** 17-21

Table 38

	SiO2	Al2O3	TiO2	FeO	MnO	MgO	CaO	Na2O	K2O	Cl	TOTAL
1	74.67	12.33	0.18	0.96	0.06	0.16	0.68	3.51	3.38	0.10	96.04
2	73.58	11.78	0.12	0.89	0.10	0.10	0.70	3.27	3.11	0.17	93.82
3	72.39	11.78	0.10	0.97	0.01	0.36	0.80	3.42	3.15	0.10	93.07
4	73.58	11.94	0.13	0.87	0.09	0.22	0.77	3.53	3.09	0.11	94.33
5	72.26	11.82	0.05	1.03	0.03	0.19	0.79	3.35	3.19	0.15	92.87
6	72.61	11.88	0.08	0.94	0.12	0.20	0.76	3.52	3.21	0.17	93.48
7	73.02	11.72	0.10	0.90	0.32	0.16	0.82	3.25	2.93	0.14	93.36
8	72.98	11.73	0.13	0.90	0.00	0.25	0.72	3.02	3.10	0.16	92.99
9	72.99	11.94	0.06	0.82	0.05	0.04	0.76	3.17	3.28	0.08	93.18

Normalised	SiO2	Al2O3	TiO2	FeO	MnO	MgO	CaO	Na2O	K2O	Cl	TOTAL
1	77.75	12.84	0.19	1.00	0.06	0.17	0.71	3.65	3.52	0.10	100
2	78.43	12.56	0.13	0.95	0.11	0.11	0.75	3.49	3.31	0.18	100
3	77.78	12.66	0.11	1.04	0.01	0.39	0.86	3.67	3.38	0.11	100
4	78.00	12.66	0.14	0.92	0.10	0.23	0.82	3.74	3.28	0.12	100
5	77.81	12.73	0.05	1.11	0.03	0.20	0.85	3.61	3.43	0.16	100
6	77.67	12.71	0.09	1.01	0.13	0.21	0.81	3.77	3.43	0.18	100
7	78.21	12.55	0.11	0.96	0.34	0.17	0.88	3.48	3.14	0.15	100
8	78.48	12.61	0.14	0.97	0.00	0.27	0.77	3.25	3.33	0.17	100
9	78.33	12.81	0.06	0.88	0.05	0.04	0.82	3.40	3.52	0.09	100
Mean	78.05	12.68	0.11	0.98	0.09	0.20	0.81	3.56	3.37	0.14	100
St. Deviation	0.32	0.10	0.04	0.07	0.10	0.10	0.06	0.17	0.12	0.04	0

Sample name: An; **Tephra ID:** Rotoehu; **Site(s) associated with the analysis:** 17-21

Table 39

	SiO2	Al2O3	TiO2	FeO	MnO	MgO	CaO	Na2O	K2O	Cl	TOTAL
1	79.20	12.18	0.15	1.11	0.22	0.17	0.93	3.90	3.18	0.23	101.26
2	76.45	12.07	0.18	0.78	0.06	0.18	0.76	3.73	3.22	0.19	97.62
3	76.58	12.09	0.16	0.81	0.09	0.13	0.77	3.87	3.23	0.14	97.86
4	76.57	12.11	0.14	1.10	0.08	0.11	0.71	3.80	3.17	0.17	97.97
5	75.31	12.01	0.10	0.67	0.08	0.11	0.71	3.65	3.43	0.11	96.17
6	76.48	12.21	0.05	0.83	0.11	0.09	0.73	3.72	3.68	0.14	98.04
7	75.53	11.91	0.08	0.86	0.01	0.09	0.81	3.77	3.41	0.15	96.62

Normalised	SiO2	Al2O3	TiO2	FeO	MnO	MgO	CaO	Na2O	K2O	Cl	TOTAL
1	78.21	12.03	0.15	1.10	0.22	0.17	0.92	3.85	3.14	0.23	100
2	78.31	12.36	0.18	0.80	0.06	0.18	0.78	3.82	3.30	0.19	100
3	78.25	12.35	0.16	0.83	0.09	0.13	0.79	3.95	3.30	0.14	100
4	78.16	12.36	0.14	1.12	0.08	0.11	0.72	3.88	3.24	0.17	100
5	78.31	12.49	0.10	0.70	0.08	0.11	0.74	3.80	3.57	0.11	100
6	78.01	12.45	0.05	0.85	0.11	0.09	0.74	3.79	3.75	0.14	100
7	78.17	12.33	0.08	0.89	0.01	0.09	0.84	3.90	3.53	0.16	100
Mean	78.20	12.34	0.13	0.90	0.09	0.13	0.79	3.86	3.40	0.16	100
St. Deviation	0.11	0.15	0.05	0.16	0.06	0.04	0.07	0.06	0.22	0.04	0

Sample name: TH/C; **Tephra ID:** Rerewhakaaitu; **Site(s) associated with the analysis:** 17-21

Table 40

	SiO2	Al2O3	TiO2	FeO	MnO	MgO	CaO	Na2O	K2O	Cl	TOTAL
1	75.47	12.08	0.14	1.04	0.01	0.13	0.94	3.36	3.21	0.15	96.53
2	75.51	11.81	0.13	0.72	0.06	0.14	0.70	3.38	3.61	0.15	96.21
3	75.73	11.80	0.10	1.09	0.00	0.14	0.98	3.80	3.25	0.10	96.98
4	75.93	11.99	0.15	1.03	0.03	0.16	0.80	3.67	3.31	0.17	97.23
5	77.05	11.83	0.14	0.78	0.04	0.14	0.93	3.78	3.32	0.14	98.13
6	75.15	12.05	0.10	1.10	0.09	0.19	0.98	3.45	3.40	0.16	96.67
7	75.88	11.64	0.11	1.03	0.01	0.09	0.66	3.44	3.59	0.11	96.57
8	75.25	12.30	0.12	1.11	0.00	0.12	0.87	3.33	3.76	0.16	97.02
9	75.44	12.05	0.17	0.89	0.05	0.18	0.93	3.27	3.24	0.13	96.35
10	75.27	11.99	0.19	1.12	0.02	0.17	0.99	3.47	3.37	0.14	96.73

Normalised	SiO2	Al2O3	TiO2	FeO	MnO	MgO	CaO	Na2O	K2O	Cl	TOTAL
1	78.18	12.51	0.15	1.08	0.01	0.13	0.97	3.48	3.33	0.16	100
2	78.48	12.28	0.14	0.75	0.06	0.15	0.73	3.51	3.75	0.16	100
3	78.09	12.17	0.10	1.12	0.00	0.14	1.01	3.92	3.35	0.10	100
4	78.09	12.33	0.15	1.06	0.03	0.16	0.82	3.77	3.40	0.17	100
5	78.52	12.06	0.14	0.79	0.04	0.14	0.95	3.85	3.38	0.14	100
6	77.74	12.47	0.10	1.14	0.09	0.20	1.01	3.57	3.52	0.17	100
7	78.58	12.05	0.11	1.07	0.01	0.09	0.68	3.56	3.72	0.11	100
8	77.56	12.68	0.12	1.14	0.00	0.12	0.90	3.43	3.88	0.16	100
9	78.30	12.51	0.18	0.92	0.05	0.19	0.97	3.39	3.36	0.13	100
10	77.81	12.40	0.20	1.16	0.02	0.18	1.02	3.59	3.48	0.14	100
Mean	78.14	12.34	0.14	1.02	0.03	0.15	0.91	3.61	3.52	0.15	100
St. Deviation	0.35	0.21	0.03	0.15	0.03	0.03	0.12	0.18	0.20	0.02	0

Sample name: GB; **Tephra ID:** Rerewhakaaitu; **Sites associated with the analysis:** 17-21

Table 41

	SiO2	Al2O3	TiO2	FeO	MnO	MgO	CaO	Na2O	K2O	Cl	TOTAL
1	74.85	11.96	0.13	0.84	0.07	0.08	0.80	3.17	3.58	0.15	95.63
2	76.47	11.95	0.11	1.40	0.04	0.10	0.93	3.38	3.00	0.16	97.54
3	76.19	11.97	0.05	1.16	0.11	0.11	1.04	3.68	2.98	0.16	97.47
4	75.47	12.35	0.15	1.02	0.05	0.13	1.05	3.44	3.00	0.18	96.85
5	75.13	11.77	0.12	1.02	0.06	0.12	0.98	3.10	3.08	0.19	95.55
6	75.83	12.01	0.20	0.97	0.06	0.08	1.04	3.30	3.09	0.16	96.75
7	76.74	12.50	0.11	1.00	0.02	0.18	0.92	3.82	3.12	0.17	98.59
8	76.17	11.84	0.13	0.96	0.07	0.11	0.82	3.15	3.16	0.23	96.64
9	75.30	12.09	0.09	1.02	0.00	0.16	0.82	3.27	3.78	0.14	96.68
10	75.06	12.05	0.19	0.98	0.07	0.14	1.00	3.28	2.88	0.20	95.85

Normalised	SiO2	Al2O3	TiO2	FeO	MnO	MgO	CaO	Na2O	K2O	Cl	TOTAL
1	78.27	12.51	0.14	0.88	0.07	0.08	0.84	3.31	3.74	0.16	100
2	78.40	12.25	0.11	1.44	0.04	0.10	0.95	3.47	3.08	0.16	100
3	78.17	12.28	0.05	1.19	0.11	0.11	1.07	3.78	3.06	0.16	100
4	77.92	12.75	0.15	1.05	0.05	0.13	1.08	3.55	3.10	0.19	100
5	78.63	12.32	0.13	1.07	0.06	0.13	1.03	3.24	3.22	0.20	100
6	78.38	12.41	0.21	1.00	0.06	0.08	1.07	3.41	3.19	0.17	100
7	77.84	12.68	0.11	1.01	0.02	0.18	0.93	3.87	3.16	0.17	100
8	78.82	12.25	0.13	0.99	0.07	0.11	0.85	3.26	3.27	0.24	100
9	77.89	12.51	0.09	1.06	0.00	0.17	0.85	3.38	3.91	0.14	100
10	78.31	12.57	0.20	1.02	0.07	0.15	1.04	3.42	3.00	0.21	100
Mean	78.26	12.45	0.13	1.07	0.06	0.12	0.97	3.47	3.27	0.18	100
St. Deviation	0.32	0.18	0.05	0.15	0.03	0.03	0.10	0.21	0.30	0.03	0

Sample name: Q3-old bus; **Tephra ID:** Rotoehu; **Site(s) associated with the analysis:** 17-21

Table 42

	SiO2	Al2O3	TiO2	FeO	MnO	MgO	CaO	Na2O	K2O	Cl	TOTAL
1	75.58	12.06	0.07	0.88	0.11	0.15	0.77	3.88	3.25	0.33	97.07
2	75.31	12.02	0.25	0.95	0.21	0.13	0.81	3.58	3.19	0.15	96.61
3	74.82	11.83	0.13	0.80	0.11	0.15	0.81	3.61	3.06	0.15	95.48
4	75.37	12.03	0.15	0.88	0.01	0.17	0.84	3.71	3.08	0.12	96.36
5	76.52	12.29	0.16	0.96	0.02	0.15	0.77	3.78	3.35	0.19	98.20
6	71.08	11.87	0.14	0.94	0.01	0.14	0.68	3.65	2.84	0.32	91.67
7	76.40	12.26	0.10	1.06	0.08	0.13	0.89	3.86	3.25	0.25	98.27
8	76.01	12.06	0.21	0.73	0.11	0.14	0.86	3.77	3.21	0.18	97.28
9	75.85	11.88	0.09	0.68	0.24	0.12	0.79	3.89	3.22	0.22	96.99
10	76.12	12.15	0.15	0.96	0.05	0.14	0.74	3.38	3.33	0.18	97.21

Normalised	SiO2	Al2O3	TiO2	FeO	MnO	MgO	CaO	Na2O	K2O	Cl	TOTAL
1	77.86	12.42	0.07	0.91	0.11	0.15	0.79	4.00	3.35	0.34	100
2	77.95	12.44	0.26	0.98	0.22	0.13	0.84	3.71	3.30	0.16	100
3	78.36	12.39	0.14	0.84	0.12	0.16	0.85	3.78	3.20	0.16	100
4	78.22	12.48	0.16	0.91	0.01	0.18	0.87	3.85	3.20	0.12	100
5	77.92	12.52	0.16	0.98	0.02	0.15	0.78	3.85	3.41	0.19	100
6	77.54	12.95	0.15	1.03	0.01	0.15	0.74	3.98	3.10	0.35	100
7	77.74	12.48	0.10	1.08	0.08	0.13	0.91	3.93	3.31	0.25	100
8	78.14	12.40	0.22	0.75	0.11	0.14	0.88	3.88	3.30	0.19	100
9	78.20	12.25	0.09	0.70	0.25	0.12	0.81	4.01	3.32	0.23	100
10	78.30	12.50	0.15	0.99	0.05	0.14	0.76	3.48	3.43	0.19	100
Mean	78.02	12.48	0.15	0.92	0.10	0.15	0.82	3.85	3.29	0.22	100
St. Deviation	0.26	0.18	0.06	0.12	0.08	0.01	0.05	0.16	0.10	0.08	0

Sample name: Q1; **Tephra ID:** Mangaone subgroup; **Sites associated with the analysis:** 17-21

Table 43

	SiO2	Al2O3	TiO2	FeO	MnO	MgO	CaO	Na2O	K2O	Cl	TOTAL
1	74.00	13.97	0.45	1.77	0.14	0.37	1.63	4.38	3.25	0.08	100.05
2	73.47	12.51	0.17	1.17	0.09	0.22	1.25	4.45	2.68	0.18	96.21
3	72.22	12.58	0.19	1.00	0.10	0.25	1.11	4.31	2.71	0.19	94.67
4	73.29	12.52	0.18	1.16	0.04	0.38	1.15	4.34	2.91	0.14	96.11
5	72.38	13.02	0.13	1.04	0.05	0.12	0.96	4.40	2.82	0.20	95.11
6	73.90	13.00	0.24	1.26	0.07	0.25	1.20	4.82	2.84	0.18	97.76
7	72.01	12.52	0.15	1.05	0.19	0.05	1.15	4.15	3.04	0.21	94.52
8	73.55	12.60	0.21	1.26	0.13	0.36	1.18	4.73	2.75	0.16	96.92

Normalised	SiO2	Al2O3	TiO2	FeO	MnO	MgO	CaO	Na2O	K2O	Cl	TOTAL
1	73.96	13.96	0.45	1.77	0.14	0.37	1.63	4.38	3.25	0.08	100
2	76.36	13.00	0.18	1.22	0.09	0.23	1.30	4.63	2.79	0.19	100
3	76.29	13.29	0.20	1.06	0.11	0.26	1.17	4.55	2.86	0.20	100
4	76.26	13.03	0.19	1.21	0.04	0.40	1.20	4.52	3.03	0.15	100
5	76.10	13.69	0.14	1.09	0.05	0.13	1.01	4.63	2.96	0.21	100
6	75.59	13.30	0.25	1.29	0.07	0.26	1.23	4.93	2.91	0.18	100
7	76.18	13.25	0.16	1.11	0.20	0.05	1.22	4.39	3.22	0.22	100
8	75.89	13.00	0.22	1.30	0.13	0.37	1.22	4.88	2.84	0.17	100
Mean	75.83	13.31	0.22	1.26	0.11	0.26	1.25	4.61	2.98	0.17	100
St. Deviation	0.79	0.35	0.10	0.23	0.05	0.12	0.18	0.20	0.17	0.05	0

WAIMANA FAULT

Waikaremoana

Sample name: Manga 1E; **Tephra ID:** Whakatane (?); **Site(s) associated with the analysis:** 82

Table 44

	SiO2	Al2O3	TiO2	FeO	MnO	MgO	CaO	Na2O	K2O	Cl	TOTAL
1	76.42	12.00	0.06	0.73	0.08	0.12	0.67	3.88	4.07	0.25	98.27
3	76.38	12.22	0.12	0.79	0.02	0.11	0.78	3.88	3.74	0.12	98.15
4	75.49	11.77	0.11	0.75	0.01	0.09	0.86	3.58	3.51	0.15	96.31
5	75.87	12.47	0.14	0.66	0.08	0.09	0.68	4.11	3.91	0.12	98.13
6	74.60	12.15	0.08	0.80	0.09	0.10	0.64	3.73	3.62	0.09	95.89
7	75.82	12.78	0.20	1.58	0.04	0.21	1.26	4.26	3.11	0.20	99.46
8	77.46	12.23	0.11	1.08	0.02	0.13	0.73	3.82	3.67	0.18	99.43
9	77.12	12.35	0.11	0.83	0.18	0.11	0.76	3.76	3.72	0.19	99.13
10	74.85	11.87	0.12	0.89	0.10	0.17	0.69	3.66	3.72	0.15	96.21

Normalised	SiO2	Al2O3	TiO2	FeO	MnO	MgO	CaO	Na2O	K2O	Cl	TOTAL
1	77.77	12.21	0.06	0.74	0.08	0.12	0.68	3.95	4.14	0.25	100
3	77.82	12.45	0.12	0.80	0.02	0.11	0.79	3.95	3.81	0.12	100
4	78.38	12.22	0.11	0.78	0.01	0.09	0.89	3.72	3.64	0.16	100
5	77.32	12.71	0.14	0.67	0.08	0.09	0.69	4.19	3.98	0.12	100
6	77.80	12.67	0.08	0.83	0.09	0.10	0.67	3.89	3.78	0.09	100
7	76.23	12.85	0.20	1.59	0.04	0.21	1.27	4.28	3.13	0.20	100
8	77.90	12.30	0.11	1.09	0.02	0.13	0.73	3.84	3.69	0.18	100
9	77.80	12.46	0.11	0.84	0.18	0.11	0.77	3.79	3.75	0.19	100
10	77.80	12.34	0.12	0.93	0.10	0.18	0.72	3.80	3.87	0.16	100
Mean	77.65	12.47	0.12	0.92	0.07	0.13	0.80	3.94	3.75	0.16	100
St. Deviation	0.59	0.23	0.04	0.28	0.05	0.04	0.19	0.19	0.28	0.05	0

Te Ahirau

Sample name: Tuh B; **Tephra ID:** Waiohau (microscope analysis: it does not contain cummingtonite); **Site(s) associated with the analysis:** 76-77

Table 45

	SiO2	Al2O3	TiO2	FeO	MnO	MgO	CaO	Na2O	K2O	Cl	TOTAL
1	75.71	11.76	0.16	0.93	0.00	0.14	0.81	3.99	3.25	0.13	96.86
2	75.93	12.08	0.14	0.94	0.09	0.09	0.84	4.00	3.05	0.20	97.36
3	75.73	11.73	0.16	0.83	0.06	0.12	0.81	2.86	3.45	0.12	95.88
4	76.96	12.29	0.15	0.85	0.17	0.10	0.82	4.01	3.10	0.07	98.53
5	76.78	11.66	0.13	0.95	0.03	0.15	0.89	3.64	3.10	0.17	97.50
6	75.65	11.71	0.15	0.96	0.04	0.15	0.83	3.87	3.37	0.17	96.88
7	76.61	12.09	0.11	0.85	0.00	0.11	0.98	3.85	3.18	0.20	97.99
8	76.48	11.85	0.15	0.89	0.07	0.10	0.78	3.60	3.28	0.18	97.38
9	76.33	11.62	0.19	0.84	0.00	0.12	0.82	3.58	3.25	0.13	96.88
10	75.89	11.76	0.07	1.14	0.08	0.14	0.87	3.45	3.32	0.13	96.84

Normalised	SiO2	Al2O3	TiO2	FeO	MnO	MgO	CaO	Na2O	K2O	Cl	TOTAL
1	78.16	12.14	0.17	0.96	0.00	0.14	0.84	4.12	3.36	0.13	100
2	77.99	12.41	0.14	0.97	0.09	0.09	0.86	4.11	3.13	0.21	100
3	78.98	12.23	0.17	0.87	0.06	0.13	0.84	2.98	3.60	0.13	100
4	78.11	12.47	0.15	0.86	0.17	0.10	0.83	4.07	3.15	0.07	100
5	78.75	11.96	0.13	0.97	0.03	0.15	0.91	3.73	3.18	0.17	100
6	78.09	12.09	0.15	0.99	0.04	0.15	0.86	3.99	3.48	0.18	100
7	78.18	12.34	0.11	0.87	0.00	0.11	1.00	3.93	3.25	0.20	100
8	78.54	12.17	0.15	0.91	0.07	0.10	0.80	3.70	3.37	0.18	100
9	78.79	11.99	0.20	0.87	0.00	0.12	0.85	3.70	3.35	0.13	100
10	78.37	12.14	0.07	1.18	0.08	0.14	0.90	3.56	3.43	0.13	100
Mean	78.40	12.19	0.15	0.94	0.06	0.13	0.87	3.79	3.33	0.15	100
St. Deviation	0.35	0.17	0.03	0.10	0.05	0.02	0.06	0.35	0.15	0.04	0

Sample name: Tuh D; **Tephra ID:** Rotoma (microscope analysis:contains cummingtonite); **Site(s) associated with the analysis:** 76-77

Table 46

	SiO2	Al2O3	TiO2	FeO	MnO	MgO	CaO	Na2O	K2O	Cl	TOTAL
1	77.58	12.38	0.13	1.03	0.05	0.09	0.79	3.37	3.02	0.09	98.55
2	77.20	12.39	0.19	0.77	0.11	0.11	0.73	3.21	3.21	0.14	98.06
3	77.06	12.30	0.21	0.97	0.03	0.12	0.83	3.09	3.21	0.13	97.94
4	75.82	12.10	0.12	0.85	0.03	0.12	0.71	3.07	3.27	0.18	96.27
5	76.65	12.16	0.13	0.88	0.01	0.10	0.80	3.31	3.17	0.18	97.39
6	77.23	12.20	0.14	0.92	0.02	0.15	0.89	3.23	3.15	0.12	98.05
7	75.88	12.17	0.11	0.90	0.00	0.15	0.91	3.09	3.05	0.16	96.42
8	78.79	12.64	0.12	1.03	0.09	0.13	0.90	3.41	3.35	0.15	100.61
9	76.11	11.93	0.06	0.86	0.10	0.09	0.63	3.45	4.25	0.12	97.62

Normalised	SiO2	Al2O3	TiO2	FeO	MnO	MgO	CaO	Na2O	K2O	Cl	TOTAL
1	78.72	12.56	0.13	1.05	0.05	0.09	0.80	3.42	3.06	0.09	100
2	78.73	12.64	0.19	0.79	0.11	0.11	0.74	3.27	3.27	0.14	100
3	78.68	12.56	0.21	0.99	0.03	0.12	0.85	3.15	3.28	0.13	100
4	78.76	12.57	0.12	0.88	0.03	0.12	0.74	3.19	3.40	0.19	100
5	78.70	12.49	0.13	0.90	0.01	0.10	0.82	3.40	3.25	0.18	100
6	78.77	12.44	0.14	0.94	0.02	0.15	0.91	3.29	3.21	0.12	100
7	78.70	12.62	0.11	0.93	0.00	0.16	0.94	3.20	3.16	0.17	100
8	78.31	12.56	0.12	1.02	0.09	0.13	0.89	3.39	3.33	0.15	100
9	77.97	12.22	0.06	0.88	0.10	0.09	0.65	3.53	4.35	0.12	100
Mean	78.59	12.52	0.14	0.93	0.05	0.12	0.82	3.32	3.37	0.14	100
St. Deviation	0.27	0.13	0.04	0.08	0.04	0.02	0.10	0.13	0.38	0.03	0

Sample name: Sunny 1; **Tephra ID:** Whakatane (microscope analysis: contains cummingtonite); **Site(s) associated with the analysis:** 79

Table 47

	SiO2	Al2O3	TiO2	FeO	MnO	MgO	CaO	Na2O	K2O	Cl	TOTAL
1	77.51	12.16	0.18	0.81	0.07	0.11	0.89	3.65	3.49	0.20	99.06
2	75.96	12.37	0.12	0.74	0.15	0.12	0.66	4.18	3.46	0.19	97.97
3	76.08	12.37	0.12	0.92	0.06	0.10	0.75	3.89	3.83	0.12	98.25
4	76.93	12.44	0.11	0.75	0.10	0.09	0.81	3.95	3.76	0.12	99.06
5	77.60	12.20	0.13	0.78	0.08	0.09	0.58	3.85	4.17	0.08	99.56
6	75.34	11.55	0.11	0.83	0.20	0.12	0.59	3.70	3.66	0.13	96.23
7	76.72	12.11	0.04	0.71	0.00	0.13	0.63	4.00	3.79	0.28	98.42
8	77.22	12.46	0.14	0.68	0.01	0.10	0.77	3.95	4.01	0.12	99.45

Normalised	SiO2	Al2O3	TiO2	FeO	MnO	MgO	CaO	Na2O	K2O	Cl	TOTAL
1	78.25	12.28	0.18	0.82	0.07	0.11	0.90	3.68	3.52	0.20	100
2	77.53	12.63	0.12	0.76	0.15	0.12	0.67	4.27	3.53	0.19	100
3	77.44	12.59	0.12	0.94	0.06	0.10	0.76	3.96	3.90	0.12	100
4	77.66	12.56	0.11	0.76	0.10	0.09	0.82	3.99	3.80	0.12	100
5	77.94	12.25	0.13	0.78	0.08	0.09	0.58	3.87	4.19	0.08	100
6	78.29	12.00	0.11	0.86	0.21	0.12	0.61	3.84	3.80	0.14	100
7	77.95	12.30	0.04	0.72	0.00	0.13	0.64	4.06	3.85	0.28	100
8	77.65	12.53	0.14	0.68	0.01	0.10	0.77	3.97	4.03	0.12	100
Mean	77.84	12.39	0.12	0.79	0.09	0.11	0.72	3.96	3.83	0.16	100
St. Deviation	0.32	0.22	0.04	0.08	0.07	0.02	0.11	0.17	0.23	0.07	0

Sample name: Auger 4; **Tephra ID:** Waiohau (microscope analysis: it does not contain no cummingtonite); **Site(s) associated with the analysis:** 73

Table 48

	SiO2	Al2O3	TiO2	FeO	MnO	MgO	CaO	Na2O	K2O	Cl	TOTAL
1	75.06	11.93	0.03	0.79	0.09	0.10	0.63	3.23	2.96	0.21	95.03
2	75.29	11.95	0.08	0.85	0.12	0.10	0.68	3.15	3.05	0.17	95.44
3	76.25	12.52	0.13	0.65	0.00	0.11	0.75	3.51	3.21	0.02	97.27
4	73.70	12.32	0.10	0.96	0.00	0.16	0.99	3.62	3.04	0.14	95.03
5	77.48	11.75	0.13	0.92	0.08	0.08	0.78	3.66	3.41	0.10	98.40
6	76.19	12.38	0.20	0.71	0.07	0.07	0.73	3.42	3.17	0.14	97.09
7	74.29	12.12	0.13	0.75	0.15	0.13	0.74	3.68	3.13	0.12	95.23
8	77.57	12.32	0.19	1.00	0.11	0.11	0.69	3.85	3.23	0.15	99.22
9	75.53	12.20	0.11	0.66	0.08	0.10	0.75	3.67	3.21	0.11	96.42
10	77.82	12.49	0.12	1.04	0.05	0.12	1.03	4.00	3.13	0.16	99.95

Normalised	SiO2	Al2O3	TiO2	FeO	MnO	MgO	CaO	Na2O	K2O	Cl	TOTAL
1	78.99	12.55	0.03	0.83	0.09	0.11	0.66	3.40	3.11	0.22	100
2	78.89	12.52	0.08	0.89	0.13	0.10	0.71	3.30	3.20	0.18	100
3	78.39	12.87	0.13	0.67	0.00	0.11	0.77	3.61	3.30	0.02	100
4	77.55	12.96	0.11	1.01	0.00	0.17	1.04	3.81	3.20	0.15	100
5	78.74	11.94	0.13	0.93	0.08	0.08	0.79	3.72	3.47	0.10	100
6	78.47	12.75	0.21	0.73	0.07	0.07	0.75	3.52	3.27	0.14	100
7	78.01	12.73	0.14	0.79	0.16	0.14	0.78	3.86	3.29	0.13	100
8	78.18	12.42	0.19	1.01	0.11	0.11	0.70	3.88	3.26	0.15	100
9	78.33	12.65	0.11	0.68	0.08	0.10	0.78	3.81	3.33	0.11	100
10	77.86	12.50	0.12	1.04	0.05	0.12	1.03	4.00	3.13	0.16	100
Mean	78.34	12.59	0.13	0.86	0.08	0.11	0.80	3.69	3.25	0.14	100
St. Deviation	0.46	0.29	0.05	0.14	0.05	0.03	0.13	0.23	0.10	0.05	0

Sample name: Ah4_D; **Tephra ID:** Mamaku (microscope analysis: it does not contain cummingtonite); **Site(s) associated with the analysis:** 75-78

Table 49

	SiO2	Al2O3	TiO2	FeO	MnO	MgO	CaO	Na2O	K2O	Cl	TOTAL
1	78.13	12.36	0.13	0.85	0.05	0.10	0.71	3.71	3.27	0.12	99.43
2	78.69	12.75	0.16	0.80	0.13	0.09	0.77	3.78	3.56	0.24	100.98
3	76.96	12.58	0.06	0.71	0.07	0.13	0.76	3.50	3.12	0.14	98.03
4	77.89	12.74	0.12	0.94	0.02	0.14	0.75	3.81	3.28	0.13	99.82
5	75.98	12.37	0.11	1.01	0.00	0.18	0.70	3.73	3.18	0.16	97.43
6	75.06	12.66	0.17	0.91	0.07	0.10	0.76	3.63	3.19	0.17	96.73
7	75.42	12.40	0.12	0.84	0.01	0.13	0.79	3.86	3.07	0.15	96.79
8	75.56	12.55	0.09	0.81	0.08	0.04	0.58	3.33	4.13	0.16	97.31
9	75.74	12.53	0.12	0.86	0.10	0.11	0.75	3.51	3.12	0.20	97.04
10	77.04	12.43	0.08	0.85	0.09	0.13	0.74	3.50	2.86	0.02	97.89

Normalised	SiO2	Al2O3	TiO2	FeO	MnO	MgO	CaO	Na2O	K2O	Cl	TOTAL
1	78.58	12.43	0.13	0.85	0.05	0.10	0.71	3.73	3.29	0.12	100
2	77.93	12.63	0.16	0.79	0.13	0.09	0.76	3.74	3.53	0.24	100
3	78.51	12.83	0.06	0.72	0.07	0.13	0.78	3.57	3.18	0.14	100
4	78.03	12.76	0.12	0.94	0.02	0.14	0.75	3.82	3.29	0.13	100
5	77.98	12.70	0.11	1.04	0.00	0.18	0.72	3.83	3.26	0.16	100
6	77.60	13.09	0.18	0.94	0.07	0.10	0.79	3.75	3.30	0.18	100
7	77.92	12.81	0.12	0.87	0.01	0.13	0.82	3.99	3.17	0.15	100
8	77.65	12.90	0.09	0.83	0.08	0.04	0.60	3.42	4.24	0.16	100
9	78.05	12.91	0.12	0.89	0.10	0.11	0.77	3.62	3.22	0.21	100
10	78.70	12.70	0.08	0.87	0.09	0.13	0.76	3.58	2.92	0.02	100
Mean	78.09	12.78	0.12	0.87	0.06	0.12	0.74	3.70	3.34	0.15	100
St. Deviation	0.38	0.18	0.03	0.09	0.04	0.04	0.06	0.16	0.35	0.06	0

Sample name: Ah4_C; **Tephra ID:** Waiohau (microscope analysis: it does not contain cummingtonite); **Site(s) associated with the analysis:** 75-78

Table 50

	SiO2	Al2O3	TiO2	FeO	MnO	MgO	CaO	Na2O	K2O	Cl	TOTAL
1	77.36	12.52	0.14	0.93	0.13	0.12	0.75	3.75	3.38	0.13	99.19
2	75.77	12.45	0.15	0.90	0.01	0.15	0.81	3.82	3.10	0.15	97.30
3	75.51	12.33	0.20	0.73	0.06	0.11	0.90	3.66	3.17	0.17	96.85
4	77.49	12.66	0.14	0.76	0.01	0.10	0.78	3.68	3.40	0.19	99.22
5	77.78	12.54	0.09	0.74	0.08	0.10	0.83	3.67	3.33	0.14	99.30
6	76.75	12.32	0.08	0.62	0.21	0.11	0.73	3.78	3.38	0.17	98.15
7	77.67	12.50	0.09	0.93	0.15	0.13	0.82	3.70	3.32	0.13	99.44

Normalised	SiO2	Al2O3	TiO2	FeO	MnO	MgO	CaO	Na2O	K2O	Cl	TOTAL
1	77.99	12.62	0.14	0.94	0.13	0.12	0.76	3.78	3.41	0.13	100
2	77.87	12.80	0.15	0.92	0.01	0.15	0.83	3.93	3.19	0.15	100
3	77.97	12.73	0.21	0.75	0.06	0.11	0.93	3.78	3.27	0.18	100
4	78.10	12.76	0.14	0.77	0.01	0.10	0.79	3.71	3.43	0.19	100
5	78.33	12.63	0.09	0.75	0.08	0.10	0.84	3.70	3.35	0.14	100
6	78.20	12.55	0.08	0.63	0.21	0.11	0.74	3.85	3.44	0.17	100
7	78.11	12.57	0.09	0.94	0.15	0.13	0.82	3.72	3.34	0.13	100
Mean	78.08	12.67	0.13	0.81	0.09	0.12	0.82	3.78	3.35	0.16	100
St. Deviation	0.15	0.10	0.04	0.12	0.08	0.02	0.06	0.08	0.09	0.02	0

Sample name: Ah1_5; **Tephra ID:** Whakatane (microscope analysis: it contains cummingtonite); **Site(s) associated with the analysis:** 76

Table 51

	SiO2	Al2O3	TiO2	FeO	MnO	MgO	CaO	Na2O	K2O	Cl	TOTAL
1	74.28	12.12	0.12	0.75	0.04	0.06	0.65	3.43	3.36	0.19	95.00
2	75.28	11.97	0.13	0.76	0.06	0.13	0.65	3.50	3.57	0.21	96.25
3	76.42	12.11	0.11	0.79	0.21	0.09	0.73	3.50	3.32	0.10	97.39
4	76.68	12.08	0.12	0.77	0.04	0.07	0.64	3.62	3.42	0.12	97.56
5	76.55	12.45	0.15	1.00	0.06	1.00	0.65	3.58	3.42	0.19	98.15
6	75.58	12.69	0.15	0.64	0.09	0.11	0.69	3.55	3.50	0.22	97.23
7	77.41	12.40	0.09	0.74	0.04	0.08	0.61	3.93	3.47	0.25	99.02
8	77.55	11.93	0.17	0.93	0.06	0.13	0.69	3.67	3.41	0.19	98.73

Normalised	SiO2	Al2O3	TiO2	FeO	MnO	MgO	CaO	Na2O	K2O	Cl	TOTAL
1	78.19	12.76	0.13	0.79	0.04	0.06	0.68	3.61	3.54	0.20	100
2	78.21	12.44	0.14	0.79	0.06	0.14	0.68	3.64	3.71	0.22	100
3	78.47	12.43	0.11	0.81	0.22	0.09	0.75	3.59	3.41	0.10	100
4	78.60	12.38	0.12	0.79	0.04	0.07	0.66	3.71	3.51	0.12	100
5	77.99	12.68	0.15	1.02	0.06	1.02	0.66	3.65	3.48	0.19	100
6	77.73	13.05	0.15	0.66	0.09	0.11	0.71	3.65	3.60	0.23	100
7	78.18	12.52	0.09	0.75	0.04	0.08	0.62	3.97	3.50	0.25	100
8	78.55	12.08	0.17	0.94	0.06	0.13	0.70	3.72	3.45	0.19	100
Mean	78.24	12.54	0.13	0.82	0.08	0.21	0.68	3.69	3.53	0.19	100
St. Deviation	0.29	0.29	0.03	0.11	0.06	0.33	0.04	0.12	0.09	0.05	0

Sample name: Ah1_2; **Tephra ID:** Taupo; **Site(s) associated with the analysis:** 76

Table 52

	SiO2	Al2O3	TiO2	FeO	MnO	MgO	CaO	Na2O	K2O	Cl	TOTAL
1	73.00	13.75	0.18	1.71	0.11	0.25	1.39	3.85	2.94	0.23	97.40
2	75.34	14.15	0.14	2.08	0.07	0.24	1.54	3.88	2.62	0.14	100.21
3	74.11	13.49	0.14	1.97	0.13	0.28	1.40	3.82	2.67	0.14	98.15
4	75.27	12.90	0.21	1.80	0.11	0.26	1.39	4.01	2.73	0.19	98.87
5	74.49	13.50	0.25	1.93	0.16	0.27	1.38	3.76	2.83	0.19	98.76
6	75.44	13.77	0.33	1.82	0.17	0.26	1.45	3.85	2.39	0.16	99.63
7	72.91	13.33	0.36	2.02	0.00	0.20	1.44	3.91	2.61	0.20	96.98

Normalised	SiO2	Al2O3	TiO2	FeO	MnO	MgO	CaO	Na2O	K2O	Cl	TOTAL
1	74.95	14.12	0.18	1.76	0.11	0.26	1.43	3.95	3.02	0.24	100
2	75.18	14.12	0.14	2.08	0.07	0.24	1.54	3.87	2.61	0.14	100
3	75.51	13.74	0.14	2.01	0.13	0.29	1.43	3.89	2.72	0.14	100
4	76.13	13.05	0.21	1.82	0.11	0.26	1.41	4.06	2.76	0.19	100
5	75.43	13.67	0.25	1.95	0.16	0.27	1.40	3.81	2.87	0.19	100
6	75.72	13.82	0.33	1.83	0.17	0.26	1.46	3.86	2.40	0.16	100
7	75.18	13.75	0.37	2.08	0.00	0.21	1.48	4.03	2.69	0.21	100
Mean	75.44	13.75	0.23	1.93	0.11	0.26	1.45	3.93	2.72	0.18	100
St. Deviation	0.39	0.36	0.09	0.13	0.06	0.03	0.05	0.09	0.19	0.04	0

Sample name: Ah1_7; **Tephra ID:** Waiohau (microscope analysis: it does not contain cummingtonite); **Site(s) associated with the analysis:** 76

Table 53

	SiO2	Al2O3	TiO2	FeO	MnO	MgO	CaO	Na2O	K2O	Cl	TOTAL
1	74.58	10.52	0.05	0.71	0.09	0.13	0.77	2.81	3.18	0.09	92.92
2	71.96	10.95	0.11	0.88	0.11	0.10	0.89	2.93	2.96	0.18	91.08
3	72.49	10.78	0.10	0.78	0.09	0.12	0.65	2.88	3.47	0.18	91.55
4	73.67	10.56	0.13	0.72	0.00	0.16	0.70	3.01	3.36	0.11	92.42
5	73.69	10.98	0.14	0.83	0.05	0.11	0.75	2.96	3.24	0.17	92.91
6	73.96	10.80	0.10	0.98	0.05	0.08	0.72	3.12	3.12	0.08	93.03
7	76.71	11.01	0.08	0.87	0.10	0.10	0.75	2.98	3.52	0.15	96.28
8	72.93	10.81	0.13	0.99	0.05	0.09	0.73	2.93	3.33	0.16	92.13
9	75.25	11.09	0.11	0.69	0.06	0.13	0.77	3.17	3.25	0.13	94.64
10	75.15	10.95	0.18	0.89	0.12	0.15	0.60	3.05	3.20	0.15	94.44

Normalised	SiO2	Al2O3	TiO2	FeO	MnO	MgO	CaO	Na2O	K2O	Cl	TOTAL
1	80.26	11.32	0.05	0.76	0.10	0.14	0.83	3.02	3.42	0.10	100
2	79.01	12.02	0.12	0.97	0.12	0.11	0.98	3.22	3.25	0.20	100
3	79.18	11.77	0.11	0.85	0.10	0.13	0.71	3.15	3.79	0.20	100
4	79.71	11.43	0.14	0.78	0.00	0.17	0.76	3.26	3.64	0.12	100
5	79.31	11.82	0.15	0.89	0.05	0.12	0.81	3.19	3.49	0.18	100
6	79.50	11.61	0.11	1.05	0.05	0.09	0.77	3.35	3.35	0.09	100
7	79.67	11.44	0.08	0.90	0.10	0.10	0.78	3.10	3.66	0.16	100
8	79.16	11.73	0.14	1.07	0.05	0.10	0.79	3.18	3.61	0.17	100
9	79.51	11.72	0.12	0.73	0.06	0.14	0.81	3.35	3.43	0.14	100
10	79.57	11.59	0.19	0.94	0.13	0.16	0.64	3.23	3.39	0.16	100
Mean	79.49	11.65	0.12	0.90	0.08	0.13	0.79	3.20	3.50	0.15	100
St. Deviation	0.36	0.21	0.04	0.12	0.04	0.03	0.09	0.10	0.17	0.04	0

Sample name: RT-b; **Tephra ID:** Reworked Whakatane; **Site(s) associated with the analysis:** 77

Table 54

	SiO2	Al2O3	TiO2	FeO	MnO	MgO	CaO	Na2O	K2O	Cl	TOTAL
1	74.04	11.43	0.11	0.72	0.12	0.12	0.73	3.63	2.92	0.21	94.12
2	75.43	12.32	0.11	0.98	0.04	0.12	0.76	3.83	3.26	0.12	97.28
3	76.52	12.46	0.93	1.00	0.11	0.09	0.78	3.58	3.45	0.11	97.88
4	73.80	11.67	0.11	0.87	0.02	0.11	0.77	3.13	3.34	0.15	94.07
5	76.12	12.38	0.13	0.81	0.04	0.09	0.67	3.26	3.44	0.22	97.53
6	76.23	12.30	0.12	0.92	0.00	0.05	0.70	3.53	3.61	0.21	97.93
7	74.15	11.65	0.38	0.88	0.03	0.12	0.82	3.42	3.33	0.10	94.88
8	76.05	12.24	0.15	0.93	0.12	0.16	0.77	3.57	3.23	0.13	97.68
9	74.40	12.18	0.27	0.99	0.12	0.15	0.68	3.62	3.60	0.17	95.86
10	73.08	11.75	0.23	0.81	0.01	0.12	0.75	3.40	3.24	0.12	93.79

Normalised	SiO2	Al2O3	TiO2	FeO	MnO	MgO	CaO	Na2O	K2O	Cl	TOTAL
1	78.67	12.14	0.12	0.76	0.13	0.13	0.78	3.86	3.10	0.22	100
2	77.54	12.66	0.11	1.01	0.04	0.12	0.78	3.94	3.35	0.12	100
3	78.18	12.73	0.95	1.02	0.11	0.09	0.80	3.66	3.52	0.11	100
4	78.45	12.41	0.12	0.92	0.02	0.12	0.82	3.33	3.55	0.16	100
5	78.05	12.69	0.13	0.83	0.04	0.09	0.69	3.34	3.53	0.23	100
6	77.84	12.56	0.12	0.94	0.00	0.05	0.71	3.60	3.69	0.21	100
7	78.15	12.28	0.40	0.93	0.03	0.13	0.86	3.60	3.51	0.11	100
8	77.86	12.53	0.15	0.95	0.12	0.16	0.79	3.65	3.31	0.13	100
9	77.61	12.71	0.28	1.03	0.13	0.16	0.71	3.78	3.76	0.18	100
10	77.92	12.53	0.25	0.86	0.01	0.13	0.80	3.63	3.45	0.13	100
Mean	78.03	12.52	0.26	0.93	0.06	0.12	0.77	3.64	3.48	0.16	100
St. Deviation	0.35	0.20	0.26	0.09	0.05	0.03	0.05	0.20	0.19	0.05	0

Tana-Tana area

Sample name: Cem 1; **Tephra ID:** Mangaone subgroup; **NZ Map Grid:** W16/160250.

Table 55

	SiO2	Al2O3	TiO2	FeO	MnO	MgO	CaO	Na2O	K2O	Cl	TOTAL
1	72.97	12.65	0.13	1.33	0.11	0.20	1.15	3.96	2.78	0.21	95.47
2	72.74	12.45	0.15	1.20	0.00	0.16	1.25	3.76	2.98	0.19	94.88
3	72.20	12.08	0.13	1.36	0.00	0.20	1.13	3.93	2.82	0.27	94.13
4	72.97	12.35	0.09	1.08	0.07	0.18	0.99	4.02	2.97	0.22	94.95
5	73.09	12.21	0.17	0.93	0.09	0.20	0.93	3.57	2.86	0.10	94.16
6	73.81	12.62	0.20	1.07	0.14	0.19	0.94	4.07	2.87	0.13	96.04
7	72.85	12.20	0.10	1.13	0.07	0.19	1.00	4.17	2.79	0.39	94.90
8	74.38	12.21	0.19	0.94	0.09	0.19	0.93	3.93	2.88	0.21	95.97
9	73.86	12.34	0.12	1.02	0.05	0.18	0.85	3.84	2.79	0.17	95.21
10	72.04	12.23	0.16	1.01	0.05	0.17	1.01	3.93	2.98	0.18	93.75

Normalised	SiO2	Al2O3	TiO2	FeO	MnO	MgO	CaO	Na2O	K2O	Cl	TOTAL
1	76.43	13.25	0.14	1.39	0.12	0.21	1.20	4.15	2.91	0.22	100
2	76.67	13.12	0.16	1.26	0.00	0.17	1.32	3.96	3.14	0.20	100
3	76.70	12.83	0.14	1.44	0.00	0.21	1.20	4.18	3.00	0.29	100
4	76.85	13.01	0.09	1.14	0.07	0.19	1.04	4.23	3.13	0.23	100
5	77.62	12.97	0.18	0.99	0.10	0.21	0.99	3.79	3.04	0.11	100
6	76.85	13.14	0.21	1.11	0.15	0.20	0.98	4.24	2.99	0.14	100
7	76.77	12.86	0.11	1.19	0.07	0.20	1.05	4.39	2.94	0.41	100
8	77.50	12.72	0.20	0.98	0.09	0.20	0.97	4.10	3.00	0.22	100
9	77.58	12.96	0.13	1.07	0.05	0.19	0.89	4.03	2.93	0.18	100
10	76.84	13.05	0.17	1.08	0.05	0.18	1.08	4.19	3.18	0.19	100
Mean	76.98	12.99	0.15	1.17	0.07	0.20	1.07	4.13	3.03	0.22	100
St. Deviation	0.42	0.16	0.04	0.16	0.05	0.01	0.13	0.17	0.09	0.08	0

Sample name: Tom 1; **Tephra ID:** uncertain; **Site(s) associated with the analysis:** 70

Table 56

	SiO2	Al2O3	TiO2	FeO	MnO	MgO	CaO	Na2O	K2O	Cl	TOTAL
1	73.05	11.73	0.18	0.75	0.10	0.10	0.98	3.36	2.73	0.20	93.18
2	74.59	12.33	0.20	1.19	0.01	0.16	0.99	4.13	2.81	0.21	96.61
3	73.79	11.71	0.13	1.18	0.08	0.13	0.87	3.44	3.01	0.18	94.53
4	73.87	12.45	0.14	1.07	0.00	0.15	1.02	4.08	2.80	0.19	95.76
5	75.42	12.47	0.17	1.08	0.09	0.15	1.05	4.00	3.07	0.18	97.69
6	73.70	12.82	0.26	1.11	0.09	0.29	1.14	4.24	2.90	0.20	96.74
7	72.81	12.14	0.14	0.83	0.07	0.18	0.86	3.80	3.14	0.25	94.22
8	76.10	12.18	0.15	1.03	0.07	0.15	1.09	3.60	3.03	0.17	97.57
9	73.63	11.64	0.08	1.03	0.09	0.10	1.03	3.60	2.96	0.16	94.32
10	74.38	12.39	0.17	1.05	0.13	0.19	0.71	3.82	2.70	0.22	95.75

Normalised	SiO2	Al2O3	TiO2	FeO	MnO	MgO	CaO	Na2O	K2O	Cl	TOTAL
1	78.40	12.59	0.19	0.80	0.11	0.11	1.05	3.61	2.93	0.21	100
2	77.21	12.76	0.21	1.23	0.01	0.17	1.02	4.27	2.91	0.22	100
3	78.06	12.39	0.14	1.25	0.08	0.14	0.92	3.64	3.18	0.19	100
4	77.14	13.00	0.15	1.12	0.00	0.16	1.07	4.26	2.92	0.20	100
5	77.20	12.76	0.17	1.11	0.09	0.15	1.07	4.09	3.14	0.18	100
6	76.18	13.25	0.27	1.15	0.09	0.30	1.18	4.38	3.00	0.21	100
7	77.28	12.88	0.15	0.88	0.07	0.19	0.91	4.03	3.33	0.27	100
8	78.00	12.48	0.15	1.06	0.07	0.15	1.12	3.69	3.11	0.17	100
9	78.06	12.34	0.08	1.09	0.10	0.11	1.09	3.82	3.14	0.17	100
10	77.68	12.94	0.18	1.10	0.14	0.20	0.74	3.99	2.82	0.23	100
Mean	77.52	12.74	0.17	1.08	0.08	0.17	1.02	3.98	3.05	0.21	100
St. Deviation	0.65	0.29	0.05	0.14	0.04	0.06	0.13	0.28	0.16	0.03	0

Sample name: Timoti D; **Tephra ID:** Mangaone subgroup; **Site(s) associated with the analysis:** 71-72

Table 57

	SiO2	Al2O3	TiO2	FeO	MnO	MgO	CaO	Na2O	K2O	Cl	TOTAL
1	73.51	12.38	0.16	0.83	0.01	0.13	0.96	3.60	2.67	0.18	94.43
2	73.70	12.73	0.34	1.03	0.24	0.14	1.02	4.20	2.94	0.16	96.49
3	73.53	12.63	0.16	1.28	0.05	0.22	1.10	3.75	2.73	0.15	95.58
4	73.58	12.43	0.14	1.52	0.10	0.16	1.01	3.67	2.83	0.20	95.64
5	75.05	12.25	0.16	0.99	0.09	0.18	1.05	4.12	2.85	0.16	96.90
6	74.66	12.53	0.18	1.11	0.01	0.18	0.87	3.86	2.89	0.19	96.47
7	74.54	12.31	0.10	1.18	0.00	0.18	0.88	3.86	2.68	0.18	95.91
8	75.38	12.85	0.17	1.14	0.03	0.19	1.02	3.68	2.69	0.18	97.33
9	74.18	12.75	0.11	1.38	0.05	0.11	1.01	3.90	2.63	0.18	96.29

Normalised	SiO2	Al2O3	TiO2	FeO	MnO	MgO	CaO	Na2O	K2O	Cl	TOTAL
1	77.85	13.11	0.17	0.88	0.01	0.14	1.02	3.81	2.83	0.19	100
2	76.38	13.19	0.35	1.07	0.25	0.15	1.06	4.35	3.05	0.17	100
3	76.93	13.21	0.17	1.34	0.05	0.23	1.15	3.92	2.86	0.16	100
4	76.93	13.00	0.15	1.59	0.10	0.17	1.06	3.84	2.96	0.21	100
5	77.45	12.64	0.17	1.02	0.09	0.19	1.08	4.25	2.94	0.17	100
6	77.39	12.99	0.19	1.15	0.01	0.19	0.90	4.00	3.00	0.20	100
7	77.72	12.83	0.10	1.23	0.00	0.19	0.92	4.02	2.79	0.19	100
8	77.45	13.20	0.17	1.17	0.03	0.20	1.05	3.78	2.76	0.18	100
9	77.04	13.24	0.11	1.43	0.05	0.11	1.05	4.05	2.73	0.19	100
Mean	77.24	13.05	0.18	1.21	0.07	0.17	1.03	4.00	2.88	0.18	100
St. Deviation	0.46	0.20	0.07	0.22	0.08	0.04	0.08	0.20	0.11	0.02	0

Sample name: Timoti B; **Tephra ID:** Rotoma (microscope analysis: it contains cummingtonite); **Site(s) associated with the analysis:** 71-72

Table 58

	SiO2	Al2O3	TiO2	FeO	MnO	MgO	CaO	Na2O	K2O	Cl	TOTAL
1	75.40	12.14	0.10	0.93	0.00	0.17	0.92	3.86	3.32	0.10	96.95
2	73.46	11.51	0.12	1.25	0.02	0.23	1.30	3.28	2.55	0.12	93.87
3	75.57	12.06	0.09	1.20	0.15	0.14	0.92	4.00	3.24	0.15	97.51
4	73.35	12.01	0.19	0.84	0.09	0.09	0.88	3.77	3.05	0.14	94.41
5	76.12	12.05	0.06	0.93	0.07	0.14	0.69	4.03	3.36	0.18	97.64
6	77.21	12.56	0.01	0.90	0.20	0.14	0.72	4.01	3.08	0.12	98.95
7	76.22	12.42	0.09	0.81	0.03	0.13	0.69	3.84	3.49	0.17	97.88
8	74.57	12.35	0.12	0.61	0.05	0.11	0.68	4.05	3.24	0.10	95.88
9	77.18	12.44	0.14	0.90	0.10	0.13	0.74	3.87	3.39	0.18	99.08
10	75.28	12.47	0.12	0.73	0.07	0.15	0.80	3.97	3.21	0.16	96.96

Normalised	SiO2	Al2O3	TiO2	FeO	MnO	MgO	CaO	Na2O	K2O	Cl	TOTAL
1	77.77	12.52	0.10	0.96	0.00	0.18	0.95	3.98	3.42	0.10	100
2	78.26	12.26	0.13	1.33	0.02	0.25	1.38	3.49	2.72	0.13	100
3	77.50	12.37	0.09	1.23	0.15	0.14	0.94	4.10	3.32	0.15	100
4	77.69	12.72	0.20	0.89	0.10	0.10	0.93	3.99	3.23	0.15	100
5	77.96	12.34	0.06	0.95	0.07	0.14	0.71	4.13	3.44	0.18	100
6	78.03	12.69	0.01	0.91	0.20	0.14	0.73	4.05	3.11	0.12	100
7	77.87	12.69	0.09	0.83	0.03	0.13	0.70	3.92	3.57	0.17	100
8	77.77	12.88	0.13	0.64	0.05	0.11	0.71	4.22	3.38	0.10	100
9	77.90	12.56	0.14	0.91	0.10	0.13	0.75	3.91	3.42	0.18	100
10	77.64	12.86	0.12	0.75	0.07	0.15	0.83	4.09	3.31	0.17	100
Mean	77.84	12.59	0.11	0.94	0.08	0.15	0.86	3.99	3.29	0.15	100
St. Deviation	0.21	0.22	0.05	0.21	0.06	0.04	0.21	0.20	0.24	0.03	0

Nukuhou North

Sample name: WP; **Tephra ID:** Rotoehu (microscope analysis: it contains cummingtonite); **Site(s) associated with the analysis:** 62-65

Table 59

	SiO2	Al2O3	TiO2	FeO	MnO	MgO	CaO	Na2O	K2O	Cl	TOTAL
1	74.59	11.69	0.19	0.78	0.00	0.13	0.74	3.99	3.47	0.17	95.76
2	74.08	11.86	0.21	0.70	0.01	0.13	0.69	3.93	3.31	0.17	95.10
3	76.50	12.00	0.13	0.85	0.00	0.11	0.72	3.74	3.24	0.18	97.48
4	76.82	11.15	0.18	0.80	0.00	0.14	0.70	3.40	2.98	0.15	96.32
5	75.39	11.81	0.16	0.71	0.06	0.15	0.81	3.88	3.19	0.14	96.30
6	77.06	12.26	0.14	0.82	0.01	0.14	0.77	3.91	3.45	0.19	98.76
7	76.05	12.15	0.12	0.82	0.04	0.11	0.79	3.90	3.04	0.15	97.16
8	75.74	12.04	0.04	0.81	0.09	0.11	0.70	3.77	3.20	0.15	96.65
9	76.73	12.26	0.16	1.03	0.07	0.15	0.86	3.73	3.43	0.11	98.53
10	76.43	12.08	0.16	0.89	0.16	0.11	0.80	3.91	3.28	0.18	97.99

Normalised	SiO2	Al2O3	TiO2	FeO	MnO	MgO	CaO	Na2O	K2O	Cl	TOTAL
1	77.89	12.21	0.20	0.81	0.00	0.14	0.77	4.17	3.62	0.18	100
2	77.90	12.47	0.22	0.74	0.01	0.14	0.73	4.13	3.48	0.18	100
3	78.48	12.31	0.13	0.87	0.00	0.11	0.74	3.84	3.32	0.18	100
4	79.75	11.58	0.19	0.83	0.00	0.15	0.73	3.53	3.09	0.16	100
5	78.29	12.26	0.17	0.74	0.06	0.16	0.84	4.03	3.31	0.15	100
6	78.03	12.41	0.14	0.83	0.01	0.14	0.78	3.96	3.49	0.19	100
7	78.27	12.51	0.12	0.84	0.04	0.11	0.81	4.01	3.13	0.15	100
8	78.37	12.46	0.04	0.84	0.09	0.11	0.72	3.90	3.31	0.16	100
9	77.87	12.44	0.16	1.05	0.07	0.15	0.87	3.79	3.48	0.11	100
10	78.00	12.33	0.16	0.91	0.16	0.11	0.82	3.99	3.35	0.18	100
Mean	78.28	12.30	0.15	0.85	0.05	0.13	0.78	3.93	3.36	0.16	100
St. Deviation	0.56	0.27	0.05	0.09	0.05	0.02	0.05	0.19	0.17	0.02	0

Sample name: Atk 1; **Tephra ID:** Mixture of Okataina and Taupo sourced-tephras; **Site(s) associated with the analysis:** 62

Table 60

	SiO2	Al2O3	TiO2	FeO	MnO	MgO	CaO	Na2O	K2O	Cl	TOTAL
1	74.71	12.16	0.20	0.63	0.00	0.13	0.66	3.58	3.82	0.18	96.08
2	75.48	12.42	0.16	0.67	0.13	0.10	0.65	3.56	3.69	0.13	96.99
3	72.24	11.94	0.21	1.66	0.21	0.11	0.97	3.87	2.83	0.19	94.22
4	76.36	11.94	0.11	0.76	0.04	0.13	0.66	3.46	3.72	0.16	97.34
5	76.73	12.09	0.04	0.66	0.05	0.12	0.66	3.78	3.91	0.16	98.19
6	74.38	13.48	0.27	1.80	0.17	0.27	1.40	3.90	2.59	0.17	98.43
7	77.02	12.23	0.11	0.78	0.07	0.09	0.53	3.64	3.69	0.13	98.28
8	75.42	12.48	0.14	1.34	0.23	0.15	0.98	3.53	3.05	0.16	97.48
9	75.19	12.31	0.04	0.62	0.00	0.08	0.58	3.58	3.79	0.14	96.34
10	72.98	12.22	0.16	1.13	0.03	0.17	0.96	3.90	3.16	0.18	94.88

Normalised	SiO2	Al2O3	TiO2	FeO	MnO	MgO	CaO	Na2O	K2O	Cl	TOTAL
1	77.76	12.66	0.21	0.66	0.00	0.14	0.69	3.73	3.98	0.19	100
2	77.82	12.81	0.16	0.69	0.13	0.10	0.67	3.67	3.80	0.13	100
3	76.67	12.67	0.22	1.76	0.22	0.12	1.03	4.11	3.00	0.20	100
4	78.45	12.27	0.11	0.78	0.04	0.13	0.68	3.55	3.82	0.16	100
5	78.14	12.31	0.04	0.67	0.05	0.12	0.67	3.85	3.98	0.16	100
6	75.57	13.70	0.27	1.83	0.17	0.27	1.42	3.96	2.63	0.17	100
7	78.37	12.44	0.11	0.79	0.07	0.09	0.54	3.70	3.75	0.13	100
8	77.37	12.80	0.14	1.37	0.24	0.15	1.01	3.62	3.13	0.16	100
9	78.05	12.78	0.04	0.64	0.00	0.08	0.60	3.72	3.93	0.15	100
10	76.92	12.88	0.17	1.19	0.03	0.18	1.01	4.11	3.33	0.19	100
Mean	77.51	12.73	0.15	1.04	0.10	0.14	0.83	3.80	3.54	0.17	100
St. Deviation	0.90	0.40	0.08	0.47	0.09	0.06	0.28	0.20	0.48	0.02	0

Sample name: Atk 5; **Tephra ID:** Rerewhakaaitu (microscope analysis: it contains biotite); **Site(s) associated with the analysis:** 62

Table 61

	SiO2	Al2O3	TiO2	FeO	MnO	MgO	CaO	Na2O	K2O	Cl	TOTAL
1	74.28	11.85	0.27	0.94	0.11	0.16	1.15	3.48	3.19	0.20	95.62
2	76.39	12.28	0.18	0.91	0.12	0.14	0.75	3.71	3.23	0.15	97.86
3	74.74	12.25	0.08	0.85	0.14	0.11	0.73	3.43	4.05	0.10	96.48
4	75.27	12.02	0.17	1.14	0.06	0.11	0.79	3.53	4.09	0.19	97.38
5	75.07	12.19	0.11	0.79	0.07	0.08	0.75	3.39	3.81	0.21	96.47
6	75.07	12.19	0.11	0.79	0.07	0.08	0.75	3.39	3.81	0.21	95.98
7	75.37	12.22	0.07	1.10	0.03	0.08	0.63	3.67	3.94	0.14	97.26
8	76.27	12.36	0.10	0.78	0.12	0.12	0.92	3.82	3.63	0.12	98.24
9	74.85	12.20	0.13	0.94	0.09	0.05	0.76	3.59	4.01	0.19	96.81
10	76.20	11.97	0.16	1.15	0.03	0.18	0.92	3.47	3.39	0.13	97.59

Normalised	SiO2	Al2O3	TiO2	FeO	MnO	MgO	CaO	Na2O	K2O	Cl	TOTAL
1	77.68	12.39	0.28	0.98	0.12	0.17	1.20	3.64	3.34	0.21	100
2	78.06	12.55	0.18	0.93	0.12	0.14	0.77	3.79	3.30	0.15	100
3	77.47	12.70	0.08	0.88	0.15	0.11	0.76	3.56	4.20	0.10	100
4	77.30	12.34	0.17	1.17	0.06	0.11	0.81	3.62	4.20	0.20	100
5	77.82	12.64	0.11	0.82	0.07	0.08	0.78	3.51	3.95	0.22	100
6	78.21	12.70	0.11	0.82	0.07	0.08	0.78	3.53	3.97	0.22	100
7	77.49	12.56	0.07	1.13	0.03	0.08	0.65	3.77	4.05	0.14	100
8	77.64	12.58	0.10	0.79	0.12	0.12	0.94	3.89	3.70	0.12	100
9	77.32	12.60	0.13	0.97	0.09	0.05	0.79	3.71	4.14	0.20	100
10	78.08	12.27	0.16	1.18	0.03	0.18	0.94	3.56	3.47	0.13	100
Mean	77.71	12.53	0.14	0.97	0.09	0.11	0.84	3.66	3.83	0.17	100
St. Deviation	0.33	0.15	0.06	0.15	0.04	0.04	0.15	0.13	0.35	0.04	0

Sample name: Atk 7; **Tephra ID:** Kawakawa; **Site(s) associated with the analysis:** 62

Table 62

	SiO2	Al2O3	TiO2	FeO	MnO	MgO	CaO	Na2O	K2O	Cl	TOTAL
1	72.63	12.37	0.21	1.17	0.10	0.23	1.08	3.50	2.71	0.13	94.15
2	75.79	12.83	0.15	1.07	0.06	0.19	1.23	3.83	2.76	0.14	98.07
3	72.41	12.34	0.13	0.83	0.11	0.26	1.07	2.82	2.65	0.19	92.81
4	73.01	12.73	0.18	1.28	0.10	0.22	1.00	3.88	2.91	0.17	95.50
5	73.28	12.62	0.20	1.07	0.05	0.26	1.10	3.67	2.74	0.17	95.15
6	73.87	12.47	0.15	0.92	0.04	0.14	0.94	3.70	2.58	0.17	94.98
7	73.47	11.82	0.11	1.07	0.02	0.12	0.95	3.24	2.87	0.19	93.86
8	73.63	12.41	0.27	1.04	0.12	0.18	0.98	3.78	2.81	0.20	95.43
9	71.61	12.76	0.20	1.37	0.26	0.25	1.21	3.87	2.60	0.22	94.35
10	73.22	11.91	0.13	0.94	0.07	0.13	1.09	3.36	3.00	0.19	94.03

Normalised	SiO2	Al2O3	TiO2	FeO	MnO	MgO	CaO	Na2O	K2O	Cl	TOTAL
1	77.14	13.14	0.22	1.24	0.11	0.24	1.15	3.72	2.88	0.14	100
2	77.28	13.08	0.15	1.09	0.06	0.19	1.25	3.91	2.81	0.14	100
3	78.02	13.30	0.14	0.89	0.12	0.28	1.15	3.04	2.86	0.20	100
4	76.45	13.33	0.19	1.34	0.10	0.23	1.05	4.06	3.05	0.18	100
5	77.02	13.26	0.21	1.12	0.05	0.27	1.16	3.86	2.88	0.18	100
6	77.77	13.13	0.16	0.97	0.04	0.15	0.99	3.90	2.72	0.18	100
7	78.28	12.59	0.12	1.14	0.02	0.13	1.01	3.45	3.06	0.20	100
8	77.16	13.00	0.28	1.09	0.13	0.19	1.03	3.96	2.94	0.21	100
9	75.90	13.52	0.21	1.45	0.28	0.26	1.28	4.10	2.76	0.23	100
10	77.87	12.67	0.14	1.00	0.07	0.14	1.16	3.57	3.19	0.20	100
Mean	77.29	13.10	0.18	1.13	0.10	0.21	1.12	3.76	2.91	0.19	100
St. Deviation	0.73	0.29	0.05	0.17	0.07	0.06	0.10	0.32	0.15	0.03	0

Sample name: M3; **Tephra ID:** Reworked Whakatane with grains of Taupo sourced tephra; **Site(s) associated with the analysis:** 65

Table 63

	SiO2	Al2O3	TiO2	FeO	MnO	MgO	CaO	Na2O	K2O	Cl	TOTAL
1	77.84	12.45	0.16	0.81	0.06	0.09	0.74	3.79	3.39	0.12	99.46
2	77.37	12.86	0.10	1.08	0.07	0.16	0.89	3.61	3.22	0.10	99.47
3	75.05	13.44	0.26	1.47	0.07	0.16	1.39	3.49	3.03	0.14	98.50
4	78.71	12.86	0.15	1.01	0.00	0.12	0.88	3.88	3.25	0.19	101.05
5	78.66	13.02	0.17	0.80	0.05	0.10	0.62	3.59	3.40	0.09	100.50
6	76.83	12.89	0.15	1.13	0.06	0.16	0.86	3.80	3.35	0.14	99.36
7	76.85	12.99	0.10	0.97	0.09	0.13	0.84	3.56	3.21	0.09	98.84
8	77.42	12.93	0.10	0.88	0.06	0.10	0.69	3.74	3.24	0.17	99.33
9	76.01	12.70	0.17	0.86	0.01	0.12	0.72	3.60	3.22	0.16	97.57
10	75.54	12.63	0.13	0.95	0.05	0.10	0.85	3.70	3.28	0.11	97.33

Normalised	SiO2	Al2O3	TiO2	FeO	MnO	MgO	CaO	Na2O	K2O	Cl	TOTAL
1	78.26	12.52	0.16	0.81	0.06	0.09	0.74	3.81	3.41	0.12	100
2	77.78	12.93	0.10	1.09	0.07	0.16	0.89	3.63	3.24	0.10	100
3	76.19	13.64	0.26	1.49	0.07	0.16	1.41	3.54	3.08	0.14	100
4	77.89	12.73	0.15	1.00	0.00	0.12	0.87	3.84	3.22	0.19	100
5	78.27	12.96	0.17	0.80	0.05	0.10	0.62	3.57	3.38	0.09	100
6	77.32	12.97	0.15	1.14	0.06	0.16	0.87	3.82	3.37	0.14	100
7	77.75	13.14	0.10	0.98	0.09	0.13	0.85	3.60	3.25	0.09	100
8	77.94	13.02	0.10	0.89	0.06	0.10	0.69	3.77	3.26	0.17	100
9	77.90	13.02	0.17	0.88	0.01	0.12	0.74	3.69	3.30	0.16	100
10	77.61	12.98	0.13	0.98	0.05	0.10	0.87	3.80	3.37	0.11	100
Mean	77.69	12.99	0.15	1.01	0.05	0.13	0.86	3.71	3.29	0.13	100
St. Deviation	0.60	0.29	0.05	0.20	0.03	0.03	0.22	0.11	0.10	0.03	0

Sample name: M4; **Tephra ID:** Whakatane (microscope analysis: it contains cummingtonite); **Site(s) associated with the analysis:** 65

Table 64

	SiO2	Al2O3	TiO2	FeO	MnO	MgO	CaO	Na2O	K2O	Cl	TOTAL
1	75.34	12.84	0.15	0.89	0.02	0.05	0.61	3.81	3.76	0.22	97.69
2	76.00	12.53	0.17	0.75	0.04	0.13	0.65	3.52	3.73	0.19	97.70
3	75.61	12.95	0.14	0.72	0.00	0.11	0.65	3.52	3.71	0.15	97.55
4	76.05	12.70	0.13	0.84	0.00	0.14	0.68	3.71	3.74	0.16	98.13
5	76.91	12.84	0.11	0.93	0.05	0.11	0.65	3.65	3.57	0.09	98.91
6	75.81	12.87	0.12	0.89	0.11	0.08	0.61	3.65	3.70	0.21	98.05
7	76.18	12.43	0.12	0.90	0.03	0.11	0.68	3.69	3.66	0.14	97.94
8	75.89	12.78	0.10	0.82	0.10	0.12	0.72	3.77	3.70	0.20	98.19
9	76.03	12.83	0.07	0.79	0.06	0.11	0.73	3.78	3.63	0.16	98.20
10	75.94	12.93	0.10	0.92	0.09	0.05	0.69	3.76	3.80	0.11	98.39

Normalised	SiO2	Al2O3	TiO2	FeO	MnO	MgO	CaO	Na2O	K2O	Cl	TOTAL
1	77.12	13.14	0.15	0.91	0.02	0.05	0.62	3.90	3.85	0.23	100
2	77.79	12.82	0.17	0.77	0.04	0.13	0.67	3.60	3.82	0.19	100
3	77.51	13.28	0.14	0.74	0.00	0.11	0.67	3.61	3.80	0.15	100
4	77.50	12.94	0.13	0.86	0.00	0.14	0.69	3.78	3.81	0.16	100
5	77.76	12.98	0.11	0.94	0.05	0.11	0.66	3.69	3.61	0.09	100
6	77.32	13.13	0.12	0.91	0.11	0.08	0.62	3.72	3.77	0.21	100
7	77.78	12.69	0.12	0.92	0.03	0.11	0.69	3.77	3.74	0.14	100
8	77.29	13.02	0.10	0.84	0.10	0.12	0.73	3.84	3.77	0.20	100
9	77.42	13.07	0.07	0.80	0.06	0.11	0.74	3.85	3.70	0.16	100
10	77.18	13.14	0.10	0.94	0.09	0.05	0.70	3.82	3.86	0.11	100
Mean	77.47	13.02	0.12	0.86	0.05	0.10	0.68	3.76	3.77	0.17	100
St. Deviation	0.25	0.17	0.03	0.07	0.04	0.03	0.04	0.10	0.08	0.04	0

Sample name: M16; **Tephra ID:** Reworked Waiohau (microscope analysis: it does not contain cummingtonite); **Site(s) associated with the analysis:** 65

Table 65

	SiO2	Al2O3	TiO2	FeO	MnO	MgO	CaO	Na2O	K2O	Cl	TOTAL
1	74.21	12.37	0.11	0.86	0.07	0.09	0.69	3.31	3.26	0.22	95.19
2	75.80	12.71	0.11	0.74	0.08	0.13	0.84	3.75	3.54	0.17	97.89
3	76.99	13.15	0.12	0.89	0.05	0.14	0.73	3.91	3.39	0.15	99.52
4	74.31	12.96	0.09	0.88	0.13	0.16	0.67	3.47	3.23	0.17	96.06
5	74.34	12.50	0.07	0.88	0.02	0.14	0.78	3.44	3.28	0.16	95.61
6	73.56	12.27	0.14	0.71	0.07	0.13	0.73	3.31	3.17	0.17	94.25
7	74.50	12.48	0.06	0.73	0.07	0.10	0.77	3.69	3.45	0.15	96.00
8	73.62	12.19	0.09	0.92	0.05	0.09	0.79	3.55	3.25	0.16	94.70
9	72.95	12.62	0.11	0.92	0.08	0.15	0.73	2.61	3.03	0.16	93.36
10	74.81	12.69	0.19	0.80	0.09	0.10	0.82	3.67	3.29	0.13	96.57

Normalised	SiO2	Al2O3	TiO2	FeO	MnO	MgO	CaO	Na2O	K2O	Cl	TOTAL
1	77.96	13.00	0.12	0.90	0.07	0.09	0.72	3.48	3.42	0.23	100
2	77.43	12.98	0.11	0.76	0.08	0.13	0.86	3.83	3.62	0.17	100
3	77.36	13.21	0.12	0.89	0.05	0.14	0.73	3.93	3.41	0.15	100
4	77.36	13.49	0.09	0.92	0.14	0.17	0.70	3.61	3.36	0.18	100
5	77.75	13.07	0.07	0.92	0.02	0.15	0.82	3.60	3.43	0.17	100
6	78.05	13.02	0.15	0.75	0.07	0.14	0.77	3.51	3.36	0.18	100
7	77.60	13.00	0.06	0.76	0.07	0.10	0.80	3.84	3.59	0.16	100
8	77.74	12.87	0.10	0.97	0.05	0.10	0.83	3.75	3.43	0.17	100
9	78.14	13.52	0.12	0.99	0.09	0.16	0.78	2.80	3.25	0.17	100
10	77.47	13.14	0.20	0.83	0.09	0.10	0.85	3.80	3.41	0.13	100
Mean	77.69	13.13	0.11	0.87	0.07	0.13	0.79	3.61	3.43	0.17	100
St. Deviation	0.29	0.22	0.04	0.09	0.03	0.03	0.05	0.33	0.11	0.03	0

Sample name: M26; **Tephra ID:** Reworked Whakatane (Microscope analysis: 1) it contains cummingtonite, 2) its glass is rounded and therefore it is water deposited reworked tephra); **Site(s) associated with the analysis:** 65

Table 66

	SiO2	Al2O3	TiO2	FeO	MnO	MgO	CaO	Na2O	K2O	Cl	TOTAL
1	73.85	12.74	0.14	0.79	0.00	0.09	0.74	3.28	3.41	0.17	95.21
2	76.92	12.88	0.09	0.83	0.09	0.12	0.52	3.71	3.71	0.21	99.08
3	73.77	12.25	0.10	0.84	0.15	0.09	0.62	3.41	3.57	0.15	94.94
4	76.32	12.86	0.13	0.76	0.08	0.09	0.60	4.38	3.73	0.17	98.21
5	73.71	12.34	0.12	0.65	0.13	0.10	0.65	3.23	3.59	0.16	94.68
6	76.00	12.77	0.08	0.87	0.12	0.12	0.77	3.79	3.66	0.15	98.35
7	76.54	12.99	0.13	0.81	0.01	0.09	0.66	3.68	3.70	0.18	98.78
8	76.61	12.89	0.11	0.82	0.02	0.13	0.72	3.85	3.65	0.11	98.93
9	73.95	12.53	0.14	0.92	0.12	0.05	0.67	3.23	3.80	0.16	95.56
10	77.43	12.86	0.07	0.97	0.11	0.11	0.73	3.53	3.62	0.15	99.58

Normalised	SiO2	Al2O3	TiO2	FeO	MnO	MgO	CaO	Na2O	K2O	Cl	TOTAL
1	77.57	13.38	0.15	0.83	0.00	0.09	0.78	3.45	3.58	0.18	100
2	77.63	13.00	0.09	0.84	0.09	0.12	0.52	3.74	3.74	0.21	100
3	77.70	12.90	0.11	0.88	0.16	0.09	0.65	3.59	3.76	0.16	100
4	77.71	13.09	0.13	0.77	0.08	0.09	0.61	4.46	3.80	0.17	100
5	77.85	13.03	0.13	0.69	0.14	0.11	0.69	3.41	3.79	0.17	100
6	77.28	12.98	0.08	0.88	0.12	0.12	0.78	3.85	3.72	0.15	100
7	77.49	13.15	0.13	0.82	0.01	0.09	0.67	3.73	3.75	0.18	100
8	77.44	13.03	0.11	0.83	0.02	0.13	0.73	3.89	3.69	0.11	100
9	77.39	13.11	0.15	0.96	0.13	0.05	0.70	3.38	3.98	0.17	100
10	77.76	12.91	0.07	0.97	0.11	0.11	0.73	3.54	3.64	0.15	100
Mean	77.58	13.06	0.11	0.85	0.09	0.10	0.69	3.70	3.74	0.17	100
St. Deviation	0.18	0.14	0.03	0.08	0.06	0.02	0.08	0.32	0.11	0.03	0

Sample name: M27; **Tephra ID:** Reworeked Whakatane (Microscope analysis: 1) it contains cummingtonite, 2) its glass is rounded and therefore it is water deposited reworked tephra); **Site(s) associated with the analysis:** 65

Table 67

	SiO2	Al2O3	TiO2	FeO	MnO	MgO	CaO	Na2O	K2O	Cl	TOTAL
1	74.43	12.54	0.17	0.94	0.08	0.12	0.83	3.34	3.13	0.16	95.74
2	75.28	12.67	0.13	0.90	0.08	0.14	0.59	2.82	3.33	0.13	96.08
3	74.38	12.72	0.10	0.76	0.15	0.14	0.76	3.48	3.20	0.12	95.81
4	74.38	12.53	0.17	0.93	0.11	0.10	0.75	3.52	3.20	0.18	95.87
5	76.45	13.01	0.16	0.81	0.12	0.15	0.78	3.46	3.22	0.14	98.31
6	77.62	13.08	0.11	0.94	0.03	0.15	0.70	3.72	3.38	0.16	99.88
7	73.29	12.89	0.16	1.01	0.07	0.08	0.73	3.18	3.31	0.22	94.94
8	75.24	12.80	0.18	0.83	0.07	0.10	0.86	3.57	3.47	0.18	97.31
9	76.51	12.81	0.10	0.87	0.01	0.14	0.70	3.55	3.38	0.10	98.17
10	75.08	12.52	0.12	0.72	0.08	0.08	0.65	3.60	3.50	0.17	96.52

Normalised	SiO2	Al2O3	TiO2	FeO	MnO	MgO	CaO	Na2O	K2O	Cl	TOTAL
1	77.74	13.10	0.18	0.98	0.08	0.13	0.87	3.49	3.27	0.17	100
2	78.35	13.19	0.14	0.94	0.08	0.15	0.61	2.94	3.47	0.14	100
3	77.63	13.28	0.10	0.79	0.16	0.15	0.79	3.63	3.34	0.13	100
4	77.58	13.07	0.18	0.97	0.11	0.10	0.78	3.67	3.34	0.19	100
5	77.76	13.23	0.16	0.82	0.12	0.15	0.79	3.52	3.28	0.14	100
6	77.71	13.10	0.11	0.94	0.03	0.15	0.70	3.72	3.38	0.16	100
7	77.20	13.58	0.17	1.06	0.07	0.08	0.77	3.35	3.49	0.23	100
8	77.32	13.15	0.18	0.85	0.07	0.10	0.88	3.67	3.57	0.18	100
9	77.94	13.05	0.10	0.89	0.01	0.14	0.71	3.62	3.44	0.10	100
10	77.79	12.97	0.12	0.75	0.08	0.08	0.67	3.73	3.63	0.18	100
Mean	77.70	13.17	0.14	0.90	0.08	0.12	0.76	3.53	3.42	0.16	100
St. Deviation	0.32	0.17	0.03	0.10	0.04	0.03	0.08	0.24	0.12	0.04	0

Sample name: M29; **Tephra ID:** Whakatane (Microscope analysis: 1) it contains cummingtonite, 2) it is airfall tephra; **Site(s) associated with the analysis:** 65

Table 68

	SiO2	Al2O3	TiO2	FeO	MnO	MgO	CaO	Na2O	K2O	Cl	TOTAL
1	74.45	12.58	0.13	1.00	0.10	0.12	0.60	3.46	3.39	0.24	96.08
3	73.81	12.81	0.06	0.75	0.07	0.07	0.58	3.34	3.47	0.21	95.18
4	76.88	12.88	0.15	1.09	0.09	0.12	0.75	3.79	3.27	0.15	99.18
5	74.36	12.52	0.10	0.76	0.14	0.14	0.83	3.61	3.23	0.09	95.78
6	76.03	12.68	0.09	0.72	0.07	0.10	0.81	3.64	3.60	0.11	97.85
7	75.79	12.18	0.12	0.78	0.17	0.13	0.69	3.60	3.31	0.15	96.92
8	73.48	12.01	0.14	0.89	0.02	0.11	0.69	3.28	3.39	0.10	94.11
9	76.68	12.61	0.14	0.94	0.08	0.18	0.86	3.58	3.16	0.14	98.36
10	76.53	12.93	0.13	1.01	0.09	0.14	0.92	3.69	3.14	0.15	98.72

Normalised	SiO2	Al2O3	TiO2	FeO	MnO	MgO	CaO	Na2O	K2O	Cl	TOTAL
1	77.49	13.09	0.14	1.04	0.10	0.12	0.62	3.60	3.53	0.25	100
3	77.55	13.46	0.06	0.79	0.07	0.07	0.61	3.51	3.65	0.22	100
4	77.52	12.99	0.15	1.10	0.09	0.12	0.76	3.82	3.30	0.15	100
5	77.64	13.07	0.10	0.79	0.15	0.15	0.87	3.77	3.37	0.09	100
6	77.70	12.96	0.09	0.74	0.07	0.10	0.83	3.72	3.68	0.11	100
7	78.20	12.57	0.12	0.80	0.18	0.13	0.71	3.71	3.42	0.15	100
8	78.08	12.76	0.15	0.95	0.02	0.12	0.73	3.49	3.60	0.11	100
9	77.96	12.82	0.14	0.96	0.08	0.18	0.87	3.64	3.21	0.14	100
10	77.52	13.10	0.13	1.02	0.09	0.14	0.93	3.74	3.18	0.15	100
Mean	77.74	12.98	0.12	0.91	0.10	0.13	0.77	3.67	3.44	0.15	100
St. Deviation	0.27	0.25	0.03	0.13	0.04	0.03	0.11	0.12	0.19	0.05	0

Sample name: M31; **Tephra ID:** Two populations, one Whakatane (reworked) and one Taupo source tephra (reworked); **Site(s) associated with the analysis:** 65

Table 69

	SiO2	Al2O3	TiO2	FeO	MnO	MgO	CaO	Na2O	K2O	Cl	TOTAL
1	73.27	12.86	0.17	1.58	0.12	0.19	1.27	3.19	2.88	0.10	95.63
2	74.82	13.67	0.25	1.76	0.12	0.22	1.42	3.57	2.87	0.16	98.86
3	75.52	13.22	0.33	2.00	0.08	0.27	1.54	3.74	2.59	0.18	99.47
4	76.10	12.55	0.09	0.72	0.09	0.10	0.72	3.97	3.43	0.10	97.86
5	78.02	13.01	0.07	0.86	0.11	0.07	0.65	3.57	3.60	0.18	100.14
6	74.56	13.80	0.19	2.05	0.09	0.22	1.36	3.65	2.84	0.15	98.92
7	74.71	12.53	0.09	0.93	0.12	0.07	0.62	3.29	4.36	0.21	96.92
8	74.67	12.61	0.10	0.79	0.05	0.10	0.65	3.09	4.16	0.20	96.42
9	72.30	13.05	0.32	1.80	0.07	0.22	1.32	3.49	2.72	0.19	95.48
10	74.70	13.84	0.26	1.99	0.13	0.26	1.44	3.76	2.88	0.17	99.43

Normalised	SiO2	Al2O3	TiO2	FeO	MnO	MgO	CaO	Na2O	K2O	Cl	TOTAL
1	76.62	13.45	0.18	1.65	0.13	0.20	1.33	3.34	3.01	0.10	100
2	75.68	13.83	0.25	1.78	0.12	0.22	1.44	3.61	2.90	0.16	100
3	75.92	13.29	0.33	2.01	0.08	0.27	1.55	3.76	2.60	0.18	100
4	77.76	12.82	0.09	0.74	0.09	0.10	0.74	4.06	3.51	0.10	100
5	77.91	12.99	0.07	0.86	0.11	0.07	0.65	3.57	3.59	0.18	100
6	75.37	13.95	0.19	2.07	0.09	0.22	1.37	3.69	2.87	0.15	100
7	77.08	12.93	0.09	0.96	0.12	0.07	0.64	3.39	4.50	0.22	100
8	77.44	13.08	0.10	0.82	0.05	0.10	0.67	3.20	4.31	0.21	100
9	75.72	13.67	0.34	1.89	0.07	0.23	1.38	3.66	2.85	0.20	100
10	75.13	13.92	0.26	2.00	0.13	0.26	1.45	3.78	2.90	0.17	100
Mean	76.47	13.39	0.19	1.48	0.10	0.18	1.12	3.61	3.30	0.17	100
St. Deviation	1.03	0.43	0.10	0.56	0.03	0.08	0.39	0.25	0.66	0.04	0

Sample name: T-1 (Moana); **Tephra ID:** Primary Waiohau; **Site(s) associated with the analysis:** 65

Table 70

	SiO2	Al2O3	TiO2	FeO	MnO	MgO	CaO	Na2O	K2O	Cl	TOTAL
1	75.69	12.31	0.12	0.94	0.20	0.10	0.86	3.43	3.02	0.16	96.82
2	75.26	12.38	0.21	1.01	0.04	0.16	0.89	3.43	3.04	0.21	96.62
3	74.94	12.28	0.17	0.93	0.00	0.11	0.88	3.39	3.05	0.14	95.89
4	76.58	12.13	0.04	0.86	0.07	0.11	0.76	3.47	3.05	0.11	97.18
5	75.14	12.21	0.12	0.76	0.00	0.16	0.70	3.44	2.96	0.15	95.64
6	74.10	12.39	0.08	0.90	0.05	0.17	0.77	3.63	3.07	0.20	95.38
7	74.30	12.37	0.17	0.92	0.03	0.11	0.68	3.42	3.02	0.18	95.21
8	74.34	12.20	0.16	0.83	0.07	0.08	0.83	3.67	3.21	0.15	95.52
9	76.16	12.62	0.10	0.98	0.04	0.19	0.85	3.51	3.17	0.18	97.81
10	76.56	12.26	0.11	0.84	0.09	0.16	0.89	3.42	2.98	0.13	97.44

Normalised	SiO2	Al2O3	TiO2	FeO	MnO	MgO	CaO	Na2O	K2O	Cl	TOTAL
1	78.18	12.71	0.12	0.97	0.21	0.10	0.89	3.54	3.12	0.17	100
2	77.89	12.81	0.22	1.05	0.04	0.17	0.92	3.55	3.15	0.22	100
3	78.15	12.81	0.18	0.97	0.00	0.11	0.92	3.54	3.18	0.15	100
4	78.80	12.48	0.04	0.88	0.07	0.11	0.78	3.57	3.14	0.11	100
5	78.57	12.77	0.13	0.79	0.00	0.17	0.73	3.60	3.09	0.16	100
6	77.69	12.99	0.08	0.94	0.05	0.18	0.81	3.81	3.22	0.21	100
7	78.04	12.99	0.18	0.97	0.03	0.12	0.71	3.59	3.17	0.19	100
8	77.83	12.77	0.17	0.87	0.07	0.08	0.87	3.84	3.36	0.16	100
9	77.87	12.90	0.10	1.00	0.04	0.19	0.87	3.59	3.24	0.18	100
10	78.57	12.58	0.11	0.86	0.09	0.16	0.91	3.51	3.06	0.13	100
Mean	78.16	12.78	0.13	0.93	0.06	0.14	0.84	3.61	3.17	0.17	100
St. Deviation	0.37	0.16	0.05	0.08	0.06	0.04	0.08	0.11	0.09	0.03	0

Sample name: M-I-3; **Tephra ID:** Two populations, one Whakatane (reworked) and one Taupo source tephra (reworked); **Site(s) associated with the analysis:** 64

Table 71

	SiO2	Al2O3	TiO2	FeO	MnO	MgO	CaO	Na2O	K2O	Cl	TOTAL
1	77.24	11.23	0.09	0.83	0.04	0.06	0.60	2.91	3.72	0.14	96.86
2	76.81	11.55	0.16	1.52	0.06	0.10	0.85	3.01	3.19	0.16	97.39
3	74.91	11.54	0.18	1.66	0.16	0.11	1.37	3.28	2.89	0.11	96.19
4	74.20	10.78	0.10	1.10	0.13	0.15	0.86	3.24	3.28	0.16	94.00
5	74.14	10.87	0.12	0.77	0.10	0.12	0.81	2.63	3.62	0.09	93.26
6	75.29	10.86	0.10	0.84	0.04	0.06	0.62	2.90	3.79	0.15	94.64
7	72.53	10.99	0.07	0.87	0.11	0.05	0.60	2.79	3.76	0.19	91.97
8	77.63	11.20	0.15	0.78	0.08	0.10	0.78	2.96	3.27	0.17	97.11
9	76.02	11.83	0.23	1.77	0.15	0.26	1.43	2.90	2.60	0.14	97.32
10	76.01	11.07	0.13	0.98	0.01	0.08	0.64	3.07	3.46	0.13	95.58

Normalised	SiO2	Al2O3	TiO2	FeO	MnO	MgO	CaO	Na2O	K2O	Cl	TOTAL
1	79.74	11.59	0.09	0.86	0.04	0.06	0.62	3.00	3.84	0.14	100
2	78.87	11.86	0.16	1.56	0.06	0.10	0.87	3.09	3.28	0.16	100
3	77.88	12.00	0.19	1.73	0.17	0.11	1.42	3.41	3.00	0.11	100
4	78.94	11.47	0.11	1.17	0.14	0.16	0.91	3.45	3.49	0.17	100
5	79.50	11.66	0.13	0.83	0.11	0.13	0.87	2.82	3.88	0.10	100
6	79.55	11.48	0.11	0.89	0.04	0.06	0.66	3.06	4.00	0.16	100
7	78.86	11.95	0.08	0.95	0.12	0.05	0.65	3.03	4.09	0.21	100
8	79.94	11.53	0.15	0.80	0.08	0.10	0.80	3.05	3.37	0.18	100
9	78.11	12.16	0.24	1.82	0.15	0.27	1.47	2.98	2.67	0.14	100
10	79.53	11.58	0.14	1.03	0.01	0.08	0.67	3.21	3.62	0.14	100
Mean	79.09	11.73	0.14	1.16	0.09	0.11	0.89	3.11	3.52	0.15	100
St. Deviation	0.69	0.24	0.05	0.39	0.05	0.06	0.31	0.19	0.46	0.03	0

WAIOTAHI FAULT

Waiotahi South

Sample name: WTH-3; **Tephra ID:** Rerewhakaaitu; **Site associated with the analysis:** 86

Table 72

	SiO2	Al2O3	TiO2	FeO	MnO	MgO	CaO	Na2O	K2O	Cl	TOTAL
1	75.69	8.04	0.06	0.83	0.07	0.13	0.84	2.34	3.41	0.15	91.57
2	75.01	8.13	0.08	0.97	0.09	0.08	0.59	2.27	3.88	0.15	91.24
3	73.49	7.72	0.09	0.84	0.04	0.07	0.83	2.06	4.43	0.14	89.70
4	72.62	8.00	0.06	0.57	0.13	0.01	0.80	2.07	3.99	0.14	88.37
5	78.07	12.52	0.20	0.84	0.13	0.10	0.71	3.60	3.55	0.12	99.85
6	78.66	11.93	0.15	1.02	0.16	0.15	0.91	3.61	3.23	0.16	99.98
7	75.07	12.16	0.13	0.99	0.10	0.15	0.84	1.96	3.33	0.17	94.89
8	76.06	12.42	0.15	1.15	0.11	0.11	0.87	3.38	3.13	0.13	97.51
9	74.41	12.30	0.19	0.84	0.09	0.07	0.63	3.51	3.59	0.15	95.80
10	75.63	12.35	0.13	0.93	0.04	0.11	0.74	3.80	3.22	0.10	97.04

Normalised	SiO2	Al2O3	TiO2	FeO	MnO	MgO	CaO	Na2O	K2O	Cl	TOTAL
1	82.66	8.78	0.07	0.91	0.08	0.14	0.92	2.56	3.72	0.16	100
2	82.21	8.91	0.09	1.06	0.10	0.09	0.65	2.49	4.25	0.16	100
3	81.93	8.61	0.10	0.94	0.04	0.08	0.93	2.30	4.94	0.16	100
4	82.18	9.05	0.07	0.65	0.15	0.01	0.91	2.34	4.52	0.16	100
5	78.19	12.54	0.20	0.84	0.13	0.10	0.71	3.61	3.56	0.12	100
6	78.68	11.93	0.15	1.02	0.16	0.15	0.91	3.61	3.23	0.16	100
7	79.11	12.81	0.14	1.04	0.11	0.16	0.89	2.07	3.51	0.18	100
8	78.00	12.74	0.15	1.18	0.11	0.11	0.89	3.47	3.21	0.13	100
9	77.67	12.84	0.20	0.88	0.09	0.07	0.66	3.66	3.75	0.16	100
10	77.94	12.73	0.13	0.96	0.04	0.11	0.76	3.92	3.32	0.10	100
Mean	79.86	11.09	0.13	0.95	0.10	0.10	0.82	3.00	3.80	0.15	100
St. Deviation	2.10	1.96	0.05	0.15	0.04	0.04	0.11	0.71	0.58	0.02	0

Waiotahi South

Sample name: Kah-2; **Tephra ID:** Rerewhakaaitu; **Site associated with the analysis:** 88

Table 73

	SiO2	Al2O3	TiO2	FeO	MnO	MgO	CaO	Na2O	K2O	Cl	TOTAL
1	73.37	12.04	0.14	0.95	0.11	0.11	0.89	3.13	3.00	0.15	93.89
2	76.16	12.33	0.14	0.98	0.09	0.16	0.90	3.59	3.29	0.15	97.78
3	76.48	12.31	0.11	0.78	0.15	0.13	0.82	3.63	3.32	0.15	97.87
4	72.97	11.91	0.16	0.71	0.10	0.17	0.92	3.26	3.35	0.17	93.72
5	72.66	12.10	0.14	0.86	0.09	0.14	0.77	3.32	3.38	0.15	93.60
6	73.79	12.32	0.08	0.98	0.04	0.10	0.77	3.40	3.26	0.13	94.89
7	73.33	12.23	0.10	1.01	0.14	0.11	0.75	3.31	3.00	0.17	94.15
8	74.35	11.90	0.16	0.87	0.16	0.12	0.97	3.31	3.17	0.15	95.17
9	75.08	12.36	0.11	0.83	0.05	0.12	0.74	3.56	3.54	0.13	96.52

Normalised	SiO2	Al2O3	TiO2	FeO	MnO	MgO	CaO	Na2O	K2O	Cl	TOTAL
1	78.14	12.82	0.15	1.01	0.12	0.12	0.95	3.33	3.20	0.16	100
2	77.89	12.61	0.14	1.00	0.09	0.16	0.92	3.67	3.36	0.15	100
3	78.14	12.58	0.11	0.80	0.15	0.13	0.84	3.71	3.39	0.15	100
4	77.86	12.71	0.17	0.76	0.11	0.18	0.98	3.48	3.57	0.18	100
5	77.63	12.93	0.15	0.92	0.10	0.15	0.82	3.55	3.61	0.16	100
6	77.76	12.98	0.08	1.03	0.04	0.11	0.81	3.58	3.44	0.14	100
7	77.89	12.99	0.11	1.07	0.15	0.12	0.80	3.52	3.19	0.18	100
8	78.12	12.50	0.17	0.91	0.17	0.13	1.02	3.48	3.33	0.16	100
9	77.79	12.81	0.11	0.86	0.05	0.12	0.77	3.69	3.67	0.13	100
Mean	77.91	12.77	0.13	0.93	0.11	0.14	0.88	3.56	3.42	0.16	100
St. Deviation	0.19	0.18	0.03	0.11	0.04	0.02	0.09	0.12	0.17	0.02	0

Sample name: A4; **Tephra ID:** Waiohau (Microscope analysis: it does not contain cummingtonite); **Site(s) associated with the analysis:** 88

Table 74

	SiO2	Al2O3	TiO2	FeO	MnO	MgO	CaO	Na2O	K2O	Cl	TOTAL
1	74.13	12.14	0.12	1.01	0.11	0.13	0.95	3.52	3.40	0.14	95.65
2	75.74	12.29	0.14	1.18	0.00	0.14	0.96	3.57	3.45	0.15	97.63
3	73.43	12.00	0.14	0.94	0.13	0.18	0.91	3.45	3.34	0.19	94.70
4	76.29	12.35	0.19	1.08	0.04	0.12	0.91	3.53	3.31	0.16	97.98
5	74.97	12.25	0.21	1.02	0.11	0.18	0.87	3.51	3.23	0.15	96.51
6	75.69	12.42	0.13	1.04	0.15	0.14	0.86	3.57	3.31	0.20	97.51
7	74.96	12.36	0.21	1.02	0.08	0.09	0.78	3.48	3.76	0.10	96.83
8	74.92	12.08	0.14	0.98	0.07	0.14	0.90	3.35	3.07	0.19	95.84
9	73.54	12.13	0.16	1.03	0.22	0.14	0.84	3.50	3.16	0.11	94.84
10	73.90	12.22	0.15	1.21	0.10	0.10	0.90	3.42	2.97	0.14	95.12

Normalised	SiO2	Al2O3	TiO2	FeO	MnO	MgO	CaO	Na2O	K2O	Cl	TOTAL
1	77.50	12.69	0.13	1.06	0.12	0.14	0.99	3.68	3.55	0.15	100
2	77.58	12.59	0.14	1.21	0.00	0.14	0.98	3.66	3.53	0.15	100
3	77.54	12.67	0.15	0.99	0.14	0.19	0.96	3.64	3.53	0.20	100
4	77.86	12.60	0.19	1.10	0.04	0.12	0.93	3.60	3.38	0.16	100
5	77.68	12.69	0.22	1.06	0.11	0.19	0.90	3.64	3.35	0.16	100
6	77.62	12.74	0.13	1.07	0.15	0.14	0.88	3.66	3.39	0.21	100
7	77.41	12.76	0.22	1.05	0.08	0.09	0.81	3.59	3.88	0.10	100
8	78.17	12.60	0.15	1.02	0.07	0.15	0.94	3.50	3.20	0.20	100
9	77.54	12.79	0.17	1.09	0.23	0.15	0.89	3.69	3.33	0.12	100
10	77.69	12.85	0.16	1.27	0.11	0.11	0.95	3.60	3.12	0.15	100
Mean	77.66	12.70	0.17	1.09	0.11	0.14	0.92	3.63	3.43	0.16	100
St. Deviation	0.22	0.09	0.03	0.09	0.06	0.03	0.06	0.06	0.21	0.03	0

References

Eden, N.D., Palmer, A.S., Froggatt, P.C., Trustrum, N.A. and Page, M.J., 1993. A multiple-source Holocene tephra sequence from Lake Tutira, Hawke's Bay, New Zealand. New Zealand Journal of Geology and Geophysics, 36, 233-242.

Froggatt, P.C. & Solloway, G.J., 1986. Correlation of Papanetu Tephra to Karapiti Tephra, central North Island, New Zealand. New Zealand Journal of Geology and Geophysics, 29, 303-314.

Lowe, J.D. & Hogg, A.G., 1986. Tephrostratigraphy and chronology of the Kaipo Lagoon, an 11,500 year-old montane peat bog in Urewera National Park, New Zealand. Journal of the Royal Society of New Zealand, 16, 1, 25-41.

Lowe, J.D., 1988. Stratigraphy, age, composition, and correlation of late Quaternary tephras interbedded with organic sediments in Waikato Lakes, North Island, New Zealand. New Zealand Journal of Geology and Geophysics, 31,125-165.

Lowe, J.D., Newnham, M.R. and Ward, M.C., 1999. Stratigraphy and chronology of a 15 Ka sequence of multi-sourced silicic tephras in a montane peat bog, eastern North Island, New Zealand. New Zealand Journal of Geology and Geophysics, 42, 566-579.

Manning, D.A., 1995. Late Pleistocene tephrostratigraphy of the eastern Bay of Plenty, North Island, New Zealand. PhD Thesis, Victoria University of Wellington, New Zealand.

Nairn, I.A., Shane, P.R., Cole, J.W., Leonard, G.J., Self, S. and Pearson, N., 2004. Rhyolite magma process of the AD 1315 Kaharoa eruption episode, Tarawera volcano, New Zealand. Journal of Volcanology and Geothermal Research, 131, 265-294.

Newnham, R.M., Lowe, D.J. and Wigley, G.N.A., 1995. Late Holocene palynology and paleovegetation of tephra-bearing mires at Papamoa and Waihi Beach, western Bay of Plenty, North Island, New Zealand. Journal of the Royal Society of New Zealand, 25, 2, 283-300.

Pillans, B. & Wright, I., 1992. Late Quaternary tephrostratigraphy from the southern Havre Trough-Bay of Plenty, northeast New Zealand. New Zealand Journal of Geology and Geophysics, 35, 129-143.

Shane, P. & Hoverd, J., 2002. Distal record of multi-sourced tephra in Onepoto basin, Auckland, New Zealand: implications for volcanic chronology, frequency and hazards. Bulletin of Volcanology, 64, 441-454.

Wilmhurst, J.M., Eden, D.N. and Froggatt, P.C., 1999. Late Holocene forest disturbance in Gisborne, New Zealand: a comparison of terrestrial and marine pollen records. New Zealand Journal of Botany, 37, 523-540.

APPENDIX IV

GRAVITY DATA

FIELD OBSERVATIONS

Field observations were undertaken by the author and Dick Beetham between 3-10 February 2005 using a LaCoste and Romberg gravimeter (serial number G106). The location and height of each observation was established with a Leica Real-Time Kinematic (RTK) differential GPS system in the post-processing mode using Trig points from New Zealand Geodetic Datum 2000. During the survey 186 new gravity stations were established and tied to the Awakeri base station of the New Zealand Primary Gravity Network (Robertson and Reilly, 1960). To determine instrumental drift, Primary Gravity Network stations were occupied at the beginning and end of each day and when practicable at various times during the day.

Observations were initially made along the roads at 0.2 km spacing. Additional readings were then made on farms. Obtaining permission for access to the farms was arranged by the author and access was generally straightforward along numerous races throughout the farms.

DATA REDUCTION

Data reduction was undertaken at GNS Science using their in-house software. The gravimeter observations were corrected for tidal effects of the Sun and the Moon before solving for the instrument drift and detection of any jumps or tares in the observations. The corrected gravity values have a standard error of about 0.02 mgal. No instrumental tares were detected throughout the entire survey period. Because the survey was tied to the Primary Gravity Network Station in the Bay of Plenty region, the gravity values are completely compatible with the historical data within the gravity anomaly database held by GNS Science.

Corrections for nearby topography (terrain corrections) were determined in the field by visual estimates of the height of the terrain relative to the observation point to Hammer D zone (170 m). Outer terrain corrections (Hammer E-M) were computed in the reduction stage using a 10 m digital terrain model (DTM). The size of these corrections ranged between 0.05 mgal in relatively flat parts of the survey area to 2.9 mgal where the observation was located among steep terrain.

Free-air and Bouguer anomalies were computed using the method described in Reilly (1970, 1972). The free air anomaly G(fa), is calculated using equation 3.2

$$G(fa) = G(obs) - \gamma_h \qquad (3.2)$$

where γ_h is composed of terms containing τ, the geographic latitude and h, the height (in kilometres).

$$\gamma_h = 978049.0 + 5149.34\sin^2\tau + 22.83\sin^4\tau + 0.12\sin^6\tau + h(-308.777 + 0.452\sin^2\tau) + h^2(0.0727 - 0.0002\sin^2\tau)\ gal$$

The Bouguer Anomaly G(ba), is calculated using equation 3.3.

$$G(ba) = G(obs) - \gamma_B \qquad (3.3)$$

Where $\gamma_B = \gamma_h + \beta(h) + \Delta b + c$

The term $\beta(h)$ is the Bouguer correction for a circular slab of a given density, a radius of 21.944 km and with a thickness equal to the height of the station above sea level. Δb is the terrain correction out to Hammer zone M (21.944 km). The term c is a terrain correction out to Hayfords O zone (166.7 km) calculated from the estimate in the average height of each degree square covering the whole of

New Zealand (Reilly 1970). A density of 2.67 Mg/m^3 is used for the Bouguer correction.

ERRORS

Errors in gravity observations can be divided into three categories;

1. Height and location errors.
2. Gravity observations errors.
3. Terrain estimation errors.

In detail:

1. Height and Location Errors

Three different Trig stations were utilized in the survey:

a) Sheet: V15d, Name: Otariki 6891 (E 2842748.11, N 6354103.35, Orthometric Height 4.12m)

b) Sheet: W15d, Name: A4V5 (Ohope) 6981 (E 2872664.32, N 6348963.79 Orthometric Height 16.46m)

c) Sheet: V15d, Name: AFQC (CC 72) (E 2845830.37, N 6349781.76) Orthometric Height 4.5743m)

Observations were made by the Leica SR530 Real Time Kinematics Global Position System equipment. Estimated errors in height and location could be up to 0.5 m, but are typically < 0.2 m.

2. Gravity Observation Errors

Errors in the calculated gravity at each station are a function of the meter dial reading and the time measurement. Time observations were used for calculating instrumental drift and the diurnal gravity variation.

The LaCoste and Romberg gravity meter dial is graduated in divisions that equate to about 0.01 mgal. Repeat measurements at stations never attained this level of accuracy, residuals having a standard deviation of 0.02 mgal. The largest residual was 0.08 mgal.

3. Terrain Estimation.

The calculation of Bouguer and isostatic gravity anomalies requires a correction for topography around the observation site. The method used in this survey is that of Hammer (1939). The area around the station is divided into a number of annular zones and each zone is further subdivided into a number of compartments. The average departure in elevation for each compartment from that of the station is used to calculate the terrain correction.

For each station the terrain out to Hammer zone D was noted in the field. Terrain corrections in Hammer zones E to M were determined from a 10 m digital terrain model (DTM) derived from the 1:50,000 topographic map sheets. All terrain corrections for topography were calculated using the GNS Science computer system (pro-prietary software).

The effect of a topographic feature on any gravity observation is inversely proportional to the distance from the observation point. Thus the largest contributing effect is from nearby valleys and hills. To some degree this is compensated for by the larger compartment size of the outer Hammer zones. However an error in estimate of 100 metres in elevation of a compartment in zone H (radius between 1530 m and 2615 m), say, will result in an error in the terrain correction of 0.01 mgals, whereas an error in elevation estimate of 100 metres in a compartment in zone C (radius between 16.6 m and 53.3 m) will result in an error in the terrain correction of 0.45 mgals. For each annular zone some estimates will be too high and others too low, so errors will tend to cancel.

REGIONAL GRAVITY FIELD

Gravity anomalies represent the departure of the observed gravity field from a standard uniform Earth and represent the effects of lateral changes in subsurface rock density. The gravity anomalies in the broader northern Bay of Plenty area result from the combined effects of the low density volcanic and sedimentary material in the upper crust and density variations in the deeper structure of the Earth. Long wavelength gravity anomalies from deep structure within the Earth produce the regional gravity field. The difference between the observed gravity anomalies and the regional gravity field is interpreted to be the gravity effect of volcanic and sedimentary material in the upper crust.

The regional field can be defined by observations on the basement greywacke rock that crops out at either end of the observations. On a regional scale, Mesozoic greywacke is geologically uniform with little variation in density. Therefore, it is inferred that any observed differences between large outcrops reflect lower crust and mantle variations. For example, Stern (1979) calculated a regional gravity field using a two-way, third-order polynomial to fit the gravity values on outcropping greywacke around the Taupo Rift. For this thesis the residual gravity field is defined by a 2^{nd} order polynomial curve connecting observations on the basement rock that crops out along the survey lines. The regional gravity field is subtracted from the Bouguer anomaly for each observation to derive residual gravity values.

RESIDUAL GRAVITY ANOMALIES

The Taupo Rift is a region of negative residual gravity that reflects the down-faulting of basement greywacke and infill with lower density volcanic rock. Residual gravity anomalies along the survey lines are up to -40 mgal. These lower gravity values are interpreted to result from thick layers of low density volcanic rocks infilling calderas and/or structural depressions formed by downfaulting on the eastern margin of the Taupo Rift.

GRAVITY MODELS

Simple two-dimensional gravity models can be used to estimate the size of buried structures. For example, Stagpoole (1994) used two-dimensional gravity models to delineate the extent of faulting along the eastern margin of the Taupo Rift. Similar models are used here to provide constraints for geological interpretations of the northern Bay of Plenty region.

Gravity modelling was undertaken using commercially available two-dimensional potential field modelling software (ModelVision Pro from ENCOM - www.encom.com.au/). Gravity anomaly data along lines were projected onto the vertical planar profile for modelling. The rock densities used in models were taken from previous studies of the TVZ (Modriniak and Studt, 1959; Hochstein and Hunt, 1970; Rogan, 1982; Stern 1982; Stagpoole, 1994). These were 2.670 kg/m^3 for basement density, 2.1 kg/m^3 and 2.3 kg/m^3 for volcanic infill (representing near-surface and deeper volcanic material, respectively) and 1.8 kg/m^3 for thin surface layer of Holocene pumice. The topography along each profile was obtained from the elevations recorded at each gravity observation site.

The models are two-dimensional in nature and have no lateral (out of section) variations in shape or density of volcanics or basement. Modelling proceeded by interactively altering the shape of bodies, representing volcanic rocks, to obtain an acceptable fit between the observed gravity anomaly and the gravity anomalies calculated for the model. Although the models do not give unique answers, they fit with the structural and density constraints provided.

Model of Northern Line

The gravity model for the east-west oriented line that crosses the eastern margin of the gravity low formed by the Taupo Rift and extends parallel to the coastline and across the Whakatane, Waimana and Waiotahi faults, is shown in Figure 4a of Chapter 6. Within the Taupo Rift and, in particular, on the hangingwall of the Edgecumbe Fault, basement is modelled at a depth of about 2800 m below sea level. Further east, on the hangingwall of Whakatane, Waimana and Waiotahi faults the basement is modelled at depths of about 600, 1000 and 500 m below sea level, respectively. The depth of the basement across the Edgecumbe Fault appears to be in good agreement with a seismic-reflection line across the Rangitaiki Plain from Nicol et al. (unpublished data) that indicate resistive rocks (basement) at c. 3000 m depth. Gravity modelling predicts that basement is down-thrown to the west by c. 2200 m across the Edgecumbe Fault, while the throw on the faults decreases eastwards with c 660, 500 and 300 m of vertical separation across the Whakatane, Waimana and Waiotahi faults, respectively. Note, however, that in this transect, the Waimana Fault is modelled to have two strands. The throw on the westermost strand appears to be nearly zero (and this is in agreement with geological observations that indicate that the fault here is mainly strike-slip; chapters 2 & 4) whereas the throw on the eastern strand, which is located c. 4 km to the east of the western 'strike-slip' strand and c. 1 km west of the Waiotahi Fault, is modeled to be c. 500 m. The fault-dip on the faults in the NIFS ranges between 60-70° and decreases westwards towards the Taupo Rift. The dip of the Edgecumbe Fault is c. 60±5°.

Model of Southern Line

The gravity model for the east-west oriented line that crosses the Waiohau, Whakatane, and Waimana faults in the NIFS is shown in Figure 4b of Chapter 6. The line runs 20 km south of, and parallel to, the Bay of Plenty coast. The basement on the hangingwalls of the Waiohau, Whakatane and Waimana faults is modelled at depths of about 800, 700 and 600 m below sea level, respectively. Gravity modelling predicts that basement is down-thrown to the west across the Waiohau Fault by c. 700 m while the throw on the Whakatane Fault is modelled to be c. 500 m (down to the west). The fault-dip on the Waiohau Fault is modelled at 65±5° W while for the Whakatane Fault at 70±5° W. The throw on the Waimana Fault appears to be nearly zero. This is in agreement with geological data (chapters 2 & 4) which indicate that the fault here is principally strike-slip with a steep (> 80°) dip. The gravity low modelled immediately southwest of Nukuhou North, Waimana

Valley, is inferred to be associated with a pre-existing topography on the basement greywacke which has been subsequently modified by drainage (inferred to be the ancient Waimana River) and is not thought to result from tectonic faulting.

Uncertainties in gravity models

The uncertainties of the gravity interpretation are related to the accuracy of the gravity observations, the non-uniqueness of gravity interpretation, the uncertainty in the shape of the regional gravity field and uncertainties regarding the rock densities used in models. In addition, the assumption that the structures represented in the models are two dimensional (or 2.5-D) limits the exactness of the interpretation.

The estimated accuracy of the gravity anomaly data from the survey is 0.02 mgal. Although they contribute to the uncertainly in the model interpretation, the effect of these errors is not considered significant, because they are appreciably less than the uncertainty in the regional gravity field and the resulting residual gravity anomalies.

Gravity models are non-unique because there is an infinite number of models that may fit the data. Several small features with a high density contrast can have the same gravity effect as a single large structure with a smaller density contrast. Modelling used simple shapes that fit the constraints imposed by all available geological/geophysical data. More complex models cannot be justified without further constraints. It is also assumed that the gravity anomalies are due to low density sediments overlying a uniformly dense basement. This assumption is reasonable from our geological knowledge of the area, but other models using lateral variations in the basement density could affect the interpretation. Large variations in basement density are, however, considered unlikely (Hatherton and Leopard, 1964).

The validity of the regional gravity field adopted for modelling, and errors in the choice of the densities of the volcanics and sediments and basement rocks used in models, affect the overall interpretation in a relatively smooth way so that the general shape of the model is not affected. The regional gravity field is well constrained from gravity measurements on each side of the survey lines. In my models I apply a 2 order polynomial trend to fit anomalies observed on basement outcrops. It is estimated that the uncertainty in the regional gravity field is up to 5 mgal in the centre of the lines, but is less than 2 mgal close to the ends where basement outcrops. The densities of the Quaternary/Tertiary sediments and basement rocks used in the models are consistent with previous studies (Williams, 1979; Vergara,1987; Woodward-Clyde, 1998) and published data for New Zealand rocks (Whiteford and Lumb, 1975).

The observed gravity value along a profile is also influenced by the density of the geological bodies in the volume out of the section, and thus 2D modelling might not always succeed to present a realistic geological model. Nevertheless, the uncertainties related to the use of simple two-dimensional structures in the models are probably small because of the uniform elongate shape of the Matahina, Taneatua and Waimana basins.

References

Hammer, S., 1939.Terrain Corrections for Gravimeter Stations. Geophysics, 4, 184-194.

Hatherton, T. & Leopard, A. E., 1964. The densities of New Zealand rocks. New Zealand Journal of Geology and Geophysics, 7, 605-614.

Hochstein, M. P. & Hunt, T. M., 1970. Seismic, gravity, and magnetic studies, Broadlands Geothermal Field, New Zealand. Geothermics Special Issue, 2, 333-346.

Modriniak, N. & Studt, F. E., 1959. Geological structure and volcanism of the Taupo-Tarawera district. New Zealand Journal of Geology and Geophysics, 2, 654-684.

Reilly W. I., 1970. Topographic-isostatic Gravity Corrections for New Zealand. New Zealand Department of Scientific and Industrial Research, Bulletin, 203.

Reilly W. I., 1972. New Zealand Gravity Map Series. New Zealand Journal of Geology and Geophysics, 15, 3-15.

Robertson, E.I. & Reilly, W.I., 1960. The New Zealand primary gravity network. New Zealand Journal of Geology and Geophysics, 3, 41-68.

Rogan, M., 1982. A geophysical study of the Taupo Volcanic Zone, New Zealand. Journal of Geophysical Research, 87, B5, 4073-4088.

Stagpoole, V. M., 1994. Interpretation of refraction seismic and gravity data across the eastern margin of the Taupo Volcanic Zone, New Zealand. Geothermics, 23, 501-510.

Stern, T.A., 1979. Regional and residual gravity fields, Central North Island, New Zealand. New Zealand Journal of Geology and Geophysics, 22, 479-485.

Stern T. A., 1982. Seismic and Gravity Investigations of the Central Volcanic Region, North Island, New Zealand. PhD thesis, Victoria University of Wellington, New Zealand.

Vergara, M.C.,1987. Gravity studies of the Whakatane graben in the Bay of Plenty, North Island, New Zealand. MSc thesis, Victoria University of Wellington, New Zealand.

Whiteford, C. M. & Lumb, J. T. 1975. A catalogue of physical properties of rocks. Department of Scientific and Industrial Research, Geophysics, New Zealand, Division Reports, 106 & 107.

Williams, L.R., 1979. A geophysical study of the Mangamako damsite area, junction of the Galatea and Waiohau basins, Eastern Bay of Plenty. BSc (Hons) thesis, University Auckland, New Zealand.

Woodward-Clyde, 1998. Matahina Dam strengthening project. Geological completion report to Electricity Corporation of New Zealand.

Table IV-1: Summary of the gravity point acquired during this survey.
SHEET: 1:250,00 Rotorua; STATION: station No.; X & Y: NZMG Coordinates E and N in NZMG; HEIGHT in meters above mean sea level; HEIGHT_CODE: type of height measurement (0 = benchmark, 1 = spot/trig, 2 = barometer; GRAVITY Absolute gravity minus 975000 in uN/kg; DATE yy mm dd (490000 = no date recorded); TERRAIN inner Hammer zones and outer Hammer zones up to zone M (22.6 km); C= a code column (used for computation); Topo_Corr = total topographic correction (includes topography beyond Hammer zone M); FAA= Free Air Anomaly; BA= Bouguer Anomaly / a density of 2.67 Mg/m^3 is used for the Bouguer correction; ISA= Isostatic Anomaly;OBS Observer code; AUTH Authority code (i.e. institution that made the observations); HT_Dif = height variation

between the recorded station height and the elevation on the NZ 10 m DTM (used to detect blunders).

Sheet	Station	X	Y	Height	Height_type	Gravity	Instrument	Date	Inner_Ter	Outer_Ter		Topo_Corr	FAA	BA	ISA	Obs	Auth	HT_dif
60	1001	2851065	6348881	7.7	0	50436	106	50203	0.4	3.9	8	-5.4	420.3	421.4	360	82	2	-5.3
60	1002	2853200	6354011	2.4	0	50172.7	106	50203	0.4	0.4	8	-4.6	181.8	184.5	90.1	82	2	2.4
60	1003	2853160	6354019	2.2	0	50170.2	106	50203	0.8	0.4	8	-4.6	178.7	182.1	87.6	82	2	2.2
60	1004	2853106	6354033	2.4	0	50166.6	106	50203	1.2	0.4	8	-4.6	175.8	179.3	84.9	82	2	2.4
60	1005	2852962	6354070	2.4	0	50157.6	106	50203	0.7	0.4	8	-4.6	167	170.1	75.8	82	2	2.4
60	1006	2852865	6354096	2.4	0	50151.3	106	50203	0.7	0.4	8	-4.6	160.9	164	69.7	82	2	2.4
60	1007	2852765	6354121	2.3	0	50146.3	106	50203	0.7	0.4	8	-4.6	155.8	159	64.7	82	2	2.3
60	1008	2852665	6354149	2.2	0	50140.9	106	50203	0.8	0.4	8	-4.6	150.2	153.6	59.4	82	2	2.2
60	1009	2852561	6354177	2.2	0	50136.1	106	50203	0.4	0.4	8	-4.6	145.7	148.6	54.4	82	2	2.2
60	1010	2852375	6354226	2.6	0	50127	106	50203	0.4	0.4	8	-4.6	138.2	140.7	46.5	82	2	2.6
60	1011	2852192	6354276	2.3	0	50120.5	106	50203	0.7	0.4	8	-4.6	131	134.2	40.1	82	2	2.3
60	1012	2851987	6354332	2.3	0	50113.1	106	50203	0.8	0.4	8	-4.5	123.9	127	33	82	2	2.3
60	1013	2851793	6354381	2.2	0	50107	106	50203	0.9	0.4	8	-4.5	117.9	121.3	27.3	82	2	2.2
60	1014	2851329	6354506	2.1	0	50096.1	106	50203	1	0.4	8	-4.7	107.5	111.2	17.3	82	2	2.1
60	1015	2851006	6354594	2.2	0	50092.1	106	50203	1	0.4	8	-4.7	104.4	108	14.4	82	2	2.2
60	1016	2850268	6355302	1.7	0	50088.9	106	50203	0.2	0.4	8	-4.6	105	108.2	12	82	2	-2.3
60	1017	2849927	6355699	2.5	0	50089.9	106	50203	0.7	0.3	8	-4.7	111.5	114.4	16.5	82	2	-5.5
60	1018	2848997	6356052	3	0	50092	106	50203	0.2	0.4	8	-4.7	117.6	119.5	21.5	82	2	-9
60	1019	2848897	6356050	2.5	0	50111.3	106	50203	0.1	0.4	8	-4.9	135.3	137.8	39.8	82	2	-9.5
60	1020	2853248	6353990	2.1	0	50176.7	106	50204	0.5	0.4	8	-4.6	184.7	187.9	93.5	82	2	2.1
60	1021	2853314	6353972	2.3	0	50181.6	106	50204	0.5	0.4	8	-4.6	190.1	193	98.6	82	2	2.3
60	1022	2853404	6353950	2.5	0	50188.1	106	50204	0.8	0.4	8	-4.6	197.1	200.1	105.7	82	2	2.5
60	1023	2853505	6353924	2.2	0	50206.7	106	50204	0.8	0.4	8	-4.6	214.6	217.9	123.4	82	2	2.2
60	1024	2853614	6353895	2.2	0	50206.1	106	50204	0.8	0.4	8	-4.6	213.8	217.2	122.6	82	2	2.2
60	1025	2853854	6353832	2.5	0	50228.6	106	50204	0.5	0.4	8	-4.6	236.8	239.5	144.9	82	2	2.5
60	1026	2854029	6353783	2.2	0	50244.8	106	50204	0.5	0.4	8	-4.7	251.8	254.9	160.3	82	2	2.2
60	1027	2854243	6353725	2.3	0	50264.8	106	50204	0.5	0.4	8	-4.7	271.7	274.6	180	82	2	2.3
60	1028	2854684	6353606	2.1	0	50299.1	106	50204	0.5	0.4	8	-4.6	304.6	307.8	213.1	82	2	2.1
60	1029	2855175	6353479	3	0	50315.5	106	50204	0.5	0.4	8	-4.6	322.9	325.1	230.3	82	2	3
60	1030	2855669	6353350	2.6	0	50325.9	106	50204	1	0.4	8	-4.6	331.2	334.4	239.4	82	2	2.6

Sheet	Station	X	Y	Height	Height type	Gravity	Instrument	Date	Inner_Ter	Outer_Ter	C	Topo_Corr	FAA	BA	ISA	Obs	Auth	HT_dif
60	1031	2856457	6353173	2.7	0	50331.8	106	50204	0.3	0.5	8	-4.7	336.3	338.8	242.7	82	2	2.7
60	1032	2856844	6352926	2.6	0	50334.4	106	50204	1	0.5	8	-4.7	336.8	340.1	244.8	82	2	2.6
60	1033	2857056	6352623	1.5	0	50339.8	106	50204	0	0.6	8	-4.8	336.5	340.1	246.3	82	2	1.5
60	1034	2857353	6352337	1.9	0	50343.7	106	50204	0.3	0.6	8	-4.8	339.5	343.1	250.5	82	2	1.9
60	1035	2857692	6351994	2.5	0	50346.3	106	50204	0.1	0.7	8	-4.9	341.4	344.3	253.1	82	2	2.5
60	1036	2858200	6351539	3.3	0	50354.8	106	50204	0.9	0.9	8	-4.9	348.9	351.9	262.7	82	2	3.3
60	1037	2858264	6350778	4.5	0	50372.7	106	50204	0	1.1	8	-4.9	364.5	365.6	281.2	82	2	4.5
60	1038	2858346	6350768	4.5	0	50372.5	106	50204	0	1.1	8	-4.9	364.3	365.4	280.9	82	2	4.5
60	1039	2858546	6350705	4.8	0	50374.7	106	50204	0.1	1.3	8	-4.9	367	367.9	283.5	82	2	4.8
60	1040	2858763	6350661	3.7	0	50382.1	106	50204	0	1.4	8	-5	370.7	373	288.5	82	2	3.7
60	1041	2859043	6350621	3.1	0	50390	106	50204	0.1	1.7	8	-5	376.5	379.8	295.1	82	2	3.1
60	1042	2859380	6350533	4.7	0	50399.7	106	50204	0.8	2.1	8	-5	390.6	393.3	308.1	82	2	1.7
60	1043	2859623	6350452	5	0	50410.6	106	50204	0	2.8	8	-5	401.9	404.1	319.1	82	2	3
60	1044	2859791	6350295	5.7	0	50423.2	106	50204	0.6	3.5	8	-5	415.5	418.2	333.9	82	2	1.7
60	1045	2859954	6350221	3.5	0	50442	106	50204	0	4.4	8	-5	427	432.5	348.4	82	2	-1.5
60	1046	2860044	6350166	3.9	0	50450.3	106	50204	0	5.4	8	-5	436.1	442.2	358.2	82	2	-0.1
60	1047	2860138	6350110	4.3	0	50461.2	106	50204	0.1	6.5	8	-5	447.8	454.7	370.9	82	2	-1.7
60	1048	2860271	6350137	7.7	0	50464.1	106	50205	0.3	9.7	8	-5	461.5	467.9	383.8	82	2	1.7
60	1049	2860342	6350141	9.6	0	50459.4	106	50205	5.8	11.9	8	-5	462.7	474.7	390.4	82	2	1.6
60	2001	2861979	6352018	91.1	0	50304.5	106	50205	0.6	3.6	8	-4.3	574.6	482	383.1	82	2	-3.9
60	2002	2863024	6351613	101.9	0	50281.2	106	50205	0.1	4.1	8	-4.3	581.9	477.3	379.4	82	2	-4.1
60	2003	2864601	6351976	4.3	0	50458	106	50205	1.1	5.3	8	-4.8	460.9	467.3	365.6	82	2	0.3
60	2004	2866531	6350963	4.3	0	50386.7	106	50205	0.1	2.3	8	-5	382.3	384.9	286.9	82	2	-1.7
60	2005	2867587	6350577	8.2	0	50357.6	106	50205	0.2	1.8	8	-5	362.6	360.5	263	82	2	2.2
60	2006	2868105	6350539	4.8	0	50354.6	106	50205	0.5	1	8	-5	349	350.2	252.7	82	2	2.8
60	2007	2869826	6349971	6.1	0	50271.4	106	50205	0	0.6	8	-5.1	265.9	264.7	168.7	82	2	6.1
60	2008	2870291	6349871	7	0	50247	106	50205	0.3	0.6	8	-4.5	243.7	241.3	146	82	2	7
60	2009	2870809	6349735	6.3	0	50223.8	106	50205	0.6	1.1	8	-4.6	217.4	216.7	121.7	82	2	-9.7
60	2010	2870904	6349571	6.1	0	50224.7	106	50205	0	0.7	8	-4.2	216.5	214.6	121	82	2	-2.9

Sheet	Station	X	Y	Height	Height type	Gravity	Instrument	Date	Inner _Ter	Outer_Ter	C	Topo_Corr	FAA	BA	ISA	Obs	Aut h	HT_dif
60	2011	2871420	6349424	4.9	0	50207	106	50205	0	0.6	8	-4.2	193.8	193.2	100	82	2	4.9
60	2012	2871606	6349375	5.4	0	50200	106	50205	0.1	0.6	8	-4.2	187.8	186.7	93.7	82	2	5.4
60	2013	2871783	6349361	6.6	0	50193	106	50205	0.1	0.5	8	-4.2	184.6	182.1	89	82	2	6.6
60	2014	2871985	6349354	7.2	0	50184	106	50205	0.4	0.5	8	-4.3	178.2	175.4	82.1	82	2	7.2
60	2015	2872188	6349293	6.5	0	50186	106	50205	0.1	0.5	8	-4.3	177.3	175	82	82	2	6.5
60	2016	2872360	6349121	4.1	0	50192	106	50205	0.5	0.5	8	-4.3	174.6	175.3	83.3	82	2	4.1
60	2017	2872469	6348991	4.2	0	50195	106	50205	0.2	0.5	8	-4.3	176.9	177.2	85.9	82	2	4.2
60	2018	2872620	6348837	2.7	0	50194	106	50205	0	0.6	8	-4.2	170.2	171.9	81.6	82	2	2.7
60	2019	2872752	6348704	3.7	0	50192	106	50205	0	0.6	8	-4.2	170.1	170.7	81.2	82	2	3.7
60	2020	2873014	6348616	3.2	0	50190	106	50205	0.2	0.6	8	-4.2	166.2	167.6	78.4	82	2	3.2
60	2021	2873259	6348548	4.3	0	50187	106	50205	0	0.6	8	-4.2	165.8	165.9	76.9	82	2	4.3
60	2022	2873517	6348510	4.6	0	50184	106	50205	0.2	0.6	8	-4.2	163.8	163.8	74.8	82	2	4.6
60	2023	2873762	6348515	2.3	0	50186	106	50205	0.1	0.6	8	-4.3	158.3	160.7	71.6	82	2	2.3
60	2024	2874032	6348507	2.2	0	50182	106	50205	0	0.6	8	-4.3	154.4	156.8	67.5	82	2	2.2
60	2025	2875224	6348589	2.5	0	50189	106	50206	0.1	1.1	8	-4.3	163.9	166.6	76.1	82	2	2.5
60	2026	2875423	6348635	4.5	0	50196	106	50206	0.1	1.5	8	-4.3	177	177.9	87	82	2	3.5
60	2027	2876623	6348390	10.1	0	50232	106	50206	1.7	4.3	8	-4.1	228.6	227.5	138.3	82	2	-3.9
60	2028	2876800	6348517	4.9	0	50249	106	50206	0.3	3.4	8	-4.2	231.1	233.5	143.4	82	2	-0.1
60	2029	2876993	6348502	5	0	50255	106	50206	0.5	3	8	-4.2	236.9	239	148.9	82	2	1
60	2030	2877240	6348469	7.9	0	50256	106	50206	4	2.7	8	-4.2	247.4	249.5	159.5	82	2	2.9
60	2031	2877523	6348355	12.5	0	50246	106	50206	6.1	1.8	8	-4.2	250.8	249	159.6	82	2	-3.5
60	2032	2877641	6348487	2.6	0	50267	106	50206	0	1.4	8	-4.2	241.8	244.5	154.2	82	2	2.6
60	2033	2877848	6348457	2.5	0	50268	106	50206	0	1.1	8	-4.2	241.9	244.4	154.1	82	2	2.5
60	2034	2878071	6348430	2.3	0	50269	106	50206	0	0.9	8	-4.2	242.5	245.2	155	82	2	2.3
60	2035	2878735	6347597	3.1	0	50247	106	50206	2.5	1.6	8	-4.2	216.8	221.7	136.8	82	2	-7.9
60	2036	2878926	6347740	3.2	0	50241	106	50206	0.2	1.4	8	-4.1	212.4	214.5	128.7	82	2	-10.8
60	2037	2879196	6347878	2.8	0	50229	106	50206	4.2	1.4	8	-3.2	199.9	205.6	119.4	82	2	-11.2
60	2038	2879664	6348166	5.8	0	50203	106	50206	2.8	2.3	8	-3.2	185.8	187.6	99.4	82	2	-7.2
60	2039	2880206	6348175	5.7	0	50193	106	50206	9.4	2.4	8	-3.2	175.7	184.3	95.8	82	2	-8.3
60	2040	2881210	6348064	10.4	0	50166	106	50206	1.3	2.1	8	-3.2	163.1	158.2	70.1	82	2	3.4

Sheet	Station	X	Y	Height	Height type	Gravity	Instrument	Date	Inner_Ter	Outer_Ter	C	Topo_Corr	FAA	BA	ISA	Obs	Auth	HT_dif
60	2041	2882088	6347998	7.3	0	50152	106	50206	2.6	1.8	8	-3.6	139.2	139	51.1	82	2	-9.7
60	2042	2876879	6333576	45.1	0	50089	106	50206	13.7	22.6	8	-6.1	77.2	69.5	72.7	82	2	-0.9
60	2043	2876717	6333709	35.3	0	50110	106	50206	1.2	22.7	8	-6.2	69	59.9	62.4	82	2	-4.7
60	2044	2876669	6333714	34.3	0	50111	106	50206	0.7	22.8	8	-6.2	66.5	58.1	60.7	82	2	-7.7
60	2045	2876610	6333734	37.2	0	50108	106	50206	3.7	22.6	8	-6.2	73.2	64.3	66.8	82	2	-9.8
60	2046	2875850	6333734	180	0	49728	106	50206	3.8	20.9	8	-4.5	133.5	-36.6	-34.4	82	2	-38
60	2047	2873566	6333023	70.2	0	50080	106	50207	7.5	10.9	8	-5.6	140.4	86.4	94	82	2	-7.8
60	2048	2873223	6333078	64.7	0	50091	106	50207	4.3	9.4	8	-5.7	134.3	81.8	89.1	82	2	1.7
60	2049	2872955	6333052	57.7	0	50107	106	50207	1.2	8.1	8	-5.7	128.6	79.5	87.3	82	2	0.7
60	2050	2872731	6332960	58.2	0	50098	106	50207	8.2	6.9	8	-5.7	120	76.3	84.7	82	2	-0.8
60	2051	2872412	6332896	35.7	0	50123	106	50207	0.1	6.9	8	-5.9	75	48.3	57.3	82	2	-3.3
60	2052	2872248	6332980	34.3	0	50114	106	50207	1.8	6.3	8	-5.9	62.6	38.5	47.1	82	2	-4.7
60	2053	2872147	6333180	30.7	0	50109	106	50207	0.1	6	8	-5.9	48	25.9	33.3	82	2	-6.3
60	2054	2871719	6333245	37.4	0	50077	106	50207	1.2	5.1	8	-5.8	36.9	7.5	14.1	82	2	-1.6
60	2055	2871646	6333173	35.7	0	50077	106	50207	0.4	5.1	8	-5.9	31.2	2.8	9.9	82	2	-3.3
60	2056	2871452	6332993	31.6	0	50084	106	50207	0.1	5.2	8	-5.9	23.8	-0.1	8.1	82	2	-4.4
60	2057	2871282	6332835	35.1	0	50075	106	50207	0.1	5.3	8	-5.9	24.4	-3.3	5.8	82	2	1.1
60	2058	2871057	6332780	34.3	0	50082	106	50207	0.1	5.2	8	-5.9	28.7	1.8	11.4	82	2	1.3
60	2059	2870839	6332769	31.9	0	50091	106	50207	0.8	5	8	-5.9	30.2	6.5	16.3	82	2	-2.1
60	2060	2870290	6332735	36.2	0	50095	106	50207	0	4.7	8	-5.9	46.7	17	27.3	82	2	-2.8
60	2061	2869726	6332776	58.2	0	50060	106	50207	2.4	3.9	8	-5.7	79.4	26.8	36.8	82	2	-2.8
60	2062	2868870	6332643	46.8	0	50112	106	50207	1.4	3.7	8	-5.8	94.9	53.8	65	82	2	-10.2
60	2063	2867946	6332930	41.7	0	50157	106	50207	0.5	4.9	8	-5.9	126.5	91.4	101.4	82	2	5.7
60	2064	2866372	6333569	41.9	0	50235	106	50207	0.8	9.1	8	-6.7	209.6	179.7	187.2	82	2	3.9
60	2065	2865109	6333631	30.3	0	50323	106	50207	1.2	8.6	8	-6.7	261.3	244	252.7	82	2	-3.7
60	2066	2864683	6334201	28.1	0	50334	106	50207	0	13.6	8	-6.5	270.4	259.2	264.9	82	2	12.1
60	2110	2871263	6349470	5.5	0	50212	106	50205	0	0.6	8	-4.2	200.9	199.7	106.4	82	2	0.5
60	2146	2876636	6333838	37.3	0	50107	106	50207	8	22.7	8	-6.1	72.8	68.1	70	82	2	-3.7
60	2147	2873843	6332639	81.9	0	50040	106	50207	0.7	10.6	8	-5.6	133.2	59.2	68.8	82	2	1.9

Sheet	Station	X	Y	Height	Height type	Gravity	Instrument	Date	Inner_Ter	Outer_Ter	C	Topo_Corr	FAA	BA	ISA	Obs	Auth	HT_dif
60	3001	2863314	6334755	96	0	50232	106	50208	1.7	7.8	8	-5.6	381.6	290.2	293.7	82	2	0
60	3002	2863010	6334929	72.9	0	50235	106	50208	1.8	6.9	8	-5.8	314.7	248.3	251.1	82	2	1.9
60	3003	2862835	6334886	51.7	0	50259	106	50208	9.9	7.3	8	-6	272.4	238.2	241.5	82	2	1.7
60	3004	2862671	6334733	32.8	0	50288	106	50208	0.4	7.5	8	-6.3	242.5	220.2	224.5	82	2	-4.2
60	3005	2862503	6334691	26.8	0	50285	106	50208	0.4	7.4	8	-6.3	220.4	204.8	209.4	82	2	0.8
60	3006	2862370	6334698	23.6	0	50280	106	50208	0	7.1	8	-6.3	205.3	192.5	197.2	82	2	4.6
60	3007	2862229	6334698	22.8	0	50272	106	50208	0	6.4	8	-6.3	195.3	182.6	187.5	82	2	5.8
60	3008	2862100	6334698	23.2	0	50264	106	50208	0	5.8	8	-7	188.2	175.2	179.4	82	2	6.2
60	3009	2861987	6334699	22.4	0	50257	106	50208	0	5.3	8	-7	178.9	166.3	170.6	82	2	4.4
60	3010	2861896	6334699	22.4	0	50253	106	50208	0	4.9	8	-7.1	174.2	161.2	165.9	82	2	2.4
60	3011	2861776	6334702	23.6	0	50247	106	50208	0	4.5	8	-7.2	172.6	158.2	162.6	82	2	2.6
60	3012	2861681	6334692	23.1	0	50245	106	50208	0	4.3	8	-7.2	168.8	154.7	159.2	82	2	1.1
60	3013	2860751	6334675	26.6	0	50229	106	50209	0	3.5	8	-6.9	163.3	144.2	149.6	82	2	8.6
60	3014	2859924	6334801	29.4	0	50226	106	50209	0.7	3.2	8	-7	169.7	147.9	153.8	82	2	10.4
60	3015	2856339	6334787	26.7	0	50329	106	50208	7.8	8	8	-8.7	263.1	257.9	266.8	82	2	-8.3
60	3016	2855446	6334872	41	0	50294	106	50208	0.8	5.9	8	-8.5	272.2	241.8	250.7	82	2	-3
60	3017	2852964	6334839	95.9	0	50212	106	50208	0.9	5.5	8	-7.6	358	265.6	278.1	82	2	1.9
60	3018	2848627	6356406	4.3	0	50097	106	50209	0	0.4	8	-4.9	129.5	129.9	30.6	82	2	-9.7
60	3019	2847514	6356648	3	0	50109	106	50209	0	0.4	8	-4.9	138.3	140.3	41.9	82	2	-12
60	3020	2847091	6356939	3	0	50111	106	50209	0	0.4	8	-4.8	143	144.9	45.8	82	2	-11
60	3021	2846945	6357040	3	0	50112	106	50209	0.1	0.4	8	-4.8	144.7	146.7	47.3	82	2	-11
60	3022	2846752	6357173	3	0	50113	106	50209	0.1	0.5	8	-4.8	146.8	148.8	48.8	82	2	-11
60	3023	2846632	6357258	3	0	50114	106	50209	0	0.5	8	-4.8	148.4	150.4	50.1	82	2	-10
60	3024	2846526	6357331	3	0	50115	106	50209	0.1	0.5	8	-4.7	150.2	152.1	50.1	82	2	-10
60	3025	2846359	6357448	3	0	50118	106	50209	0	0.5	8	-4.7	153.3	155.2	52.8	82	2	-9
60	3026	2845948	6357742	3	0	50121	106	50209	0.1	0.5	8	-4.7	158.4	160.4	57.4	82	2	-7
60	3027	2845516	6358051	3	0	50125	106	50209	0.1	0.6	8	-4.7	165.5	167.6	63.8	82	2	-4
60	3028	2845090	6358829	3	0	50134	106	50209	0.1	0.6	8	-4.5	179.8	181.7	74.7	82	2	-2
60	3029	2844480	6358978	3	0	50150	106	50209	0.4	0.8	8	-4.5	197.1	199.4	92.7	82	2	2

Sheet	Station	X	Y	Height	Height type	Gravity	Instrum ent	Date	Inner_Ter	Outer_ Ter	C	Topo_Co rr	FAA	BA	ISA	Obs	Auth	HT_dif
60	3030	2843588	6359720	3	0	50192	106	50209	0	1	8	-4.5	244.6	246.7	137.8	82	2	3
60	3031	2842691	6359902	3.1	0	50236	106	50209	0.3	1.4	8	-4.6	289.7	292.5	184.8	82	2	3.1
60	3032	2840800	6360064	14.2	0	50330	106	50209	2.2	12.6	8	-4.6	418.5	422.2	318.2	82	2	11.2
60	3033	2847936	6336037	272.5	0	49918	106	50210	1.7	6.5	8	-5.9	617.6	330.5	344.1	82	2	11.5
60	3034	2846630	6336121	265.8	0	49946	106	50210	0.5	6.2	8	-6.1	624.3	343.3	358.5	82	2	8.8
60	3035	2846473	6336406	250.9	0	49970	106	50210	1.5	6.9	8	-6.3	604.7	341.9	355.9	82	2	-8.1
60	3036	2845842	6336426	206.3	0	50036	106	50210	0.8	9.9	8	-6.8	532.7	321.8	336.8	82	2	3.3
60	3037	2845670	6336279	204.1	0	50033	106	50210	0.3	10.9	8	-6.8	522.7	314.8	330.8	82	2	6.1
60	3038	2845508	6336165	181.5	0	50068	106	50210	1.2	12.1	8	-7.1	486.9	306.3	323.3	82	2	3.5
60	3039	2845347	6336065	153.1	0	50115	106	50210	1.2	13.3	8	-7.4	445.3	297.5	315.4	82	2	-0.9
60	3040	2845178	6336031	126.2	0	50156	106	50210	1.7	14.9	8	-7.7	402.5	286.9	305.3	82	2	1.2
60	3041	2845005	6336070	83.1	0	50234	106	50210	10.7	17.3	8	-8.2	347.6	291.5	310.1	82	2	7.1
60	3042	2844862	6336209	25.7	0	50338	106	50210	7.6	30.5	8	-9.1	276.3	294.8	313.1	82	2	10.7
60	3043	2844790	6336211	25.3	0	50337	106	50210	1.4	26.5	8	-9.1	273.9	282.7	301.1	82	2	8.3
60	3044	2844691	6336200	22.9	0	50330	106	50210	0.7	24.6	8	-9.1	259.2	268.1	286.7	82	2	7.9
60	3045	2844587	6336172	25.4	0	50322	106	50210	2.2	25.9	8	-9.1	258.2	267.1	286	82	2	16.4
60	3046	2844490	6336201	23.2	0	50316	106	50210	2.6	29.2	8	-9.1	245.6	260.7	279.6	82	2	23.2
60	3047	2844290	6336107	83	0	50148	106	50210	4.4	16.6	8	-8.2	261.3	198.4	218	82	2	20
60	3048	2844016	6336067	116.1	0	50092	106	50210	0	11.6	8	-7.9	307	197.7	217.9	82	2	1.1
60	3049	2843856	6335918	140.4	0	50039	106	50210	0.9	8.3	8	-7.6	328	189.2	210.4	82	2	4.4
60	3050	2843690	6335798	161.1	0	49993	106	50210	0.3	6.5	8	-7.4	344.6	180.2	202.3	82	2	2.1
60	3051	2843699	6335629	157.5	0	49999	106	50210	0.6	6.6	8	-7.4	338.5	178.7	201.7	82	2	2.5
60	3052	2843532	6335788	159	0	49984	106	50210	0.1	5.7	8	-7.4	329.2	166.3	188.8	82	2	0
60	3053	2843199	6335713	165.4	0	49967	106	50210	0.5	4.4	8	-7.2	331.9	160.7	184.1	82	2	-8.6
60	3054	2842934	6335711	178	0	49951	106	50210	0	3.9	8	-6.9	354.3	167.9	191.3	82	2	0
60	3055	2842705	6335955	184.8	0	49926	106	50210	0.1	3.8	8	-6.8	352.1	158.2	180.8	82	2	5.8
60	3056	2841811	6335906	181	0	49920	106	50210	0.5	3.9	8	-6.9	333.5	144.3	168.8	82	2	0
60	3057	2841272	6335973	195.8	0	49918	106	50210	0.8	3.7	8	-6.7	378	172.4	197.6	82	2	-2.2
60	3058	2840706	6335837	200.3	0	49924	106	50210	0.5	4.3	8	-6.7	396.3	186.1	213.4	82	2	2.3
60	3059	2839778	6335956	233	0	49917	106	50210	0.1	6.3	8	-6.5	491.1	246.2	275.2	82	2	0
60	3060	2838577	6336073	246.4	0	49887	106	50210	0.6	16	8	-6.3	503.2	253.6	284.2	82	2	-10.6
60	3112	2861610	6334625	23.4	0	50243	106	50208	0	4.3	8	-7.3	167.5	153	158	82	2	1.4
60	3114	2859646	6334661	27.6	0	50237	106	50209	0	3.3	8	-8	174	154.6	160.8	82	2	8.6
60	3212	2861430	6334459	23.6	0	50236	106	50208	0	4.2	8	-7.2	159.7	144.8	150.8	82	2	1.6
60	3214	2859051	6334699	27.5	0	50259	106	50209	2.6	4.2	8	-8.3	195.4	180	186.4	82	2	8.5
60	3312	2860959	6334697	25.6	0	50245	106	50208	0	3.6	8	-7.2	175.8	158.2	163.4	82	2	7.6
60	3412	2861363	6334736	23	0	50241	106	50208	0	3.8	8	-7.2	164.4	149.9	154.4	82	2	0
60	3512	2861622	6334747	24.3	0	50231	106	50209	0	4.1	8	-7.2	159.2	143.6	147.9	82	2	1.3
60	3612	2861500	6334742	26.8	0	50239	106	50209	0	4	8	-7.2	174.2	155.6	160	82	2	3.8

APPENDIX V

R A D I O C A R B O N D A T I N G

The University of Waikato

Radiocarbon Dating Laboratory

Private Bag 3105
Hamilton,
New Zealand.
Fax +64 7 838 4192
Ph +64 7 838 4278
email c14@waikato.ac.nz
Head: Dr Alan Hogg

Report on Radiocarbon Age Determination for Wk- 14588

Submitter	D Chambers
Submitter's Code	R28527/1 A1
Site & Location	, New Zealand
Sample Material	Peat
Physical Pretreatment	Visible contaminants removed.
Chemical Pretreatment	Acid washed using 10% conc. HCl, rinsed. Washed in hot 1% NaOH, then acid washed in 10% conc. HCL, rinsed and dried. The base insoluble fraction was selected for dating.

$d^{14}C$	-461.7 ± 3.0	‰
$\delta^{13}C$	-29.2 ± 0.2	‰
$D^{14}C$	-457.2 ± 3.0	‰
% Modern	54.3 ± 0.3	%
Result	**4908 ± 45 BP**	

Comments

AG Hogg
9/6/04

- Result is *Conventional Age or % Modern* as per Stuiver and Polach, 1977, Radiocarbon 19, 355-363. This is based on the Libby half-life of 5568 yr with correction for isotopic fractionation applied. This age is normally quoted in publications and must include the appropriate error term and Wk number.
- Quoted errors are 1 standard deviation due to counting statistics multiplied by an experimentally determined Laboratory Error Multiplier of 1 .
- The isotopic fractionation, $\delta^{13}C$, is expressed as ‰ wrt PDB.
- Results are reported as *% Modern* when the conventional age is younger than 200 yr BP.

RAFTER RADIOCARBON LABORATORY R28527/1

INSTITUTE OF GEOLOGICAL AND NUCLEAR SCIENCES LTD.
PO Box 31312, Lower Hutt, New Zealand
Phone (+64 4) 570 4671, Fax (+64 4) 570 4657

RADIOCARBON CALIBRATION REPORT

WK 14588 CONVENTIONAL RADIOCARBON AGE 4908 ± 45 years BP

INTCAL98_14C
1998 Atmospheric delta 14C and radiocarbon ages from:
Stuiver, M., Reimer, P.J., Bard,E., Beck, J.W., Burr, G.S.,
Hughen, K.A., Kromer, B., McCormac, F.G., v.d. Plicht, J., and
Spurk,M. 1998, Radiocarbon 40(3):1041-1083

CALIBRATED AGE in terms of cofidence intervals (Smoothing parameter: 1, Offset: 0)

2 sigma interval is 3779 BC to 3637 BC	5728 BP to 5586 BP (95.6% of area)
1 sigma interval is 3706 BC to 3648 BC	5655 BP to 5597 BP (61.6% of area)

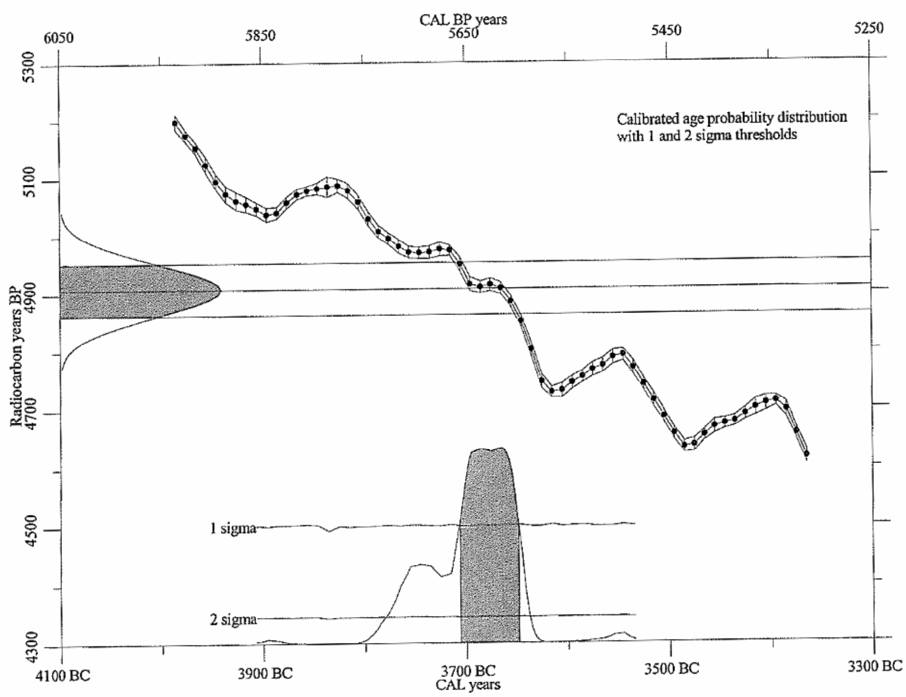

The University of Waikato

Radiocarbon Dating Laboratory

Private Bag 3105
Hamilton,
New Zealand.
Fax +64 7 838 4192
Ph +64 7 838 4278
email c14@waikato.ac.nz
Head: Dr Alan Hogg

Report on Radiocarbon Age Determination for Wk- 14588

Submitter	D Chambers
Submitter's Code	R28527/1 A1
Site & Location	, New Zealand
Sample Material	Peat
Physical Pretreatment	Visible contaminants removed.
Chemical Pretreatment	Acid washed using 10% conc. HCl, rinsed. Washed in hot 1% NaOH, then acid washed in 10% conc. HCL, rinsed and dried. The base insoluble fraction was selected for dating.

$d^{14}C$	-461.7 ± 3.0	‰
$\delta^{13}C$	-29.2 ± 0.2	‰
$D^{14}C$	-457.2 ± 3.0	‰
% Modern	54.3 ± 0.3	%
Result	**4908 ± 45 BP**	

Comments

9/6/04

- Result is *Conventional Age or % Modern* as per Stuiver and Polach, 1977, Radiocarbon 19, 355-363. This is based on the Libby half-life of 5568 yr with correction for isotopic fractionation applied. This age is normally quoted in publications and must include the appropriate error term and Wk number.
- Quoted errors are 1 standard deviation due to counting statistics multiplied by an experimentally determined Laboratory Error Multiplier of 1 .
- The isotopic fractionation, $\delta^{13}C$, is expressed as ‰ wrt PDB.
- Results are reported as *% Modern* when the conventional age is younger than 200 yr BP.

The University of Waikato

Radiocarbon Dating Laboratory

Private Bag 3105
Hamilton,
New Zealand.
Fax +64 7 838 4192
Ph +64 7 838 4278
email c14@waikato.ac.nz
Head: Dr Alan Hogg

Report on Radiocarbon Age Determination for Wk- 14590

Submitter	D Chambers
Submitter's Code	R28527/3 THb
Site & Location	, New Zealand
Sample Material	Peat
Physical Pretreatment	Visible contaminants removed.
Chemical Pretreatment	Acid washed using 10% conc. HCl, rinsed. Washed in hot 1% NaOH, then acid washed in 10% conc. HCL, rinsed and dried. The base insoluble fraction was selected for dating.

$d^{14}C$	-229.1 ± 3.9	‰
$\delta^{13}C$	-28.7 ± 0.2	‰
$D^{14}C$	-223.4 ± 3.9	‰
% Modern	77.7 ± 0.4	%
Result	**2031 ± 40 BP**	

Comments

AG Hogg
9/6/04

- Result is *Conventional Age or % Modern* as per Stuiver and Polach, 1977, Radiocarbon 19, 355-363. This is based on the Libby half-life of 5568 yr with correction for isotopic fractionation applied. This age is normally quoted in publications and must include the appropriate error term and Wk number.
- Quoted errors are 1 standard deviation due to counting statistics multiplied by an experimentally determined Laboratory Error Multiplier of 1 .
- The isotopic fractionation, $\delta^{13}C$, is expressed as ‰ wrt PDB.
- Results are reported as *% Modern* when the conventional age is younger than 200 yr BP.

RAFTER RADIOCARBON LABORATORY R28527/3

INSTITUTE OF GEOLOGICAL AND NUCLEAR SCIENCES LTD.
PO Box 31312, Lower Hutt, New Zealand
Phone (+64 4) 570 4671, Fax (+64 4) 570 4657

RADIOCARBON CALIBRATION REPORT

WK 14590 CONVENTIONAL RADIOCARBON AGE 2031 ± 40 years BP

INTCAL98_14C
1998 Atmospheric delta 14C and radiocarbon ages from:
Stuiver, M., Reimer, P.J., Bard,E., Beck, J.W., Burr, G.S.,
Hughen, K.A., Kromer, B., McCormac, F.G., v.d. Plicht, J., and
Spurk,M. 1998, Radiocarbon 40(3):1041-1083

CALIBRATED AGE in terms of cofidence intervals (Smoothing parameter: 1, Offset: 0)

2 sigma interval is 162 BC to 64 AD	2111 BP to 1886 BP (97.3% of area)
1 sigma interval is 58 BC to 19 AD	2007 BP to 1931 BP (54.4% of area)

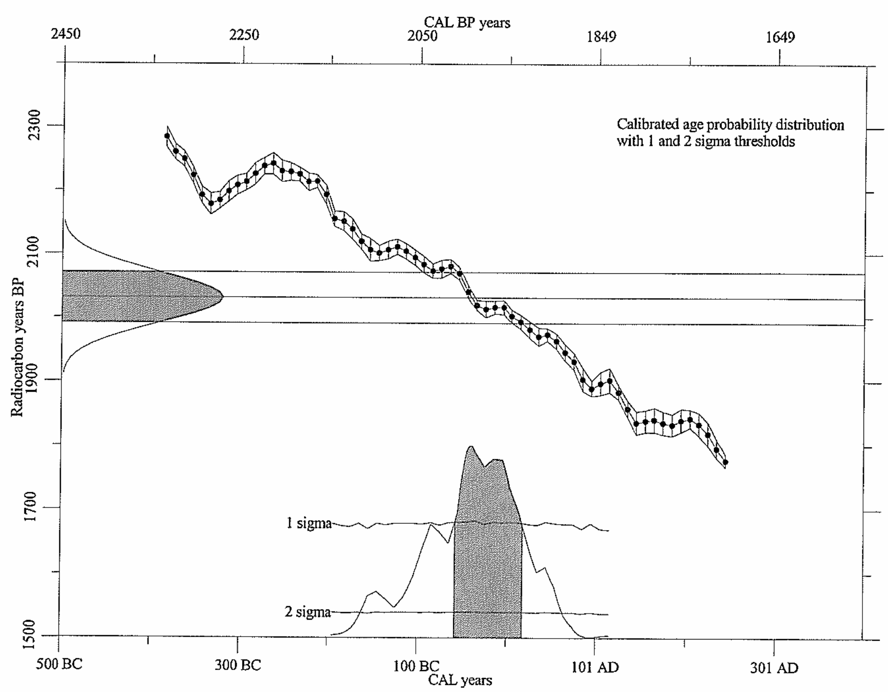

The University of Waikato

Radiocarbon Dating Laboratory

Private Bag 3105
Hamilton,
New Zealand.
Fax +64 7 838 4192
Ph +64 7 838 4278
email c14@waikato.ac.nz
Head: Dr Alan Hogg

Report on Radiocarbon Age Determination for Wk- 18346

Submitter	D Chambers
Submitter's Code	MT-1a/b R 2934
Site & Location	, New Zealand
Sample Material	Soil, organics
Physical Pretreatment	Visible contaminants removed.
Chemical Pretreatment	Washed in hot 10% HCl, rinsed and treated with hot 1% NaOH. The NaOH insoluble fraction was treated with hot 10% HCl, filtered, rinsed and dried.

$d^{14}C$	-114.1 ± 7.0	‰
$\delta^{13}C$	-29.6 ± 0.2	‰
$D^{14}C$	-106.0 ± 7.1	‰
% Modern	89.4 ± 0.7	%
Result	**900 ± 64 BP**	

Comments

AG Hogg
24/3/06

- Result is *Conventional Age or % Modern* as per Stuiver and Polach, 1977, Radiocarbon 19, 355-363. This is based on the Libby half-life of 5568 yr with correction for isotopic fractionation applied. This age is normally quoted in publications and must include the appropriate error term and Wk number.
- Quoted errors are 1 standard deviation due to counting statistics multiplied by an experimentally determined Laboratory Error Multiplier of 1 .
- The isotopic fractionation, $\delta^{13}C$, is expressed as ‰ wrt PDB.
- Results are reported as *% Modern* when the conventional age is younger than 200 yr BP.

RAFTER RADIOCARBON LABORATORY R29134

INSTITUTE OF GEOLOGICAL AND NUCLEAR SCIENCES LTD.
PO Box 31312, Lower Hutt, New Zealand
Phone (+64 4) 570 4671, Fax (+64 4) 570 4657

RADIOCARBON CALIBRATION REPORT

WK-18346 CONVENTIONAL RADIOCARBON AGE 900 ± 64 years BP

Southern Hemisphere Atmospheric data from McCormac et al (2004);
FG McCormac, AG Hogg, PG Blackwell, CE Buck, TFG Higham, and PJ Reimer (2004)
Radiocarbon 46, 1087-1092

CALIBRATED AGE in terms of confidence intervals (Smoothing parameter: 1, Offset: 0)

2 sigma interval is 1030 AD to 1282 AD	920 BP to 668 BP (98.2% of area)
1 sigma interval is 1055 AD to 1065 AD	895 BP to 885 BP (4.2% of area)
plus 1150 AD to 1230 AD	800 BP to 720 BP (48.7% of area)
plus 1252 AD to 1259 AD	698 BP to 691 BP (2.9% of area)

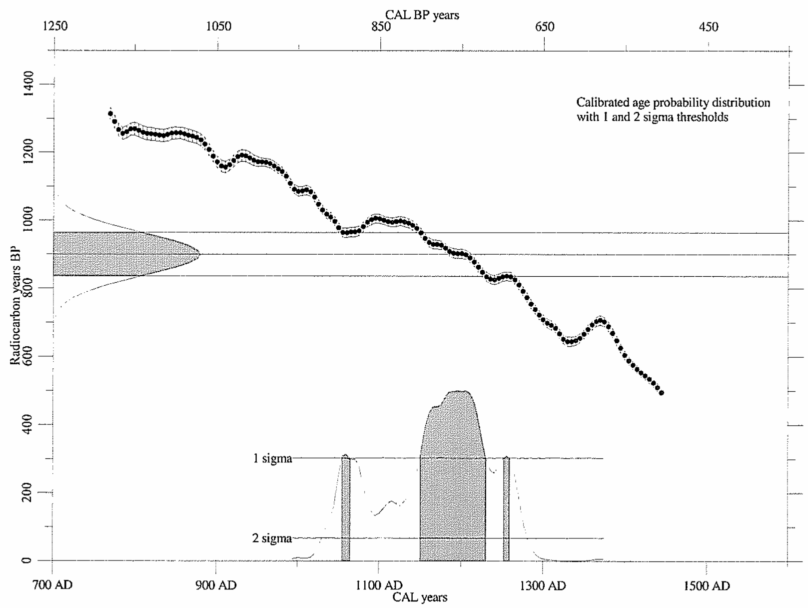

Institute of
Geological &
Nuclear Sciences
Limited

Rafter Radiocarbon Laboratory

Accelerator Mass Spectrometry Result

Sample	**R 28527/4**
Description	Peat
Sample ID	THc
Submitter	Vasso Mouslopoulou
	GNS McKay

Laboratory Code	**NZA 19822**
Date measured	20-May-04
$\delta^{13}C$	-29.9 ‰
* **Radiocarbon Age**	920 ± 40 BP
$\delta^{14}C$	-123 ± 4.4 ‰
$\Delta^{14}C$	-114.1 ± 4.5 ‰
** **Per cent modern**	88.59 ± 0.45

Job No. 29972

Issued 24/05/2004 D.M. Chambers

* Reported age is the conventional radiocarbon age before present (BP)

** Per cent modern means absolute per cent modern relative to the NBS oxalic acid standard, (HOxI) corrected for decay since 1950.

Age, $\Delta^{14}C$, $\delta^{14}C$ and absolute per cent modern are as defined by Stuiver and Polach, Radiocarbon 19:355-363 (1977)

The reported errors comprise statistical errors in sample and standard determinations, combined in quadrature with a system error component that is based on the analysis of an ongoing series of measurements on oxalic acid secondary standard. For the present result the system error component is conservatively estimated as 0.18% (= ± 14 radiocarbon years).

Environment Group, Institute of Geological and Nuclear Sciences Ltd., PO Box 31-312, Lower Hutt, New Zealand
Fax +64 4 570 4657 Phone +64 4 570 4671

Institute Form NSR-303 Rev 9 January 2003

RAFTER RADIOCARBON LABORATORY R28527/4

INSTITUTE OF GEOLOGICAL AND NUCLEAR SCIENCES LTD.
PO Box 31312, Lower Hutt, New Zealand
Phone (+64 4) 570 4671, Fax (+64 4) 570 4657

RADIOCARBON CALIBRATION REPORT

NZA 19822 CONVENTIONAL RADIOCARBON AGE 920 ± 40 years BP

INTCAL98_14C
1998 Atmospheric delta 14C and radiocarbon ages from:
Stuiver, M., Reimer, P.J., Bard,E., Beck, J.W., Burr, G.S.,
Hughen, K.A., Kromer, B., McCormac, F.G., v.d. Plicht, J., and
Spurk,M. 1998, Radiocarbon 40(3):1041-1083

CALIBRATED AGE in terms of cofidence intervals (Smoothing parameter: 1, Offset: 0)

2 sigma interval is 1020 AD to 1214 AD	930 BP to 736 BP (98.3% of area)
1 sigma interval is 1032 AD to 1174 AD	918 BP to 776 BP (84.7% of area)

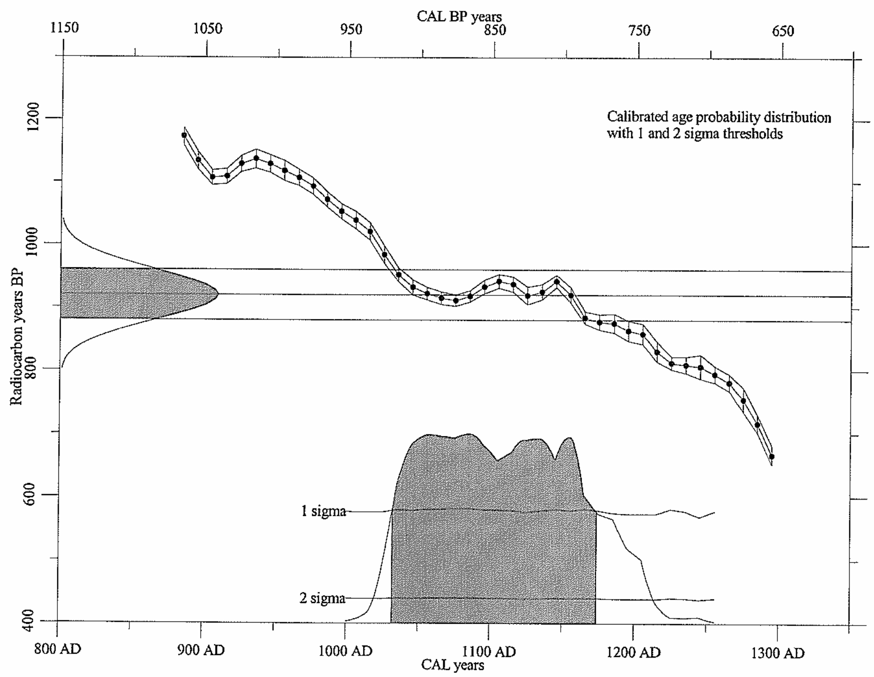

Institute of
Geological &
Nuclear Sciences
Limited

Rafter Radiocarbon Laboratory

Accelerator Mass Spectrometry Result

Sample	**R 28744/1**
Description	Peat
Sample ID	Ahirau1-1
Submitter	Vasiliki (Vasso) Mouslopoulou
	GNS McKay

Laboratory Code	**NZA 21341**
Date measured	14-Dec-04
$\delta^{13}C$	-26.6 ‰
* **Radiocarbon Age**	8566 ± 45 BP
$\delta^{14}C$	-659.1 ± 1.9 ‰
$\Delta^{14}C$	-658 ± 1.9 ‰
** **Per cent modern**	34.2 ± 0.19

Job No. 31756

Issued 15/12/2004 D.M. Chambers

* Reported age is the conventional radiocarbon age before present (BP)

** Per cent modern means absolute per cent modern relative to the NBS oxalic acid standard, (HOxI) corrected for decay since 1950.

Age, $\Delta^{14}C$, $\delta^{14}C$ and absolute per cent modern are as defined by Stuiver and Polach, Radiocarbon 19:355-363 (1977)

The reported errors comprise statistical errors in sample and standard determinations, combined in quadrature with a system error component that is based on the analysis of an ongoing series of measurements on oxalic acid secondary standard. For the present result the system error component is conservatively estimated as 0.18% (= ± 14 radiocarbon years).

Environment Group, Institute of Geological and Nuclear Sciences Ltd., PO Box 31-312, Lower Hutt, New Zealand
Fax +64 4 570 4657 Phone +64 4 570 4671

Institute Form NSR-303 Rev 9 January 2003

RAFTER RADIOCARBON LABORATORY R28744/1

INSTITUTE OF GEOLOGICAL AND NUCLEAR SCIENCES LTD.
PO Box 31312, Lower Hutt, New Zealand
Phone (+64 4) 570 4671, Fax (+64 4) 570 4657

RADIOCARBON CALIBRATION REPORT

NZA 21341 CONVENTIONAL RADIOCARBON AGE 8566 ± 45 years BP

INTCAL98_14C
1998 Atmospheric delta 14C and radiocarbon ages from:
Stuiver, M., Reimer, P.J., Bard,E., Beck, J.W., Burr, G.S.,
Hughen, K.A., Kromer, B., McCormac, F.G., v.d. Plicht, J., and
Spurk,M. 1998, Radiocarbon 40(3):1041-1083

CALIBRATED AGE in terms of cofidence intervals (Smoothing parameter: 1, Offset: 0)

2 sigma interval is 7608 BC to 7534 BC	9557 BP to 9483 BP (82.4% of area)
1 sigma interval is 7597 BC to 7575 BC	9546 BP to 9524 BP (43.9% of area)

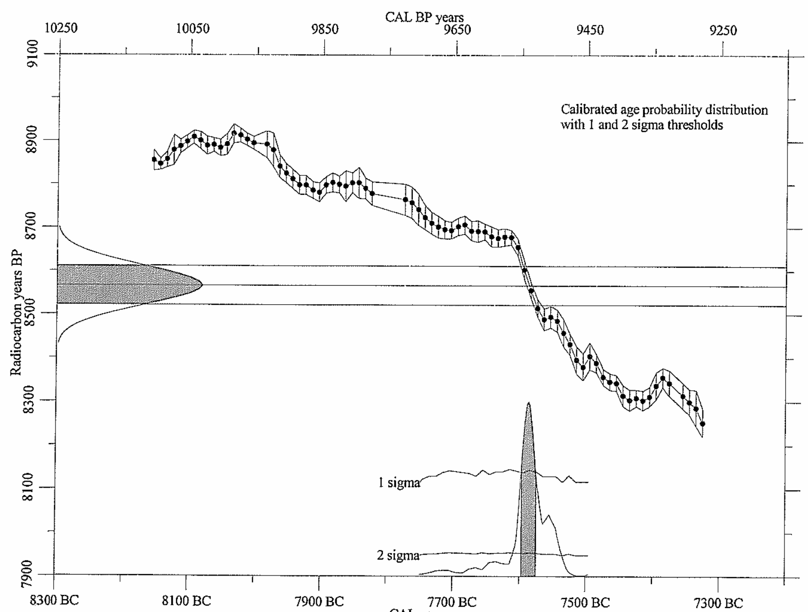

Institute of
Geological &
Nuclear Sciences
Limited

Rafter Radiocarbon Laboratory

Accelerator Mass Spectrometry Result

Sample	**R 28744/2**
Description	Peaty paleosol
Sample ID	Ahirau1-4
Submitter	Vasiliki (Vasso) Mouslopoulou
	GNS McKay

Laboratory Code	**NZA 21342**
Date measured	14-Dec-04
$\delta^{13}C$	-25.6 ‰
* **Radiocarbon Age**	2873 ± 35 BP
$\delta^{14}C$	-306.1 ± 2.8 ‰
$\Delta^{14}C$	-305.2 ± 2.8 ‰
** **Per cent modern**	69.48 ± 0.28

Job No. 31757

Issued 15/12/2004 DM Chambers

* Reported age is the conventional radiocarbon age before present (BP)

** Per cent modern means absolute per cent modern relative to the NBS oxalic acid standard, (HOxI) corrected for decay since 1950.

Age, $\Delta^{14}C$, $\delta^{14}C$ and absolute per cent modern are as defined by Stuiver and Polach, Radiocarbon 19:355-363 (1977)

The reported errors comprise statistical errors in sample and standard determinations, combined in quadrature with a system error component that is based on the analysis of an ongoing series of measurements on oxalic acid secondary standard. For the present result the system error component is conservatively estimated as 0.18% (= ± 14 radiocarbon years).

Environment Group, Institute of Geological and Nuclear Sciences Ltd., PO Box 31-312, Lower Hutt, New Zealand
Fax +64 4 570 4657 Phone +64 4 570 4671

Institute Form NSR-303 Rev 9 January 2003

RAFTER RADIOCARBON LABORATORY R28744/2

INSTITUTE OF GEOLOGICAL AND NUCLEAR SCIENCES LTD.
PO Box 31312, Lower Hutt, New Zealand
Phone (+64 4) 570 4671, Fax (+64 4) 570 4657

RADIOCARBON CALIBRATION REPORT

NZA 21342 CONVENTIONAL RADIOCARBON AGE 2873 ± 35 years BP

INTCAL98_14C
1998 Atmospheric delta 14C and radiocarbon ages from:
Stuiver, M., Reimer, P.J., Bard,E., Beck, J.W., Burr, G.S.,
Hughen, K.A., Kromer, B., McCormac, F.G., v.d. Plicht, J., and
Spurk,M. 1998, Radiocarbon 40(3):1041-1083

CALIBRATED AGE in terms of cofidence intervals (Smoothing parameter: 1, Offset: 0)

2 sigma interval is 1157 BC to 1150 BC	3106 BP to 3099 BP (0.7% of area)
plus 1129 BC to 924 BC	3078 BP to 2873 BP (93.0% of area)
1 sigma interval is 1115 BC to 991 BC	3064 BP to 2940 BP (72.3% of area)

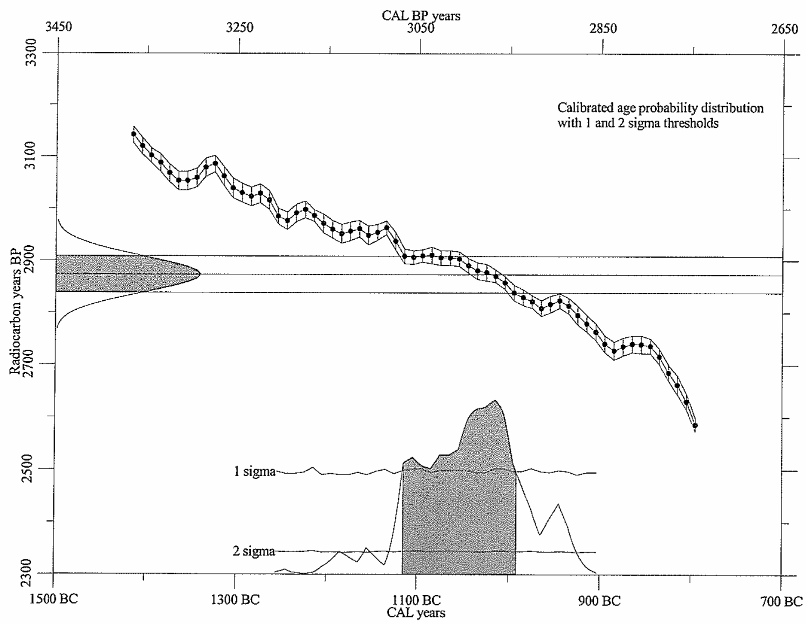

Institute of
Geological &
Nuclear Sciences
Limited

Rafter Radiocarbon Laboratory

Accelerator Mass Spectrometry Result

Sample	**R 28744/3**
Description	Peat
Sample ID	Ahirau1-9
Submitter	Vasiliki (Vasso) Mouslopoulou GNS McKay

Laboratory Code	**NZA 21343**
Date measured	14-Dec-04
$\delta^{13}C$	-25.9 ‰
* **Radiocarbon Age**	2801 ± 35 BP
$\delta^{14}C$	-300.3 ± 3 ‰
$\Delta^{14}C$	-299 ± 3 ‰
** **Per cent modern**	70.1 ± 0.3

Job No. 31758

Issued 15/12/2004 D.M. Chambers

* Reported age is the conventional radiocarbon age before present (BP)

** Per cent modern means absolute per cent modern relative to the NBS oxalic acid standard, (HOxI) corrected for decay since 1950.

Age, $\Delta^{14}C$, $\delta^{14}C$ and absolute per cent modern are as defined by Stuiver and Polach, Radiocarbon 19:355-363 (1977)

The reported errors comprise statistical errors in sample and standard determinations, combined in quadrature with a system error component that is based on the analysis of an ongoing series of measurements on oxalic acid secondary standard. For the present result the system error component is conservatively estimated as 0.18% (= ± 14 radiocarbon years).

Environment Group, Institute of Geological and Nuclear Sciences Ltd., PO Box 31-312, Lower Hutt, New Zealand
Fax +64 4 570 4657 Phone +64 4 570 4671

Institute Form NSR-303 Rev 9 January 2003

RAFTER RADIOCARBON LABORATORY R28744/3

INSTITUTE OF GEOLOGICAL AND NUCLEAR SCIENCES LTD.
PO Box 31312, Lower Hutt, New Zealand
Phone (+64 4) 570 4671, Fax (+64 4) 570 4657

RADIOCARBON CALIBRATION REPORT

NZA 21343 CONVENTIONAL RADIOCARBON AGE 2801 ± 35 years BP

INTCAL98_14C
1998 Atmospheric delta 14C and radiocarbon ages from:
Stuiver, M., Reimer, P.J., Bard,E., Beck, J.W., Burr, G.S.,
Hughen, K.A., Kromer, B., McCormac, F.G., v.d. Plicht, J., and
Spurk,M. 1998, Radiocarbon 40(3):1041-1083

CALIBRATED AGE in terms of cofidence intervals (Smoothing parameter: 1, Offset: 0)

2 sigma interval is 1028 BC to 839 BC	2977 BP tó 2788 BP (96.0% of area)
1 sigma interval is 995 BC to 904 BC	2944 BP to 2853 BP (72.2% of area)

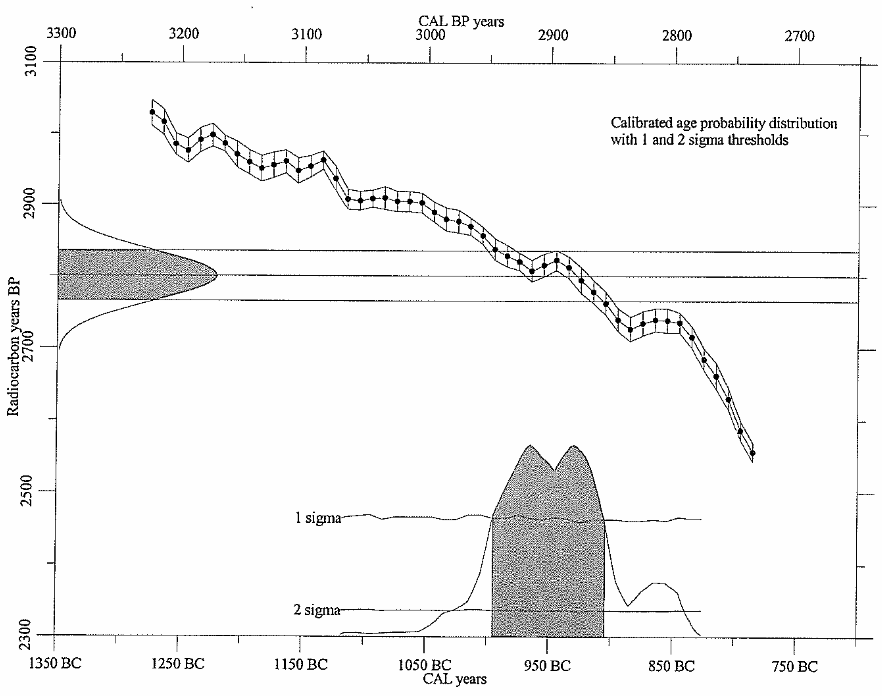

Institute of
Geological &
Nuclear Sciences
Limited

Rafter Radiocarbon Laboratory

Accelerator Mass Spectrometry Result

Sample	**R 28744/4**
Description	Peat
Sample ID	Moana/P1
Submitter	Vasiliki (Vasso) Mouslopoulou
	GNS McKay

Laboratory Code	**NZA 21344**
Date measured	14-Dec-04
$\delta^{13}C$	-26 ‰
* **Radiocarbon Age**	12433 ± 50 BP
$\delta^{14}C$	-789.1 ± 1.4 ‰
$\Delta^{14}C$	-788.7 ± 1.4 ‰
** **Per cent modern**	21.13 ± 0.14

Job No. 31759

Issued 15/12/2004 D.M. Chambers

* Reported age is the conventional radiocarbon age before present (BP)

** Per cent modern means absolute per cent modern relative to the NBS oxalic acid standard, (HOxI) corrected for decay since 1950.

Age, $\Delta^{14}C$, $\delta^{14}C$ and absolute per cent modern are as defined by Stuiver and Polach, Radiocarbon 19:355-363 (1977)

The reported errors comprise statistical errors in sample and standard determinations, combined in quadrature with a system error component that is based on the analysis of an ongoing series of measurements on oxalic acid secondary standard. For the present result the system error component is conservatively estimated as 0.18% (= ± 14 radiocarbon years).

Environment Group, Institute of Geological and Nuclear Sciences Ltd., PO Box 31-312, Lower Hutt, New Zealand
Fax +64 4 570 4657 Phone +64 4 570 4671

Institute Form NSR-303 Rev 9 January 2003

RAFTER RADIOCARBON LABORATORY R28744/4

INSTITUTE OF GEOLOGICAL AND NUCLEAR SCIENCES LTD.
PO Box 31312, Lower Hutt, New Zealand
Phone (+64 4) 570 4671, Fax (+64 4) 570 4657

RADIOCARBON CALIBRATION REPORT

NZA 21344 CONVENTIONAL RADIOCARBON AGE 12433 ± 50 years BP

INTCAL98_14C
1998 Atmospheric delta 14C and radiocarbon ages from:
Stuiver, M., Reimer, P.J., Bard,E., Beck, J.W., Burr, G.S.,
Hughen, K.A., Kromer, B., McCormac, F.G., v.d. Plicht, J., and
Spurk,M. 1998, Radiocarbon 40(3):1041-1083

CALIBRATED AGE in terms of cofidence intervals (Smoothing parameter: 1, Offset: 0)

2 sigma interval is	13563 BC to 12204 BC	15512 BP to 14153 BP (98.7% of area)
1 sigma interval is	13425 BC to 12628 BC	15374 BP to 14577 BP (52.1% of area)
plus	12475 BC to 12281 BC	14424 BP to 14230 BP (25.0% of area)

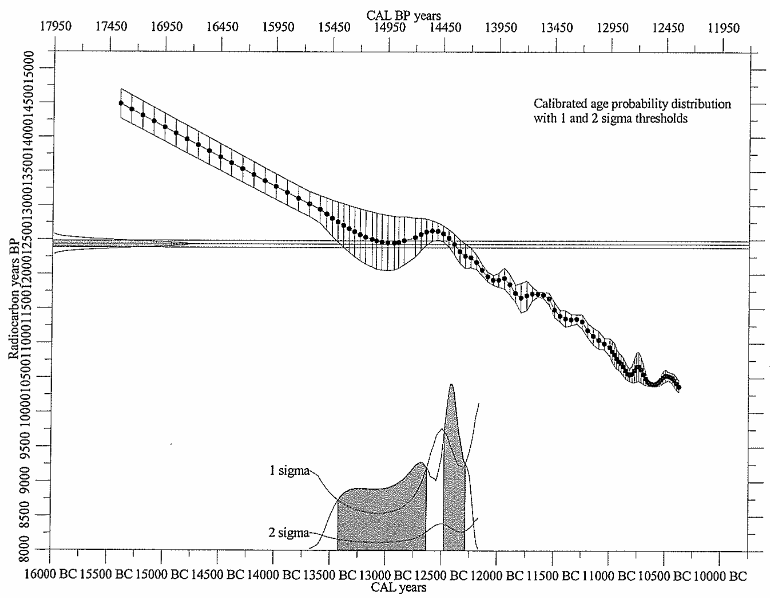

Institute of Geological & Nuclear Sciences Limited

Rafter Radiocarbon Laboratory

Accelerator Mass Spectrometry Result

Sample	**R 28744/5**
Description	Peat
Sample ID	Moana/P2
Submitter	Vasiliki (Vasso) Mouslopoulou GNS McKay

Laboratory Code	**NZA 21345**
Date measured	14-Dec-04
$\delta^{13}C$	-24 ‰
* **Radiocarbon Age**	12336 ± 45 BP
$\delta^{14}C$	-785.6 ± 1.3 ‰
$\Delta^{14}C$	-786.1 ± 1.3 ‰
** **Per cent modern**	21.39 ± 0.13

Job No. 31760

Issued 15/12/2004 D.M. Chambers

* Reported age is the conventional radiocarbon age before present (BP)

** Per cent modern means absolute per cent modern relative to the NBS oxalic acid standard, (HOxI) corrected for decay since 1950.

Age, $\Delta^{14}C$, $\delta^{14}C$ and absolute per cent modern are as defined by Stuiver and Polach, Radiocarbon 19:355-363 (1977)

The reported errors comprise statistical errors in sample and standard determinations, combined in quadrature with a system error component that is based on the analysis of an ongoing series of measurements on oxalic acid secondary standard. For the present result the system error component is conservatively estimated as 0.18% (= ± 14 radiocarbon years).

Environment Group, Institute of Geological and Nuclear Sciences Ltd., PO Box 31-312, Lower Hutt, New Zealand
Fax +64 4 570 4657 Phone +64 4 570 4671

Institute Form NSR-303 Rev 9 January 2003

RAFTER RADIOCARBON LABORATORY R28744/5

INSTITUTE OF GEOLOGICAL AND NUCLEAR SCIENCES LTD.
PO Box 31312, Lower Hutt, New Zealand
Phone (+64 4) 570 4671, Fax (+64 4) 570 4657

RADIOCARBON CALIBRATION REPORT

NZA 21345 CONVENTIONAL RADIOCARBON AGE 12336 ± 45 years BP

INTCAL98_14C
1998 Atmospheric delta 14C and radiocarbon ages from:
Stuiver, M., Reimer, P.J., Bard,E., Beck, J.W., Burr, G.S.,
Hughen, K.A., Kromer, B., McCormac, F.G., v.d. Plicht, J., and
Spurk,M. 1998, Radiocarbon 40(3):1041-1083

CALIBRATED AGE in terms of cofidence intervals (Smoothing parameter: 1, Offset: 0)

2 sigma interval is 13520 BC to 12173 BC	15469 BP to 14122 BP (96.4% of area)
1 sigma interval is 13358 BC to 12694 BC	15307 BP to 14643 BP (45.0% of area)
plus 12420 BC to 12218 BC	14369 BP to 14167 BP (30.6% of area)

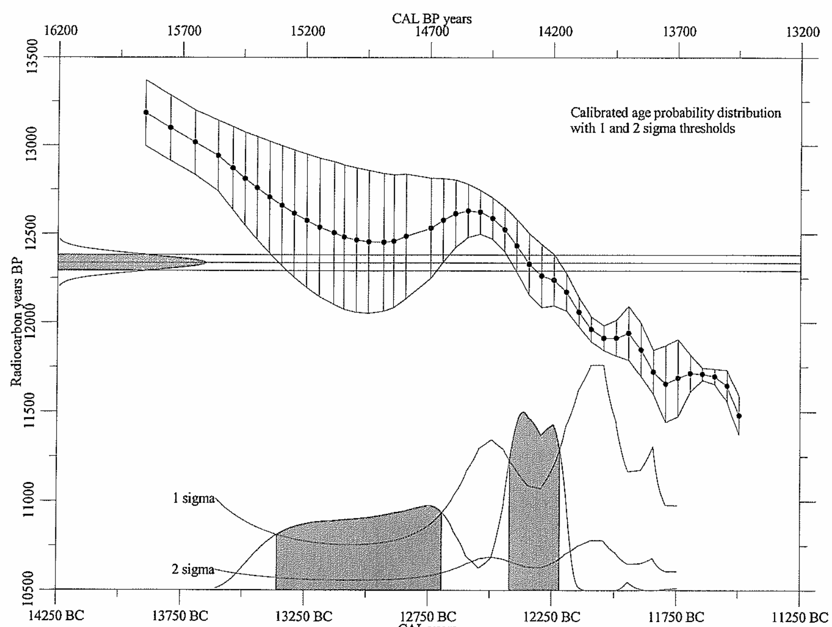

Institute of
Geological &
Nuclear Sciences
Limited

Rafter Radiocarbon Laboratory

Accelerator Mass Spectrometry Result

Sample	**R 28744/6**
Description	Peat
Sample ID	M-28 (Moana 28)
Submitter	Vasiliki (Vasso) Mouslopoulou
	GNS McKay

Laboratory Code	**NZA 21346**
Date measured	14-Dec-04
$\delta^{13}C$	-29.4 ‰
* **Radiocarbon Age**	6803 ± 35 BP
$\delta^{14}C$	-577.9 ± 1.8 ‰
$\Delta^{14}C$	-574 ± 1.8 ‰
** **Per cent modern**	42.6 ± 0.18

Job No. 31761

Issued 15/12/2004 D.M. Chambers

* Reported age is the conventional radiocarbon age before present (BP)

** Per cent modern means absolute per cent modern relative to the NBS oxalic acid standard, (HOxI) corrected for decay since 1950.

Age, $\Delta^{14}C$, $\delta^{14}C$ and absolute per cent modern are as defined by Stuiver and Polach, Radiocarbon 19:355-363 (1977)

The reported errors comprise statistical errors in sample and standard determinations, combined in quadrature with a system error component that is based on the analysis of an ongoing series of measurements on oxalic acid secondary standard. For the present result the system error component is conservatively estimated as 0.18% (= ± 14 radiocarbon years).

Environment Group, Institute of Geological and Nuclear Sciences Ltd., PO Box 31-312, Lower Hutt, New Zealand
Fax +64 4 570 4657 Phone +64 4 570 4671

Institute Form NSR-303 Rev 9 January 2003

RAFTER RADIOCARBON LABORATORY R28744/6

INSTITUTE OF GEOLOGICAL AND NUCLEAR SCIENCES LTD.
PO Box 31312, Lower Hutt, New Zealand
Phone (+64 4) 570 4671, Fax (+64 4) 570 4657

RADIOCARBON CALIBRATION REPORT

NZA 21346 CONVENTIONAL RADIOCARBON AGE 6803 ± 35 years BP

INTCAL98_14C
1998 Atmospheric delta 14C and radiocarbon ages from:
Stuiver, M., Reimer, P.J., Bard,E., Beck, J.W., Burr, G.S.,
Hughen, K.A., Kromer, B., McCormac, F.G., v.d. Plicht, J., and
Spurk,M. 1998, Radiocarbon 40(3):1041-1083

CALIBRATED AGE in terms of cofidence intervals (Smoothing parameter: 1, Offset: 0)

2 sigma interval is 5734 BC to 5631 BC	7683 BP to 7580 BP (95.9% of area)
1 sigma interval is 5725 BC to 5659 BC	7674 BP to 7608 BP (76.9% of area)

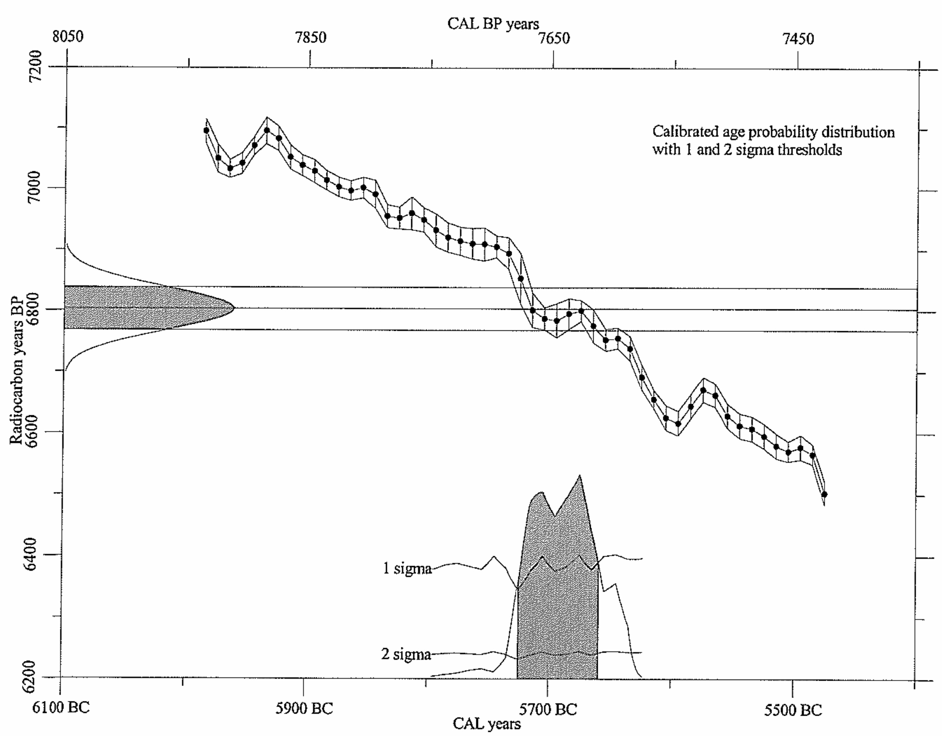

Institute of
Geological &
Nuclear Sciences
Limited

Rafter Radiocarbon Laboratory

Accelerator Mass Spectrometry Result

Sample	R 28757/2
Description	Organic soil
Sample ID	M-I-5
Submitter	Vasiliki (Vasso) Mouslopoulou
	GNS McKay

Laboratory Code	**NZA 21389**
Date measured	16-Dec-04
$\delta^{13}C$	-32.6 ‰
* **Radiocarbon Age**	3139 ± 30 BP
$\delta^{14}C$	-338.4 ± 2.3 ‰
$\Delta^{14}C$	-327.9 ± 2.4 ‰
** **Per cent modern**	67.21 ± 0.24

Job No. 31918

Issued 20/12/2004 O.M. Chambers

* Reported age is the conventional radiocarbon age before present (BP)

** Per cent modern means absolute per cent modern relative to the NBS oxalic acid standard, (HOxI) corrected for decay since 1950.

Age, $\Delta^{14}C$, $\delta^{14}C$ and absolute per cent modern are as defined by Stuiver and Polach, Radiocarbon 19:355-363 (1977)

The reported errors comprise statistical errors in sample and standard determinations, combined in quadrature with a system error component that is based on the analysis of an ongoing series of measurements on oxalic acid secondary standard. For the present result the system error component is conservatively estimated as 0.18% (= ± 14 radiocarbon years).

Environment Group, Institute of Geological and Nuclear Sciences Ltd., PO Box 31-312, Lower Hutt, New Zealand
Fax +64 4 570 4657 Phone +64 4 570 4671

Institute Form NSR-303 Rev 9 January 2003

RAFTER RADIOCARBON LABORATORY R28757/2

INSTITUTE OF GEOLOGICAL AND NUCLEAR SCIENCES LTD.
PO Box 31312, Lower Hutt, New Zealand
Phone (+64 4) 570 4671, Fax (+64 4) 570 4657

RADIOCARBON CALIBRATION REPORT

M-I-5

NZA 21389 CONVENTIONAL RADIOCARBON AGE 3139 ± 30 years BP

INTCAL98_14C
1998 Atmospheric delta 14C and radiocarbon ages from:
Stuiver, M., Reimer, P.J., Bard,E., Beck, J.W., Burr, G.S.,
Hughen, K.A., Kromer, B., McCormac, F.G., v.d. Plicht, J., and
Spurk,M. 1998, Radiocarbon 40(3):1041-1083

CALIBRATED AGE in terms of cofidence intervals (Smoothing parameter: 1, Offset: 0)

2 sigma interval is 1494 BC to 1479 BC	3443 BP to 3428 BP (4.2% of area)
plus 1453 BC to 1376 BC	3402 BP to 3325 BP (74.9% of area)
plus 1339 BC to 1318 BC	3288 BP to 3267 BP (8.1% of area)
1 sigma interval is 1431 BC to 1397 BC	3380 BP to 3346 BP (49.6% of area)

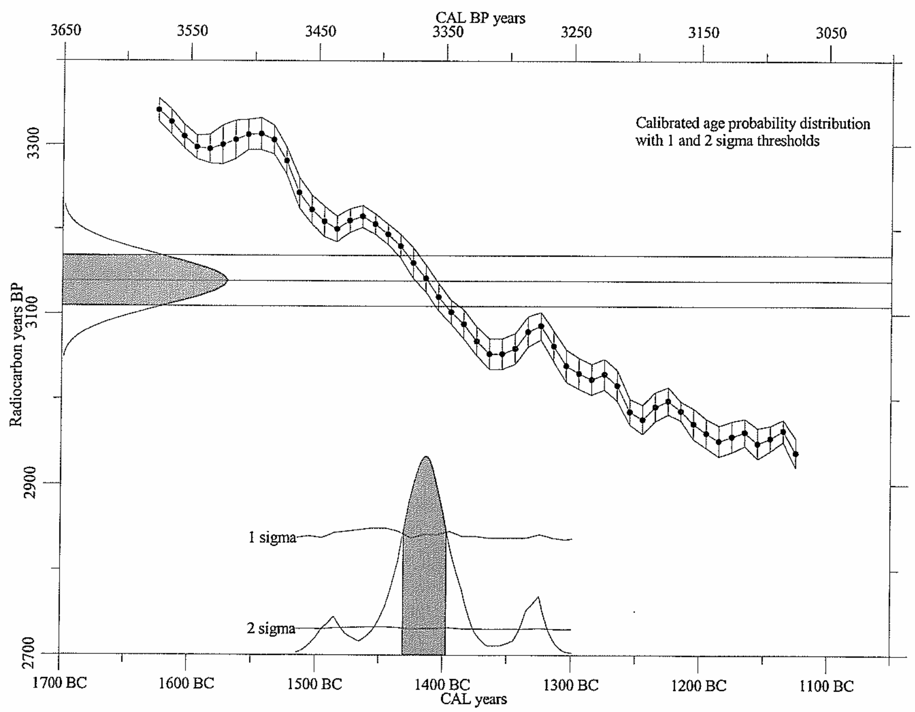

Institute of
Geological &
Nuclear Sciences
Limited

Rafter Radiocarbon Laboratory

Accelerator Mass Spectrometry Result

Sample	**R 28757/3**
Description	Organic soil
Sample ID	M-I-6
Submitter	Vasiliki (Vasso) Mouslopoulou GNS McKay

Laboratory Code	**NZA 21391**
Date measured	16-Dec-04
$\delta^{13}C$	-27 ‰
* **Radiocarbon Age**	2039 ± 30 BP
$\delta^{14}C$	-232.3 ± 2.8 ‰
$\Delta^{14}C$	-229.2 ± 2.8 ‰
** **Per cent modern**	77.08 ± 0.28

Job No. 31919

Issued 20/12/2004 O.M. Chambers

* Reported age is the conventional radiocarbon age before present (BP)

** Per cent modern means absolute per cent modern relative to the NBS oxalic acid standard, (HOxI) corrected for decay since 1950.

Age, $\Delta^{14}C$, $\delta^{14}C$ and absolute per cent modern are as defined by Stuiver and Polach, Radiocarbon 19:355-363 (1977)

The reported errors comprise statistical errors in sample and standard determinations, combined in quadrature with a system error component that is based on the analysis of an ongoing series of measurements on oxalic acid secondary standard. For the present result the system error component is conservatively estimated as 0.18% (= ± 14 radiocarbon years).

Environment Group, Institute of Geological and Nuclear Sciences Ltd., PO Box 31-312, Lower Hutt, New Zealand
Fax +64 4 570 4657 Phone +64 4 570 4671

Institute Form NSR-303 Rev 9 January 2003

R28757/3

RAFTER RADIOCARBON LABORATORY

INSTITUTE OF GEOLOGICAL AND NUCLEAR SCIENCES LTD.
PO Box 31312, Lower Hutt, New Zealand
Phone (+64 4) 570 4671, Fax (+64 4) 570 4657

RADIOCARBON CALIBRATION REPORT

NZA 21391 CONVENTIONAL RADIOCARBON AGE 2039 ± 30 years BP

INTCAL98_14C
1998 Atmospheric delta 14C and radiocarbon ages from:
Stuiver, M., Reimer, P.J., Bard,E., Beck, J.W., Burr, G.S.,
Hughen, K.A., Kromer, B., McCormac, F.G., v.d. Plicht, J., and
Spurk,M. 1998, Radiocarbon 40(3):1041-1083

CALIBRATED AGE in terms of cofidence intervals (Smoothing parameter: 1, Offset: 0)

2 sigma interval is 156 BC to 137 BC	2105 BP to 2086 BP (3.1% of area)
plus 114 BC to 33 AD	2063 BP to 1917 BP (89.9% of area)
1 sigma interval is 56 BC to 2 AD	2005 BP to 1948 BP (51.3% of area)

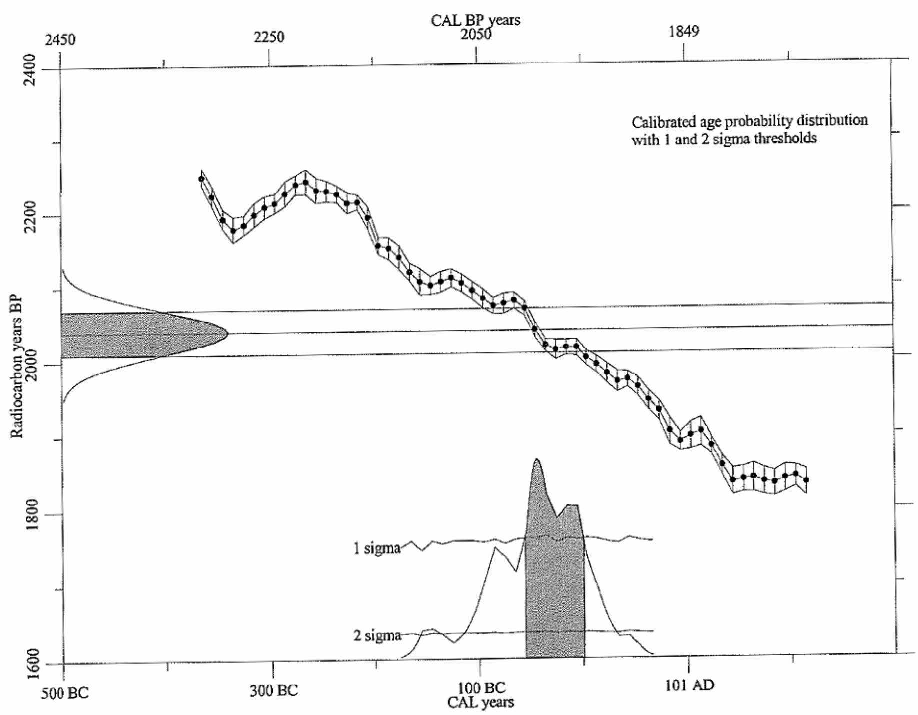

RAFTER
GNS SCIENCE

Accelerator Mass Spectrometry Result

Sample	**R 28757/1**
Description	Peat
Submitter ID	M-I-4
Submitter	Vasiliki (Vasso) Mouslopoulou GNS McKay

Laboratory Code	**NZA 21392**
Date measured	16-Dec-04
$\delta^{13}C$	-30.1 ‰
* **Radiocarbon Age**	23080 ± 160 BP
$\delta^{14}C$	-944.4 ± 1.1 ‰
$\Delta^{14}C$	-943.9 ± 1.1 ‰
** **Per cent modern**	5.61 ± 0.11

Job No. 31917

Issued 12/06/2006

* Reported age is the conventional radiocarbon age before present (BP)

** Per cent modern means absolute per cent modern relative to the NBS oxalic acid standard, (HOxI) corrected for decay since 1950.

Age, $\Delta^{14}C$, $\delta^{14}C$ and absolute per cent modern are as defined by Stuiver and Polach, Radiocarbon 19:355-363 (1977)

The reported errors comprise statistical errors in sample and standard determinations, combined in quadrature with a system error component that is based on the analysis of an ongoing series of measurements on oxalic acid secondary standard. For the present result the system error component is conservatively estimated as 0.18% (= ± 14 radiocarbon years).

National Isotope Centre, Institute of Geological and Nuclear Sciences Ltd (GNS Science)
PO Box 31-312 Lower Hutt, New Zealand Fax +64 4 570 4657 Phone +64 4 570 4644
www.RafterRadiocarbon.co.nz

RAFTER RADIOCARBON LABORATORY

R28527/1

INSTITUTE OF GEOLOGICAL AND NUCLEAR SCIENCES LTD.
PO Box 31312, Lower Hutt, New Zealand
Phone (+64 4) 570 4671, Fax (+64 4) 570 4657

RADIOCARBON CALIBRATION REPORT

WK 14588 CONVENTIONAL RADIOCARBON AGE 4908 ± 45 years BP

Southern Hemisphere Atmospheric data from McCormac et al (2004);
FG McCormac, AG Hogg, PG Blackwell, CE Buck, TFG Higham, and PJ Reimer (2004)
Radiocarbon 46, 1087-1092

CALIBRATED AGE in terms of confidence intervals (Smoothing parameter: 1, Offset: 0)

2 sigma interval is 3708 BC to 3624 BC	5657 BP to 5573 BP (59.9% of area)
plus 3593 BC to 3525 BC	5542 BP to 5474 BP (28.6% of area)
1 sigma interval is 3659 BC to 3634 BC	5608 BP to 5583 BP (27.6% of area)

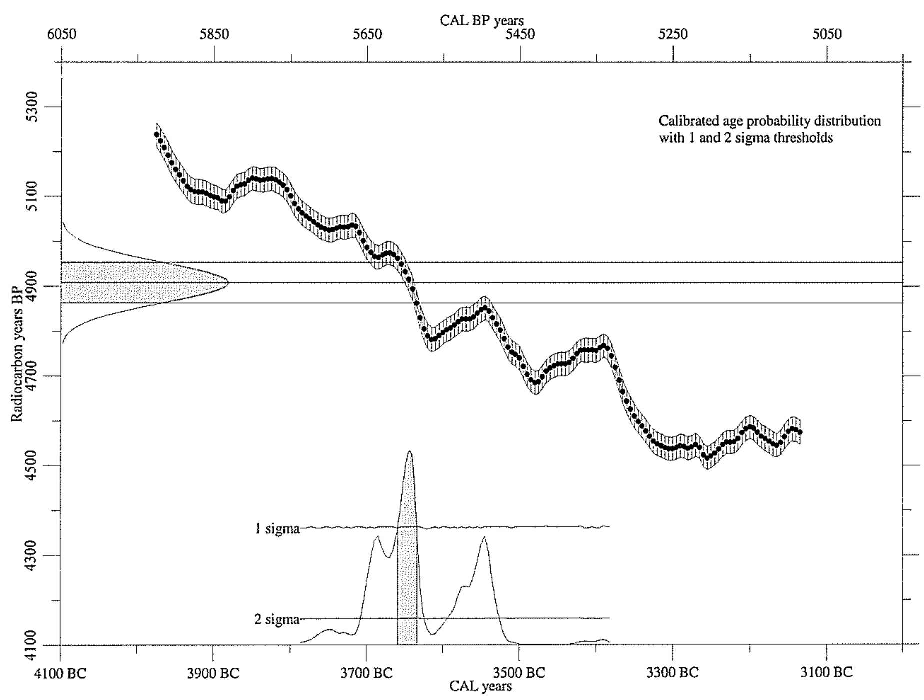

Institute of
Geological &
Nuclear Sciences
Limited

Rafter Radiocarbon Laboratory

Accelerator Mass Spectrometry Result

Sample	**R 28904/1**
Description	Peat
Sample ID	RT-A
Submitter	Vasiliki (Vasso) Mouslopoulou GNS McKay

Laboratory Code	**NZA 22386**
Date measured	15-Jun-05
$\delta^{13}C$	-27.9 ‰
* **Radiocarbon Age**	708 ± 30 BP
$\delta^{14}C$	-95.8 ± 3.5 ‰
$\Delta^{14}C$	-90.5 ± 3.5 ‰
** **Per cent modern**	90.95 ± 0.35

Job No. 33322

Issued 21/06/2005 D.M. Chambers

* Reported age is the conventional radiocarbon age before present (BP)

** Per cent modern means absolute per cent modern relative to the NBS oxalic acid standard, (HOxI) corrected for decay since 1950.

Age, $\Delta^{14}C$, $\delta^{14}C$ and absolute per cent modern are as defined by Stuiver and Polach, Radiocarbon 19:355-363 (1977)

The reported errors comprise statistical errors in sample and standard determinations, combined in quadrature with a system error component that is based on the analysis of an ongoing series of measurements on oxalic acid secondary standard. For the present result the system error component is conservatively estimated as 0.18% (= ± 14 radiocarbon years).

Environment Group, Institute of Geological and Nuclear Sciences Ltd., PO Box 31-312, Lower Hutt, New Zealand
Fax +64 4 570 4657 Phone +64 4 570 4671

Institute Form NSR-303 Rev 13 May 2005

RAFTER RADIOCARBON LABORATORY R28904/1

INSTITUTE OF GEOLOGICAL AND NUCLEAR SCIENCES LTD.
PO Box 31312, Lower Hutt, New Zealand
Phone (+64 4) 570 4671, Fax (+64 4) 570 4657

RADIOCARBON CALIBRATION REPORT

NZA 22386 CONVENTIONAL RADIOCARBON AGE 708 ± 30 years BP

Atmospheric data from Reimer et al (2004);

PJ Reimer, MGL Baillie, E Bard, A Bayliss, JW Beck, C Bertrand, PG Blackwell, CE Buck, G Burr, KB Cutler, PE Damon, RL Edwards, RG Fairbanks, M Friedrich, TP Guilderson, KA Hughen, B Kromer, FG McCormac, S Manning, C Bronk Ramsey, RW Reimer, S Remmele, JR Southon, M Stuiver, S Talamo, FW Taylor, J van der Plicht, and CE Weyhenmeyer (2004), Radiocarbon 46:1029-1058

CALIBRATED AGE in terms of confidence intervals (Smoothing parameter: 1, Offset: 0)

2 sigma interval is 1264 AD to 1300 AD	686 BP to 650 BP (80.0% of area)
plus 1370 AD to 1380 AD	580 BP to 570 BP (6.6% of area)
1 sigma interval is 1274 AD to 1290 AD	676 BP to 660 BP (53.6% of area)

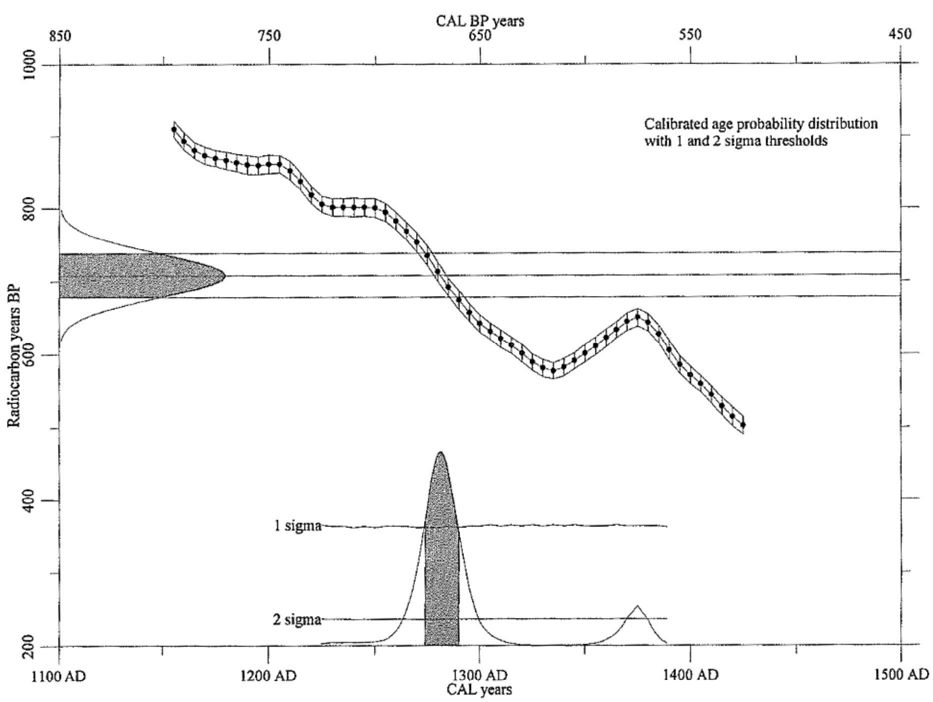

RAFTER
GNS SCIENCE

Accelerator Mass Spectrometry Result

Sample	**R 28904/2**
Description	Organic palaesol
Submitter ID	RT-E
Submitter	Vasiliki (Vasso) Mouslopoulou
	GNS McKay

Laboratory Code	**NZA 22387**
Date measured	15-Jun-05
$\delta^{13}C$	-27.3 ‰
* **Radiocarbon Age**	-1114 ± 30 BP
$\delta^{14}C$	135.9 ± 4 ‰
$\Delta^{14}C$	141.2 ± 4 ‰
** **Per cent modern**	114.12 ± 0.4

Job No. 33323

Issued 12/06/2006

This result for the sample submitted is for the exclusive use of the submitter. All liability whatsoever to any third party is excluded.

* Reported age is the conventional radiocarbon age before present (BP)

** Per cent modern means absolute per cent modern relative to the NBS oxalic acid standard, (HOxI) corrected for decay since 1950.

Age, $\Delta^{14}C$, $\delta^{14}C$ and absolute per cent modern are as defined by Stuiver and Polach, Radiocarbon 19:355-363 (1977)

The reported errors comprise statistical errors in sample and standard determinations, combined in quadrature with a system error component that is based on the analysis of an ongoing series of measurements on oxalic acid secondary standard. For the present result the system error component is conservatively estimated as 0.18% (= ± 14 radiocarbon years).

National Isotope Centre, Institute of Geological and Nuclear Sciences Ltd (GNS Science)
PO Box 31-312 Lower Hutt, New Zealand Fax +64 4 570 4657 Phone +64 4 570 4644
www.RafterRadiocarbon.co.nz

RAFTER
GNS SCIENCE

Accelerator Mass Spectrometry Result

Sample	**R 28744/6**
Description	Peat
Submitter ID	M-28 (Moana 28)
Submitter	Vasiliki (Vasso) Mouslopoulou GNS McKay

Laboratory Code	**NZA 21346**
Date measured	14-Dec-04
$\delta^{13}C$	-29.4 ‰
* **Radiocarbon Age**	6803 ± 35 BP
$\delta^{14}C$	-577.9 ± 1.8 ‰
$\Delta^{14}C$	-574 ± 1.8 ‰
** **Per cent modern**	42.6 ± 0.18

Job No. 31761

Issued 12/06/2006

This result for the sample submitted is for the exclusive use of the submitter. All liability whatsoever to any third party is excluded.

* Reported age is the conventional radiocarbon age before present (BP)

** Per cent modern means absolute per cent modern relative to the NBS oxalic acid standard, (HOxI) corrected for decay since 1950.

Age, $\Delta^{14}C$, $\delta^{14}C$ and absolute per cent modern are as defined by Stuiver and Polach, Radiocarbon 19:355-363 (1977)

The reported errors comprise statistical errors in sample and standard determinations, combined in quadrature with a system error component that is based on the analysis of an ongoing series of measurements on oxalic acid secondary standard. For the present result the system error component is conservatively estimated as 0.18% (= ± 14 radiocarbon years).

National Isotope Centre, Institute of Geological and Nuclear Sciences Ltd (GNS Science)
PO Box 31-312 Lower Hutt, New Zealand Fax +64 4 570 4657 Phone +64 4 570 4644
www.RafterRadiocarbon.co.nz

RAFTER RADIOCARBON LABORATORY R28744/6

INSTITUTE OF GEOLOGICAL AND NUCLEAR SCIENCES LTD.
PO Box 31312, Lower Hutt, New Zealand
Phone (+64 4) 570 4671, Fax (+64 4) 570 4657

RADIOCARBON CALIBRATION REPORT

NZA 21346 CONVENTIONAL RADIOCARBON AGE 6803 ± 35 years BP

Southern Hemisphere Atmospheric data from McCormac et al (2004);
FG McCormac, AG Hogg, PG Blackwell, CE Buck, TFG Higham, and PJ Reimer (2004)
Radiocarbon 46, 1087-1092

CALIBRATED AGE in terms of confidence intervals (Smoothing parameter: 1, Offset: 0)

2 sigma interval is 5722 BC to 5614 BC	7671 BP to 7563 BP (92.1% of area)
plus 5582 BC to 5569 BC	7531 BP to 7518 BP (2.7% of area)
1 sigma interval is 5698 BC to 5689 BC	7647 BP to 7638 BP (7.1% of area)
plus 5672 BC to 5625 BC	7621 BP to 7574 BP (54.6% of area)

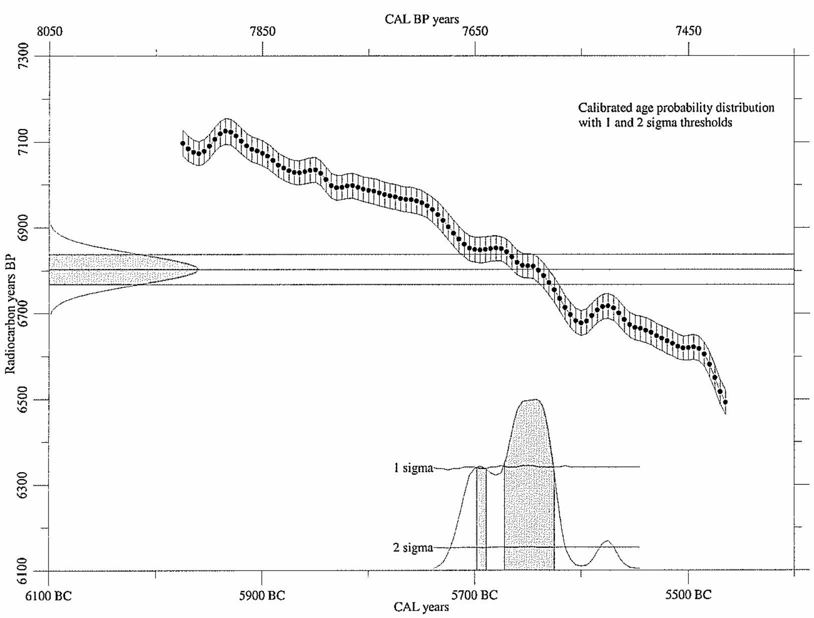

The University of Waikato

Radiocarbon Dating Laboratory

Private Bag 3105
Hamilton,
New Zealand.
Fax +64 7 838 4192
Ph +64 7 838 4278
email c14@waikato.ac.nz
Head: Dr Alan Hogg

Report on Radiocarbon Age Determination for Wk- 14589

Submitter	D Chambers
Submitter's Code	R28527/2 THa
Site & Location	, New Zealand
Sample Material	Peat
Physical Pretreatment	Visible contaminants removed.
Chemical Pretreatment	Acid washed using 10% conc. HCl, rinsed. Washed in hot 1% NaOH, then acid washed in 10% conc. HCL, rinsed and dried. The base insoluble fraction was selected for dating.

$d^{14}C$	-283.7 ± 3.7	‰
$\delta^{13}C$	-28.2 ± 0.2	‰
$D^{14}C$	-279.0 ± 3.7	‰
% Modern	72.1 ± 0.4	%
Result	**2628 ± 41 BP**	

Comments

AG Hogg
9/6/04

- Result is *Conventional Age or % Modern* as per Stuiver and Polach, 1977, Radiocarbon 19, 355-363. This is based on the Libby half-life of 5568 yr with correction for isotopic fractionation applied. This age is normally quoted in publications and must include the appropriate error term and Wk number.
- Quoted errors are 1 standard deviation due to counting statistics multiplied by an experimentally determined Laboratory Error Multiplier of 1 .
- The isotopic fractionation, $\delta^{13}C$, is expressed as ‰ wrt PDB.
- Results are reported as *% Modern* when the conventional age is younger than 200 yr BP.

RAFTER RADIOCARBON LABORATORY R28527/2

INSTITUTE OF GEOLOGICAL AND NUCLEAR SCIENCES LTD.
PO Box 31312, Lower Hutt, New Zealand
Phone (+64 4) 570 4671, Fax (+64 4) 570 4657

RADIOCARBON CALIBRATION REPORT

WK 14589 CONVENTIONAL RADIOCARBON AGE 2628 ± 41 years BP

INTCAL98_14C
1998 Atmospheric delta 14C and radiocarbon ages from:
Stuiver, M., Reimer, P.J., Bard,E., Beck, J.W., Burr, G.S.,
Hughen, K.A., Kromer, B., McCormac, F.G., v.d. Plicht, J., and
Spurk,M. 1998, Radiocarbon 40(3):1041-1083

CALIBRATED AGE in terms of cofidence intervals (Smoothing parameter: 1, Offset: 0)

2 sigma interval is 834 BC to 773 BC	2783 BP to 2722 BP (84.6% of area)
1 sigma interval is 819 BC to 794 BC	2768 BP to 2743 BP (54.6% of area)

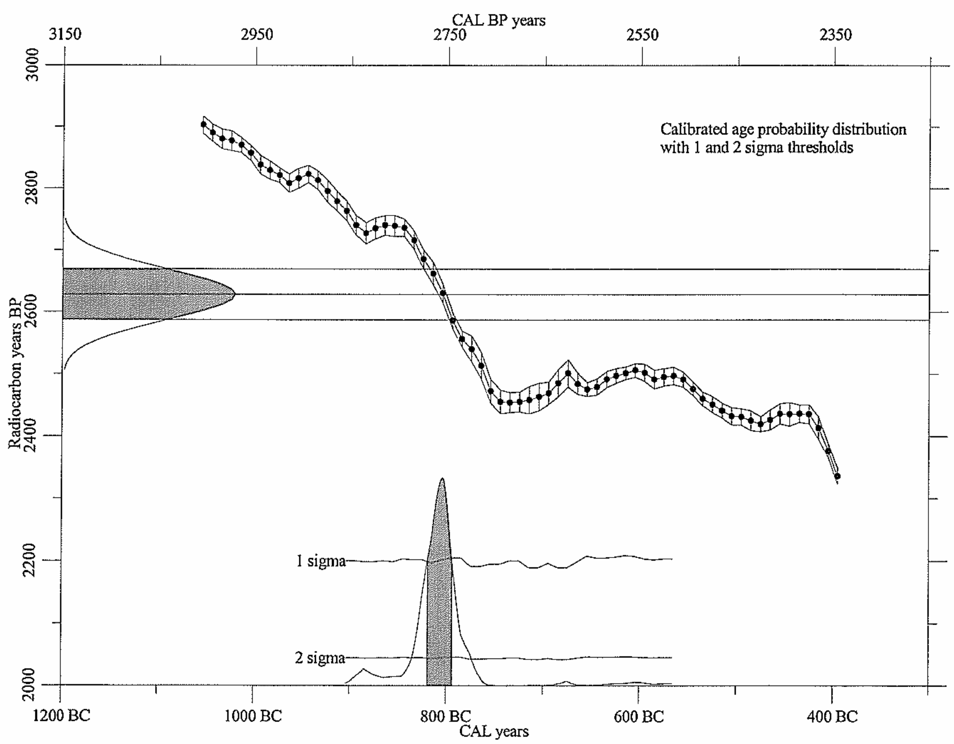

Institute of
Geological &
Nuclear Sciences
Limited

Rafter Radiocarbon Laboratory

Accelerator Mass Spectrometry Result

Sample	**R 28904/4**
Description	Paleosol with charcoal
Sample ID	RT-F
Submitter	Vasiliki (Vasso) Mouslopoulou
	GNS McKay

Laboratory Code	**NZA 22530**
Date measured	29-Jun-05
$\delta^{13}C$	-27.1 ‰
* **Radiocarbon Age**	535 ± 35 BP
$\delta^{14}C$	-74.7 ± 3.8 ‰
$\Delta^{14}C$	-70.7 ± 3.8 ‰
** **Per cent modern**	92.93 ± 0.38

Job No. 33325

Issued 7/07/2005 D.M. Chambers

* Reported age is the conventional radiocarbon age before present (BP)

** Per cent modern means absolute per cent modern relative to the NBS oxalic acid standard, (HOxI) corrected for decay since 1950.

Age, $\Delta^{14}C$, $\delta^{14}C$ and absolute per cent modern are as defined by Stuiver and Polach, Radiocarbon 19:355-363 (1977)

The reported errors comprise statistical errors in sample and standard determinations, combined in quadrature with a system error component that is based on the analysis of an ongoing series of measurements on oxalic acid secondary standard. For the present result the system error component is conservatively estimated as 0.18% (= ± 14 radiocarbon years).

Environment Group, Institute of Geological and Nuclear Sciences Ltd., PO Box 31-312, Lower Hutt, New Zealand
Fax +64 4 570 4657 Phone +64 4 570 4671

Institute Form NSR-303 Rev 13 May 2005

RAFTER RADIOCARBON LABORATORY

R28904/4

INSTITUTE OF GEOLOGICAL AND NUCLEAR SCIENCES LTD.
PO Box 31312, Lower Hutt, New Zealand
Phone (+64 4) 570 4671, Fax (+64 4) 570 4657

RADIOCARBON CALIBRATION REPORT

NZA 22530 CONVENTIONAL RADIOCARBON AGE 535 ± 35 years BP

Southern Hemisphere Atmospheric data from McCormac et al (2004);
FG McCormac, AG Hogg, PG Blackwell, CE Buck, TFG Higham, and PJ Reimer (2004)
Radiocarbon 46, 1087-1092

CALIBRATED AGE in terms of confidence intervals (Smoothing parameter: 1, Offset: 0)

2 sigma interval is 1399 AD to 1454 AD	551 BP to 496 BP (96.2% of area)
1 sigma interval is 1412 AD to 1444 AD	538 BP to 506 BP (74.1% of area)

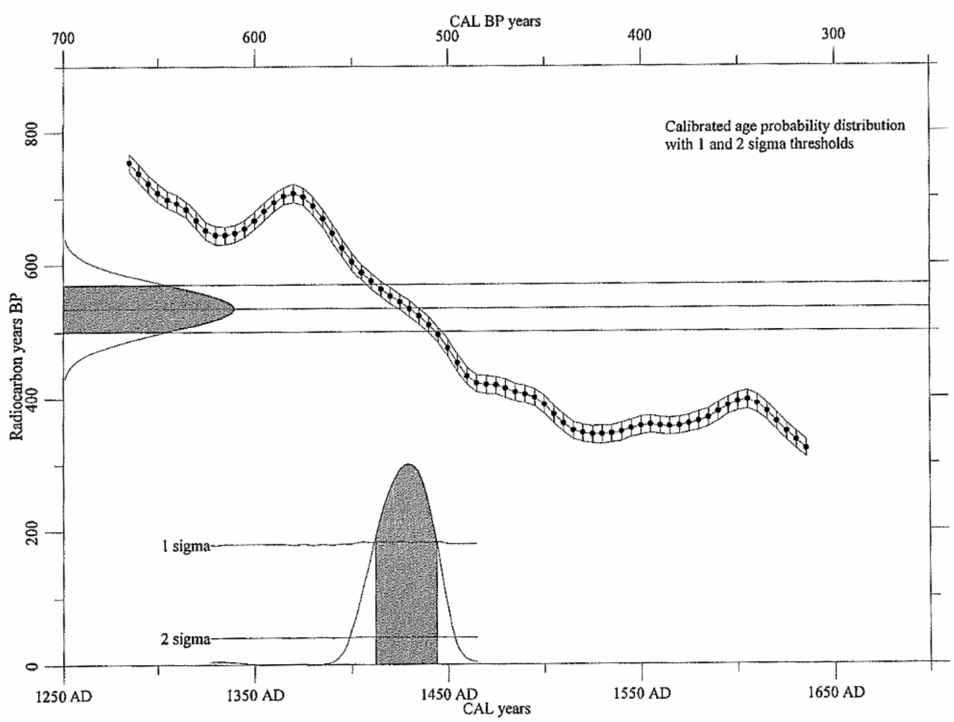

Institute of
Geological &
Nuclear Sciences
Limited

Rafter Radiocarbon Laboratory

Accelerator Mass Spectrometry Result

Sample	**R 28904/5**
Description	Wood
Sample ID	RT-G
Submitter	Vasiliki (Vasso) Mouslopoulou GNS McKay

Laboratory Code	**NZA 22388**
Date measured	15-Jun-05
$\delta^{13}C$	-23.5 ‰
* **Radiocarbon Age**	402 ± 30 BP
$\delta^{14}C$	-52.1 ± 3.6 ‰
$\Delta^{14}C$	-55.1 ± 3.5 ‰
** **Per cent modern**	94.49 ± 0.35

Job No. 33326

Issued 21/06/2005 D.M. Chambers

* Reported age is the conventional radiocarbon age before present (BP)

** Per cent modern means absolute per cent modern relative to the NBS oxalic acid standard, (HOxI) corrected for decay since 1950.

Age, $\Delta^{14}C$, $\delta^{14}C$ and absolute per cent modern are as defined by Stuiver and Polach, Radiocarbon 19:355-363 (1977)

The reported errors comprise statistical errors in sample and standard determinations, combined in quadrature with a system error component that is based on the analysis of an ongoing series of measurements on oxalic acid secondary standard. For the present result the system error component is conservatively estimated as 0.18% (= ± 14 radiocarbon years).

Environment Group, Institute of Geological and Nuclear Sciences Ltd., PO Box 31-312, Lower Hutt, New Zealand
Fax +64 4 570 4657 Phone +64 4 570 4671

Institute Form NSR-303 Rev 13 May 2005

RAFTER RADIOCARBON LABORATORY

R28904/3

INSTITUTE OF GEOLOGICAL AND NUCLEAR SCIENCES LTD.
PO Box 31312, Lower Hutt, New Zealand
Phone (+64 4) 570 4671, Fax (+64 4) 570 4657

RADIOCARBON CALIBRATION REPORT

NZA 22388 CONVENTIONAL RADIOCARBON AGE 402 ± 30 years BP

Atmospheric data from Reimer et al (2004);

PJ Reimer, MGL Baillie, E Bard, A Bayliss, JW Beck, C Bertrand, PG Blackwell, CE Buck, G Burr, KB Cutler, PE Damon, RL Edwards, RG Fairbanks, M Friedrich, TP Guilderson, KA Hughen, B Kromer, FG McCormac, S Manning, C Bronk Ramsey, RW Reimer, S Remmele, JR Southon, M Stuiver, S Talamo, FW Taylor, J van der Plicht, and CE Weyhenmeyer (2004), Radiocarbon 46:1029-1058

CALIBRATED AGE in terms of confidence intervals (Smoothing parameter: 1, Offset: 0)

2 sigma interval is 1438 AD to 1518 AD	512 BP to 432 BP (77.5% of area)
plus 1595 AD to 1620 AD	355 BP to 330 BP (13.0% of area)
1 sigma interval is 1446 AD to 1482 AD	504 BP to 468 BP (52.2% of area)

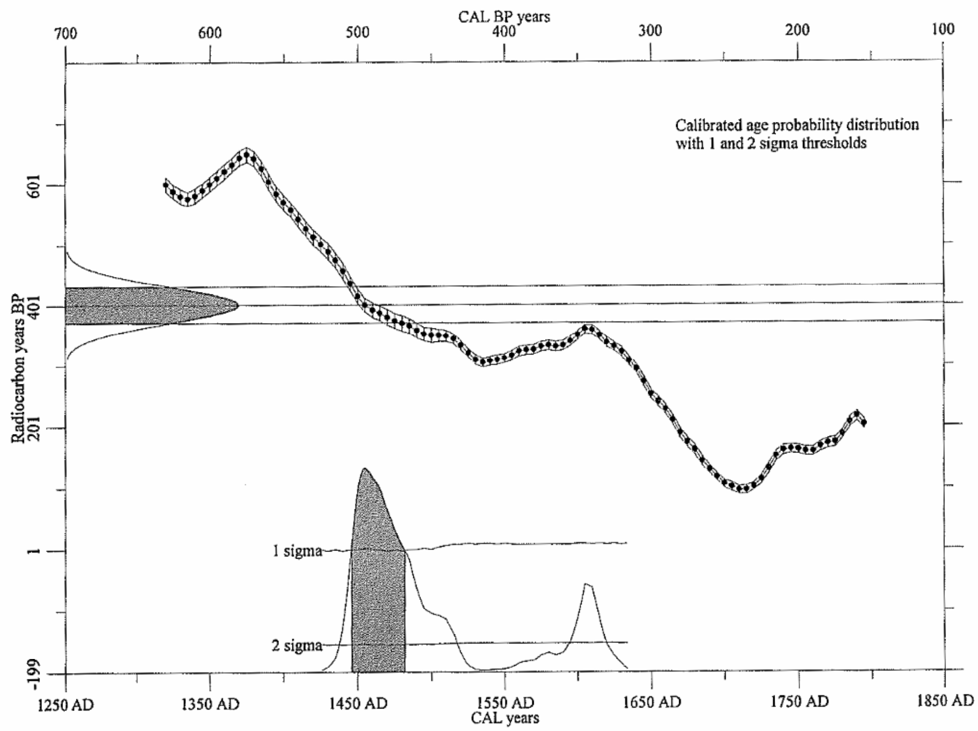

Institute of
Geological &
Nuclear Sciences
Limited

Rafter Radiocarbon Laboratory

Accelerator Mass Spectrometry Result

Sample	**R 28904/3**
Description	Organic palaesol
Sample ID	RT-H
Submitter	Vasiliki (Vasso) Mouslopoulou GNS McKay

Laboratory Code	**NZA 22455**
Date measured	22-Jun-05
$\delta^{13}C$	-33.1 ‰
* **Radiocarbon Age**	4258 ± 35 BP
$\delta^{14}C$	-425 ± 2.6 ‰
$\Delta^{14}C$	-415.3 ± 2.6 ‰
** **Per cent modern**	58.47 ± 0.26

Job No. 33324

Issued 7/07/2005 D.M. Chambers

* Reported age is the conventional radiocarbon age before present (BP)

** Per cent modern means absolute per cent modern relative to the NBS oxalic acid standard, (HOxI) corrected for decay since 1950.

Age, $\Delta^{14}C$, $\delta^{14}C$ and absolute per cent modern are as defined by Stuiver and Polach, Radiocarbon 19:355-363 (1977)

The reported errors comprise statistical errors in sample and standard determinations, combined in quadrature with a system error component that is based on the analysis of an ongoing series of measurements on oxalic acid secondary standard. For the present result the system error component is conservatively estimated as 0.18% (= ± 14 radiocarbon years).

Environment Group, Institute of Geological and Nuclear Sciences Ltd., PO Box 31-312, Lower Hutt, New Zealand
Fax +64 4 570 4657 Phone +64 4 570 4671

Institute Form NSR-303 Rev 13 May 2005

R28904/3

RAFTER RADIOCARBON LABORATORY

INSTITUTE OF GEOLOGICAL AND NUCLEAR SCIENCES LTD.
PO Box 31312, Lower Hutt, New Zealand
Phone (+64 4) 570 4671, Fax (+64 4) 570 4657

RADIOCARBON CALIBRATION REPORT

NZA 22455 CONVENTIONAL RADIOCARBON AGE 4258 ± 35 years BP

Southern Hemisphere Atmospheric data from McCormac et al (2004);
FG McCormac, AG Hogg, PG Blackwell, CE Buck, TFG Higham, and PJ Reimer (2004)
Radiocarbon 46, 1087-1092

CALIBRATED AGE in terms of confidence intervals (Smoothing parameter: 1, Offset: 0)

2 sigma interval is 2900 BC to 2634 BC	4849 BP to 4583 BP (95.8% of area)
1 sigma interval is 2886 BC to 2858 BC	4835 BP to 4807 BP (17.7% of area)
plus 2807 BC to 2752 BC	4756 BP to 4701 BP (34.3% of area)
plus 2719 BC to 2702 BC	4668 BP to 4651 BP (8.8% of area)